UNIVERSITEIT VAN PRETORIA
UNIVERSITY OF PRETORIA
YUNIBESITHI YA PRETORIA

Synthesis, electronic structure and reactivity of rhodium(I) and iridium(I) bis(imino)acenaphthene complexes.

By

Wynand Johannes Louw

Student Number: u04393805

Supervisor: Daniela I. Bezuidenhout

Co-supervisor: Shankara G. Radhakrishnan

Submitted in fulfilment of the requirements for the degree

Doctor of Philosophy in Chemistry

in the Faculty of Natural and Agricultural Sciences

University of Pretoria

2022

Date Submitted: 28 November 2022

© University of Pretoria

Declaration of Originality

I, Wynand Johannes Louw (u04393805), hereby declare that the following these, which I submit in fulfilment of the requirements of the degree Doctor of Philosophy in Chemistry at the University of Pretoria, is my own original work and has not been previously submitted by me for a degree at this or any other tertiary institution. Secondary materials, where used, have been carefully acknowledged and referenced in accordance with the University requirements. I am aware of the University's policies and implications regarding plagiarism.

Contributing researchers are hereby accredited:

The crystal structure data collection as well as structure refinements were performed by Dr Frederick Malan, University of Pretoria. Collection of mass spectrometric data was performed by Dr Madelien Wooding, University of Pretoria. Computational modelling was performed utilising the computational resources of the Centre for High Performance Computing (CHPC Cape Town, South Africa, http://www.chpc.ac.za) with the assistance of Dr Shankara Radhakrishnan (University of Pretoria), Dr Krishna K. Govender (University of Johannesburg), and Mr Shane de Beer (Stellenbosch University).

Thank you to the University of Pretoria, as well as Sasol Technology R&D Pty. Ltd. for their financial support of this project. A special note of thanks to the South African National Research Foundation (NRF) for their support of this research via the CSUR funding element, UID: 116317, as well as the Renewable and Sustainable Energy Masters and Doctoral Scholarship.

Outcomes from this PhD thesis have been published in:

Synthesis, electronic structure and interaction of rhodium(I) and iridium(I) bisimine-acenaphthalene complexes with CO_2. Louw, W. J., Radhakrishnan, S. G., Malan, F. P., & Bezuidenhout, D. I. (2023). *Polyhedron*, *235*, 116350. https://doi.org/10.1016/j.poly.2023.116350

SIGNATURE:  DATE: 22 / 06 / 23

© University of Pretoria

Acknowledgments

When you start your postgraduate studies, few people tell you about the journey that you are embarking on – what the adventure ahead may entail or in fact, what it may demand of you. As I had expected, in many regards, my postgraduate voyage has been fraught with intellectual challenges enroute to mastering my chosen crafts. However, I could not have foreseen the number of interpersonal and professional skills that I would need to master in a short amount of time to navigate the research environment. Although the disillusionments were startling, I found comfort and renewed purpose in encouraging my fellow students with what I had learnt, sharing the wisdom I desired someone had taught me sooner. I could not have achieved this hard-fought victory of completing a PhD degree without the care, support, encouragement, and wisdom of so many along the way.

During the hardest of times, God gave my parents and I a promise that I would study at His hand, that He will ensure that I will be able to learn. Through many a miracle of provision, protection, and inspiration, I have made it this far, in the grace of God.

From a very young age, my parents have fostered my curiosity and love for reading. Whenever I asked them questions about how or why things worked the way they do, they guided me to a book where I could find an answer and said: “I am not sure. But when you find the answer in here, come and tell me too!”. Thank you, *Mom* and *Dad*! You have made me into the scientist, the man, that I am today.

When things went awry, and we all know that they inevitable do in scientific research (as in life), I always had my go-to person who I could lean on. Together against the world! *Leonie*, my amazing sister, I love you, and I appreciate you driving me around even though I “stank of lab chemicals” tremendously!

Through all my successes and failures, I have made wonderful friends on campus who have carried me through so much of the daily turmoil. *Clarissa*, *Shane*, *Jessie*, *Mike*, *Quinn*, *Kyle*, *Paul*, *Simphewe*: thank you all for making this possible; for your advice, encouragement, and all of the COFFEE! And a special thank you to my mentor, *Dr Ruric Vogel* – you helped me become a better lecturer, friend, and man.

I would not have life work out any differently, because it has all lead to meeting my best friend and partner: my sound board, my encourager, my helper and comforter, my joker when things get too much… *Sergio*, thank you for all the hours that you spent alongside me in the lab! Your continued inspiration, picking me up when I was at my lowest, holding me close to earth when I thought I could float away. I love you!

Lastly, but by no means the least – my incredible supervisor *Prof Daniela Bezuidenhout*: you have taught me to master not only chemistry, but how navigate professional situations that often felt like minefields. Thank you for your unconditional support, for always rising to the challenge. I am infinitely grateful! *Dr Shankara Radhakrishnan*, thank you for your co-supervision, assistance with the computational and electrochemistry work, and your inspired ideas on the CO_2 reactivity work. I think the three of us have made something great together! *Dr Frederick Malan*, thank you for your friendship and all the hard work you have put into the SC-XRD for this thesis. *Dr Madelien Wooding*, thank you for all the MS samples that you ran over the years. And, thank you to the South African NRF and the University of Pretoria, as well as Sasol Technology R&D Pty. Ltd. for their financial support of this project.

© University of Pretoria

Table of Contents

Declaration of Originality i
Acknowledgments ii
Table of Contents iii
Summary vi
List of Complexes viii
List of Abbreviations x

Chapter 1: Background and Research Objectives 1
1.1) Project Background on BIANs 1
1.1.1) What are Bis(aryl-imino)acenaphthenes? 1
1.1.2) Coordination complexes of Bis(aryl-imino)acenaphthenes 2
1.1.3) Characterisation of Redox Non-innocence in BIAN Compounds 4
1.2) Research Rationale and Motivation 7
1.3) Research Objectives 8
1.4) References 10

Chapter 2: Rhodium(I) and Iridium(I) BIAN Complexes: Synthesis and Characterisation 24
2.1) Introduction 24
2.1.1) Characteristics and preparation of bis(aryl-imino)acenaphthene compounds 24
2.1.2) Coordination complexes of bis(aryl-imino)acenaphthene 26
2.2) Synthesis Methodologies, Observations, and Characterisation 28
2.2.1) Dipp- and MesBIAN Ligands 28
2.2.2) Rh(I) and Ir(I) BIAN complexes with ancillary 1,5-cyclooctadiene ligand: **1a**–**d** 30
2.2.3) Rh(I) and Ir(I) BIAN complexes with ancillary dicarbonyl ligands: **2a**–**d** 32
2.2.4) Rh(I) and Ir(I) BIAN complexes with ancillary triethylphosphine and monocarbonyl ligands: **3a**–**b** 34
2.2.5) Rh(I) and Ir(I) BIAN complexes with ancillary 1,5-cyclooctadiene and chlorido ligands: **4a**–**d** 37
2.3) Single crystal XRD 40
2.3.1) **1b** [RhMB(cod)]PF_6 41
2.3.2) **1d** [IrMB(cod)]PF_6 42
2.3.3) **2a** [RhDB$(CO)_2$]PF_6 42
2.3.4) **2b** [RhMB$(CO)_2$]PF_6 44
2.3.5) **2c** [IrDB$(CO)_2$]PF_6 44
2.3.6) **3a** [RhDB(CO)(PEt_3)]PF_6 45
2.3.7) **4c** [IrDB(cod)Cl] 46
2.4) Conclusions 48
2.5) Experimental Details 50

© University of Pretoria

2.5.1) Materials 50
2.5.2) Instrumentation 50
2.5.3) Synthesis Methods and Compound Characterisation 51
2.6) References 60

Chapter 3: Electrochemical Behaviour and Molecular Orbital Calculations 74
3.1) Introduction 74
3.2) Methods and Materials 76
3.2.1) Voltammetry 76
3.2.2) Molecular Modelling 76
3.3) Results and Discussion 78
3.3.1) Electrochemical Behaviour and Molecular Orbital Calculations 78
3.3.2) Analysis Methodology and Rationale 80
3.3.3) Comparative Discussion 95
3.4) Conclusions 100
3.5) References 101

Chapter 4: Linear Free Energy Relationships 106
4.1) Introduction 106
4.2) Methodology and Rationale 107
4.2.1) Molecular Modelling Methodology 107
4.2.2) Analysis and Nomenclature Conventions 108
4.2.3) Thermodynamic Half-Reaction Cycles 110
4.3) Results and Discussion 112
4.3.1) Outlier Analyses and the Peak Characterisation Model 112
4.3.2) HOMO / LUMO vs E_{DPV} 114
4.3.3) –EA vs E_{DPV} 117
4.3.4) $-\Delta G_{rxn}$ vs E_{DPV} 120
4.3.5) E_{cell} vs E_{DPV} 124
4.4) Conclusions 126
4.4.1) Peak Characterisation Model and Revised E_{DPV} Assignments 127
4.5) References 129

Chapter 5: Catalytic Activity Screening 134
5.1) Introduction 134
5.1.1) Metal Complexes of BIANs as Catalysts 134
5.1.2) General Catalytic Applications of Rhodium and Iridium Complexes 136
5.1.3) NMR-scale Catalytic Reactivity Screening Assays of Complex Series **1**–**4** 140
5.1.4) Screening Catalytic Activity for Electroreduction of CO_2 by Complex Series **1**–**4** 142
5.2) Methods and Materials 145
5.2.1) General aspects 145
5.2.2) Catalytic Reactivity Samples 145

© University of Pretoria

5.3) Results and Discussion 148
5.3.1) NMR based Catalytic Reactivity Investigation 148
5.3.2) Reductant Activation of Catalytic Reactivity 157
5.3.3) CO_2 Electrochemical Reduction and Interactions 162
5.4) Conclusion 174
5.5) References 178

Chapter 6: Conclusions and Research Outlook 186
6.1) Conclusions 186
6.1.1) Critical Comparison and Evaluation 186
6.1.2) Systematic Electrochemical Characterisation 187
6.1.3) Computational Analysis of Electronic Structure 188
6.1.4) Peak Characterisation Model and Revised E_{DPV} Assignments 188
6.1.5) Catalytic Reactivity Screening and Redox Activation 189
6.1.6) Electrocatalytic CO_2 Reduction Ability Screening 191
6.1.7) Non-innocent Behaviour of BIANs 191
6.2) Notes on Prospective Research 192
6.3) References 195

© University of Pretoria

Summary

Among α-diimine ligands, the group of bis(aryl-imino)acenaphthenes (BIANs) are unique due to the relatively inflexibility of the N=C–C=N bisimine moiety, their ability to act as a reservoir for electron density, as well as the redox non-innocent behaviour that they have exhibited in coordination complexes. These factors have led to an upsurge in studies on the physiochemical properties and catalytic applications of BIAN complexes, featuring primarily 3*d*- and coinage metals.

Rhodium(I) and iridium(I) catalysts are known to be tolerant of various functional groups and have been shown to be active in hydroelementation and copolymerisation reactions of alkenes and alkynes. Even though BIAN ligands have been employed as ligands in catalysts since the 1990's, limited literature data is available for BIAN complexes of rhodium and iridium in oxidation state +1 specifically.

In this study, a range of new Rh(I)- and Ir(I)-BIAN complexes of 4- and 5-coordinate geometries were synthesised utilising archetypal BIAN ligands (i.e., Dipp- and MesBIAN) and ancillary ligands from across the spectrochemical series (low, mid and high field). The series of complexes are divided into four groups based on the ancillary ligands that were targeted in this study: (**1**) 1,5-cyclooctadiene (cod), (**2**) dicarbonyl, (**3**) triethylphosphine and carbonyl, as well as (**4**) cod and chloride. Using a multi-technique approach (NMR, IR, UV-Vis, SC-XRD, electrochemistry, and DFT computations), the electronic structure and catalytic reactivity of the series of BIAN complexes **1**–**4**, featuring ancillary ligands with various electron donating and withdrawing characteristics, were critically examined.

The crystal structures of the square planar complexes **1b** [Rh(MesBIAN)(cod)]PF_6, **1d** [Ir(MesBIAN)(cod)]PF_6, **2a** [Rh(DippBIAN)$(CO)_2$]PF_6, **2b** [Rh(MesBIAN)$(CO)_2$]PF_6, **2c** [Ir(DippBIAN)$(CO)_2$]PF_6 and **3a** [Rh(DippBIAN)(CO)(PEt_3)]PF_6 are reported herein, as well as the square pyramidal structure of **4c** [Ir(DippBIAN)(cod)Cl]. The electrochemical study performed in the non-coordinating solvent CH_2Cl_2 revealed that all complexes featured at least one reversible, ligand-centred reduction event at less negative potentials (above –1.0 V vs Ag/Ag^+) compared to the free ligands.

Contrasting results between the bisimine moiety C–N and C–C bond lengths within the structures of **2a** and **4c**, and all other data from our multi-technique analyses, illustrate the non-innocent behaviour of the DippBIAN accepting additional electron density from the metal centre due to push-pull interactions between the ancillary and BIAN ligands.

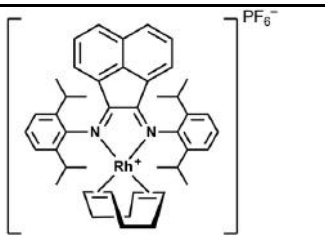
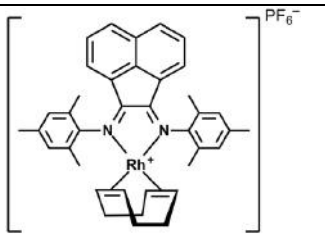
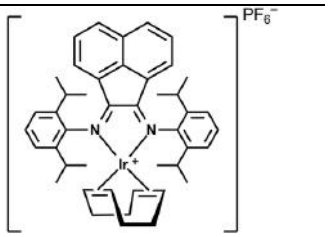
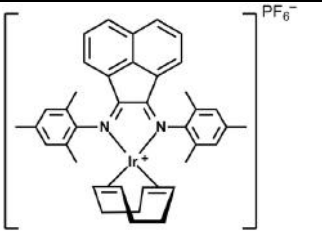
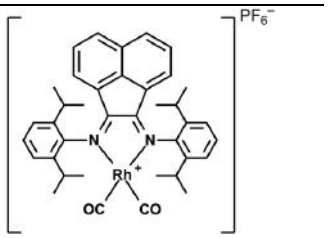
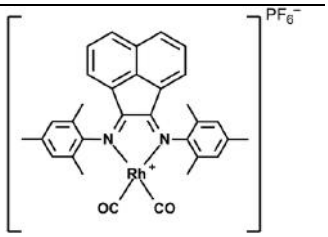
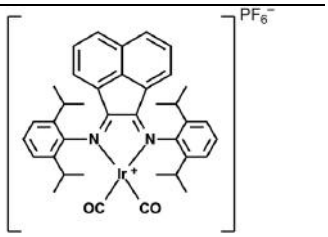
© University of Pretoria

The statistically-based Peak Characterisation Model (PCM) was developed from Linear Free Energy Relationships (LFERs) between experimentally recorded DPV peak potentials, and various calculated theoretical properties of each reported compound. The PCM aided differentiation between voltametric peaks associated with the primary electrochemical reaction of the analyte and voltammetry peaks of impurities or secondary reactions in the electrolyte solution.

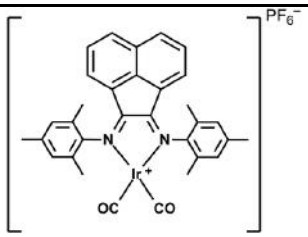
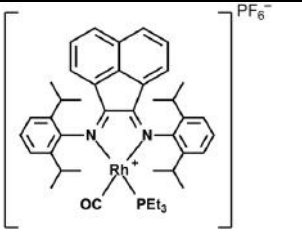
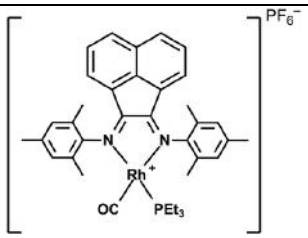
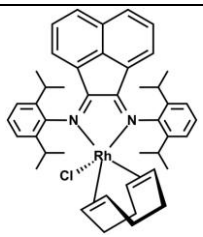
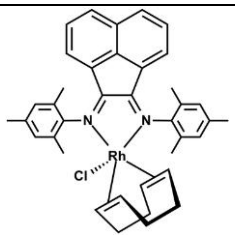
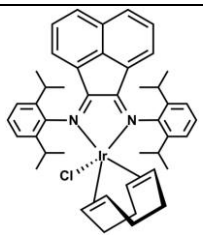
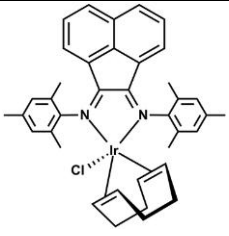
In our preliminary electrocatalytic CO_2 reduction study, complex **3a** showed a promising interaction with CO_2 under aprotic conditions. The catalytic reactivity of the series of complexes **1**–**4** was preliminarily screened in NMR-scale tests, both in the absence and presence of a reductant, towards several reactions: dimerization, hydroamination (with t-butylamine), and hydrothiolation (with t-butylthiol) of 1-hexene and 1-hexyne. The most promising results in terms of both catalytic activity and regioselectivity were obtained for the alkyne hydrothiolation reaction.

© University of Pretoria

List of Complexes

Complex Number	Abbreviated Formula	Complex Structure
1a	[Rh(DB)(cod)]PF_6	
1b	[Rh(MB)(cod)]PF_6	
1c	[Ir(DB)(cod)]PF_6	
1d	[Ir(MB)(cod)]PF_6	
2a	[Rh(DB)$(CO)_2$]PF_6	
2b	[Rh(MB)$(CO)_2$]PF_6	
2c	[Ir(DB)$(CO)_2$]PF_6	

© University of Pretoria

Complex Number	Abbreviated Formula	Complex Structure
2d	$[Ir(MB)(CO)_2]PF_6$	
3a	$[Rh(DB)(CO)(PEt_3)]PF_6$	
3b	$[Rh(MB)(CO)(PEt_3)]PF_6$	
4a	[Rh(DB)(cod)(Cl)]	
4b	[Rh(MB)(cod)(Cl)]	
4c	[Ir(DB)(cod)(Cl)]	
4d	[Ir(MB)(cod)(Cl)]	

© University of Pretoria

List of Abbreviations

Å	Angstrom, measurement of interatomic bond length
Ac	Descriptive abbreviation for Acenaphthene, as used in "C_{Ac}"; used to delineate an atom that located the Acenaphthene moiety
AceNQ	Acenaphthalenequinone
Ar	Aryl, or Aromatic
a.u.	atomic units, measurement of computed electronic energy (also known as Hartrees)
av.	Average of a set of values
BIAN	Bis(aryl-imino)acenaphthene
ca.	*circa*, meaning "about" or "approximately"
CHPC	Centre for High Performance Computing (Cape Town, South Africa)
cod	1,5-cyclooctadiene
Cp	1,3-cyclopentadienyl
CV or CVs	Cyclic Voltammetry, or Cyclic Voltammogram(s)
DB	1,2-bis[(2,6-diisopropylphenyl)imino]acenaphthene
DFT	Density Functional Theory
Dipp	2,6-diisopropylphenyl
DippBIAN	1,2-bis[(2,6-diisopropylphenyl)imino]acenaphthene
$DippNH_2$	2,6-diisopropylaniline
DPV or DPVs	Differential Pulse Voltammetry, or Differential Pulse Voltammogram(s)
e	electron
EA	Electron Affinity
% ee	Enantiomeric excess percentage
EE_{ZPV}	Zero-Point Vibrational Electronic Energy
e.g.	*exempli gratia*, meaning "for example"
eq	Molar equivalents
ESI+	Electron Spray Ionisation, Positive Mode
ESI-TOFMS	Electron Spray Ionisation – Time-Of-Flight Mass Spectrometry
ESP	Electrostatic Surface Potential
eV	Electron Volts; 1 Hartree = 27.2116 eV
E_{cell}	Theoretical half-cell reaction potentials
E_{cell}^{Ox}	Oxidation Half-cell Potential

© University of Pretoria

E_{cell}^{Red}	Reduction Half-cell Potential
E_{DPV}	Peak potential of an electrochemical event observed during the DPV analysis of an analyte (V vs Ag/Ag^{+})
E_{pa}	Anodic peak potential of an electrochemical event on a cyclic voltammogram
E_{pc}	Cathodic peak potential of an electrochemical event on a cyclic voltammogram
E_{Ref}^{Ag}	Standard potential of a silver reference electrode
E°'	Formal reaction potential of an electrochemical event calculated as the midpoint value between the cathodic and anodic peak potentials (E_{pc} and E_{pa} respectively) of a fully reversible electrochemical event
$E_{½}$	The potential (half-peak potential) of an electrochemical event on a cyclic voltammogram measured at half-peak height
$FcH^{0/+1}$	Ferrocene/Ferrocenium redox couple
$[Fe(\eta\text{-}C_5Me_5)_2]^{0/+1}$	Decamethylferrocene/Decamethylferrocenium redox couple
FMO or FMOs	Frontier Molecular Orbital(s)
GCE	Glassy Carbon Electrode, 3 mm working electrode
(g)	Gaseous phase
$G_{gas}^{\circ}(x)$	Theoretical free energy for species "x" calculated in a gaseous state
HOMO or HOMOs	Highest Occupied Molecular Orbital(s)
H(S)OMO or H(S)OMOs	Highest (or Singly) Occupied Molecular Orbital(s)
H_{corr}	Thermal correction factor to enthalpy
IE	Ionisation Energy
IR	Infrared
i.e.	in explanation
LFER or LFERs	Linear Free Energy Relationship(s)
LUMO or LUMOs	Lowest Unoccupied Molecular Orbital(s)
MAD	Mean Absolute Deviation
MB	1,2-bis[(2,4,6-trimethylphenyl)imino]acenaphthene
Me	Methyl, with reference to a methyl group or substituent
Mes	2,4,6-trimethylphenyl
MesBIAN	1,2-bis[(2,4,6-trimethylphenyl)imino]acenaphthene
MO or MO(s)	Molecular Orbital(s)
MS	Mass Spectrometry or Mass Spectrometry spectra
mol%	Molar percentage: a measure of catalyst load in a chemical reaction, relating the moles of catalyst added to the moles of substrate present in the reaction mixture as a percentage value
m/z	Mass to charge ratio, Mass Spectrometric unit of measurement

© University of Pretoria

NHE	Natural Hydrogen Electrode (Theoretical Reference Electrode)
NMR	Nuclear Magnetic Resonance or Nuclear Magnetic Resonance spectra
n = *integer*	Nomenclature adopted to specify the charged state a molecule was modelled in, where the integer value of "*n*" represents the number of electrons which had been added to, or removed from, the molecule's standard charged state (n = 0)
PEt_3	Triethylphosphine
RMSD	Root Mean Standard Deviation
R^2	Coefficient of determination
S	The molecular spin state in which a molecule's charged state was modelled
SOMO or SOMOs	Singly Occupied Molecular Orbital(s)
S_{tot}	Theoretical total entropy
TBAPF6	Tetrabutylammonium hexafluorophosphate
tert	Tertiary substitution, as in *tert*-butylamine
$\mathbf{t_0}$ and $\mathbf{t_{24}}$	Time designations when measurements were taken, as in time 0 hours, and time 24 hours
UV-Vis	Ultra-Violet and Visible light Spectroscopy or Ultra-Violet and Visible light spectra
XRD / SC-XRD	X-Ray Diffraction, or Single Crystal X-Ray Diffraction Spectrometry
ZPE_{corr}	Zero-point vibrational correction energy
ΔG_{corr}	Thermal correction to free energy change
ΔG°_{gas}	Standard state free energy change of a gaseous reaction
ΔG_{Ox}	Free energy change of the oxidation half-reaction
ΔG_{Red}	Free energy change of the reduction half-reaction
ΔG_{rxn}	Theoretical free energy change of a reaction
ΔG°_{solv}	Standard state free energy change of solvation
Δθ	Change in the size of an angle
$\mu A.mm^{-2}$	Current density, expressed as microampere per millimetre surface area of the working electrode

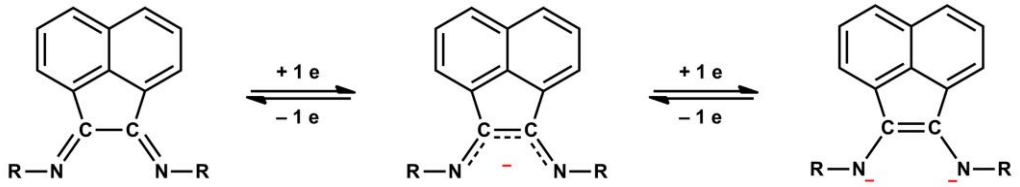
© University of Pretoria

Chapter 1: Background and Research Objectives

1.1) Project Background on BIANs

1.1.1) What are Bis(aryl-imino)acenaphthenes?

As a unique class among α-diimine ligands, research into bis(aryl-imino)acenaphthene (BIAN) compounds has enjoyed renewed interest in recent years due to the promising redox non-innocent properties that they have displayed.[1,2] The electrochemical "non-innocent" behaviour of a compound or ligand may be described as the ability of the compound/ligand to function as a reservoir for electron density during oxidation or reduction reactions.[3–6] In this context, redox non-innocent ligands (such as BIAN ligands) are able to reversibly accept and release electrons to assist in mediating reactions at the metal centre of a complex (e.g., changes in the oxidation state).[3–6] The prolific research team(s) of Fedushkin *et al*. has demonstrated the non-innocent abilities of BIAN ligands to accept and stabilise additional electron density in coordination complexes, with the ligands being reduced by up to four electrons.[7–12]



*Scheme 1.1–1: Charge delocalisation across the bisimine N=C–C=N moiety of a generic BIAN compound, with "*R*" representing an aryl-substituent. Addition of one electron forms the semiquinonate in which the radical electron is stabilised through resonance between the two imine nitrogen terminals. Addition of a subsequent electron produces the quinonate dianion, resulting in the formal change of bond orders in the bisimine moiety to a bisamide N–C=C–N moiety.*[1,7,13–17]

The α-diimine moiety in BIAN compounds is affixed to the rigid, planar framework of the acenaphthene aromatic rings, with aryl-substituents located on each of the sp^2-hybridised imine nitrogens (Scheme 1.1–1).[1,17] As with other α-diimine ligands, charge delocalisation can readily occur between the two imine nitrogen atoms of the bisimine moiety due to resonance stabilisation (Scheme 1.1–1).[1,7,13–17] The orbital conjugation within the BIAN molecules has been noted to extend into the acenaphthene rings as well, enabling this class of compounds to accommodate a total of up to four additional electrons between the bisimine moiety and acenaphthene rings.[7,9,18]

In this chapter, the class of compounds that was utilised in this study, as well as some of their physiochemical properties and salient features that are of relevance to the aims and objectives for this research study, will be succinctly discussed. A review and discussion of the literature which is

© University of Pretoria

pertinent to the research themes and objectives for each subsequent chapter (Chapter 2 to Chapter 5), will be presented in the respective introductory sections.

1.1.2) Coordination complexes of Bis(aryl-imino)acenaphthenes

Research into compounds of the α-diimine BIANs has enjoyed an upsurge in literature reports since the late 1990's and early 2010's, primarily as ligands in transition metal and main group metal complexes.[17] Compared to other α-diimine ligands, the relatively inflexible N=C–C=N bisimine moiety of BIAN ligands are already in the correct *cis*-geometry that is required for chelation to a metal, and it imparts additional stability to central C–C bond of the thusly formed five-membered metallocycles which are prone to hydrolysis and rupture in some α-diimine catalyst systems.[1,17] The initial studies on BIAN complexes were chiefly focused on their application as homogeneous catalysts, with the aim of exploiting the bulky aryl-substituents on the BIAN ligands to create a sterically hindered coordination sphere.[19–24] One of the well-studied groups of catalysts is known as Brookhart-type catalysts, Pd(II)- or Ni(II)-based α-diimine complexes recognised for their high ethylene and α-olefin polymerisation activity.[19,23,25–29]

Catalytic application of the BIAN ligands were by no means limited to nickel and palladium, however, with cationic vanadyl BIAN complexes having been shown to selectively oxidise alkenes to epoxides,[30] whereas an oxidovanadium(IV) complex of DippBIAN has been reported as an efficient alkane oxygenation catalyst in the presence of H_2O_2 under mild conditions.[31] Other catalytic reactions have also been investigated, including the successful hydrosilylation of alkenes by Fe(II) complexes of Dipp- and MesBIAN,[32] and the hydroformylation of 1-octene by a water-soluble Rh(I)-cod complex bearing a sulphonated-DippBIAN type ligand.[33]

Very few studies, such as the report on cobaloxime BIAN complexes by Williams *et al*.,[34] have correlated the influence that the redox non-innocent behaviour of BIAN ligands on the catalytic reactivity of metal complexes. The authors noted that the BIAN ligand acted as an electron sink during multi-electron reduction events, resulting in the delocalisation of unpaired electron spin density from the metal centre into the organic framework, and thus decreasing the hydrogen reduction activity of the reported BIAN complexes compared to those of previously reported cobaloxime complexes.[34] Recently, Krisch *et al*. demonstrated the redox non-innocence of BIAN ligands in their series of bischelated Ag(I)$BIAN_2$ complexes.[35] The authors reported that the BIANs participated during the electrocatalytic reduction cycle of CO_2 by accepting or donating electron density to the metal centre.[35] A few other BIAN complexes have also been reported to show potential as catalysts for the

© University of Pretoria

electrochemical reduction of CO_2, such as the octahedral Re(I)-tricarbonyl complexes of Dipp- and MesBIAN,[36–38] and the neutral Rh(III)-trichloride complex of DippBIAN.[39]

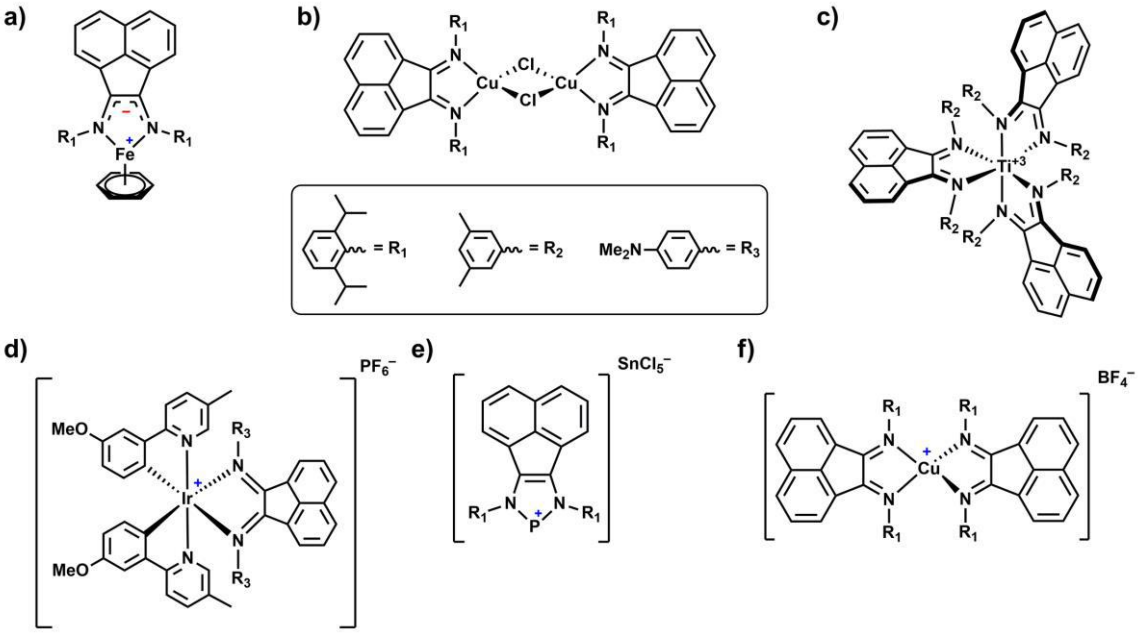


*Figure 1.1–1: Selected literature examples of mono-chelated (**a**, **b**, **d**, **e**), bis-chelated (**f**), and tris-chelated (**c**) coordination geometries for complexes of BIAN ligands. Structure have been reproduced as reported by (**a**) Larson et al.,[3] (**b**) Fliedel et al.,[40] (**c**) Clark et al.,[13] (**d**) Hasan et al.,[41] (**e**) Reeske et al.,[42] and (**f**) Li et al.[43]*

A rich variety of coordination structures are attainable with BIAN ligands as illustrated in the collage of previously reported mono- (a, b, d, e), bis- (f) and tris-chelated BIAN complexes (c, Figure 1.1–1). Although the steric bulk of the aryl-substituents on the imine nitrogens have been shown to influence the stability of the coordination sphere,[17] the aryl groups of the BIAN ligand may be readily modified or functionalised through a modular approach to the synthesis of the BIAN ligand. The structural modality thus offered by BIAN ligands is further enriched by the ease with which steric and electronic properties of the ligands may be altered, through the modifications of the aryl-substituents on the imine nitrogens.[1,44–50]

Hua *et al*. has demonstrated that the donating ability of their asymmetric bidentate N-donor ligands were affected by the steric and electronic environment of the N-donor moiety,[51] which directly influenced the catalytic activity of their Rh(I) and Ir(I) complexes. By applying the modular functionality of the α-diimine BIAN ligands in coordination complexes, the electronic environment of the coordination sphere may be modulated,[33,52] with the aim of enhancing the catalytic reactivity of the metal centre.

© University of Pretoria

The electronic character of a metal centre may be highly dependent on the electron donating/accepting character of the ancillary ligands in the complex, not only those of the BIAN ligand. For example, Romashev *et al*. and Shaffer *et al*. described the Rh(I)-centre of their diimine complexes is as nucleophilic,[52,53] whereas Rumble *et al*. described the Rh(I)-centres of their α-diimine complexes as having low electron density on the metal centre (i.e., electrophilic).[54] The source which gives rise to the contrasting descriptions for the electronic character of metal centres of these Rh(I)-diimine complexes is the electronic properties of the other ancillary ligands present in the complexes. The diimine complexes which were described as having a more nucleophilic (i.e., electron rich) metal centre featured ancillary ligands that are more electron donating in character (e.g., alkenes, bisimines, halogens); whereas the complexes with electrophilic metal centres featured electron withdrawing ancillary ligands (e.g., carbonyls).[52–54]

The ancillary ligands which have featured among previously reported transition metal BIAN complexes span across the breadth of the spectrochemical series – from strong field ligands such as CO and H_2O, to weak field donors such as Cl^- and Br^- (Figure 1.1–1.b).[36–39,41,43,47,48,53–62] Larger organic ancillary ligands such as arenes (ex. cyclopentadiene, 1,5-cyclooctadiene and phenyl; Figure 1.1–1.a) and organometallic carbenes (ex. phenylpyridine) have also been reported (Figure 1.1–1.d).[33,41,47,53,54,57,58,62–64] To the best of our efforts, systematic literature investigations regarding the effects of ancillary ligands on the electronic properties of the BIAN-metal interaction, and/or the influence of the BIAN ligand redox non-innocence on the electronic properties and reactivities of BIAN complexes, were not found.

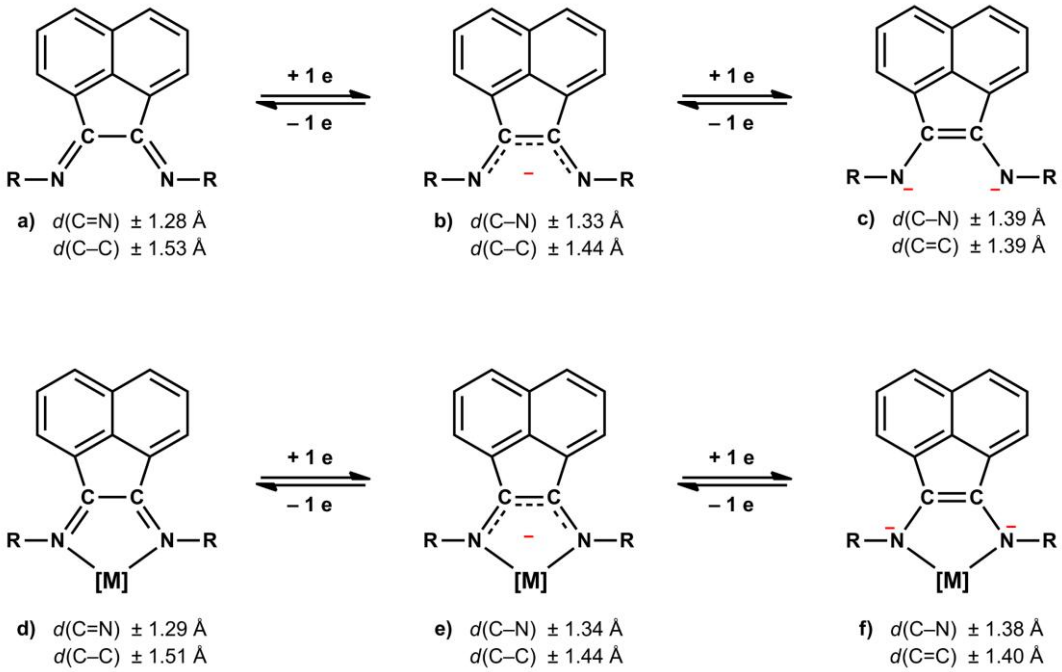
1.1.3) Characterisation of Redox Non-innocence in BIAN Compounds

Nuclear Magnetic Resonance (NMR) characterisation has become a fundamental requirement in modern synthetic reports; however, it is not a tool that has been ubiquitously applied throughout the literature publications on BIAN complex, and several previous literature reports on topics such as the catalytic activity of BIAN complexes do not feature any characterisation data of the reported compounds themselves.[20,54,65–67] Coordination of the BIAN ligands have been confirmed in some reports using vibrational spectroscopy, with authors noting a decrease in the wavenumbers associated with the ν(C=N) vibrational bands in coordination complexes compared to the spectra of the free ligands.[2,33,59,68,69] These techniques alone cannot provide distinctive evidence of redox non-innocent properties at work within a BIAN complex, as they do not provide direct information of the oxidation states of either the BIAN ligands or the metal centre of the BIAN complex.

© University of Pretoria

The electrochemical characterisation of BIAN ligands and complexes has been reported with increased frequency in recent years, however, the data interpretations presented in some reports are speculative or inconclusive due to the multitude of consecutive redox events that are observed within a small potential range.[39,53] Computational modelling of BIAN complexes has seen increasing application in recent years, largely focusing on the determination of optimised coordination geometries and theoretical spectroscopic properties of the BIAN complexes, as well as and molecular orbital distributions which assisted the authors in assigning the localisation of the first reduction and oxidation events.[1–3,12,13,26,29–32,34,37–41,43,50,53,63,64,66,70–91]

Two remarkable papers from the research group of Skara *et al*.[4,92] investigated what influence the structural rearrangement of their α-diimine complexes had on the electrochemical reaction potentials observed that they observed. Theoretical reduction reactions energies were calculated by modelling the complexes in different charged states and showed good correlation with the experimental data of the group, enabling the researchers to assign and describe each observed electrochemical event to specific changes in the molecular and electronic structures of their complexes.[4,92]



*Scheme 1.1–2: The bond lengths of the BIAN bisimine C–N and C–C are characteristic of the reduced state of the compound, and have been recorded for free BIAN ligands in their (**a**) neutral,[1,3] (**b**) semiquinonate,[1,7] and (**c**) quinonate charged states.[1,7] Ligand centred reduction, or non-innocent charge transfer, in BIAN coordination complexes display similar changes in the average bond lengths of the BIAN bisimine C–N and C–C, illustrated by BIAN ligands associated with a formal charge of (**d**) zero,[14–16,39,53,93] (**e**) –1,[13–16] and (**f**) –2 respectively.[15,16,42]*

Amongst all the characterisation methods, the importance of Single Crystal X-Ray Diffraction (SC-XRD) analyses for BIAN compounds cannot be overstated. Free BIAN ligands have been noted to

© University of Pretoria

present distinctive changes in colouration that are associated with the charged state of the ligand, whereas the formal charge of coordinated BIAN ligands is not as easily distinguishable. The charge delocalisation which occurs across the bisimine N=C–C=N moiety of the semiquinonate [BIAN^{1-}] and quinonate [BIAN^{2-}] states, result in idiosyncratic changes of the C–N and C–C bond lengths which may be best determined from SC-XRD (Scheme 1.1–2.a–c).[1,3,7] Upon reduction of the bisimine moiety, the C=N double bonds become elongated to interatomic distances comparable with C–N single bonds in the quinonate [BIAN^{2-}] state. Conversely, the C–C single bond shortens to a bond length akin to that of a C=C double bond. Analogous changes in the bond lengths of the bisimine N=C–C=N moiety are observed for BIAN ligands after coordination to a metal centre, despite the structural limitations that are imposed by the formation of the five-membered metallocycle (Scheme 1.1–2.d–f).[13–16,39,42,53,93]

Determination of the C–N and C–C bond lengths of the bisimine N=C–C=N moiety in BIAN coordination complexes has proven to be vital data to interpret the interactions between the BIAN ligand and the metal centre for the presence of any non-innocent interactions between them. In their discussion regarding identification of ligand non-innocent behaviour, Milstein *et al*.[6] emphasised that the non-innocence of a ligand should not be based solely on the ligand's structural data. The group of Cowley *et al*.[34] echoed this cautionary advice, noting that differences in the coordination environment of various BIAN complexes may influence the comparability of the structural data of the ligands. The oxidation state of the metal, and consequently the electronic structure of the complex, may be vastly influenced by back-bonding and valence tautomerism between the metal and BIAN ligand. These interactions may in turn also be influenced by the electronic properties of the ancillary ligands that are present in the complex.

Such valence tautomerism was observed by Larson *et al*.[3] in their study on Fe(II)-BIAN complexes (Figure 1.1–1.a). The authors observed C–C bond shortening and C–N bond elongation in the SC-XRD data for some of their Fe(II)-complexes that was comparable to previously reported values for monoanionic BIAN ligands. Investigation of these compounds using electrochemical analysis and computational modelling suggested that these complexes featured a Fe(I)-centre and [BIAN^{1-}] ligand, with strong antiferromagnetic coupling between the metal centre and radical anion ligand.

Applying multi-technique methodologies to examine the electronic structure and bonding interactions of the BIAN complexes in this body of work is therefore essential to accurately designate the oxidation states of both the central metal and the ligand(s) that are presenting non-innocent behaviour characteristics.[6]

© University of Pretoria

1.2) Research Rationale and Motivation

Limited experimental and reactivity data is available in literature for BIAN complexes of rhodium and iridium in oxidation state +1 specifically, [33,53,54,58] compared to the large number of BIAN complexes of different first row transition metals which have been investigated to date.[3,12–15,23,26,29–32,34,40,43,45,48,55,59,61,69,71,74,79,83,89,91,93–111] Complexes of rhodium and iridium have found application in a diverse range of catalytic reactions including hydroamination,[51,54,112,113] hydrothiolation,[114–116] copolymerisation of olefins,[117] as well as alkyne dimerization and trimerization.[19,113,116] Moreover, complexes of late transition metals, such as rhodium(I) and iridium(I), have been reported to be more resilient catalysts compared to their lanthanide, actinide, and early transition metal counterparts.[51,54,118]

Rhodium(I) complexes are well known for their catalytic activity in homogeneous hydroformylation and hydrogenation of olefins,[33,117,119,120] ethylene and olefin polymerisation,[19,117] as well as the hydrosilylation of alkenes and alkynes to yield mixtures of *cis* and *trans* isomer products.[117] Rhodium catalysts have also proven to catalysts for H–X and C–F bond activation, H_2 production, and CO_2 reduction.[52] For their part, a number of iridium(I) and iridium(III) complexes have been reported to demonstrate ligand-cooperative or redox-switchable behaviour which facilitated their catalytic activity.[121–123]

Precious metals often catalyse multielectron reactions more efficiently since they typically undergo 2 electron oxidation or reduction events (e.g., Ir(I) ⇌ Ir(III) ⇌ Ir (V)).[124] Consecutive 1 electron transfer reactions may not be as favourable as a single 2 electron transfer reaction, due to the highly reactive nature of the radical intermediate that is formed during the former process.[124] The BIAN ligand moiety has demonstrated the potential to fulfil a similar electron sink role when coordinated to redox active metals.[3,34,35]

As noted earlier, several BIAN complexes have been reported as catalysts for the electrochemical reduction of CO_2, and featured metals such as Re(I), Mo(II), Ag(I) and Rh(III).[35,36,39,80] Reports of BIAN complexes of iridium largely focussed on iridium(III) and the photochemical properties of the complexes.[41,54,64,85] However, a methodical electrochemical analysis of Rh(I)- and/or Ir(I)-BIAN complexes, with DFT assisted assignment of redox events, has not been reported.

© University of Pretoria

This study was prompted by the possibility of combining the following characteristics of rhodium(I) and iridium(I) catalysts with the known redox non-innocent behaviour of BIAN ligands to modulate the catalytic reactivity of the new Rh(I)- and Ir(I)-BIAN complexes:[3,34,35]

- The robustness of rhodium(I) and iridium(I) catalysts and their tolerance to various functional groups and exposure to atmospheric conditions; [51,54,118]
- their ability to demonstrate redox-switchable and/or ligand-cooperative behaviour;[121–123]
- their ability to facilitate multiple catalytic reaction pathways contingent on the electronic parameters of the coordination environment.[33,51,115,117]

1.3) Research Objectives

The complexes synthesised as part of this body of work are subdivided into four groups based on the ancillary ligands that are present in the Rh(I)- and Ir(I)-BIAN complexes. The ancillary ligands were chosen from across the spectrochemical series to include low, mid and high field ligands, and consist of the σ-donor/π-acceptor ligands (1,5-cyclooctadiene, triethylphosphine and carbonyl), as well as a σ-donor/π-donor ligand (chloride). In addition, the complexes in this body of work will be subjected to an array of reactivity screening test to evaluate their potential application as catalysts or pre-catalysts in a variety of catalytic reactions, and to investigate how the ancillary ligands modulate electronic environment (and reactivity) of the coordination sphere.[33,52]

A combination of both physical characterisation techniques (such as NMR spectrometry, XRD and electrochemistry methods) and computational DFT studies were employed in this study to facilitate the analysis of intramolecular interactions in the reported BIAN complexes, and to establish a description of the electronic structure of these BIAN complexes. Critical assessment of the characterisation results data for these groups of complexes is anticipated to yield information on the impact that the electronic properties of ancillary ligands may have on the ability of the BIAN ligand to function as a non-innocent ligand. The information and understanding thusly gained may shed light on underlying physiochemical characteristics of the complexes that affect their catalytic reactivity.

Throughout this body of work, the present study aims to address the following research objectives:

- To critically compare the bonding patterns, physiochemical properties, and electrochemical reactivity of the synthesised series of Rh(I)-BIAN and Ir(I)-BIAN complexes.
- To evaluate what influence the electronic characteristics of different ancillary ligands have on the bonding patterns, physiochemical properties, electrochemical reactivity, and catalytic

© University of Pretoria

reactivity of the series of Rh(I)- and Ir(I)-BIAN complexes in this study.

- To facilitate the interpretation of multi-electron reactions observed during the electrochemical analysis by applying DFT computational modelling of the series of Rh(I)- and Ir(I)-BIAN complexes.
- To screen the catalytic reactivity of the series of Rh(I)- and Ir(I)-BIAN complexes towards various catalytic reactions, in the presence and absence of a chemical reducing agent (cobaltocene), to investigate how the redox non-innocent characteristics of the BIAN ligand may influence the catalytic reactivity of the complexes.
- To screen the electrocatalytic CO_2 reduction reactivity of the series of Rh(I)- and Ir(I)-BIAN complexes in preliminary qualitative electrochemical measurements.
- To appraise whether the BIAN ligands exhibited non-innocent behaviour in any of the series of Rh(I)- and Ir(I)-BIAN complexes.

The thesis presented across the following five chapters will cover the synthesis and physiochemical characterisation of the series of Rh(I)- and Ir(I)-BIAN complexes (Chapter 2); the systematic electrochemical reactivity analysis (Chapter 3); a computationally grounded elucidation of the electrochemical reactivity of the complexes (Chapter 4); a qualitative catalytic reactivity screening of the series of Rh(I)- and Ir(I)-BIAN complexes towards alkene and alkyne dimerization, hydroamination and hydrothiolation, as well as their electrocatalytic reactivity towards CO_2 reduction (Chapter 5); and finally, the critical evaluations, comparisons and noteworthy findings of the study will be reviewed in Chapter 6, along with a survey of prospective research notes.

© University of Pretoria

1.4) References

(1) Viganò, M.; Ferretti, F.; Caselli, A.; Ragaini, F.; Rossi, M.; Mussini, P.; Macchi, P. Easy Entry into Reduced Ar-BIANH 2 Compounds: A New Class of Quinone/Hydroquinone-Type Redox-Active Couples with an Easily Tunable Potential. *Chemistry - European Journal* **2014**, *20* (44), 14451–14464. https://doi.org/10.1002/chem.201403594.

(2) Hasan, K.; Zysman-Colman, E. Synthesis, UV-Vis and CV Properties of a Structurally Related Series of Bis(Arylimino)Acenaphthenes (Ar-BIANs). *J Phys Org Chem* **2013**, *26* (3), 274–279. https://doi.org/10.1002/poc.3081.

(3) Larson, P. J.; Wekesa, F. S.; Singh, A.; Smith, C. R.; Rajput, A.; McGovern, G. P.; Unruh, D. K.; Cozzolino, A. F.; Findlater, M. Synthesis, Characterization, Electrochemical Properties and Theoretical Calculations of (BIAN) Iron Complexes. *Polyhedron* **2019**, *159*, 365–374. https://doi.org/10.1016/j.poly.2018.11.060.

(4) Skara, G.; Pinter, B.; Geerlings, P.; De Proft, F. Revealing the Thermodynamic Driving Force for Ligand-Based Reductions in Quinoids; Conceptual Rules for Designing Redox Active and Non-Innocent Ligands. *Chem Sci* **2015**, *6* (7), 4109–4117. https://doi.org/10.1039/C5SC01140J.

(5) Allan, C. J.; Cooper, B. F. T.; Cowley, H. J.; Rawson, J. M.; Macdonald, C. L. B. Non-Innocent Ligand Effects on Low-Oxidation-State Indium Complexes. *Chemistry - European Journal* **2013**, *19* (43), 14470–14483. https://doi.org/10.1002/chem.201301881.

(6) Butschke, B.; Fillman, K. L.; Bendikov, T.; Shimon, L. J. W.; Diskin-Posner, Y.; Leitus, G.; Gorelsky, S. I.; Neidig, M. L.; Milstein, D. How Innocent Are Potentially Redox Non-Innocent Ligands? Electronic Structure and Metal Oxidation States in Iron-PNN Complexes as a Representative Case Study. *Inorg Chem* **2015**, *54* (10), 4909–4926. https://doi.org/10.1021/acs.inorgchem.5b00509.

(7) Fedushkin, I. L.; Skatova, A. A.; Chudakova, V. A.; Fukin, G. K. Four-Step Reduction of Dpp-bian with Sodium Metal: Crystal Structures of the Sodium Salts of the Mono-, Di-, Tri- and Tetraanions of Dpp-bian. *Angewandte Chemie* **2003**, *115* (28), 3416–3420. https://doi.org/10.1002/ange.200351408.

(8) Fedushkin, I. L.; Skatova, A. A.; Chudakova, V. A.; Fukin, G. K.; Dechert, S.; Schumann, H. Monomeric Magnesium and Calcium Complexes Containing the Bidentate, Dianionic 1,2-Bis[(2,6-Diisopropylphenyl)Imino]Acenaphthene Ligand. *Eur J Inorg Chem* **2003**, No. 18, 3336–3346. https://doi.org/10.1002/ejic.200300181.

(9) Fedushkin, I. L.; Skatova, A. A.; Chudakova, V. A.; Cherkasov, V. K.; Fukin, G. K.; Lopatin, M. A. Reduction of 1,2-Bis[(2,6-Diisopropylphenyl)Imino]Acenaphthene (Dpp-Bian) with Alkali Metals− A Study of the Solution Behaviour of (Dpp-Bian)N−[M^+]n (M = Li, Na;n = 1−4) with

© University of Pretoria

UV/Vis, ESR and 1H NMR Spectroscopy. *Eur J Inorg Chem* **2004**, *2004* (2), 388–393. https://doi.org/10.1002/ejic.200300351.

(10) Fedushkin, I. L.; Khvoinova, N. M.; Baurin, A. Y.; Chudakova, V. A.; Skatova, A. A.; Cherkasov, V. K.; Fukin, G. K.; Baranov, E. V. Reactions of Germanium(II), Tin(II), and Antimony(III) Chlorides with Acenaphthene-1,2-Diimines. *Russian Chemical Bulletin* **2006**, *55* (1), 74–83. https://doi.org/10.1007/s11172-006-0217-z.

(11) Moskalev, M. V.; Lukoyanov, A. N.; Baranov, E. V.; Fedushkin, I. L. Unexpected Reactivity of an Alkylaluminum Complex of a Non-Innocent 1,2-Bis[(2,6-Diisopropylphenyl)Imino]Acenaphthene Ligand (Dpp-Bian). *Dalton Transactions* **2016**, *45* (40), 15872–15878. https://doi.org/10.1039/C6DT01750A.

(12) Morozov, A. G.; Fedushkin, I. L.; Irran, E.; Grohmann, A. Titanium(IV) Complexes Supported by a Dianionic Acenaphthenediimine Ligand: X-Ray and Spectroscopic Studies of the Metal Coordination Sphere. *Inorg Chem Commun* **2018**, *95* (June), 50–55. https://doi.org/10.1016/j.inoche.2018.07.006.

(13) Clark, K. M.; Bendix, J.; Heyduk, A. F.; Ziller, J. W. Synthesis and Characterization of a Neutral Titanium Tris(Iminosemiquinone) Complex Featuring Redox-Active Ligands. *Inorg Chem* **2012**, *51* (14), 7457–7459. https://doi.org/10.1021/ic301059p.

(14) Bendix, J.; Clark, K. M. Delocalization and Valence Tautomerism in Vanadium Tris(Iminosemiquinone) Complexes. *Angewandte Chemie - International Edition* **2016**, *55* (8), 2748–2752. https://doi.org/10.1002/anie.201510403.

(15) Khusniyarov, M. M.; Harms, K.; Burghaus, O.; Sundermeyer, J. Molecular and Electronic Structures of Homoleptic Nickel and Cobalt Complexes with Non-Innocent Bulky Diimine Ligands Derived from Fluorinated 1,4-Diaza-1,3-Butadiene (DAD) and Bis(Arylimino)Acenaphthene (BIAN). *Eur J Inorg Chem* **2006**, No. 15, 2985–2996. https://doi.org/10.1002/ejic.200600236.

(16) Vasudevan, K.; Cowley, A. H. Synthesis and Structures of 1,2-Bis(Imino)Acenaphthene (BIAN) Lanthanide Complexes That Involve the Transfer of Zero, One, or Two Electrons. *Chemical Communications* **2007**, No. 33, 3464–3466. https://doi.org/10.1039/b708758f.

(17) Hill, N. J.; Vargas-Baca, I.; Cowley, A. H. Recent Developments in the Coordination Chemistry of Bis(Imino)Acenaphthene (BIAN) Ligands with s- and p-Block Elements. *Dalton Transactions* **2009**, *9226* (2), 240–253. https://doi.org/10.1039/b815079f.

(18) Caulton, K. G. Systematics and Future Projections Concerning Redox-Noninnocent Amide/Imine Ligands. *Eur J Inorg Chem* **2012**, No. 3, 435–443. https://doi.org/10.1002/ejic.201100623.

© University of Pretoria

(19) Daugulis, O.; Macarthur, A. H. R.; Rix, F. C.; Templeton, J. L. A Career in Catalysis: Maurice Brookhart. *ACS Catal* **2016**, *6* (3), 1518–1532. https://doi.org/10.1021/acscatal.5b02216.

(20) van Asselt, R.; Elsevier, C. J. Homogeneous Catalytic Hydrogenation of Alkenes by Zero-Valent Palladium Complexes of Cis-Fixed Dinitrogen Ligands. *Journal of Molecular Catalysis* **1991**, *65* (3). https://doi.org/10.1016/0304-5102(91)85057-9.

(21) van Asselt, R.; Gielens, E. E. C. G.; Rulke, R. E.; Vrieze, K.; Elsevier, C. J. Rigid Bidentate Nitrogen Ligands in Organometallic Chemistry and Homogeneous Catalysis. 3. Insertion of Carbon Monoxide and Alkenes into Palladium-Carbon Bonds of Complexes Containing Rigid Bidentate Nitrogen Ligands: The First Example of Isolated Complex. *J Am Chem Soc* **1994**, *116* (3), 977–985. https://doi.org/10.1021/ja00082a020.

(22) van Asselt, R.; Elsevier, C. J. New Palladium Complexes of Cis-Fixed Bidentate Nitrogen Ligands as Catalysts for Carbon-Carbon Bond Formation. *Organometallics* **1992**, *11* (6), 1999–2001.

(23) Johnson, L. K.; Killian, C. M.; Brookhart, M. New Pd(II)- and Ni(II)-Based Catalysts for Polymerization of Ethylene and α-Olefins. *J Am Chem Soc* **1995**, *117* (23), 6414–6415. https://doi.org/10.1021/ja00128a054.

(24) van Asselt, R.; Elsevier, C. J.; Smeets, W. J. J.; Spek, A. L.; Benedix, R. Synthesis and Characterization of Rigid Bidentate Nitrogen Ligands and Some Examples of Coordination to Divalent Palladium. X-Ray Crystal Structures of Bis (p-Tolylimino) Acenaphthene and Methylchloro [Bis(o,O'-Diisopropylphenyl-Imino) Acenaphthene] Palla. *Recueil des Travaux Chimiques des Pays-Bas* **1994**, *113* (2), 88–98. https://doi.org/10.1002/recl.19941130204.

(25) Liu, W.; Brookhart, M. Mechanistic Studies of Palladium(II)-a-Diimine-Catalyzed Polymerizations of Cis- and Trans-2-Butenes. *Organometallics* **2004**, *23* (26), 6099–6107. https://doi.org/10.1021/om040077m.

(26) Williams, B. S.; Leatherman, M. D.; White, P. S.; Brookhart, M. Reactions of Vinyl Acetate and Vinyl Trifluoroacetate with Cationic Diimine Pd(II) and Ni(II) Alkyl Complexes: Identification of Problems Connected with Copolymerizations of These Monomers with Ethylene. *J Am Chem Soc* **2005**, *127* (14), 5132–5146. https://doi.org/10.1021/ja045969s.

(27) Shiotsuki, M.; White, P. S.; Brookhart, M.; Templeton, J. L. Mechanistic Studies of Platinum(II)-Catalyzed Ethylene Dimerization: Determination of Barriers to Migratory Insertion in Diimine Pt(II) Hydrido Ethylene and Ethyl Ethylene Intermediates. *J Am Chem Soc* **2007**, *129* (13), 4058–4067. https://doi.org/10.1021/ja068118o.

(28) Khlebnikov, V.; Meduri, A.; Mueller-Bunz, H.; Montini, T.; Fornasiero, P.; Zangrando, E.; Milani, B.; Albrecht, M. Palladium Carbene Complexes for Selective Alkene Di- and Oligomerization. *Organometallics* **2012**, *31* (3), 976–986. https://doi.org/10.1021/om201027y.

© University of Pretoria

(29) Zhang, D.; Nadres, E. T.; Brookhart, M.; Daugulis, O. Synthesis of Highly Branched Polyethylene Using "Sandwich" (8-p-Tolyl Naphthyl α-Diimine)Nickel(II) Catalysts. *Organometallics* **2013**, *32* (18), 5136–5143. https://doi.org/10.1021/om400704h.

(30) Nunes, C. D.; Vaz, P. D.; Félix, V.; Veiros, L. F.; Moniz, T.; Rangel, M.; Realista, S.; Mourato, A. C.; Calhorda, M. J. Vanadyl Cationic Complexes as Catalysts in Olefin Oxidation. *Dalton Transactions* **2015**, *44* (11), 5125–5138. https://doi.org/10.1039/C4DT03174A.

(31) Fomenko, I. S.; Gushchin, A. L.; Shul'pina, L. S.; Ikonnikov, N. S.; Abramov, P. A.; Romashev, N. F.; Poryvaev, A. S.; Sheveleva, A. M.; Bogomyakov, A. S.; Shmelev, N. Y.; Fedin, M. V.; Shul'pin, G. B.; Sokolov, M. N. New Oxidovanadium(Iv) Complex with a BIAN Ligand: Synthesis, Structure, Redox Properties and Catalytic Activity. *New Journal of Chemistry* **2018**, *42* (19), 16200–16210. https://doi.org/10.1039/C8NJ03358G.

(32) Supej, M. J.; Volkov, A.; Darko, L.; West, R. A.; Darmon, J. M.; Schulz, C. E.; Wheeler, K. A.; Hoyt, H. M. Aryl-Substituted BIAN Complexes of Iron Dibromide: Synthesis, X-Ray and Electronic Structure, and Catalytic Hydrosilylation Activity. *Polyhedron* **2016**, *114*, 403–414. https://doi.org/10.1016/j.poly.2016.02.020.

(33) Omosun, N. N.; Smith, G. S. Water-Soluble, Disulfonated Alpha-Diimine Rhodium(I) Complexes: Synthesis, Characterisation and Application as Catalyst Precursors in the Hydroformylation of 1-Octene. *Eur J Inorg Chem* **2019**, *2019* (20), 2558–2564. https://doi.org/10.1002/ejic.201900317.

(34) Williams, O. M.; Cowley, A. H.; Rose, M. J. Structural and Electronic Characterization of Multi-Electron Reduced Naphthalene (BIAN) Cobaloximes. *Dalton Transactions* **2015**, *44* (29), 13017–13029. https://doi.org/10.1039/C5DT00924C.

(35) Krisch, D.; Sun, H.; Pellumbi, K.; Faust, K.; Apfel, U.-P.; Schöfberger, W. Tuning the Electronic Properties of Homoleptic Silver(I) Bis-BIAN Complexes towards Efficient Electrocatalytic CO2 Reduction. *Catalysts* **2022**, *12* (5), 545. https://doi.org/10.3390/catal12050545.

(36) Portenkirchner, E.; Kianfar, E.; Sariciftci, N. S.; Knör, G. Two-Electron Carbon Dioxide Reduction Catalyzed by Rhenium(I) Bis(Imino)Acenaphthene Carbonyl Complexes. *ChemSusChem* **2014**, *7* (5), 1347–1351. https://doi.org/10.1002/cssc.201301116.

(37) Kianfar, E.; Monkowius, U.; Portenkirchner, E.; Knör, G. Synthesis and Characterization of Novel Re(BIAN)(CO)3Cl Derivatives Including the First Example of a Water-Soluble Tricarbonyl Rhenium(I) Complex with Bis(Imino)Acenaphthene Ligands. *Zeitschrift fur Naturforschung - Section B Journal of Chemical Sciences* **2014**, *69* (6), 691–698. https://doi.org/10.5560/ZNB.2014-4016.

© University of Pretoria

(38) Abramov, P. A.; Dmitriev, A. A.; Kholin, K. V.; Gritsan, N. P.; Kadirov, M. K.; Gushchin, A. L.; Sokolov, M. N. Mechanistic Study of the [(Dpp-Bian)Re(CO)3Br] Electrochemical Reduction Using in Situ EPR Spectroscopy and Computational Chemistry. *Electrochim Acta* **2018**, *270*, 526–534. https://doi.org/10.1016/j.electacta.2018.03.111.

(39) Gushchin, A. L.; Romashev, N. F.; Shmakova, A. A.; Abramov, P. A.; Ryzhikov, M. R.; Fomenko, I. S.; Sokolov, M. N. Novel Redox Active Rhodium(III) Complex with Bis(Arylimino)Acenaphthene Ligand: Synthesis, Structure and Electrochemical Studies. *Mendeleev Communications* **2020**, *30* (1), 81–83. https://doi.org/10.1016/j.mencom.2020.01.027.

(40) Fliedel, C.; Rosa, V.; Santos, C. I. M.; Gonzalez, P. J.; Almeida, R. M.; Gomes, C. S. B.; Gomes, P. T.; Lemos, M. A. N. D. A.; Aullón, G.; Welter, R.; Avilés, T. Copper(Ii) Complexes of Bis(Aryl-Imino)Acenaphthene Ligands: Synthesis, Structure, DFT Studies and Evaluation in Reverse ATRP of Styrene. *Dalton Transactions* **2014**, *43* (34), 13041–13054. https://doi.org/10.1039/c4dt01069h.

(41) Hasan, K.; Zysman-Colman, E. The Effect of Aryl Substitution on the Properties of a Series of Highly Absorptive Cationic Iridium(III) Complexes Bearing Ancillary Bis(Arylimino)Acenaphthene Ligands. *Eur J Inorg Chem* **2013**, *2013* (25), 4421–4429. https://doi.org/10.1002/ejic.201300583.

(42) Reeske, G.; Hoberg, C. R.; Hill, N. J.; Cowley, A. H. Capture of Phosphorus(I) and Arsenic(I) Moieties by a 1,2-Bis(Arylimino) Acenaphthene (Aryl-BIAN) Ligand. A Case of Intramolecular Charge Transfer. *J Am Chem Soc* **2006**, *128* (9), 2800–2801. https://doi.org/10.1021/ja058459m.

(43) Li, L.; Lopes, P. S.; Rosa, V.; Figueira, C. A.; Lemos, M. A. N. D. A.; Duarte, M. T.; Avilés, T.; Gomes, P. T. Synthesis and Structural Characterisation of (Aryl-BIAN)Copper(i) Complexes and Their Application as Catalysts for the Cycloaddition of Azides and Alkynes. *Dalton Transactions* **2012**, *41* (17), 5144. https://doi.org/10.1039/c2dt11854h.

(44) Viganò, M.; Ragaini, F.; Buonomenna, M. G.; Lariccia, R.; Caselli, A.; Gallo, E.; Cenini, S.; Jansen, J. C.; Drioli, E. Catalytic Polymer Membranes under Forcing Conditions: Reduction of Nitrobenzene by CO/H2O Catalyzed by Ruthenium Bis(Arylimino)Acenaphthene Complexes. *ChemCatChem* **2010**, *2* (9), 1150–1164. https://doi.org/10.1002/cctc.201000044.

(45) Hagar, M.; Ragaini, F.; Monticelli, E.; Caselli, A.; Macchi, P.; Casati, N. Chiral Cyclopropylamines in the Synthesis of New Ligands; First Asymmetric Alkyl-BIAN Compounds. *Chemical Communications* **2010**, *46* (33), 6153. https://doi.org/10.1039/c0cc00977f.

© University of Pretoria

(46) Ragaini, F.; Cenini, S.; Turra, F.; Caselli, A. Allylic Amination of Unfunctionalyzed Olefins by Nitroarenes and CO, Catalyzed by Ru3(CO)12/Ph-BIAN (Ph-BIAN=bis(Phenylimino) Acenaphthenequinone): Extension to the Synthesis of Allylic Amines with Strongly Electron-Withdrawing or Electron-Donating Groups. *Tetrahedron* **2004**, *60* (23), 4989–4994. https://doi.org/10.1016/j.tet.2004.04.034.

(47) Gasperini, M.; Ragaini, F.; Cenini, S. Synthesis of Ar-BIAN Ligands (Ar-BIAN = Bis(Aryl)Acenaphthenequinonediimine) Having Strong Electron-Withdrawing Substituents on the Aryl Rings and Their Relative Coordination Strength toward Palladium(0) and -(II) Complexes. *Organometallics* **2002**, *21* (14), 2950–2957. https://doi.org/10.1021/om020147u.

(48) Villa, M.; Miesel, D.; Hildebrandt, A.; Ragaini, F.; Schaarschmidt, D.; Jacobi von Wangelin, A. Synthesis and Catalysis of Redox-Active Bis(Imino)Acenaphthene (BIAN) Iron Complexes. *ChemCatChem* **2017**, *9* (16), 3203–3209. https://doi.org/10.1002/cctc.201700144.

(49) Ragaini, F.; Gasperini, M.; Gallo, E.; Macchi, P. Using Ring Strain to Inhibit a Decomposition Path: First Synthesis of an Alkyl-BIAN Ligand (Alkyl-BIAN = Bis(Alkyl)Acenaphthenequinonediimine). *Chemical Communications* **2005**, *2* (8), 1031–1033. https://doi.org/10.1039/b415767b.

(50) Gasperini, M.; Ragaini, F.; Gazzola, E.; Caselli, A.; Macchi, P. Synthesis of Mixed Ar,Ar'-BIAN Ligands (Ar,Ar'-BIAN = Bis(Aryl)Acenaphthenequinonediimine). Measurement of the Coordination Strength of Hemilabile Ligands with Respect to Their Symmetric Counterparts. *Dalton Trans.* **2004**, *33* (20), 3376–3382. https://doi.org/10.1039/B406582D.

(51) Hua, C.; Vuong, K. Q.; Bhadbhade, M.; Messerle, B. A. New Rhodium(I) and Iridium(I) Complexes Containing Mixed Pyrazolyl-1,2,3-Triazolyl Ligands as Catalysts for Hydroamination. *Organometallics* **2012**, *31* (5), 1790–1800. https://doi.org/10.1021/om201171b.

(52) Shaffer, D. W.; Ryken, S. A.; Zarkesh, R. A.; Heyduk, A. F. Redox Behavior of Rhodium 9,10-Phenanthrenediimine Complexes. *Inorg Chem* **2011**, *50* (1), 13–21. https://doi.org/10.1021/ic1007632.

(53) Romashev, N. F.; Gushchin, A. L.; Fomenko, I. S.; Abramov, P. A.; Mirzaeva, I. V.; Kompan'kov, N. B.; Kal'nyi, D. B.; Sokolov, M. N. A New Organometallic Rhodium(I) Complex with Dpp-Bian Ligand: Synthesis, Structure and Redox Behaviour. *Polyhedron* **2019**, *173*, 114110. https://doi.org/10.1016/j.poly.2019.114110.

(54) Rumble, S. L.; Page, M. J.; Field, L. D.; Messerle, B. A. In Situ Catalysts for the Intramolecular Hydroamination of Aminoalkynes - What Ligand Properties Determine Catalyst Activity? *Eur J Inorg Chem* **2012**, *2012* (13), 2226–2231. https://doi.org/10.1002/ejic.201101307.

© University of Pretoria

(55) Khrizanforova, V. V.; Morozov, V. I.; Khrizanforov, M. N.; Lukoyanov, A. N.; Kataeva, O. N.; Fedushkin, I. L.; Budnikova, Yu. H. Iron Complexes of BIANs: Redox Trends and Electrocatalysis of Hydrogen Evolution. *Polyhedron* **2018**, *154*, 77–82. https://doi.org/10.1016/j.poly.2018.07.041.

(56) Raghavan, A.; Venugopal, A. Review: Structurally Characterized α-Diimine Complexes of s- and p-Block Elements. *J Coord Chem* **2014**, *67* (15), 2530–2549. https://doi.org/10.1080/00958972.2014.931576.

(57) Van Belzen, R.; Hoffmann, H.; Elsevier, C. J. Catalytic Three-Component Synthesis of Conjugated Dienes from Alkynes via Pd0, PdII, and PdIV Intermediates Containing 1,2-Diimine. *Angewandte Chemie (International Edition in English)* **1997**, *36* (16), 1743–1745. https://doi.org/10.1002/anie.199717431.

(58) Rumble, S. L. The Synthesis of Amines and Imines Using Organometallic Catalysts. Doctor of Philosophy, University of New South Wales, 2005.

(59) Paulovicova, A.; El-Ayaan, U.; Shibayama, K.; Morita, T.; Fukuda, Y. Mixed-Ligand Copper(II) Complexes with the Rigid Bidentate Bis(N-Arylimino)Acenaphthene Ligand: Synthesis, Spectroscopic-, and X-Ray Structural Characterization. *Eur J Inorg Chem* **2001**, *2001* (10), 2641–2646. https://doi.org/10.1002/1099-0682(200109)2001:10<2641::AID-EJIC2641>3.0.CO;2-C.

(60) Mahabiersing, T.; Luytenn, H.; Nieuwendam, R. C.; Hartl, F. Synthesis, Spectroscopy and Spectroelectrochemistry of Chlorocarbonyl {1,2-Bis[(2,6-Diisopropylphenyl)Imino]-Acenaphthene-K2-N, N'}rhodium(I). *Collect Czechoslov Chem Commun* **2003**, *68* (9), 1687–1709. https://doi.org/10.1135/cccc20031687.

(61) Yambulatov, D. S.; Nikolaevskii, S. A.; Kiskin, M. A.; Magdesieva, T. V.; Levitskiy, O. A.; Korchagin, D. V.; Efimov, N. N.; Vasil'ev, P. N.; Goloveshkin, A. S.; Sidorov, A. A.; Eremenko, I. L. Complexes of Cobalt(II) Iodide with Pyridine and Redox Active 1,2-Bis(Arylimino)Acenaphthene: Synthesis, Structure, Electrochemical, and Single Ion Magnet Properties. *Molecules* **2020**, *25* (9), 2054. https://doi.org/10.3390/molecules25092054.

(62) Van Der Poel, H.; Van Koten, G.; Vrieze, K. Syntheses and NMR Studies of Five-Co-Ordinate Rhodium(I) Complexes with α-Diimines (RNC(H)C(H)NR): [RhCl(CO)(H2-C2H4)(α-Diimine)] and [RhCl(L)2(α-Diimine)] (R = t-Bu, EtMe2C-; L = CO,PF3). *Inorganica Chim Acta* **1981**, *51* (C), 241–252. https://doi.org/10.1016/S0020-1693(00)88344-9.

(63) Liu, B.; Gao, M.; Dang, L.; Zhao, H.; Marder, T. B.; Lin, Z. DFT Studies on the Mechanisms of the Platinum-Catalyzed Diboration of Acyclic α,β-Unsaturated Carbonyl Compounds. *Organometallics* **2012**, *31* (8), 3410–3425. https://doi.org/10.1021/om3002153.

© University of Pretoria

(64) Hasan, K.; Zysman-Colman, E. Panchromic Cationic Iridium(III) Complexes. *Inorg Chem* **2012**, *51* (22), 12560–12564. https://doi.org/10.1021/ic301998t.

(65) Klein, R. A.; Elsevier, C. J.; Hartl, F. Redox Properties of Zerovalent Palladium Complexes Containing α-Diimine and p -Quinone Ligands. *Organometallics* **1997**, *16* (6), 1284–1291. https://doi.org/10.1021/om960809d.

(66) Donkervoort, J. G.; Bühl, M.; Ernsting, J. M.; Elsevier, C. J. Steric and Electronic Effects on the 103Rh NMR Chemical Shifts of Rh1(Cyclooctadiene) Compounds Bearing N-Donor Ligands. *Eur J Inorg Chem* **1999**, *1999* (1), 27–33. https://doi.org/10.1002/(sici)1099-0682(199901)1999:1<27::aid-ejic27>3.0.co;2-4.

(67) van Laren, M. W.; Elsevier, C. J. Selective Homogeneous Palladium(0)- Catalyzed Hydrogenation of Alkynes to (Z)- Alkenes. *Angew. Chem. Int. Ed.* **1999**, *38* (24), 3715–3717.

(68) Harding, D. A. J.; Hope, E. G.; Singh, K.; Solan, G. A. Cationic Rhodium(I) and Iridium(I) α-Diimine Complexes. *Polyhedron* **2012**, *33* (1), 360–366. https://doi.org/10.1016/j.poly.2011.11.058.

(69) Zhou, M.; Li, X.; Bu, D.; Lei, H. Synthesis, Crystal Structures and Electrochemical Properties of Co(II) and Mn(II) Complexes with Asymmetric Bulky BIAN Ligands. *Polyhedron* **2018**, *148*, 88–99. https://doi.org/10.1016/j.poly.2018.03.034.

(70) Schelter, E. J.; Wu, R.; Scott, B. L.; Thompson, J. D.; Cantat, T.; John, K. D.; Batista, E. R.; Morris, D. E.; Kiplinger, J. L. Actinide Redox-Active Ligand Complexes: Reversible Intramolecular Electron-Transfer in U(Dpp-BIAN)2/U(Dpp-BIAN)2(THF). *Inorg Chem* **2010**, *49* (3), 924–933. https://doi.org/10.1021/ic901636f.

(71) Rosa, V.; Avilés, T.; Aullon, G.; Covelo, B.; Lodeiro, C. A New Bis(1-Naphthylimino)Acenaphthene Compound and Its Pd(II) and Zn(II) Complexes: Synthesis, Characterization, Solid-State Structures and Density Functional Theory Studies on the Syn and Anti Isomers. *Inorg Chem* **2008**, *47* (17), 7734–7744. https://doi.org/10.1021/ic800790u.

(72) Schaefer, B. A.; Margulieux, G. W.; Small, B. L.; Chirik, P. J. Evaluation of Cobalt Complexes Bearing Tridentate Pincer Ligands for Catalytic C-H Borylation. *Organometallics* **2015**, *34* (7), 1307–1320. https://doi.org/10.1021/acs.organomet.5b00044.

(73) Housecroft, C. E.; Constable, E. C. The Emergence of Copper(I)-Based Dye Sensitized Solar Cells. *Chem Soc Rev* **2015**, *44* (23), 8386–8398. https://doi.org/10.1039/c5cs00215j.

(74) Evans, D. A.; Lee, L. M.; Vargas-Baca, I.; Cowley, A. H. Photophysical Tuning of the Aggregation-Induced Emission of a Series of Para-Substituted Aryl Bis(Imino)Acenaphthene Zinc Complexes. *Dalton Transactions* **2015**, *44* (26), 11984–11996. https://doi.org/10.1039/C5DT01529D.

(75) Papanikolaou, P. A.; Gdaniec, M.; Wicher, B.; Akrivos, P. D.; Tkachenko, N. V. Bis(Aryl)Acenaphthenequinonediimine Substituent Effect on the Properties and Coordination

© University of Pretoria

Environment of Ligands and Their Bis-Chelate Ag I Complexes. *Eur J Inorg Chem* **2013**, *2013* (29), 5196–5205. https://doi.org/10.1002/ejic.201300828.

(76) Wang, J.; Ganguly, R.; Yongxin, L.; Díaz, J.; Soo, H. Sen; García, F. A Multi-Step Solvent-Free Mechanochemical Route to Indium(III) Complexes. *Dalton Transactions* **2016**, *45* (19), 7941–7946. https://doi.org/10.1039/c6dt00978f.

(77) Henwood, A. F.; Hu, Y.; Sajjad, M. T.; Thalluri, G. K. V. V.; Ghosh, S. S.; Cordes, D. B.; Slawin, A. M. Z.; Samuel, I. D. W.; Robertson, N.; Zysman-Colman, E. Unprecedented Strong Panchromic Absorption from Proton-Switchable Iridium(III) Azoimidazolate Complexes. *Chemistry - European Journal* **2015**, *21* (52), 19128–19135. https://doi.org/10.1002/chem.201503546.

(78) Mak, C. S. K.; Wong, H. L.; Leung, Q. Y.; Tam, W. Y.; Chan, W. K.; Djurišić, A. B. The Use of Sublimable Chlorotricarbonyl Bis(Phenylimino)Acenaphthene Rhenium(I) Complexes as Photosensitizers in Bulk-Heterojunction Photovoltaic Devices. *J Organomet Chem* **2009**, *694* (17), 2770–2776. https://doi.org/10.1016/j.jorganchem.2009.04.037.

(79) Papanikolaou, P.; Akrivos, P. D.; Czapik, A.; Wicher, B.; Gdaniec, M.; Tkachenko, N. Homoleptic Bis(Aryl)Acenaphthenequinonediimine–Cu I Complexes – Synthesis and Characterization of a Family of Compounds with Improved Light-Gathering Characteristics. *Eur J Inorg Chem* **2013**, *2013* (13), 2418–2431. https://doi.org/10.1002/ejic.201201507.

(80) Tory, J.; Gobaille-Shaw, G.; Chippindale, A. M.; Hartl, F. Spectroelectrochemical Study of Complexes [Mo(CO)2(η 3-Allyl)(α-Diimine)(NCS)] (α-Diimine = Bis(2,6-Dimethylphenyl)-Acenaphthenequinonediimine and 2,2'-Bipyridine) Exhibiting Different Molecular Structure and Redox Reactivity Dedicated to Professor Maria. *J Organomet Chem* **2014**, *760*, 30–41. https://doi.org/10.1016/j.jorganchem.2014.01.015.

(81) Rosa, V.; Santos, C. I. M.; Welter, R.; Aullón, G.; Lodeiro, C.; Avilés, T. Comparison of the Structure and Stability of New α-Diimine Complexes of Copper(I) and Silver(I): Density Functional Theory versus Experimental. *Inorg Chem* **2010**, *49* (19), 8699–8708. https://doi.org/10.1021/ic100450y.

(82) Dokić, M.; Soo, H. Sen. Artificial Photosynthesis by Light Absorption, Charge Separation, and Multielectron Catalysis. *Chemical Communications* **2018**, *54* (50), 6554–6572. https://doi.org/10.1039/c8cc02156b.

(83) Ahmadjo, S.; Damavandi, S.; Zohuri, G. H.; Farhadipour, A.; Etemadinia, Z. Mechanisms for the Effects of Fluorine and α-Diimine Backbone Structure on the Catalyst Behavior and Catalyst Deactivation in Ethylene Polymerization by Ni Catalysts. *J Organomet Chem* **2017**, *835*, 43–51. https://doi.org/10.1016/j.jorganchem.2017.02.043.

© University of Pretoria

(84) Ladouceur, S.; Fortin, D.; Zysman-Colman, E. Enhanced Luminescent Iridium(III) Complexes Bearing Aryltriazole Cyclometallated Ligands. *Inorg Chem* **2011**, *50* (22), 11514–11526. https://doi.org/10.1021/ic2014013.

(85) Hasan, K.; Wang, J.; Pal, A. K.; Hierlinger, C.; Guerchais, V.; Sen Soo, H.; García, F.; Zysman-Colman, E. Bay-Region Functionalisation of Ar-BIAN Ligands and Their Use Within Highly Absorptive Cationic Iridium(III) Dyes. *Sci Rep* **2017**, *7* (1), 15520. https://doi.org/10.1038/s41598-017-14996-4.

(86) Hazari, A. S.; Das, A.; Ray, R.; Agarwala, H.; Maji, S.; Mobin, S. M.; Lahiri, G. K. Tunable Electrochemical and Catalytic Features of BIAN- and BIAO-Derived Ruthenium Complexes. *Inorg Chem* **2015**, *54* (10), 4998–5012. https://doi.org/10.1021/acs.inorgchem.5b00615.

(87) Singha Hazari, A.; Ray, R.; Hoque, M. A.; Lahiri, G. K. Electronic Structure and Multicatalytic Features of Redox-Active Bis(Arylimino)Acenaphthene (BIAN)-Derived Ruthenium Complexes. *Inorg Chem* **2016**, *55* (16), 8160–8173. https://doi.org/10.1021/acs.inorgchem.6b01280.

(88) Wang, J.; Ganguly, R.; Yongxin, L.; Díaz, J.; Soo, H. Sen; García, F. Synthesis and the Optical and Electrochemical Properties of Indium(III) Bis(Arylimino)Acenaphthene Complexes. *Inorg Chem* **2017**, *56* (14), 7811–7820. https://doi.org/10.1021/acs.inorgchem.7b00539.

(89) Evans, D. A.; Lee, L. M.; Vargas-Baca, I.; Cowley, A. H. Aggregation-Induced Emission of Bis(Imino)Acenaphthene Zinc Complexes: Photophysical Tuning via Methylation of the Flanking Aryl Substituents. *Organometallics* **2015**, *34* (11), 2422–2428. https://doi.org/10.1021/om501191c.

(90) Mondal, P.; Agarwala, H.; Jana, R. D.; Plebst, S.; Grupp, A.; Ehret, F.; Mobin, S. M.; Kaim, W.; Lahiri, G. K. Sensitivity of a Strained C-C Single Bond to Charge Transfer: Redox Activity in Mononuclear and Dinuclear Ruthenium Complexes of Bis(Arylimino)Acenaphthene (BIAN) Ligands. *Inorg Chem* **2014**, *53* (14), 7389–7403. https://doi.org/10.1021/ic500730m.

(91) Kee, J. W.; Ng, Y. Y.; Kulkarni, S. A.; Muduli, S. K.; Xu, K.; Ganguly, R.; Lu, Y.; Hirao, H.; Soo, H. S. Development of Bis(Arylimino)Acenaphthene (BIAN) Copper Complexes as Visible Light Harvesters for Potential Photovoltaic Applications. *Inorg Chem Front* **2016**, *3* (5), 651–662. https://doi.org/10.1039/c5qi00221d.

(92) Skara, G.; Gimferrer, M.; De Proft, F.; Salvador, P.; Pinter, B. Scrutinizing the Noninnocence of Quinone Ligands in Ruthenium Complexes: Insights from Structural, Electronic, Energy, and Effective Oxidation State Analyses. *Inorg Chem* **2016**, *55* (5), 2185–2199. https://doi.org/10.1021/acs.inorgchem.5b02543.

© University of Pretoria

(93) Moore, J. A.; Vasudevan, K.; Hill, N. J.; Reeske, G.; Cowley, A. H. Facile Routes to Alkyl-BIAN Ligands. *Chemical Communications* **2006**, *2006* (27), 2913–2915. https://doi.org/10.1039/b606390j.

(94) Small, B. L.; Rios, R.; Fernandez, E. R.; Carney, M. J. Oligomerization of Ethylene Using New Iron Catalysts Bearing Pendant Donor Modified α-Diimine Ligands. *Organometallics* **2007**, *26* (7), 1744–1749. https://doi.org/10.1021/om0611406.

(95) Schmiege, B. M.; Carney, M. J.; Small, B. L.; Gerlach, D. L.; Halfen, J. A. Alternatives to Pyridinediimine Ligands: Syntheses and Structures of Metal Complexes Supported by Donor-Modified α-Diimine Ligands. *Dalton Transactions* **2007**, No. 24, 2547–2562. https://doi.org/10.1039/b702197f.

(96) Wekesa, F. S.; Arias-Ugarte, R.; Kong, L.; Sumner, Z.; McGovern, G. P.; Findlater, M. Iron-Catalyzed Hydrosilylation of Aldehydes and Ketones under Solvent-Free Conditions. *Organometallics* **2015**, *34* (20), 5051–5056. https://doi.org/10.1021/acs.organomet.5b00630.

(97) Brown, L. A.; Wekesa, F. S.; Unruh, D. K.; Findlater, M.; Long, B. K. BIAN-Fe(H6-C6H6): Synthesis, Characterization, and l-Lactide Polymerization. *J Polym Sci A Polym Chem* **2017**, *55* (17), 2824–2830. https://doi.org/10.1002/pola.28688.

(98) Yu, X.; Zhu, F.; Bu, D.; Lei, H. Ferrous Complexes Supported by Sterically Encumbered Asymmetric Bis(Arylimino)Acenaphthene (BIAN) Ligands: Synthesis, Characterization and Screening for Catalytic Hydrosilylation of Carbonyl Compounds. *RSC Adv* **2017**, *7* (25), 15321–15329. https://doi.org/10.1039/c7ra01511a.

(99) Rosa, V.; Carabineiro, S. A.; Avilés, T.; Gomes, P. T.; Welter, R.; Campos, J. M.; Ribeiro, M. R. Synthesis, Characterisation and Solid State Structures of α-Diimine Cobalt(II) Complexes: Ethylene Polymerisation Tests. *J Organomet Chem* **2008**, *693* (4), 769–775. https://doi.org/10.1016/j.jorganchem.2007.12.007.

(100) Gomes, C. S. B.; Gomes, P. T.; Duarte, M. T. α-Diimine Transition-Metal Complexes: Mechanochemistry − A New Synthetic Approach. *J Organomet Chem* **2014**, *760* (3), 101–107. https://doi.org/10.1016/j.jorganchem.2013.11.040.

(101) Maldanis, R. J.; Wood, J. S.; Chandrasekaran, A.; Rausch, M. D.; Chien, J. C. W. The Formation and Polymerization Behavior of Ni(II) α-Diimine Complexes Using Various Aluminum Activators. *Journal of Organometalic Chemistry* **2002**, *645* (1–2), 158–167. https://doi.org/10.1016/S0022-328X(01)01340-7.

(102) Camacho, D. H.; Salo, E. V.; Ziller, J. W.; Guan, Z. Cyclophane-Based Highly Active Late-Transition-Metal Catalysts for Ethylene Polymerization. *Angewandte Chemie - International Edition* **2004**, *43* (14), 1821–1825. https://doi.org/10.1002/anie.200353226.

© University of Pretoria

(103) Liu, H.; Zhao, W.; Hao, X.; Redshaw, C.; Huang, W.; Sun, W. H. 2,6-Dibenzhydryl- N -(2-Phenyliminoacenaphthylenylidene)-4- Methylbenzenamine Nickel Dibromides: Synthesis, Characterization, and Ethylene Polymerization. *Organometallics* **2011**, *30* (8), 2418–2424. https://doi.org/10.1021/om200154a.

(104) Rhinehart, J. L.; Mitchell, N. E.; Long, B. K. Enhancing α-Diimine Catalysts for High-Temperature Ethylene Polymerization. *ACS Catal* **2014**, *4* (8), 2501–2504. https://doi.org/10.1021/cs500694m.

(105) Katla, V.; Yue, E.; Rajendran, N. M.; Liang, T.; Sun, W.-H. Synthesis, Characterization and Ethylene Polymerization of 1-(2,6-Dimethyl-4-Fluorenylphenylimino)-2-Aryliminoacenaphthylnickel Bromides. *Comptes Rendus Chimie* **2016**, *19* (5), 604–613. https://doi.org/10.1016/j.crci.2016.01.005.

(106) Khrizanforova, V. V; Fayzullin, R. R.; Musina, E. I.; Karasik, A. A.; Budnikova, Y. H. Electrochemical and Catalytic Properties of Nickel(II) Complexes with Bis(Imino)Acenaphthene and Diazadiphosphacyclooctane Ligands. *Mendeleev Communications* **2020**, *30* (3), 302–304. https://doi.org/10.1016/j.mencom.2020.05.013.

(107) El-Ayaan, U.; Abdel-Aziz, A. A.-M.; Al-Shihry, S. Solvatochromism, DNA Binding, Antitumor Activity and Molecular Modeling Study of Mixed-Ligand Copper(II) Complexes Containing the Bulky Ligand: Bis[N-(p-Tolyl)Imino]Acenaphthene. *Eur J Med Chem* **2007**, *42* (11–12), 1325–1333. https://doi.org/10.1016/j.ejmech.2007.02.014.

(108) Li, L.; Lopes, P. S.; Figueira, C. A.; Gomes, C. S. B.; Duarte, M. T.; Rosa, V.; Fliedel, C.; Avilés, T.; Gomes, P. T. Cationic and Neutral (Ar-BIAN)Copper(I) Complexes Containing Phosphane and Arsane Ancillary Ligands: Synthesis, Molecular Structure and Catalytic Behaviour in Cycloaddition Reactions of Azides and Alkynes. *Eur J Inorg Chem* **2013**, No. 9, 1404–1417. https://doi.org/10.1002/ejic.201201211.

(109) Ng, Y. Y.; Tan, L. J.; Ng, S. M.; Chai, Y. T.; Ganguly, R.; Du, Y.; Yeow, E. K. L.; Soo, H. Sen. Spectroscopic Characterization and Mechanistic Studies on Visible Light Photoredox Carbon-Carbon Bond Formation by Bis(Arylimino)Acenaphthene Copper Photosensitizers. *ACS Catal* **2018**, *8* (12), 11277–11286. https://doi.org/10.1021/acscatal.8b02502.

(110) Makarov, V. M.; Koptseva, T. S.; Sokolov, V. G.; Dodonov, V. A.; Skatova, A. A.; Baranov, E. V.; Fedushkin, I. L. New Bromine-Containing Bis(Arylimino)Acenaphthenes and Related Metal Complexes. *Russian Journal of Coordination Chemistry/Koordinatsionnaya Khimiya* **2020**, *46* (4), 215–223. https://doi.org/10.1134/S1070328420030045.

© University of Pretoria

(111) Coventry, D. N.; Batsanov, A. S.; Goeta, A. E.; Howard, J. A. K.; Marder, T. B. Synthesis and Molecular Structures of α-Diimines and Their Zinc and Palladium Dichloride Complexes. *Polyhedron* **2004**, *23* (17 SPEC.ISS.), 2789–2795. https://doi.org/10.1016/j.poly.2004.06.023.

(112) Tregubov, A. A.; Vuong, K. Q.; Luais, E.; Gooding, J. J.; Messerle, B. A. Rh(I) Complexes Bearing N, N and N,P Ligands Anchored on Glassy Carbon Electrodes: Toward Recyclable Hydroamination Catalysts. *J Am Chem Soc* **2013**, *135* (44), 16429–16437. https://doi.org/10.1021/ja405783g.

(113) Colby, D. A.; Bergman, R. G.; Ellman, J. A. Rhodium-Catalyzed C-C Bond Formation via Heteroatom-Directed C-H Bond Activation. *Chem Rev* **2010**, *110* (2), 624–655. https://doi.org/10.1021/cr900005n.

(114) Burling, S.; Field, L. D.; Messerle, B. A.; Vuong, K. Q.; Turner, P. Rhodium(I) and Iridium(I) Complexes with Bidentate N,N and P,N Ligands as Catalysts for the Hydrothiolation of Alkynes. *Dalton Transactions* **2003**, *3* (21), 4181–4191. https://doi.org/10.1039/B303774F.

(115) Strydom, I.; Guisado-Barrios, G.; Fernández, I.; Liles, D. C.; Peris, E.; Bezuidenhout, D. I. A Hemilabile and Cooperative N-Donor-Functionalized 1,2,3-Triazol-5-Ylidene Ligand for Alkyne Hydrothiolation Reactions. *Chemistry - European Journal* **2017**, *1* (I), 1393–1401. https://doi.org/10.1002/chem.201604567.

(116) Kleinhans, G.; Guisado-Barrios, G.; Liles, D. C.; Bertrand, G.; Bezuidenhout, D. I. A Rhodium(i)-Oxygen Adduct as a Selective Catalyst for One-Pot Sequential Alkyne Dimerization-Hydrothiolation Tandem Reactions. *Chemical Communications* **2016**, *52* (17), 3504–3507. https://doi.org/10.1039/c6cc00029k.

(117) Bourissou, D.; Guerret, O.; Gabbaï, F. P.; Bertrand, G. Stable Carbenes. *Chem Rev* **2000**, *100* (1), 39–91. https://doi.org/10.1021/cr940472u.

(118) Field, L. D.; Messerle, B. A.; Vuong, K. Q.; Turner, P. Rhodium(I) and Iridium(I) Complexes Containing Bidentate Phosphine-Imidazolyl Donor Ligands as Catalysts for the Hydroamination and Hydrothiolation of Alkynes. *Dalton Transactions* **2009**, *38* (18), 3599. https://doi.org/10.1039/b821188d.

(119) Bikrani, M.; Garralda, M. A.; Ibarlucea, L.; Pinilla, E.; Torres, M. R. Pentacoordinated Cationic Rhodium(I) and Iridium(I) Organocomplexes with α-Diimine Ligands Derived from Glyoxal: Crystal Structure of [Rh(Norbornadiene) (Glyoxalbis(4-Dimethylamino-Anil))-(PPh3)]BF4·1/2CH2Cl2. *Inorganica Chim Acta* **1998**, *282* (2), 230–236. https://doi.org/10.1016/s0020-1693(98)00237-0.

(120) Aucamp, D.; Witteler, T.; Dielmann, F.; Siangwata, S.; Liles, D. C.; Smith, G. S.; Bezuidenhout, D. I. A Triarylated 1,2,3-Triazol-5-Ylidene Ligand with a Redox-Active Ferrocenyl Substituent for

© University of Pretoria

Rhodium(I)-Catalyzed Hydroformylation of 1-Octene. *Eur J Inorg Chem* **2017**, *2017* (9), 1227–1236. https://doi.org/10.1002/ejic.201700164.

(121) Broere, D. L. J.; Plessius, R.; Van Der Vlugt, J. I. New Avenues for Ligand-Mediated Processes-Expanding Metal Reactivity by the Use of Redox-Active Catechol, o-Aminophenol and o-Phenylenediamine Ligands. *Chem Soc Rev* **2015**, *44* (19), 6886–6915. https://doi.org/10.1039/c5cs00161g.

(122) Gunanathan, C.; Milstein, D. Bond Activation and Catalysis by Ruthenium Pincer Complexes. *Chem Rev* **2014**, *114* (24), 12024–12087. https://doi.org/10.1021/cr5002782.

(123) Munz, D. Pushing Electrons - Which Carbene Ligand for Which Application? *Organometallics* **2018**, *37* (3), 275–289. https://doi.org/10.1021/acs.organomet.7b00720.

(124) Luca, O. R.; Crabtree, R. H. Redox-Active Ligands in Catalysis. *Chem. Soc. Rev.* **2013**, *42* (4), 1440–1459. https://doi.org/10.1039/C2CS35228A.

© University of Pretoria

Chapter 2: Rhodium(I) and Iridium(I) BIAN Complexes: Synthesis and Characterisation

2.1) Introduction

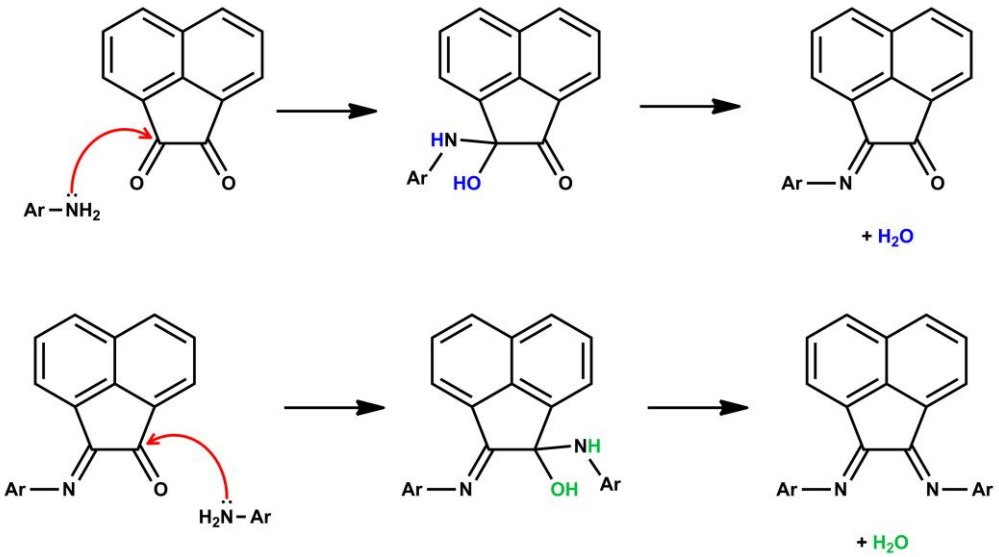
2.1.1) Characteristics and preparation of bis(aryl-imino)acenaphthene compounds

As a unique class among α-diimines ligands, research into bis(aryl-imino)acenaphthene (BIAN) compounds has enjoyed renewed interest in recent years due to the promising redox non-innocent properties they have displayed.[1,2] While the first reports of the synthesis of the BIAN framework dates to the late 1960's, it was not until the 1990's that the use of BIAN derivatives as ligands for the preparation of transition metal complexes gained attention following works published by the research groups of Elsevier, van Asselt and Brookhart.[3–6] The investigations into BIAN coordination complexes were initially focused on the development of homogeneous catalysts which may exploit the sterically hindered coordination sphere, resulting from the bulky aryl-substituents of the BIAN ligand.[3–5,7–9] Emphasis later shifted to the functionalisation of these aryl-substituents to alter the steric and electronic properties of the BIAN ligands and complexes, leading to an extensive library of derivative BIAN ligands and complexes.[1,2,10–12]

Even though the synthetic procedures and characterisation data for numerous variants of BIAN ligands are presently available, solely the 1,2-bis[(2,6-diisopropylphenyl)imino]acenaphthene (DippBIAN, or DB) and 1,2-bis[(2,4,6-trimethylphenyl)imino]acenaphthene (MesBIAN, or MB) archetype ligands are utilised in this study. Not only are these ligands easy to synthesise routinely in high yields, but a large body of judiciously reviewed data is available for the reactivity and physicochemical properties of these ligands with an assortment of first row transition metals, as well as main group metals.[2,13] The results and understanding which may be gleaned from these studies, on the influence that different structural and chemical factors may have on the electronic structure and physicochemical properties of BIAN complexes, form an integral part of the foundation of the present study on new BIAN complexes with late transition metals.

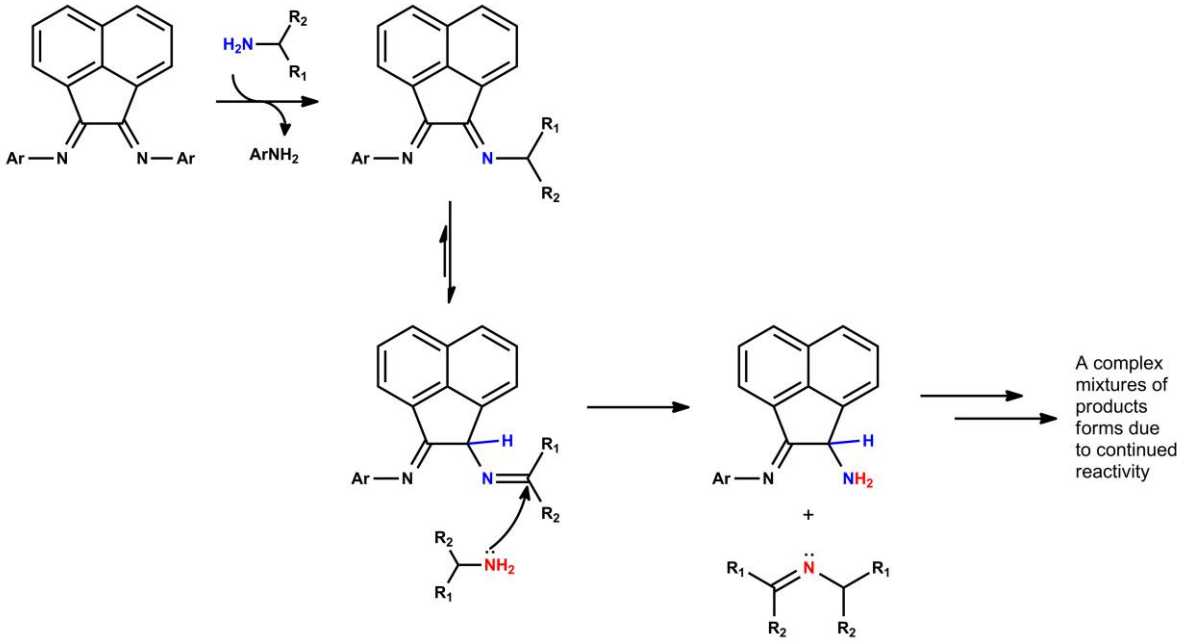
Synthesis of a BIAN ligand is achieved through a double Schiff base condensation of arylamines (Ar-NH_2) with the α-diketone acenaphthalenequinone, with concomitant release of H_2O (Scheme 2.1–1).[14] Symmetrical bis(aryl)-substituted BIAN ligands are by far the most commonly employed in literature, while asymmetrical bis(aryl)-substituted BIAN ligands and mono(aryl)-substituted imine-ketone derivatives have also been reported.[15–20]

© University of Pretoria



Scheme 2.1–1: A simplified reaction scheme depicting the double Schiff base condensation of two arylamines onto acenaphthalenequinone, resulting in the release of two molecules of water.[14]

The successful synthesis and isolation of numerous BIAN ligand derivatives depend heavily on the product's solubility in the reaction medium to affect the Schiff base condensation reactions' equilibrium.[2,21] Selective precipitation of the desired product from the reaction mixture is therefore a prominent feature in many BIAN ligand synthetic methodologies, routinely involving the formation of an intermediate BIAN transition metal complex.[2,21]



Scheme 2.1–2: The transimination reaction mechanism proposed by Ragaini et al.[12] *for the complex mixture of products formed during the attempted syntheses of alkyl-functionalised BIAN ligands. Primary alkylamines with a proton in the α-position to the nitrogen readily enable a hydride-shift reaction with the adjacent sp^2-carbon of the five-membered ring, resulting in a cascade of reactions, and ultimately forming multiple derivative amine products.*

© University of Pretoria

Despite the abundance of aryl-substituted BIAN ligands, only a very limited number of publications were found describing alkyl substituted analogues in the literature. These include the initial reports from the late 2000's involving extremely bulky alkyls such as 1-aminoadamantane and *tert*-butylamine, or sterically strained alkyls such as 1-cyclopropylamine.[12,22,23] The group of Ragaini *et al*. noted that synthetic procedures involving primary or secondary alkylamines,[12] with protons on the α-position relative to the nitrogen, results in transimination reactions between the alkylamines, alkylimines and acenaphthene scaffold (Scheme 2.1–2), ultimately yielding a complex mixture of products.

2.1.2) Coordination complexes of bis(aryl-imino)acenaphthene

As previously noted in Section 1.1.2, BIAN complexes have been synthesised with a wide variety of transition metals in various oxidation states (Figures 1.1–1 and 2.1–1), including:

- 3d metals such as titanium,[24,25] vanadium,[26–28] iron,[29–36] cobalt,[20,37–41] nickel,[5,19,37,39,42–49] copper,[50–58] and zinc;[12,21–23,58–62]
- 4d and 5d metals such as iridium,[10,11,63] palladium,[5,8,9,12,15,17,21,43,44,59,60,64–70] platinum,[65,68,71–76] rhenium,[77–81] rhodium,[6,82–87] and ruthenium;[18,88–91] as well as
- f-block metals such as lanthanum [92,93] and uranium.[93–95]

The initial reports of Rh(I)-BIAN complexes have chiefly been as part of synthetic [6] or catalytic studies,[84] however, the protocols employed to synthesise these complexes were not always reported. In the original thesis by the Rumble,[83] the author details the synthesis of a Rh(I) complex of MesBIAN with a cod co-ligand (Figure 2.1–1.a). In addition, the author notes that although they experienced difficulty in isolating an analogous Rh(I)-MesBIAN dicarbonyl complex $[Rh(MesBIAN)(CO)_2]^+$, they were able to generate and isolate a neutral carbonyl-chloride derivative complex [Rh(MesBIAN)(CO)Cl].[83] Further reports of rhodium BIAN complexes only appeared much later (2019) in the form of water soluble $[Rh(BIAN)(cod)]^+$ complexes (Figure 2.1–1.b),[87] and an octahedral Rh(III)-trichlorido complex of DippBIAN that showed promising electrocatalytic CO_2 reduction ability (Figure 2.1–1.c).[85] The research group of Romashev *et al*.[85,86] also reported the crystal structure and electrochemical characterisation of a neutral [Rh(DippBIAN)(cod)Cl] complex, noting specifically the unusual 5-coordinate molecular geometry and elongated Rh–Cl bond that were observed.

Literature reports of iridium-BIAN complexes are far more limited, however, most reports primarily detail the characterisation of Ir(III)-BIAN complexes that exhibited highly UV-Vis absorptive characteristics and panchromic absorption properties (Figure 2.1–1.d–e).[10,11,63] However, descriptions

© University of Pretoria

of structurally related cationic Rh(I) and Ir(I) α-diimine complexes, featuring Dipp- and Mes-functionalised 1,4-diazabutadiene ligands with cod and $(CO)_2$ co-ligands, were found (Figure 2.1–1.f).[96]

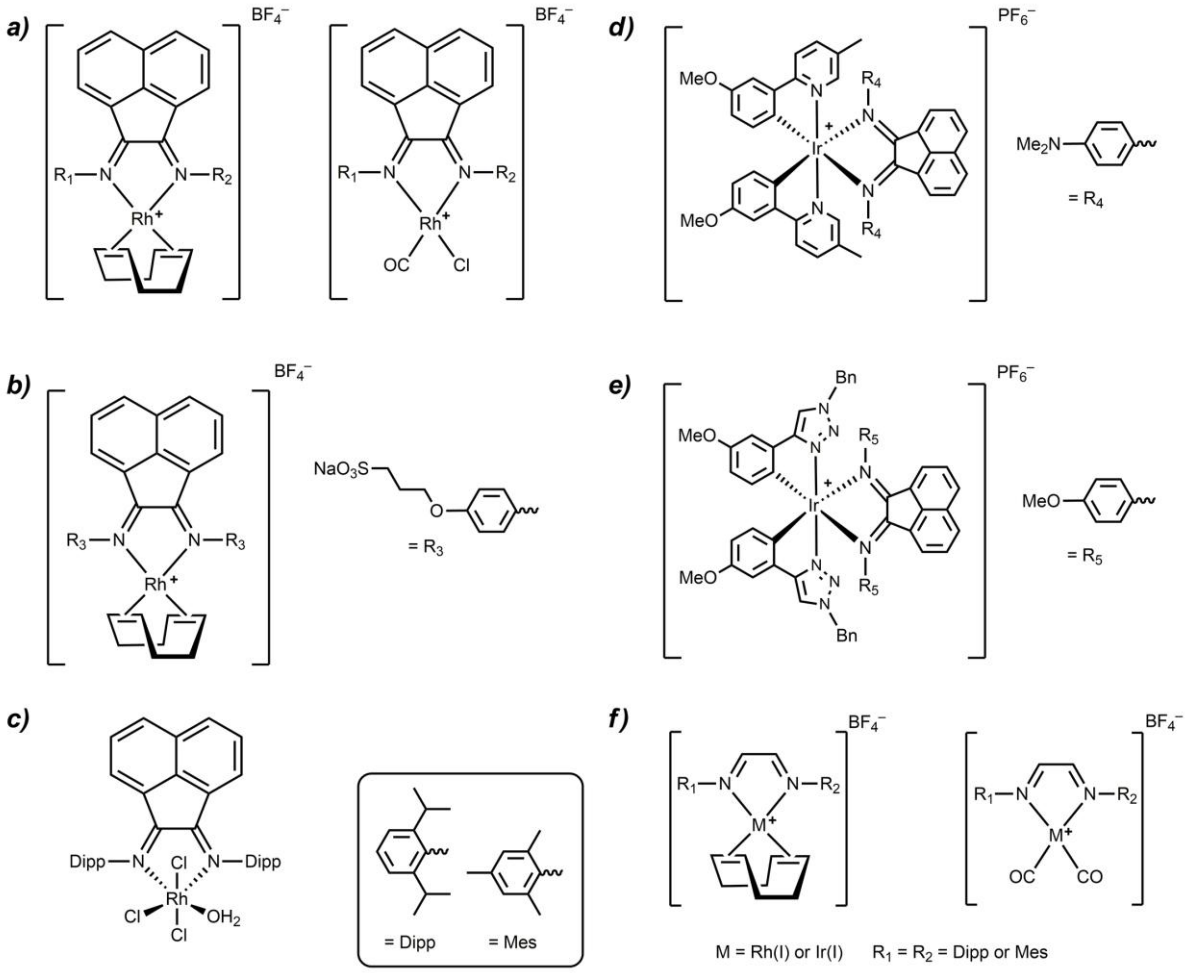


Figure 2.1–1: A selection of rhodium and iridium α-diimine complexes that are structurally related to the BIAN complexes that are targeted in this study, as reported by (a) Rumble et al.,[83,84] (b) Omosun et al.,[87] (c) Romashev et al.,[86] (d and e) Hasan et al.,[10,11,63] and (f) Harding et al.[96]

Limited experimental and reactivity data is available in literature for BIAN complexes of rhodium and iridium in oxidation state +1 specifically, [83–85,87] compared to the number of different BIAN complexes of first row transition metals which have been investigated to date.[5,16,19,20,22–62] This study was prompted by the possibility of combining the robust characteristics of rhodium(I) and iridium(I) catalysts to tolerate a variety of functional groups and exposure to oxygen and/or moisture,[84,97,98] their ability to demonstrate ligand-cooperative or redox-switchable behaviour,[99–101] as well as to mediate multiple catalytic reaction pathways depending on the electronic parameters of the coordination environment,[87,97,102,103] with the known redox non-innocent behaviour of BIAN ligands to facilitate the catalytic reactivity of Rh(I)- and Ir(I)-BIAN complexes.[36,40,104]

© University of Pretoria

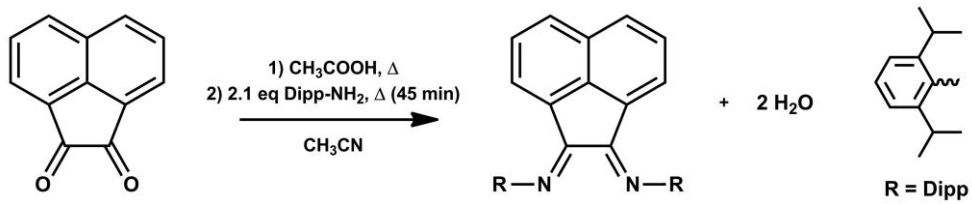
The complexes that were synthesised as part of this work are subdivided into four groups based on the ancillary ligands present. The ancillary ligands were chosen from across the spectrochemical series to include low, mid and high field ligands, and consist of σ-donor/π-donor (chloride), and σ-donor/π-acceptor ligands (1,5-cyclooctadiene, triethylphosphine and carbonyl). Assessment of the characterisation results data of these groups of complexes is anticipated to yield information regarding the impact on the ability of the BIAN ligand to function as a non-innocent ligand.

The synthetic methodologies that were applied in this study, and important experimental observations, will be discussed in Section 2.2 along with comparative discussions on the characterisation of the free Dipp- and MesBIAN ligands, as well as the series of complexes **1**–**4**. Details pertaining to the experimental procedure and characterisation data of the reported compounds are presented in Section 2.5. The NMR, MS, IR, and UV-Vis spectra for the reported compounds, as well as comparative data tables, are presented in Appendix A–D.

2.2) Synthesis Methodologies, Observations, and Characterisation

2.2.1) Dipp- and MesBIAN Ligands

As mentioned in Section 2.1, the synthesis of BIAN compounds involves a double Schiff base reaction between acenaphthalenequinone (AceNQ) and two equivalents of arylamine (aniline). Formation of the imine bonds between the aniline and AceNQ are typically an equilibrium reaction in the acidic reaction conditions. In the reaction between 2,6-diisopropylaniline ($DippNH_2$) and AceNQ, the DippBIAN product quickly precipitates from the solution acting as a thermodynamic driving force favouring product formation (Scheme 2.2–1).[50] The low solubility of DippBIAN compared to other BIAN ligands has been attributed to the steric bulk of the isopropyl substituents hindering accessibility to the polar imine nitrogens for solvent-solute interactions.[21]

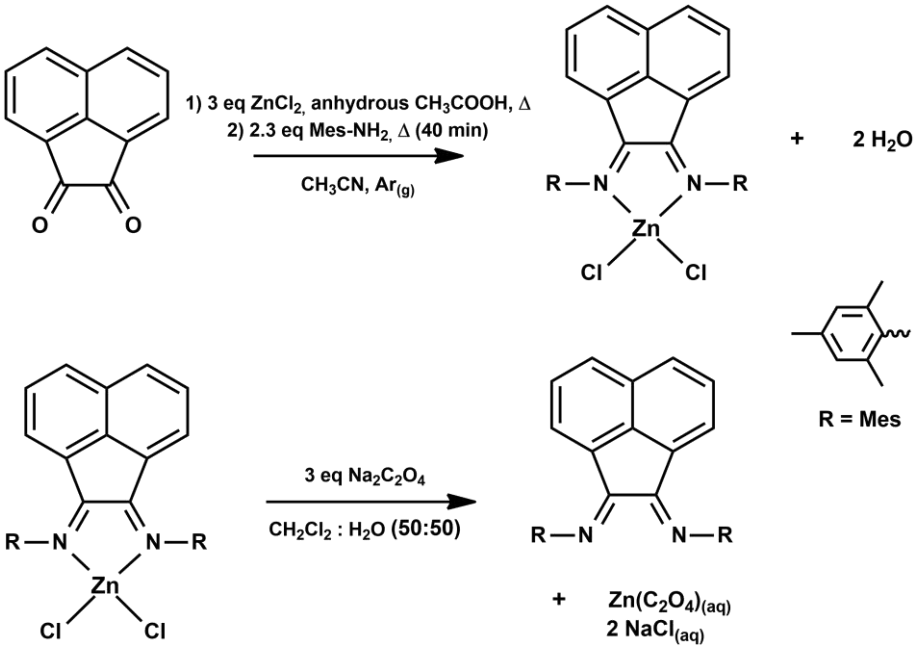


Scheme 2.2–1: Reaction scheme for the synthesis of DippBIAN, adapted from the methods of Paulovikova et al.[50]

The synthesis of other aryl-BIAN derivatives, such as MesBIAN (Scheme 2.2–2), may be readily achieved by introducing an additional reaction step to form an intermediate Zn(II)-BIAN coordination complex that is less soluble in the reaction solvent than the free aryl-BIAN.[2,21] The same

© University of Pretoria

thermodynamic driving force which favoured the formation of DippBIAN may thereby be exploited to achieve greater product yields in the synthesis of other aryl-BIAN derivatives.[2,21] The desired aryl-BIAN is liberated from the intermediate Zn(II)-complex in a subsequent procedure by reaction with aqueous sodium oxalate and extraction with dichloromethane (Scheme 2.2–2).[21] During the reaction workup, however, care must be taken to avoid introduction of any acids to the (CH_2Cl_2:H_2O) emulsion as even trace amounts may be sufficient to initiate rehydration of the imine bonds, reforming two equivalents of the anilines and the acenaphthalenequinone.[21]



Scheme 2.2–2: Reaction scheme for the two-step synthesis of MesBIAN, adapted from the methods of Hasan et al.[2,21]

The observations on the NMR spectra of the free BIAN ligands are briefly reviewed in the interest of informing the characterisation discussion of the complex series **1**–**4** in the following sections. The Dipp- and MesBIAN ligands were isolated as air stable orange and red-orange solids that readily dissolve in CH_2Cl_2, $CDCl_3$ and C_6D_6. The ^1H and ^{13}C NMR spectra recorded for Dipp- and MesBIAN are in good agreement with previously reported results (Table A.2–1 and Table A.2–2 respectively).[2,50]

The ^1H NMR spectra of Dipp- and MesBIAN display a characteristic set of three signals with a "*d-dd-d*" splitting pattern between 8.0–6.5 ppm, associated with the aromatic BIAN–C**H** groups. The pair of doublet-of-doublet (*dd*) signals which are typically observed in the NMR spectra for the (*E*,*Z*)-stereoisomers of symmetrically substituted BIANs or asymmetrically substituted BIANs, present as a single overlapping *dd* signal in the distinctive "*d-dd-d*" splitting pattern observed in the spectra of the (*E*,*E*)-stereoisomers of symmetrically substituted BIANs, as well as symmetrical BIAN coordination complexes.[2,22,56,105,106]

© University of Pretoria

Two sets of doublets are observed for the protons of the isopropyl-CH_3 groups of DippBIAN [Dipp(iso)–C**H**$_3$], integrating for twelve protons each. In addition, two separate Dipp(iso)–**C**H_3 carbon signals (at 23.5 and 23.3 ppm) are also observed, indicating that the isopropyl-CH_3 groups occupy two distinct electronic environments. Due to the rigid nature of the imine double bonds and the molecular geometry of the (*E*,*E*)-DippBIAN stereoisomer, the two electronic environments may be described as the methyls either pointing away from the aryl and acenaphthene moieties, or towards the main acenaphthene plane (a sterically less favourable environment). The ^{1}H spectra of MesBIAN displayed a pair of singlets (at 2.37 and 2.12 ppm) which integrate for six and twelve protons respectively. These peaks correspond to the *para*- and *ortho*-methyl groups in turn. As expected, the electronegative nitrogen atoms deshield the adjacent BIAN and aryl quaternary carbons (BIAN–N=**C**$_q$ and Ar–N–**C**$_q$), resulting in a downfield shift of their ^{13}C NMR signals relative to the aromatic BIAN–**C**H and Ar–**C**H signals (Table A.2–2).

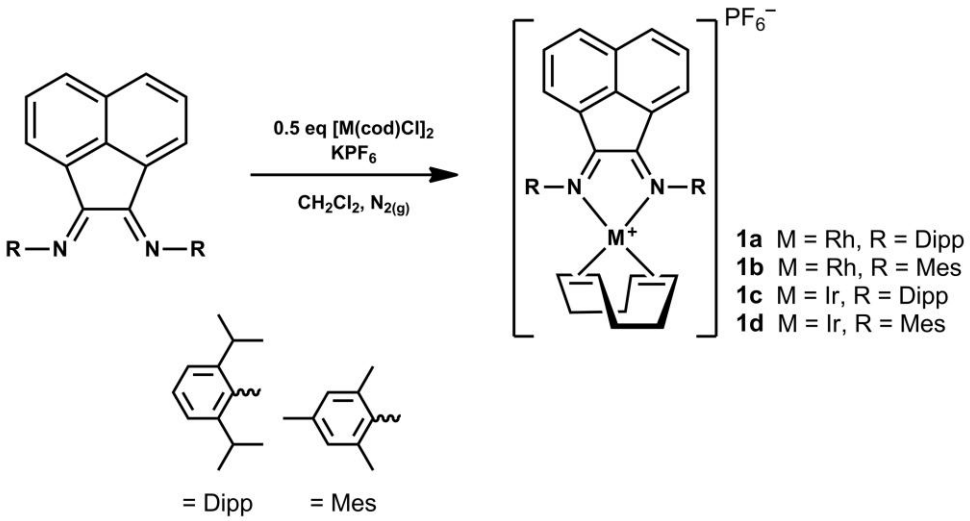
The IR and UV-Vis spectroscopic data for the free Dipp- and MesBIAN ligands are in good agreement with previously reported data (Figures C.1–1, C.1–2, D.1–1 and D.1–2).[2,50] Moderate intensity IR absorbance bands were observed in the 1680–1580 cm^{-1} range, which are attributable to the stretching vibrations of the C=N bonds (Table C.2–1).[2,50] The UV-Vis spectra of the free ligands in CH_2Cl_2 showed a strong, high energy absorption band at 231 nm; two moderate intensity absorptions bands between 270–300 nm; a moderate intensity shoulder band around 325 nm; and a low energy, weak absorption band around 421 nm (Table D.2–1). Assignments of the absorption transitions have been done in accordance with computationally supported literature data.[2] The high energy absorptions between 200–310 nm may be assigned as ligand-centred π-π* transitions, originating from both the acenaphthene rings and aryl-substituents.[2] The lower energy absorptions in the 320–450 nm range are likely the result of intraligand charge transfer (ILCT) transitions between the arylimine moieties and acenathphene rings.[2,50]

2.2.2) Rh(I) and Ir(I) BIAN complexes with ancillary 1,5-cyclooctadiene ligand: 1a–d

The Rh(I) and Ir(I) 1,5-cyclooctadiene complexes with DippBIAN (**1a**, **1c**) and MesBIAN (**1b**, **1d**) were synthesised by means of a concurrent ligand addition and anion substitution reaction (Scheme 2.2–3). The admixtures of the free ligands, KPF_6, and the respective metal cod-chloride dimer in a CH_2Cl_2 solution were stirred overnight to allow sufficient time for the large metallic cations to coordinate to the sterically encumbered BIAN ligands. The colour of the rhodium reaction mixtures slowly changed from orange to brown as the reaction progressed, whereas the iridium reactions changed colour from orange to dark green. It was noted that the amount of time required for the

© University of Pretoria

1c–**d** reaction solutions to exhibit a visible colour change was nearly double the amount of time required for the **1a**–**b** reaction solutions under the same experimental conditions. The delay in reactivity between the Ir(I)-centre and BIAN ligand may be due to a greater degree of steric strain experienced by the larger Ir(I)-cation from the aryl-substituents of the ligand. The solids and solution were separated by cannula filtration, after which the Rh(I) complexes **1a** and **1b** were isolated as brown solids, and the Ir(I) complexes **1c** and **1d** as dark green solids.



*Scheme 2.2–3: Reaction scheme for the synthesis of cationic BIAN complex series **1a–d**, containing a 1,5-cyclooctadiene ancillary ligand.*

Coordination of the Dipp- and MesBIAN ligands to the Rh(I)-cod (**1a**, **1b**) and Ir(I)-cod (**1c**, **1d**) metal centres resulted in the expected downfield shift of all ^{1}H peaks associated with the BIAN ligands (Table A.2–1). The peak separation between the characteristic "*d-dd-d*" BIAN–C**H** peaks is increased following coordination, occurring between 8.4–6.4 ppm for complex series **1a**–**d**. The Dipp–Ar–C**H** signals in **1a** and **1c** no longer overlap as observed for the free ligand (Table A.2–1), instead presenting as two distinct signals. In addition to the characteristic "*d-dd-d*" BIAN–C**H** peaks, the olefinic cod-C**H** signals in **1a**–**d** are observed as single broad peaks, indicating that the complexes adopt a symmetric molecular geometry in solution

The ^{13}C peaks for the complex series **1a**–**d** don't show the same extent of downfield shifts as observed in the ^{1}H NMR spectra (Table A.2–2). The quaternary BIAN–N=**C**$_q$ are notably deshielded by the σ-donation of the nitrogens to the metal centre, resulting in a downfield shift of ≥ +14 ppm relative to the free DippBIAN. Interestingly, the chemical shift of Ar–N–**C**$_q$ in the series of Rh(I) complex series **1a**–**b** is nearly unchanged compared to the free ligands, whereas an upfield shift of *ca*. 10 ppm is noted for the Ir(I) complex series **1c**–**d**. The chemical shifts recorded for the coordinated cod–**C**H in the series

© University of Pretoria

of complexes **1a**–**d** are in good agreement with previously reported values for rhodium(I) and iridium(I) complexes.[83,85,96,107] As expected, the cod–**C**H for the series of complexes **1a**–**b** presented as doublets due to spin coupling between NMR-active ^{13}C and ^{103}Rh nuclei.[6,102,108,109]

Weak intensity C=N vibration bands were observed in the 1670–1550 cm^{-1} range for complex **1c**, comparable to the vibrations observed for previous DippBIAN complexes (Table C.2–1).[50,96] The C=N vibration bands of complexes **1a**, **1b** and **1d** show a larger decrease in wavenumber relative to those recorded for the free ligands,[50,96] indicating the partial weakening of the C=N bond in the bisimine moiety after coordination to the metal centre. In addition, the series of complexes **1a**–**d** displayed strong absorption bands near 835 cm^{-1} and 555 cm^{-1} which are associated with the PF_6^- counter ion.

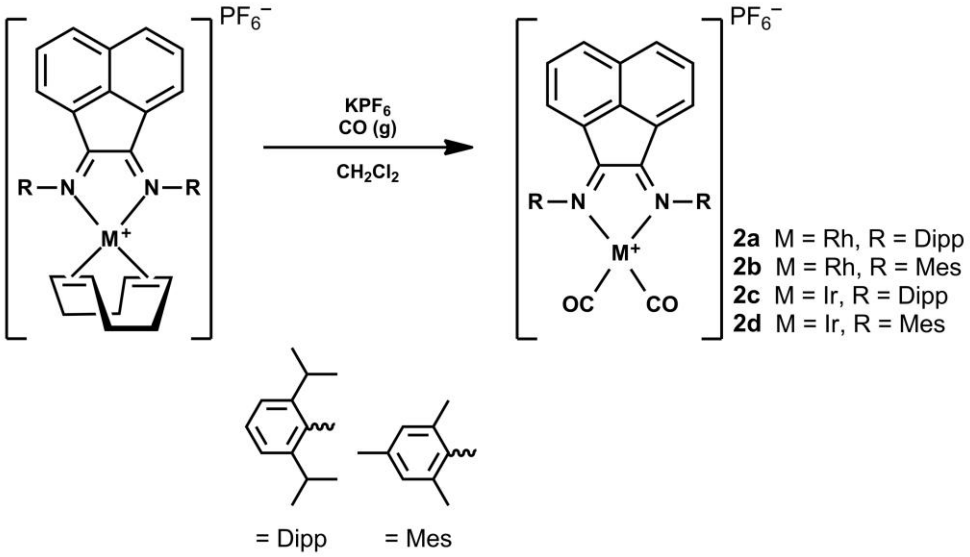
In the UV-Vis spectra of the complex series **1a**–**d**, strong, high-energy absorption peaks were observed in the 230–232 nm range comparable to the ligand-centred π-π* transitions noted in the spectra of the free ligands.[2] Moderate intensity absorption bands were noted for complex **1a** at 272 nm, and at 268 nm for complex **1b** (with a shoulder peak visible at 275 nm). In contrast, the Ir(I) complexes **1c**–**d** displayed two moderate intensity absorption bands in the 270–300 nm range that are comparable to those observed for the free ligands. The lower energy ILCT transitions that are noted in the spectra of complexes **1a**–**b** and **1d**, in the range 330–435 nm, are red-shifted relative to the ILCT transitions which were observed in the free ligands. Interestingly, low intensity absorptions were observed in the spectra of the Ir(I) complexes **1c**–**d** around 669 nm, which may be assigned as metal-to-ligand charge transfer (MLCT) transitions.[35,50,90]

2.2.3) Rh(I) and Ir(I) BIAN complexes with ancillary dicarbonyl ligands: 2a–d

The series of complexes **2a**–**d** was synthesised either from previously isolated portions of the corresponding series of cod-complexes **1a**–**d** (Scheme 2.2–4), or alternatively from *in situ* generated aliquots of complexes **1a**–**d** with direct treatment of the reaction mixtures (see Scheme 2.2–3) with CO (g) (Scheme 2.2–4) and trituration of the desired product with hexanes. Similar yields were obtained when using either isolated or *in situ* generated complexes **1a**–**d** as precursors, thus the more convenient *in situ* route was employed to circumvent the process of isolating complexes **1a**–**d**. The solids thus obtained were washed with hexane, while maintaining a CO(g) atmosphere. The relative reaction times required to synthesise each of the derivatives were similar, however, the intense colouration of the Ir(I) complexes' reaction solutions impeded visibility of the precipitated product during the reaction workup. Complexes **2a** and **2c** were isolated as dark brown solids, and complexes **2b** and **2d** were iridescent brown solids. It was noted that complexes in the series **2a**–**d** showed signs

© University of Pretoria

of decomposition in solution (e.g., discolouration) when exposed to atmospheric conditions for prolonged periods of time.



*Scheme 2.2–4: Reaction scheme for the synthesis of cationic BIAN complex series **2a–d**, bearing two carbonyl ancillary ligands.*

The ^{1}H NMR signals and splitting patterns for the series of complexes **2a**–**d** (Table A.2–1) appear overall similar to those of the complex series **1a**–**d** (Table A.2–1). The influence of the π-acceptor carbonyl ancillary ligands is, however, evident in the 10–30 ppm downfield shift of the proton peaks. Retention of the characteristic BIAN–C**H** peaks' "*d-dd-d*" splitting pattern observed in the spectra of the free Dipp- and MesBIAN ligands (Table A.2–1), among other features, indicate that the complexes likely adopt a symmetrical coordination geometry.[56,106] It is interesting to note that the Mes-aryl substituents in complexes **2b** and **2d** experience greater deshielding of the *para*-position Mes–C**H**$_3$ than in complexes **1b** and **1d**, resulting in a single Mes–C**H**$_3$ signal that integrates for 18 hydrogens.

A fully resolved ^{13}C NMR spectrum for **2c** could not be obtained, even after prolonged acquisition times. The quaternary BIAN–N=**C**$_q$ of **2a** and **2b** are shifted *ca*. 17 ppm downfield (Table A.2–2), relative to their recorded shifts in the free ligands (Table A.2–2). In contrast to the strong deshielding observed for BIAN–N=**C**$_q$ in the series of Ir(I) complexes **1c**–**d** (Table A.2–2), the downfield shift for **2d** is decreased appreciably to 7 ppm. However, the BIAN–**C**H and Ar–N–**C**$_q$ signals of **2d** show a significant downfield shift relative to those of **1d**. The chemical shifts of the carbonyl Ir–**C**O and Rh–**C**O signals (*ca*. 180 ppm) correlate well with previously reported values for Ir(I) and Rh(I) complexes, and the Rh–**C**O signals of complexes **2a** and **2b** presented as a set of doublets ($J_{C–Rh}$ = 70. 3 Hz and 70.1 Hz respectively) due to spin coupling between the carbonyl ^{13}C and ^{103}Rh(I) nuclei. [6,83,85,96,102,107–109]

© University of Pretoria

The presence of two carbonyl ancillary ligands were confirmed by the IR transmittance spectra of complex series **2a**–**d**. Two bands were observed between 2100–2000 cm^{-1} corresponding to the in-phase and out-of-phase bending motions of two *cis*-coordinated carbonyl ligands (Table C.2–1). The carbonyl stretching frequencies of the series **2a**–**b** occur at slightly higher wavenumbers than those of the **2c**–**d** series, indicating enhanced π-backbonding in the Ir–CO interactions compared to the analogous Rh–CO due to the iridium's π-basic character. The ν(C=N) bands of complex series **2a**–**b** are very similar in intensity and wavenumber to those of the **1a**–**b** series. Overall, the upper limit wavenumbers determined for the ν(C=N) band in complex series **2a**–**d** are lower than those of the free ligands, indicating a partial decrease in the C=N bond strength after coordination. As noted for the complex series **1a**–**d** in Section 2.2.2, the vibrational bands that are observed in IR spectra of the complex series **2a**–**d** at 833 cm^{-1} and 555 cm^{-1} confirm the presence of the PF_6^- counter ion.

A strong, high energy absorption peak is observed in the UV-Vis spectra of the complex series **2a**–**d** around 231 nm, comparable to that of the free ligands and the complex series **1a**–**d**. Moderate intensity absorptions were noted between 265–290 nm, which is slightly blue-shifted compared to the moderate intensity ligand-centred π-π* transitions of the free ligands.[2] While all the complexes in the series **2a**–**d** showed a moderate ILCT transition around 336 nm, only complexes **2b**–**d** showed additional ILCT transitions in the range 340–430 nm.[2,50] In addition, Ir(I)-DippBIAN complex **2c** was the only dicarbonyl analogue to show a MLCT transition, localised about 598 nm as a low intensity peak.[35,50,90]

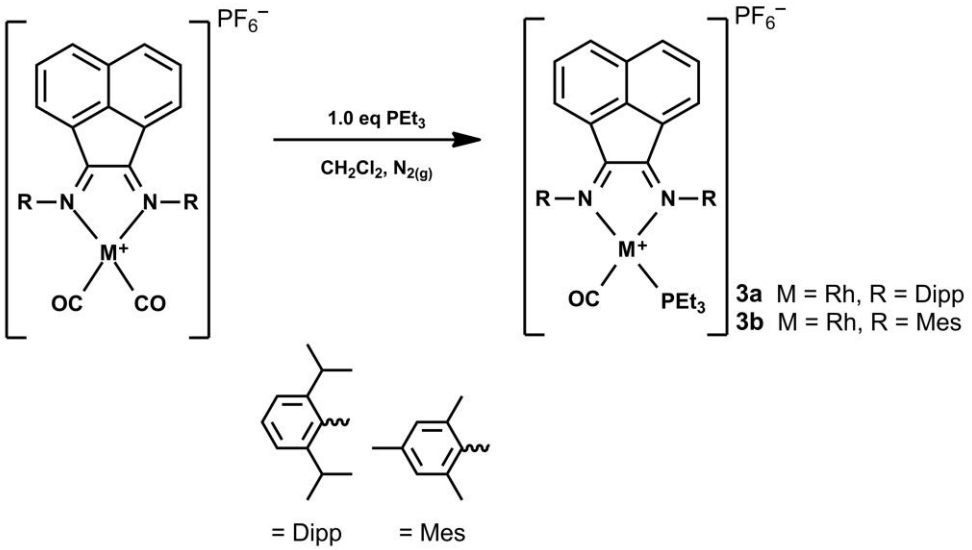
2.2.4) Rh(I) and Ir(I) BIAN complexes with ancillary triethylphosphine and monocarbonyl ligands: 3a–b

The asymmetric Rh(I) triethylphosphine (PEt_3) complexes of DippBIAN (**3a**) and MesBIAN (**3b**) were synthesised from the purified dicarbonyl complexes **2a** and **2b** respectively (Scheme 2.2–5). Complexes **2a**–**b** were noted to react with PEt_3 immediately after the first portion of reagent was added since a colour change in the reaction mixture from dark brown to deep purple was observed. The phosphine reagent was dispensed sparingly into dilute reaction mixtures to minimise the probability of substituting both carbonyl ligands on the metal centre. The series of complexes **3a**–**b** were isolated as purple solids.

The synthesis of analogous Ir(I) Dipp- and MesBIAN complexes were also attempted. The reaction solutions of these two complexes exhibited a similar deep-purple colour to what was observed during the synthesis of series **3a**–**b**, however, the Ir(I)-BIAN phosphine complexes could not be isolated with

© University of Pretoria

sufficient purity to establish definitive characterisation. The purple solids that were isolated during the Ir(I)-BIAN phosphine synthesis attempts proved to be highly reactive when not under an inert atmosphere, decomposing over time in both solution and solid state.



*Scheme 2.2–5: Reaction scheme for the synthesis of cationic BIAN complex series **3a–b**, with a carbonyl and triethylphosphine as ancillary ligands.*

As mentioned in Section 2.3.1, the ^{1}H NMR spectra of symmetrical BIAN–coordination complexes display a characteristic "*d-dd-d*" splitting pattern for the BIAN–C**H** peaks. As much as this presence of this pattern was diagnostic in the successful characterisation of complex series **1**–**2**, it is the absences of these features in the NMR spectra of complex series **3a**–**b** that are distinctively informative.[56,105,106]

Interpretation of the ^{1}H and ^{13}C NMR spectra of **3a**–**b** proved non-trivial, and the peak assignments have been made using additional 2D NMR techniques. The BIAN–C**H** peaks of **3a**–**b** are spread between 8.3–6.3 ppm as five separate peaks (Figure A.1–20 and A.1–23), the most downfield of which integrates for two protons. The Ar–C**H** peaks of the Dipp- and Mes-substituents overlap to some extent with the BIAN–C**H** peaks between 7.6–7.4 ppm (Table A.2–1). The Dipp(iso)–C**H** signals of **3a** appear as a pair of septets shifted downfield relative to free DippBIAN, by 0.5 and 0.2 ppm respectively, indicating that the two aryl-substituents are not in equivalent electronic environments. The observation of four sets of Dipp(iso)–C**H$_3$** signals, reaffirms this observation. The Mes–C**H$_3$** signals of complex **3b** displayed similar disparity and were observed as five peaks between 2.6–2.3 ppm. Interestingly, two of the Mes–C**H$_3$** signals displayed through-space coupling to the PEt_3 ligand, presenting a doublet and multiplet that integrates for 3 hydrogens each.

© University of Pretoria

The two aryl-substituents of **3a**–**b** experience divergent electronic environments due to steric interactions between their *ortho*-substituents and the ethyl fragments of the PEt_3, in addition to the *trans* influence exerted by the CO and PEt_3 ancillary ligands.[6,109–113] The protons of the aryl-substituent *trans* of the stronger π-acid CO are expected to be more deshielded than those *trans* of the PEt_3.[6,109–113] Thus, the Mes-substituent which displayed through-space coupling to the PEt_3 ligand must be *trans* of the CO ancillary ligand.[6,109–113]

The large number of unique carbon signals observed in the ^{13}C NMR spectra of **3a**–**b** provided additional confirmation of the asymmetric molecular geometry of these complexes (Figure A.1–21 and A.1–24). The BIAN–N=**C**$_q$ signals of **3a**–**b** show a downfield shift of *ca*. 10 ppm compared to the free ligands, while the Ar–N–**C**$_q$ of **3a** show a minor 3 ppm upfield shift. The Ar–N–**C**$_q$ of **3b** could not be definitively identified. The chemical shift for the aromatic BIAN–**C**H and Ar–**C**H peaks of series of complexes **3a**–**b** (Table A.2–2) relate closely to the results obtained for the series of complexes **1a**–**d** (which featured σ-donor and weak π-acceptor cod ligands) as well as the **2a**–**d** series (with ancillary carbonyl ligands that exhibit σ-donor and strong π-acceptor properties).

The Rh–**C**O peak of **3a** was observed at 177.26 ppm as a doublet due to spin coupling between the ^{13}C and $^{103}Rh(I)$ nuclei.[6,83,85,96,102,107–109] The Rh–**C**O peak of **3b** presented as a peak at 177.6 ppm, however, coupling between the ^{13}C and $^{103}Rh(I)$ nuclei was not observable due to the low intensity of the signal. [6,83,85,96,102,107–109] The chemical shifts associated with the monocarbonyls of **3a**–**b** are in line with previously reported values for Rh(I) complexes bearing phosphine ligands.[113] The presence of the two very π-acidic carbonyl ligands in **2a**–**b**, compared to **3a**–**b** with one carbonyl ligand and one more basic/weaker π-acceptor phosphine ligand, results in an overall more electron-deficient complex cation with consequent greater deshielding of the carbonyl carbon atom resonances observed in the downfield ^{13}C NMR shifts of **2a**–**b**, compared to **3a**–**b**.

The phosphine PEt_3–**C**H_2 peaks were also observed as doublets, with coupling constants comparable to literature values,[109,114,115] due to spin coupling between the ^{13}C and ^{31}P nuclei. The chemical shift for the phosphine PEt_3–**C**H_3 peaks was surprisingly upfield between 8.5–5.8 ppm. The ^{31}P MNR spectra of complex series **3a**–**b** displayed a doublet for the coordinated PEt_3 ligand at 28–30 ppm ($J_{P–Rh}$ = 142 Hz),[115,116] and a septet at –144 ppm ($J_{P–F}$ = 712 Hz) associated with the PF_6^- anion (Figures A.1–22 and A.1–25).[109]

© University of Pretoria

The successful substitution of one carbonyl ligand by PEt_3 was confirmed by the presence of only a single Rh–CO vibrational frequency peak in the IR spectra of the complex series **3a**–**b** (Table C.2–1), which is observed *ca*. 100 cm^{-1} lower than the ν(C=O) bands of complex series **2a**–**b** (Table C.2–1). The C=N and P–F vibrations of **3a**–**b** are comparable to those observed for the series of complexes **1a**–**b** and **2a**–**b** in terms of their relative intensity and wavenumber (Table C.2–1). Due to the large number of peaks in the fingerprint region of the IR spectra (1500–500 cm^{-1}), characteristic P–C vibrations could not be conclusively assigned (Figures C.1–11 and C.1–12).

The UV-Vis spectra of the phosphine complex series **3a**–**b** showed a strong, high-energy absorption at 229 nm as well as a moderate intensity absorption at 269 nm that may be assigned to ligand-centred π-π* transitions (Table D.2–1).[2] Two moderate intensity absorption bands are observed at 337 nm and 427 nm, which may be assigned as ILCT transitions.[2,50] The π-π* transitions of series **3a**–**b** are slightly blue-shifted, and the ILCT transitions slightly red-shifted, relative the same transition bands in the spectra of the free ligands and the Rh(I)-DippBIAN complexes **1a** and **2a** (Table D.2–1). The transitions of the series **3a**–**b** correspond more closely with the absorption bands observed in the spectra of the Rh(I)-MesBIAN complexes **1b** and **2b**.

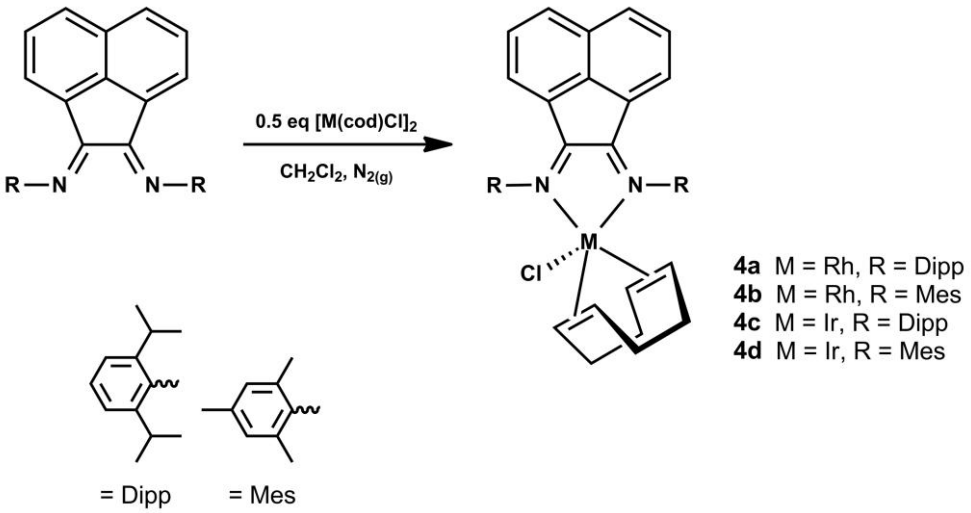
2.2.5) Rh(I) and Ir(I) BIAN complexes with ancillary 1,5-cyclooctadiene and chlorido ligands: 4a–d

Neutral, 5-coordiante chlorido derivatives of the series of Rh(I) and Ir(I) 1,5-cyclooctadiene (cod) complexes with DippBIAN (**4a**, **4c**) and MesBIAN (**4b**, **4d**) were synthesised in a procedure similarly to that employed for the complex series **1a**–**d**. The reaction between free Dipp- and MesBIAN ligands with Rh(I) (**4a**, **4b**) and Ir(I) (**4c**, **4d**) cod-chloride dimers in the absence of an anion exchange reagent (e.g. KPF_6) were projected to yield 5-coordinate neutral complexes (Scheme 2.2–6).[85,114] The reaction mixtures slowly changed colour from bright orange suspensions to dark green and dark blue solutions for Rh(I) and Ir(I) respectively. The non-coordinating solvents CH_2Cl_2 and $CDCl_3$ were purposely utilised to preclude substitution of the chlorido ligand during reaction and analysis conditions, as previously observed by Romashev *et al*. for acetonitrile solutions of [Rh(DippBIAN)(cod)Cl].[85]

Purification of **4a**–**d** presented a greater challenge than the other complexes due to their partial solubility in less polar solvents such as hexane and diethyl ether. After chromatographic purification using CH_2Cl_2 and EtOH, complexes in the series **4a**–**b** and **4c**–**d** were isolated as dark green and dark blue solids. It was noted that the series of complexes **4a**–**d** showed signs of decomposition in the solid

© University of Pretoria

state (e.g., discolouration) over the course of several weeks, and slowly decomposed in solution, when exposed to atmospheric conditions.



*Scheme 2.2–6: Reaction scheme for the synthesis of neutral BIAN complex series **4a–d**, with a 1,5-cyclooctadiene and chloride as ancillary ligands.*

The ^{1}H NMR spectra of the MesBIAN complexes **4b** and **4d** display the characteristic "*d-dd-d*" BIAN–C**H** and singlet Mes–C**H** patterns which were noted for the complexes **1b** and **1d** (Section 2.2.2), as well as a single olefinic cod-C**H** signal between 4.0–3.7 ppm, which indicate that complexes **4b** and **4d** adopt a symmetrical molecular geometry in solution (Table A.2–1). The chemical shifts of all proton peaks for **4d** are shifted upfield relative to those recorded for **1d** (Table A.2–1), indicating an increased degree of shielding across the MesBIAN ligand of **4d**. The increased shielding of the BIAN ligand suggests that the π-donor chlorido ligand increases the electron density on the Ir(I)-centre, resulting in a partially decreased N–Ir σ-donation interaction compared to complex **1d**.

A similar upfield shift is observed between **4b** and **1b**, however, the *ortho*-C**H$_3$** signals of **4b** are observed downfield from the *para*-C**H$_3$** signals (Figure A.1–28). Even though both **4b** and **4d** bear the same ligands in a 5-coordinate geometry, the smaller ionic radius of Rh(I) compared to Ir(I) would result in a more sterically congested coordination centre for complex **4b**. The apparent inversion of the chemical shifts for the *ortho*- and *para*-C**H$_3$** signals are unique to complex **4b** and may be attributed to steric interference between the *ortho*-C**H$_3$** groups with the cod and chlorido ancillary ligands.

As noted for **4b** and **4d**, the splitting patterns observed on the ^{1}H NMR spectra of **4c** suggest that the complex adopts a largely symmetrical molecular geometry in solution. However, the presence of two separate Dipp–Ar–C**H** peaks, as well as six individual ^{13}C BIAN–**C**H peaks (Table A.2–2), indicate that

© University of Pretoria

the electronic environment around the DippBIAN ligand and its two aryl-substituents may not be distributed equivalently with the molecular geometry (Section 2.3.4).

The ^{1}H and ^{13}C NMR splitting patterns observed for **4a** appear very similar to those of the asymmetric complex series **3a**–**b**, with six individual signals for each BIAN–C**H** proton and four distinct Dipp(iso)–C**H$_3$** signals (Table A.2–1), illustrating the inequivalence in the electronic environment for the two Dipp-substituents. In addition, the ^{13}C NMR of **4a** displayed six unique Dipp–Ar–**C**H peaks (Table A.2–2). As noted for **4b**, the smaller ionic size of the Rh(I)-cation compared to Ir(I) is expected to result in a sterically overcrowded coordination centre where the isopropyl substituents in **4a** must compete for space around the metal centre with the cod- and chloro and ancillary ligands. Unlike the Mes–CH$_3$ groups, however, the Dipp(iso)–CH groups are able to alleviate some steric strain by rotation of the isopropyl group to minimal energy gauche interactions between the Dipp(iso)–C**H$_3$** and ancillary ligands.

The cod–**C**H signals for **4b** showed spin coupling between the ^{13}C and ^{103}Rh nuclei and presented chemical shifts and coupling constants which correlate well with previously reported values (Table A.2–2).[83,85,96,102,107,108] Interestingly, two cod–**C**H signals were observed for **4a** as a doublet and doublet-of-doublets respectively. The unexpected carbon splitting and coupling pattern is the result of the strained coordination sphere of the complex. The quaternary BIAN–N=**C$_q$** signals of the complex series **4a**–**d** are shifted upfield relative to those observed for the series **1a**–**d** (Table A.2–2), but are still downfield relative to the values recorded for the free ligands. The Ar–N–**C$_q$** peaks of the complex series **4c**–**d** are shifted downfield by *ca*. 5 ppm relative to **1c**–**d** series, whereas the Ar–N–**C$_q$** peak of complex **4b** and second Ar–N–**C$_q$** peak of **4a** are shifted upfield compared to their cationic analogues (complex series **1a**–**b**). Interestingly, the chemical shifts of the second BIAN–N=**C$_q$** peak, and first Ar–N–**C$_q$** peak, of complex **4a** are near identical to those of the free DippBIAN ligand.

The lack of any signals in the ^{19}F and ^{31}P NMR spectra, as well as the absence of the strong P–F vibrational bands at 833 cm^{-1} and 555 cm^{-1} in the IR spectra of the series complexes **4a**–**d**, confirm the absence of PF_6^- counter ions in these complexes compared to the cationic series of complexes **1a**–**d**. Weak to moderate intensity C=N vibration bands were observed in the IR spectra for the complex series **4a**–**d** in the 1670–1540 cm^{-1} range (Table C.2–1). The C=N vibrations of the Ir(I) complexes **4c** and **4d** are shifted to lower wavenumbers compared to that of complex **4b**, indicating a more pronounced weakening of the C=N bond in complexes **4c**–**d** after coordination to the metal centre than in **4b**.[50,96] The C=N vibrations of **4b** are comparable to those of **1b**, whereas those of **4c**–**d** are

© University of Pretoria

comparable to those of **1d**. Interestingly, the C=N vibrations of the Rh(I)-DippBIAN complex **4a** show a small decrease in wavenumber compared to that of the free DippBIAN ligand, and are in closer agreement with the values recorded for the Ir(I)-DippBIAN complex **1c**.

The UV-Vis spectra of the complex series **4a**–**d** showed a strong, high-energy absorption peak at 231 nm which closely parallels the observations for the free ligands and complex series **1a**–**d**. Complexes **4a**, **4c** and **4d** displayed a moderate intensity absorption band in the 270–290 nm range, with a shoulder band around 313 nm which may be assigned as ligand-centred π-π* transitions. In contrast, the moderate intensity π-π* transitions of **4b** are slightly blue-shifted and are observed between 265–278 nm. The ILCT transitions of the Rh(I) complexes **4a**–**b** were observed around 327 nm and 422 nm, whereas the Ir(I) complexes **4c**–**d** only displayed a single ILCT transition around 402 nm. However, two MLCT transitions were observed in the spectra of the Ir(I) complexes around 466 nm and *ca*. 680 nm. Interestingly, the lower-energy MLCT transitions of complexes **4c**–**d** (i.e., around 680 nm) have the highest absorptivity among all of the MLCT transitions recorded for the series of complexes **1**–**4**.

2.3) Single crystal XRD

Single crystals suitable for XRD analysis were prepared through slow evaporation of CH_2Cl_2 or $CDCl_3$ solutions of complexes **1b**, **1d**, **2a**, **2b**, **2c**, **3a** and **4c**. The molecular structures for these complexes are shown in Figures 2.3–1 to 2.3–7, with hydrogen atoms and PF_6^- anions excluded for the sake of clarity. Additional crystallographic data and parameters are also presented in Appendix E.1. A selection of experimental bond lengths, bond angles and dihedral angles are presented in Tables E.2–1 to E.2–3 in Appendix E.2. For comparative purposes, selected bond lengths, bond angles and dihedral angles from the computationally optimised molecular geometries of complexes **1b**, **1d**, **2a**, **2b**, **2c**, **3a** and **4c**, *vide infra*, are included in the discussions below and Tables E.2–1 to E.2–3. The computational methodology and results pertaining to the DFT modelling will be discussed in Chapter 4.

When considering the centre of each cod-alkene bond as a measuring point, the coordination geometry of the four coordinate complexes are described in terms of the τ_4 geometry index as defined by Yang *et al*.,[117] where τ_4 = 0.00 represents square planar coordination geometry and τ_4 = 1.00 tetrahedral coordination.[118] Similarly, the geometry of the five coordinate complex **4c** is described using the τ_5 geometric parameter for which τ_5 = 1.00 denotes a trigonal bipyramidal geometry and τ_5 = 0.00 a square pyramidal coordination sphere.[117,119]

© University of Pretoria

2.3.1) **1b** [RhMB(cod)]PF_6

The hexagonal symmetry crystals of complex **1b** (space group $P6_522$) presented a slightly distorted square planar coordination geometry (τ_4 = 0.08) which is often observed for Rh(I) complexes (Figure 2.3–1).

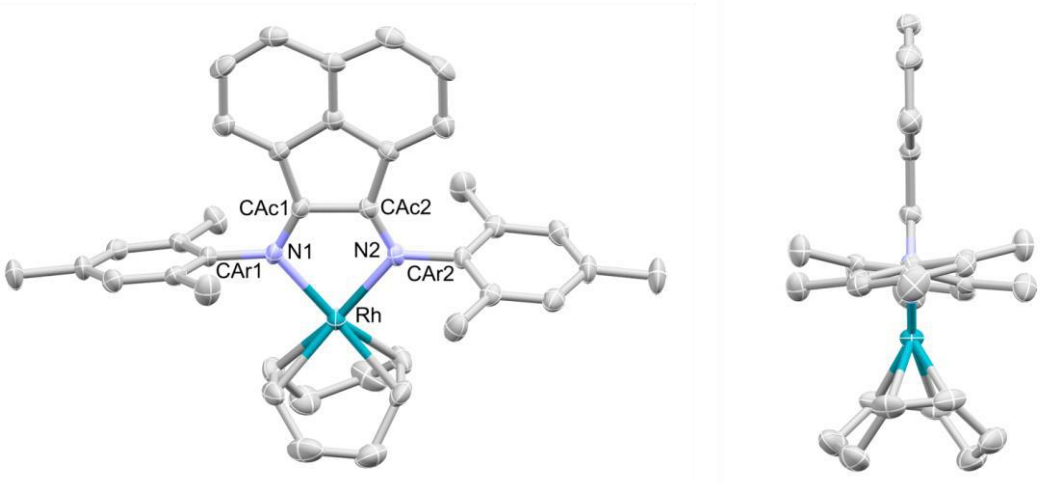


*Figure 2.3–1: The molecular structure of **1b** [RhMB(cod)]PF_6 with partial atom-numbering scheme (left), and side-on view (right), thermal ellipsoids shown at 50 % probability. Hydrogen atoms, PF_6^- counterion and CH_2Cl_2 solvent molecule are omitted for clarity.*

The fused aromatic rings that make up the acenaphthene moiety of the MesBIAN ligand largely retain its planar molecular geometry upon coordination to the Rh(I)–cod centre, however, a marginal deformation of –3.0(8)° the bisimine N=C–C=N moiety is observed. The planar Mes-substituents are rotated at a 23.97° angle relative to one another, and are slanted away from the acenaphthene plane by 10.4°. The bond angles about the imine nitrogens (av. C_{Ac}–N–C_{Ar} = 120.6(5)°) are consistent with *sp*^{2}-hybridized nitrogen atoms, increased slightly from the ideal 120° due to the bite angle between the bisimine chelate and Rh(I)-centre (N1–Rh–N2 = 78.9(2)°). The N–C_{Ac} and C_{Ac}–C_{Ac} bond lengths in the bisimine N=C–C=N moiety are typical of N–C double bonds and C–C single bonds for a coordinated BIAN ligand bearing no formal charge.

Overall, the bond lengths and angles for computationally modelled molecular geometry of **1b** correspond well to those observed in the SC-XRD data. However, the modelled geometry underestimates the extent to which the Mes-substituents rotate relative to one another, and the acenaphthene plane, to accommodate the steric bulk of the cod-ligand in the coordination sphere.

© University of Pretoria

2.3.2) **1d** [IrMB(cod)]PF_6

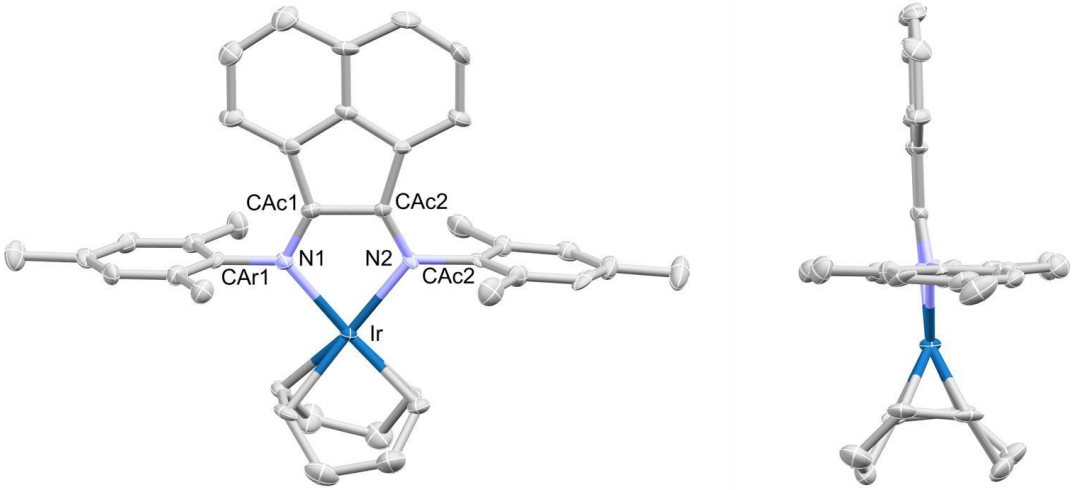


*Figure 2.3–2: The molecular structure of **1d** [IrMB(cod)]PF_6 with partial atom-numbering scheme (left), and side-on view (right), thermal ellipsoids shown at 50 % probability. Hydrogen atoms, PF_6^- counterion and two $CDCl_3$ solvent molecules are omitted for clarity.*

The cationic Ir(I)-cod complex **1d** crystallised in a monoclinic P$2_1/n$ symmetry with two $CDCl_3$ molecules in the unit cell. Unlike the Mes-substituents of **1b**, the aryl-substituents in **1d** are nearly co-planar (7.31°) and virtually orthogonal to the acenaphthene moiety (88.61°). Slight distortions of the expected square planar coordination geometry of the Ir(I)-centre (τ_4 = 0.06) is evidenced by the variance in the two Ir–N=C–C dihedral angles (2.6(10)° and –6.4(10)°). The C_{Ac}–N–C_{Ar} bond angles of the imine nitrogens (av. 119.6°) correlate well to the expected value for sp^2-hybridized nitrogen atoms (Figure 2.3–2), and the bite angle (N1–Ir–N2 = 78.8(3)°) is in good agreement with values reported for other Ir(I) α-diimine complexes.[96] As observed for complex **1b**, the N–C_{Ac} and C_{Ac}–C_{Ac} bond lengths in the N=C–C=N moiety are typical of N–C double bonds and C–C single bonds for a neutrally charged coordinated BIAN ligand.

2.3.3) **2a** [RhDB$(CO)_2$]PF_6

The orthorhombic crystals of complex **2a** (space group P*nma*) show an almost rectangular Rh(I) coordination centre due to the small bite angle formed by the DippBIAN chelate (Figure 2.3–3, N1–Rh–N2 = 69.4(2)°) and the diminished angle between the carbonyl ligands (C1–Rh–C2 = 80.8(4)°). While the bond and dihedral angles between the Rh(I) and carbonyl ligands are indicative of a near planar relationship, the coordination sphere distortion is exemplified by the non-linear angle between the bisimine nitrogens and their *trans* carbonyl carbons (av. 173.9(2)°), and the Rh–N=C–C dihedral angles (± 4.3(4)°). The co-planar Dipp-substituents (0.91°) are pitched away from the acenaphthene plane (av. 13.3°) with two isopropyl groups in close proximity to one another, partially shrouding the dorsal coordination sphere.

© University of Pretoria

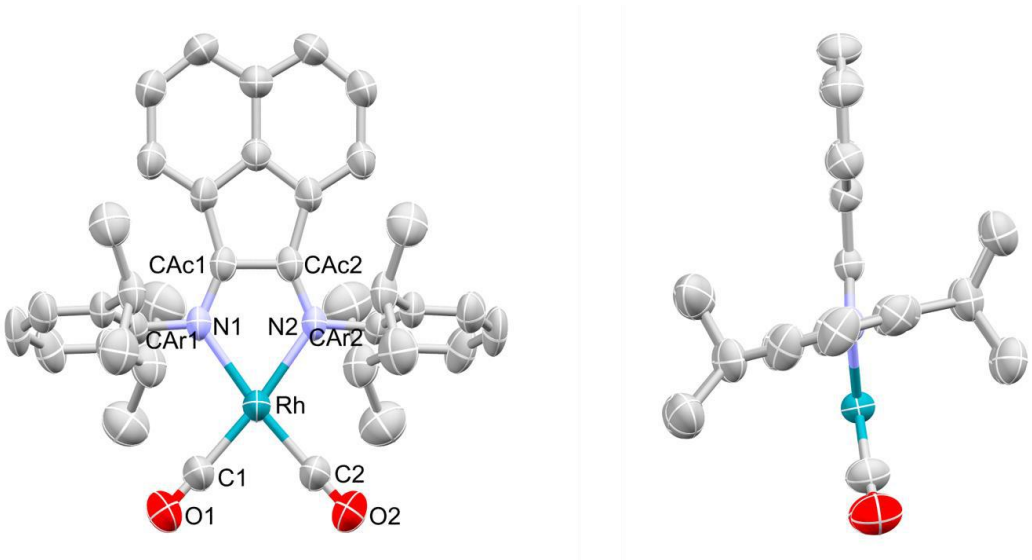


*Figure 2.3–3: The molecular structure of **2a** [RhDB(CO)$_2$]PF$_6$ with partial atom-numbering scheme (left), and side-on view (right), thermal ellipsoids shown at 50 % probability. Hydrogen atoms and PF$_6^-$ counterion are omitted for clarity.*

The planar relationship in the bisimine N=C–C=N moiety of the free DippBIAN ligand is retained in **2a** despite these distortions (N1–C$_{Ac2}$–C$_{Ac1}$–N2 = 0.0(6)°). The C$_{Ac}$–N–C$_{Ar}$ bond angles (av. 116.0(4)°) are slightly smaller than the expected 120° for *sp*^{2}-hybridized nitrogen atoms. The extended N–C$_{Ac}$ and shortened C$_{Ac}$–C$_{Ac}$ bond lengths in the N=C–C=N moiety of **2a** correlate to literature reports of the DippBIAN quinonate dianion [DippBIAN^{2-}].[1,24,27,36,37,120]

It should be noted, however, that in the crystal structure of **2a** the rhodium centre adopts a distorted square planar geometry (τ_4 = 0.09) which is indicative of a Rh(I) complex (as opposed to an octahedral Rh(III) centre) with a single PF$_6^-$ counter ion. The absence of additional counter cations therefore further negates the possibility of a reduced ligand being coordinated in **2a**. It is thus proposed that the small bite angle of the chelate coordination enforces a partial change in the atomic hybridization of the N-atoms to accommodate the strained geometry. Although somewhat simplified, the linear combination of atomic orbitals available for interatomic overlap (i.e., MO formation) between the imine nitrogens, C$_{Ar}$ and C$_{Ac}$ are modified. The orbital alterations across all six atoms could feasibly result in the observed decrease C$_{Ac}$–N–C$_{Ar}$ in bond angle (partial *sp*^{2} → *sp*^{3}) as well as the changes in bond lengths (partial N=C → N–C and C–C → C=C deformation).

© University of Pretoria

2.3.4) **2b** [RhMB(CO)$_2$]PF$_6$

The coordination centre of complex **2b** in its orthorhombic (P*bcn*) crystals adopted a distorted square planar geometry common among Rh(I) complexes (τ_4 = 0.09), with significantly decreased angular distortions of the aryl-substituents and bisimine moiety compared to complex **2a** (Figure 2.3–4).

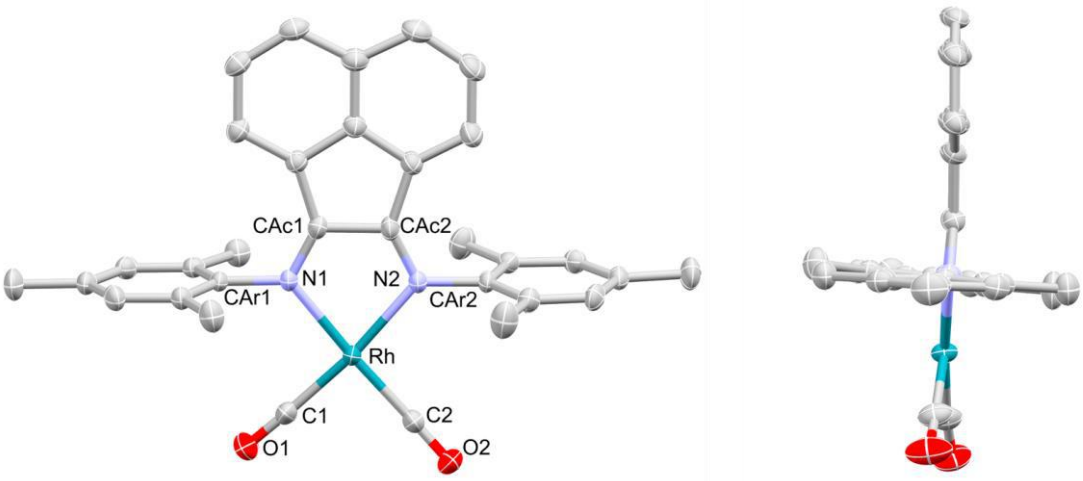


*Figure 2.3–4: The molecular structure of **2b** [RhMB(CO)$_2$]PF$_6$ with partial atom-numbering scheme (left), and side-on view (right), thermal ellipsoids shown at 50 % probability. Hydrogen atoms and PF$_6^-$ counterion are omitted for clarity.*

The two carbonyl ligands are bonded at a right angle (C1–Rh–C2 = 89.89(8)°), although they are not entirely parallel to with one another (O1–C1–C2–O2 = –7.3(4)°). The two Mes-substituents are nearly co-planar (5.18°) and depart only marginally from orthogonality with the acenaphthene plane. The shallow dihedral angles across the bisimine N=C–C=N moiety (av. 0.4(3)°) and its coordination to Rh(I)-centre (Rh–N=C–C = 1.5(2)° and –2.0(2)°) indicate a nearly linear molecular geometry between the rhodium and BIAN ligand. The average N–C$_{Ac}$ and C$_{Ac}$–C$_{Ac}$ bond lengths are comparable to those observed in the structures of complexes **1b** and **1d**, and point towards a coordinated BIAN ligand of neutral charge.

2.3.5) **2c** [IrDB(CO)$_2$]PF$_6$

The Dipp-substituents of complex **2c** are observed to adopt a twisted configuration in the orthorhombic (*P2$_1$2$_1$2$_1$*) crystal structure (Figure 2.3–5). The least squares planes of the two Dipp-substituents (Dipp$_{plane(C_{Ar1})}$ and Dipp$_{plane(C_{Ar2})}$) are rotated 17.41° relative to one another, with the Dipp$_{plane(C_{Ar1})}$ nearly orthogonal to the acenaphthene plane, and Dipp$_{plane(C_{Ar2})}$ slated 14.6° away from it. The steric strain induced by the distortion of the aryl-substituents results in a slightly deformed square planar Ir(I) coordination centre (τ_4 = 0.10), evidenced by the differences in Ir–CO bond angles (O1–C1–Ir = 175.8(4)° and O2–C2–Ir = 177.9(4)°) and Ir–N=C–C dihedral angles (0.6(5)° and –4.5(5)°).

© University of Pretoria

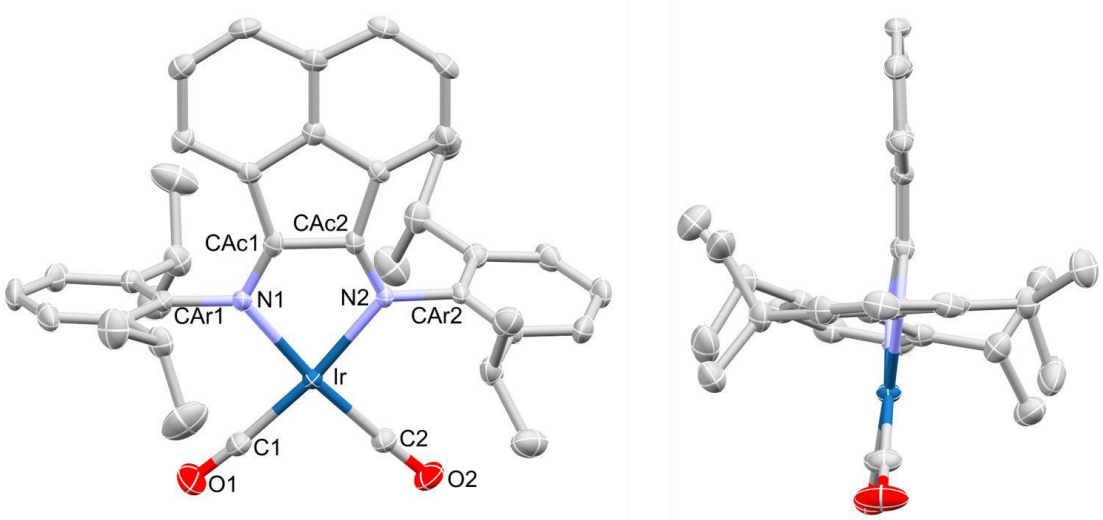


Figure 2.3–5: The molecular structure of ***2c*** *$[IrDB(CO)_2]PF_6$ with partial atom-numbering scheme (left), and side-on view (right), thermal ellipsoids shown at 50 % probability. Hydrogen atoms and PF_6^- counterion are omitted for clarity.*

A slight distortion is also noted in the bisimine N=C–C=N moiety (2.7(6)°). The recorded Ir–C bond lengths are comparable to the some of the largest previously reported values for related dicarbonyl-bisimine complexes of iridium.[96,97] The C_{Ac}–N–C_{Ar} bond angle in **2c** (av. 119.75°) is very similar to the expected 120° angle for sp^2-hybridized nitrogen atoms. The N–C_{Ac} and C_{Ac}–C_{Ac} bond lengths are closely comparable to those observed in complexes **1d** and **2b**, and are typical of N–C double bonds and C–C single bonds respectively. The DippBIAN ligand in **2c** is thus anticipated to have a neutral charge.

2.3.6) **3a** $[RhDB(CO)(PEt_3)]PF_6$

As observed in the crystal structure of **1d** and **2b**, the Dipp-substituents of complex **3a** adopt a nearly co-planar geometry (7.30°) in the orthorhombic (P*bca*) crystal structure, tilted away from the acenaphthene plane by *ca*. 8.22° (Figure 2.3–6). The heteroleptic composition of complex **3a** results in notable dissimilarities in the bond lengths and bond angles between similar molecular moieties within the molecular structure. For example, the Rh–N1 bond *trans* of the σ-donor/π-acceptor PEt_3 ligand (2.3053(13) Å) is slightly longer than the Rh–N2 bond *trans* of the strong field σ-donor carbonyl ligand (2.163(4) Å), indicating that the *trans* influence applied by the carbonyl is weaker compared to that of the phosphine. The Rh–N1 bond is *ca*. 0.2 Å longer than the Rh–N bonds in the other Rh(I) complexes (av. 2.11 Å), whereas the Rh–N2 bond length is comparable to those observed in the Rh(I)-dicarbonyl complex **2a**. The Rh–C bond in **3a** is slight shorter relative to the M–C bonds recorded for the series of complexes **2a**–**c**, but is still comparable to previously reported values for Rh(I)-carbonyls.[96,98,116]

© University of Pretoria

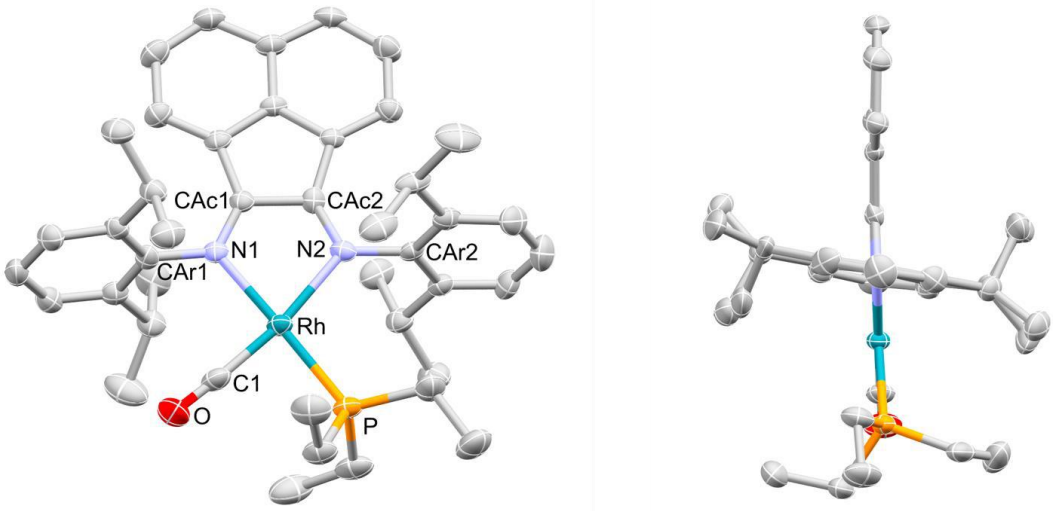


*Figure 2.3–6: The molecular structure of **3a** [RhDB(CO)(PEt$_3$)]PF$_6$ with partial atom-numbering scheme (left), and side-on view (right), thermal ellipsoids shown at 50 % probability. Hydrogen atoms and PF$_6^-$ counterion are omitted for clarity.*

The Rh–P bond is marginally shorter compared to an analogous 5-coordinate Rh(I)-diimine complexes bearing phosphine co-ligands, but well within the range of known literature Rh–P bond lengths.[98,106,116,121] The Rh(I) coordination sphere can nonetheless be described as slightly distorted square planar (τ_4 = 0.08), with an angle of 85.24(16)° between the carbonyl and PEt$_3$ ligands, and a BIAN chelate bite angle comparable to those of complexes **1b**, **1d**, **2b** and **2c** (N1–Rh–N2 = 77.30(15)°). As with these complexes as well, the imine nitrogens' C_{Ac}–N–C_{Ar} bond angles indicate *sp*^{2}-hybridizion of the nitrogen atoms, and the N–C_{Ac} and C_{Ac}–C_{Ac} bond lengths reveal that the DippBIAN ligand has a neutral formal charge.

2.3.7) **4c** [IrDB(cod)Cl]

The neutral cod-chloride complex **4c** crystallised in an orthorhombic (P*nma*) symmetry, featuring near ideal square pyramidal geometry about the Ir(I) (τ_5 = 0.00) centre in which the chlorido ligand shows slight axial distortion. The N–Ir–Cl bonds bend towards the acenaphthene plane (av. 88.3°) to reduce steric interaction with the cod-ligand (Figure 2.3–7, Cl–Ir–Ac$_{plane}$ = 79.66°). The unusual 5-coordinate structure of the Ir(I) complex is made possible, in part, by the metallocycle formed between the bisimine N=C–C=N moiety and iridium which is deformed to a greater extent compared to what has been observed in the other cationic 4-coordinate complexes. The five-membered metallocycle in **4c** takes on an "envelope" geometry reminiscent of a cyclopentane ring with Ir–N=C–C dihedral angles of ± 12.12(9)°.

© University of Pretoria

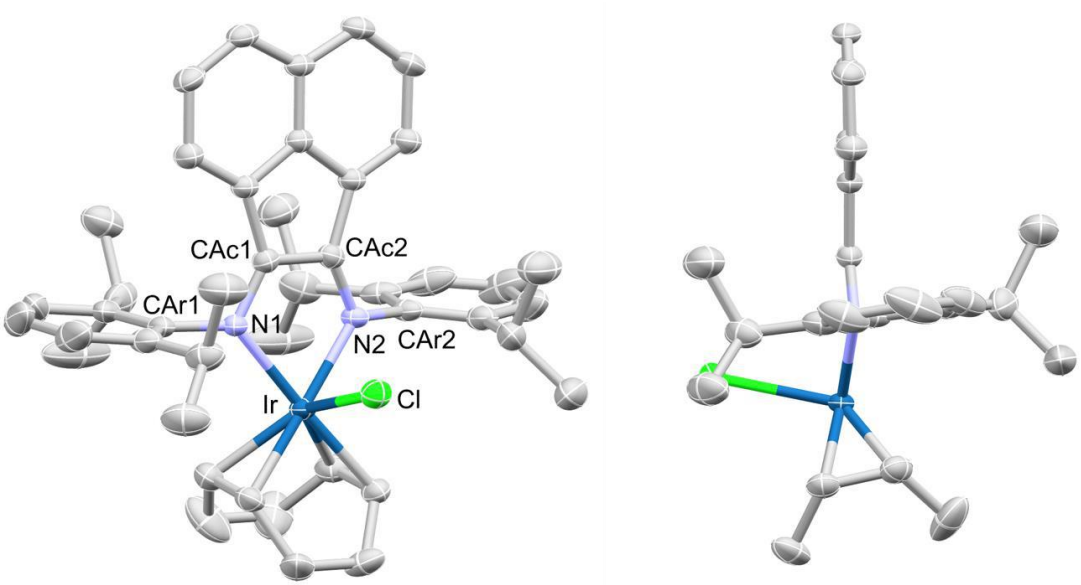


*Figure 2.3–7: The molecular structure of **4c** [IrDB(cod)Cl] with partial atom-numbering scheme (left), and side-on view (right), thermal ellipsoids shown at 50 % probability. Hydrogen atoms are omitted for clarity.*

The Ir–Cl bond length (2.4754(11) Å) is on the upper boundary of average bond lengths which have been reported for Ir(I) or Ir(III) chloride complexes.[112,122–128] The Ir–Cl bond thus shows similar elongation as reported by Ramoshev *et al*. for the Rh–Cl bond in their Rh(I) complex analogous to **4a**.[85] As observed in complex **2a**, the nitrogen C_{Ac}–N–C_{Ar} bond angles of **4c** (av. 116.8(2)°) are slightly smaller than the 120° expected for sp^2-hybridized nitrogen atoms, and the N–C_{Ac} bond lengths are slightly longer than those in the other complexes (av. 1.321(4) Å). However, the N–C_{Ar} and C_{Ac}–C_{Ac} bond lengths are in good agreement with N–C and C–C single bond lengths. The slight elongation of the bisimine double bond, and decrease in bonding angle around the nitrogens, parallel previous reports for the DippBIAN ligand in a radical monoanionic state as a [DippBIAN^{1-}] semiquinonate ligand.[1,24,27,36,37,120]

It should be noted that the absence of any counter ions in the crystal structure of **4c**, as well as the likeness of the square pyramidal coordination structures between **4c** and the previously reported structure of **4a**,[85] with rhodium in oxidation state +1, render the possibility of DippBIAN coordinating as a reduced ligand implausible. The variances observed in the bond lengths and angles of the ligands are therefore likely artefacts of the σ-donor/π-donor character of the chlorido ligand, with electron density from the metal donated to the non-innocent BIAN ligand.

© University of Pretoria

2.4) Conclusions

Two bis(aryl-imino)acenaphthene ligands, Dipp- and MesBIAN, were synthesised using known procedures, and utilised to generate new Rh(I) and Ir(I) complexes of 4- and 5-coordinate geometries. Four groups of complexes were synthesised featuring ancillary ligands from across the spectrochemical series (low, mid and high field) to access their impact on the ability of the BIAN ligand to function as a non-innocent ligand. The ancillary ligands included σ-donor (1,5-cyclooctadiene), π-donor (chloride), and π-acceptor (triethylphosphine and carbonyl) functionalities. Cationic Rh(I) and Ir(I) 1,5-cyclooctadiene complexes with Dipp- and MesBIAN ligands (complex series **1a**–**d**) were isolated as brown [Rh(I)] and dark green [Ir(I)] solids. Dicarbonyl complexes of Rh(I) and Ir(I) with Dipp- and MesBIAN ligands (complex series **2a**–**d**) were synthesised by trituration form a concentrated solution of **1a**–**d** under CO(g). The heteroleptic Rh(I) complexes of Dipp- (**3a**) and MesBIAN (**3b**) bearing a carbonyl and triethylphosphine ligand were synthesised from **2a** and **2b** respectively via ligand substitution reaction. Reacting Rh(I) and Ir(I) 1,5-cyclooctadiene chloride dimers with Dipp- and MesBIAN produced unusual 5-coordinate series of complexes **4a**–**d** as neutral products of green [Rh(I)] and dark blue [Ir(I)] colouration.

The ^{1}H and ^{13}C NMR spectra of the series of complexes **1a**–**d, 2a**–**d**, **4b** and **4d** indicated that the complexes adopted a symmetrical molecular geometry in solution, as noted by the BIAN–C**H** peaks' characteristic "*d-dd-d*" splitting patterns. The aromatic-C**H** and quaternary imine carbon N=**C$_q$** signals were shifted significantly downfield due to electron withdrawal following coordination to the metal centre, with the greatest shifts observed in complexes with the high field carbonyl ligands. In contrast, the NMR spectra of the series of complexes **3a**–**b** and **4a** showed that the complexes were in an asymmetric molecular geometry as the BIAN–C**H**'s characteristic "*d-dd-d*" peaks were not observed, while multiple upfield alkyl signals were observed for the Dipp- and Mes-C**H$_3$** groups occupying different electronic environments. The NMR spectra of **4c** displayed a mixture of these symmetric and asymmetric substitution characteristics due to the steric interactions between the chloride and cod ancillary ligands, with the isopropyl-substituents of the Dipp-moieties.

The UV-Vis spectra of the free Dipp- and MesBIAN ligands, as well as the series of complexes **1**–**4** showed a strong, high-energy absorption band around 231 nm, as well as moderate intensity bands between 265–310 nm that may be assigned as ligand-centred π-π* transitions, originating from both the acenaphthene rings and aryl-substituents.[2] Moderate to low intensity absorptions were observed in the 320–435 nm range which may be attributed to intraligand charge transfer (ILCT) transitions between the arylimine moieties and acenathphene rings.[2,50] In addition, metal-to-ligand charge

© University of Pretoria

transfer (MLCT) transitions were observed in the UV-Vis spectra of the Ir(I)-BIAN complexes **1c**–**d** and **2c** around 669 nm and 598 nm respectively; whereas two MLCT transitions were observed for the neutral Ir(I)-BIAN complexes **4c**–**d** around 466 nm and *ca*. 680 nm.[35,50,90]

The molecular structures of the series of complexes **1b**, **1d**, **2a**–**c**, **3a** and **4c** were determined using SC-XRD analysis of single crystals prepared from CH_2Cl_2 or $CDCl_3$ solutions. The pseudo-square planar coordination geometry of complex series **1b**, **1d**, **2a**–**c** and **3a** is in good agreement with known geometries for complexes of Rh(I) and Ir(I). The square pyramidal geometry of the 5-coordinate **4c** correlates well to the previously reported crystal structure of **4a**,[85] both featuring axial M–Cl bonds with slight angular distortions.

The oxidation state of BIAN ligands in a coordination complex is often assigned based on the experimentally determined bond lengths of the N–C_{Ac} and C_{Ac}–C_{Ac} bonds within the bisimine N=C–C=N moiety.[1,24,27,36,37,120] The N–C_{Ac} bond lengths complexes of **2a** and **4c** were slightly longer than those observed in the crystal structures of the other complexes, whereas the C_{Ac}–C_{Ac} bond lengths were slightly shorter. The elongated N–C_{Ac} bond, and shortened C_{Ac}–C_{Ac} bond lengths, correlate closely to previously reported values for the DippBIAN ligand coordinated in an anionic state. More specifically, the structural deviations observed in **2a** and **4c** parallel those of the dianionic [DippBIAN^{2-}] quinonate and the radical monoanionic [DippBIAN^{1-}] semiquinonate species respectively.[1,24,27,36,37,120]

Authors have recently expressed caution against relying exclusively on comparative changes in bond lengths for the determination of the reduced state of a ligand within a complex.[36,40,129] It should thus be pointed out that the crystal structures of **2a** and **4c** lack additional counter ions to stabilise a reduced ligands' charge, and that the square pyramidal coordination structures of **4c** and the reported structure of **4a**,[85] in which rhodium is in oxidation state +1, are strikingly similar. No additional evidence was obtained from collective analysis of the characterisation and electrochemical data, as well as the computational modelling of **2a** and **4c** (*vide infra*) to substantiate the assignment of an anionic charge to the DippBIAN ligands in these complexes. It is therefore implausible that the DippBIAN ligand could coordinate as a reduced ligand in complexes **2a** and **4c**, and the structural anomalies are the result of electronic interactions between the ancillary and BIAN ligands and demonstrates the non-innocent of the DippBIAN ligand in complexes **2a** and **4c**. These observations are in good agreement with the observations and conclusions drawn from the electrochemical, EPR and computational results which have previously been reported for BIAN complexes of various transition metals.[18,40,81,82,85,90,91,130]

© University of Pretoria

2.5) Experimental Details

2.5.1) Materials

Standard Schlenk line techniques were utilised with N_2 atmosphere, unless otherwise specified. All reagents were purchased from Sigma-Aldrich and used without prior purification. The precursor $[Rh(cod)Cl]_2$ and $[Ir(cod)Cl]_2$ dimers were prepared according to published procedures.[131,132] The 1,2-bis[(2,6-diisopropylphenyl)imino]acenaphthene (DippBIAN, or DB) and 1,2-bis[(2,4,6-trimethylphenyl)imino]acenaphthene (MesBIAN, or MB) ligands were synthesised according to the modified procedures published by Paulovikova [50] and Gasperini [21] respectively. Dichloromethane (CH_2Cl_2) was distilled over P_2O_5 under a N_2 atmosphere. Hexane and toluene were distilled over Na-wire under N_2 atmosphere. Diethyl ether and tetrahydrofuran were distilled from Na-wire and benzophenone under an atmosphere of N_2 (g). HPLC grade CH_2Cl_2 purged with Ar (g) was used for all UV-Vis and electrochemical measurements.

2.5.2) Instrumentation

Nuclear Magnetic Resonance (NMR) spectra were recorded on a Bruker Ultrashield Plus 400 AVANCE 3 or Ultrashield 300 AVANCE 3 spectrometers, at 25 °C, using $CDCl_3$ as solvent. The ^1H NMR spectra were recorded at 400.13 or 300.13 MHz, the ^{13}C NMR spectra at 100.613 or 75.468 MHz, ^{31}P spectra at 162.01 or 121.49 MHz, and ^{19}F spectra at 376.57 or 282.40 MHz respectively. All ^1H and ^{13}C chemical shifts reported are referenced to the residual hydrogen peak of deuterated chloroform ($CDCl_3$) at 7.26 ppm for δH, and 77.00 ppm for δC. All coupling constants (*J*) are reported in Hz. Spectral coupling patterns as assigned as: **s**–singlet, **d**–doublet, **t**–triplet, **q**–quartet, **quint**–quintet, **sept**–septet, **m**–multiplet, **br**–broad signal. Quaternary carbons that could be definitively identified are labelled as $\mathbf{C_q}$. NMR spectra for the free ligands and the series of complexes **1**–**4** are presented in Appendix A.

Electron Spray Ionisation – Time-Of-Flight Mass Spectrometry (ESI-TOF MS) analysis was done using a Waters Synapt G2 HDMS system with direct infusion in positive and negative ionisation modes. Samples were prepared using HPLC grade methanol (MeOH) at a concentration of *ca.* 10 µg cm^{-3} (100 µg cm^{-3} for sample with an exact mass greater than 850 amu). MS spectra for the series of complexes **1**–**4** are presented in Appendix B.

Solid state infrared (IR) transmittance spectra were recorded on a Bruker Alpha II FT-IR spectrometer with the platinum-ATR module (monolithic diamond crystal window). The normalised IR spectra for the free ligands and the series of complexes **1**–**4** are presented in Appendix C.

© University of Pretoria

Single crystal X-rays diffraction (SC-XRD) experiments of complexes **1b**, **1d**, and **3a** were analysed using Quazar multi-layer optics monochromated Mo Kα radiation (k = 0.71073 Å) on a Bruker D8 Venture kappa geometry diffractometer with duo Iμs sources, a Photon 100 CMOS detector and APEX III control software.[133] Data reduction was performed using SAINT+ [133] and the intensities were corrected for absorption using SADABS-2016.[133] Single crystal diffraction experiments of complexes **2a**, **2b**, **2c**, and **4c** were performed on a Rigaku XtaLAB Synergy R diffractometer, with a rotating-anode X-ray source and a HyPix CCD detector. Data reduction and absorption were carried out using the CrysAlisPro (version 1.171.40.23a) software package.[134] All X-ray diffraction measurements were performed at 150(1) K, using an Oxford Cryogenics Cryostat. All structures were solved by direct methods with SHELXT-2018 [135] and refined using SHELXL-2018 packages.[136] All H atoms were placed in geometrically idealised positions and constrained to ride on their parent atoms. Additional images and data on the SC-XRD results for complex series **1b**, **1d**, **2a**–**c**, **3a** and **4c** are available in Appendix E.

2.5.3) Synthesis Methods and Compound Characterisation

2.5.3.i) DippBIAN

The synthetic methodology was adapted from the method published by Paulovicova *et al*.[50] To 5.504 g (30.2 mmol) acenaphthalenequinone in a round bottomed flask was added 100 mL distilled acetonitrile and 30 mL (0.5 mol) glacial acetic acid. The solution was heated to reflux before addition of 12 mL (63.6 mmol) 2,6-diisopropylaniline in one portion. The yellow suspension immediately became a clear red solution, gradually forming an orange-red precipitate. The mixture was refluxed for 45 minutes, slowly cooled until just cold enough to handle, and promptly vacuum filtered. The resulting orange solids were rinsed with 100 mL acetonitrile, followed by small portions (50 mL) of hexane. The solids were allowed to dry on the vacuum filter, and DippBIAN was isolated as a light orange powder. (13.16 g, 87 % yield). **^{1}H NMR** (300 MHz, C_6D_6) δ 7.77 (d, *J* = 8.3 Hz, 2H, BIAN–C**H**), 7.26 (t, *J* = 7.8 Hz, 2H, BIAN–C**H**), 7.22–7.10 (m, *J* = 6.7 Hz, 8H, Dipp–C**H**), 6.53 (d, *J* = 7.2 Hz, 2H, BIAN–C**H**), 2.93 (sept, 4H, Dipp(iso)–C**H**), 1.22–1.06 (m, 12H, Dipp(iso)–C**H**$_3$), 0.87 (d, *J* = 6.9 Hz, 12H, Dipp(iso)–C**H**$_3$). **^{1}H NMR** (300 MHz, $CDCl_3$) δ 7.86 (d, *J* = 8.3 Hz, 2H, BIAN–C**H**), 7.35 (dd, *J* = 8.3, 7.2 Hz, 2H, BIAN–C**H**), 7.31–7.19 (m, 6H, Dipp–C**H**), 6.63 (d, *J* = 7.2 Hz, 2H, BIAN–C**H**), 3.03 (sept, *J* = 6.8 Hz, 4H, Dipp(iso)–C**H**), 1.23 (d, *J* = 6.8 Hz, 12H, Dipp(iso)–C**H**$_3$), 0.97 (d, *J* = 6.8 Hz, 12H, Dipp(iso)–C**H**$_3$). **^{13}C NMR** (75 MHz, $CDCl_3$) δ 161.1 (BIAN–**C**$_q$=N), 147.6 (Dipp–**C**$_q$–N), 140.9 (BIAN–**C**$_q$), 135.5 (Dipp–**C**H), 131.2 (BIAN–**C**$_q$), 129.6 (BIAN–**C**$_q$), 129.0 (Dipp(iso)–**C**$_q$), 128.0 (BIAN–**C**H), 124.4 (BIAN–**C**H), 123.6 (Dipp–**C**H), 123.5 (BIAN–**C**H), 28.7 (Dipp(iso)–**C**H), 23.5, 23.3 (Dipp(iso)–**C**H$_3$). **IR** (cm^{-1}) **ν(C=N)** 1668

© University of Pretoria

(m), 1652 (m, sh), 1590 (m). **UV-Vis** in CH_2Cl_2, λ_{max} [nm] (ε [M^{-1} cm^{-1}]): 231 (45 126), 274 (4 699), 310 (4 436), 327 (3 372), 420 (501).

2.5.3.ii) MesBIAN

Adapted from the method published by Gasperini *et al*.[21] and Hasan *et al*.[2] To a mixture of 5.517 g (30.3 mmol) acenaphthalenequinone and 12.130 g (89.7 mmol) anhydrous $ZnCl_2$ under an argon atmosphere in a round bottomed flask was added 75 mL glacial acetic acid. The mixture was heated to 85°C for 35 minutes under reflux, where after 10 mL (71.3 mmol) 2,4,6-trimethylaniline was added dropwise. The yellow suspension was refluxed for 40 minutes at 85°C. The dark red solution was cooled to *ca*. 50°C and warm filtered, rinsed well with 50 mL portions of diethyl ether, and the resulting orange solids dried well. The MesBIAN ligand may be liberated from the orange Zn-Cl adduct intermediate by treatment with 12 g sodium oxalate in 500 mL distilled water and extraction with dichloromethane. The deep red organic fraction was separated from the cloudy zinc oxalate aqueous fraction, stirred with excess $MgSO_4$ and vacuum filtered. The solution was dried and MesBIAN was isolated as an orange solid. (10.70 g, 85 % yield). **^{1}H NMR** (300 MHz, C_6D_6) δ 7.79 (d, *J* = 8.3 Hz, 2H, BIAN–C**H**), 7.30 (dd, *J* = 8.3, 7.2 Hz, 2H, BIAN–C**H**), 6.87 (s, 4H, Mes–C**H**), 6.67 (d, *J* = 7.2 Hz, 2H, BIAN–C**H**), 2.28 (s, 6H, Mes–C**H**$_3$), 1.99 (s, 12H, Mes–C**H**$_3$). **^{1}H NMR** (300 MHz, $CDCl_3$) δ 7.89 (d, *J* = 8.3 Hz, 2H, BIAN–C**H**), 7.37 (dd, *J* = 8.3, 7.1 Hz, 2H, BIAN–C**H**), 6.98 (s, 4H, Mes–C**H**), 6.80 (d, *J* = 7.1 Hz, 2H, BIAN–C**H**), 2.37 (s, 6H, Mes–C**H**$_3$), 2.12 (s, 12H, Mes–C**H**$_3$). **^{13}C NMR** (75 MHz, $CDCl_3$) δ 161.1 (BIAN–**C**$_q$=N), 146.8 (Mes–**C**$_q$–N), 140.5 (BIAN–**C**$_q$), 132.8 (Mes–**C**$_q$), 131.0 (BIAN–**C**$_q$), 129.6 (BIAN–**C**H), 128.9 (Mes–**C**H), 128.8 (BIAN–**C**$_q$), 128.2 (Mes–**C**$_q$), 124.5 (BIAN–**C**H), 122.4 (BIAN–**C**H), 20.90, 20.87 (*p*–Mes–**C**H$_3$), 17.70, 17.66 (*o*–Mes–**C**H$_3$). **IR** (cm^{-1}) **ν(C=N)** 1673 (m), 1648 (m), 1594 (w). **UV-Vis** in CH_2Cl_2, λ_{max} [nm] (ε [M^{-1} cm^{-1}]): 231 (91 675), 280 (11 090), 308 (10 139), 324 (8 082), 422 (1 397).

2.5.3.iii) **1a** [RhDB(cod)]PF_6

To 0.148 g (0.3 mmol, 1eq) $[Rh(cod)Cl]_2$, 0.301 g (0.6 mmol, 2eq) DippBIAN and 0.135 g (0.7 mmol, 2.44eq) KPF_6 in a Schlenk tube was added 20 mL CH_2Cl_2 at RT and the brown solution stirred overnight. The dark brown solution was filtered and dried *in vacuo*. The resulting brown powder was washed with 50 mL hexane, and **1a** was isolated as a dark brown solid. (0.44 g, 85 % yield). **^{1}H NMR** (300 MHz, $CDCl_3$) δ 8.24 (d, *J* = 8.3 Hz, 2H, BIAN–C**H**), 7.56 (dd, *J* = 7.3, 3.6 Hz, 2H, BIAN–C**H**), 7.53 (dd, *J* = 7.5, 3.3 Hz, 2H, Dipp–C**H**), 7.42 (d, *J* = 7.5 Hz, 4H, Dipp–C**H**), 6.40 (d, *J* = 7.3 Hz, 2H, BIAN–C**H**), 4.01 (br, 4H, cod–C**H**), 3.46 (sept, *J* = 6.7 Hz, 4H, Dipp(iso)–C**H**), 2.59–2.36 (m, 4H, cod–C**H**$_2$), 2.10–1.91 (m, 4H, cod–C**H**$_2$), 1.52 (d, *J* = 6.8 Hz, 12H, Dipp(iso)–C**H**$_3$), 0.93 (d, *J* = 6.8 Hz, 12H, Dipp(iso)–C**H**$_3$). **^{13}C NMR**

© University of Pretoria

(75 MHz, $CDCl_3$) δ 175.9 (BIAN–N=**C**$_q$), 147.1 (Dipp–N-**C**$_q$), 139.1 (BIAN–**C**$_q$), 139.00 (Dipp(iso)–**C**$_q$), 134.2 (BIAN–**C**H), 131.6 (**C**$_q$), 129.8 (**C**$_q$), 129.4 (Dipp–**C**H), 129.4 (Dipp–**C**H), 126.9 (BIAN–**C**H), 126.9 (BIAN–**C**H), 125.5 (Dipp–**C**H), 124.4 (BIAN–**C**$_q$), 124.4 (BIAN–**C**$_q$), 89.9 (d, $J_{C–Rh}$ = 12.2 Hz, cod–**C**H), 30.4 (cod–**C**H_2), 29.7 (Dipp(iso)–**C**H), 29.7 (cod–**C**H_2), 25.3 (Dipp(iso)–**C**H_3), 23.7, 23.6 (Dipp(iso)–**C**H_3). **^{19}F NMR** (282 MHz, $CDCl_3$) δ –73.8 (d, $J_{F–P}$ = 712.3 Hz, P**F**$_6$). **^{31}P NMR** (121 MHz, $CDCl_3$) δ –144.3 (sept, $J_{P–F}$ = 712.4 Hz, **P**F_6). **MS** (ESI+, CH_3OH): m/z [**1a**]$^+$ calculated 711.31855; found 711.318. **IR** (cm^{-1}) **ν(C=N)** 1629 (vw), 1619 (vw), 1596 (w, sh), 1580 (w); **ν(P–F)** 831 (vs); **δ(P–F)** 555 (vs). **UV-Vis** in CH_2Cl_2, **λ$_{max}$** [nm] (**ε** [M^{-1} cm^{-1}]): 232 (43 928), 272 (17 744), 335 (8 024), 353 (7 069), 432 (5 188).

2.5.3.iv) 1b [RhMB(cod)]PF_6

Complex **1b** was prepared in a procedure similar to that reported for **1a**. 0.291 g (0.6 mmol, 1.01eq) $[Rh(cod)Cl]_2$, 0.473 g (1.16 mmol, 2eq) MesBIAN and 0.243 g (1.3 mmol, 2.2eq) KPF_6 were employed, and **1b** was isolated as an iridescent dark brown solid. (0.82 g, 92 % yield). **^{1}H NMR** (300 MHz, $CDCl_3$) δ 8.21 (d, *J* = 8.3 Hz, 2H, BIAN–C**H**), 7.56 (dd, *J* = 8.3, 7.3 Hz, 2H, BIAN–C**H**), 7.11 (s, 3H, Mes–C**H**), 6.59 (d, *J* = 7.3 Hz, 2H, BIAN–C**H**), 3.86 (br, 4H, cod–C**H**), 2.51 (br, 4H, cod–CH_2), 2.40 (s, 6H, Mes–CH_3), 2.38 (s, 12H, Mes–CH_3), 2.06–1.90 (m, 4H, cod–CH_2). **^{13}C NMR** (75 MHz, $CDCl_3$) δ 175.7 (BIAN–N=**C**$_q$), 147.6 (Mes–N-**C**$_q$), 138.9 (BIAN–**C**$_q$), 138.7 (BIAN–**C**H), 133.8 (BIAN–**C**H), 131.6 (**C**$_q$), 130.4 (BIAN–**C**H), 129.8 (**C**$_q$), 127.9 (Mes–**C**H), 125.5 (**C**$_q$), 124.2 (BIAN–**C**$_q$), 90.0 (d, $J_{C–Rh}$ = 10.1 Hz, cod–**C**H), 30.8 (cod–**C**H_2), 21.22, 21.17, 18.00, 17.95 (Mes–**C**H_3). **^{19}F NMR** (282 MHz, $CDCl_3$) δ –73.9 (d, $J_{F–P}$ = 712.4 Hz, P**F**$_6$). **^{31}P NMR** (121 MHz, $CDCl_3$) δ –144.4 (sept, $J_{P–F}$ = 712.1 Hz, **P**F_6). **MS** (ESI+, CH_3OH): m/z [**1b**]$^+$ calculated 627.225; found 627.224. **IR** (cm^{-1}) **ν(C=N)** 1633 (vw), 1601 (vw), 1621 (vw, sh), 1582 (w); **ν(P–F)** 833 (vs); **δ(P–F)** 555 (s). **UV-Vis** in CH_2Cl_2, **λ$_{max}$** [nm] (**ε** [M^{-1} cm^{-1}]): 230 (49 406), 268 (23 442), 275 (22 616), 333 (9 404), 427 (6 324).

2.5.3.v) 1c [IrDB(cod)]PF_6

To 0.327 g (0.48 mmol, 1.01 eq) $[Ir(cod)Cl]_2$, 0.474 g (0.7 mmol, 2 eq) DippBIAN and 0.220 g (1.2 mmol, 2.5 eq) KPF_6 in a Schlenk tube was added 10 mL CH_2Cl_2 at RT and the orange suspension stirred for four days. The dark green solution was filtered and dried *in vacuo*. The resulting dark green powder was washed with 50 mL hexane, and **1c** was isolated as a dark green solid. (0.65 g, 72 % yield). **^{1}H NMR** (300 MHz, $CDCl_3$) δ 8.36 (d, *J* = 8.2 Hz, 2H, BIAN–C**H**), 7.61–7.53 (m, 4H, Dipp–C**H** and BIAN–C**H**), 7.47 (d, *J* = 7.8 Hz, 4H, Dipp–C**H**), 6.50 (d, *J* = 7.3 Hz, 2H, BIAN–C**H**), 4.11 (br, 4H, cod–C**H**), 3.40 (sept, *J* = 6.4 Hz, 4H, Dipp(iso)–C**H**), 2.35–2.22 (m, 4H, cod–CH_2), 1.99–1.86 (m, 4H, cod–CH_2), 1.49 (d, *J* = 6.7 Hz, 12H, Dipp(iso)–CH_3), 0.93 (d, *J* = 6.7 Hz, 12H, Dipp(iso)–CH_3). **^{13}C NMR** (75 MHz, $CDCl_3$) δ 179.63 (BIAN–N=**C**$_q$), 179.61 (BIAN–N=**C**$_q$), 139.8 (Dipp(iso)–**C**$_q$), 138.3 (Dipp–N-**C**$_q$),

© University of Pretoria

134.9 (BIAN–**C**H), 132.2 (BIAN–**C**$_q$), 130.3 (Dipp–**C**H), 129.9 (BIAN–**C**H), 127.4 (BIAN–**C**H), 127.4 (BIAN–**C**H), 125.5 (Dipp–**C**H), 124.1 (BIAN–**C**$_q$), 77.5 (from dept135, cod–**C**H), 77.4 (cod–**C**H), 31.6 (cod–**C**H$_2$), 29.6 (Dipp(iso)–**C**H), 25.3 (Dipp(iso)–**C**H$_3$), 23.7 (Dipp(iso)–**C**H$_3$). **^{19}F NMR** (282 MHz, $CDCl_3$) δ –73.8 (d, $J_{F–P}$ = 712.5 Hz, P**F**$_6$). **^{31}P NMR** (121 MHz, $CDCl_3$) δ –144.4 (sept, $J_{P–F}$ = 712.6 Hz, **P**F$_6$). **MS** (ESI+, CH_3OH): m/z [**1c**]$^+$ calculated 801.3759; found 801.377. **IR** (cm^{-1}) **ν(C=N str)** 1666 (vw), 1594(w), 1549 (vw, sh); **ν(P–F)** 839 (vs); **δ(P–F)** 555 (s). **UV-Vis** in CH_2Cl_2, **λ$_{max}$** [nm] (**ε** [M^{-1} cm^{-1}]): 231 (53 363), 275 (10 798), 317 (7 063), 668 (1 005).

2.5.3.vi) 1d [IrMB(cod)]PF_6

Complex **1d** was prepared in a procedure similar to that reported for **1c**. 0.282 g (0.4 mmol, 1.01 eq) $[Ir(COD)Cl]_2$, 0.349 g (0.84 mmol, 2 eq) MesBIAN and 0.217 g (1.2 mmol, 2.8 eq) KPF_6 were employed, and **1d** was isolated as an iridescent dark brown solid. (0.63 g, 88 % yield). **^{1}H NMR** (300 MHz, $CDCl_3$) δ 8.23 (d, *J* = 8.3 Hz, 2H, BIAN–C**H**), 7.50 (dd, *J* = 8.3, 7.2 Hz, 2H, BIAN–C**H**), 7.11 (s, 4H, Mes–C**H**), 6.68 (d, *J* = 7.2 Hz, 2H, BIAN–C**H**), 3.92 (br, 4H, cod–C**H**), 2.43 (s, 6H, Mes–C**H**$_3$), 2.36 (s, 12H, Mes–C**H**$_3$), 2.32 (br, 4H, cod–C**H**$_2$), 1.90 (br, 4H, cod–C**H**$_2$). **^{13}C NMR** (75 MHz, $CDCl_3$) δ 176.6 (BIAN–N=**C**$_q$), 139.9 (Mes–N-**C**$_q$), 138.2 (BIAN–**C**$_q$), 132.7 (BIAN–**C**H), 132.4, 131.9, 129.9 (Mes–**C**H), 129.7 (BIAN–**C**H), 128.93, 128.87, 128.2, 126.0, 124.5 (BIAN–**C**H), 122.4 (BIAN–**C**$_q$), 74.4 (cod–**C**H), 32.1 (cod–**C**H$_2$), 21.0, 18.0 (Mes–**C**H$_3$). **^{19}F NMR** (282 MHz, $CDCl_3$) δ –73.8 (d, $J_{F–P}$ = 712.6 Hz, P**F**$_6$). **^{31}P NMR** (121 MHz, $CDCl_3$) δ –144.5 (sept, $J_{P–F}$ = 712.2 Hz, **P**F$_6$). **MS** (ESI+, CH_3OH): m/z [**1d**]$^+$ calculated 717.28207; found 717.283. **IR** (cm^{-1}) **ν(C=N str)** 1605 (w), 1561 (w); **ν(P–F)** 839 (vs, sh); **δ(P–F)** 555 (s). **UV-Vis** in CH_2Cl_2, **λ$_{max}$** [nm] (**ε** [M^{-1} cm^{-1}]): 230 (34 200), 271 (9 319), 317 (5 795), 378 (3 955), 670 (1 663).

2.5.3.vii) 2a [RhDB$(CO)_2$]PF_6

Complex **2a** was prepared from complex **1a** generated *in situ*. To 0.266 g (0.53 mmol, 1.01eq) $[Rh(cod)Cl]_2$, 0.519 g (1.05 mmol, 2eq) DippBIAN and 0.219 g (1.2 mmol, 2.2eq) KPF_6 in a Schlenk tube, were added 15 mL CH_2Cl_2 at RT and the brown solution stirred overnight. The dark brown solution was cannula filtered and dried *in vacuo*. The residue was dissolved in a minimum of CH_2Cl_2 (2 mL) and CO (g) was bubbled through the solution for 5 minutes, resulting in a slow colour change from dark brown to brick red. Hexane was added slowly while passing CO (g) through the solution for 45 minutes to form a brown precipitate. The lightly green coloured solution was decanted off and the solids rinsed with hexane whilst under a flow of CO (g). The brown solid was dried *in vacuo*, and **2a** isolated as a dark brown solid. (0.74 g, 98 % yield). **^{1}H NMR** (300 MHz, $CDCl_3$) δ 8.37 (d, *J* = 8.3 Hz, 2H, BIAN–C**H**), 7.66 (dd, *J* = 8.3, 7.4 Hz, 2H, BIAN–C**H**), 7.60 (dd, *J* = 8.7, 7.1 Hz, 2H, Dipp–C**H**), 7.47 (d, *J* = 7.9 Hz, 2H, Dipp–C**H**), 6.72 (d, *J* = 7.4 Hz, 2H, BIAN–C**H**), 3.38 (sept, *J* = 6.7 Hz, 4H, Dipp(iso)–C**H**), 1.51 (d,

© University of Pretoria

J = 6.8 Hz, 12H, Dipp(iso)–C**H**$_3$), 1.10 (d, *J* = 6.8 Hz, 12H, Dipp(iso)–C**H**$_3$). **^{13}C NMR** (75 MHz, $CDCl_3$) δ 180.2 (d, $J_{C–Rh}$ = 70.3 Hz, **C**O), 178.6 (BIAN–N=**C**$_q$), 149.3 (Dipp–N-**C**$_q$), 142.9 (BIAN–**C**$_q$), 142.9 (BIAN–**C**$_q$), 138.3 (Dipp–**C**H), 135.7 (BIAN–**C**H), 132.0 (Dipp–**C**H), 130.6 (Dipp(iso)–**C**$_q$), 130.0 (Dipp(iso)–**C**$_q$), 126.8 (BIAN–**C**H), 125.5 (BIAN–**C**H), 123.2 (Dipp–**C**H), 123.2 (Dipp–**C**H), 30.0, 29.9 (Dipp(iso)–**C**H), 23.9, 23.4, 23.4 (Dipp(iso)–**C**H). **^{19}F NMR** (377 MHz, $CDCl_3$) δ –73.7 (d, $J_{F–P}$ = 712.6 Hz, P**F**$_6$). **^{31}P NMR** (162 MHz, $CDCl_3$) δ –144.5 (sept, $J_{P–F}$ = 712.4 Hz, **P**F_6). **MS** (ESI+, CH_3OH): m/z [**2a**-CO]$^+$ calculated 631.220; found 631.225. **IR** (cm^{-1}) **ν(CO)** 2096 (m), 2045 (m); **ν(C=N)** 1623 (w), 1596 (w, sh), 1580 (w); **ν(P–F)** 833 (vs); **δ(P–F)** 555 (s). **UV-Vis** in CH_2Cl_2, **λ$_{max}$** [nm] (**ε** [M^{-1} cm^{-1}]): 234 (75 053), 273 (26 503), 280 (26 323), 338 (21 691).

2.5.3.viii) 2b [RhMB(CO)$_2$]PF$_6$

Complex **2b** was prepared in a procedure similar to that reported for **2a**. 0.247 g (0.5 mmol, 1.01eq) [Rh(cod)Cl]$_2$, 0.414 g (1.0 mmol, 2eq) MesBIAN and 0.225 g (1.2 mmol, 2.4eq) KPF_6 were used, and **2b** was isolated as an iridescent brown solid. (0.67 g, 93 % yield). **^{1}H NMR** (300 MHz, $CDCl_3$) δ 8.28 (d, *J* = 8.3 Hz, 2H, BIAN–C**H**), 7.63 (dd, *J* = 8.3, 7.3 Hz, 2H, BIAN–C**H**), 7.14 (s, 4H, Mes–C**H**), 6.78 (d, *J* = 7.3 Hz, 2H, BIAN–C**H**), 2.42 (s, 18H, Mes–C**H**$_3$). **^{13}C NMR** (75 MHz, $CDCl_3$) δ 180.19 (d, J_{C-Rh} = 70.1 Hz, Rh=**C**=O), 178.5 (BIAN–N=**C**$_q$), 149.3 (Mes–N-**C**$_q$), 142.8 (BIAN–**C**$_q$), 139.5 (BIAN–**C**H), 134.9 (BIAN–**C**H), 131.6 (**C**$_q$), 130.5 (Mes–**C**H), 130.0 (**C**$_q$), 127.5 (BIAN–**C**H), 126.3 (BIAN–**C**$_q$), 123.3 (**C**$_q$), 21.2, 21.1, 18.3, 18.2 (Mes–**C**H$_3$). **^{19}F NMR** (282 MHz, $CDCl_3$) δ –73.7 (d, $J_{F–P}$ = 712.9 Hz, P**F**$_6$). **^{31}P NMR** (121 MHz, $CDCl_3$) δ –144.6 (sept, $J_{P–F}$ = 713.3 Hz, **P**F_6). **MS** (ESI+, CH_3OH): m/z [**2b**]$^+$ calculated 575.121; found 575.125, [**2b**-CO]$^+$ calculated 547.126; found 547.125, [**2b**-(CO)$_2$]$^+$ calculated 519.131; found 519.126. **IR** (cm^{-1}) **ν(CO)** 2098 (m), 2041 (m); **ν(C=N)** 1623 (w), 1603 (vw, sh), 1582 (m); **ν(P–F)** 831 (vs); **δ(P–F)** 555 (vs). **UV-Vis** in CH_2Cl_2, **λ$_{max}$** [nm] (**ε** [M^{-1} cm^{-1}]): 230 (30 050), 268 (13 438), 274 (12 901), 335 (6 936), 427 (3 376).

2.5.3.ix) 2c [IrDB(CO)$_2$]PF$_6$

Complex **2c** was prepared in a procedure similar to that reported for **2a**. To 0.269 g (0.4 mmol, 1.01 eq) [Ir(cod)Cl]$_2$, 0.399 g (0.8 mmol, 2 eq) DippBIAN and 0.198 g (1.01 mmol, 2.7 eq) KPF_6 were used, and **2c** isolated as a dark brown solid. (0.41 g, 57 % yield). **^{1}H NMR** (300 MHz, $CDCl_3$) δ 8.45 (br, 2H, BIAN–C**H**), 7.70 (dd, *J* = 7.9, 7.3 Hz, 2H, BIAN–C**H**), 7.61 (dd, *J* = 8.7, 6.8 Hz, 2H, Dipp–C**H**), 7.51 (d, *J* = 7.7 Hz, 4H, Dipp–C**H**), 6.82 (d, *J* = 7.3 Hz, 2H, BIAN–C**H**), 3.39 (sept, *J* = 6.8 Hz, 4H, Dipp(iso)–C**H**), 1.50 (d, *J* = 6.8 Hz, 12H, Dipp(iso)–C**H**$_3$), 1.11 (d, *J* = 6.8 Hz, 12H, Dipp(iso)–C**H**$_3$). No well-resolved **^{13}C NMR** spectrum of this compound could be obtained, even after extended data

© University of Pretoria

acquisition times. **^{19}F NMR** (282 MHz, $CDCl_3$) δ –73.7 (d, $J_{F–P}$ = 712.7 Hz, PF_6). **^{31}P NMR** (121 MHz, $CDCl_3$) δ –144.5 (sept, $J_{P–F}$ = 712.3 Hz, PF_6). **MS** (ESI+, CH_3OH): m/z [**2c**]$^+$ calculated 749.27190; found 749.268. **IR** (cm^{-1}) **ν(CO)** 2082 (s), 2020 (s), 1985 (vw, sh); **ν(C=N)** 1623 (w), 1599 (w), 1576 (m); **ν(P–F)** 833 (vs); **δ(P–F)** 555 (s). **UV-Vis** in CH_2Cl_2, **λ_{max}** [nm] (**ε** [M^{-1} cm^{-1}]): 232 (30 303), 286 (10 477), 334 (10 253), 342 (10 353), 408 (3 285), 598 (682).

2.5.3.x) 2d [IrMB(CO)$_2$]PF$_6$

Complex **2d** was prepared in a procedure similar to that reported for **2a**. To 0.284 g (0.42 mmol, 1.01 eq) $[Ir(COD)Cl]_2$, 0.349 g (0.84 mmol, 2 eq) MesBIAN and 0.184 g (1.0 mmol, 2.4 eq) KPF_6 were used, and **2d** isolated as an iridescent brown solid. (0.48 g, 70 % yield). **^{1}H NMR** (300 MHz, $CDCl_3$) δ 8.33 (d, *J* = 8.3 Hz, 2H, BIAN–C**H**), 7.66 (dd, *J* = 8.3, 7.3 Hz, 2H, BIAN–C**H**), 7.18 (s, 4H, Mes–C**H**), 6.87 (d, *J* = 7.3 Hz, 2H, BIAN–C**H**), 2.46 (s, 18H, Mes–C$\mathbf{H}_3$). **^{13}C NMR** (75 MHz, $CDCl_3$) δ 180.4 (Ir=**C**=O), 168.7 (BIAN–N=**C**$_q$), 151.1 (Mes–N-**C**$_q$), 142.0 (BIAN–**C**$_q$), 140.1 (BIAN–**C**H), 135.5 (BIAN–**C**H), 132.0, 130.5 (Mes–**C**H), 130.4, 128.3 (BIAN–**C**H), 126.7, 123.1, 21.3, 18.3 (Mes–**C**H_3). **^{19}F NMR** (282 MHz, $CDCl_3$) δ –73.7 (d, $J_{F–P}$ = 712.9 Hz, PF_6). **^{31}P NMR** (121 MHz, $CDCl_3$) δ –144.8 (sept, $J_{P–F}$ = 712.9 Hz, PF_6). **MS** (ESI+, CH_3OH): m/z [**2d**]$^+$ calculated 665.178; found 665.178. **IR** (cm^{-1}) **ν(C=O)** 2078 (s), 2010 (s); **ν(C=N)** 1625 (w), 1603 (vw), 1578 (m); **ν(P–F)** 833 (vs); **δ(P–F)** 555 (s). **UV-Vis** in CH_2Cl_2, **λ_{max}** [nm] (**ε** [M^{-1} cm^{-1}]): 230 (21 646), 273 (7 033), 283 (7 201), 335 (6 506), 410 (2 289).

2.5.3.xi) 3a [RhDB(CO)(PEt$_3$)]PF$_6$

Complex **3a** was prepared from complex **2a**. To 0.569 g (0.7 mmol, 1eq) **2a** dissolved in 15 mL CH_2Cl_2 was added drop wise 0.71 mL (0.71 mmol, 1.1eq) triethylphosphine (PEt_3) solution (1.0 M in THF), and the reaction mixture stirred for 3 hours. The solvent was evaporated and the residue was washed with small portions of Et_2O. The solids were dried *in vacuo*, and **3a** isolated as a dark brown solid. (0.55 g, 87 % yield). **^{1}H NMR** (300 MHz, $CDCl_3$) δ 8.25 (d, *J* = 8.4 Hz, 2H, BIAN–C**H**), 7.63–7.50 (m, 4H, Dipp–C**H** and BIAN–C**H**), 7.48–7.41 (m, 4H, Dipp–C**H** and BIAN–C**H**), 6.67 (d, *J* = 7.3 Hz, 1H, BIAN–C**H**), 6.31 (d, *J* = 7.4 Hz, 1H, BIAN–C**H**), 3.53 (sept, *J* = 6.9 Hz, 2H, Dipp(iso)–C**H**), 3.21 (sept, *J* = 6.7 Hz, 2H, Dipp(iso)–C**H**), 1.49 (d, *J* = 6.8 Hz, 6H, Dipp(iso)–C$\mathbf{H}_3$), 1.45 (d, *J* = 6.8 Hz, 6H, Dipp(iso)–C$\mathbf{H}_3$), 1.37 (q, *J* = 7.9 Hz, 6H, PEt_3–C$\mathbf{H}_2$), 1.15–1.01 (m, 15H, Dipp(iso)–C$\mathbf{H}_3$ and PEt_3–C$\mathbf{H}_3$), 0.93 (d, *J* = 6.8 Hz, 6H, Dipp(iso)–C$\mathbf{H}_3$). **^{13}C NMR** (75 MHz, $CDCl_3$) δ 177.27 (d, $J_{C–Rh}$ = 63.2 Hz, **C**O), 171.6 (BIAN–N=**C**$_q$), 171.5 (BIAN–N=**C**$_q$), 146.6 (BIAN–**C**$_q$), 144.5 (Dipp–N-**C**$_q$), 144.0(Dipp–N-**C**$_q$), 138.4 (BIAN–**C**$_q$), 138.0 (BIAN–**C**$_q$), 134.3 (BIAN–**C**H), 133.3 (BIAN–**C**H), 131.7 (BIAN–**C**$_q$), 129.9 (Dipp–**C**H), 129.6, 129.5 (Dipp–**C**H), 129.4 (Dipp–**C**H), 129.4 (BIAN–**C**$_q$), 126.83 (BIAN–**C**H), 126.78 (BIAN–**C**H), 125.7 (BIAN–**C**H), 125.5 (Dipp(iso)–**C**$_q$), 125.4 (Dipp(iso)–**C**$_q$), 125.23 (Dipp–**C**H), 125.21 (BIAN–**C**H),

© University of Pretoria

125.0 (Dipp–**C**H), 124.6 (Dipp–**C**H), 29.69, 29.66, 29.6, 29.5 (Dipp(iso)–**C**H), 24.0, 23.31, 23.26, 23.21 (Dipp(iso)–**C**H_3), 16.45 (d, $J_{C–P}$ = 30.1 Hz, PEt_3–**C**H_2), 8.38, 8.35 (PEt_3–**C**H_3). **^{19}F NMR** (282 MHz, $CDCl_3$) δ –73.8 (d, $J_{F–P}$ = 712.5 Hz, P**F**$_6$). **^{31}P NMR** (121 MHz, $CDCl_3$) δ –144.4 (sept, $J_{P–F}$ = 712.2 Hz, **P**F_6), 28.8 (d, $J_{P–Rh}$ = 141.4 Hz, **P**Et_3). **MS** (ESI+, CH_3OH): m/z [**3a**]$^+$ calculated 749.310; found 749.313. **IR** (cm^{-1}) **ν(CO)** 1991 (s); **ν(C=N)** 1631 (vw), 1594 (vw, sh), 1576 (w); **ν(P–F)** 831 (vs); **δ(P–F)** 555 (s). **UV-Vis** in CH_2Cl_2, **λ_{max}** [nm] (**ε** [M^{-1} cm^{-1}]): 229 (28 804), 269 (11 525), 337 (5 571), 427 (3 050).

2.5.3.xii) 3b [RhMB(CO)(PEt_3)]PF_6

Complex **3b** was prepared in a procedure similar to that reported for **3a**. 0.526 g (0.73 mmol, 1eq) **2b** and 0.71 mL (0.71 mmol, 1.1 eq) PEt_3 solution (1.0 M in THF) were used and **3b** isolated as a dark brown powder. (0.44 g, 74 % yield). **^{1}H NMR** (300 MHz, $CDCl_3$) δ 8.22 (dd, *J* = 8.3, 3.9 Hz, 2H, BIAN–C**H**), 7.56 (m, 2H, Mes–C**H** and BIAN–C**H**), 7.16 (s, 1H, Mes–C**H**), 7.13 (s, 1H, Mes–C**H**), 7.10 (s, 1H, Mes–C**H**), 6.76 (d, *J* = 7.2 Hz, 1H, BIAN–C**H**), 6.59 (d, *J* = 7.2 Hz, 1H, BIAN–C**H**), 6.53 (d, *J* = 7.3 Hz, 1H, BIAN–C**H**), 2.55–2.46 (m, 3H, Mes–CH_3), 2.44 (d, *J* = 3.8 Hz, 3H, Mes–CH_3), 2.41 (s, 6H, Mes–CH_3), 2.38 (s, 3H, Mes–CH_3), 2.25 (s, 3H, Mes–CH_3), 1.66 (br, 2H, PEt_3–CH_2), 1.36 (dq, $J_{P–H}$ = 8.0 Hz, $J_{H–H}$ = 7.6, 7.4 Hz, 4H, PEt_3–CH_2), 1.11 (dt, $J_{P–H}$ = 17.0 Hz, $J_{H–H}$ = 7.4, 7.4 Hz, 9H, PEt_3–CH_3). **^{13}C NMR** (75 MHz, $CDCl_3$) δ 177.6 (Rh=**C**=O), 175.7 (BIAN-N=**C**$_q$), 171.7 (BIAN-N=**C**$_q$), 147.0 (BIAN-**C**$_q$), 143.9 (Mes-N-**C**$_q$), 143.0 (Mes-N-**C**$_q$), 139.2, 138.9, 138.6, 138.2, 133.9 (BIAN–**C**H), 133.8, 132.8 (BIAN–**C**H), 131.6, 130.7 (Mes–**C**H), 130.4 (Mes–**C**H), 130.1 (Mes–**C**H), 129.82 (Mes–**C**H), 129.77 (BIAN–**C**H), 128.0, 127.9, 127.2 (BIAN–**C**$_q$), 125.8 (BIAN–**C**H), 125.5 (BIAN–**C**H), 124.5 (BIAN–**C**H), 124.2, 30.88, 21.3, 21.2 (Mes–**C**H_3), 19.71 (d, $J_{C–P}$ = 65.8 Hz, PEt_3–**C**H_2), 18.24, 18.19, 17.96 (Mes–**C**H_3), 16.06 (d, $J_{C–P}$ = 29.7 Hz, PEt_3–**C**H_2), 8.5, 5.8 (PEt_3–**C**H_3). **^{19}F NMR** (282 MHz, $CDCl_3$) δ –73.5 (d, $J_{F–P}$ = 713.1 Hz, P**F**$_6$). **^{31}P NMR** (121 MHz, $CDCl_3$) δ 29.7 (d, $J_{P–Rh}$ = 143.0 Hz), –144.4 (sept, $J_{P–F}$ = 712.4 Hz, **P**F_6). **MS** (ESI+, CH_3OH): m/z [**3b**]$^+$ calculated 749.311; found 749.310. **IR** (cm^{-1}) **ν(CO)** 1989 (m); **ν(C=N)** 1621 (vw), 1603 (vw, sh), 1582 (w); **ν(P–F)** 833 (vs); **δ(P–F)** 555 (s). **UV-Vis** in CH_2Cl_2, **λ_{max}** [nm] (**ε** [M^{-1} cm^{-1}]): 229 (31 589), 269 (13 742), 337 (6 010), 427 (3 373).

2.5.3.xiii) 4a [RhDB(cod)Cl]

0.220 g (0.44 mmol, 1.01eq) $[Rh(cod)Cl]_2$, 0.432 g (0.87 mmol, 2eq) DippBIAN were dissolved in *ca.* 20 mL degassed CH_2Cl_2 and stirred for 24 hours at RT. The orange suspension slowly changed to a dark green solution and was dried *in vacuo*. The resulting green-brown solid was purified by column chromatography (aluminium oxide resin), eluting residual starting material with CH_2Cl_2, thereafter flushing the product from the column with EtOH:CH_2Cl_2 (1:15). The dark brown ethanolic fractions were combined and dried *in vacuo* to yield **4a** as a dark green solid. (0.30 g, 46 % yield). **^{1}H NMR**

© University of Pretoria

(300 MHz, $CDCl_3$) δ 8.14 (d, *J* = 8.3 Hz, 1H, BIAN–C**H**), 7.87 (d, *J* = 8.3 Hz, 1H, BIAN–C**H**), 7.52–7.31 (m, 6H, Dipp–C**H** and BIAN–C**H**), 7.31–7.19 (m, 1H), 6.62 (d, *J* = 7.2 Hz, 1H, BIAN–C**H**), 6.41 (d, *J* = 7.3 Hz, 1H, BIAN–C**H**), 4.23 (br, 2H, cod–C**H**), 3.85 (s, 2H, cod–C**H**), 3.75 (sept, *J* = 6.7 Hz, 2H, Dipp(iso)–C**H**), 3.02 (sept, *J* = 6.7 Hz, 2H, Dipp(iso)–C**H**), 2.55–2.36 (m, 4H, cod–C$\mathbf{H}_2$), 1.93–1.81 (m, 2H, cod–C$\mathbf{H}_2$), 1.77–1.64 (m, 2H, cod–C$\mathbf{H}_2$), 1.45 (d, *J* = 6.8 Hz, 6H, Dipp(iso)–C$\mathbf{H}_3$), 1.23 (d, *J* = 6.9 Hz, 6H, Dipp(iso)–C$\mathbf{H}_3$), 0.96 (d, *J* = 6.9 Hz, 6H, Dipp(iso)–C$\mathbf{H}_3$), 0.88 (d, *J* = 6.8 Hz, 6H, Dipp(iso)–C$\mathbf{H}_3$). **^{13}C NMR** (75 MHz, $CDCl_3$) δ 173.3 (BIAN–N=**C**$_q$), 161.1 (BIAN–N=**C**$_q$), 147.6 (Dipp–N-**C**$_q$), 144.0 (Dipp–N-**C**$_q$), 141.4 (BIAN–**C**$_q$), 140.9 (BIAN–**C**$_q$), 139.9 (**C**$_q$), 135.5 (**C**$_q$), 132.2, 132.1 (BIAN–**C**H), 131.3, 131.2 (Dipp(iso)–**C**$_q$), 129.6 (**C**$_q$), 129.0, 128.8 (Dipp–**C**H), 128.0 (BIAN–**C**H), 126.8 (**C**$_q$), 125.8, 125.7 (Dipp–**C**H), 125.2, 124.4 (BIAN–**C**H), 123.6, 123.5 (Dipp–**C**H), 84.35 (dd, $J_{C–Rh}$ = 10.9, 4.9 Hz, cod–**C**H), 77.36 (d, $J_{C–Rh}$ = 4.8 Hz, cod–**C**H), 31.1 (cod–**C**$\mathbf{H}_2$), 30.6 (cod–**C**$\mathbf{H}_2$), 28.9, 28.8, 28.7 (Dipp(iso)–**C**H), 25.5 (cod–**C**$\mathbf{H}_2$), 25.5 (Dipp(iso)–**C**$\mathbf{H}_3$), 24.2 (cod–**C**$\mathbf{H}_2$), 24.2, 23.5, 23.3 (Dipp(iso)–**C**$\mathbf{H}_3$). **MS** (ESI+, CH_3OH): m/z [**4a**-Cl]$^+$ calculated 711.3186; found 711.325. **IR** (cm^{-1}) **ν(C=N)** 1666 (m), 1646 (w, sh), 1590 (m). **UV-Vis** in CH_2Cl_2, **λ$_{max}$** [nm] (**ε** [M^{-1} cm^{-1}]): 231 (37 783), 271 (8 664), 314 (4 445), 326 (4 414), 413 (1 913).

2.5.3.xiv) 4b [RhMB(cod)Cl]

Complex **4b** was prepared in a procedure similar to that reported for **4a**. 0.246 g (0.5 mmol, 1.01eq) $[Rh(cod)Cl]_2$ and 0.404 g (0.98 mmol, 2eq) MesBIAN were employed, and **4b** isolated as a dark green solid. (0.44 g, 72 % yield). **^{1}H NMR** (300 MHz, $CDCl_3$) δ 8.14 (d, *J* = 8.3 Hz, 2H, BIAN–C**H**), 7.47 (dd, *J* = 8.3, 7.3 Hz, 2H, BIAN–C**H**), 7.05 (s, 4H, Mes–C**H**), 6.55 (d, *J* = 7.2 Hz, 2H, BIAN–C**H**), 3.75 (br, 4H, cod–C**H**), 2.52–2.47 (m, 4H, cod–C$\mathbf{H}_2$), 2.40 (s, 12H, Mes–C$\mathbf{H}_3$), 2.37 (s, 6H, Mes–C$\mathbf{H}_3$), 1.98–1.81 (m, 4H, cod–C$\mathbf{H}_2$). **^{13}C NMR** (75 MHz, $CDCl_3$) δ 173.3 (BIAN–N=**C**$_q$), 140.7 (Mes–N-**C**$_q$), 137.7 (BIAN–**C**H), 132.2 (BIAN–**C**$_q$), 132.2 (BIAN–**C**$_q$), 131.4 (**C**$_q$), 130.1 (Mes–**C**H), 129.4 (**C**$_q$), 128.6 (BIAN–**C**H), 126.0 (**C**$_q$), 124.7 (BIAN–**C**$_q$), 124.5 (BIAN–**C**H), 124.4 (BIAN–**C**H), 85.9 (d, $J_{C–Rh}$ = 11.0 Hz, cod–**C**H), 30.9 (cod–**C**$\mathbf{H}_2$), 21.2, 21.1, 18.5, 18.4 (Mes–**C**$\mathbf{H}_3$). **MS** (ESI+, CH_3OH): m/z [**4b**-Cl]$^+$ calculated 627.225; found 627.247. **IR** (cm^{-1}) **ν(C=N)** 1631 (vw, sh), 1603 (m), 1535 (w). **UV-Vis** in CH_2Cl_2, **λ$_{max}$** [nm] (**ε** [M^{-1} cm^{-1}]): 231 (44 817), 268 (17 306), 275 (16 828), 329 (7 067), 431 (4 523).

2.5.3.xv) 4c [IrDB(cod)Cl]

Complex **4c** was prepared in a procedure similar to that reported for **4a**. 0.245 g (0.4 mmol, 1.01 eq) $[Ir(cod)Cl]_2$, 0.359 g (0.7 mmol, 2 eq) DippBIAN were employed, and **4c** isolated as a dark blue solid. (0.39 g, 66 % yield). **^{1}H NMR** (300 MHz, $CDCl_3$) δ 7.94 (d, *J* = 8.2 Hz, 2H, BIAN–C**H**), 7.44 (dd,

© University of Pretoria

J = 7.6 Hz, 2H, Dipp–C**H**), 7.31 (br, 4H, Dipp–C**H**), 7.19 (dd, *J* = 8.3, 7.2 Hz, 2H, 2H, BIAN–C**H**), 6.51 (d, *J* = 7.2 Hz, 2H, BIAN–C**H**), 4.01 (br, 4H, cod–C**H**), 2.29 (br, 4H, Dipp(iso)–C**H**), 1.95–1.84 (m, 4H, cod–C$\mathbf{H}_2$), 1.60 (br, 2H, cod–C$\mathbf{H}_2$), 1.30 (d, *J* = 6.7 Hz, 12H, Dipp(iso)–C$\mathbf{H}_3$), 0.87 (br, 12H, Dipp(iso)–C$\mathbf{H}_3$). **^{13}C NMR** (75 MHz, $CDCl_3$) δ 172.1 (BIAN–N=**C**$_q$), 144.2 (Dipp–N-**C**$_q$), 139.0 (BIAN–**C**$_q$), 131.9, 131.7 (Dipp(iso)–**C**$_q$), 128.59, 128.57 (BIAN–**C**H), 128.5, 128.4 (BIAN–**C**$_q$), 128.03, 128.00 (BIAN–**C**H), 124.93, 124.90, 124.85 (Dipp–**C**H), 123.6 (BIAN–**C**H), 123.6 (BIAN–**C**$_q$), 123.5 (BIAN–**C**H), 67.4 (br, cod–**C**H), 32.7 (cod–**C**H_2), 32.5 (br, Dipp(iso)–**C**H), 27.7 (br, cod–**C**H_2), 25.6, 25.5, 24.8, 24.6 (Dipp(iso)–**C**H_3). **MS** (ESI+, CH_3OH): m/z [**4c**-Cl]$^+$ calculated 801.376; found 801.373. **IR** (cm^{-1}) **ν(C=N)** 1603 (vw), 1584 (vw), 1549 (m). **UV-Vis** in CH_2Cl_2, **λ$_{max}$** [nm] (**ε** [M^{-1} cm^{-1}]): 231 (31 161), 284 (6 980), 313 (6 188), 401 (2 809), 468 (1 734), 683 (4 043).

2.5.3.xvi) 4d [IrMB(cod)Cl]

Complex **4d** was prepared in a procedure similar to that reported for **4a**. 0.298 g (0.4 mmol, 1.01 eq) $[Ir(COD)Cl]_2$, 0.358 g (0.7 mmol, 2 eq) MesBIAN were employed, and **4d** isolated as a dark blue solid. (0.57 g, 87 % yield). **^{1}H NMR** (300 MHz, $CDCl_3$) δ 7.96 (d, *J* = 8.2 Hz, 2H, BIAN–C**H**), 7.26–7.20 (m, 2H, BIAN–C**H**), 6.99 (s, 4H, Mes–C**H**), 6.64 (d, *J* = 7.1 Hz, 2H, BIAN–C**H**), 3.92 (br, 4H, cod–C**H**), 2.39 (s, 6H, Mes–C$\mathbf{H}_3$), 2.32 (br, 16H, Mes–C$\mathbf{H}_3$ and cod–C$\mathbf{H}_2$), 1.95–1.83 (m, 4H, cod–C$\mathbf{H}_2$). **^{13}C NMR** (75 MHz, $CDCl_3$) δ 171.3 (BIAN–N=**C**$_q$), 144.1 (Mes–N-**C**$_q$), 139.3 (BIAN–**C**$_q$), 136.6, 132.0 (BIAN–**C**$_q$), 131.3, 129.8 (Mes–**C**H), 129.1 (BIAN–**C**H), 128.4 (BIAN–**C**H), 121.9 (BIAN–**C**H), 77.4 (cod–**C**H), 32.8, 32.8, 32.7, 32.6 (cod–**C**H_2), 21.1, 18.8 (Mes–**C**H_3). **MS** (ESI+, CH_3OH): m/z [**4d**-Cl]$^+$ calculated 717.282; found 717.283. **IR** (cm^{-1}) **ν(C=N)** 1607 (vw), 1564 (m). **UV-Vis** in CH_2Cl_2, **λ$_{max}$** [nm] (**ε** [M^{-1} cm^{-1}]): 231 (14 169), 281 (3 348), 313 (2 740), 403 (1 234), 462 (848), 676 (1 862).

© University of Pretoria

2.6) References

(1) Viganò, M.; Ferretti, F.; Caselli, A.; Ragaini, F.; Rossi, M.; Mussini, P.; Macchi, P. Easy Entry into Reduced Ar-BIANH 2 Compounds: A New Class of Quinone/Hydroquinone-Type Redox-Active Couples with an Easily Tunable Potential. *Chemistry - European Journal* **2014**, *20* (44), 14451–14464. https://doi.org/10.1002/chem.201403594.

(2) Hasan, K.; Zysman-Colman, E. Synthesis, UV-Vis and CV Properties of a Structurally Related Series of Bis(Arylimino)Acenaphthenes (Ar-BIANs). *J Phys Org Chem* **2013**, *26* (3), 274–279. https://doi.org/10.1002/poc.3081.

(3) van Asselt, R.; Elsevier, C. J. Homogeneous Catalytic Hydrogenation of Alkenes by Zero-Valent Palladium Complexes of Cis-Fixed Dinitrogen Ligands. *Journal of Molecular Catalysis* **1991**, *65* (3). https://doi.org/10.1016/0304-5102(91)85057-9.

(4) van Asselt, R.; Elsevier, C. J.; Smeets, W. J. J.; Spek, A. L.; Benedix, R. Synthesis and Characterization of Rigid Bidentate Nitrogen Ligands and Some Examples of Coordination to Divalent Palladium. X-Ray Crystal Structures of Bis (p-Tolylimino) Acenaphthene and Methylchloro [Bis(o,O'-Diisopropylphenyl-Imino) Acenaphthene] Palla. *Recueil des Travaux Chimiques des Pays-Bas* **1994**, *113* (2), 88–98. https://doi.org/10.1002/recl.19941130204.

(5) Johnson, L. K.; Killian, C. M.; Brookhart, M. New Pd(II)- and Ni(II)-Based Catalysts for Polymerization of Ethylene and α-Olefins. *J Am Chem Soc* **1995**, *117* (23), 6414–6415. https://doi.org/10.1021/ja00128a054.

(6) Donkervoort, J. G.; Bühl, M.; Ernsting, J. M.; Elsevier, C. J. Steric and Electronic Effects on the 103Rh NMR Chemical Shifts of Rh1(Cyclooctadiene) Compounds Bearing N-Donor Ligands. *Eur J Inorg Chem* **1999**, *1999* (1), 27–33. https://doi.org/10.1002/(sici)1099-0682(199901)1999:1<27::aid-ejic27>3.0.co;2-4.

(7) Daugulis, O.; Macarthur, A. H. R.; Rix, F. C.; Templeton, J. L. A Career in Catalysis: Maurice Brookhart. *ACS Catal* **2016**, *6* (3), 1518–1532. https://doi.org/10.1021/acscatal.5b02216.

(8) van Asselt, R.; Gielens, E. E. C. G.; Rulke, R. E.; Vrieze, K.; Elsevier, C. J. Rigid Bidentate Nitrogen Ligands in Organometallic Chemistry and Homogeneous Catalysis. 3. Insertion of Carbon Monoxide and Alkenes into Palladium-Carbon Bonds of Complexes Containing Rigid Bidentate Nitrogen Ligands: The First Example of Isolated Complex. *J Am Chem Soc* **1994**, *116* (3), 977–985. https://doi.org/10.1021/ja00082a020.

(9) van Asselt, R.; Elsevier, C. J. New Palladium Complexes of Cis-Fixed Bidentate Nitrogen Ligands as Catalysts for Carbon-Carbon Bond Formation. *Organometallics* **1992**, *11* (6), 1999–2001.

(10) Hasan, K.; Zysman-Colman, E. The Effect of Aryl Substitution on the Properties of a Series of Highly Absorptive Cationic Iridium(III) Complexes Bearing Ancillary

© University of Pretoria

Bis(Arylimino)Acenaphthene Ligands. *Eur J Inorg Chem* **2013**, *2013* (25), 4421–4429. https://doi.org/10.1002/ejic.201300583.

(11) Hasan, K.; Wang, J.; Pal, A. K.; Hierlinger, C.; Guerchais, V.; Sen Soo, H.; García, F.; Zysman-Colman, E. Bay-Region Functionalisation of Ar-BIAN Ligands and Their Use Within Highly Absorptive Cationic Iridium(III) Dyes. *Sci Rep* **2017**, *7* (1), 15520. https://doi.org/10.1038/s41598-017-14996-4.

(12) Ragaini, F.; Gasperini, M.; Gallo, E.; Macchi, P. Using Ring Strain to Inhibit a Decomposition Path: First Synthesis of an Alkyl-BIAN Ligand (Alkyl-BIAN = Bis(Alkyl)Acenaphthenequinonediimine). *Chemical Communications* **2005**, *2* (8), 1031–1033. https://doi.org/10.1039/b415767b.

(13) Hill, N. J.; Vargas-Baca, I.; Cowley, A. H. Recent Developments in the Coordination Chemistry of Bis(Imino)Acenaphthene (BIAN) Ligands with s- and p-Block Elements. *Dalton Transactions* **2009**, *9226* (2), 240–253. https://doi.org/10.1039/b815079f.

(14) Smith, J. G. Aldehydes and Ketones–Nucleaophilic Addition: Addition of 1° Amines. In *Organic Chemistry, Third Ed. (Int.)*; McGraw-Hill Education: New York, NY, 2011; pp 797–801.

(15) Gasperini, M.; Ragaini, F.; Gazzola, E.; Caselli, A.; Macchi, P. Synthesis of Mixed Ar,Ar'-BIAN Ligands (Ar,Ar'-BIAN = Bis(Aryl)Acenaphthenequinonediimine). Measurement of the Coordination Strength of Hemilabile Ligands with Respect to Their Symmetric Counterparts. *Dalton Trans.* **2004**, *33* (20), 3376–3382. https://doi.org/10.1039/B406582D.

(16) Schmiege, B. M.; Carney, M. J.; Small, B. L.; Gerlach, D. L.; Halfen, J. A. Alternatives to Pyridinediimine Ligands: Syntheses and Structures of Metal Complexes Supported by Donor-Modified α-Diimine Ligands. *Dalton Transactions* **2007**, No. 24, 2547–2562. https://doi.org/10.1039/b702197f.

(17) Szalontai, G.; Szabó, P.; Besenyei, G. A New Heterotopic Ar-BIAN Ligand with a Pendant P Donor Site. *Polyhedron* **2015**, *92*, 156–165. https://doi.org/10.1016/j.poly.2015.03.008.

(18) Hazari, A. S.; Das, A.; Ray, R.; Agarwala, H.; Maji, S.; Mobin, S. M.; Lahiri, G. K. Tunable Electrochemical and Catalytic Features of BIAN- and BIAO-Derived Ruthenium Complexes. *Inorg Chem* **2015**, *54* (10), 4998–5012. https://doi.org/10.1021/acs.inorgchem.5b00615.

(19) Katla, V.; Yue, E.; Rajendran, N. M.; Liang, T.; Sun, W.-H. Synthesis, Characterization and Ethylene Polymerization of 1-(2,6-Dimethyl-4-Fluorenylphenylimino)-2-Aryliminoacenaphthylnickel Bromides. *Comptes Rendus Chimie* **2016**, *19* (5), 604–613. https://doi.org/10.1016/j.crci.2016.01.005.

© University of Pretoria

(20) Zhou, M.; Li, X.; Bu, D.; Lei, H. Synthesis, Crystal Structures and Electrochemical Properties of Co(II) and Mn(II) Complexes with Asymmetric Bulky BIAN Ligands. *Polyhedron* **2018**, *148*, 88–99. https://doi.org/10.1016/j.poly.2018.03.034.

(21) Gasperini, M.; Ragaini, F.; Cenini, S. Synthesis of Ar-BIAN Ligands (Ar-BIAN = Bis(Aryl)Acenaphthenequinonediimine) Having Strong Electron-Withdrawing Substituents on the Aryl Rings and Their Relative Coordination Strength toward Palladium(0) and -(II) Complexes. *Organometallics* **2002**, *21* (14), 2950–2957. https://doi.org/10.1021/om020147u.

(22) Moore, J. A.; Vasudevan, K.; Hill, N. J.; Reeske, G.; Cowley, A. H. Facile Routes to Alkyl-BIAN Ligands. *Chemical Communications* **2006**, *2006* (27), 2913–2915. https://doi.org/10.1039/b606390j.

(23) Hagar, M.; Ragaini, F.; Monticelli, E.; Caselli, A.; Macchi, P.; Casati, N. Chiral Cyclopropylamines in the Synthesis of New Ligands; First Asymmetric Alkyl-BIAN Compounds. *Chemical Communications* **2010**, *46* (33), 6153. https://doi.org/10.1039/c0cc00977f.

(24) Clark, K. M.; Bendix, J.; Heyduk, A. F.; Ziller, J. W. Synthesis and Characterization of a Neutral Titanium Tris(Iminosemiquinone) Complex Featuring Redox-Active Ligands. *Inorg Chem* **2012**, *51* (14), 7457–7459. https://doi.org/10.1021/ic301059p.

(25) Morozov, A. G.; Fedushkin, I. L.; Irran, E.; Grohmann, A. Titanium(IV) Complexes Supported by a Dianionic Acenaphthenediimine Ligand: X-Ray and Spectroscopic Studies of the Metal Coordination Sphere. *Inorg Chem Commun* **2018**, *95* (June), 50–55. https://doi.org/10.1016/j.inoche.2018.07.006.

(26) Nunes, C. D.; Vaz, P. D.; Félix, V.; Veiros, L. F.; Moniz, T.; Rangel, M.; Realista, S.; Mourato, A. C.; Calhorda, M. J. Vanadyl Cationic Complexes as Catalysts in Olefin Oxidation. *Dalton Transactions* **2015**, *44* (11), 5125–5138. https://doi.org/10.1039/C4DT03174A.

(27) Bendix, J.; Clark, K. M. Delocalization and Valence Tautomerism in Vanadium Tris(Iminosemiquinone) Complexes. *Angewandte Chemie - International Edition* **2016**, *55* (8), 2748–2752. https://doi.org/10.1002/anie.201510403.

(28) Fomenko, I. S.; Gushchin, A. L.; Shul'pina, L. S.; Ikonnikov, N. S.; Abramov, P. A.; Romashev, N. F.; Poryvaev, A. S.; Sheveleva, A. M.; Bogomyakov, A. S.; Shmelev, N. Y.; Fedin, M. V.; Shul'pin, G. B.; Sokolov, M. N. New Oxidovanadium(Iv) Complex with a BIAN Ligand: Synthesis, Structure, Redox Properties and Catalytic Activity. *New Journal of Chemistry* **2018**, *42* (19), 16200–16210. https://doi.org/10.1039/C8NJ03358G.

(29) Small, B. L.; Rios, R.; Fernandez, E. R.; Carney, M. J. Oligomerization of Ethylene Using New Iron Catalysts Bearing Pendant Donor Modified α-Diimine Ligands. *Organometallics* **2007**, *26* (7), 1744–1749. https://doi.org/10.1021/om0611406.

© University of Pretoria

(30) Wekesa, F. S.; Arias-Ugarte, R.; Kong, L.; Sumner, Z.; McGovern, G. P.; Findlater, M. Iron-Catalyzed Hydrosilylation of Aldehydes and Ketones under Solvent-Free Conditions. *Organometallics* **2015**, *34* (20), 5051–5056. https://doi.org/10.1021/acs.organomet.5b00630.

(31) Supej, M. J.; Volkov, A.; Darko, L.; West, R. A.; Darmon, J. M.; Schulz, C. E.; Wheeler, K. A.; Hoyt, H. M. Aryl-Substituted BIAN Complexes of Iron Dibromide: Synthesis, X-Ray and Electronic Structure, and Catalytic Hydrosilylation Activity. *Polyhedron* **2016**, *114*, 403–414. https://doi.org/10.1016/j.poly.2016.02.020.

(32) Brown, L. A.; Wekesa, F. S.; Unruh, D. K.; Findlater, M.; Long, B. K. BIAN-Fe(H6-C6H6): Synthesis, Characterization, and l-Lactide Polymerization. *J Polym Sci A Polym Chem* **2017**, *55* (17), 2824–2830. https://doi.org/10.1002/pola.28688.

(33) Villa, M.; Miesel, D.; Hildebrandt, A.; Ragaini, F.; Schaarschmidt, D.; Jacobi von Wangelin, A. Synthesis and Catalysis of Redox-Active Bis(Imino)Acenaphthene (BIAN) Iron Complexes. *ChemCatChem* **2017**, *9* (16), 3203–3209. https://doi.org/10.1002/cctc.201700144.

(34) Yu, X.; Zhu, F.; Bu, D.; Lei, H. Ferrous Complexes Supported by Sterically Encumbered Asymmetric Bis(Arylimino)Acenaphthene (BIAN) Ligands: Synthesis, Characterization and Screening for Catalytic Hydrosilylation of Carbonyl Compounds. *RSC Adv* **2017**, *7* (25), 15321–15329. https://doi.org/10.1039/c7ra01511a.

(35) Khrizanforova, V. V.; Morozov, V. I.; Khrizanforov, M. N.; Lukoyanov, A. N.; Kataeva, O. N.; Fedushkin, I. L.; Budnikova, Yu. H. Iron Complexes of BIANs: Redox Trends and Electrocatalysis of Hydrogen Evolution. *Polyhedron* **2018**, *154*, 77–82. https://doi.org/10.1016/j.poly.2018.07.041.

(36) Larson, P. J.; Wekesa, F. S.; Singh, A.; Smith, C. R.; Rajput, A.; McGovern, G. P.; Unruh, D. K.; Cozzolino, A. F.; Findlater, M. Synthesis, Characterization, Electrochemical Properties and Theoretical Calculations of (BIAN) Iron Complexes. *Polyhedron* **2019**, *159*, 365–374. https://doi.org/10.1016/j.poly.2018.11.060.

(37) Khusniyarov, M. M.; Harms, K.; Burghaus, O.; Sundermeyer, J. Molecular and Electronic Structures of Homoleptic Nickel and Cobalt Complexes with Non-Innocent Bulky Diimine Ligands Derived from Fluorinated 1,4-Diaza-1,3-Butadiene (DAD) and Bis(Arylimino)Acenaphthene (BIAN). *Eur J Inorg Chem* **2006**, No. 15, 2985–2996. https://doi.org/10.1002/ejic.200600236.

(38) Rosa, V.; Carabineiro, S. A.; Avilés, T.; Gomes, P. T.; Welter, R.; Campos, J. M.; Ribeiro, M. R. Synthesis, Characterisation and Solid State Structures of α-Diimine Cobalt(II) Complexes: Ethylene Polymerisation Tests. *J Organomet Chem* **2008**, *693* (4), 769–775. https://doi.org/10.1016/j.jorganchem.2007.12.007.

© University of Pretoria

(39) Gomes, C. S. B.; Gomes, P. T.; Duarte, M. T. α-Diimine Transition-Metal Complexes: Mechanochemistry − A New Synthetic Approach. *J Organomet Chem* **2014**, *760* (3), 101–107. https://doi.org/10.1016/j.jorganchem.2013.11.040.

(40) Williams, O. M.; Cowley, A. H.; Rose, M. J. Structural and Electronic Characterization of Multi-Electron Reduced Naphthalene (BIAN) Cobaloximes. *Dalton Transactions* **2015**, *44* (29), 13017–13029. https://doi.org/10.1039/C5DT00924C.

(41) Yambulatov, D. S.; Nikolaevskii, S. A.; Kiskin, M. A.; Magdesieva, T. V.; Levitskiy, O. A.; Korchagin, D. V.; Efimov, N. N.; Vasil'ev, P. N.; Goloveshkin, A. S.; Sidorov, A. A.; Eremenko, I. L. Complexes of Cobalt(II) Iodide with Pyridine and Redox Active 1,2-Bis(Arylimino)Acenaphthene: Synthesis, Structure, Electrochemical, and Single Ion Magnet Properties. *Molecules* **2020**, *25* (9), 2054. https://doi.org/10.3390/molecules25092054.

(42) Maldanis, R. J.; Wood, J. S.; Chandrasekaran, A.; Rausch, M. D.; Chien, J. C. W. The Formation and Polymerization Behavior of Ni(II) α-Diimine Complexes Using Various Aluminum Activators. *Journal of Organometalic Chemistry* **2002**, *645* (1–2), 158–167. https://doi.org/10.1016/S0022-328X(01)01340-7.

(43) Camacho, D. H.; Salo, E. V.; Ziller, J. W.; Guan, Z. Cyclophane-Based Highly Active Late-Transition-Metal Catalysts for Ethylene Polymerization. *Angewandte Chemie - International Edition* **2004**, *43* (14), 1821–1825. https://doi.org/10.1002/anie.200353226.

(44) Williams, B. S.; Leatherman, M. D.; White, P. S.; Brookhart, M. Reactions of Vinyl Acetate and Vinyl Trifluoroacetate with Cationic Diimine Pd(II) and Ni(II) Alkyl Complexes: Identification of Problems Connected with Copolymerizations of These Monomers with Ethylene. *J Am Chem Soc* **2005**, *127* (14), 5132–5146. https://doi.org/10.1021/ja045969s.

(45) Liu, H.; Zhao, W.; Hao, X.; Redshaw, C.; Huang, W.; Sun, W. H. 2,6-Dibenzhydryl- N -(2-Phenyliminoacenaphthylenylidene)-4- Methylbenzenamine Nickel Dibromides: Synthesis, Characterization, and Ethylene Polymerization. *Organometallics* **2011**, *30* (8), 2418–2424. https://doi.org/10.1021/om200154a.

(46) Zhang, D.; Nadres, E. T.; Brookhart, M.; Daugulis, O. Synthesis of Highly Branched Polyethylene Using "Sandwich" (8-p-Tolyl Naphthyl α-Diimine)Nickel(II) Catalysts. *Organometallics* **2013**, *32* (18), 5136–5143. https://doi.org/10.1021/om400704h.

(47) Rhinehart, J. L.; Mitchell, N. E.; Long, B. K. Enhancing α-Diimine Catalysts for High-Temperature Ethylene Polymerization. *ACS Catal* **2014**, *4* (8), 2501–2504. https://doi.org/10.1021/cs500694m.

(48) Ahmadjo, S.; Damavandi, S.; Zohuri, G. H.; Farhadipour, A.; Etemadinia, Z. Mechanisms for the Effects of Fluorine and α-Diimine Backbone Structure on the Catalyst Behavior and Catalyst

© University of Pretoria

Deactivation in Ethylene Polymerization by Ni Catalysts. *J Organomet Chem* **2017**, *835*, 43–51. https://doi.org/10.1016/j.jorganchem.2017.02.043.

(49) Khrizanforova, V. V; Fayzullin, R. R.; Musina, E. I.; Karasik, A. A.; Budnikova, Y. H. Electrochemical and Catalytic Properties of Nickel(II) Complexes with Bis(Imino)Acenaphthene and Diazadiphosphacyclooctane Ligands. *Mendeleev Communications* **2020**, *30* (3), 302–304. https://doi.org/10.1016/j.mencom.2020.05.013.

(50) Paulovicova, A.; El-Ayaan, U.; Shibayama, K.; Morita, T.; Fukuda, Y. Mixed-Ligand Copper(II) Complexes with the Rigid Bidentate Bis(N-Arylimino)Acenaphthene Ligand: Synthesis, Spectroscopic-, and X-Ray Structural Characterization. *Eur J Inorg Chem* **2001**, *2001* (10), 2641–2646. https://doi.org/10.1002/1099-0682(200109)2001:10<2641::AID-EJIC2641>3.0.CO;2-C.

(51) El-Ayaan, U.; Abdel-Aziz, A. A.-M.; Al-Shihry, S. Solvatochromism, DNA Binding, Antitumor Activity and Molecular Modeling Study of Mixed-Ligand Copper(II) Complexes Containing the Bulky Ligand: Bis[N-(p-Tolyl)Imino]Acenaphthene. *Eur J Med Chem* **2007**, *42* (11–12), 1325–1333. https://doi.org/10.1016/j.ejmech.2007.02.014.

(52) Li, L.; Lopes, P. S.; Rosa, V.; Figueira, C. A.; Lemos, M. A. N. D. A.; Duarte, M. T.; Avilés, T.; Gomes, P. T. Synthesis and Structural Characterisation of (Aryl-BIAN)Copper(i) Complexes and Their Application as Catalysts for the Cycloaddition of Azides and Alkynes. *Dalton Transactions* **2012**, *41* (17), 5144. https://doi.org/10.1039/c2dt11854h.

(53) Li, L.; Lopes, P. S.; Figueira, C. A.; Gomes, C. S. B.; Duarte, M. T.; Rosa, V.; Fliedel, C.; Avilés, T.; Gomes, P. T. Cationic and Neutral (Ar-BIAN)Copper(I) Complexes Containing Phosphane and Arsane Ancillary Ligands: Synthesis, Molecular Structure and Catalytic Behaviour in Cycloaddition Reactions of Azides and Alkynes. *Eur J Inorg Chem* **2013**, No. 9, 1404–1417. https://doi.org/10.1002/ejic.201201211.

(54) Papanikolaou, P.; Akrivos, P. D.; Czapik, A.; Wicher, B.; Gdaniec, M.; Tkachenko, N. Homoleptic Bis(Aryl)Acenaphthenequinonediimine–Cu I Complexes – Synthesis and Characterization of a Family of Compounds with Improved Light-Gathering Characteristics. *Eur J Inorg Chem* **2013**, *2013* (13), 2418–2431. https://doi.org/10.1002/ejic.201201507.

(55) Fliedel, C.; Rosa, V.; Santos, C. I. M.; Gonzalez, P. J.; Almeida, R. M.; Gomes, C. S. B.; Gomes, P. T.; Lemos, M. A. N. D. A.; Aullón, G.; Welter, R.; Avilés, T. Copper(Ii) Complexes of Bis(Aryl-Imino)Acenaphthene Ligands: Synthesis, Structure, DFT Studies and Evaluation in Reverse ATRP of Styrene. *Dalton Transactions* **2014**, *43* (34), 13041–13054. https://doi.org/10.1039/c4dt01069h.

(56) Kee, J. W.; Ng, Y. Y.; Kulkarni, S. A.; Muduli, S. K.; Xu, K.; Ganguly, R.; Lu, Y.; Hirao, H.; Soo, H. S. Development of Bis(Arylimino)Acenaphthene (BIAN) Copper Complexes as Visible Light

© University of Pretoria

Harvesters for Potential Photovoltaic Applications. *Inorg Chem Front* **2016**, *3* (5), 651–662. https://doi.org/10.1039/c5qi00221d.

(57) Ng, Y. Y.; Tan, L. J.; Ng, S. M.; Chai, Y. T.; Ganguly, R.; Du, Y.; Yeow, E. K. L.; Soo, H. Sen. Spectroscopic Characterization and Mechanistic Studies on Visible Light Photoredox Carbon-Carbon Bond Formation by Bis(Arylimino)Acenaphthene Copper Photosensitizers. *ACS Catal* **2018**, *8* (12), 11277–11286. https://doi.org/10.1021/acscatal.8b02502.

(58) Makarov, V. M.; Koptseva, T. S.; Sokolov, V. G.; Dodonov, V. A.; Skatova, A. A.; Baranov, E. V.; Fedushkin, I. L. New Bromine-Containing Bis(Arylimino)Acenaphthenes and Related Metal Complexes. *Russian Journal of Coordination Chemistry/Koordinatsionnaya Khimiya* **2020**, *46* (4), 215–223. https://doi.org/10.1134/S1070328420030045.

(59) Coventry, D. N.; Batsanov, A. S.; Goeta, A. E.; Howard, J. A. K.; Marder, T. B. Synthesis and Molecular Structures of α-Diimines and Their Zinc and Palladium Dichloride Complexes. *Polyhedron* **2004**, *23* (17 SPEC.ISS.), 2789–2795. https://doi.org/10.1016/j.poly.2004.06.023.

(60) Rosa, V.; Avilés, T.; Aullon, G.; Covelo, B.; Lodeiro, C. A New Bis(1-Naphthylimino)Acenaphthene Compound and Its Pd(II) and Zn(II) Complexes: Synthesis, Characterization, Solid-State Structures and Density Functional Theory Studies on the Syn and Anti Isomers. *Inorg Chem* **2008**, *47* (17), 7734–7744. https://doi.org/10.1021/ic800790u.

(61) Evans, D. A.; Lee, L. M.; Vargas-Baca, I.; Cowley, A. H. Aggregation-Induced Emission of Bis(Imino)Acenaphthene Zinc Complexes: Photophysical Tuning via Methylation of the Flanking Aryl Substituents. *Organometallics* **2015**, *34* (11), 2422–2428. https://doi.org/10.1021/om501191c.

(62) Evans, D. A.; Lee, L. M.; Vargas-Baca, I.; Cowley, A. H. Photophysical Tuning of the Aggregation-Induced Emission of a Series of Para-Substituted Aryl Bis(Imino)Acenaphthene Zinc Complexes. *Dalton Transactions* **2015**, *44* (26), 11984–11996. https://doi.org/10.1039/C5DT01529D.

(63) Hasan, K.; Zysman-Colman, E. Panchromic Cationic Iridium(III) Complexes. *Inorg Chem* **2012**, *51* (22), 12560–12564. https://doi.org/10.1021/ic301998t.

(64) Van Belzen, R.; Hoffmann, H.; Elsevier, C. J. Catalytic Three-Component Synthesis of Conjugated Dienes from Alkynes via Pd0, PdII, and PdIV Intermediates Containing 1,2-Diimine. *Angewandte Chemie (International Edition in English)* **1997**, *36* (16), 1743–1745. https://doi.org/10.1002/anie.199717431.

(65) Van Asselt, R.; Elsevier, C. J.; Amatore, C.; Jutand, A. Divalent Palladium and Platinum Complexes Containing Rigid Bidentate Nitrogen Ligands and Electrochemistry of the Palladium Complexes. *Organometallics* **1997**, *16* (3), 317–328. https://doi.org/10.1021/om960578a.

© University of Pretoria

(66) Klein, R. A.; Elsevier, C. J.; Hartl, F. Redox Properties of Zerovalent Palladium Complexes Containing α-Diimine and p -Quinone Ligands. *Organometallics* **1997**, *16* (6), 1284–1291. https://doi.org/10.1021/om960809d.

(67) van Laren, M. W.; Elsevier, C. J. Selective Homogeneous Palladium(0)- Catalyzed Hydrogenation of Alkynes to (Z)- Alkenes. *Angew. Chem. Int. Ed.* **1999**, *38* (24), 3715–3717.

(68) Kannan, S.; James, A. J.; Sharp, P. R. Dinuclear Diimine Palladium(II) and Platinum(II) Hydroxo and Amido Complexes: Synthesis and X-Ray Crystal Structures. *Polyhedron* **2000**, *19* (2), 155–163. https://doi.org/10.1016/S0277-5387(99)00338-1.

(69) Liu, W.; Brookhart, M. Mechanistic Studies of Palladium(II)-a-Diimine-Catalyzed Polymerizations of Cis- and Trans-2-Butenes. *Organometallics* **2004**, *23* (26), 6099–6107. https://doi.org/10.1021/om040077m.

(70) Flapper, J.; Reek, J. N. H. Templated Encapsulation of Pyridyl-Bian Palladium Complexes: Tunable Catalysts for CO/4-Tert-Butylstyrene Copolymerization. *Angewandte Chemie - International Edition* **2007**, *46* (45), 8590–8592. https://doi.org/10.1002/anie.200703294.

(71) Sprengers, J. W.; de Greef, M.; Duin, M. A.; Elsevier, C. J. Stable Platinum(0) Catalysts for Catalytic Hydrosilylation of Styrene and Synthesis of [Pt(Ar-bian)(η 2 -alkene)] Complexes. *Eur J Inorg Chem* **2003**, *2003* (20), 3811–3819. https://doi.org/10.1002/ejic.200300088.

(72) Adams, C. J.; Fey, N.; Weinstein, J. A. Near-Infrared Luminescence from Platinum(II) Diimine Compounds. *Inorg Chem* **2006**, *45* (16), 6105–6107. https://doi.org/10.1021/ic060399d.

(73) Parmene, J.; Krivokapic, A.; Tilset, M. Synthesis, Characterization, and Protonation Reactions of Ar-BIAN and Ar-BICAT Diimine Platinum Diphenyl Complexes. *Eur J Inorg Chem* **2010**, *2010* (9), 1381–1394. https://doi.org/10.1002/ejic.200900975.

(74) Liu, B.; Gao, M.; Dang, L.; Zhao, H.; Marder, T. B.; Lin, Z. DFT Studies on the Mechanisms of the Platinum-Catalyzed Diboration of Acyclic α,β-Unsaturated Carbonyl Compounds. *Organometallics* **2012**, *31* (8), 3410–3425. https://doi.org/10.1021/om3002153.

(75) Lohr, T. L.; Piers, W. E.; Parvez, M. Reversible Insertion of Carbon Dioxide into Pt(Ii)-Hydroxo Bonds. *Dalton Transactions* **2013**, *42* (41), 14742–14748. https://doi.org/10.1039/c3dt51701b.

(76) O'Brien, C.; Wong, M. Y.; Cordes, D. B.; Slawin, A. M. Z.; Zysman-Colman, E. Cationic Platinum(II) Complexes Bearing Aryl-BIAN Ligands: Synthesis and Structural and Optoelectronic Characterization. *Organometallics* **2015**, *34* (1), 13–22. https://doi.org/10.1021/om5006512.

(77) Knör, G.; Leirer, M.; Keyes, T. E.; Vos, J. G.; Vogler, A. Non-Luminescent 1,2-Diiminetricarbonylrhenium(I) Chloride Complexes - Synthesis, Electrochemical and Spectroscopic Properties of Re(DIAN)(CO)3Cl with DIAN = p-Substituted

© University of Pretoria

Bis(Arylimino)Acenaphthene. *Eur J Inorg Chem* **2000**, *2000* (4), 749–751. https://doi.org/10.1002/(sici)1099-0682(200004)2000:4<749::aid-ejic749>3.0.co;2-b.

(78) Portenkirchner, E.; Kianfar, E.; Sariciftci, N. S.; Knör, G. Two-Electron Carbon Dioxide Reduction Catalyzed by Rhenium(I) Bis(Imino)Acenaphthene Carbonyl Complexes. *ChemSusChem* **2014**, *7* (5), 1347–1351. https://doi.org/10.1002/cssc.201301116.

(79) Kianfar, E.; Monkowius, U.; Portenkirchner, E.; Knör, G. Synthesis and Characterization of Novel Re(BIAN)(CO)3Cl Derivatives Including the First Example of a Water-Soluble Tricarbonyl Rhenium(I) Complex with Bis(Imino)Acenaphthene Ligands. *Zeitschrift fur Naturforschung - Section B Journal of Chemical Sciences* **2014**, *69* (6), 691–698. https://doi.org/10.5560/ZNB.2014-4016.

(80) Mak, C. S. K.; Wong, H. L.; Leung, Q. Y.; Tam, W. Y.; Chan, W. K.; Djurišić, A. B. The Use of Sublimable Chlorotricarbonyl Bis(Phenylimino)Acenaphthene Rhenium(I) Complexes as Photosensitizers in Bulk-Heterojunction Photovoltaic Devices. *J Organomet Chem* **2009**, *694* (17), 2770–2776. https://doi.org/10.1016/j.jorganchem.2009.04.037.

(81) Abramov, P. A.; Dmitriev, A. A.; Kholin, K. V.; Gritsan, N. P.; Kadirov, M. K.; Gushchin, A. L.; Sokolov, M. N. Mechanistic Study of the [(Dpp-Bian)Re(CO)3Br] Electrochemical Reduction Using in Situ EPR Spectroscopy and Computational Chemistry. *Electrochim Acta* **2018**, *270*, 526–534. https://doi.org/10.1016/j.electacta.2018.03.111.

(82) Mahabiersing, T.; Luytenn, H.; Nieuwendam, R. C.; Hartl, F. Synthesis, Spectroscopy and Spectroelectrochemistry of Chlorocarbonyl {1,2-Bis[(2,6-Diisopropylphenyl)Imino]-Acenaphthene-K2-N, N'}rhodium(I). *Collect Czechoslov Chem Commun* **2003**, *68* (9), 1687–1709. https://doi.org/10.1135/cccc20031687.

(83) Rumble, S. L. The Synthesis of Amines and Imines Using Organometallic Catalysts. Doctor of Philosophy, University of New South Wales, 2005.

(84) Rumble, S. L.; Page, M. J.; Field, L. D.; Messerle, B. A. In Situ Catalysts for the Intramolecular Hydroamination of Aminoalkynes - What Ligand Properties Determine Catalyst Activity? *Eur J Inorg Chem* **2012**, *2012* (13), 2226–2231. https://doi.org/10.1002/ejic.201101307.

(85) Romashev, N. F.; Gushchin, A. L.; Fomenko, I. S.; Abramov, P. A.; Mirzaeva, I. V.; Kompan'kov, N. B.; Kal'nyi, D. B.; Sokolov, M. N. A New Organometallic Rhodium(I) Complex with Dpp-Bian Ligand: Synthesis, Structure and Redox Behaviour. *Polyhedron* **2019**, *173*, 114110. https://doi.org/10.1016/j.poly.2019.114110.

(86) Gushchin, A. L.; Romashev, N. F.; Shmakova, A. A.; Abramov, P. A.; Ryzhikov, M. R.; Fomenko, I. S.; Sokolov, M. N. Novel Redox Active Rhodium(III) Complex with Bis(Arylimino)Acenaphthene Ligand: Synthesis, Structure and Electrochemical Studies.

© University of Pretoria

Mendeleev Communications **2020**, *30* (1), 81–83. https://doi.org/10.1016/j.mencom.2020.01.027.

(87) Omosun, N. N.; Smith, G. S. Water-Soluble, Disulfonated Alpha-Diimine Rhodium(I) Complexes: Synthesis, Characterisation and Application as Catalyst Precursors in the Hydroformylation of 1-Octene. *Eur J Inorg Chem* **2019**, *2019* (20), 2558–2564. https://doi.org/10.1002/ejic.201900317.

(88) Ragaini, F.; Cenini, S.; Turra, F.; Caselli, A. Allylic Amination of Unfunctionalyzed Olefins by Nitroarenes and CO, Catalyzed by Ru3(CO)12/Ph-BIAN (Ph-BIAN=bis(Phenylimino) Acenaphthenequinone): Extension to the Synthesis of Allylic Amines with Strongly Electron-Withdrawing or Electron-Donating Groups. *Tetrahedron* **2004**, *60* (23), 4989–4994. https://doi.org/10.1016/j.tet.2004.04.034.

(89) Viganò, M.; Ragaini, F.; Buonomenna, M. G.; Lariccia, R.; Caselli, A.; Gallo, E.; Cenini, S.; Jansen, J. C.; Drioli, E. Catalytic Polymer Membranes under Forcing Conditions: Reduction of Nitrobenzene by CO/H2O Catalyzed by Ruthenium Bis(Arylimino)Acenaphthene Complexes. *ChemCatChem* **2010**, *2* (9), 1150–1164. https://doi.org/10.1002/cctc.201000044.

(90) Mondal, P.; Agarwala, H.; Jana, R. D.; Plebst, S.; Grupp, A.; Ehret, F.; Mobin, S. M.; Kaim, W.; Lahiri, G. K. Sensitivity of a Strained C-C Single Bond to Charge Transfer: Redox Activity in Mononuclear and Dinuclear Ruthenium Complexes of Bis(Arylimino)Acenaphthene (BIAN) Ligands. *Inorg Chem* **2014**, *53* (14), 7389–7403. https://doi.org/10.1021/ic500730m.

(91) Singha Hazari, A.; Ray, R.; Hoque, M. A.; Lahiri, G. K. Electronic Structure and Multicatalytic Features of Redox-Active Bis(Arylimino)Acenaphthene (BIAN)-Derived Ruthenium Complexes. *Inorg Chem* **2016**, *55* (16), 8160–8173. https://doi.org/10.1021/acs.inorgchem.6b01280.

(92) Vasudevan, K.; Cowley, A. H. Synthesis and Structures of 1,2-Bis(Imino)Acenaphthene (BIAN) Lanthanide Complexes That Involve the Transfer of Zero, One, or Two Electrons. *Chemical Communications* **2007**, No. 33, 3464–3466. https://doi.org/10.1039/b708758f.

(93) Fedushkin, I. L.; Lukoyanov, A. N.; Baranov, E. V. Lanthanum Complexes with a Diimine Ligand in Three Different Redox States. *Inorg Chem* **2018**, *57* (8), 4301–4309. https://doi.org/10.1021/acs.inorgchem.7b03112.

(94) Wang, J.; Ganguly, R.; Yongxin, L.; Díaz, J.; Soo, H. Sen; García, F. A Multi-Step Solvent-Free Mechanochemical Route to Indium(III) Complexes. *Dalton Transactions* **2016**, *45* (19), 7941–7946. https://doi.org/10.1039/c6dt00978f.

(95) Schelter, E. J.; Wu, R.; Scott, B. L.; Thompson, J. D.; Cantat, T.; John, K. D.; Batista, E. R.; Morris, D. E.; Kiplinger, J. L. Actinide Redox-Active Ligand Complexes: Reversible Intramolecular

© University of Pretoria

Electron-Transfer in U(Dpp-BIAN)2/U(Dpp-BIAN)2(THF). *Inorg Chem* **2010**, *49* (3), 924–933. https://doi.org/10.1021/ic901636f.

(96) Harding, D. A. J.; Hope, E. G.; Singh, K.; Solan, G. A. Cationic Rhodium(I) and Iridium(I) α-Diimine Complexes. *Polyhedron* **2012**, *33* (1), 360–366. https://doi.org/10.1016/j.poly.2011.11.058.

(97) Hua, C.; Vuong, K. Q.; Bhadbhade, M.; Messerle, B. A. New Rhodium(I) and Iridium(I) Complexes Containing Mixed Pyrazolyl-1,2,3-Triazolyl Ligands as Catalysts for Hydroamination. *Organometallics* **2012**, *31* (5), 1790–1800. https://doi.org/10.1021/om201171b.

(98) Field, L. D.; Messerle, B. A.; Vuong, K. Q.; Turner, P. Rhodium(I) and Iridium(I) Complexes Containing Bidentate Phosphine-Imidazolyl Donor Ligands as Catalysts for the Hydroamination and Hydrothiolation of Alkynes. *Dalton Transactions* **2009**, *38* (18), 3599. https://doi.org/10.1039/b821188d.

(99) Broere, D. L. J.; Plessius, R.; Van Der Vlugt, J. I. New Avenues for Ligand-Mediated Processes-Expanding Metal Reactivity by the Use of Redox-Active Catechol, o-Aminophenol and o-Phenylenediamine Ligands. *Chem Soc Rev* **2015**, *44* (19), 6886–6915. https://doi.org/10.1039/c5cs00161g.

(100) Gunanathan, C.; Milstein, D. Bond Activation and Catalysis by Ruthenium Pincer Complexes. *Chem Rev* **2014**, *114* (24), 12024–12087. https://doi.org/10.1021/cr5002782.

(101) Munz, D. Pushing Electrons - Which Carbene Ligand for Which Application? *Organometallics* **2018**, *37* (3), 275–289. https://doi.org/10.1021/acs.organomet.7b00720.

(102) Strydom, I.; Guisado-Barrios, G.; Fernández, I.; Liles, D. C.; Peris, E.; Bezuidenhout, D. I. A Hemilabile and Cooperative N-Donor-Functionalized 1,2,3-Triazol-5-Ylidene Ligand for Alkyne Hydrothiolation Reactions. *Chemistry - European Journal* **2017**, *1* (I), 1393–1401. https://doi.org/10.1002/chem.201604567.

(103) Bourissou, D.; Guerret, O.; Gabbaï, F. P.; Bertrand, G. Stable Carbenes. *Chem Rev* **2000**, *100* (1), 39–91. https://doi.org/10.1021/cr940472u.

(104) Krisch, D.; Sun, H.; Pellumbi, K.; Faust, K.; Apfel, U.-P.; Schöfberger, W. Tuning the Electronic Properties of Homoleptic Silver(I) Bis-BIAN Complexes towards Efficient Electrocatalytic CO2 Reduction. *Catalysts* **2022**, *12* (5), 545. https://doi.org/10.3390/catal12050545.

(105) Papanikolaou, P. A.; Gdaniec, M.; Wicher, B.; Akrivos, P. D.; Tkachenko, N. V. Bis(Aryl)Acenaphthenequinonediimine Substituent Effect on the Properties and Coordination Environment of Ligands and Their Bis-Chelate Ag I Complexes. *Eur J Inorg Chem* **2013**, *2013* (29), 5196–5205. https://doi.org/10.1002/ejic.201300828.

(106) Bikrani, M.; Garralda, M. A.; Ibarlucea, L.; Pinilla, E.; Torres, M. R. Pentacoordinated Cationic Rhodium(I) and Iridium(I) Organocomplexes with α-Diimine Ligands Derived from Glyoxal:

© University of Pretoria

Crystal Structure of [Rh(Norbornadiene) (Glyoxalbis(4-Dimethylamino-Anil))-(PPh3)]BF4·1/2CH2Cl2. *Inorganica Chim Acta* **1998**, *282* (2), 230–236. https://doi.org/10.1016/s0020-1693(98)00237-0.

(107) Oro, L. A.; Ciriano, M. A.; Viguri, F.; Foces-Foces, C.; Cano, F. H. Rhodium(I) and Iridium(I) Complexes of 2,2'-Dipyridylamine and Its Deprotonated Form. *Inorganica Chim Acta* **1986**, *115* (1), 65–73. https://doi.org/10.1016/S0020-1693(00)87699-9.

(108) Aucamp, D.; Witteler, T.; Dielmann, F.; Siangwata, S.; Liles, D. C.; Smith, G. S.; Bezuidenhout, D. I. A Triarylated 1,2,3-Triazol-5-Ylidene Ligand with a Redox-Active Ferrocenyl Substituent for Rhodium(I)-Catalyzed Hydroformylation of 1-Octene. *Eur J Inorg Chem* **2017**, *2017* (9), 1227–1236. https://doi.org/10.1002/ejic.201700164.

(109) Ernsting, J. M.; Gaemers, S.; Elsevier, C. J. 103Rh NMR Spectroscopy and Its Application to Rhodium Chemistry. *Magnetic Resonance in Chemistry* **2004**, *42* (9), 721–736. https://doi.org/10.1002/mrc.1439.

(110) Berners Price, S. J.; DiMartino, M. J.; Hill, D. T.; Kuroda, R.; Mazid, M. A.; Sadler, P. J. Addition and Corrections: Tertiary Phosphine Complexes of Gold(I) and Gold(III) with Imido Ligands: 1H, 31P, and 15N NMR Spectroscopy, Antiinflammatory Activity, and X-Ray Crystal Structure of (Phthalimido)(Triethylphosphine)Gold(I). *Inorg Chem* **1986**, *25* (7), 1072–1072. https://doi.org/10.1021/ic00227a040.

(111) Wehman-Ooyevaar, I. C. M.; Drenth, W.; Grove, D. M.; van Koten, G. Stereoselective Isomerization in Organoiridium(III) Complexes Induced by the Presence of Rigid C,N Chelating Ligands. *Inorg Chem* **1993**, *32* (15), 3347–3356. https://doi.org/10.1021/ic00067a027.

(112) Bezman, S. A.; Bird, P. H.; Fraser, A. R.; Osborn, J. A. Metallacyclic Complexes of Iridium. *Inorg Chem* **1980**, *19* (12), 3755–3763. https://doi.org/10.1021/ic50214a035.

(113) Bresler, L. S.; Buzina, N. A.; Varshavsky, Y. S.; Kiseleva, N. V; Cherkasova, T. G.; Lebedev, S. V. CARBON-13 NUCLEAR MAGNETIC RESONANCE SPECTRA OF RHODIUM CARBONYL COMPLEXES. *J Organomet Chem* **1979**, *171*, 229–235.

(114) Van Der Poel, H.; Van Koten, G.; Vrieze, K. Syntheses and NMR Studies of Five-Co-Ordinate Rhodium(I) Complexes with α-Diimines (RNC(H)C(H)NR): [RhCl(CO)(H2-C2H4)(α-Diimine)] and [RhCl(L)2(α-Diimine)] (R = t-Bu, EtMe2C-; L = CO,PF3). *Inorganica Chim Acta* **1981**, *51* (C), 241–252. https://doi.org/10.1016/S0020-1693(00)88344-9.

(115) Köcher, C.; Herrmann, W. A. Heterocyclic Carbenes. One-Pot Synthesis of Rhodium and Iridium Carbene Complexes. *J Organomet Chem* **1997**, *532* (1–2), 261–265. https://doi.org/10.1016/S0022-328X(96)06732-0.

© University of Pretoria

(116) Wajda-Hermanowicz, K.; Kochel, A.; Wróbel, R. Coordination Studies of Nitrogen-Containing Aryl Phosphine Ligands PˆN and PˆNˆN with Rhodium. *J Organomet Chem* **2018**, *860*, 30–48. https://doi.org/10.1016/j.jorganchem.2018.01.060.

(117) Yang, L.; Powell, D. R.; Houser, R. P. Structural Variation in Copper(i) Complexes with Pyridylmethylamide Ligands: Structural Analysis with a New Four-Coordinate Geometry Index, T4. *Dalton Transactions* **2007**, No. 9, 955–964. https://doi.org/10.1039/b617136b.

(118) Sekiguchi, Y.; Kuriyama, S.; Eizawa, A.; Arashiba, K.; Nakajima, K.; Nishibayashi, Y. Synthesis and Reactivity of Iron-Dinitrogen Complexes Bearing Anionic Methyl- and Phenyl-Substituted Pyrrole-Based PNP-Type Pincer Ligands toward Catalytic Nitrogen Fixation. *Chemical Communications* **2017**, *53* (88), 12040–12043. https://doi.org/10.1039/c7cc06987a.

(119) Addison, A. W.; Rao, T. N.; Reedijk, J.; Van Rijn, J.; Verschoor, G. C. Synthesis, Structure, and Spectroscopic Properties of Copper(II) Compounds Containing Nitrogen-Sulphur Donor Ligands; the Crystal and Molecular Structure of Aqua[1,7-Bis(N-Methylbenzimidazol-2';-Yl)-2,6-Dithiaheptane]Copper(II) Perchlorate. *Dalton Transactions* **1984**, No. 7, 1349–1356. https://doi.org/10.1039/DT9840001349.

(120) Fedushkin, I. L.; Skatova, A. A.; Chudakova, V. A.; Fukin, G. K. Four-Step Reduction of Dpp-bian with Sodium Metal: Crystal Structures of the Sodium Salts of the Mono-, Di-, Tri- and Tetraanions of Dpp-bian. *Angewandte Chemie* **2003**, *115* (28), 3416–3420. https://doi.org/10.1002/ange.200351408.

(121) Bikrani, M.; El Mail, R.; Garralda, M. A.; Ibarlucea, L.; Pinilla, E.; Torres, M. R. Pentacoordinated Diolefinic Rhodium(I) Organocomplexes with α-Diimine Ligands. Crystal Structures of [Rh(Nbd)(LL)(PPh3)]ClO4 (Nbd=norbornadiene; LL=Bdh, Biacetylidihydrazone; Pvdh, Pyruvaldihydrazone; Bda, Biacetyldianil). *J Organomet Chem* **2000**, *601* (2), 311–319. https://doi.org/10.1016/S0022-328X(00)00090-5.

(122) Li, J. J.; Tian, Z.; Xu, Z.; Zhang, S.; Feng, Y.; Zhang, L.; Liu, Z. Highly Potent Half-Sandwich Iridium and Ruthenium Complexes as Lysosome-Targeted Imaging and Anticancer Agents. *Dalton Transactions* **2018**, *47* (44), 15772–15782. https://doi.org/10.1039/C8DT02963F.

(123) Sieh, D.; Schöffel, J.; Burger, P. Synthesis of a Chloro Protected Iridium Nitrido Complex. *Dalton Transactions* **2011**, *40* (37), 9512–9524. https://doi.org/10.1039/c1dt10886g.

(124) Wang, Z.; Lu, S. M.; Li, J.; Wang, J.; Li, C. Unprecedentedly High Formic Acid Dehydrogenation Activity on an Iridium Complex with an N,N'-Diimine Ligand in Water. *Chemistry - European Journal* **2015**, *21* (36), 12592–12595. https://doi.org/10.1002/chem.201502086.

© University of Pretoria

(125) Gonell, S.; Poyatos, M.; Peris, E. Pyrene-Based Bisazolium Salts: From Luminescence Properties to Janus-Type Bis-N-Heterocyclic Carbenes. *Chemistry - European Journal* **2014**, *20* (31), 9716–9724. https://doi.org/10.1002/chem.201304952.

(126) Petronilho, A.; Rahman, M.; Woods, J. A.; Al-Sayyed, H.; Müller-Bunz, H.; Don MacElroy, J. M.; Bernhard, S.; Albrecht, M. Photolytic Water Oxidation Catalyzed by a Molecular Carbene Iridium Complex. *Dalton Transactions* **2012**, *41* (42), 13074. https://doi.org/10.1039/c2dt30403a.

(127) Donnelly, K. F.; Lalrempuia, R.; Müller-Bunz, H.; Albrecht, M. Regioselective Electrophilic C-H Bond Activation in Triazolylidene Metal Complexes Containing a N-Bound Phenyl Substituent. *Organometallics* **2012**, *31* (23), 8414–8419. https://doi.org/10.1021/om300983m.

(128) Vasudevan, K. V.; Butorac, R. R.; Abernethy, C. D.; Cowley, A. H. Synthesis and Coordination Compounds of a Bis(Imino)Acenaphthene (BIAN)-Supported N-Heterocyclic Carbene. *Dalton Transactions* **2010**, *39* (31), 7401–7408. https://doi.org/10.1039/c0dt00278j.

(129) Butschke, B.; Fillman, K. L.; Bendikov, T.; Shimon, L. J. W.; Diskin-Posner, Y.; Leitus, G.; Gorelsky, S. I.; Neidig, M. L.; Milstein, D. How Innocent Are Potentially Redox Non-Innocent Ligands? Electronic Structure and Metal Oxidation States in Iron-PNN Complexes as a Representative Case Study. *Inorg Chem* **2015**, *54* (10), 4909–4926. https://doi.org/10.1021/acs.inorgchem.5b00509.

(130) Allan, C. J.; Cooper, B. F. T.; Cowley, H. J.; Rawson, J. M.; Macdonald, C. L. B. Non-Innocent Ligand Effects on Low-Oxidation-State Indium Complexes. *Chemistry - European Journal* **2013**, *19* (43), 14470–14483. https://doi.org/10.1002/chem.201301881.

(131) Giordano, G.; Crabtree, R. H.; Heintz, R. M.; Forster, D.; Morris, D. E. Di-μ-Chloro-Bis(η 4 -1,5-Cyclooctadiene)-Dirhodium(I). In *Inorganic Syntheses*; 2007; pp 88–90. https://doi.org/10.1002/9780470132593.ch22.

(132) Choudhury, J.; Podder, S.; Roy, S. Cooperative Friedel-Crafts Catalysis in Heterobimetallic Regime: Alkylation of Aromatics by π-Activated Alcohols. *J Am Chem Soc* **2005**, *127* (17), 6162–6163. https://doi.org/10.1021/ja0506004.

(133) APEX3 (Including SAINT and SADABS), Bruker AXS Inc., Madison, WI. Bruker AXS Inc. 2016.

(134) Rigaku Oxford Diffraction, CrysAlisPro Software System. Rigaku Corporation: Oxford, UK 2018.

(135) Sheldrick, G. M. SHELXT – Integrated Space-Group and Crystal-Structure Determination. *Acta Crystallogr A Found Adv* **2015**, *71* (1), 3–8. https://doi.org/10.1107/S2053273314026370.

(136) Sheldrick, G. M. Crystal Structure Refinement with SHELXL. *Acta Crystallogr C Struct Chem* **2015**, *71* (1), 3–8. https://doi.org/10.1107/S2053229614024218.

© University of Pretoria

Chapter 3: Electrochemical Behaviour and Molecular Orbital Calculations

3.1) Introduction

The electrochemical "non-innocent" behaviour of a ligand may broadly be described as a ligand's ability to act as an electron reservoir during reduction or oxidation reactions of the complex, where the ligand can reversibly accept and release electrons to facilitate reactions at the metal, (e.g., changes in oxidation state).[1–4]

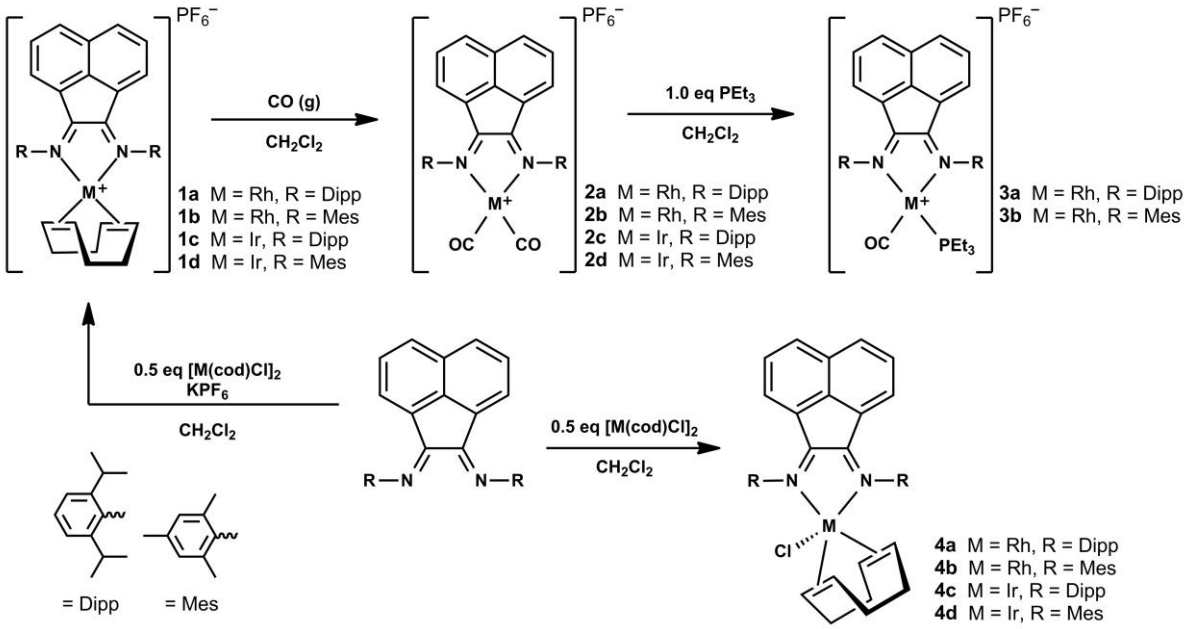
The team of Fedushkin *et al*. has demonstrated the non-innocent abilities of DippBIAN and MesBIAN ligands to accept and stabilise additional electron density in complexes with the ligands reduced by up to four electrons.[5–10] An extensive collection of BIAN complexes with s- and p-block elements is also discussed in a review by Hill, Vargas-Baca and Cowley.[11]

More pertinent perhaps are the redox non-innocent characteristics of BIAN ligands in coordination complexes with transition metals. A neutral, pseudo-octahedral titanium(III) complex bearing three radical BIAN ligands has been reported.[12] Electrochemical analysis of the complexes displayed four quasi-reversible processes, illustrating the ability of the BIAN ligands to stabilise the complex over a range of five different oxidation states. A vanadium(III) complex of three BIAN ligands was also reported which showed reversible and delocalised valence tautomerism between the three BIAN ligands.[13] A tetrahedral copper(I) complex featuring two BIAN ligands has been reported as an active photosensitiser for carbon-carbon bond formation catalysis.[14]

The electrochemical reduction of CO_2 by BIAN complexes has been reported for a rhenium(I) carbonyl, a molybdenum(II) dicarbonyl, as well as a rhodium(III) trichloride complex.[15–17] Before these studies, Rh(I)-BIAN complexes were chiefly reported as part of synthetic[18,19] or catalytic studies,[20,21] while reactivity of the complex with solvent acetonitrile complicated the electrochemical analyses of the single five-coordinate complex previously reported.[17,22] Similarly, reported BIAN complexes of iridium have largely been limited to iridium(III).[21,23–25] However, a methodical electrochemical study of BIAN complexes of Rh and Ir (featuring 4- and 5-coordinate geometries), with DFT assisted assignment of redox events has not been reported.

© University of Pretoria

The electrochemical investigations performed as part of the present study were therefore aimed at expanding our understanding of the intramolecular electronic interactions of the four groups of new Rh(I)- and Ir(I)-BIAN complexes, each group featuring ancillary ligands that are known to exhibit different degrees of electron withdrawal or donating characteristics within in coordination complexes. These ancillary ligands were chosen from across the spectrochemical series to include low, mid and high field ligands (Scheme 3.1–1), and consist of σ-donor/π-donor (chloride), and σ-donor/π-acceptor ligands (1,5-cyclooctadiene, triethylphosphine and carbonyl).



Scheme 3–1: Reaction scheme of reported complexes.

The frontier molecular orbitals (FMOs) of these modelled states, along with the calculated Electrostatic Surface Potential (ESP) maps and Spin density plots were applied to establish the localisation of observed redox events.

© University of Pretoria

3.2) Methods and Materials

3.2.1) Voltammetry

Electrochemical studies were carried out on a Metrohm Autolab PGSTAT100, using NOVA 2.1 electrochemistry software interface. Cyclic voltammograms (CVs) were recorded between –2.0 and +1.8 V and scan rate of 100 mV s^{-1}. Differential pulse voltammograms (DPVs) were recorded from 0.0 V to –2.0 V and 0.0 V to +1.8 V, with a step potential of 5 mV. All measurements were made using a three-electrode cell with a 3 mm glassy carbon working electrode (GCE), platinum wire counter electrode, and silver wire pseudo-reference electrode.[26,27] The GCE was polished using a suspension of 0.05 µm alumina on a micro-cloth polishing pad prior to each measurement.

Sample solutions were prepared using 1.0 mM analyte concentration, 0.1 M tetrabutylammonium hexafluorophosphate ($TBAPF_6$) supporting electrolyte in HPLC grade CH_2Cl_2, deoxygenated with Ar (g) before starting analyses.

All potentials from the cyclic voltammograms (CVs) and differential pulse voltammograms (DPVs) are reported relative to the silver wire pseudo-reference electrode, as addition of internal electrochemical standards (i.e. the $FcH^{0/+1}$ or $[Fe(\eta\text{-}C_5Me_5)_2]^{0/+1}$ couples respectively) to the analyte solutions cause significant shifts in the analyte's peak potentials, leading to the formation of additional secondary chemical reaction peaks, as well as the notable irreversibility of the internal standards' redox peaks between first and second scans. In addition, it should be noted that the electrochemical analyses were not performed at variable scan rates due to the irreversible nature of the majority of redox events for the reported series of complexes.

3.2.2) Molecular Modelling

Structural optimisations and frequency calculations were performed on both the free ligands and all of the above reported complexes using Gaussian 16 B.01.[28] The series of charged oxidation states that were modelled for each complex are labelled using "(n = integer)", where *n* represents the number of electrons that have been removed or added to the molecule (ex. "n = –1" representing the first oxidised state, and "n = +2" the second reduction state). The hybrid functional B3LYP[29,30] was employed with the def2SVP[31] split valence basis set on all atoms, including unrestricted basis functions for all calculations of open shell charged state molecules. Long range electron correlations resulting from electron delocalisation were accounted for with the addition of Grimme's D3 Empirical Dispersion function.[32,33] The effects of solvation were modelled using continuum potential surfaces functions[34,35] (denoted cPCM) for CH_2Cl_2. The thermodynamic energies, frontier orbitals and

© University of Pretoria

Electrostatic Surface Potential surfaces (ESP) were calculated for all molecules and their charged states. Spin density plots were generated for charged state calculations to visualise the (de)localisation of the unpaired electrons. Discussions on the computational procedures and methodology will be presented in Chapter 4. Additional orbital diagrams, ESP diagrams, spin density plots and Mulliken charge diagrams are available in Appendix G.1 for the interested reader. The stationary point coordinates for all calculated compounds, in both gas-phase and cPCM, may be found in Appendix J.

Total Energies (EE_{ZPV}) are reported in a.u. and include the zero-point vibrational correction. Diagrams of H(S)OMO and LUMO orbitals were generated with [Isovalue] = 0.02, and Spin Density plots with [Isovalue] = 0.0004. Mulliken Spin diagrams were generated with symmetric colour shading (unless specified otherwise) where brightly coloured areas indicate the localisation of unpaired spin densities. Alpha FMOs are presented for reduced species (n = +1) to (n = +4) in the Charge Localisation Tables, and Beta FMOs for oxidised species (n = –1) to (n = –3).

© University of Pretoria

3.3) Results and Discussion

3.3.1) Electrochemical Behaviour and Molecular Orbital Calculations

Uncertainty has been expressed in some literature sources regarding the exact nature of electrochemical events of BIAN complexes as both the ligand and metal may show reactivity within the same potential range, leading to intricate voltammograms that are difficult to interpret unambiguously.[36] The possibility of ligand dissociation during the analysis adds additional complexity to interpretation of the electrochemical reactivity of these complexes.[22] The assignments of the electrochemical events presented in this chapter are therefore informed by changes observed in the MO compositions, spin density plots as well as charge distribution diagrams as calculated for each compound and their various charged states.

Interpretation of CVs were done in conjunction with the recorded DPVs. The peak potentials observed in DPVs are closely related to the half-peak potentials of an electrochemical reaction ($E_{½}$), while the midpoint between the cathodic (E_{pc}) and anodic peak (E_{pa}) potentials in the CVs of an electrochemically reversible one electron reaction may be used to calculate the formal reaction potential ($E°'$).[37] However, due to the large number of irreversible events observed in the CVs of the free ligands and complexes, reaction peak potentials in this work are reported as recorded in the DPV experiments unless otherwise stated (e.g. Figure 3.3–1).

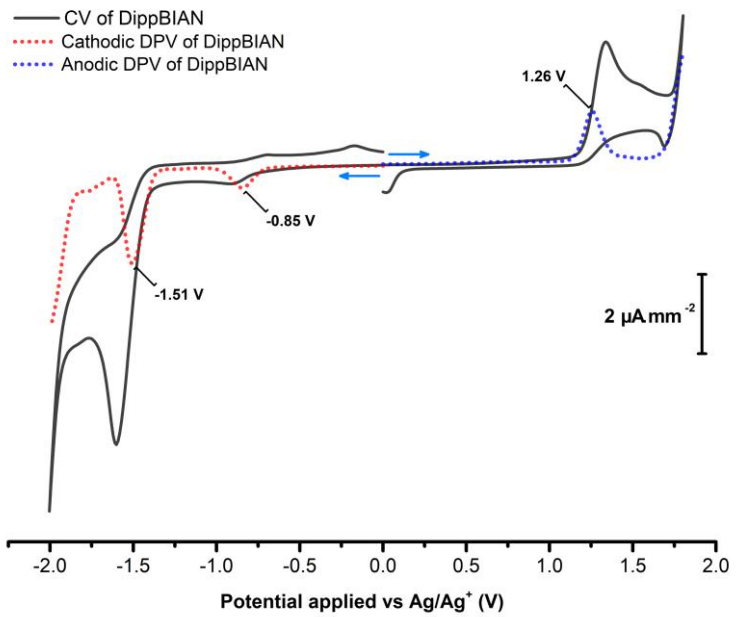


Figure 3–1: CV and DPV of DippBIAN recorded in CH_2Cl_2 with 1.0 mM analyte and 0.1 M $TBAPF_6$ supporting electrolyte.

© University of Pretoria

Cyclic voltammetry potential cycles were applied twofold in all measurements to ascertain the repeatability of electrochemical events under the experimental conditions. These cycles are designated as “First pass” and “Second Pass” scans respectively (e.g., Figure 3.3–2), and aided in identifying the electrochemical signals which originate from secondary chemical reactions within the analyte solutions. Additional voltammograms of the free ligands and complexes recorded under Ar (g) are available in Appendix F.1.

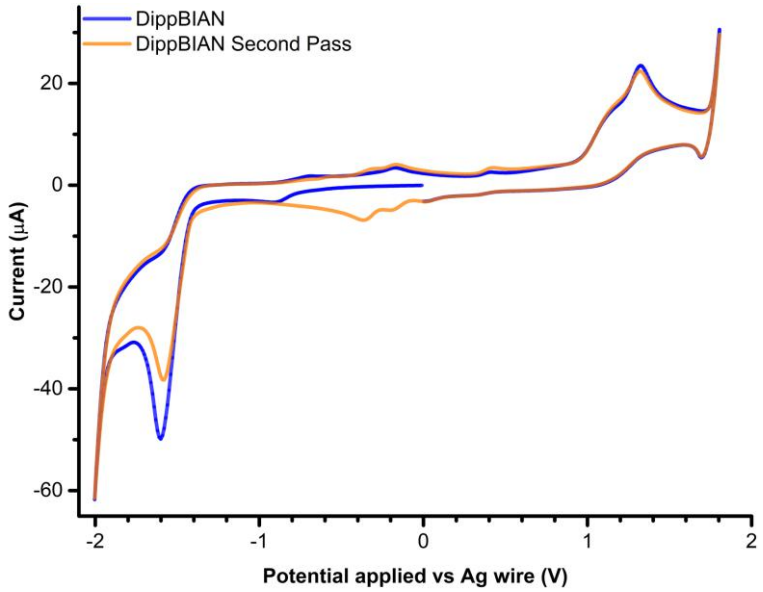


Figure 3–2: Cathodic first CV of the free DippBIAN ligand recorded in CH_2Cl_2 with 1.0 mM analyte and 0.1 M $TBAPF_6$ supporting electrolyte. The second pass scan (orange) is included to assist in differentiating analyte peaks from decomposition or secondary reaction peaks.

Primary and secondary electrochemical events could thus largely be delineated by simultaneous examination of the first and second pass CV scans, as well as the recorded DPVs for the respective analyte.

Table 3–1: The modelled charged states are labelled with the "(n = integer)" moniker. The integer value of “n” represents how many electrons have been added to, or removed from, the starting molecular geometry to model changes in its charged state during reductive or oxidative electrochemical processes.

“n” label	(n = +2)	(n = +1)	(n = 0)	(n = –1)	(n = –2)
Electrons added	2	1	0	-	-
Electrons removed	-	-	0	1	2
Compound Examples	$[DippBIAN]^{2-}$	$[DippBIAN]^{-}$	DippBIAN	$[DippBIAN]^{+}$	$[DippBIAN]^{2+}$
	$[RhDB(CO)_2]^{-}$	$[RhDB(CO)_2]$	$[RhDB(CO)_2]^{+}$	$[RhDB(CO)_2]^{2+}$	$[RhDB(CO)_2]^{3+}$

To assist in the assignment of primary electrochemical events related directly to the reduction and oxidation of the analyte, each compound was computationally modelled in eight different charged

© University of Pretoria

states – representative of the initial ground state for the compounds, after losing 1 to 3 electrons, as well as after gaining 1 to 4 electrons. The series of charged states are labelled using a "(n = integer)" moniker, where "*n*" represents the number of electrons that have been removed or added to the molecule (Table 3.1–1).

Visualisations of the Frontier Molecular Orbitals (FMOs) were critically evaluated for parallels and contrasts – in terms of orbital distribution across the molecule as well as atomic orbital contributions to the overall MO – between proximate "(n = integer)" charged states of the same compound.[38–40] The FMO evaluation was enriched by examination of the charged states for theoretical Electrostatic Surface Potential (ESP) maps, Mulliken Spin diagrams and Spin density plots to establish the (de)localisation of charges resulting from changes in the electron count between the modelled states.[40–42]

Numerous similarities were noted in the electrochemical and computational results of the studied compounds due to communal structural and chemical characteristics among them (*vide infra*). In an effort to avoid exhaustive repetition, the results are presented as an abridged report. Formative examples of how the analysis methodology and rationale was applied are presented in the following subsection (Section 3.3.2), after which a comparative discussion of the results for the free Dipp- and MesBIAN ligands, and the series of complexes **1**–**4** will be presented (Section 3.3.3).

3.3.2) Analysis Methodology and Rationale

3.3.2.i) MesBIAN

Two reduction events are observed at –1.43 V and –1.92 V in the CV and DPV of the free MesBIAN ligand (Figure 3.3–3). The first oxidation event is observed at +1.20 V, and a second oxidation event appears near the edge of the DPV potential window (+1.73 V). However, the apex of the second oxidation peak falls beyond the potential window of solvent used for the CV analysis. Inclusion of the DPV peak at +1.73 V as part of the experimentally measured oxidation events for MesBIAN is supported by the sharp increase in the anodic current of the CV as the anodic sweep approach +1.8 V (Figure 3.3–4, left), as well as by previously reported electrochemical results for the MesBIAN ligand.[36]

© University of Pretoria

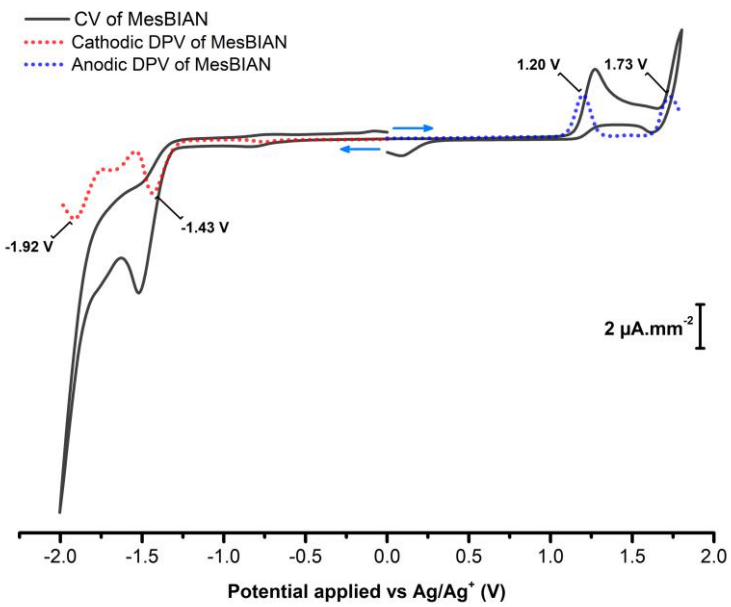


Figure 3–3: CV and DPV of MesBIAN recorded in CH_2Cl_2 with 1.0 mM analyte and 0.1 M $TBAPF_6$ supporting electrolyte.

The second pass anodic current is observed to increase by an average of 10 µA at potentials above +1.0 V following a full cathodic sweep to –2.0 V (Figure 3.3–4, left), with a concomitant broadening of the oxidation peak at +1.20 V. Following any anodic sweeps from potentials above +1.5 V, additional reduction peaks are observed in the cathodic return scan between +0.3 V and –0.6 V (Figure 3.3–4, right; Figure 3.3–5, left). A similar pair of peaks has previously been reported for both Dipp- and MesBIAN, only observed following the irreversible first oxidation of the ligands.[36] A decrease in the second pass cathodic current at potentials below –1.4 V is also noted (Figure 3.3–5, right).

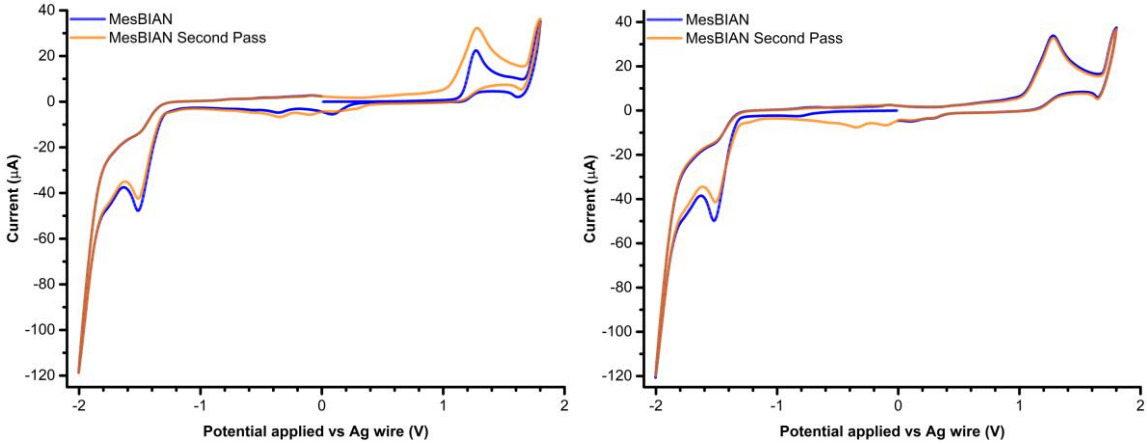


Figure 3–4: Anodic first (left) and Cathodic first (right) CVs of the free MesBIAN ligand recorded in CH_2Cl_2 with 1.0 mM analyte and 0.1 M $TBAPF_6$ supporting electrolyte. The second pass scans (orange) are included to assist in differentiating analyte peaks from decomposition or secondary reaction peaks.

© University of Pretoria

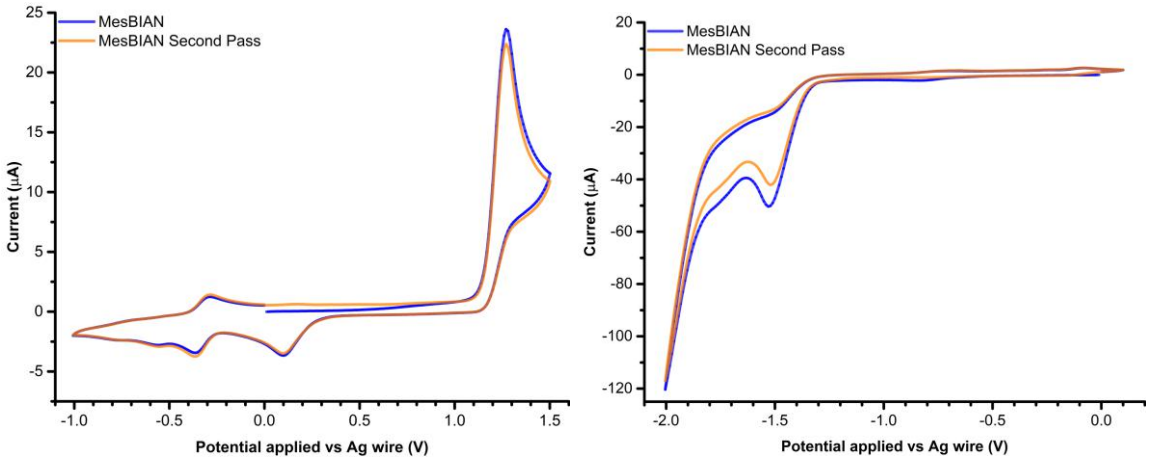


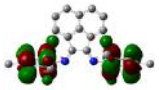
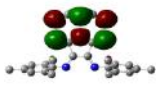
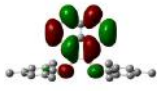
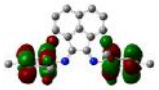
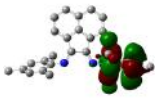
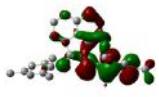
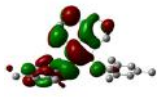
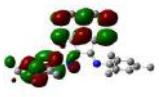
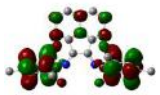
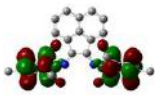
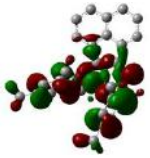
Figure 3–5: Narrowed potential window CVs the free MesBIAN ligand, anodic first (left) and cathodic first (right), recorded in CH_2Cl_2 with 1.0 mM analyte and 0.1 M $TBAPF_6$ supporting electrolyte. The second pass scans (orange) are included to assist in differentiating analyte peaks from decomposition or secondary reaction peaks.

The FMO visualisations for the eight modelled states of MesBIAN are present in Table 3.3–2 below and are very similar in appearance to those of DippBIAN in terms of orbital distributions and symmetry changes. The orbital overlap of the (n = 0) HOMO of MesBIAN displays largely antibonding character and is laterally delocalised across the aryl rings of the two Mes-substituents and the bisimine N=C–C=N moiety. The *para*-methyl groups show a greater amount of involvement in the HOMO composition than the *ortho*-methyl groups. In contrast, the (n = 0) LUMO is comprised of contributions from the acenaphthene rings, and out-of-phase interactions between the nitrogens and carbons of the bisimine moiety, with only minor contributions from the aryl-substituents. The orbital distributions of (n = +1) $HOMO_\alpha$ appears in good agreement with those of (n = 0) LUMO.

The orbital distribution of the (n = 0) LUMO and (n = +1) $HOMO_\alpha$ suggest the first reduction event at –1.43 V is delocalised mainly between the two bisimine nitrogen atoms (Table 3.3–2), with an increase in bonding-type orbital overlap between the two bisimine carbons, and minor stabilising contributions from the acenaphthene π-electron cloud. The orbital overlap patterns seen across the acenaphthene rings in (n = 0) LUMO and (n = +1) $HOMO_\alpha$ show a lack of orbital contributions from any pair of adjacent carbon atoms, which indicate a partial non-bonding character of the molecular orbital on the acenaphthene backbone itself.[43] The out-of-phase interaction between the *p*-orbitals of the bisimine nitrogens and the bisimine carbons, as well as the bonding interaction between bisimine carbons themselves, support the experimentally observed bond order change from (N=C–C=N) to $(N–C=C–N)^-$ which has been reported for the reduction of DippBIAN.[5,11]

© University of Pretoria

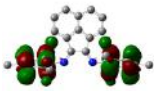
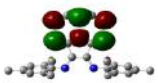
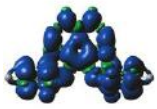
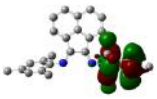
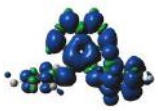
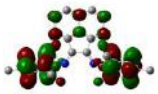
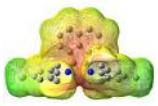
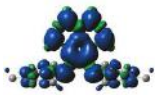
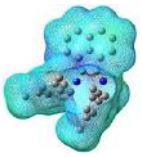
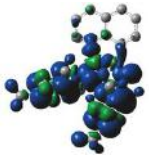
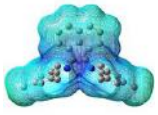
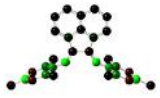
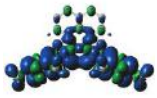
Table 3–2: H(S)OMO and LUMO Diagrams and Energies of MesBIAN, modelled in different charged states. Total Energies (EE_{ZPV}) in a.u. include zero-point vibrational correction. H(S)OMO and LUMO orbitals were generated with [Isovalue] = 0.02. All calculations were performed at B3LYP-D3/def2-SVP level of theory in CH_2Cl_2 using cPCM.

EE_{ZPV} (a.u.)	S	H(S)OMO$_\alpha$ (eV)	LUMO$_\alpha$ (eV)	H(S)OMO$_\beta$ (eV)	LUMO$_\beta$ (eV)	Other (eV)
–1268.36 (n = +4)	5/2	 0.712	 2.127	 –2.328	 1.136	 HOMO -1$_\alpha$ 0.703
–1268.39 (n = +3)	2	 0.432	 1.337	 –2.770	 0.291	 LUMO +1$_\alpha$ 1.632
–1268.41 (n = +2)	3/2	 –1.602	 0.999	 –3.534	 –0.204	 LUMO +1$_\alpha$ 1.022
–1268.35 (n = +1)	1	 –2.800	 –1.298	 –4.678	 –1.071	 HOMO -1$_\beta$ –4.715
–1268.25 (n = 0)	1/2	 –5.827	 –2.375			
–1268.06 (n = –1)	1	 –6.442	 –3.513	 –6.646	 –4.951	
–1267.83 (n = –2)	3/2	 –7.630	 –4.485	 –7.660	 –5.637	 LUMO +1$_\beta$ –5.594

The ESP map of the MesBIAN (n = 0) state indicates that the area nearest the bisimine nitrogens has a partial negative charge (red colouration) compared to the rest of the molecule's surface area due to their high electronegativity (Table 3.3–3).

© University of Pretoria

Table 3–3: Electrostatic Surface Potential and Spin Density diagrams of MesBIAN. Total Energies (EE_{ZPV}) in a.u. include zero-point vibrational correction. H(S)OMO and LUMO orbitals were generated with [Isovalue] = 0.02, and Spin Density plots with [Isovalue] = 0.0004. Mulliken Spin diagrams were generated with symmetric colour shading where brightly coloured areas indicate the localisation of unpaired alpha- or beta-spin densities. Alpha FMOs are presented for reduced species, and Beta FMOs for oxidised species. All calculations were performed at B3LYP-D3/def2-SVP level of theory in CH_2Cl_2 using cPCM.

EE_{ZPV} (a.u.)	S	H(S)OMO	LUMO	ESP	Mulliken Spin	Spin Density
–1268.36 (n = +4)	5/2					
–1268.39 (n = +3)	2					
–1268.41 (n = +2)	3/2					
–1268.35 (n = +1)	1					
–1268.25 (n = 0)	1/2					
–1268.06 (n = –1)	1					
–1267.83 (n = –2)	3/2					

The ESP map of the (n = +1) state of MesBIAN indicates a coalescence of negative charge in the region of the bisimine moiety. The bright green colouration in Mulliken spin diagram shows that the unpaired electron density is localised chiefly on the bisimine nitrogen atoms themselves. The acenaphthene rings provide some stabilisation to the reduced states of MesBIAN by delocalising the electron density over a greater surface area as indicated by their contribution in the Spin density plot.

The (n = +1) $LUMO_{\alpha}$ and (n = +2) $HOMO_{\alpha}$ orbitals have comparable atomic orbital compositions and may be best described as a π* antibonding MO (Table 3.3–2). Comparison between the Mulliken spin

© University of Pretoria

diagrams of the (n = +1) and (n = +2) states (Table 3.3–3), indicate a considerable increase in the amount of unpaired electron density in the acenaphthene rings and the bisimine moiety of the (n = +2) state. The ESP map of (n = +2) shows an increased negative charge surrounding the bisimine as well as the acenaphthene rings. Interestingly, the Spin density plot shows that both aryl rings participate to some small degree to the stabilisation of the additional electron density, although the bulk of the spin density is delocalised across the bisimine and acenaphthene rings. The second reduction of MesBIAN at –1.92 V can therefore be described as delocalised across the bisimine moiety and acenaphthene rings.

Although the third and fourth reduction events of MesBIAN were not experimentally observed during the electrochemical measurements, the (n = +3) and (n = +4) states were modelled to inform our interpretation of changes in the FMOs and spin density between the free coordinated ligand at these highly reduced states, which were observed for some of the complexes, ex. **1c**–**d** and **4a**–**d** (*vide infra)*.

The (n = +2) $LUMO_{\alpha}$ [0.999 eV] and (n = +2) LUMO $+1_{\alpha}$ [1.022 eV] orbitals were calculated to be energetically degenerate (Table 3.3–2), and both included a pair of π* antibonding orbitals on the aryl ring substituents of the MesBIAN ligand. In contrast, however, the (n = +3) $HOMO_{\alpha}$ featured a π* antibonding orbital on only one of the aryl rings. The dissimilarity in orbital composition between the (n = +3) $HOMO_{\alpha}$ and (n = +2) $LUMO_{\alpha}$ may be due to orbital rearrangement taking place upon reduction to the (n = +3) state. None the less, based on the charge and spin localisation observed in the ESP map, Mulliken Spin diagram and Spin density plot, the third reduction of MesBIAN is anticipated to be chiefly confined to one of the aryl ring substituents (Table 3.3–3).

The (n = +4) $HOMO_{\alpha}$ [0.712 eV] and (n = +4) HOMO -1_{α} [0.703 eV] orbitals were found to be energetically degenerate (Table 3.3–2), and their orbital distributions are nearly identical. The pair of π* antibonding orbitals are geometrically nearly identical, but the orbital phasing of the left-hand aryl-substituent's contributions is inverted in $HOMO_{\alpha}$ compared to HOMO -1_{α}. The orbital distributions of (n = +3) $LUMO_{\alpha}$ and (n = +3) LUMO $+1_{\alpha}$ were anticipated to be fairly comparable to those of (n = +4) $HOMO_{\alpha}$ and (n = +4) $LUMO_{\alpha}$ respectively. However, the (n = +3) $LUMO_{\alpha}$ features a π* antibonding orbital on only the left-hand aryl ring, and (n = +3) LUMO $+1_{\alpha}$ presents π* antibonding orbitals on the left-hand aryl ring and acenaphthene ring. The dissimilarity in orbital distributions between the (n = +3) to (n = +4) states invoke the possibility of further orbital rearrangement occurring between the third and fourth reduction to stabilise the increased charge and electron density. The ESP map of the (n = +4) state indicates the negative charges are delocalised across the acenaphthene

© University of Pretoria

rings and both aryl-substituents (Table 3.3–3). Comparing the Mulliken spin diagrams and Spin density plots of (n = +3) and (n = +4), a marked increase in electron density is noted on the left-hand aryl-substituent of the (n = +4) state. The fourth reduction of MesBIAN is thus anticipated to be localised on the opposite aryl ring substituent as the third reduction event.

Turning our attention now to the oxidation events of MesBIAN – for the first oxidation of MesBIAN (+1.20 V) the optimised molecular geometry of the (n = –1) state showed a deformation of the typical (*E*,*E*)-BIAN conformer to the (*E*,*Z*)-conformer (Table 3.3–2).[11] The (n = 0) HOMO and (n = –1) $LUMO_{\beta}$ presented antibonding character and are delocalised equivalently across both aryl-substituents. It is known that the C=N bonds in BIAN compounds may interconvert between (*E*,*E*)- and (*E*,*Z*)-configurations in solution, without affecting the chelation ability of the ligand.[11] Closer examination of (n = –1) $HOMO_{\beta}$ revealed an in-phase orbital overlap interaction between the left nitrogen and the π-cloud electrons of the right aryl ring. It should be noted that the shortest interatomic distance between the left nitrogen and right aryl ring is 2.630 Å. The Mulliken Spin diagrams show that the unpaired electron density is delocalised between the two aryl ring substituents and the bisimine nitrogens (Table 3.3–3). The (*E*,*Z*)-isomerisation that is observed in the (n = –1) state of MesBIAN may enable constructive orbital overlap between the right aryl ring and the left nitrogen atom, facilitating the exchange of electron density between these two otherwise isolated regions of the molecule, resulting in the intramolecular charge delocalisation that is observed in the Mulliken Spin diagrams.

The molecular geometry of the (n = –1) state of DippBIAN optimised to a similar (*E*,*Z*)-conformation as determined for the (n = –1) MesBIAN, however, the (n = –1) $LUMO_{\beta}$ of DippBIAN was localised on the distorted *Z*-aryl substituent and its adjacent bisimine nitrogen (Table G.1–1). No in-phase orbital overlap interactions were observed between the aryl-substituent and imine nitrogen, likely due to the steric bulk of the isopropyl groups precluding close enough proximity between the π-electrons of the *Z*-aryl substituent and imine nitrogen. The Mulliken spin and ESP diagrams indicate that the positive charge on the DippBIAN (n = –1) state is consequently localised on the *Z*-aryl substituent.

The (n = –2) $LUMO_{\beta}$ [–5.637 eV] and LUMO $+1_{\beta}$ [–5.594 eV] orbitals were observed to be nearly degenerate in energy and displayed orbital distributions comparable to those observed in the (n = –1) $HOMO_{\beta}$ and $LUMO_{\beta}$ (Table 3.3–2). The second oxidation of MesBIAN (+1.73 V) induces a subsequent structural deformation of the (*E*,*Z*)-conformer. The modified bond angles around the nitrogen atoms suggest a loss of the sp^2 trigonal planar hybridisation in favour of a geometry approaching sp^3 tetrahedral hybridisation. The ESP map and Mulliken spin diagrams indicate

© University of Pretoria

that the positive electrostatic charge and spin density is distributed across both aryl-substituents (Table 3.3–3).

Summary: The computational results quite accurately reproduce the charge distribution patterns which have been described by Fedushkin *et al.*,[5] in their report of the crystal structures of DippBIAN in four different reduced states; as well as the charge delocalisation behaviour which has been observed in various BIAN complexes.[12–14]

The first reduction of MesBIAN at –1.43 V is mainly delocalised within the bisimine moiety due to a changes in the N–C and C–C bond order upon reduction from (N=C–C=N) to (N–C=C–N)$^{-}$. The second reduction (at –1.92 V) is delocalised between the bisimine moiety and acenaphthene rings. The third and fourth reductions are projected to be localised to one of the aryl-substituents each. The first oxidation of MesBIAN (+1.20 V) is delocalised between the two aryl ring substituents and the bisimine nitrogens, causing isomerisation of the (*E*,*E*)-BIAN conformer to the (*E*,*Z*)-conformer. The second oxidation of MesBIAN (+1.73 V) is distributed across both aryl-substituents and results in further distortion of the bonding geometry of the two imino nitrogens.

3.3.2.ii) **2b** [RhMB(CO)$_2$]PF$_6$

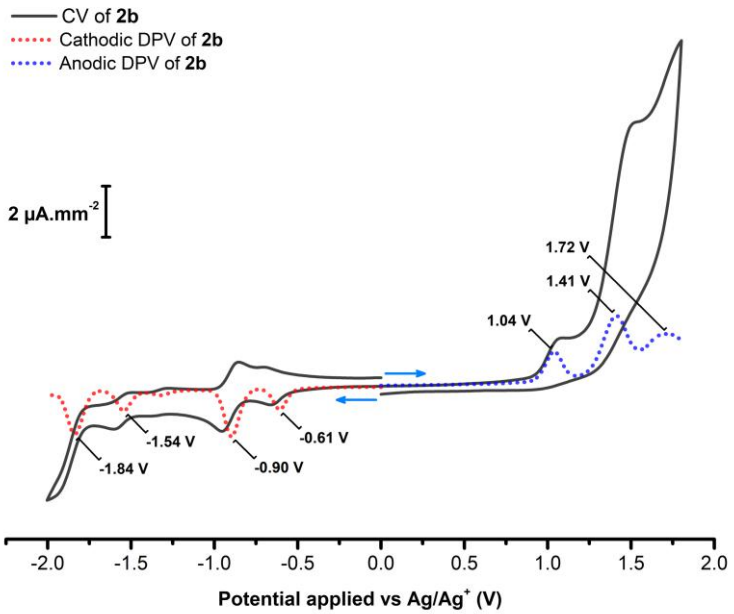


Figure 3–6: CV and DPV of ***2b*** *[RhMB(CO)$_2$]PF$_6$ recorded in CH_2Cl_2 with 1.0 mM analyte and 0.1 M $TBAPF_6$ supporting electrolyte.*

© University of Pretoria

In the cathodic CV and DPV of **2b**, two major reduction events are observed at –0.90 V and –1.84 V along with two minor events at –0.61 V and –1.54 V (Figure 3.3–6). Three oxidations are observed in the anodic scan DPV at +1.04 V, +1.41 V and +1.72 V. The third oxidation event is poorly resolved in the CV scans due to the sharp increase in anodic peak current associated with the oxidation event at +1.41 V, as well as its close proximity to the edge of the potential window for the solvent.

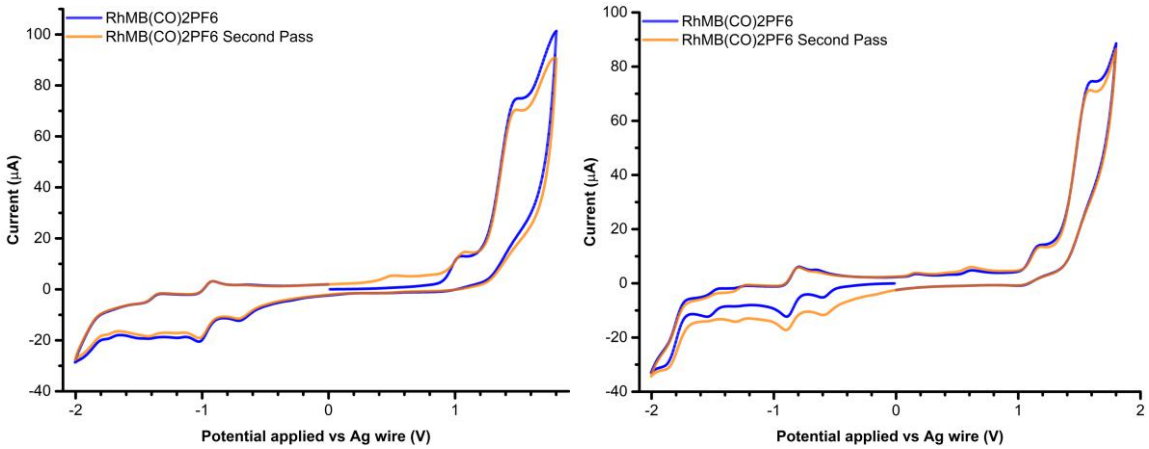


*Figure 3–7: Anodic first (left) and Cathodic first (right) CVs of **2b** recorded in CH_2Cl_2 with 1.0 mM analyte and 0.1 M $TBAPF_6$ supporting electrolyte. The second pass scans (orange) are included to assist in differentiating analyte peaks from decomposition or secondary reaction peaks.*

Anodic scans following a cathodic sweep to potentials below –1.8 V display an additional minor oxidation peak at +0.5 V (Figure 3.3–7, left), as well as a decrease in anodic peak current of the second and third oxidation events. Limiting the anodic scan potential to +1.3 V revealed the first oxidation event at +1.04 V to be electrochemically reversible, but not fully chemically reversible on the timescale of the experiment (Figure 3.3–8).

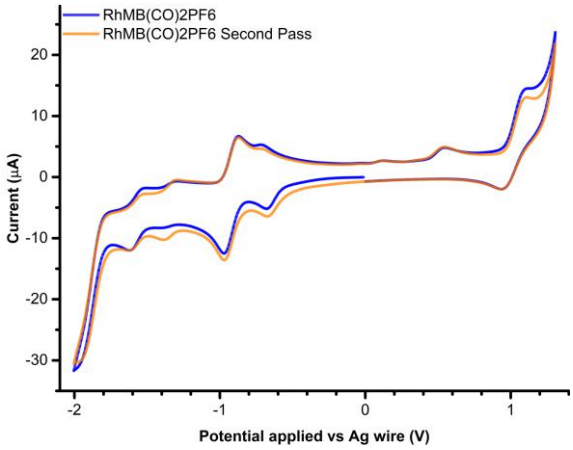


*Figure 3–8: Narrowed potential window CV of **2b** recorded in CH_2Cl_2 with 1.0 mM analyte and 0.1 M $TBAPF_6$ supporting electrolyte. The second pass scan (orange) is included to assist in differentiating analyte peaks from decomposition or secondary reaction peaks.*

© University of Pretoria

An overall increase in the second pass cathodic current is noted between 0.0 V and –1.7 V in the second pass cathodic scans following an anodic sweep to +1.8 V (Figure 3.3–7, right). The reduction peaks are poorly resolved due to overlapping secondary reduction peaks between 0.0 and –2.0 V. However, when the maximum anodic sweep potential is limited to +1.3 V (Figure 3.3–8), the cathodic reduction peak profiles remain clearly defined and appear nearly repeatable.

The 10–20 µA decrease in second pass anodic current observed in the –0.1 V to +1.8 V CV analysis indicates a large extent of complex decomposition resulting from the irreversible oxidation events (Figure 3.3–9, left). The second pass cathodic current between –0.5 V and –1.8 V is decreases by *ca*. 5 µA following a cathodic sweep to –2.0 V and a maximum anodic sweep potential of +0.1 V (Figure 3.3–9, right), indicating decomposition of the analyte at potentials below –1.8 V.

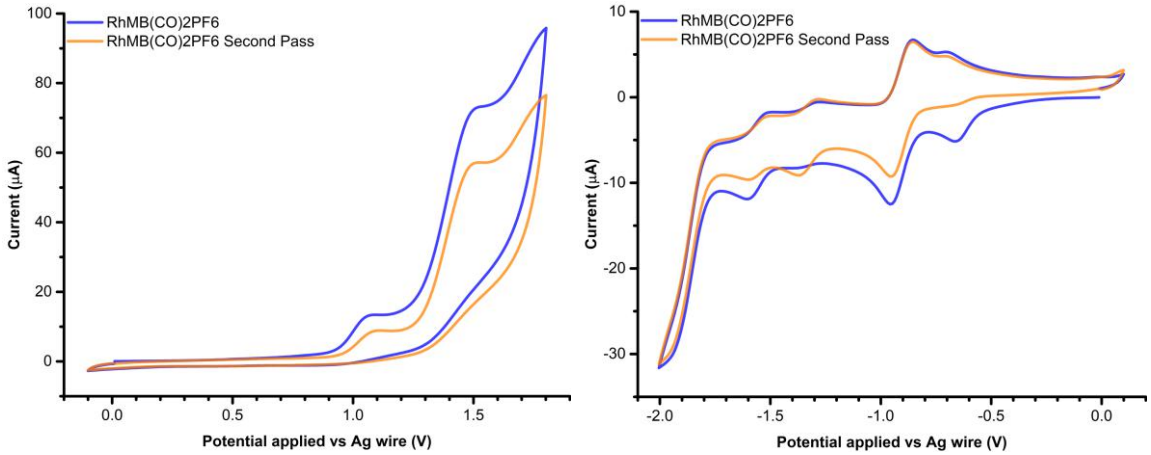


*Figure 3–9: Narrowed potential window CVs of **2b**, anodic first (left) and cathodic first (right), recorded in CH_2Cl_2 with 1.0 mM analyte and 0.1 M $TBAPF_6$ supporting electrolyte. The second pass scans (orange) are included to assist in differentiating analyte peaks from decomposition or secondary reaction peaks.*

The third oxidation event of **2b** (+1.72 V) occurs at nearly the same potential as the second oxidation event of the free MesBIAN ligand (+1.73 V, Figure 3.3–3). A similar third oxidation was also observed for **1d**. Two scenarios which may explain the similarity in oxidation potential for these different events are:

- That the ligand-centred second oxidation event is largely unaffected by the coordination of the metal, and the oxidation potential therefore remains unchanged; or,
- That ligand dissociation from the intermediary [**2b**$^{2+}$] complex occurs following the oxidation event at +1.41 V, yielding a [MesBIAN]$^{+}$, cation which is then further oxidised to form [MesBIAN]$^{2+}$ at +1.72 V.

© University of Pretoria

Despite employing acetonitrile as solvent, recent work by Romashev *et al*. on [Rh(DippBIAN)((cod)Cl] reported observing a similar electrochemical reduction peak for free DippBIAN ligand, which dissociated from the analyte during analysis.[22]

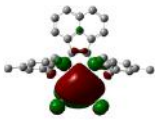
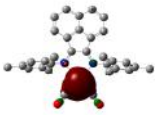
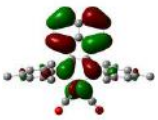
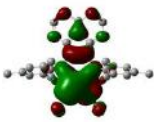
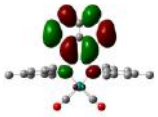
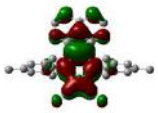
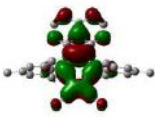
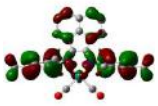
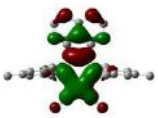
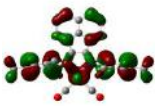
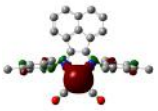
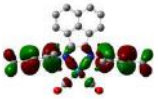
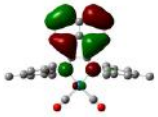
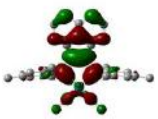
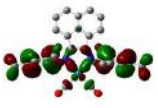
The secondary reduction peak observed in Figure 3.3–8 and Figure 3.3–9 (right) provides additional information. The peak potential of this event (*ca.* –1.4 V) corresponds closely to the first reduction potential of the free MesBIAN ligand (–1.43 V, Figure 3.3–3). The fact that this secondary event is only observed after anodic sweeps to potentials higher than +1.3 V, and cathodic sweeps to potentials below –1.8 V, indicates that ligand dissociation is taking place as a result of the decomposition of **2b**.

The orbital composition of (n = +1) $HOMO_{\alpha}$ appears identical to that of (n = 0) LUMO, but with opposite orbital phasing (Table 3.3–4). The MOs are distributed across both carbonyl ligands, the bisimine moiety, and acenaphthene rings along a single plane. The orbital contribution of the acenaphthene rings appears to be of non-bonding symmetry, whereas the bisimine N=C and carbonyl C=O contributions display more antibonding character. Examination of the ESP map reveals an increase in negative surface potential across the acenaphthene rings, near the bisimine moiety, as well as towards the oxygen atoms of the two carbonyl ligands (Table 3.3–5). The Mulliken spin diagram indicates majority localisation of the unpaired electron density on the bisimine N=C–C=N moiety, consistent with what was observed for the first reductions of complexes **1a**–**d** as well as the free Dipp- and MesBIAN ligands.

The (n = +2) $HOMO_{\alpha}$ is comparable to the (n = +1) $LUMO_{\alpha}$ (Table 3.3–4), a π* antibonding orbital composed of majority contribution from the acenaphthene rings and bisimine moiety, with minor *d*-orbital symmetry contributions visible from the rhodium centre. The ESP map for the second reduction indicates an increase in negative charge on the acenaphthene rings and bisimine moiety with unpaired electron density delocalised across the same molecular regions (Table 3.3–5). Analogous orbital and charge distributions were observed for the free ligands as well as the other modelled complexes.

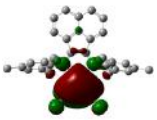
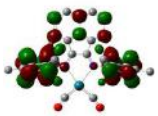
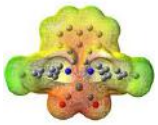
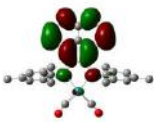
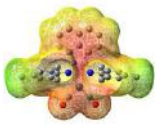
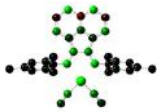
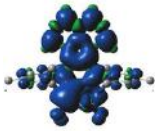
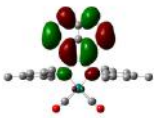
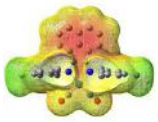
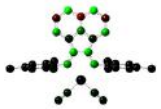
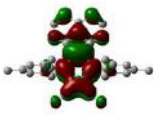
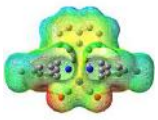
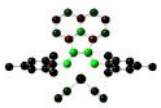
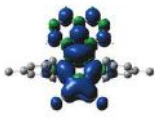
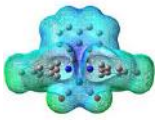
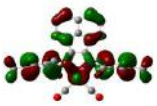
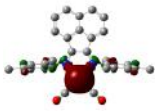
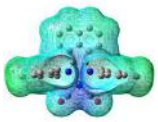
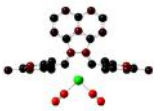
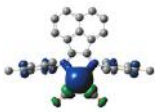
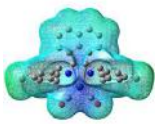
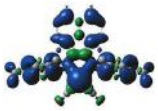
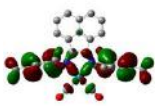
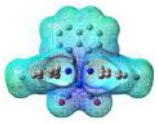
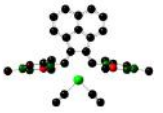
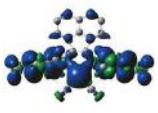
© University of Pretoria

*Table 3–4: H(S)OMO and LUMO Diagrams and Energies of **2b**, modelled in different charged states. Total Energies (EE_{ZPV}) in a.u. include zero-point vibrational correction. H(S)OMO and LUMO orbitals were generated with [Isovalue] = 0.02. All calculations were performed at B3LYP-D3/def2-SVP level of theory in CH_2Cl_2 using cPCM.*

EE_{ZPV} (a.u.)	S	H(S)OMO$_\alpha$ (eV)	LUMO$_\alpha$ (eV)	H(S)OMO$_\beta$ (eV)	LUMO$_\beta$ (eV)	Other (eV)
–1605.60 (n = +4)	5/2	 –0.716	 1.123	 –3.427	 –0.203	
–1605.59 (n = +3)	2	 –1.932	 20.841	 –3.928	 –1.014	 HOMO -1$_\alpha$ –2.240
–1605.53 (n = +2)	3/2	 –2.488	 –0.841	 –4.634	 –1.817	 LUMO +1$_\alpha$ –0.386
–1605.44 (n = +1)	1	 –4.432	 –2.206	 –6.076	 –2.756	 HOMO -1$_\beta$ –6.115
–1605.28 (n = 0)	1/2	 –6.880	 –4.037			
–1605.04 (n = –1)	1	 –7.543	 –4.817	 –7.577	 –5.979	 HOMO -1$_\beta$ –7.590
–1604.77 (n = –2)	3/2	 –8.346	 –5.562	 –8.023	 –7.305	
–1604.48 (n = –3)	2	 –8.744	 –6.107	 –8.716	 –7.718	 LUMO +1$_\beta$ –7.704

© University of Pretoria

*Table 3–5: Electrostatic Surface Potential and Spin Density diagrams of **2b**. Total Energies (EE_{ZPV}) in a.u. include zero-point vibrational correction. H(S)OMO and LUMO orbitals were generated with [Isovalue] = 0.02, and Spin Density plots with [Isovalue] = 0.0004. Mulliken Spin diagrams were generated with symmetric colour shading where brightly coloured areas indicate the localisation of unpaired alpha- or beta-spin densities. Alpha FMOs are presented for reduced species, and Beta FMOs for oxidised species. All calculations were performed at B3LYP-D3/def2-SVP level of theory in CH_2Cl_2 using cPCM. *Asymmetric colour shading applied for clarity.*

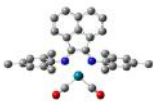
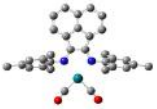
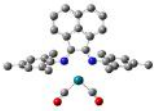
EE_{ZPV} (a.u.)	S	H(S)OMO	LUMO	ESP	Mulliken Spin	Spin Density
–1605.60 (n = +4)	5/2				 *	
–1605.59 (n = +3)	2					
–1605.53 (n = +2)	3/2					
–1605.44 (n = +1)	1					
–1605.28 (n = 0)	1/2					
–1605.04 (n = –1)	1				 *	
–1604.77 (n = –2)	3/2				 *	
–1604.48 (n = –3)	2				 *	

The optimised molecular geometries calculated for the (n = +3) and (n = +4) states of **2b** showed significant distortion of the coordination centre and ancillary ligands with increased molecular charge (Table 3.3–6). In particular, a loss of co-planarity is observed between the two Mes-aryl substituents (Mes_{Ar}–Mes_{Ar} dihedral = 35.06°), as well as an angular distortion (Δθ = ±17°) in the square planar

© University of Pretoria

geometry of the coordination sphere of the (n = +3) state. The optimised molecular geometries of **2a**, **2c** and **2d** showed similar distortions.

*Table 3–6: Optimised molecular geometries of **2b** modelled in different charged states. All calculations were performed at B3LYP-D3/def2-SVP level of theory in CH_2Cl_2 using cPCM. The integer "n" designates the number of electrons that were added to the starting geometry before optimisation to simulate the effect of electrochemical reduction.*

n = 0	n = +1	n = +2	n = +3	n = +4
				

The (n = +3) $HOMO_\alpha$ and $LUMO_\alpha$ orbital compositions appear very similar to those of the (n = +2) $HOMO_\alpha$ and $LUMO_\alpha$ respectively. Examination of the orbital distribution of (n = +3) HOMO -1_α alongside the Spin density plot and Mulliken spin diagram indicate that the third reduction event for **2b** is mainly localised to the rhodium centre and carbon atoms of the carbonyl ligands (Table 3.3–5), accompanied by Rh–N antibonding interactions (Table 3.3–4). During the course of the third reduction event (–1.54 V), orbital rearrangement takes place to lower the energy of the (n = +3) HOMO -1_α, favouring its occupation, resulting in a decrease in the Rh–N bond order and an increase in the level of metal-to-carbonyl back-bonding. The latter decreases the strength of the carbon-oxygen triple bond, tolerating more flexibility in the Rh–C–O bond angles of an otherwise rigid, linear system (Rh–C–O = 167.62° and 162.55°).

The orbital distribution of (n = +4) $HOMO_\alpha$ is surprisingly comparable to that of (n = +2) $LUMO_\alpha$ as well as (n = +3) $LUMO_\alpha$, however, the optimised molecular geometry of the (n = +4) state shows slightly less structural deformation than in the (n = +3) state. The orbital interactions between the rhodium and carbons of the carbonyl ligands shows constructive overlap (bonding interaction), whereas the Rh–N and C≡O orbital interactions present antibonding character. Comparison of the ESP map and Mulliken spin diagram of (n = +4) to that of (n = +3) indicates a marked increase in both negative charge and unpaired electron density surrounding the metal and carbonyl carbons compared to the rest of the molecule. The fourth reduction of **2b** (–1.84 V) is thus firmly localised across the rhodium centre and carbonyl ligands, resulting in an increase in metal-to-carbonyl back bonding, and subsequent partial decrease in the C≡O bond order.

The antibonding orbital interactions present between the carbon and oxygen of the carbonyl ligands in the (n = +4) $HOMO_\alpha$ provide further influence to decreased C≡O bond order, resulting in the bending observed in the Rh–C–O bond (Rh–C–O = 166.33° and 164.98°). The Rh–N antibonding interaction in

© University of Pretoria

the (n = +4) $HOMO_{\alpha}$ could feasibly facilitate ligand dissociation from the [**2b**$^{4-}$] complex, resulting in the observed spike in cathodic current as well as the irreversibility of the fourth reduction event.

The (n = –1) $LUMO_{\beta}$ shows decreased contribution from the Mes-aryl orbitals than in the (n = 0) HOMO (Table 3.3–4), however, both MOs present majority metal centred d_{z^2}-symmetry orbital contributions. The (n = –1) ESP map displays an increased positive charge near the rhodium centre (Table 3.3–5), correlating with the Mulliken spin diagram and spin density plot which indicate a localisation of the unpaired electron density on the metal centre of **2b** for the first oxidation event. The green colouration on the carbonyl ligands in the spin density plot indicates an increase in electron donation towards the metal centre due to its increased positive charge.

The energetically degenerate (n = –1) $HOMO_{\beta}$ and (n = –1) HOMO -1_{β} orbitals are both chiefly laterally distributed in π* antibonding orbitals across the Mes-aryl substituents, however, the $HOMO_{\beta}$ has a larger orbital contribution from the rhodium and acenaphthene rings, whereas the HOMO -1_{β} shows contributions from the carbonyl carbons (Table 3.3–4). The orbital distribution of (n = –2) $LUMO_{\beta}$ resembles a combination of the (n = –1) $HOMO_{\beta}$ and (n = –1) HOMO -1_{β} orbitals, displaying lateral π* antibonding orbitals spanning across the Mes-aryl substituents, and contributions from both the carbonyl carbons and acenaphthene rings. Comparison of the ESP maps of (n = –2) to that (n = –1) show an increase in the overall positive charge of the molecule (Table 3.3–5). The Mulliken spin diagram and spin density plot point towards an extensive delocalisation of the oxidation event and the resulting spin density across both of the aryl-substituents and the acenaphthene rings.

Summary – The first reduction event of **2b** (–0.61 V), and the electrochemically reversible second reduction (–0.90 V), are delocalised between the bisimine moiety and acenaphthene rings. The third reduction (–1.54 V) and irreversible fourth reduction events (–1.84 V) are delocalised between the two ancillary carbonyl ligands and the metal centre, resulting in structural deformation of the coordination centre of **2b** due to elongation of the Rh–N bonds and bending of the Rh–C–O bonds. The metal centred first oxidation event (+1.04 V) is electrochemically reversible, but not fully chemically reversible under the experimental conditions. Electron donation effects from the carbonyl ligands towards the rhodium to stabilise the increased positive charge is visible on the (n = –1) state Mulliken spin diagram. The irreversible second oxidation (+1.41 V) is ligand centred, with the spin density and associated positive charge delocalised across both aryl rings. The third oxidation (+1.72 V) is tentatively attributed to the oxidation of the free MesBIAN ligand in the solution, following ligand

© University of Pretoria

dissociation of a $[MesBIAN]^+$ intermediary from the analyte subsequent to the irreversible oxidation at +1.41 V.

3.3.3) Comparative Discussion

Frequent similarities were noticeable among the computationally assisted descriptions of the electrochemical events for the free Dipp- and MesBIAN ligands and the complex series **1**–**4**. The DPV peak potentials attributed as primary electrochemical events (i.e., resulting from the electrochemical reactivity of the analyte only) for all studied compounds are summarised in Table 3.3–7. As detailed in Section 3.3.2.ii, DPV peaks with potentials similar to those of the free ligands were observed in the analyses of complexes **1c**, **1d**, and **4b**, and provisionally attributed to the reactivity of a free ligand in the solution resulting from ligand dissociation.[22] Selected full scan and narrowed potential window CVs and DPVs of all studies compounds are available in Appendix F.

*Table 3–7: Summary of the DPV peak potentials (V vs Ag/Ag^+) recorded for DippBIAN, MesBIAN, and complex series **1**–**4**. Electrochemically reversible events are marked with an "*" symbol; quasi-reversible events (electrochemically reversible but not fully chemically reversible) are marked with a "†" symbol. Analyses where ligand dissociation is suspected, are indicated by the "lig-dis" note.*

Compound	Red. 4	Red. 3	Red. 2	Red. 1	Ox. 1	Ox. 2	Notes
DippBIAN			–1.51	–0.85	+1.26		
MesBIAN			–1.92	–1.43	+1.20	+1.73	
1a			–1.53	–0.56*	+1.31*	+1.61	
1b			–1.64	–0.70*	+1.26	+1.63	
1c	–1.53	–1.14*	–0.91	–0.19*	+0.58†	+1.50	lig-dis
1d	–1.52	–1.11*	–0.85†	–0.21*	+0.58	+1.47	lig-dis
2a	–1.68	–1.41*	–0.70	–0.43*	+1.12	+1.40	
2b	–1.84	–1.54	–0.90*	–0.61	+1.04†	+1.41	lig-dis
2c			–1.19*	–0.22*	+1.56		
2d			–1.18*	–0.25*	+1.56		
3a			–1.79	–0.77*	+1.36	+1.60	
3b		–1.78	–1.70	–0.82*	+1.25	+1.59	
4a	–1.88	–1.37	–1.15	–0.18*	+0.77	+1.46	
4b	–1.78	–1.53	–1.14	–0.20*	+0.89		lig-dis
4c	–1.79	–1.45	–1.02*	–0.16*	+0.70†	+1.64	
4d	–1.80	–1.40	–1.00*	–0.16*	+0.67	+1.58†	

The first and second reduction events of all compounds were observed to be delocalised between the bisimine N=C–C=N moiety and acenaphthene rings. While the third and fourth reduction events of the free ligands were not experimentally observed, their computational descriptions correlate closely with

© University of Pretoria

those previously reported for single crystal structures of DippBIAN in various reduced states.[5] Unlike the free ligands, however, the third reduction events of the complexes (if observed) were identified as largely metal-centred events. The fourth reduction events of **2a**–**b** also presented metal-centred characteristics, whereas those of complexes **1c**–**d** and **4a**–**d** closely resembled the ligand localised reduction as observed for the third reduction events of the free ligands.

The first oxidation reaction for all complexes may be described as a metal-centred event, with the Mulliken spin diagrams of all complexes revealing an increase in electron donation from the ancillary ligands towards the metal to stabilise the Rh(II)/Ir(II) centres. The second and third (where observed) oxidation events were in all case centred on the BIAN ligand. The charge localisation of the second oxidation varied between the different complexes and ancillary ligands, being either centred in a π*-orbital of one of the aryl-substituents, or delocalised between the bisimine moiety and acenaphthene rings. The third oxidation event is localised on the other aryl-substituent – it was noted that orbital rearrangement may often be necessary between the second and third oxidations, as well as between the second and third reduction events.

The first reduction potentials of **1c** and **1d** are *ca*. 430 mV more positive than those of **1a** and **1b**, and the second reduction potentials of **1c** and **1d** are an average of 700 mV more positive than those of **1a** or **1b**. The positive shift indicates a greater extent of electron withdrawal from the bisimine moiety and acenaphthene rings due to enhanced orbital interactions with the large Ir(I)-centre compared to Rh(I). Interestingly, the metal-centred first oxidations of **1c** and **1d** occur at more negative potentials than the first oxidations of **1a** and **1b**, pointing towards an increased π-basic character of Ir(I) compared to Rh(I). The ligand-centred second oxidation events of **1a**–**b** are an average of 320 mV more positive than the oxidation of the free Dipp- and MesBIAN ligands, correlating with an increase in difficulty of oxidising a ligand from which electrons are being withdrawn by the coordinated metal. The increased π-basic character of Ir(I) results in a negative shift of the second oxidation potentials for **1c**–**d** compared to **1a**–**b** as well.

First reductions of **2a**–**b** occur at more negative potential than those of **2c**–**d**, but the second reductions occur at more positive potentials. Third and fourth reductions of **2a**–**b** fall within solvent potential window, and are localised on the dicarbonyl ancillary ligands, indicating that the Rh–CO bonds are more reactive than the Ir–CO bonds. The increased reactivity of the carbonyl ancillary ligand points towards a possible enhancement of the catalytic activity via ligand substitution reactions. Metal-centred oxidations of **2a**–**b** occur at more negative potentials than in **2c**–**d**, indicating a greater

© University of Pretoria

extent of carbonyl π-acceptor character in the bonding of the carbonyl ligands to the iridium metal centre compared to the rhodium, with consequent increased Ir–CO back-bonding from the more π-basic 5d metal centre. The oxidation potentials of **2c** and **2d** are almost 1 V greater than in **1c** and **1d**, highlighting the influence that ancillary ligands may have on the electron density (and thus reaction potentials) of structurally related complexes. The π-basic characteristics of Ir(I) evident in the reaction potentials of **1c** and **1d** is partly overturned in the observed reaction potentials of **2c** and **2d**, offset by the π-acidic nature of the carbonyl ligands.

The first reduction potentials of **3a**–**b** are about 200–300 mV more negative than in **2a**–**b**, indicating an increase in the σ-donor character of the phosphine ligand which decreases the extent of electron withdrawal from the BIAN ligand. The second reduction potentials of **3a**–**b** are almost 1 V more negative than in **2a**–**b**, and 200 mV more negative than those of the free BIAN ligands, suggesting that a large degree of electron density is delocalised from the metal centre onto the ligand due to the electron donating character of the phosphine ligand. The first and second oxidation potentials are shifted roughly 200 mV more positive than in **2a**–**b**, but are very similar to those recorded for **1a**–**b**.

The electrochemically reversible ligand centred first reduction potentials of **4a**–**d** are similar, whereas the ligand centred second reduction potentials of **4c** and **4d** are quasi-reversible (electrochemically reversible, but not fully chemically reversible under the experimental conditions) and shifted to 100 mV more positive potentials than those of **4a** and **4b**. The metal-centred third reduction events of all four complexes are irreversible, however, the reduction event of **4b** is shifted *ca*. 100 mV more negative than the other complexes. An upsurge in cathodic current is observed in CVs of all four complexes. The metal centred first oxidation of **4d** occurs at a slightly less positive potential relative to the other three complexes, and **4c** is the only complex that showed signs of an electrochemically reversible first oxidation. Surprisingly, the ligand based second oxidation of **4d** is quasi-reversible, whereas the second oxidations of the other three complexes are irreversible.

The first reductions of the chlorido derivatives **4a**–**d** are shifted to more positive potentials relative to those of **1a**–**d**. The difference in potentials is presumably due to the presence of the electronegative chlorido ligand in these complexes, although the effect of an additional ligand (five coordinate complexes **4a**–**d**, compared to the square planar **1a**–**d**) cannot be discounted. The ligand centred second reduction potentials of **4a**–**b** are shifted to more positive potentials compared to those of **1a**–**b**. While the ligand centred second reductions potentials of **4c**–**d** are shifted *ca*. 100 mV more negative than in **1c**–**d**, the metal centred third reduction potentials are shifted nearly 300 mV more

© University of Pretoria

negative. The first oxidation potentials of **4a**–**b** are shifted more negative than in **1a**–**b** due to the Rh–Cl bonding orbital overlap, which delocalises the spatial distribution of the positive charge and unpaired electron density. The first oxidations of **4c**–**d** are, however, shifted to slightly more positive potentials than in **1c**–**d** due to the delocalisation of their positive charge and unpaired electron density onto one of the BIAN aryl-substituents into nonbonding symmetry MOs.

The dissimilarity observed in the comparisons of **4a**–**b**, and **4c**–**d**, with **1a**–**d** may be due to the variance seen in the metal–chlorine bond lengths of the optimised molecular geometries of the reduced states. The Rh–Cl bond length in **4a**–**b** increased considerably between the (n = 0) and (n = +4) states (± 2.741 Å), whereas the Ir–Cl bond of **4c**–**d** showed only a modest increase in length (± 0.200 Å), indicating a much stronger Ir–Cl than Rh–Cl association throughout the reductive process. Consequently, the iridium centre of **4c**–**d** would be more electron rich than in **4a**–**b**, decreasing the extent to which electrons are withdrawn from the bisimine moiety towards the coordination centre. This is in good agreement with the literature results that have been reported for the octahedral BIAN complex *mer*-[Rh(DippBIAN)$(Cl)_3(H_2O)$],[17] signifying that the steep increase in cathodic current observed in the CVs of the complex series **4a**–**d** at potentials more negative than –1.65 V likely results from the irreversible reductive dissociation of the chlorido ligand from the complexes. The BIAN ligand dissociates from the reduced complex either subsequently or concurrently to the loss of the chloride ligand, ultimately resulting in the decomposition of the complexes at larger negative potentials.

The structural differences between **1** and **4** are due to steric competition between the isopropyl-groups and chlorido ligand in the coordination sphere of **4**. While the increased reaction times required to synthesise complexes **4** may reasonable be attributed to the increased steric bulk surrounding the coordination centres, the inefficient orbital overlap and structural deformation shown in the computational data of **4c** may explain why the reaction times required for the synthesis of **4c** were longer than for any of the other complexes.

The electrochemical data obtained for **4a** correlates reasonably well with the results reported by Romashev *et al*. for [RhDB(cod)Cl], even though the authors used acetonitrile as solvent.[22] The authors proposed that the chlorido ligand dissociates from the complex immediately upon dissolution due to the elongated Rh–Cl bond length in the complex, in the crystal structure as well as modelled geometries. The electrochemical data was therefore attributed to the reactivity of a $[Rh(cod)DippBIAN]^+$ intermediate which formed upon dissolution of **4a**. The electrochemical results in CH_2Cl_2 for the analogous complex, **1a**, do not correlate with the results presented by the authors,

© University of Pretoria

suggesting that further investigation is required. The solvent used for the analyses may have a significant influence on the reactivity of the complexes and their intermediates. Although acetonitrile has a wider potential window for electrochemical analysis than CH_2Cl_2, it is a known coordinating solvent, which could result in the formation of solvent-adducts during analysis.

The differences noted between the electrochemical results of **1a**, **4a**, and those reported by Romashev *et al*. may thus largely be due to changes in the interactions between the complexes and the solvent.[22] The second reduction event observed by Romashev *et al*. was fully reversible,[22] however, the second reduction recorded for both **1a** and **4a** was irreversible. The increased polarity of acetonitrile compared to CH_2Cl_2 may assist in stabilising the reduced complex. The third reduction event reported by the authors is observed in the results for **4a**, however, it is not observed in the scans of **1a**. The first oxidation process reported by the authors and recorded for **4a** is irreversible, whereas first oxidation recorded for **1a** is electrochemically reversible. The irreversible second oxidation peaks observed by the authors and recorded for **4a** was attributed to the oxidation of free chloride ions in the solution. However, the absence of any correlating peaks between the anodic scans of **1a** and **4a** indicate that the second oxidation events that are observed are intrinsic to the coordinated chlorido ligand complex.

The cathodic CVs of DippBIAN, MesBIAN, **1c**–**d** and **4a**–**d** showed an upsurge in cathodic current at potentials below –1.7 V. The increase in current may be due to the chemical reduction of the solvent (CH_2Cl_2) by the decomposing analyte. The reduced intermediates of the free Dipp- and MesBIAN ligands were observed to be sufficiently strong chemical reducing agents to increase the reduction potential of the CH_2Cl_2 by nearly 300 mV (Figure 3.3–3), resulting in the observed spike in cathodic current at potentials below –1.7 V. Upon coordination of the ligands, their third reduction potentials are increased to well within the potential window for the solvent (Table 3.3–7). Ligand dissociations or analyte decompositions occurring during the analysis of complexes **1c**–**d** and **4a**–**d** at potentials below –1.7 V, could result in the liberation of $[DippBIAN]^{-3}$ or $[MesBIAN]^{-3}$ intermediates. The highly reduced ligand intermediates are anticipated to be sufficiently strong reducing agents to react with the CH_2Cl_2, producing cathodic currents up to 60 µA greater than those recorded for the free Dipp- and MesBIAN ligands.

Interestingly, the cathodic current of **4c** and **4d** below –1.7 V is *ca*. 30 µA lower than the cathodic current of **4a** and **4b**, and roughly 40 µA greater than the current recorded for **1c** and **1d**. In the optimised molecular geometries of the reduced states of **4a** and **4b**, the elongation of the Rh–Cl bond

© University of Pretoria

length, and distortion of the coordination sphere, points towards ligand dissociation during the transition from third to fourth reduced states. Moderate elongation of the Ir–N bonds are observed in the molecular geometries of **4c** and **4d** as well. The change in Ir–Cl bond lengths are modest compared to the change in Rh–Cl bond lengths of the same reduced states, indicating that the Ir–Cl interaction is stronger than the Rh–Cl interaction. The chlorido ligand of **4a** and **4b** is anticipated to dissociate more easily from the complex than in **4c** and **4d**, leading to an increased degree of decomposition (and therefore cathodic current) in the CVs of **4a** and **4b**.

3.4) Conclusions

The systematic electrochemical study in non-coordinating solvent CH_2Cl_2, revealed that all the complexes featured at least one electrochemically reversible, ligand-centred, reduction event at more positive potentials than the reduction potentials of the free ligands. The ligand-centred second reduction events of **2a**–**d** and **4c**–**d** were also electrochemically reversible, indicating improved stabilisation of the reduced ligand by the electron withdrawing dicarbonyl ligands and the iridium-chloride coordination sphere. Complexes **1c**–**d**, **2a**–**b** and **4a**–**d** showed evidence of the metal-centred third reduction event, however, this reduction event proved to be largely irreversible and resulted in ligand dissociation and/or decomposition of the complexes at potentials lower than –1.6 V.

Complex **1a** was the only complex to show a fully reversible metal-centred oxidation, while **1c**, **2b**, and **4c** showed metal-centred oxidation events which are electrochemically reversible, but not chemically reversible on the timescale of the scan rate employed during the analyses. The second oxidation events that were observed for complexes **1a**–**d**, **2a**–**b**, **3a**–**b**, and **4a**–**c** were all irreversible and ligand-centred events. Interestingly, the second oxidation of **4d** showed quasi-reversible characteristics.

© University of Pretoria

3.5) References

(1) Larson, P. J.; Wekesa, F. S.; Singh, A.; Smith, C. R.; Rajput, A.; McGovern, G. P.; Unruh, D. K.; Cozzolino, A. F.; Findlater, M. Synthesis, Characterization, Electrochemical Properties and Theoretical Calculations of (BIAN) Iron Complexes. *Polyhedron* **2019**, *159*, 365–374. https://doi.org/10.1016/j.poly.2018.11.060.

(2) Skara, G.; Pinter, B.; Geerlings, P.; De Proft, F. Revealing the Thermodynamic Driving Force for Ligand-Based Reductions in Quinoids; Conceptual Rules for Designing Redox Active and Non-Innocent Ligands. *Chem Sci* **2015**, *6* (7), 4109–4117. https://doi.org/10.1039/C5SC01140J.

(3) Allan, C. J.; Cooper, B. F. T.; Cowley, H. J.; Rawson, J. M.; Macdonald, C. L. B. Non-Innocent Ligand Effects on Low-Oxidation-State Indium Complexes. *Chemistry - European Journal* **2013**, *19* (43), 14470–14483. https://doi.org/10.1002/chem.201301881.

(4) Butschke, B.; Fillman, K. L.; Bendikov, T.; Shimon, L. J. W.; Diskin-Posner, Y.; Leitus, G.; Gorelsky, S. I.; Neidig, M. L.; Milstein, D. How Innocent Are Potentially Redox Non-Innocent Ligands? Electronic Structure and Metal Oxidation States in Iron-PNN Complexes as a Representative Case Study. *Inorg Chem* **2015**, *54* (10), 4909–4926. https://doi.org/10.1021/acs.inorgchem.5b00509.

(5) Fedushkin, I. L.; Skatova, A. A.; Chudakova, V. A.; Fukin, G. K. Four-Step Reduction of Dpp-bian with Sodium Metal: Crystal Structures of the Sodium Salts of the Mono-, Di-, Tri- and Tetraanions of Dpp-bian. *Angewandte Chemie* **2003**, *115* (28), 3416–3420. https://doi.org/10.1002/ange.200351408.

(6) Fedushkin, I. L.; Skatova, A. A.; Chudakova, V. A.; Fukin, G. K.; Dechert, S.; Schumann, H. Monomeric Magnesium and Calcium Complexes Containing the Bidentate, Dianionic 1,2-Bis[(2,6-Diisopropylphenyl)Imino]Acenaphthene Ligand. *Eur J Inorg Chem* **2003**, No. 18, 3336–3346. https://doi.org/10.1002/ejic.200300181.

(7) Fedushkin, I. L.; Skatova, A. A.; Chudakova, V. A.; Cherkasov, V. K.; Fukin, G. K.; Lopatin, M. A. Reduction of 1,2-Bis[(2,6-Diisopropylphenyl)Imino]Acenaphthene (Dpp-Bian) with Alkali Metals− A Study of the Solution Behaviour of (Dpp-Bian)N−[M^+]n (M = Li, Na;n = 1−4) with UV/Vis, ESR and 1H NMR Spectroscopy. *Eur J Inorg Chem* **2004**, *2004* (2), 388–393. https://doi.org/10.1002/ejic.200300351.

(8) Fedushkin, I. L.; Khvoinova, N. M.; Baurin, A. Y.; Chudakova, V. A.; Skatova, A. A.; Cherkasov, V. K.; Fukin, G. K.; Baranov, E. V. Reactions of Germanium(II), Tin(II), and Antimony(III) Chlorides with Acenaphthene-1,2-Diimines. *Russian Chemical Bulletin* **2006**, *55* (1), 74–83. https://doi.org/10.1007/s11172-006-0217-z.

© University of Pretoria

(9) Moskalev, M. V.; Lukoyanov, A. N.; Baranov, E. V.; Fedushkin, I. L. Unexpected Reactivity of an Alkylaluminum Complex of a Non-Innocent 1,2-Bis[(2,6-Diisopropylphenyl)Imino]Acenaphthene Ligand (Dpp-Bian). *Dalton Transactions* **2016**, *45* (40), 15872–15878. https://doi.org/10.1039/C6DT01750A.

(10) Morozov, A. G.; Fedushkin, I. L.; Irran, E.; Grohmann, A. Titanium(IV) Complexes Supported by a Dianionic Acenaphthenediimine Ligand: X-Ray and Spectroscopic Studies of the Metal Coordination Sphere. *Inorg Chem Commun* **2018**, *95* (June), 50–55. https://doi.org/10.1016/j.inoche.2018.07.006.

(11) Hill, N. J.; Vargas-Baca, I.; Cowley, A. H. Recent Developments in the Coordination Chemistry of Bis(Imino)Acenaphthene (BIAN) Ligands with s- and p-Block Elements. *Dalton Transactions* **2009**, *9226* (2), 240–253. https://doi.org/10.1039/b815079f.

(12) Clark, K. M.; Bendix, J.; Heyduk, A. F.; Ziller, J. W. Synthesis and Characterization of a Neutral Titanium Tris(Iminosemiquinone) Complex Featuring Redox-Active Ligands. *Inorg Chem* **2012**, *51* (14), 7457–7459. https://doi.org/10.1021/ic301059p.

(13) Bendix, J.; Clark, K. M. Delocalization and Valence Tautomerism in Vanadium Tris(Iminosemiquinone) Complexes. *Angewandte Chemie - International Edition* **2016**, *55* (8), 2748–2752. https://doi.org/10.1002/anie.201510403.

(14) Ng, Y. Y.; Tan, L. J.; Ng, S. M.; Chai, Y. T.; Ganguly, R.; Du, Y.; Yeow, E. K. L.; Soo, H. Sen. Spectroscopic Characterization and Mechanistic Studies on Visible Light Photoredox Carbon-Carbon Bond Formation by Bis(Arylimino)Acenaphthene Copper Photosensitizers. *ACS Catal* **2018**, *8* (12), 11277–11286. https://doi.org/10.1021/acscatal.8b02502.

(15) Portenkirchner, E.; Kianfar, E.; Sariciftci, N. S.; Knör, G. Two-Electron Carbon Dioxide Reduction Catalyzed by Rhenium(I) Bis(Imino)Acenaphthene Carbonyl Complexes. *ChemSusChem* **2014**, *7* (5), 1347–1351. https://doi.org/10.1002/cssc.201301116.

(16) Tory, J.; Gobaille-Shaw, G.; Chippindale, A. M.; Hartl, F. Spectroelectrochemical Study of Complexes [Mo(CO)2(η 3-Allyl)(α-Diimine)(NCS)] (α-Diimine = Bis(2,6-Dimethylphenyl)-Acenaphthenequinonediimine and 2,2′-Bipyridine) Exhibiting Different Molecular Structure and Redox Reactivity Dedicated to Professor Maria. *J Organomet Chem* **2014**, *760*, 30–41. https://doi.org/10.1016/j.jorganchem.2014.01.015.

(17) Gushchin, A. L.; Romashev, N. F.; Shmakova, A. A.; Abramov, P. A.; Ryzhikov, M. R.; Fomenko, I. S.; Sokolov, M. N. Novel Redox Active Rhodium(III) Complex with Bis(Arylimino)Acenaphthene Ligand: Synthesis, Structure and Electrochemical Studies. *Mendeleev Communications* **2020**, *30* (1), 81–83. https://doi.org/10.1016/j.mencom.2020.01.027.

© University of Pretoria

(18) Donkervoort, J. G.; Bühl, M.; Ernsting, J. M.; Elsevier, C. J. Steric and Electronic Effects on the 103Rh NMR Chemical Shifts of Rh1(Cyclooctadiene) Compounds Bearing N-Donor Ligands. *Eur J Inorg Chem* **1999**, *1999* (1), 27–33. https://doi.org/10.1002/(sici)1099-0682(199901)1999:1<27::aid-ejic27>3.0.co;2-4.

(19) Van Der Poel, H.; Van Koten, G.; Vrieze, K. Syntheses and NMR Studies of Five-Co-Ordinate Rhodium(I) Complexes with α-Diimines (RNC(H)C(H)NR): [RhCl(CO)(H2-C2H4)(α-Diimine)] and [RhCl(L)2(α-Diimine)] (R = t-Bu, EtMe2C-; L = CO,PF3). *Inorganica Chim Acta* **1981**, *51* (C), 241–252. https://doi.org/10.1016/S0020-1693(00)88344-9.

(20) Rumble, S. L. The Synthesis of Amines and Imines Using Organometallic Catalysts. Doctor of Philosophy, University of New South Wales, 2005.

(21) Rumble, S. L.; Page, M. J.; Field, L. D.; Messerle, B. A. In Situ Catalysts for the Intramolecular Hydroamination of Aminoalkynes - What Ligand Properties Determine Catalyst Activity? *Eur J Inorg Chem* **2012**, *2012* (13), 2226–2231. https://doi.org/10.1002/ejic.201101307.

(22) Romashev, N. F.; Gushchin, A. L.; Fomenko, I. S.; Abramov, P. A.; Mirzaeva, I. V.; Kompan'kov, N. B.; Kal'nyi, D. B.; Sokolov, M. N. A New Organometallic Rhodium(I) Complex with Dpp-Bian Ligand: Synthesis, Structure and Redox Behaviour. *Polyhedron* **2019**, *173*, 114110. https://doi.org/10.1016/j.poly.2019.114110.

(23) Hasan, K.; Zysman-Colman, E. Panchromic Cationic Iridium(III) Complexes. *Inorg Chem* **2012**, *51* (22), 12560–12564. https://doi.org/10.1021/ic301998t.

(24) Hasan, K.; Zysman-Colman, E. The Effect of Aryl Substitution on the Properties of a Series of Highly Absorptive Cationic Iridium(III) Complexes Bearing Ancillary Bis(Arylimino)Acenaphthene Ligands. *Eur J Inorg Chem* **2013**, *2013* (25), 4421–4429. https://doi.org/10.1002/ejic.201300583.

(25) Hasan, K.; Wang, J.; Pal, A. K.; Hierlinger, C.; Guerchais, V.; Sen Soo, H.; García, F.; Zysman-Colman, E. Bay-Region Functionalisation of Ar-BIAN Ligands and Their Use Within Highly Absorptive Cationic Iridium(III) Dyes. *Sci Rep* **2017**, *7* (1), 15520. https://doi.org/10.1038/s41598-017-14996-4.

(26) Inzelt, G.; Lewenstam, A.; Scholz, F. *Handbook of Reference Electrodes*; 2013. https://doi.org/10.1007/978-3-642-36188-3.

(27) Gayathri, S. S.; Wielopolski, M.; Pérez, E. M.; Fernández, G.; Sánchez, L.; Viruela, R.; Ortí, E.; Guldi, D. M.; Martín, N. Discrete Supramolecular Donor–Acceptor Complexes. *Angewandte Chemie International Edition* **2009**, *48* (4), 815–819. https://doi.org/10.1002/ANIE.200803984.

(28) Frisch, M. J.; Trucks, G. W.; Schlegel, H. B.; Scuseria, G. E.; Robb, M. A.; Cheeseman, J. R.; Scalmani, G.; Barone, V.; Petersson, G. A.; Nakatsuji, H.; Li, X.; Caricato, M.; Marenich, A. V.;

© University of Pretoria

Bloino, J.; Janesko, B. G.; Gomperts, R.; Mennucci, B.; Hratchian, H. P.; Ortiz, J. V.; Izmaylov, A. F.; Sonnenberg, J. L.; Williams-Young, D.; Ding, F.; Lipparini, F.; Egidi, F.; Goings, J.; Peng, B.; Petrone, A.; Henderson, T.; Ranasinghe, D.; Zakrzewski, V. G.; Gao, J.; Rega, N.; Zheng, G.; Liang, W.; Hada, M.; Ehara, M.; Toyota, K.; Fukuda, R.; Hasegawa, J.; Ishida, M.; Nakajima, T.; Honda, Y.; Kitao, O.; Nakai, H.; Vreven, T.; Throssell, K.; Montgomery, Jr., J. A.; Peralta, J. E.; Ogliaro, F.; Bearpark, M. J.; Heyd, J. J.; Brothers, E. N.; Kudin, K. N.; Staroverov, V. N.; Keith, T. A.; Kobayashi, R.; Normand, J.; Raghavachari, K.; Rendell, A. P.; Burant, J. C.; Iyengar, S. S.; Tomasi, J.; Cossi, M.; Millam, J. M.; Klene, M.; Adamo, C.; Cammi, R.; Ochterski, J. W.; Martin, R. L.; Morokuma, K.; Farkas, O.; Foresman, J. B.; Fox, D. J. Gaussian 16, Revision B.01. Gaussian Inc. Wallingford CT 2016.

(29) Becke, A. D. Density-functional Thermochemistry. III. The Role of Exact Exchange. *J Chem Phys* **1993**, *98* (7), 5648–5652. https://doi.org/10.1063/1.464913.

(30) Lee, C.; Yang, W.; Parr, R. G. Development of the Colle-Salvetti Correlation-Energy Formula into a Functional of the Electron Density. *Phys Rev B* **1988**, *37* (2), 785–789. https://doi.org/10.1103/PhysRevB.37.785.

(31) Weigend, F.; Ahlrichs, R. Balanced Basis Sets of Split Valence, Triple Zeta Valence and Quadruple Zeta Valence Quality for H to Rn: Design and Assessment of Accuracy. *Physical Chemistry Chemical Physics* **2005**, *7* (18), 3297–3305. https://doi.org/10.1039/b508541a.

(32) Steinmetz, M.; Grimme, S. Benchmark Study of the Performance of Density Functional Theory for Bond Activations with (Ni,Pd)-Based Transition-Metal Catalysts. *ChemistryOpen* **2013**, *2* (3), 115–124. https://doi.org/10.1002/open.201300012.

(33) Grimme, S.; Antony, J.; Ehrlich, S.; Krieg, H. A Consistent and Accurate Ab Initio Parametrization of Density Functional Dispersion Correction (DFT-D) for the 94 Elements H-Pu. *J Chem Phys* **2010**, *132* (15), 154104. https://doi.org/10.1063/1.3382344.

(34) Cossi, M.; Rega, N.; Scalmani, G.; Barone, V. Energies, Structures, and Electronic Properties of Molecules in Solution with the C-PCM Solvation Model. *J Comput Chem* **2003**, *24* (6), 669–681. https://doi.org/10.1002/jcc.10189.

(35) Barone, V.; Cossi, M. Quantum Calculation of Molecular Energies and Energy Gradients in Solution by a Conductor Solvent Model. *Journal of Physical Chemistry A* **1998**, *102* (11), 1995–2001. https://doi.org/10.1021/jp9716997.

(36) Li, L.; Lopes, P. S.; Rosa, V.; Figueira, C. A.; Lemos, M. A. N. D. A.; Duarte, M. T.; Avilés, T.; Gomes, P. T. Synthesis and Structural Characterisation of (Aryl-BIAN)Copper(i) Complexes and Their Application as Catalysts for the Cycloaddition of Azides and Alkynes. *Dalton Transactions* **2012**, *41* (17), 5144. https://doi.org/10.1039/c2dt11854h.

© University of Pretoria

(37) Bard, A. J.; Faulkner, L. R. *Electrochemical Methods: Fundamentals and Applications*, Second Edi.; John Wiley & Sons, Inc: New York, NY, 2001. https://doi.org/10.1038/s41929-019-0277-8.

(38) Williams, O. M.; Cowley, A. H.; Rose, M. J. Structural and Electronic Characterization of Multi-Electron Reduced Naphthalene (BIAN) Cobaloximes. *Dalton Transactions* **2015**, *44* (29), 13017–13029. https://doi.org/10.1039/C5DT00924C.

(39) Schultz, F. A.; Lord, R. L.; Baik, M.-H. Multifaceted Examination of Multielectron Transfer Reactions. *Inorganica Chim Acta* **2020**, *510*, 119746. https://doi.org/10.1016/j.ica.2020.119746.

(40) Popov, I. A.; Mehio, N.; Chu, T.; Davis, B. L.; Mukundan, R.; Yang, P.; Batista, E. R. Impact of Ligand Substitutions on Multielectron Redox Properties of Fe Complexes Supported by Nitrogenous Chelates. *ACS Omega* **2018**, *3* (11), 14766–14778. https://doi.org/10.1021/acsomega.8b01921.

(41) Matson, B. D.; McLoughlin, E. A.; Armstrong, K. C.; Waymouth, R. M.; Sarangi, R. Effect of Redox Active Ligands on the Electrochemical Properties of Manganese Tricarbonyl Complexes. *Inorg Chem* **2019**, *58* (11), 7453–7465. https://doi.org/10.1021/acs.inorgchem.9b00652.

(42) Chandra Patra, S.; Saha Roy, A.; Manivannan, V.; Weyhermüller, T.; Ghosh, P. Ruthenium, Osmium and Rhodium Complexes of 1,4-Diaryl 1,4-Diazabutadiene: Radical versus Non-Radical States. *Dalton Transactions* **2014**, *43* (36), 13731–13741. https://doi.org/10.1039/c4dt01241k.

(43) Orchin, M.; Jaffe, H. H. *The Importance of Antibonding Orbitals*; Houghton Mifflin: Boston, 1967. https://doi.org/10.1021/ed044p773.1.

© University of Pretoria

Chapter 4: Linear Free Energy Relationships

4.1) Introduction

During the experimental data analysis of voltammograms presented in Chapter 3, a question arose regarding peaks in the voltammograms of complexes with peak potentials near identical to those observed in the voltammograms of the free ligands. "*Were these peaks the result of ligand dissociation from the complex, or could they in fact be part of the characteristic electrochemical reactivity for the metal complex unexpectedly occurring at similar reaction potentials to those of the free ligands?*" The similarity in peak potentials between the ligand and metal complex, if not coincidental, points towards underlying metal-ligand interactions that are present in the charged states of the complex during these electrochemical reactions.

Consider for example the second oxidation events of **1d**, observed to occur at nearly the same potential as the first oxidation of the free MesBIAN ligand (Chapter 3, Section 3.3.1.vi). Examination of the FMO visualisations for the (n = 0, –1, and –2) states of **1d** and MesBIAN revealed that the second and third oxidation of **1d** are localised to similar molecular regions as the first and second oxidation of the free MesBIAN. If the voltammetry peaks are indeed part of the characteristic electrochemical reactivity profile of the complex, the similarity in peak potentials would indicate that the coordinated metal has very little influence on the energy required to oxidise the ligand due to limited metal-ligand interactions in the (n = 0, –1, and –2) states of **1d**.

Computational chemistry has become a powerful tool with which chemists can not only visualise the intra- and interatomic interactions of molecules, but also calculate a wide variety of physiochemical properties. Linear free energy relationships (LFERs) are a theoretically guided method for assessing the correlation between computed properties – such as frontier molecular orbital energies, ionisation energies, and electron affinities – and experimentally observable properties such as reduction and oxidation potentials.[1–4] Literature LFER comparisons and theoretical reaction potential correlation studies often focus solely on the first reduction or oxidation reaction, seldom extending their correlations or predictive models beyond one electron transfer events due to the immense computational costs it entails.[5–7]

The accuracy with which computational functions are able to reproduce experimental results has greatly improved in recent years.[8,9] The availability of large scale computational hardware dedicated to research initiatives, such as the computer clusters of the Centre for High Performance Computing

© University of Pretoria

(CHPC) South Africa utilised for this study, has significantly increased the number of active researchers and complexity of investigations that can be performed in a reasonable amount of time. Sponsored research infrastructure as provided by the CHPC are shared among many research groups and companies, therefore submitted projects are required to make use of the services as efficiently as possible.

The objective of the investigation was to identify qualitative correlations between theoretical and experimental properties, not to deliver quantitative comparatives between the properties of the compounds. The computational protocols for this study were therefore designed to minimise the CPU time that would be required for the calculations, while maintaining acceptable levels of accuracy of both the optimised molecular geometries and calculated energies. The computational and modelling methodologies, and data analysis rationale applied were informed by literature recommendations and guidelines.[1,2,5,8–16]

4.2) Methodology and Rationale

4.2.1) Molecular Modelling Methodology

Structural optimisations and frequency calculations were performed on both the free ligands and all the reported complexes using Gaussian 16 B.01.[17] The hybrid functional B3LYP [18,19] was employed with the def2SVP [11] split valence basis set on all atoms, including unrestricted basis functions for all calculations of open shell charged state molecules. Long range electron correlations resulting from electron delocalisation were accounted for with the addition of Grimme's D3 Empirical Dispersion function.[8,20] The effects of solvation were modelled using continuum potential surfaces functions (denoted cPCM) [21,22] for CH_2Cl_2. The electronic and thermodynamic energies, frontier orbitals and electrostatic potential surfaces were calculated for all molecules and their charged states.

A rigorous, systematic workflow was followed for modelling all of the complexes, ligands, and their associated charged states. The series of charged states that were modelled for each compound is labelled using a "(n = integer)" moniker, where *n* represents the number of electrons that have either been removed or added to the modelled molecule.[23] Thus, "n = –1" represents the first oxidised state, and "n = +2" the second reduced state of the molecule. The initial molecular geometries of all compounds were derived from previously reported four and five coordinate Aryl-BIAN transition metal complexes,[24–34] and minimised using MM2 molecular mechanics with a minimum RMS Gradient of 0.010.

© University of Pretoria

The stability of the all modelled wave function states were tested and optimised before further calculations were conducted using the Gaussian keyword "stable=opt".[10,14] Gas phase geometries were then optimised and confirmed to be at a minimum if a subsequent frequency calculation showed no imaginary vibrational frequencies.[10,14] The optimised gas phase geometry of the (n = 0) state for each molecule was used as the initial guess for modelling the solvated molecular geometries with cPCM.[5] Similarly, the obtained solvated geometries were established to be at a minimum by confirming that there were no imaginary vibrational frequencies in the subsequent frequency calculations.

4.2.2) Analysis and Nomenclature Conventions

When an analyte is dissolved in an electrochemical cell, and no external potential is applied over the electrodes (i.e., 0.0 V), chemical intuition may lead one to accept that the compound is in an electronically unchanged state. In other words, that the analyte has not yet undergone any reduction, oxidation, or other chemical reactions during the dissolution process. This state is consistent with the (n = 0) modelled charged state, representing the optimised molecular geometry of the molecule in a CH_2Cl_2 solution (at STP) before any electrons have been added or removed.

*Table 4.2–1: Exemplar of how the computational and electrochemical data for each compound were arranged and processed before correlation analyses were performed. The data values presented are those of complex **1a**.*

E_{DPV} vs Ag/Ag^+ (V)	Modelled State	HOMO (eV)	LUMO (eV)	FMO (eV)	E_{cell} vs NHE (eV)	–EA(M) (kJ/mol)	$-\Delta G_{rxn}$ (kJ/mol)
--	n = +4	0.33144	1.12139	1.12139	–4.72069	577.64929	–27.08272
--	n = +3	–1.63215	0.65471	0.65471	–3.54157	238.67367	86.68543
–1.53	n = +2	–2.32578	–0.14286	–0.14286	–2.16238	–83.67467	219.75625
–0.56	n = +1	–4.15712	–2.07951	–2.07951	–0.42498	–482.33578	387.38915
1.31	n = –1	–7.53544	–5.25157	–7.53544	1.4008	–906.45636	563.54967
1.61	n = –2	–7.98361	–7.38523	–7.98361	2.91183	–1237.86793	709.34104
--	n = –3	–8.48376	–7.79612	–8.48376	3.32637	–1477.85434	749.3379

At the first oxidation potential the molecule may be best described by the (n = –1) modelled state, which is the optimised molecular geometry of the molecule in a CH_2Cl_2 solution (at STP) after one electron has been removed. Similarly, at the first reduction potential the molecule may be best described as the (n = +1) modelled state, where one electron has been added to the original (n = 0) molecule. Measurements of the (n = 0) state itself are not necessarily recorded during the CV and DPV analyses, but rather variations in the current and potential associated with the molecule(s) changing between different charged states. Therefore, unless otherwise stated, the following correlation models do not include a "zero-point" related to the (n = 0) modelled state at potentials of {x = 0.0 V} (Table 4.2–1).

© University of Pretoria

Grouping the data for all of the modelled compounds together (*All*) in this manner proved to be an ineffective descriptor for a correlation analysis due to the diversity of both organic and inorganic compounds in a single dataset. Marginal improvement in the degree of linear correlations is noted when the dataset was limited to the metal complexes series (***1–4***), however, the Root Mean Squared Deviation (RMSD, equation 1)[35,36] and Mean Absolute Deviation (MAD, equation 2)[36–38] of the dataset were still relatively large given the diversity of coordination geometries and the variety of ancillary ligands present among the various complexes.

$$RMSD = \sqrt{\sum_{i=1}^{N} \frac{(x_i - \bar{x})^2}{N-1}} \qquad MAD = \sum_{i=1}^{N} \frac{|x_i - \bar{x}|}{N} \qquad (1\ \&\ 2)$$

$$with:\ \bar{x} = dataset\ mean,\ x_i = individual\ datapoint,\ and\ N = number\ of\ datapoints$$

The dataset for the series of complexes ***1–4*** may be further subdivided into two pairs of groups, namely:

- all modelled metal complexes of Rhodium (*All Rh*) all modelled complexes of Iridium (*All Ir*); as well as,
- all modelled complexes with either DippBIAN (*All DippBIAN*) or MesBIAN (*All MesBIAN*) ligands.

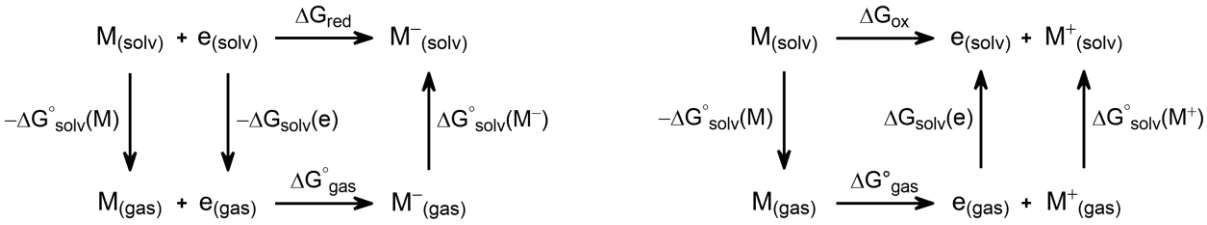
The orbital energy correlations and reaction energy correlations between the *All DippBIAN* and *All MesBIAN* complexes are closely comparable, however, the degree of linear correlation of the dataset for the iridium complexes is greater than those of the rhodium complexes. While the linear correlation between the theoretical and experimental properties has improved by separating the dataset into broad groups of complexes, the variances in the coordination geometries between different compounds, as well as the electronic properties of the coordinated ancillary ligands, are anticipated to contribute significantly to the mean deviations observed in the datasets.

The data in the datasets may also be described by grouping complexes which feature similar ancillary ligands together, giving rise to data-groups ***1a–d***, ***2a–d***, ***3a–b***, and ***4a–d***. The experimental results and theoretical properties of each group of complexes show reasonable ($R^2 \approx 0.94$) to excellent correlation ($R^2 \geq 0.98$), *vide infra*. The correlations for many of the theoretical parameters of group ***1a–d*** proved to be lower than those of the other groups. Closer inspection of the data revealed that the trends presented by complexes **1a** and **1b** were quite different from those of complexes **1c** and **1d**. The origin of these variances between complexes **1a**–**b** and **1c**–**d** needed to be established before further

© University of Pretoria

meaningful interpretations could be carried out, therefore outlier analyses were performed on all statistical results.

4.2.3) Thermodynamic Half-Reaction Cycles



Scheme 4–1: Thermodynamic reaction cycles were used to calculate the theoretical Gibbs Free Energy change of the reduction half-cell reaction (left), and oxidation half-cell reaction (right), of compound "M" in solution.

Theoretical E_{cell} potentials may be calculated by applying a half-cell reaction thermodynamic cycle method as depicted in Scheme 4.2–1.[1–3,39] The reduction potential (E_{cell}^{Red}) of a reaction may be calculated from the standard state free energy change (ΔG_{Red}) of the half-reaction using equation 3. [2,3,7,39–42]

$$E_{cell}^{Red} = \left(\frac{-\Delta G_{Red}}{nF}\right) - E_{Ref} \qquad (3)$$

The number of electrons transferred during the reaction is represented by n, F is Faraday's constant (96.485 kJ/V.e) and E_{Ref} is the standard reduction potential of a reference electrode, relative to which E_{cell}^{Red} is being calculated. E_{Ref} here serves a similar function as a reference electrode in an electrochemical cell, whereby the reaction potential is measured relative to the potential of the reference electrode.[1–3,39] The ΔG_{Red} is calculated as shown in the thermodynamic half-cell reaction cycle and equation 4,

$$\Delta G_{Red} = \Delta G_{gas}^{\circ} + \Delta G_{solv}(e) + \left[\Delta G_{solv}^{\circ}(M^{-}) - \Delta G_{solv}^{\circ}(M)\right] \qquad (4)$$

where ΔG_{gas}° is the standard state free energy change of the gaseous reduction reaction, and ΔG_{solv}° denotes the free energy of solvation. Note: as previously reported in literature, the $\Delta G_{solv}(e)$ was treated as 0 (zero). [2,3,40,41] The ΔG_{gas}° may be calculated as a function of the Electronic Energy "EE" and the thermal correction to the free energy "ΔG_{corr}" for all products and reactants (Equation 5) – which include contributions for their individual zero-point energy corrections "E_{ZPV}" (Equation 6).[2,3,10,15,39] The free energy contribution of the gaseous electron at 298.15 K (in kJ/mol) is also taken into account, as determined using Fermi-Dirac statistics.[2,43]

© University of Pretoria

$$\Delta G^{\circ}_{gas} = G^{\circ}_{gas}(M^{-}) - G^{\circ}_{gas}(M) - G^{\circ}_{gas}(e) \quad (5)$$
$$= \left[EE(M^{-})_{gas} + \Delta G_{corr}(M^{-})_{gas}\right] - \left[EE(M)_{gas} + \Delta G_{corr}(M)_{gas}\right] - (-3.6106)$$

and

$$\Delta G_{corr} = H_{corr} - TS_{corr} = (ZPE_{corr} + k_B T) - TS_{tot} \quad (6)$$

The "S_{tot}" represents the total Entropy, and the thermal correction factor to enthalpy "H_{corr}" includes the zero-point vibrational correction energy "ZPE_{corr}".[2,3,10,15,39]

The last remaining variables in equation 4 are the solvation free energies "ΔG°_{solv}" of the product and reactant, which are critical to account for energy differences between the two states that are not directly associated with the reaction itself.[2,3,10,15,39] For example, conformational changes that are induced by solvation between the optimised gas-phase and solvated geometries will result in energy differences between the two states that is not related to the reduction/oxidation reaction. Equation 7, written here for the reduced "(M^{-})" species, also includes the change in the thermal correction to free energy.

$$\Delta G^{\circ}_{solv}(M^{-}) = G^{\circ}_{solv}(M^{-}) - G^{\circ}_{gas}(M^{-}) \quad (7)$$
$$= [EE(M^{-})_{solv} + \Delta G_{corr}(M^{-})_{solv}] - \left[EE(M^{-})_{gas} + \Delta G_{corr}(M^{-})_{gas}\right]$$

The energy that is released by the addition of one electron to compound "*M*" may be described as the Electron Affinity (EA),[3,14] and the energy required to remove an electron from "*M*" as the Ionisation Energy (IE),[3,14] which may be estimated using equations 8 and 9:

$$EA(M) = EE(M) - EE(M^{-}) \quad (8)$$
$$IE(M) = EE(M^{+}) - EE(M) \quad (9)$$

Substituting equation 8 into equation 5 yields:

$$\Delta G^{\circ}_{gas} = \left[EE(M^{-})_{gas} + \Delta G_{corr}(M^{-})_{gas}\right] - \left[EE(M)_{gas} + \Delta G_{corr}(M)_{gas}\right] - G^{\circ}_{gas}(e)$$
$$= -EA(M)_{gas} + \left[\Delta G_{corr}(M^{-})_{gas} - \Delta G_{corr}(M)_{gas}\right] - (-3.6106)$$
$$= -EA(M)_{gas} + \Delta\Delta G_{corr} + 3.6106 \quad (10)$$

© University of Pretoria

A linear relationship between the ΔG_{Red} and $-EA(M)_{gas}$ becomes apparent when substituting equation 10 into equation 4:

$$\Delta G_{Red} = \left[-EA(M)_{gas} + \Delta\Delta G_{corr} - G^{\circ}_{gas}(e)\right] + \Delta G_{solv}(e) + \left[\Delta G^{\circ}_{solv}(M^{-}) - \Delta G^{\circ}_{solv}(M)\right] \quad (11)$$

After which it therefore follows that a linear relationship exists between the theoretical E_{cell} potentials and $-EA(M)_{gas}$ as well:

$$E^{Red}_{cell} = \left(\frac{-(\left[-EA(M)_{gas}+\Delta\Delta G_{corr}-G^{\circ}_{gas}(e)\right]+\Delta G_{solv}(e)+\left[\Delta G^{\circ}_{solv}(M^{-})-\Delta G^{\circ}_{solv}(M)\right])}{nF}\right) - E_{Ref} \quad (12)$$

The theoretical E_{cell} potentials, and by extension the experimental E_{DPV} potentials, can thus be correlated to a range of different calculated thermodynamic quantities. The equivalent set of equations for calculating the theoretical oxidation potential (E^{Ox}_{cell}) from the standard state free energy change (ΔG_{Ox}) of the thermodynamic half-cell reaction cycle depicted in Scheme 4.2–1 may be found in Appendix G.2.1.

4.3) Results and Discussion

4.3.1) Outlier Analyses and the Peak Characterisation Model

Initial LFER plots were drawn up from the experimentally analysed E_{DPV} data as presented Chapter 3 (Table 3.3–41), for all calculated compounds (Limited dataset). Exclusion of E_{DPV} data points solely based on their similarity to the data recorded for the free ligands may result in the introduction of bias and an egregious amount of error to the linear correlation analyses. Thus, a second population of dependant data points, which utilised the complete E_{DPV} data (Full dataset), was subjected to the same linear correlation examinations.

The correlation analyses of the Full dataset showed increased mean deviations for linear correlations of the collective group comparisons (*All*, ***1–4***, *All Rh* and *All Ir*, *All DippBIAN* and *All MesBIAN*) compared to those of the Limited dataset. However, the R^2 values of the collective group comparisons for the LFER plots of LUMO energy, FMO energy, and –EA using the Full dataset showed a notable upturn in linear agreement.

© University of Pretoria

Statistical inspections of all the LFER plots from both the Limited dataset and Full dataset were done for outlier data points, and any identified outlier dependant variable points (E_{DPV}) were rigorously examined according to the following three criteria:

1. Does the outlier point significantly differ from the other data points in the plot? In other words, does the outlier point have a studentised residual > |2.5|?
2. Is the dependant variable point a significant outlier in multiple LFER plots?
3. Is there a chemically meaningful justification as to why the data point may be an outlier?

A pair of outlier data points associated with E_{DPV} data from **1c** (x = –0.58 V) and **1d** (x = –0.58 V) were identified during these examinations as significantly different from other data points on the orbital energy plots for ***1a–d***. However, the pair was not significantly different from data points in other LFER plots, and their removal could not be chemically justified. Subdivision of the ***1a–d*** group into ***1ab*** and ***1cd*** substantially increased the groups' linear correlations across a number of different LFER plots, and decreased the significance of the outlier points. In addition, a sizeable difference in the slope of the best fit lines for ***1ab*** and ***1cd*** on several LFER plots was revealed, indicating a notable difference in the electrochemical characteristics of the two subgroups even though they are structurally and chemically very similar. Examination of the best fit graphs for the individual complexes of the ***2a–d*** group revealed variances in the slope and Y-intercept for the graphs of –EA, $-\Delta G_{rxn}$ and E_{cell} between complexes **2a** and **2b**, and complexes **2c** and **2d.** However, no significant variance was observed in the orbital energy correlations between the ***2ab*** and ***2cd*** subgroups.

An additional E_{DPV} data point (**4d**, x = –1.8 V) was identified as significantly different in the LFER plots for E_{cell} and $-\Delta G_{rxn}$. As discussed in Chapter 3 (Section 3.3.1.xvi), when subjecting **4d** to potentials below –1.7 V it resulted in a steep increase in the recorded cathodic current of a highly irreversible reduction event. The voltammetric reactivity of **4d** indicates analyte decomposition taking place, providing experimental support for the exclusion of the (**4d**, x = –1.8 V) data point as an outlier. Removal of this data point yielded a third population of E_{DPV} data (All – Outlier dataset) which was submitted to identical linear correlation examinations as the previous datasets. Many increased linear correlations were noted for a variety of LFERs compared to those observed with the Full dataset or Limited dataset.

The linear correlations of the Full dataset and All – Outlier dataset are overall superior to those obtained when using the Limited dataset, indicating that the voltammetric peaks with potentials

© University of Pretoria

similar to those of the free ligands are, in fact, an intrinsic part of the electrochemical reactivity characteristics for the complexes.

The computational workflow and data analysis applied to the current systems, hereafter referred to as the Peak Characterisation Model, were thus utilised to distinguish characteristic voltammetric peaks for an analyte from among otherwise convoluted voltammograms. The LFERs that will be discussed in the following sections are representative results from the All – Outlier dataset. For the interested reader, additional results from the Full dataset and Limited dataset are available in Appendix G.2.2.

4.3.2) HOMO / LUMO vs E_{DPV}

The comparison of calculated HOMO/LUMO orbital energy values and experimentally determined redox potentials as a LFER has become a fairly common place practice for synthetic chemists branching out into computational chemistry.[4,14,44,45] Ideally, it is anticipated that the LUMO and HOMO orbital energies of a compound would parallel the experimentally observed reduction and oxidation potentials, respectively, since they represent the orbitals that are most likely to be involved in these electrochemical reactions.[4,14,40,44,46] Such MO energy LFER models are narrowed to correlations of the first reduction and/or oxidation potentials of a compound, seldom encompassing the full electrochemical reaction profile. In the models presented here, linear correlations are observed between the MO energies of compounds in a series of seven different charged states and their experimental reduction and oxidation reaction potentials spanning a 3.8 V potential window.

As illustrated in Table 4.2–1, the (n = +1) charged state of each complex, and its computational results, were utilised as the independent variables associated with the recorded first reduction potential of that complex. Similarly, the second reduction potentials were linked to the computational results of the (n = +2) states for the complexes, the first oxidation potentials with the computational results of the (n = –1) states for the complexes, etc.

© University of Pretoria

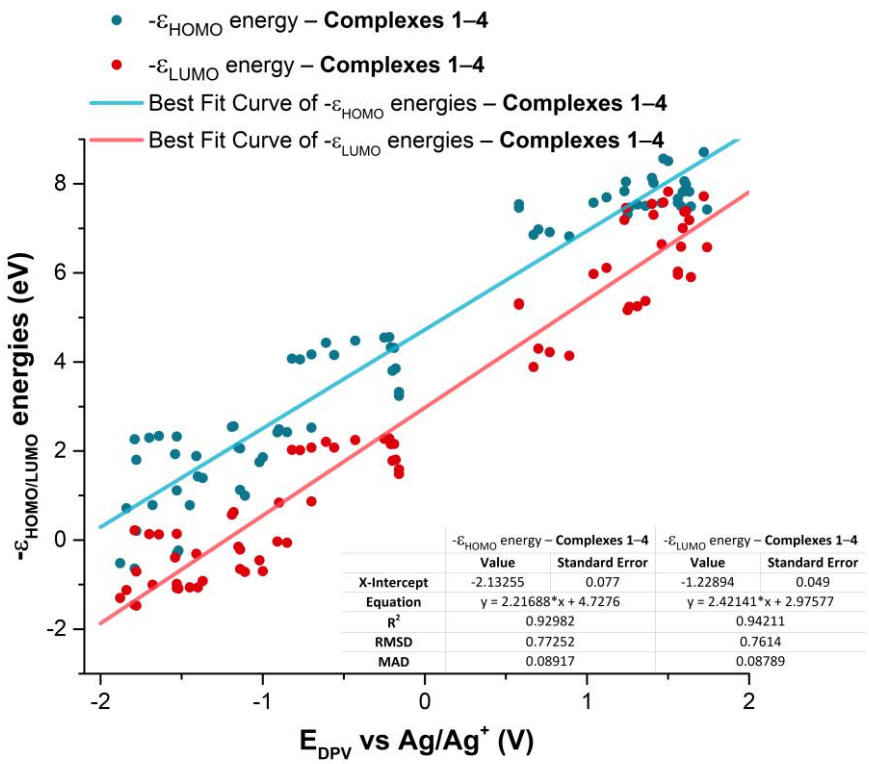


*Figure 4.3–1: Linear Free Energy Relationship between the HOMO (blue) and LUMO (red) orbital energies ($-\varepsilon_{HOMO/LUMO}$) calculated for all modelled states of the complex series **1–4**, and their experimental DPV reaction potentials (E_{DPV}).*

The HOMO and LUMO orbital energies for the collective group ***1–4*** showed a good linear relationship relative to the recorded DPV potentials (Figure 4.3–1). The relationships for complexes from specific groups showed excellent linear correlation (Table 4.`3–2).

Table 4.3–1: Correlations of the HOMO/LUMO orbital energies (eV) and the experimental DPV reaction potentials (V vs Ag/Ag⁺) based on linear best fit trend lines using the All – Outlier dataset.

Plot	Compounds	Y-Intercept (eV)	Slope (eV/V)	X-Intercept (V)	R^2	RMSD	MAD
HOMO	**1a–b**	5.174	1.745	–2.965	0.99691	0.14917	0.04568
HOMO	**1c–d**	4.685	2.958	–1.584	0.97172	0.59872	0.14814
HOMO	**2a–d**	4.918	2.142	–2.285	0.97328	0.46748	0.10144
HOMO	**3a–b**	5.223	1.712	–3.051	0.99514	0.19669	0.05782
HOMO	**4a–d**	4.299	2.305	–1.865	0.96287	0.57295	0.11416
LUMO	**1a–b**	3.333	2.046	–1.629	0.96828	0.56873	0.17414
LUMO	**1c–d**	3.155	3.171	–0.995	0.98817	0.41167	0.10186
LUMO	**2a–d**	3.207	2.424	–1.323	0.97332	0.5261	0.11417
LUMO	**3a–b**	3.413	1.983	–1.721	0.96808	0.59166	0.17393
LUMO	**4a–d**	2.391	2.355	–1.015	0.98252	0.39773	0.07925

A second series of LFER plots were generated to investigate the cooperative correlation between the calculated HOMO and LUMO energies of a complex relative to its recorded DPV reaction potentials.[4] The LUMO energies for the (n = +1 to +4) states of the complexes, and the HOMO energies for the

© University of Pretoria

(n = –1 to –3) states of the complexes, were used as the independent variables for these "reactive" FMO correlation plots.[4]

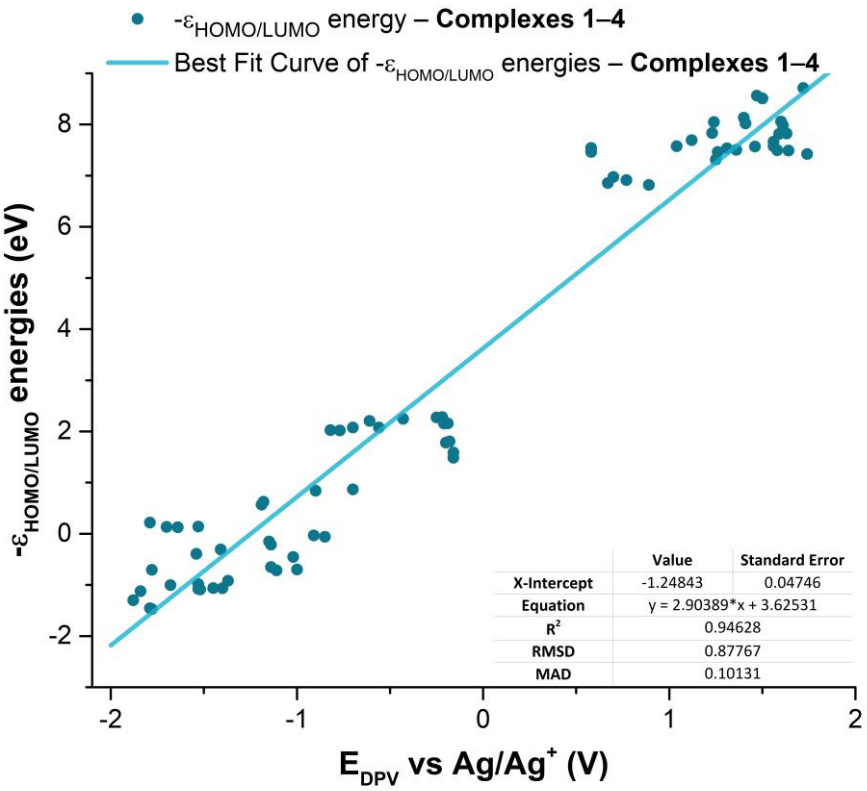


*Figure 4.3–2: LFER between the reactive FMO energies ($-\varepsilon_{HOMO/LUMO}$) and experimental DPV reaction potentials (E_{DPV}) for all modelled states of the complex series **1**–**4**. LUMO energies were used at negative potentials, and HOMO energies at positive potentials, to model reductive and oxidative reactivity respectively.*

Overall, the "reactive" FMO plots of the collective group comparisons showed a small increase in the average R^2 value compared to individual HOMO and LUMO energy plots (Figure 4.3–2). None of the correlations for complexes from specific groups showed similar improvement in their linearity index (Table 4.3–3). The high degree of linearity observed for the "reactive" FMO vs E_{DPV} correlation plots may nonetheless be a viable descriptor for the electrochemical reactivity of the charged species of the complexes alongside their individual HOMO vs E_{DPV} and LUMO vs E_{DPV} correlation plots.

Table 4.3–2: Correlations of the reactive Frontier Molecular Orbital energies (eV) and the experimental DPV reaction potentials (V vs Ag/Ag⁺) based on linear best fit trend lines using the All – Outlier dataset.

Plot	Compounds	Y-Intercept (eV)	Slope (eV/V)	X-Intercept (V)	R^2	RMSD	MAD
FMO	**1a–b**	3.968	2.527	–1.570	0.99374	0.3081	0.09434
FMO	**1c–d**	3.703	3.585	–1.033	0.95616	0.91097	0.22541
FMO	**2a–d**	3.717	2.870	–1.295	0.98049	0.53068	0.11516
FMO	**3a–b**	4.409	2.441	–1.684	0.99476	0.29097	0.08554
FMO	**4a–d**	3.228	2.940	–1.098	0.94312	0.91409	0.18213

© University of Pretoria

4.3.3) –EA vs E_{DPV}

Classically, the electron affinity (EA) of an element or compound is described as the amount of energy that is released when one additional electron is taken up by the element or compound while in the gas phase.[3,14] In computation terms, however, one of the possible descriptions of electron affinity is as the difference in electronic energy between a modelled molecule in its initial (M) and first reduced (M^-) states (Equation 6).[3,14] When applying a thermodynamic half-reaction cycle approach to calculate the theoretical reaction potentials, as discussed in Section 4.2, a linear proportionality is observed between the gas phase EA of a molecule and its cell reaction potentials (simplified from equation 12),

$$E_{cell} \propto \left(-EA(M)_{gas}\right) \times m + c \qquad (13)$$

where m represents the slope and c represents the Y-intercept of the linear fit line. The latter may be interrelated to the standard potential of the reference electrode which was used during the experimental measurements. For the purposes of this study, the Y-intercept value for data with ideal correlation is anticipated to be equal to the standard potential of a silver electrode (E_{Ref}^{Ag}) in a non-aqueous solution. Using conventional electrode potential conversion methods,[47] the standard potential of the NHE reference electrode (E_{Ref}) utilised in the computational methodology may be converted to E_{Ref}^{Ag} using equation 14:

$$E_{Ref}^{Ag} = E_{Ref} - 1.34\,V \quad = (-4.44) - 1.34 \quad = -5.78\,eV \qquad (14)$$

The LFER observed between –EA(M) and E_{DPV} showed only modest linear correlations ($0.84 \leq R^2 \geq 0.89$) in all three datasets when considering the results for the collective groups (*All*, ***1–4***, *All Rh* and *All Ir*, *All DippBIAN* and *All MesBIAN*) (Figure 4.3–3). A much-improved correlation ($0.92 \leq R^2 \geq 0.98$) is observed when considering the complex specific groups, indicating that the –EA(M) correlation model is sensitive to dissimilarities among the compounds that are being compared (Table 4.3–4).

Variants among the compounds in the collective group data which may affect –EA(M) are not limited to only the coordinated metal but may also include difference in the coordination geometries and the specific ancillary ligands that are present in the complexes. No doubt, the thermodynamic basis from which –EA(M) is calculated has a big influence on the sensitivity of the correlation model, as the number and type of atoms present in the molecules being compared would directly affect the individual values of –EA(M).

© University of Pretoria

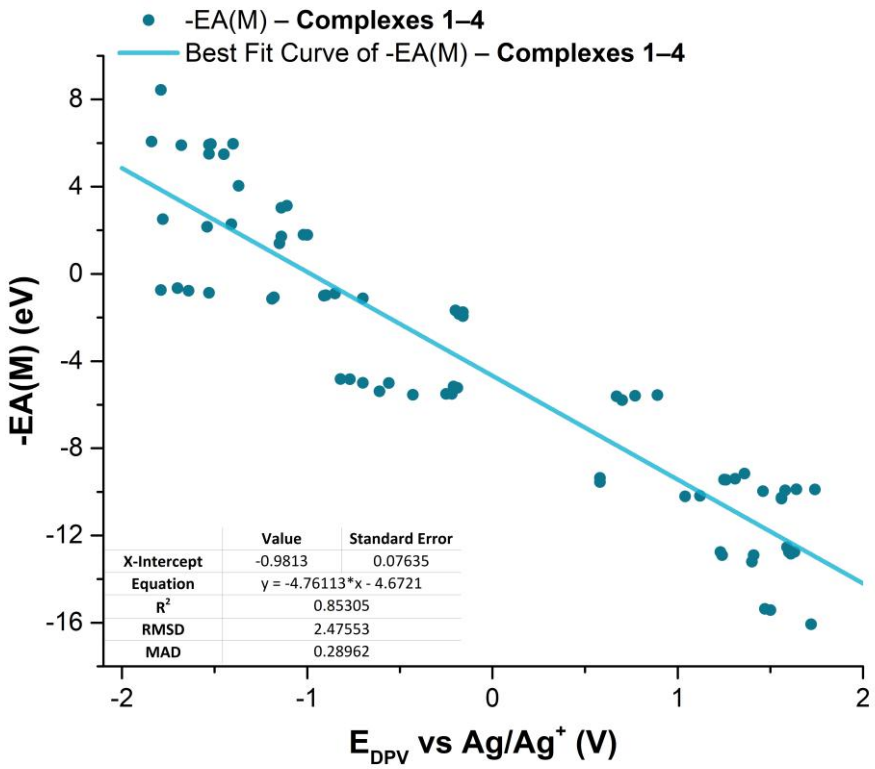


*Figure 4.3–3: LFER between the theoretical Electron Affinity ($-EA_{gas}$) and the experimental DPV reaction potentials (E_{DPV}) for all modelled states of the complex series all modelled states of the complex series all modelled states of the complex series **1–4**.*

The R^2 linear correlation of the complex specific groups ***1a–d*** and ***2a–d*** showed a marked improvement when subdivided into the ***1ab***, ***1cd***, ***2ab*** and ***2cd*** subgroupings mentioned in Section 4.3.1.

*Table 4.3–3: Correlations of the theoretical Electron Affinity **–EA** (eV) and the experimental DPV reaction potentials (V vs Ag/Ag⁺) based on linear best fit trend lines using the All – Outlier dataset.*

Compounds	Y-Intercept (eV)	Slope (eV/V)	X-Intercept (V)	R^2	RMSD	MAD
All	–4.590	–4.550	–1.009	0.84249	2.50114	0.27954
1–4	–4.672	–4.761	–0.981	0.85305	2.47553	0.28962
All Rh	–5.038	–4.294	–1.173	0.85636	2.3583	0.36344
All Ir	–4.233	–5.551	–0.763	0.88675	2.3277	0.40436
All DippBIAN	–4.546	–4.830	–0.941	0.85578	2.47916	0.4069
All MesBIAN	–4.796	–4.696	–1.021	0.85132	2.53411	0.4145
1a–d	–5.586	–5.218	–1.070	0.88353	2.37097	0.48197
2a–d	–5.446	–4.927	–1.105	0.92146	1.88541	0.40915
3a–b	–6.229	–3.444	–1.809	0.9299	1.5539	0.4568
4a–d	–2.293	–4.807	–0.477	0.97433	0.95536	0.1983
1a–b	–6.432	–3.33	–1.933	0.96039	1.03786	0.31778
1c–d	–5.383	–6.744	–0.798	0.98375	1.02845	0.25448
2a–b	–5.582	–5.543	–1.007	0.95792	1.61345	0.41163
2c–d	–5.478	–3.253	–1.684	0.97695	0.69657	0.23219

© University of Pretoria

The increased degree of linearity indicates a dissimilarity in the computational gas phase energetics of rhodium and iridium complexes with analogous ligands, which may result from difference in the valence orbitals of the metals.

Table 4.3–4: Correlations of the theoretical Electron Affinity (eV) and the experimental DPV reaction potentials (V vs Ag/Ag^+) based on linear best fit trend lines for each complex using the All – Outlier dataset.

Compounds	Y-Intercept (eV)	Slope (eV/V)	X-Intercept (V)	R^2	RMSD	MAD
1a	–6.320	–3.388	–1.865	0.95848	1.29936	0.45939
1b	–6.539	–3.276	–1.996	0.9638	1.21692	0.43025
1c	–5.420	–6.677	–0.812	0.98329	1.14159	0.36467
1d	–5.345	–6.813	–0.785	0.98447	1.10218	0.35208
2a	5.230	–5.601	–0.934	0.95444	1.75419	0.58473
2b	–5.891	–5.475	–1.076	0.9633	1.71605	0.54817
2c	–5.473	–3.233	–1.693	0.97967	0.91865	0.30622
2d	–5.484	–3.273	–1.676	0.97438	1.04577	0.34859
3a	–6.562	–3.070	–2.137	0.94324	1.52189	0.53807
3b	–6.065	–3.693	–1.642	0.935	1.81247	0.62786
4a	–2.817	–4.531	–0.622	0.98196	0.86201	0.29861
4b	–2.187	–4.363	–0.501	0.98223	0.92719	0.32119
4c	–2.099	–5.152	–0.407	0.9812	1.05949	0.35316
4d	–2.220	–5.056	–0.439	0.98355	0.91787	0.31796

The Y-intercept for the of group ***4a–d***, which relates to E_{Ref}^{Ag} using equation 14, greatly underestimates the expected value for the experimental reference electrode potential (E_{Ref}^{Ag} = –2.293 eV). The presence of the chlorido ligands in complex series **4a–d** may be a contributing factor to this observed deviation due to interactions with the silver quasi-reference electrode in the experimental system. Moreover, any irreversible dissociation of the chlorido ligand from the complexes during the electrochemical analyses would result in fundamental change in what compound is giving rise to the subsequent electrochemical reactions.

The –EA(M) vs E_{DPV} correlations of groups ***1ab*** and ***3a–b*** overestimate the expected values of E_{Ref}^{Ag} (Table 4.3–4). The square planar complexes in groups ***1ab*** and ***3a–b*** does not have common ancillary ligands, suggesting that the shift in potential may be due to systemic overestimations of the rhodium gas phase energies for these complexes and their charged states.

Correlation models utilising only gas-phase optimised structures require additional computational parameters, expanded basis sets, and often need to be calibrated with existing experimental data in order to reach the desired level of predictive accuracy.[5] The functional applicability of the modelled gas-phase –EA(M) correlation to other compounds is therefore severely limited, and may prove

© University of Pretoria

inadequate when utilised for chemical systems beyond that for which it was originally calculated. By including the energies of the solvent optimised structures into the correlation models, the accuracy with which the computations may correlate to the experimental observations may be improved. Thus, the LFER of the experimental data to the theoretical reaction free energy changes (ΔG_{rxn}) was also investigated.

4.3.4) $-\Delta G_{rxn}$ vs E_{DPV}

Several statistical thermodynamics parameters, such as enthalpy (H), entropy (S) and Gibbs Free energy (G), are calculated automatically during the frequency calculations that were performed to ensure the optimised molecular geometries were at minima.[10,14] These parameters are an intrinsic part of the internal equations the software uses to calculate the vibrational frequencies of the molecule. For example, the Free energy correction factor "ΔG_{corr}", described by equation 6, accounts for an increase in the thermodynamic energies of both enthalpy and entropy resulting from the system being modelled under standard conditions (298.15 K) instead of standard temperature (0 K).[10] Furthermore, the thermodynamics parameters calculated for the same molecule in different energetic or electronic states may be used in conjunction with one another to calculate more practically applicable thermodynamic quantities such as the free energy change of reactions (ΔG_{rxn}) or theoretical half-cell reaction potentials (E_{cell}).

As discussed earlier, the reduction and oxidation half-reactions of an analyte molecule "*M*" at the electrode surface may be written as separate thermodynamic half-cell reactions (Scheme 4.2–3). The Free energy change of the electrochemical reaction in solution (ΔG_{rxn}) was then calculated for all modelled compounds using a thermodynamic half-cell reaction cycle (see equations 4–10) and the thermodynamic parameters calculated for the modelled charged states of each compound. The directly proportional relationship between ΔG_{rxn} and E_{cell} may be clarified by simplifying equation 3,

$$E_{cell} = -\Delta G_{rxn} \times m + c \qquad (15)$$

where m represents the slope of the linear best fit line between the calculated ΔG_{rxn} and experimental E_{DPV} measurements, and c the Y-intercept. The value of the Y-intercept for the data with ideal correlation is anticipated to be equal to the standard potential of the standard potential of the theoretical NHE reference electrode ($E_{Ref} = 4.44\ eV$).

© University of Pretoria

*Table 4.3–5: An example set of the Thermodynamic Parameter extracted from the cPCM frequency calculations for **1a** [Rh(DippBIAN)(cod)]⁺ in its various charged states.*

[RhDB(cod)]⁺ n = ? (cPCM)	EE *(eV)*	ZPE_{Corr} *(eV)*	H_{corr} *(eV)*	G_{corr} *(eV)*	S_{tot} *(eV)*
a, +4	–52428.91	22.644	23.924	20.540	0.01135
a, +3	–52434.90	22.940	24.195	20.870	0.01115
a, +2	–52437.37	23.109	24.351	21.042	0.01110
a, +1	–52436.50	23.223	24.462	21.163	0.01106
ab, 0	–52431.50	23.279	24.523	21.224	0.01107
b, –1	–52422.11	23.269	24.515	21.198	0.01112
b, –2	–52409.28	23.158	24.422	21.036	0.01136
b, –3	–52393.96	23.054	24.339	20.898	0.01154

An exemplar of the initial thermodynamic parameters obtained from the frequency calculations of the eight modelled charged states of **1a** is provided in Table 4.3–6. Following the application of equations 3 through 10, the various Free energy changes, Electron Affinity and theoretical half-cell potential associated with each of the first four reduction reactions, and first three oxidation reactions, were calculated (Table 4.3–7).

*Table 4.3–6: An example set of the calculated Free Energies and Electron Affinity of **1a** [Rh(DippBIAN)(cod)]⁺ that were used to calculate the theoretical E_{cell} redox potentials relative to the Standard Hydrogen Electrode (E_{Ref} = 4.44 V).*

[RhDB(cod)]⁺	E_{cell} vs NHE *(eV)*	ΔG_{rxn} *(kJ/mol)*	ΔG_{gas} *(kJ/mol)*	–EA(M) *(kJ/mol)*	$\Delta\Delta G_{thermal}$ *(kJ/mol)*	$\Delta G_{solv}(M^-)$ *(kJ/mol)*	$\Delta G_{solv}(M)$ *(kJ/mol)*
Red 4	–4.721	27.083	549.444	577.649	–31.821	–978.335	–455.973
Red 3	–3.542	–86.685	225.702	238.674	–16.588	–455.973	–143.586
Red 2	–2.162	–219.756	–91.771	–83.675	–11.712	–143.586	–15.6007
Red 1	–0.425	–387.389	–484.533	–482.336	–5.813	–15.6007	–112.744
Ox 1	1.401	–563.550	–900.370	–906.456	2.471	–112.744	–449.564
Ox 2	2.912	–709.341	–1218.630	–1237.868	15.622	–449.564	–958.853
Ox 3	3.326	–749.338	–1460.940	–1477.854	13.298	–958.853	–1670.46

A comprehensive set of tables with the linear best fit and statistical analysis results of the linear correlations between the theoretical Gibbs Free energy change of reaction and the experimental E_{DPV} data for all three datasets is available in Appendix G.2.2.

The collective grouped comparisons (*All*, ***1–4***, *All Rh* and *All Ir*, *All DippBIAN* and *All MesBIAN*) presented modest to fair linear correlations ($0.88 \leq R^2 \geq 0.92$), whereas very good linear correlations were observed for the ***1cd***, ***2cd*** and ***4a–d*** subgroups of complexes (Table 4.3–8).

© University of Pretoria

Table 4.3–7: Correlations of the theoretical reaction free energy change $-\Delta G_{rxn}$ (eV) and the experimental DPV reaction potentials (V vs Ag/Ag$^+$) based on linear best fit trend lines using the All – Outlier dataset.

Compounds	Y-Intercept (eV)	Slope (eV/V)	X-Intercept (V)	R^2	RMSD	MAD
All	4.092	1.827	–2.239	0.88428	0.84029	0.09392
1–4	4.103	1.896	–2.164	0.88918	0.83857	0.09811
All Rh	4.258	1.706	–2.496	0.89606	0.77923	0.12009
All Ir	3.916	2.218	–1.766	0.92351	0.74871	0.13006
All DippBIAN	4.088	1.958	–2.088	0.89066	0.85756	0.14075
All MesBIAN	4.119	1.840	–2.239	0.88945	0.83752	0.13565
1a–d	4.222	2.099	–2.012	0.88785	0.93358	0.18978
2a–d	4.422	1.937	–2.284	0.93956	0.64389	0.13973
3a–b	4.539	1.423	–3.190	0.93151	0.63405	0.18639
4a–d	3.480	1.917	–1.815	0.97207	0.39784	0.08258
1a–b	4.602	1.387	–3.317	0.9514	0.48154	0.14744
1c–d	4.110	2.666	–1.542	0.97876	0.46602	0.11531
2a–b	4.464	2.115	–2.111	0.95784	0.61615	0.1572
2c–d	4.425	1.454	–3.044	0.97723	0.30935	0.10312

The stark difference between the linear correlations of the collective groups and specific groups of complexes is similar to what was observed for the –EA(M) vs E_{DPV} plots, and results from the same underlying thermodynamic difference between the groups of compounds that are being compared (see Section 4.3.3).

Table 4.3–8: Correlations of the theoretical reaction free energy change $-\Delta G_{rxn}$ (eV) and the experimental DPV reaction potentials (V vs Ag/Ag$^+$) based on linear best fit trend lines for each complex using the All – Outlier dataset.

Compounds	Y-Intercept (eV)	Slope (eV/V)	X-Intercept (V)	R^2	RMSD	MAD
1a	4.575	1.430	–3.199	0.95436	0.57629	0.20372
1b	4.626	1.349	–3.431	0.95018	0.59193	0.20928
1c	4.164	2.647	–1.573	0.97968	0.49981	0.15966
1d	4.057	2.687	–1.510	0.97863	0.51144	0.16337
2a	4.423	2.257	–1.959	0.95153	0.73031	0.24344
2b	4.525	2.017	–2.243	0.96902	0.57912	0.18499
2c	4.464	1.458	–3.063	0.98336	0.37393	0.12464
2d	4.387	1.450	–3.026	0.97216	0.48342	0.16114
3a	4.700	1.309	–3.592	0.94349	0.64709	0.22878
3b	4.439	1.490	–2.978	0.93289	0.74408	0.25776
4a	3.710	1.880	–1.973	0.9627	0.51952	0.17997
4b	3.457	1.700	–2.034	0.97191	0.45651	0.15814
4c	3.356	2.068	–1.623	0.98946	0.31713	0.10571
4d	3.472	1.960	–1.771	0.994	0.21377	0.07405

Examining the linear correlation data for each individual compound reveals a splendid degree of linearity ($0.93 \leq R^2 \geq 0.99$) between the theoretical reaction free energy change ($-\Delta G_{rxn}$) and E_{DPV}

© University of Pretoria

potentials (Table 4.3–9). A closer look at plots for the complex specific groups reveal interesting similarities between the different groups of complexes (Figure 4.3–4). As observed for the –EA(M), the slope and intercept of the best fit lines for the ***1ab*** and ***3a–b*** subgroups are very similar. The best fit curves for groups ***2a–d*** and ***4a–d*** are near parallel, whereas the ***1cd*** group presents a vastly steeper slope than any of the other subgroupings.

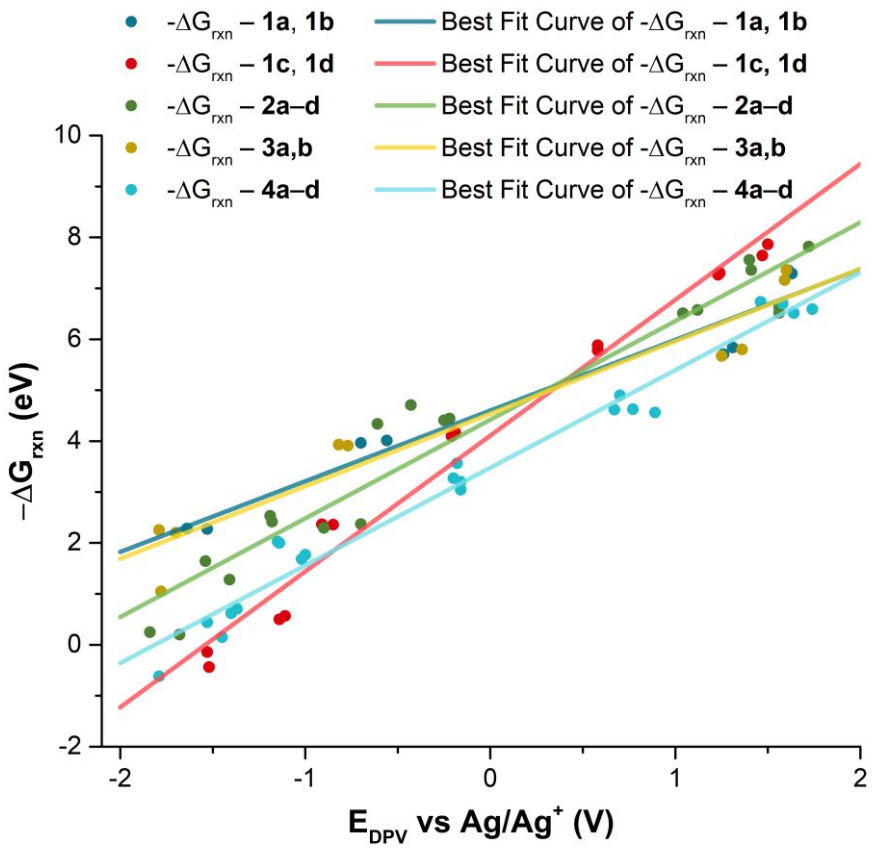


*Figure 4.3–4: LFER between the theoretical reaction free energy change ($-\Delta G_{rxn}$) and the experimental DPV reaction potentials (E_{DPV}) for all modelled states of the complex series **1–4**.*

Using the relationship presented in equation 15, the Y-intercept of the best fit lines are anticipated to correlate to the standard potential of the NHE reference electrode ($E_{Ref} = 4.44\ eV$). The linear correlation plots for most of the groups yielded Y-intercept values within ± 0.4 eV of the expected reference potential, with the notable exception of the ***4a–d*** group which underestimated the expected reference potential by *c.a.* 1 eV.

Previous LFER models have interpreted the slope of the linear correlations as an indicator of systematic errors in the calculations due to an overestimation of the charged states' energies.[5] Future work following this computational methodology would thus benefit from including additional diffuse functions to the basis set that is employed.[5] Even though the present $-\Delta G_{rxn}$ vs E_{DPV} model does not

© University of Pretoria

predict the reference potentials accurately for all of the modelled compounds, the high degree of linear correlation observed among the complex specific groups, as well as the individual LFER plots for the complexes, show the capacity for the model to be applied to compounds with multi-electron electrochemical reactivity.

4.3.5) E_{cell} vs E_{DPV}

The theoretical E_{cell} half-reaction potentials of the first four reduction events, and first three oxidation events, were calculated for all modelled complexes to formulate a qualitative comparison with the experimental E_{DPV} data. In order to achieve a satisfactory level of accuracy in the calculated energy values for this study to carry quantitative comparability, all of the modelled compounds and their charged states (in both gas phase and cPCM) would need to be submitted for further energy calculations using an expanded functional that includes additional basis functions for valence shell of each atom.[9,11] The additional computational cost was deemed prohibitively high for the purposes of the current study.

Table 4.3–9: Correlations of the theoretical reaction cell potential E_{cell} (V vs NHE) and the experimental DPV reaction potentials (V vs Ag/Ag^+) based on linear best fit trend lines using the All – Outlier dataset.

Compounds	Y-Intercept (V)	Slope (V/V)	X-Intercept (V)	R^2	RMSD	MAD
All	–0.348	1.827	0.191	0.88428	0.84029	0.09392
1–4	–0.337	1.896	0.178	0.88918	0.83857	0.09811
All Rh	–0.182	1.706	0.107	0.89606	0.77923	0.12009
All Ir	–0.524	2.217	0.237	0.92351	0.74871	0.13006
All DippBIAN	–0.352	1.958	0.180	0.89066	0.85756	0.14075
All MesBIAN	–0.321	1.840	0.174	0.88945	0.83752	0.13565
1a–d	–0.218	2.099	0.104	0.88785	0.93358	0.18978
2a–d	–0.018	1.937	0.009	0.93956	0.64389	0.13973
3a–b	0.099	1.423	–0.070	0.93151	0.63405	0.18639
4a–d	–0.960	1.917	0.501	0.97207	0.39784	0.08258
1a–b	0.162	1.387	–0.117	0.9514	0.48154	0.14744
1c–d	–0.330	2.666	0.124	0.97876	0.46602	0.11531
2a–b	0.024	2.115	–0.012	0.95784	0.61615	0.1572
2c–d	–0.015	1.454	0.010	0.97723	0.30935	0.10312

All values of E_{cell} are calculated and reported as Formal potentials relative to the Natural Hydrogen Electrode (NHE), with the half-cell potential taken as E_{Ref} = 4.44 eV.[1,39,48] Literature reports for the E_{Ref} value of the NHE vary widely due to differences in the solvents employed during experimental preparations, as well as variance in the statistical models (Boltzmann vs Fermi-Dirac statistics)[2] utilised to calculate the enthalpy, entropy and Gibbs free energy involved in the reference electrode's reactions. The qualitative assessment of correlation between the theoretical E_{cell} and experimental

© University of Pretoria

reaction potentials in this study are performed using LFERs in which the experimental potentials are reported relative to the experimental quasi-reference Ag/Ag^+ electrode, and E_{cell} values relative to the NHE.

The collective grouped comparisons (*All*, ***1–4***, *All Rh* and *All Ir*, *All DippBIAN* and *All MesBIAN*) showed fair linear correlations between the theoretical E_{cell} and experimental E_{DPV} potentials (Table 4.3–10) near identical to those observed for the $-\Delta G_{rxn}$ vs E_{DPV} correlations in Table 4.3-8. The ***1cd*** and ***4a–d*** subgroupings showed the best linear agreement (Figure 4.3–5), with R^2 = 0.98 and 0.97 respectively.

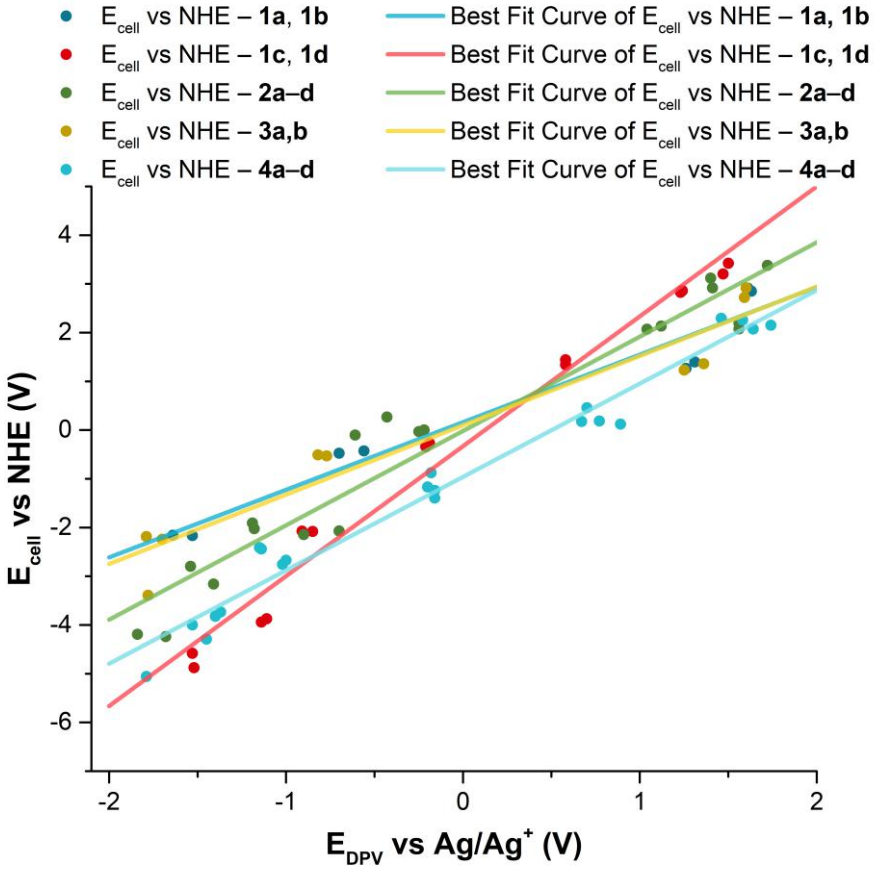


*Figure 4.3–5: LFER between the theoretical reaction cell potential (E_{cell}) and the experimental DPV reaction potentials (E_{DPV}) for all modelled states of the complex series **1–4**.*

As noted in Section 4.3.4, the $-\Delta G_{rxn}$ vs E_{DPV} plots for most of the groups yielded predicted E_{Ref} potentials within ± 0.4 eV of the expected value, corresponding to the Y-intercept values shown in Table 4.3–10. The underestimated E_{Ref} potential predicted by group ***4a–d*** can be easily identified using the E_{cell} vs E_{DPV} graphs.

© University of Pretoria

Examining the linear fit of the data for the individual complexes reveals excellent correlation between the theoretical and experimental reaction potentials (Table 4.3–11), with an average MAD of 0.1753 between all of the modelled complexes.

Table 4.3–10: Correlations of the theoretical reaction cell potential E_{cell} (V vs NHE) and the experimental DPV reaction potentials (V vs Ag/Ag$^+$) based on linear best fit trend lines for each complex using the All – Outlier dataset.

Compounds	Y-Intercept (V)	Slope (V)	X-Intercept (V)	R^2	RMSD	MAD
1a	0.135	1.430	–0.094	0.95436	0.57629	0.20375
1b	0.186	1.349	–0.138	0.95018	0.59193	0.20928
1c	–0.276	2.647	0.104	0.97968	0.49981	0.15966
1d	–0.383	2.687	0.143	0.97863	0.51144	0.16337
2a	–0.017	2.257	0.008	0.95153	0.73031	0.24344
2b	0.085	2.017	–0.042	0.96902	0.57912	0.18499
2c	0.024	1.458	–0.017	0.98336	0.37393	0.12464
2d	–0.053	1.450	0.369	0.97216	0.48342	0.16114
3a	0.260	1.309	–0.199	0.94349	0.64709	0.22878
3b	–0.001	0.001	0.001	0.93289	0.74408	0.25776
4a	–0.730	1.880	0.388	0.9627	0.51952	0.17997
4b	–0.983	1.700	0.579	0.97191	0.45651	0.15814
4c	–1.084	2.068	0.524	0.98946	0.31713	0.10571
4d	–0.968	1.960	0.494	0.994	0.21377	0.07405

4.4) Conclusions

Linear free energy relationships (LFERs) between experimentally recorded DPV peak potentials and computed theoretical properties of the DippBIAN and MesBIAN ligands, and the complex series **1**–**4** (e.g., HOMO/LUMO energies, Electron Affinity and Reaction Free energy change) were investigated.

In addition to conventional HOMO/LUMO energy correlation plots, "reactive" FMO correlation plots were generated using the LUMO energies of the complexes' (n = +1 to +4) states, and HOMO energies of the (n = –1 to –3) states, as the plots' independent variables. A high degree of linearity was observed for the "reactive" FMO vs E_{DPV} correlation plots. These LFERs may provide enhanced projections of the electrochemical reactivity of a complex's charged species alongside the HOMO vs E_{DPV} and LUMO vs E_{DPV} correlation plots of the complex.

The linear correlations between the Electron Affinity (–EA(M)), Free energy change of reaction ($-\Delta G_{rxn}$), and theoretical half-reaction potentials (E_{cell}) of the complexes proved to be sensitive to dissimilarities among the compounds that were being compared. The –EA(M), $-\Delta G_{rxn}$, and E_{cell} vs E_{DPV} plots showed only modest linear correlations ($0.84 \leq R^2 \geq 0.92$) when comparing the collective groups

© University of Pretoria

of results (ex. all rhodium complexes, iridium complexes, DippBIAN complexes, etc.). This sensitivity results from the thermodynamic basis from which the properties are calculated, and caution must be exercised when setting up (and interpreting) comparisons between compounds. It is advised that chemically or structurally closer related compounds be compared with one another for a more accurate reflection of linear correlation. Indeed, among the groups of complexes (***1a–b***, ***2a–b***, etc.), and for the individual complexes', the –EA(M), $-\Delta G_{rxn}$, and E_{cell} vs E_{DPV} plots showed good to excellent linear correlations ($0.93 \leq R^2 \geq 0.99$).

4.4.1) Peak Characterisation Model and Revised E_{DPV} Assignments

An integrated computational and experimental Peak Characterisation Model has been developed and applied to distinguish characteristic analyte voltametric peaks, in convoluted voltammograms, from peaks which originate from secondary reactions or impurities in the electrolyte solution. The Peak Characterisation Model utilised the LFERs between experimentally recorded DPV peak potentials and computed theoretical properties of the complex series **1**–**4** to probe the statistical influence of queried DPV peaks on the LFERs of the analyte. DPV peaks which were not part of the characteristic voltametric reactivity of the analyte decreased the linear correlation observed between the data points of the plot, whereas DPV peaks which were an inherent part of the voltametric reactivity of the analyte improved the linear correlation (R^2), or decreased the absolute deviations (MAD and RMSD), observed in the data plot.

The changes in the LFERs were investigated utilising three datasets of experimental E_{DPV} values, namely:

* The Full dataset (consisting of all measured E_{DPV} data points);
* The All – Outlier dataset (containing the majority of E_{DPV} data points, with statistical outliers removed); and
* The Limited dataset (comprised of the E_{DPV} data points as assigned and discussed in Chapter 3).

The linear correlations of the Full dataset and All – Outlier dataset were overall superior to those obtained using the Limited dataset. Following the application of the Peak Characterisation Model, it was observed that the DPV peaks with potentials similar to those observed for the free ligands are not the result of ligand dissociation occurring during the electrochemical analysis. These peaks are in fact part of the characteristic electrochemical reactivity of the complexes, and the similarity in peak

© University of Pretoria

potential to those observed for the free ligands yields important information about the metal-BIAN interactions within these complexes.

The unchanged reaction potentials indicate that coordination of the metal centre (as well as the presence of the ancillary ligands) does not affect the electronic properties of the chelated BIAN ligand as expected. Coordination of the positively charged metal is anticipated to withdraw electron density from the BIAN ligand due to the ligand σ-donor interaction with the metal. A decrease in electron density on the BIAN ligand would facilitate ligand reduction and hamper ligand oxidation (i.e., shift the E_{DPV} values to more positive potentials). The ligand-based redox events that are occurring at potentials equivalent to those of the free ligands, may be associated with the MO composition that is isolated on the ligand itself, which features minimal contribution from the metal centre or ancillary ligands.

The revised E_{DPV} assignments for the series of complexes **1**–**4**, after application of the Peak Characterisation Model, are presented in Table 4.4-1 below.

*Table 4.4–1: Summary of the DPV peak potentials (V vs Ag/Ag^+) recorded for DippBIAN, MesBIAN, and the series of complexes **1**–**4**, revised after application of the Peak Characterisation Model. Reversible events are marked with an "*" symbol.*

Compound	Red. 4	Red. 3	Red. 2	Red. 1	Ox. 1	Ox. 2	Ox. 3
DippBIAN			–1.51	–0.85	+1.26		
MesBIAN			–1.92	–1.43	+1.20	+1.73	
1a			–1.53	–0.56*	+1.31*	+1.61	
1b			–1.64	–0.70*	+1.26	+1.63	
1c	–1.53	–1.14*	–0.91	–0.19*	+0.58	+1.24	+1.50
1d	–1.52	–1.11*	–0.85	–0.21*	+0.58	+1.23	+1.47
2a	–1.68	–1.41*	–0.70	–0.43*	+1.12	+1.40	
2b	–1.84	–1.54	–0.90*	–0.61	+1.04	+1.41	+1.72
2c			–1.19*	–0.22*	+1.56		
2d			–1.18*	–0.25*	+1.56		
3a			–1.79	–0.77*	+1.36	+1.60	
3b		–1.78	–1.70	–0.82*	+1.25	+1.59	
4a	–1.88	–1.37	–1.15	–0.18*	+0.77	+1.46	
4b	–1.78	–1.53	–1.14	–0.20*	+0.89	+1.74	
4c	–1.79	–1.45	–1.02*	–0.16*	+0.70	+1.64	
4d		–1.40	–1.00*	–0.16*	+0.67	+1.58	

© University of Pretoria

4.5) References

(1) Winget, P.; Weber, E. J.; Cramer, C. J.; Truhlar, D. G. Computational Electrochemistry: Aqueous One-Electron Oxidation Potentials for Substituted Anilines. *Physical Chemistry Chemical Physics* **2000**, *2* (6), 1231–1239. https://doi.org/10.1039/a909076b.

(2) Marenich, A. V.; Ho, J.; Coote, M. L.; Cramer, C. J.; Truhlar, D. G. Computational Electrochemistry: Prediction of Liquid-Phase Reduction Potentials. *Physical Chemistry Chemical Physics* **2014**, *16* (29), 15068–15106. https://doi.org/10.1039/c4cp01572j.

(3) Ho, J.; Coote, M. L.; Cramer, C. J.; Truhlar, D. G. Theoretical Calculation Of Reduction Potentials. In *Organic Electrochemistry*; CRC Press, 2015; pp 249–280. https://doi.org/10.1201/b19122-12.

(4) Méndez-Hernández, D. D.; Tarakeshwar, P.; Gust, D.; Moore, T. A.; Moore, A. L.; Mujica, V. Simple and Accurate Correlation of Experimental Redox Potentials and DFT-Calculated HOMO/LUMO Energies of Polycyclic Aromatic Hydrocarbons. In *Journal of Molecular Modeling*; Springer, 2013; Vol. 19, pp 2845–2848. https://doi.org/10.1007/s00894-012-1694-7.

(5) Lynch, E. J.; Speelman, A. L.; Curry, B. A.; Murillo, C. S.; Gillmore, J. G. Expanding and Testing a Computational Method for Predicting the Ground State Reduction Potentials of Organic Molecules on the Basis of Empirical Correlation to Experiment. *Journal of Organic Chemistry* **2012**, *77* (15), 6423–6430. https://doi.org/10.1021/jo300853k.

(6) Méndez-Hernández, D. D.; Gillmore, J. G.; Montano, L. A.; Gust, D.; Moore, T. A.; Moore, A. L.; Mujica, V. Building and Testing Correlations for the Estimation of One-Electron Reduction Potentials of a Diverse Set of Organic Molecules. *J Phys Org Chem* **2015**, *28* (5), 320–328. https://doi.org/10.1002/poc.3413.

(7) Baik, M.-H.; Friesner, R. A. Computing Redox Potentials in Solution: Density Functional Theory as A Tool for Rational Design of Redox Agents. *J Phys Chem A* **2002**, *106* (32), 7407–7412. https://doi.org/10.1021/jp025853n.

(8) Steinmetz, M.; Grimme, S. Benchmark Study of the Performance of Density Functional Theory for Bond Activations with (Ni,Pd)-Based Transition-Metal Catalysts. *ChemistryOpen* **2013**, *2* (3), 115–124. https://doi.org/10.1002/open.201300012.

(9) Jäger, M.; Freitag, L.; González, L. Using Computational Chemistry to Design Ru Photosensitizers with Directional Charge Transfer. *Coord Chem Rev* **2015**, *304–305*, 146–165. https://doi.org/10.1016/j.ccr.2015.03.019.

(10) Ochterski, J. W. Thermochemistry in Gaussian. *Gaussian Inc Pittsburgh PA* **2000**, *264* (1), 1–19.

© University of Pretoria

(11) Weigend, F.; Ahlrichs, R. Balanced Basis Sets of Split Valence, Triple Zeta Valence and Quadruple Zeta Valence Quality for H to Rn: Design and Assessment of Accuracy. *Physical Chemistry Chemical Physics* **2005**, *7* (18), 3297–3305. https://doi.org/10.1039/b508541a.

(12) Lage, M. L.; Fernández, I.; Mancheño, M. J.; Sierra, M. A. Electronic Structure of Alkoxychromium(0) Carbene Complexes: A Joint TD-DFT/Experimental Study. *Inorg Chem* **2008**, *47* (12), 5253–5258. https://doi.org/10.1021/ic800187r.

(13) Adamo, C.; Jacquemin, D. The Calculations of Excited-State Properties with Time-Dependent Density Functional Theory. *Chem Soc Rev* **2013**, *42* (3), 845–856. https://doi.org/10.1039/c2cs35394f.

(14) Foresman, J. B.; Frisch, Æ. *Exploring Chemistry with Electronic Structure Methods*, 3rd ed.; Gaussian, Inc.: Wallingford, CT, 2015.

(15) Ryu, H.; Park, J.; Kim, H. K.; Park, J. Y.; Kim, S.-T.; Baik, M.-H. Pitfalls in Computational Modeling of Chemical Reactions and How To Avoid Them. *Organometallics* **2018**, *37* (19), 3228–3239. https://doi.org/10.1021/acs.organomet.8b00456.

(16) Kleinhans, G.; Chan, A. K. -W.; Leung, M.; Liles, D. C.; Fernandes, M. A.; Yam, V. W. -W.; Fernández, I.; Bezuidenhout, D. I. Synthesis and Photophysical Properties of T-Shaped Coinage-Metal Complexes. *Chemistry - European Journal* **2020**, *26* (31), 6993–6998. https://doi.org/10.1002/chem.202000726.

(17) Frisch, M. J.; Trucks, G. W.; Schlegel, H. B.; Scuseria, G. E.; Robb, M. A.; Cheeseman, J. R.; Scalmani, G.; Barone, V.; Petersson, G. A.; Nakatsuji, H.; Li, X.; Caricato, M.; Marenich, A. V.; Bloino, J.; Janesko, B. G.; Gomperts, R.; Mennucci, B.; Hratchian, H. P.; Ortiz, J. V.; Izmaylov, A. F.; Sonnenberg, J. L.; Williams-Young, D.; Ding, F.; Lipparini, F.; Egidi, F.; Goings, J.; Peng, B.; Petrone, A.; Henderson, T.; Ranasinghe, D.; Zakrzewski, V. G.; Gao, J.; Rega, N.; Zheng, G.; Liang, W.; Hada, M.; Ehara, M.; Toyota, K.; Fukuda, R.; Hasegawa, J.; Ishida, M.; Nakajima, T.; Honda, Y.; Kitao, O.; Nakai, H.; Vreven, T.; Throssell, K.; Montgomery, Jr., J. A.; Peralta, J. E.; Ogliaro, F.; Bearpark, M. J.; Heyd, J. J.; Brothers, E. N.; Kudin, K. N.; Staroverov, V. N.; Keith, T. A.; Kobayashi, R.; Normand, J.; Raghavachari, K.; Rendell, A. P.; Burant, J. C.; Iyengar, S. S.; Tomasi, J.; Cossi, M.; Millam, J. M.; Klene, M.; Adamo, C.; Cammi, R.; Ochterski, J. W.; Martin, R. L.; Morokuma, K.; Farkas, O.; Foresman, J. B.; Fox, D. J. Gaussian 16, Revision B.01. Gaussian Inc. Wallingford CT 2016.

(18) Becke, A. D. Density-functional Thermochemistry. III. The Role of Exact Exchange. *J Chem Phys* **1993**, *98* (7), 5648–5652. https://doi.org/10.1063/1.464913.

© University of Pretoria

(19) Lee, C.; Yang, W.; Parr, R. G. Development of the Colle-Salvetti Correlation-Energy Formula into a Functional of the Electron Density. *Phys Rev B* **1988**, *37* (2), 785–789. https://doi.org/10.1103/PhysRevB.37.785.

(20) Grimme, S.; Antony, J.; Ehrlich, S.; Krieg, H. A Consistent and Accurate Ab Initio Parametrization of Density Functional Dispersion Correction (DFT-D) for the 94 Elements H-Pu. *J Chem Phys* **2010**, *132* (15), 154104. https://doi.org/10.1063/1.3382344.

(21) Cossi, M.; Rega, N.; Scalmani, G.; Barone, V. Energies, Structures, and Electronic Properties of Molecules in Solution with the C-PCM Solvation Model. *J Comput Chem* **2003**, *24* (6), 669–681. https://doi.org/10.1002/jcc.10189.

(22) Barone, V.; Cossi, M. Quantum Calculation of Molecular Energies and Energy Gradients in Solution by a Conductor Solvent Model. *Journal of Physical Chemistry A* **1998**, *102* (11), 1995–2001. https://doi.org/10.1021/jp9716997.

(23) Popov, I. A.; Mehio, N.; Chu, T.; Davis, B. L.; Mukundan, R.; Yang, P.; Batista, E. R. Impact of Ligand Substitutions on Multielectron Redox Properties of Fe Complexes Supported by Nitrogenous Chelates. *ACS Omega* **2018**, *3* (11), 14766–14778. https://doi.org/10.1021/acsomega.8b01921.

(24) van Asselt, R.; Elsevier, C. J. New Palladium Complexes of Cis-Fixed Bidentate Nitrogen Ligands as Catalysts for Carbon-Carbon Bond Formation. *Organometallics* **1992**, *11* (6), 1999–2001.

(25) Klein, R. A.; Elsevier, C. J.; Hartl, F. Redox Properties of Zerovalent Palladium Complexes Containing α-Diimine and p -Quinone Ligands. *Organometallics* **1997**, *16* (6), 1284–1291. https://doi.org/10.1021/om960809d.

(26) Kannan, S.; James, A. J.; Sharp, P. R. Dinuclear Diimine Palladium(II) and Platinum(II) Hydroxo and Amido Complexes: Synthesis and X-Ray Crystal Structures. *Polyhedron* **2000**, *19* (2), 155–163. https://doi.org/10.1016/S0277-5387(99)00338-1.

(27) Coventry, D. N.; Batsanov, A. S.; Goeta, A. E.; Howard, J. A. K.; Marder, T. B. Synthesis and Molecular Structures of α-Diimines and Their Zinc and Palladium Dichloride Complexes. *Polyhedron* **2004**, *23* (17 SPEC.ISS.), 2789–2795. https://doi.org/10.1016/j.poly.2004.06.023.

(28) Adams, C. J.; Fey, N.; Weinstein, J. A. Near-Infrared Luminescence from Platinum(II) Diimine Compounds. *Inorg Chem* **2006**, *45* (16), 6105–6107. https://doi.org/10.1021/ic060399d.

(29) Fliedel, C.; Rosa, V.; Santos, C. I. M.; Gonzalez, P. J.; Almeida, R. M.; Gomes, C. S. B.; Gomes, P. T.; Lemos, M. A. N. D. A.; Aullón, G.; Welter, R.; Avilés, T. Copper(Ii) Complexes of Bis(Aryl-Imino)Acenaphthene Ligands: Synthesis, Structure, DFT Studies and Evaluation in Reverse ATRP of Styrene. *Dalton Transactions* **2014**, *43* (34), 13041–13054. https://doi.org/10.1039/c4dt01069h.

© University of Pretoria

(30) Evans, D. A.; Lee, L. M.; Vargas-Baca, I.; Cowley, A. H. Aggregation-Induced Emission of Bis(Imino)Acenaphthene Zinc Complexes: Photophysical Tuning via Methylation of the Flanking Aryl Substituents. *Organometallics* **2015**, *34* (11), 2422–2428. https://doi.org/10.1021/om501191c.

(31) Supej, M. J.; Volkov, A.; Darko, L.; West, R. A.; Darmon, J. M.; Schulz, C. E.; Wheeler, K. A.; Hoyt, H. M. Aryl-Substituted BIAN Complexes of Iron Dibromide: Synthesis, X-Ray and Electronic Structure, and Catalytic Hydrosilylation Activity. *Polyhedron* **2016**, *114*, 403–414. https://doi.org/10.1016/j.poly.2016.02.020.

(32) Romashev, N. F.; Gushchin, A. L.; Fomenko, I. S.; Abramov, P. A.; Mirzaeva, I. V.; Kompan'kov, N. B.; Kal'nyi, D. B.; Sokolov, M. N. A New Organometallic Rhodium(I) Complex with Dpp-Bian Ligand: Synthesis, Structure and Redox Behaviour. *Polyhedron* **2019**, *173*, 114110. https://doi.org/10.1016/j.poly.2019.114110.

(33) Yambulatov, D. S.; Nikolaevskii, S. A.; Kiskin, M. A.; Magdesieva, T. V.; Levitskiy, O. A.; Korchagin, D. V.; Efimov, N. N.; Vasil'ev, P. N.; Goloveshkin, A. S.; Sidorov, A. A.; Eremenko, I. L. Complexes of Cobalt(II) Iodide with Pyridine and Redox Active 1,2-Bis(Arylimino)Acenaphthene: Synthesis, Structure, Electrochemical, and Single Ion Magnet Properties. *Molecules* **2020**, *25* (9), 2054. https://doi.org/10.3390/molecules25092054.

(34) De Frémont, P.; Clavier, H.; Rosa, V.; Avilés, T.; Braunstein, P. Synthesis, Characterization, and Reactivity of Cationic Gold(I) α-Diimine Complexes. *Organometallics* **2011**, *30* (8), 2241–2251. https://doi.org/10.1021/om2000426.

(35) Glen, S. *RMSE: Root Mean Square Error*. Statistics How To: Elementary Statistics for the rest of us! https://www.statisticshowto.com/probability-and-statistics/regression-analysis/rmse-root-mean-square-error (accessed 2022-10-04).

(36) OriginLab. *Origin Help - The Statistics on Columns Dialog Box*. OriginLab Online Help. https://www.originlab.com/doc/Origin-Help/DescStats-Dialog (accessed 2022-10-04).

(37) Konvexity. *Range, mean absolute deviation, standard deviation, and variance*. CFA Exam Prep & Study Material - Konvexity. http://konvexity.com/range-mean-absolute-deviation-standard-deviation-and-variance (accessed 2022-10-04).

(38) Arcidiacono, G. *Mean Absolute Deviation*. alcula.com. http://www.alcula.com/calculators/statistics/mean-absolute-deviation (accessed 2022-10-04).

(39) Schultz, F. A.; Lord, R. L.; Baik, M.-H. Multifaceted Examination of Multielectron Transfer Reactions. *Inorganica Chim Acta* **2020**, *510*, 119746. https://doi.org/10.1016/j.ica.2020.119746.

© University of Pretoria

(40) Adeniyi, A. A.; Conradie, J. Computational Insight into the Contribution of Para-Substituents on the Reduction Potential, Proton Affinity, and Electronic Properties of Nitrobenzene Compounds. *J Mol Model* **2019**, *25* (3), 78. https://doi.org/10.1007/s00894-019-3946-2.

(41) Fu, Y.; Liu, L.; Yu, H. Z.; Wang, Y. M.; Guo, Q. X. Quantum-Chemical Predictions of Absolute Standard Redox Potentials of Diverse Organic Molecules and Free Radicals in Acetonitrile. *J Am Chem Soc* **2005**, *127* (19), 7227–7234. https://doi.org/10.1021/ja0421856.

(42) Roy, L. E.; Jakubikova, E.; Guthrie, M. G.; Batista, E. R. Calculation of One-Electron Redox Potentials Revisited. Is It Possible to Calculate Accurate Potentials with Density Functional Methods? *J Phys Chem A* **2009**, *113* (24), 6745–6750. https://doi.org/10.1021/jp811388w.

(43) Fifen, J. J. Thermodynamics of the Electron Revisited and Generalized. *J Chem Theory Comput* **2013**, *9* (7), 3165–3169. https://doi.org/10.1021/ct400212t.

(44) Hosseini-Yazdi, S. A.; Samadzadeh-Aghdam, P.; Ghadari, R. Computational DFT Study on Nickel Symmetric Bis(Thiosemicarbazone) Complexes: Electronic Absorption and Redox Potentials. *Polyhedron* **2019**, *160*, 35–41. https://doi.org/10.1016/j.poly.2018.12.019.

(45) Adeniyi, A. A.; Conradie, J. Substituent and Isomeric Effects on the Reduction and Oxidation Potential of Tris(β-Diketonato) Manganese (III) Complexes: DFT and MESP Analysis. *Suid-Afrikaanse Tydskrif vir Natuurwetenskap en Tegnologie* **2019**, *38* (1). https://doi.org/10.36303/SATNT.2019.38.1.728.

(46) Toma, M.; Kuvek, T.; Vrcek, V. Ionization Energy and Reduction Potential in Ferrocene Derivatives: Comparison of Hybrid and Pure DFT Functionals. *Journal of Physical Chemistry A* **2020**, *124* (39), 8029–8039. https://doi.org/10.1021/acs.jpca.0c06663.

(47) Connelly, N. G.; Geiger, W. E. Chemical Redox Agents for Organometallic Chemistry. *Chem Rev* **1996**, *96* (2), 877–910. https://doi.org/10.1021/cr940053x.

(48) Patterson, E. V.; Cramer, C. J.; Truhlar, D. G. Reductive Dechlorination of Hexachloroethane in the Environment: Mechanistic Studies via Computational Electrochemistry. *J Am Chem Soc* **2001**, *123* (9), 2025–2031. https://doi.org/10.1021/ja0035349.

© University of Pretoria

Chapter 5: Catalytic Activity Screening

5.1) Introduction

5.1.1) Metal Complexes of BIANs as Catalysts

The bidentate rigidity of the α-diimine moiety, the modality of the N-aryl steric bulk near the coordination centre, as well as the potential non-innocent behaviour within a complex have all made BIAN ligands an attractive topic in the study of much of the catalytic activity research. Indeed, one of the well-studied groups of transition metal BIAN catalysts is known as Brookhart-type catalysts, Pd(II)- or Ni(II)-based α-diimine complexes with sterically encumbered active sites, that have found industrial application due to their high ethylene and α-olefin polymerisation activity.[1–7]

Elsewhere, stereoselective CO (g) insertion onto alkenes by Pd(II)-BIAN complexes have also been reported, as well as the co-polymerisation of alkenes with CO (g) by these complexes to yield polyketones.[8] In another study, Pd(0)-BIAN complexes were reported to act as stereoselective alkyne hydrogenation catalysts under very mild conditions (20 °C), reacting chemoselectively with alkyne groups even in the presence of carboxylic acid, ester or nitro substituents to yield *Z*-alkenes.[9]

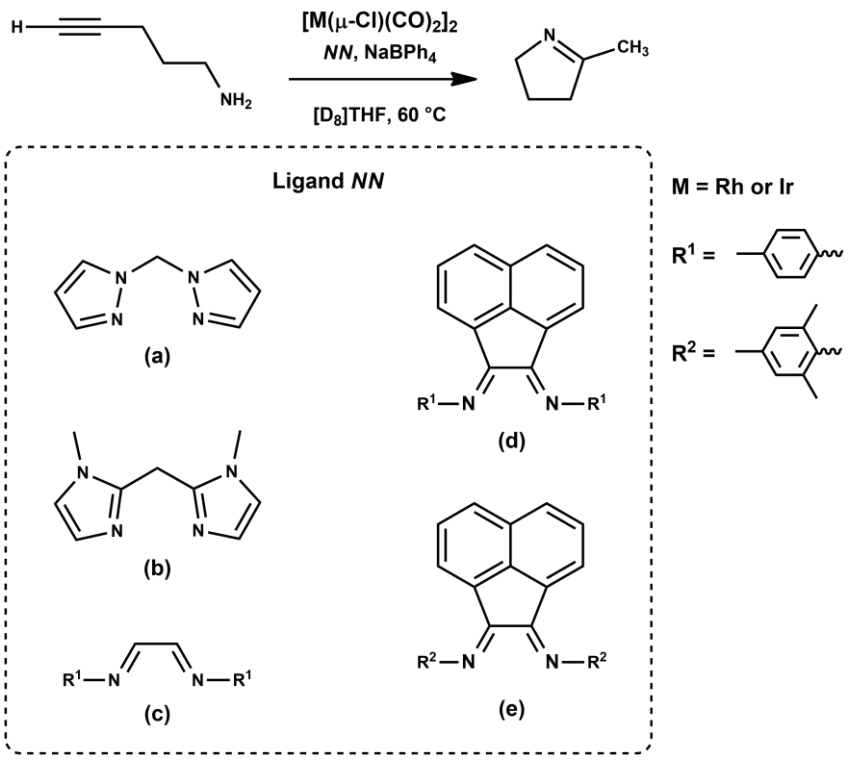
Catalytic application of the BIAN ligands were by no means limited to nickel and palladium, however, with cationic vanadyl BIAN complexes having been shown to selectively oxidise alkenes to epoxides,[10] whereas an oxidovanadium(IV) complex of DippBIAN has been reported as an efficient alkane oxygenation catalyst in the presence of H_2O_2 under mild conditions.[11] Other catalytic reactions have also been investigated, including the successful hydrosilylation of alkenes by Fe(II) complexes of Dipp- and MesBIAN,[12] and the hydroformylation of 1-octene by a water-soluble Rh(I)-cod complex bearing a sulphonated-DippBIAN type ligand.[13]

Even though the redox non-innocent behaviour of BIAN ligands has been noted in literature with specific reference to their effect on the structural and physiochemical properties of complexes, little research has explicitly explored the benefit (or detriment) of these non-innocent characteristics of the BIAN ligands towards the catalytic reactivity of metal complexes. One example of such an investigation includes a report on cobaloxime BIAN complexes.[14] Williams *et al*. demonstrated the capacity of the BIAN ligand in these complexes to act as an electron sink in their observation of multi-electron reduction events.[14] The authors remarked that the ability of the BIAN ligand to act as an electron sink resulted in the delocalisation of unpaired electron spin density from the metal centre into the organic

© University of Pretoria

framework.[14] Consequently, the reported complexes showed a decrease in hydrogen reduction activity compared to those of previously reported cobaloxime complexes. More recently, the non-innocence of BIAN ligands was demonstrated in a report of Ag(I)BIAN$_2$ complexes, in which the auxiliary ligands were shown to participate in the electrocatalytic reduction cycle of CO_2 by accepting or donating electron density during.[15]

To date, relatively few rhodium and iridium BIAN complexes have been reported compared to the number of reports for BIAN complexes of other early transition metals.[13,16–20] Amongst these reports are iridium(III) complexes featuring BIAN ligands as π-acceptor ligands that have been tested as catalysts for hydroamination and hydrogenation reactions,[17] the water soluble Rh(I)-BIAN complexes featuring the sulphonated BIAN ligands,[13] as well as neutral Rh(I)- and Rh(III)-DippBIAN complexes which exhibited potential as catalysts for the electrochemical reduction of CO_2.[16,18]



Scheme 5.1–1: An illustration of the intramolecular hydroamination reaction catalysed by in situ generated Rh(I)- and Ir(I)-carbonyl complexes, as investigated by Rumble et al. in NMR-scale reactivity studies.[19,20]

NMR-scale reactivity studies were conducted by Rumble *et al*. on the catalytic intramolecular hydroamination ability of *in situ* generated Rh(I)-carbonyl complexes bearing various diimine ligands, including MesBIAN (Scheme 5.1–1).[20] As mentioned in Chapter 2, the authors of this study described the isolation of the Rh(I)-MesBIAN complex elsewhere as a neutral [Rh(MesBIAN)(CO)Cl] monocarbonyl.[19] However, they were not able to isolate the cationic Rh(I)-MesBIAN dicarbonyl

© University of Pretoria

complex with a chloride anion (comparable in structure to complex **2b**), likely due to the strong electrostatic interactions between the Rh(I) and Cl^- ions.[19] Thus, the catalytic activity reported for the *in situ* generated Rh(I)-MesBIAN complex is unlikely to be that of a $[Rh(MesBIAN)(CO)_2]^+$ complex due to the presence of Cl^- in the reaction solutions.

Indeed, Rumble *et al*. noted an increase in the catalytic activity of their *in situ* generated chloride containing Rh(I)-BIAN complexes when additional counterions were added to the reaction mixture to stabilise the metal centre.[20] The authors proposed that the decreased reactivity of the chloride containing complexes is due to the strength with which the chloride binds to the metal centre, resulting in an increase of electron density on the metal centre, as well as the occupation of a coordination site which could be used for substrate binding.[20]

It is therefore feasible that the cationic complexes in the series **1**–**3** that contain PF_6^- counterions may show greater catalytic reactivity than their neutral chloride containing analogues **4a**–**d**, due to decreased competition between the chloride ions and the substrate for access to metal centre.

5.1.2) General Catalytic Applications of Rhodium and Iridium Complexes

Complexes of rhodium and iridium have found application in a diverse range of catalytic reactions including hydroamination,[20–23] hydrothiolation,[24–26] copolymerisation of olefins,[27] alkyne dimerization and trimerization,[7,23,26] as well as the hydroformylation,[13,28,29] hydrosilylation,[27] hydrogenation,[27,30,31] hydroxylation,[24,32] and dehydrogenation of various substrates.[7,33,34]

Rhodium(I) complexes are well known for their catalytic activity in homogeneous hydroformylation and hydrogenation of olefins,[13,27–29] ethylene and olefin polymerisation,[7,27] as well as the hydrosilylation of alkenes and alkynes to yield mixtures of *cis* and *trans* isomer products.[27] Rhodium catalysts have also proven to be catalytically reactive towards functional groups other than alkenes and alkynes, for example, in the dehydrogenative coupling of alcohols to amines,[35] and the application of rhodium(I) complexes applied as catalysts for H–X and C–F bond activation, H_2 production, and CO_2 reduction.[36] Both rhodium and iridium complexes have been reported as active catalysts in alcohol hydrogenation of ketones and aldehydes, as well as the dehydrogenation of alkanes.[33] However, iridium complexes haven proven to be more active catalysts in the latter reaction.[33]

For their part, iridium complexes have been shown to be active as water oxidation catalysts,[37–39] and pincer complexes of iridium have been utilized to catalyse in a variety of reactions including alcohol

© University of Pretoria

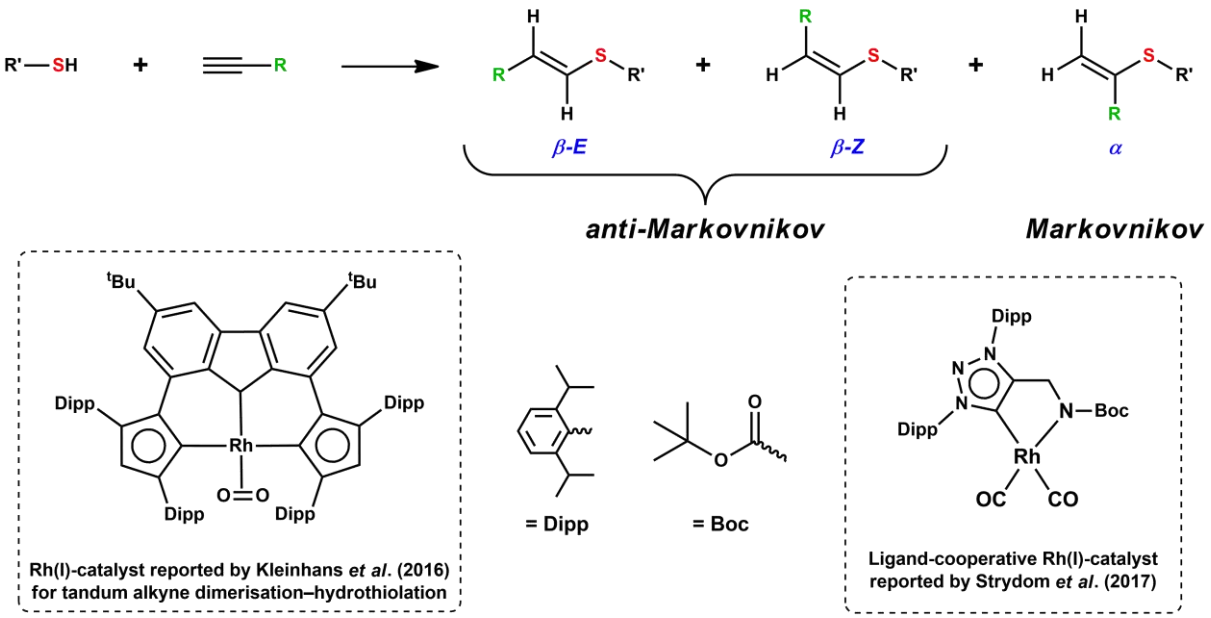
dehydrogenation,[33] alkane dehydrogenation and metathesis,[7] as well as the dehydroaromatization of n-alkanes to yield aromatic compounds.[7] A number of iridium(I) and iridium(III) complexes have been reported to demonstrate ligand-cooperative or redox-switchable behaviour which facilitates their catalytic activity,[31,33,40] such as the Ir(III)-cyclopentadienyl complexes reported by Navarro *et al*.,[39] that featured zwitterionic flexible donor ligands as part of the catalytic mechanism for water oxidation.

Precious metals often catalyse multielectron reactions more efficiently since they typically undergo 2 electron oxidation or reduction events (e.g., Ir(I) ⇌ Ir(III) ⇌ Ir (V)).[41] Consecutive 1 electron transfer reactions may not be as favourable as a single 2 electron transfer reaction, due to the highly reactive nature of the radical intermediate that is formed during the former process.[41] However, redox non-innocent ligands may confer additional stability to this intermediate radical state by forming a spin-coupled species in which the ligand and metal each bare a single additional electron.[41] Rhodium and iridium carbene complexes of quinones have been produced that were able to exploit the ability of these metals to undergo multielectron reactions, in which the quinone moiety functioned as an electron sink to facilitate the formation of s spin-coupled species.[41] The BIAN ligand moiety has demonstrated the potential to fulfil a similar electron sink role when coordinated to redox active metals.[14,15,42]

Late transition metal complexes of rhodium(I) and iridium(I) have proven to function as more robust hydroamination catalysts compared to their lanthanide, actinide, and early transition metal counterparts, showing tolerance of substrates which feature various functional groups, as well as being less sensitive towards oxygen and/or moisture exposure.[20,21,32] Rhodium(I) and iridium(I) complexes have been reported as effective catalysts for intramolecular hydroamination of alkynamines and alkenamines,[22] as well as highly active catalysts for the hydrogenation of CO_2 to formic acid or formates.[30] Complexes of Rh(I) and Ir(I) featuring bidentate N,N- and P,N-donor ligands have also been reported as catalytically active towards the hydroamination and hydroxylation of alkynes,[24,32] however, the authors noted that the N-donor ligands could readily be displaced by the strong binding thiol substrates, which limited their activity towards hydrothiolation.[24]

Nonetheless, a number of Rh(I) complexes have been reported to catalyse hydrothiolation reactions with high activity and selectivity. For example, the Rh(I)-CNC pincer complex reported by Kleinhans *et al*. that facilitated the one-pot tandem catalysis of 1-hexyne dimerization-hydrothiolation (Scheme 5.1–2),[26] and the N-donor functionalised Rh(I)-1,2,3-triazol-5-ylidene complexes of Strydom *et al*. which demonstrated ligand-assisted hydrothiolation of terminal alkynes (Scheme 5.1–2).[25]

© University of Pretoria



Scheme 5.1–2: General reaction scheme depicting the 1,2-addition (Markovnikov) and 1,1-addition (anti-Markovnikov) products that may form during alkyne hydrothiolation. The Markovnikov and anti-Markovnikov addition products are separated into two groups of regio-isomers (α- and β-isomers), while the β-isomers may be further divided into (E) and (Z) stereoisomers. The Rh(I) catalysts reported by Kleinhans et al. (left) and Strydom et al. (right) have shown excellent regioselectivity to produce the α-isomer during alkyne hydrothiolation.[25,26]

Strydom *et al*. discussed in their paper that the ability of rhodium catalysts to produce both the Markovnikov (α-isomer) and anti-Markovnikov (β-isomer) addition products of alkyne hydrothiolation is in part attributable to the ability of the metal centre to mediate multiple catalytic reaction pathways (Scheme 5.1–2).[25] The authors continued, stating that the selectivity of the reaction may be altered by changing the electronic parameters of the coordination environment.[25]

The electronic character of a metal centre may be highly dependent on the electron donating/accepting character of the ligands in the complex. For example, in the report on the structure and electrochemical behaviour of [Rh(DippBIAN)(cod)(Cl)] by Romashev *et al*.,[18] as well as the redox non-innocence illustrated by Shaffer *et al*. for their Rh(I) complex with 9,10-phenanthrenediimine,[36] the Rh(I)-centre of the complexes is described as nucleophilic. The nucleophilicity of square-planar Rh(I) complexes is noted by Shaffer *et al*. to facilitate the binding of substrates to the coordination sphere.[36] In contrast, the enhanced catalytic hydroamination performance of the Rh(I)-diimine complexes reported by Rumble *et al*. was ascribed to low electron density on the metal centre.[20] A factor which may distinguish the apparent juxtaposition in the electronic characteristic of the metal centres in these complexes is the electronic properties of the ancillary ligands that are present. The Rh(I) complexes described as nucleophilic featured ancillary ligands which are more electron donating (cod, bisimine, and chloride),[18,36] whereas the Rh(I)

© University of Pretoria

complexes described as electrophilic featured ancillary ligands which are more electron withdrawing (strong π-acceptor dicarbonyl ligands).[18,20,36]

In a landmark recent study by Jay, Banerjee *et al*.,[43] the authors utilised time-resolved X-ray fluorescence spectroscopy and computational modelling to show that C–H bond activation of an alkane substrate occurs after the formation of the Rh(I)alkane complex. The clear association between orbital rearrangements of the metal centre, spectator ligands, and the substrate during the process of alkane coordination and subsequent C–H bond activation was reported.[43] The authors related the computational modelling results for the Rh(I)-alkane complexes with cyclopentadienyl (Cp) [Rh(Cp)(CO)(octane)] and acetylacetonate (*acac*) [Rh(*acac*)(CO)(octane)].[43] Compared to the Cp ligand, the *acac* ligand showed a stronger ionic interaction with the metal centre, resulting in enhanced electron donation from the alkane C–H σ-bonding orbital to an empty metal 4d-orbital on the Rh(I)*acac* complex, and a diminished degree of π-backbonding to the C–H σ*-orbitals.[43] Ultimately, the catalytic inactivity of the Rh(I)*acac* complex towards C–H bond activation was determined to be the result of a decreased extent of orbital hybridization between the metal 4d-orbitals and the orbitals of the spectator ligands, resulting in unfavourable changes to the metal-to-ligand charge transfer interactions between the Rh(I)-centre and the substrate.[43]

The influential role that ancillary ligands play in the ultimate catalytic activity of a complex has been noted by Bourissou *et al*. for Rh(I)-carbene complexes that feature a mixture of electron donor and acceptor ligands tend to show greater catalytic activity and stability due to the modulation of electron density at the metal centre.[27] For example, Rh(I)-carbene complexes with a greater number of π-acceptor ligands (ex. phosphines) have shown improved H_2-activation ability due to a decrease in electron density on the metal.[27] It has been demonstrated by Hua *et al*. that the donating ability of their asymmetric bidentate N-donor ligands were affected by the steric and electronic environment of the N-donor moiety,[21] which in turn directly influenced the catalytic hydroamination activity of their Rh(I) and Ir(I) complexes.

Utilising α-diimine ligands in coordination complexes may thus present key benefits through which the electronic environment of the coordination sphere may be modulated.[13,36] These benefits arise from the strong σ-donor/π-acceptor properties of the α-diimine ligands due to the *exo*-positioned imines relative to the α-carbons, as well as the ease with which the stereo-electronic properties of the substituents bonded to the imines may be altered through modular control of the α-diimine ligand synthesis.[13]

© University of Pretoria

It is therefore feasible that the complexes between the different series of complexes **1**, **2**, **3**, and **4** may show some variance in catalytic reactivity for towards the various types of catalytic conversion reactions that will be screened in this study, due to the unique range of electron donating and withdrawing characteristics that are afforded to the metal centres of each series of complexes by the ancillary ligands.

5.1.3) NMR-scale Catalytic Reactivity Screening Assays of Complex Series 1–4

This study was prompted by the possibility of combining the robust characteristics of rhodium(I) and iridium(I) catalysts to tolerate a variety of functional groups as well as exposure to oxygen and/or moisture,[20,21,32] their ability to demonstrate ligand-cooperative or redox-switchable behaviour,[31,33,40] and to mediate multiple catalytic reaction pathways depending on the electronic parameters of the coordination environment,[13,21,25,27] with the know redox non-innocent behaviour of BIAN ligands to facilitate the catalytic reactivity of Rh(I)- and Ir(I)-BIAN complexes.[14,15,42]

Bidentate N,N'-complexes of rhodium(I) and iridium(I) have been noted to be effective catalysts for intramolecular hydroamination of alkynamines as well as alkenamines.[22,24,32] Iridium(III) complexes featuring BIAN ligands have been reported as catalysts for hydroamination and hydrogenation reactions,[17] while *in situ* generated Rh(I)-carbonyl complexes bearing various diimine ligands, including MesBIAN, have been noted for their catalytic intramolecular hydroamination ability.[20]

The application of hydrothiolation catalysts has been limited due to the propensity of sulphur-containing substrates to bond strongly to transition metals, resulting in deactivation of the catalyst.[24] Under normal, non-catalysed conditions, hydrothiolation reactions which proceed via a radical mediated mechanism produce the anti-Markovnikov addition product with low selectivity.[32] Markovnikov addition may be achieved, however, this requires long reaction times and harsh reaction conditions.[32] As noted in Section 5.1.2, rhodium catalysts can produce both the α- and β-isomers of hydrothiolation (Scheme 5.1–2), and the selectivity of the reaction may be altered by changing the electronic environment of the coordination sphere since the metal centre is capable of mediating multiple catalytic reaction pathways.[25]

Based on these known catalytic applications of Rh(I), Ir(I) and BIAN complexes, a limited collection of qualitative catalytic activity screening assays were performed on the series of complexes **1**–**4** to investigate the influence that the redox non-innocent BIAN ligand may have on the catalytic reactivity of the Rh(I) and Ir(I) metal centres towards the dimerization, hydroamination and hydrothiolation of

© University of Pretoria

both alkene (*vide infra* Schemes 5.3–1 to 5.3–3) and alkyne substrates (*vide infra* Schemes 5.3–4 to 5.3–6). The catalytic reactivity was analysed using NMR-scale reactions as previously demonstrated in literature.[4,24–26] The results obtained from this investigation will be assessed to inform the feasibility of future research into the catalytic reactivity of the reported complexes.

As a preliminary qualitative investigation into the possible catalytic reactivities of the complex series **1**–**4**, NMR-scale catalytic reactivity screening assays were performed to identify whether any catalytic conversion of the reaction substrates could be observed. A subsequent series of NMR-scale catalytic reactivity screening assays were also performed with a select number of complexes, in which a chemical reducing agent (cobaltocene) was introduced to the reaction mixture, to investigate how the redox non-innocent characteristics of the BIAN ligand may influence the catalytic reactivity of the complexes. The identification of any by-products or decomposition products resulting from the assay reactions, the determination of kinetic activity data, the optimisation of the catalytic reaction conditions, as well as the determination of possible catalytic reaction mechanisms were therefor beyond the scope of the present study. However, the results obtained from the current research will assist in delineating which catalytic reactions to pursue in our future research projects on this topic.

In accordance with literature procedures, a fractional amount of non-nucleophilic base (0.25 eq) was included in the catalytic reaction mixtures to facilitate the initiation of the catalytic reactions by labilization of the substrate C−H (with reference to dimerization reactions) or S−H/N−H (hydrothiolation/hydroamination) protons.[25,26] Two non-nucleophilic bases were tested for this purpose: imidazole and K_2CO_3, however, reactions utilising imidazole resulted in the decomposition of the catalysts without any conversion of the substrates. Therefore, all NMR-scale catalytic activity screening reactions were done using K_2CO_3.[25,26]

Transient charged species often form as part of a catalytic reaction cycle, and may be directly influenced by the extent to which their charge can be stabilised in the reaction medium.[44,45] The polarity of the reaction solvent employed may feasibly have an impact not only the product yield of a catalytic reaction, but also on whether or not the reaction is able to place efficiently.[44,45] The NMR-scale catalytic reactivity tests of complex series **1**–**4** were thus conducted in both a polar aprotic ($CDCl_3$) and a non-polar (C_6D_6) solvent.

© University of Pretoria

5.1.4) Screening Catalytic Activity for Electroreduction of CO_2 by Complex Series 1–4

To date, only a few BIAN complexes have been reported to show potential as catalysts for the electrochemical reduction of CO_2, with reports of bidentate N,N'-ligand containing catalysts of this reaction being largely dominated by complexes of porphyrin type ligands. Among the few examples of such BIAN-containing electroreduction catalysts are the octahedral Re(I)-tricarbonyl complexes of Dipp- and MesBIAN,[46–48] the neutral Rh(III)- complex of DippBIAN,[16] and more recently a series of bischelated Ag(I)$BIAN_2$ complexes (Figure 5.1–1).[15]

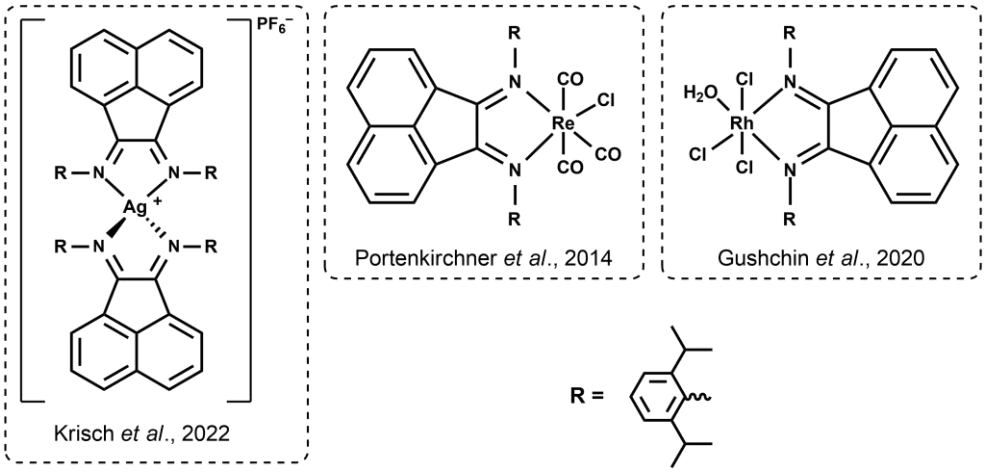


Figure 5.1–1: Molecular representations of selected DippBIAN complexes which have been reported by Krisch et al. (left), Portenkirchner et al. (middle), and Gushchin et al. (right) as catalysts for the electroreduction of CO_2.[15,16,46,47]

Rhodium and iridium complexes have been noted to be highly active towards the hydrogenation of CO_2 to formic acid or formate.[30,49,50] Rh(III)- and Ir(III)-2,2'-bipyridine complexes were reported back in 1997 as CO_2 electrocatalysts capable of producing formate in aqueous organic solutions.[51] Polypyridyl complexes that have shown CO_2 reduction applications have recently been reviewed by Elgrishi *et al.*,[52] and included a number of Rh(III)- and Ir(III) complexes which showed electrocatalytic CO_2 reduction activity. Elsewhere, Ir(III) and Rh(III)-diimine complexes have been reported to catalyse the one-step hydrogenation of CO_2 to formate using H_2.[53]

Many literature reports are available on the CO_2 reduction and hydrogenation ability of iridium(III) complexes. A noteworthy example comes from Sato *et al*. who reported the selective photocatalytic reduction of CO_2 to CO by an Ir(III) complex of terpyridine and 2-phenylpyridine in 2013.[54] A number of these reports pertain to Ir(III)-trihydride complexes featuring pincer ligands,[30,35,55,56] such as the water-stable Ir(III)H_3-pincer complex which had been reported by the Brookhart group.[30,55] The authors noted that complex reacted with acetonitrile to form an adduct, which then continues to react with CO_2 in a rapid equilibrium process as part of the electrocatalytic reduction of CO_2 to formate.[30,55]

© University of Pretoria

They noted that addition of H_2O to the reaction mixture resulted in a decrease of the observed electrocatalysis reduction potential, and the inhibition of background reduction of protons to H_2.[55]

In their review on the activation of CO_2 by iridium complexes, Fernández-Alvarez *et al*.[30] cautioned fellow researchers to consider the interaction between the iridium centre and the coordinated CO_2, as this interaction appears to be influenced not only by the nature of the CO_2 molecule (which features both Lewis acidic and basic coordination sites) but also the oxidation state of the iridium.[30] The authors noted as well that Ir(I) complexes favoured coordination of CO_2 via the Lewis acidic carbon in a η^1-coordination mode, which results in the increased the nucleophilicity of the oxygen atoms.[30]

Protic medium	Aprotic medium
$CO_2 + 2\,H^+_{(solv)} + 2\,e^- \xrightarrow{catalyst} HCOOH_{(solv)}$	$2\,CO_2 + 2\,e^- \xrightarrow{catalyst} CO_3^{2-} + CO$
$CO_2 + 2\,H^+_{(solv)} + 2\,e^- \xrightarrow{catalyst} CO + H_2O_{(solv)}$	$2\,CO_2 + 2\,e^- \xrightarrow{catalyst} C_2O_4^{2-}$

Scheme 5.1–3: Selected CO_2 electrocatalytic reduction processes that may occur in non-aqueous electrolyte solutions under protic (left) and aprotic (right) reaction conditions.[46,56]

The presence of a proton source (such as H^+, H_2O or organic alcohols) in the electrolyte solution used to assess CO_2 electroreduction has been remarked to be important factor that may determine whether or not successful CO_2 reduction can occur.[15,57,58] However, conversion of CO_2 in an aprotic environment has been observed and results in the production of carbonate or oxalate anions (Scheme 5.1–3).[46,59] For the interested reader, an extensive review of catalysed CO_2 electroreduction has been published by Francke, Schille and Roemelt,[56] which includes discussions on previously reported catalytic reduction pathways, CO_2 reduction reaction equations, as well as the influence of protons on the reduction reaction mechanism.

The evaluation of CO_2 reduction activity is often performed using electrochemical methods such as cyclic voltammetry, during which the confirmation of CO_2 reduction activity is associated with an increase in the cathodic peak current of a reduction event in a CO_2 saturated solution, or the positive shift in the onset potential of reduction events in the presence of CO_2.[15,52,57–59] In 2015 Vollmer *et al*. reported on the CO_2 reduction activity of their tricarbonyl complexes of manganese(I) and rhenium(I) with α-diimine ligands, noting that the cathodic current of the cyclic voltammograms increased upon introduction of CO_2 to the electrolytic solution.[60] The cathodic current showed a substantial additional increase when a proton source was included in the solution, which the authors indicated suggests that

© University of Pretoria

the catalytic activity of the complexes were kinetically limited by the dissociation of the product from the complex.[60]

The Re(I)-BIAN complexes of Portenkirchner *et al*. were also reported to show CO_2 electroreduction to CO (g) as an enhancement of the cathodic current at potentials below –1.6 V (vs NHE) in the presence of CO_2.[46] Their report includes GC headspace and gas-phase FTIR analysis following a prolonged controlled potential electrolysis at –1.85 V (vs NHE), which confirmed the presence of CO (g).[46] The catalytic reaction mechanism was not determined, however, the authors suggested that based on catalytic mechanisms of similar complexes, a vacant site on the metal centre is required for the CO_2 substrate to bind, which may be achieved through the dissociation of the Cl^- ligand from their Re(BIAN) complexes.[46]

Francke *et al*. notes that CV is a useful tool for the preliminary assessment of the CO_2 reduction ability of a complex, as this method enables one to compare the characteristic electrochemical behaviour of the complex in the absence and presence of CO_2.[56] Key criteria that the authors, and other literature sources, advise to look for when investigating the reactivity of complexes with CO_2 using CV analysis include:

- A positive shift in the reduction peak potential(s) of the complex between analyses done in the absence and presence of CO_2; [15,16,52,56–59,61]
- An enhancement of cathodic peak current(s) in the presence of CO_2; [15,16,46,52,56,57,60] and,
- Changes in the reversibility of electrochemical events or the shape of the CV graph in the presence of CO_2. [16,52,56–59,61]

Alterations in the reversibility of electrochemical events of the complex, after introduction of CO_2 to the electrolyte solution, may provide additional information on the reaction kinetics that are involved in the CO_2 electroreduction mechanism at the electrode surface.[56] In addition, changes in the cathodic peak current may be correlated to the CO_2 electroreduction catalytic efficiency of the complex.[56]

Building upon the work of Gushchin *et al*. and Krisch *et al*. on the electrocatalytic CO_2 reduction activity of their BIAN complexes,[15,16] as well as additional experimental and data analysis methodologies from literature,[15,16,46,52,56–58,60–62] an array of preliminary qualitative electrochemical measurements were preformed to investigate whether the electrochemical reactivity of the complex series **1**–**4** changed in the presence of CO_2. The results from these analyses will inform our future research into the potential application of the series of complexes **1**–**4** as homogeneous CO_2 electroreduction catalysts. The

© University of Pretoria

determination of catalytic reduction reaction mechanisms, *in situ* product identification and yield determination, as well as the calculation of the Faradaic efficiency of the electroreduction processes are therefore beyond the scope of the current research project.

5.2) Methods and Materials

5.2.1) General aspects

5.2.1.i) Nuclear Magnetic Resonance (NMR) Analyses

All reagents were purchased from Sigma-Aldrich and used without prior purification. Deuterated solvents were purged with Ar (g) before use. ^{1}H NMR spectra of the catalysis samples were recorded on a Bruker Ultrashield 300 AVANCE 3 spectrometer at 25°C, using $CDCl_3$ or C_6D_6 as solvent, at 300.13 MHz. All chemical shifts reported are referenced to the residual hydrogen peak of either deuterated chloroform ($CDCl_3$) at 7.26 ppm, or deuterated benzene (C_6D_6) at 7.16 ppm.

5.2.1.ii) Cyclic Voltammetry (CV) and Differential Pulse Voltammetry (DPV) Analyses

Electrochemical studies were carried out as detailed in Chapter 3, Section 3.2.1. Cyclic voltammograms were recorded between –2.0 V and +1.8 V and scan rate of 100 mV s^{-1}. Differential pulse voltammograms were recorded from 0.0 V to –2.0 V and 0.0 V to +1.8 V, with a step potential of 5 mV. Sample solutions were prepared using 1.0 mM analyte concentration, 0.1 M tetrabutylammonium hexafluorophosphate ($TBAPF_6$) supporting electrolyte in HPLC grade CH_2Cl_2, deoxygenated with Ar (g) before starting analyses. Reactivity of the DippBIAN, MesBIAN and the series of complexes **1**–**4** towards electrochemical CO_2 reduction were tested after electrochemical characterisation using the same sample solutions as described in Chapter 3, purging the solutions with CO_2 for 30 minutes before starting the analyses.

5.2.2) Catalytic Reactivity Samples

5.2.2.i) NMR Sample Preparation

To oven dried NMR tubes were added pre-weighed aliquots of 2 mol % catalyst (± 5 mg) and 10.2 mg (0.25 eq) K_2CO_3, before the solid reagents were covered with 8.05 µL (0.25 eq) anisole. One equivalent each of substrates 1 and 2 were carefully layered atop the internal standard (Table 5.2–1), followed by 1 mL of deuterated solvent. Each NMR sample was carefully sealed with a tight-fitting cap, secured

© University of Pretoria

onto the tube with parafilm tape and electrical insulation tape. The samples were vigorously mixed immediately prior to $\mathbf{t_0}$ data acquisition, then heated to reflux for 24 hours. Sample tubes were cooled to room temperature before $\mathbf{t_{24}}$ data acquisition was recorded. The mass of catalyst used in each test reaction has been tabulated alongside the catalytic activity results in Appendix H.2.

Table 5–1: The calculated mass (mg) and volume (µL) amounts of substrate that were required for one equivalent of reactant in the catalytic reactivity tests.

Substrate	Mass Required for 2 mol % catalyst (mg)	Volume Required for 2 mol % catalyst (µL)
1-hexene	24.9	37
1-hexyne	24.3	34
n-butylamine	21.7	29
t-butylthiol	26.7	33

5.2.2.ii) Reactivity Data Analysis

Post processing, the chemical shift scale (x-axis) of the $\mathbf{t_0}$ and $\mathbf{t_{24}}$ NMR spectra were calibrated relative to the known chemical shift for the methoxy group of the anisole internal standard (i.e., Ar-OC**H**$_3$ 3.80 ppm in $CDCl_3$; and Ar-OC**H**$_3$ 3.32 ppm in C_6D_6). The proton signals for some of the products which formed during the catalytic reactions overlapped with the methoxy-OC**H**$_3$ signal. The integration for the spectra was therefore calibrated relative to the internal standard using an upfield aromatic multiplet of anisole (Ar-C**H** 6.9 ppm).

The relative concentrations of the substrates and products from the catalysis reactions in the mixtures are proportional to the concentration of the unreactive internal standard (i.e., the anisole).[4,19,24–26] Therefore, changes in the concentration of the substrates and products may be evaluated by comparing the changes in the peak area of the unique NMR peaks for a product relative to the standardised peak area for anisole (i.e., Ar-C**H** 6.9 ppm, set equal to 1H).[4] For each of the products that were expected may be present in a reaction mixture, at least one unique NMR peak was identified to serve as a characteristic marker for the quantification of the concentration of that product in the reaction mixture.[4] Selected exemplar NMR spectra of $\mathbf{t_0}$ and $\mathbf{t_{24}}$ measurements are presented in Appendix H.1 (Figures H.1–1 to H.1–20) for the catalytic dimerization, hydroamination and hydrothiolation reactions of 1-hexene and 1-hexyne that were investigated.

© University of Pretoria

The amount of substrate which was consumed during the catalytic reaction may therefore be expressed in terms of percentage Conversion using equation 1,

$$Conversion\ \% = 1 - \frac{\int S1_{t_{24}}}{\int S1_{t_0}} \times 100\ \% \qquad (1)$$

where $\int S1_{t_0}$ and $\int S1_{t_{24}}$ represent the average peak integral of substrate 1 at t_0 and t_{24} respectively. When comparing the peak integrals of two different peaks, however, it is important to take into account the number of protons that are present in the functional groups corresponding to each of the NMR signals. In order to calculate the yield for one of the products from the catalytic reaction (equation 2), the peak integrals of both the substrate (S1) and product (P1) are therefore expressed as *per proton* values (denoted $t_{x/H}$, equation 3 and 4),

$$Yield\ \%\ P1 = \frac{\int P1_{t_{24/H}}}{\int S1_{t_{0/H}}} \times 100\ \% \qquad (2)$$

where

$$\int P1_{t_{24/H}} = \frac{\int P1_{t_{24}}}{number\ of\ protons} \quad \text{and} \quad \int S1_{t_{0/H}} = \frac{\int S1_{t_0}}{number\ of\ protons} \qquad (3\ \&\ 4)$$

Due to the large number of reactions that were tested, Section 5.3 will focus on an abridged discussion of general reactivity trends that were observed. Complexes which showed notable catalytic performance will be highlighted, however, the conversion and yield percentages calculated based on NMR integrations for all the catalytic reactivity tests have been summarised in Appendix H.2 (Tables H.2–1 to H.2–12).

© University of Pretoria

5.3) Results and Discussion

5.3.1) NMR based Catalytic Reactivity Investigation

The variety of primary products which are expected to form in each of the following catalytic reactions (illustrated in Schemes 5.3–1 to 5.3–6) are described as 1,2–addition products (or Markovnikov) and 1,1–addition (or anti-Markovnikov) products.[32] The 1,1–addition products of the alkyne reactions, along with the 1,1– and 1,2–addition products of the alkene dimerization, are further subdivided into two possible stereoisomers: (*Z*) and (*E*). Where clear identification of the (*Z*) and (*E*) isomers were possible, the percentage yield of each isomer has been reported separately. Repeating the catalytic reactions under the same reaction conditions in the absence of catalyst or base does not result in product formation, although a blank experiment (absence of catalyst) with the inclusion of 5 mol% base K_2CO_3 leads to conversion with formation of the β-E and β-Z vinyl sulphides in a ratio of approximately 1:1.[25,26]

A number of unprecedented changes in the catalytic reaction solutions were observed during the course of the reactivity investigation. While changes in the colour of the reaction solutions were anticipated as ligand exchange with the substrate molecules takes place, distinctive changes in the viscosity of the reaction solutions and formation of precipitates were often observed, indicative of possible polymerisation. In addition, the glass sample tubes were frequently stained with insoluble organic films after the reactions.

In several cases (e.g., the alkene dimerization reaction of complex **3b** (Appendix H.2.1) and alkyne dimerization reaction of complex **1b** (Appendix H.2.4)) the total yield of products that could be detected was much less than the percentage conversion of the substrate that was observed as determined by integration of the NMR signals (see Section 5.2.2.ii). In addition, thin films and/or globular precipitates were observed to have formed in some of the reaction tubes after the $\mathbf{t_{24}}$ reflux period.

Complexes of rhodium and iridium in various oxidation states,[7,23,26,27] as well as complexes of BIAN ligands such as the Brookhart-type catalysts,[1–7] are known to have application as ethylene and olefin polymerisation catalysts. It is therefore postulated that the aberrant conversion and yield percentages, in conjunction with the precipitation that is observed in some of the catalytic reactivity assays, may indicate the formation of polymerisation products that proved to be insoluble in the reaction media. However, future research into these catalytic reactions will need to be conducted on a larger molar scale to allow for the isolation, purification, and characterization of the end-products,

© University of Pretoria

not only to eliminate the possibility that the observed precipitates are due to the decomposition of the catalysts, but also to establish the chemical and structural nature of the polymerisation product (if detected).

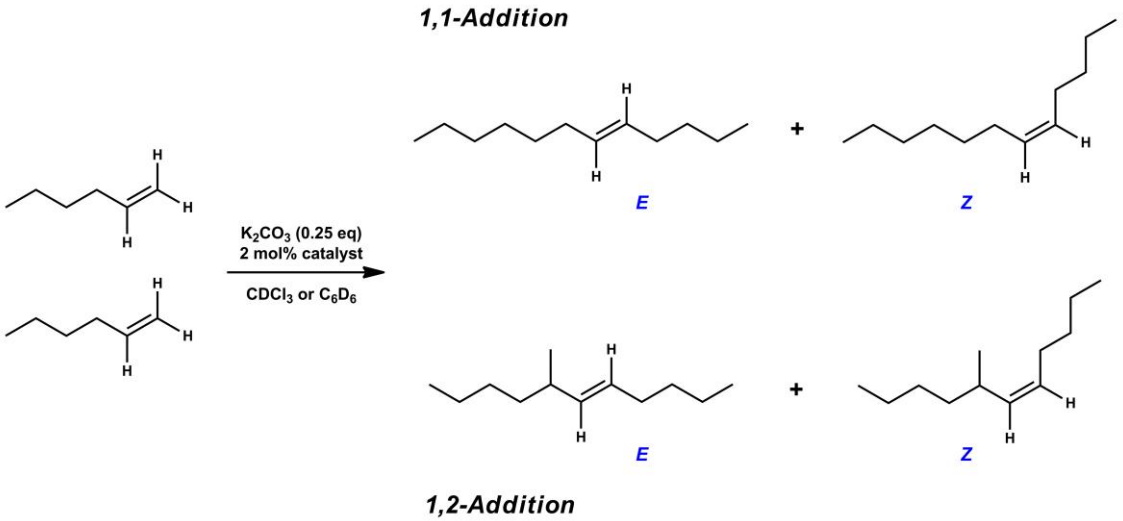
Contrary to theoretical expectations, the total percentage yield of 1,1– and 1,2–addition products in a few test reactions were noted to exceed the overall percentage conversion of the two substrate materials (e.g., the alkene dimerization of complex **1c** (Table 5.3–1) and alkene hydroamination of complex **4c** (Table 5.3–2)). The overall conversion and the total percentage yields of 1,1– and 1,2–addition products were determined based on the integration of the unique identified NMR signal(s) of the substrates and products using equations 1–4 (Section 5.2.2.ii). The excess yields are likely due to complexes reacting with the alkene or amine moieties within the 1,1–addition products as supplementary substrates, in addition to original substrates, resulting in a multifaceted mixture of products with overlapping NMR signals. Indeed, literature reports have noted the propensity of rhodium complexes to catalyse alkyne dimerization (or trimerization) in addition to hydroalkylation and hydrothiolation reactions within the same reaction mixtures.[23,26] Future investigation of these experiments would be conducted on a larger mass scale to facilitate the identification of the individual constituents of the product mixtures.

In addition to these unforeseen complications in product identification, a small amount of product formation was observed in the $\mathbf{t_0}$ spectra of numerous reaction mixtures with little increase in peak intensity noted in the $\mathbf{t_{24}}$ spectra. This suggest that the complexes may be moderately active catalysts at very mild temperature conditions (25–30 °C), as observed with previous Co(II)-BIAN complexes that become somewhat deactivated at higher temperatures.[63] Future investigations of these reactions at variable temperatures may shed light on the optimal thermal environment for catalytic activity.

5.3.1.i) Alkene dimerization

All complexes showed moderate to poor alkene conversions (Figures H.1–1 and H.1–2; Tables 5.3–1, H.2–1 and H.2–2), however, the Ir(I)-MesBIAN complexes **1d** and **4d** stand out among the rest as they selectively yielded 1,1–addition products in $CDCl_3$ solutions (Scheme 5.3–1) but 1,2–addition products in C_6D_6. In the case of complex **1c**, the percentage total yield of products is noted to exceed the percentage conversion of the alkene substrate.

© University of Pretoria



Scheme 5.3–1: Some of the principal products which may form during catalysis of the 1-hexene dimerization reaction. Note that two stereoisomers (E and Z) as well as two constitutional isomers may form depending on the regioselectively of the catalyst.

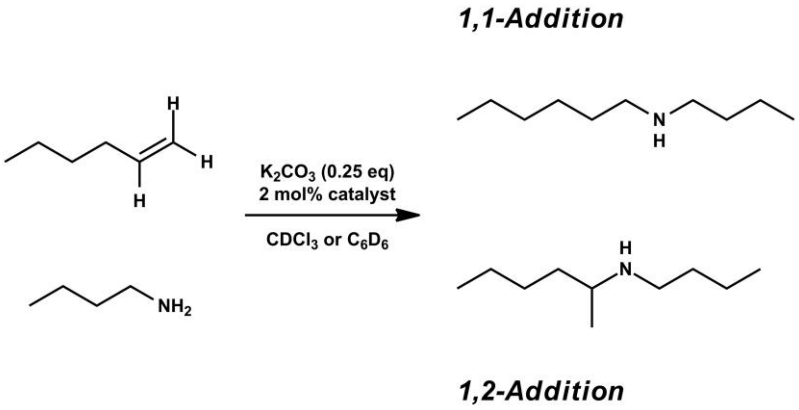
The excess yield is likely due to **1c** reacting with the alkenes in the 1,1– and 1,2–addition products as secondary substrates, resulting in a mixture of products with NMR peaks that overlap with those of the expected 1,1– and 1,2–addition products. In the reaction of complex **3b**, the total yield of products detected is much less than the percentage conversion of substrate, likely due to polymerisation of the alkene substrate to form products that are insoluble in the reaction solvent.

Table 5–2: Selected catalysis results for alkene dimerization reaction recorded in 0.5 mL $CDCl_3$ or 0.5 mL C_6D_6. Reactions performed with 2 mol% complex. Substrate 1 & 2: 1-hexene; Additives: 0.25 eq K_2CO_3. Conversion and Yield based on NMR integration. ‡ Yield in excess of Conversion % is likely due to the catalyst reacting with the products in addition to the substrate, resulting in the complex overlapping alkyl proton ^1H NMR peaks.

	Complex	Catalyst Mass (mg)	Conversion (%)	Total Yield (%)	Yield of 1,1 (%)	Yield of 1,2 (%)	Ratio 1,1 : 1,2
$CDCl_3$	**1c**	5.5	13	14 ‡	8	6	5:4
	1d	5.1	20	6	6	0	6:0
	2b	5.0	12	< 1	< 1	0	-
	3a	5.5	11	2	2	< 1	4:1
	3b	5.0	17	1	1	0	1:0
	4c	4.6	12	9	2	7	2:7
	4d	5.5	14	6	6	0	6:0
	Complex	**Catalyst Mass (mg)**	**Conversion (%)**	**Total Yield (%)**	**Yield of 1,1 (%)**	**Yield of 1,2 (%)**	**Ratio 1,1 : 1,2**
C_6D_6	**1c**	5.2	54	20	20	0	20:0
	1d	5.1	49	11	0	11	0:11
	2b	5.4	57	6	6	0	6:0
	3a	4.6	31	1	1	0	1:0
	3b	4.7	49	8	8	0	8:0
	4c	4.6	48	12	12	0	12:0
	4d	4.9	36	9	< 1	8	1:22

© University of Pretoria

5.3.1.ii) Alkene hydroamination



Scheme 5.3–2: Some of the principal products which may form during catalysis of the 1-hexene hydroamination reaction with n-butylamine. Note that two constitutional isomers may form depending on the regioselectively of the catalyst.

The percentage conversions of the alkene and amine substrates by complex series **1–4** were on average greater in C_6D_6 compared to the reactions done in $CDCl_3$ (Figures H.1–3 and H.1–4; Tables 5.3–2, H.2–3 and H.2–4), however, all of the reactions showed a greater amount of conversions of the hexene compared to the amine. In the majority of cases, the percentage yield of the 1,1-products (Scheme 5.3–2) were in excess of the percentage conversion of amine substrate, due in part to peak overlap between the products of the alkene dimerization and hydrothiolation reactions. However, the catalysts may also be utilising the secondary alkylamine products as substrates to react with a second alkene molecule to yield tertiary amines or amine functionalised polyolefins.

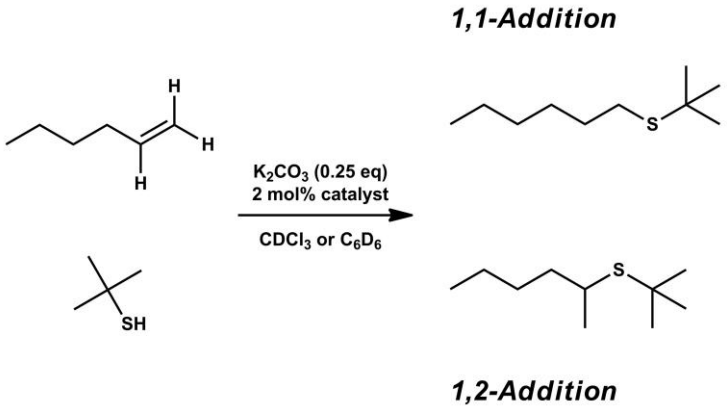
Table 5–3: Selected catalysis results for alkene hydroamination reaction recorded in 0.5 mL $CDCl_3$ or 0.5 mL C_6D_6. Reactions performed with 2 mol% complex. Substrate 1: 1-hexene, Substrate 2: nBu-NH_2; Additives: 0.25 eq K_2CO_3. Conversion and Yield based on NMR integration. ‡ Yields in excess of substrate 2 Conversion are due to the formation of alkene dimerization products. † Yields are in excess of substrate 2 Conversion due to the catalyst reacting with the 1,1 products in addition to the substrate, and minimal dimerization by-products were observed. § Traces of dimerization noted.

	Complex	Catalyst Mass (mg)	Conv. Sub.1 (%)	Conv. Sub.2 (%)	Total Yield (%)	Yield of 1,1 (%)	Yield of 1,2 (%)	Ratio 1,1 : 1,2
$CDCl_3$	**1d**	5.3	14	10	8 §	8	0	8:0
	2b	4.6	20	8	7 §	7	0	7:0
	3a	5.3	14	12	6	0	6	0:6
	3b	5.0	28	10	16 §	16	0	16:0
	4c	5.2	8	2	7 ‡	7	0	7:0
	4d	5.5	17	5	17 ‡	17	0	17:0
	Complex	**Catalyst Mass (mg)**	**Conv. Sub.1 (%)**	**Conv. Sub.2 (%)**	**Total Yield (%)**	**Yield of 1,1 (%)**	**Yield of 1,2 (%)**	**Ratio 1,1 : 1,2**
C_6D_6	**1d**	5.4	64	9	4	4	0	4:0
	2b	4.8	76	25	7	6	1	4:1
	3a	5.3	49	18	10	5	5	1:1
	3b	4.6	91	25	< 5	5	< 1	11:2
	4c	5.2	50	24	28 ‡	16	12	4:3
	4d	5.0	29	11	7 ‡	6	1	4:1

© University of Pretoria

The reactions done in $CDCl_3$ showed an increased degree of selectivity towards hydroamination than dimerization reactions (Table H.2–3). Interestingly, the regioselectivity of the catalytic reactions for **2b**, **3b**, **4c**, and **4d** in done in $CDCl_3$ favour the formation of the 1,1-addition product, whereas the corresponding reactions done in C_6D_6 produced an increased amount of the 1,2-addition products. Complexes **1d** and **2b** in particular largely formed the 1,1-addition hydroamination product, whereas complex **3a** formed the 1,2-addition hydroamination product exclusively (Scheme 5.3–2).

5.3.1.iii) Alkene hydrothiolation



Scheme 5.3–3: Some of the principal products which may form during catalysis of the 1-hexene hydrothiolation reaction with t-butylthiol. Note that two constitutional isomers may form depending on the regioselectively of the catalyst.

The percentage conversions of both the alkene and mercaptan substrates by complex series **1**–**4** were considerably lower in the $CDCl_3$ solutions than in the C_6D_6 solutions (Figures H.1–7 and H.1–8; Tables 5.3–3, H.2–5 and H.2–6). While the complex **2a** and **4a** showed a near quantitative conversion of both substrates, a minimal amount of product formation was detected (*ca*. 2 %) pointing towards the possible insolubility of the reaction products in the solvent. However, the reactions of complexes **1c**, **1d** and **4d** showed yields of 10 %, 17 % and 11 % respectively.

Even though the series of complexes **1**–**4** showed a low overall reactivity towards alkene hydrothiolation in $CDCl_3$, it is noted that the complexes **1b**, **1c**, **2b**, and **4d** displayed a clear regioselectivity towards the formation of the 1,1-addition product (Scheme 5.3–3) in both $CDCl_3$ and C_6D_6, with **1c** producing the 1,1–addition product exclusively in C_6D_6. Interestingly, trace amounts of alkene dimerization products were observed in some of the reactions done in $CDCl_3$, but not in any of the C_6D_6 samples.

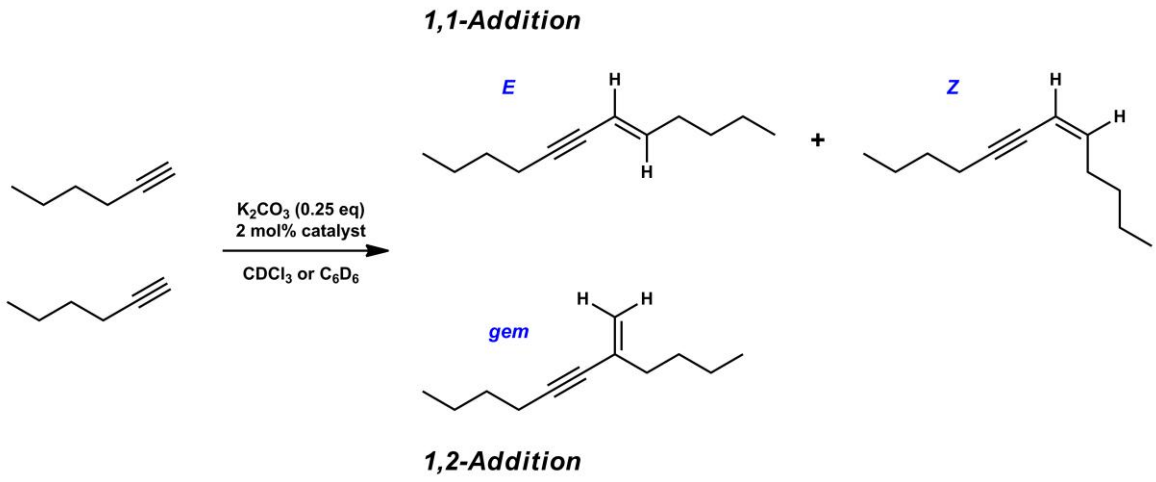
© University of Pretoria

Table 5–4: Selected catalysis results for alkene hydrothiolation reaction recorded in 0.5 mL $CDCl_3$ or 0.5 mL C_6D_6. Reactions performed with 2 mol% complex. Substrate 1: 1-hexene, Substrate 2: tBu-SH; Additives = 0.25 eq K_2CO_3. Conversion and Yield based on NMR integration. ‡ Yields in excess of substrate 2 Conversion are due to the formation of alkene dimerization products.

	Complex	Catalyst Mass (mg)	Conv. Sub.1 (%)	Conv. Sub.2 (%)	Total Yield (%)	Yield of 1,1 (%)	Yield of 1,2 (%)	Ratio 1,1 : 1,2
$CDCl_3$	**1c**	4.8	16	0	< 1 ‡	< 1	0	1:0
	1d	5.2	45	12	0	0	0	-
	2b	4.8	22	0	1 ‡	1	0	1:0
	4c	5.5	21	0	< 1 ‡	< 1	0	1:0
	4d	4.2	21	2	4 ‡	3	< 1	6:1
	Complex	**Catalyst Mass (mg)**	**Conv. Sub.1 (%)**	**Conv. Sub.2 (%)**	**Total Yield (%)**	**Yield of 1,1 (%)**	**Yield of 1,2 (%)**	**Ratio 1,1 : 1,2**
C_6D_6	**1c**	5.4	72	42	10	10	0	10:0
	1d	5.3	64	35	17	12	5	2:1
	2a	4.8	100	94	1	< 1	1	1:2
	2b	5.0	83	55	4	4	< 1	27:1
	3a	5.3	54	32	< 1	0	< 1	0:1
	4a	5.2	100	98	2	1	1	3:2
	4c	5.3	45	29	9	6	3	2:1
	4d	4.6	58	19	11	10	1	8:1

5.3.1.iv) Alkyne dimerization

The percentage substrate conversion by complex series **1**–**4** is observed to increase notably in C_6D_6 compared to the results recorded in $CDCl_3$ solutions (Figures H.1–11 and H.1–12; Tables 5.3–4, H.2–7 and H.2–8), however, the greatest total yield recorded was a mere 4 % by complex **4b**. Complex **2c** showed the highest regioselectivity with a 4 % yield of exclusively the 1,1–addition product in C_6D_6 (Scheme 5.3–4), however, the total conversion for was very low (10 %) considering the extended reaction time.



Scheme 5.3–4: Some of the principal products which may form during catalysis of the 1-hexyne dimerization reaction. Note that two stereoisomers (E and Z) as well as two constitutional isomers may form depending on the regioselectively of the catalyst.

© University of Pretoria

Table 5–5: Selected catalysis results for alkyne dimerization reaction recorded in 0.5 mL $CDCl_3$ or 0.5 mL C_6D_6. Reactions performed with 2 mol% complex. Substrate 1 & 2: 1-hexyne; Additives: 0.25 eq K_2CO_3. Conversion and Yield based on NMR integration.

	Complex	Catalyst Mass (mg)	Conversion (%)	Total Yield (%)	Yield of 1,1 (%)	Yield of 1,2 (%)	Ratio 1,1 : 1,2
$CDCl_3$	**1d**	5.0	5	< 1	< 1	0	1:0
	2b	4.7	7	0	0	0	-
	2c	5.3	4	0	0	0	-
	3a	5.4	10	0	0	0	-
	4b	5.4	18	4	2	3	3:5
	4c	4.6	12	2	2	< 1	4:1
	Complex	**Catalyst Mass (mg)**	**Conversion (%)**	**Total Yield (%)**	**Yield of 1,1 (%)**	**Yield of 1,2 (%)**	**Ratio 1,1 : 1,2**
C_6D_6	**1d**	5.2	15	< 1	0	< 1	0:1
	2b	4.6	17	< 1	0	< 1	0:1
	2c	5.3	10	4	4	0	4:0
	3a	4.9	19	0	0	0	-
	4b	4.9	31	0	0	0	-
	4c	5.2	25	1	0	1	0:1

Two possible explanations may be presented for the disproportionate relationship that is observed between the product yields and substrate conversions:

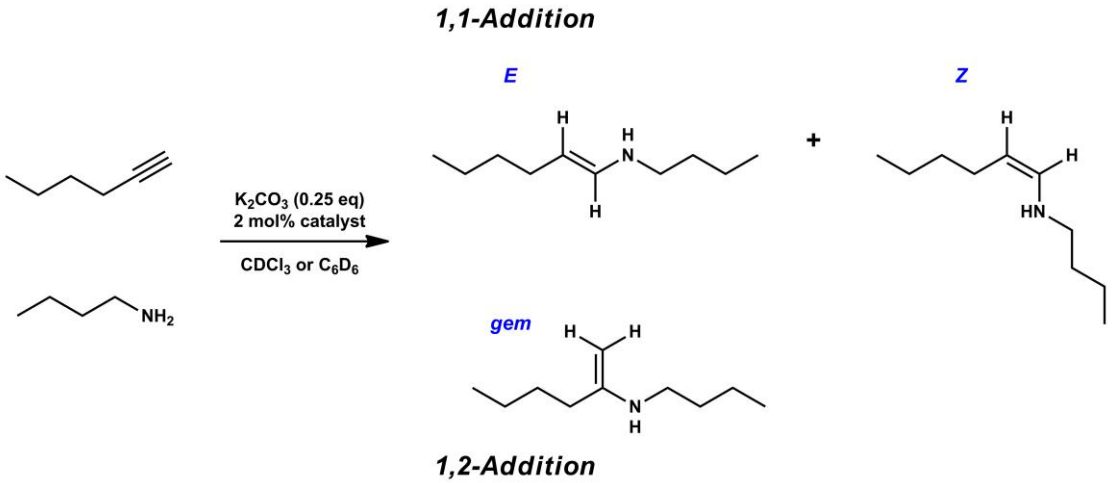
- ~ The products formed during the catalytic reaction are insoluble in the reaction solvent, and are therefore only detected in trace amounts; or,
- ~ That the catalysts react with the alkene and/or alkyne moieties within the 1,1– and 1,2–addition products as well as the 1-hexyne substrate in polymerisation reaction cycles.

Repeat analyses of these reactions on a larger reaction scale may enable not only the identification of the products that are formed, but also more accurate quantification of the extent to which the complexes are able to react with the alkyne substrate.

5.3.1.v) Alkyne hydroamination

As noted for the alkyne dimerization, most of the test reactions showed an increased percentage of substrate conversion by the series of complexes **1**–**4** in C_6D_6 compared to $CDCl_3$ (Figures H.1–13 and H.1–14; Tables 5.3–5, H.2–9 and H.2–10), showing a slight upturn in the overall yields of products as well. Interestingly, the reactions of the Rh(I)-MesBIAN complexes (**1b**, **2b**, **3b**, and **4b**) in C_6D_6 showed a distinct change in the colour of the reaction solutions before (orange) and after reflux (purple).

© University of Pretoria



Scheme 5.3–5: Some of the principal products which may form during catalysis of the 1-hexyne hydroamination reaction with n-butylamine. Note that two stereoisomers (E and Z) as well as two constitutional isomers may form depending on the regioselectively of the catalyst.

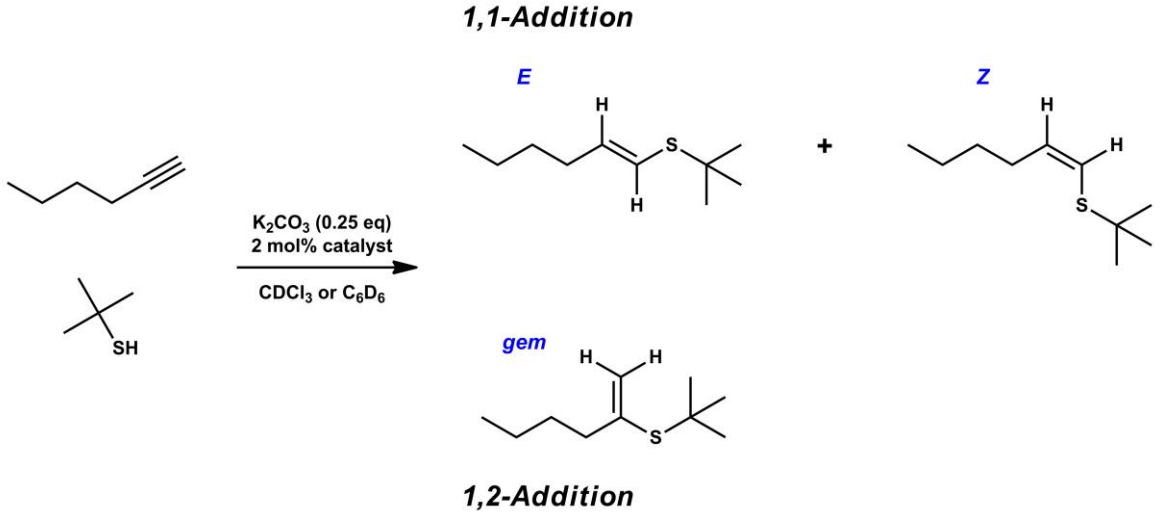
The percentage conversion of the amine substrate in many of the reaction mixtures is lower than that of the 1-hexyne substrate, while a limited number of reactions showed a near equivalent amount of conversion of both substrates. The highest overall yield (6 %) was observed in the reaction of complex **4d** in C_6D_6. No significant change in the selectivity of the catalysts could be determined due to relatively small amounts of products that were formed during the test reactions.

Table 5–6: Selected catalysis results for alkyne hydroamination reaction recorded in 0.5 mL $CDCl_3$ or 0.5 mL C_6D_6. Reactions performed with 2 mol% complex. Substrate 1: 1-hexyne, Substrate 2: nBu-NH_2; Additives = 0.25 eq K_2CO_3. Conversion and Yield based on NMR integration. ‡ Yields in excess of substrate 2 Conversion are due to the formation of alkyne dimerization products. § Orange reaction mixture changed colour to purple during reflux.

	Complex	Catalyst Mass (mg)	Conv. Sub.1 (%)	Conv. Sub.2 (%)	Total Yield (%)	Yield of 1,1 (%)	Yield of 1,2 (%)	Ratio 1,1 : 1,2
$CDCl_3$	**1b**	5.1	0	17	1	1	< 1	2:1
	1d	5.4	41	13	0	0	0	-
	2b	4.8	13	11	0	0	0	-
	3a	5.1	4	9	< 1	< 1	0	1:0
	3b	4.5	12	15	0	0	0	-
	4b	4.9	11	15	1	< 1	< 1	1:1
	4c	5.2	21	0	4	3 ‡	1	3:1
	4d	5.0	32	12	1	< 1	< 1	1:1
	Complex	**Catalyst Mass (mg)**	**Conv. Sub.1 (%)**	**Conv. Sub.2 (%)**	**Total Yield (%)**	**Yield of 1,1 (%)**	**Yield of 1,2 (%)**	**Ratio 1,1 : 1,2**
C_6D_6	**1b §**	5.2	23	17	4	2	2	1:1
	1d	5.0	17	12	4	3	1	2:1
	2b §	4.6	14	7	2	1	< 1	3:1
	3a	4.9	19	11	1	1	0	1:0
	3b §	4.7	12	13	2	1	1	1:1
	4b §	4.7	36	15	2	1	1	2:3
	4c	4.9	24	17	4	2	2	5:4
	4d	4.7	19	7	6	3	3	7:6

© University of Pretoria

5.3.1.vi) Alkyne hydrothiolation



Scheme 5.3–6: Some of the principal products which may form during catalysis of the 1-hexyne hydrothiolation reaction with t-butylthiol. Note that two stereoisomers (E and Z) as well as two constitutional isomers may form depending on the regioselectively of the catalyst.

The alkyne hydrothiolation reactions performed in $CDCl_3$ showed a diverse degree of substrate conversions and product yields between the different complexes (Figures H.1–17 and H.1–18; Tables 5.3–6, H.2–11, and H.2–12). The alkyne and thiol substrate conversions percentages of many reactions were near equivalent, unlike the majority of alkyne hydroamination reactions. In general, the catalysts displayed an enhanced degree of regioselectivity for the production of the 1,1-addition products in $CDCl_3$, however, the reactions done in C_6D_6 showed overall higher yields.

Minimal traces of alkyne dimerization by-products were observed for some reactions in $CDCl_3$ solutions, whereas no traces of dimerization were detected in the reactions done in C_6D_6 (Tables 5.3–6 and H.2–12), corresponding to the poor dimerization activity results of the complexes as observed in Section 5.3.1.iv. Complexes **4c** and **4d** displayed the highest overall yields of all reactions done in $CDCl_3$ (58 % and 53 % respectively). The complexes regioselectively produced 1,1–addition products (Scheme 5.3–6), and their stereoselective partiality was evidenced by the *ca*. 82 % enantiomeric excess of the 1,1–(*E*)–addition product (% $ee_{1,1\text{-}E}$). Although the total yields for the reactions of complexes **4c** and **4d** in C_6D_6 decreased notably, the stereoselectivity with which the complexes produced the 1,1–(*E*)–addition product was greatly enhanced (100 % $ee_{1,1\text{-}E}$). Complex **1c** showed comparable catalytic performance to that of **4d** in the same solvent, however, it retained a higher degree of regioselectivity to produce the 1,1-adittion product.

© University of Pretoria

Table 5–7: Selected catalysis results for alkyne hydrothiolation reaction recorded in 0.5 mL $CDCl_3$ or 0.5 mL C_6D_6. Reactions performed with 2 mol% complex. Substrate 1: 1-hexyne, Substrate 2: tBu-SH; Additives = 0.25 eq K_2CO_3. Conversion and Yield based on NMR integration. The ratios of 1,1- and 1,2-addition products, as well as the percentage enantiomeric excess of the 1,1-(E) product are given in Table H.2–11 and H.2–12. † Yields are in excess of substrate 1 Conversion due to the catalyst reacting with the alkene products in addition to the alkyne substrate. No alkyne dimerization by-products were observed.

	Complex	Catalyst Mass (mg)	Conv. Sub.1 (%)	Conv. Sub.2 (%)	Total Yield (%)	Yield of 1,1–*Z* (%)	Yield of 1,1–*E* (%)	Yield of 1,2 (%)	Total Yield (%)
$CDCl_3$	**1d**	5.5	12	17	13 †	0	13	0	< 1
	2b	5.0	54	53	49	13	35	1	0
	3a	4.9	16	12	7	2	5	0	0
	4a	4.7	29	17	17	6	10	1	0
	4b	4.9	46	45	39	7	32	< 1	4
	4c	4.7	74	61	58	10	47	< 1	2
	4d	4.9	51	58	53 †	9	43	< 0	< 1
	Complex	**Catalyst Mass (mg)**	**Conv. Sub.1 (%)**	**Conv. Sub.2 (%)**	**Total Yield (%)**	**Yield of 1,1–*Z* (%)**	**Yield of 1,1–*E* (%)**	**Yield of 1,2 (%)**	**Total Yield (%)**
C_6D_6	**1d**	4.7	46	62	15	0	12	3	< 1
	2b	4.9	79	87	56	26	30	< 1	< 1
	3a	4.7	52	69	36	6	29	1	0
	4a	4.8	66	72	47	9	23	15	0
	4b	5.3	72	79	62	15	37	10	0
	4c	5.5	41	37	22	0	21	2	1
	4d	4.7	65	82	41	0	38	3	2

Excerpt of Alkyne Dimerization Results (Table 5.3–4)

While complexes **4a** and **4b** showed poor and moderate catalytic reactivity in $CDCl_3$, 17 % and 39 % respectively, the overall yields for their reactions in C_6D_6 increased nearly two-fold (47 % and 62 %) and outperforming complexes **4c** and **4d** in terms of total yield (Table 5.3–6). Interestingly, the alkyne hydrothiolation reactions complexes **4a** and **4b** in C_6D_6 showed the greatest yield of the geminal 1,2–addition product (Scheme 5.3–6) out of all the reactions tested (15 % and 10 % respectively).

5.3.2) Reductant Activation of Catalytic Reactivity

An additional set of catalytic activity experiments were performed which included a chemical reducing agent additive in a preliminary investigation into whether the catalytic activity of the Rh(I)- and Ir(I)-BIAN complexes may be enhanced through redox activation of the complexes' reaction centre.[64] Following the identification of electrochemical CO_2 interaction (Section 5.3.3 below), four complexes were selected as representative examples of the different ancillary ligand groups utilised in the series of complexes **1**–**4**, namely complexes **1d**, **2b**, **3a** and **4c**. More specifically, two complexes that showed evidence of interaction with CO_2 in solution (**2b** and **3a**, *vide infra*), as well as two complexes that showed no change in electrochemical behaviour in the presence of CO_2 (**1d** and **4c**, *vide infra*), were selected to investigate whether their catalytic reactivity may be affected through a change in their charged state. These experiments were conducted solely in C_6D_6 solutions due to the increased

© University of Pretoria

catalytic reactivity and yields that were observed for most of the reactions in Section 5.3.1 in this solvent.

The series of complexes **1**–**4** all showed a one electron reduction event at potentials above –1.0 V (vs Ag/Ag^+) (see Chapter 3), thus the addition of a suitably strong chemical reducing agent to the catalytic reaction mixture was anticipated to afford the respective complexes in a singly reduced state. To such effect, equimolar amounts (*ca*. 2 mol %) of catalyst and the chemical reducing agent cobaltocene ($CoCp_2$) was added to the reaction mixtures to induce a one electron reduction of the BIAN complexes.[65] The catalytic activity of reaction mixtures containing $CoCp_2$ as the sole metal complex were also tested to ensure that any changes observed in the reactivity of complexes were not the result of the chemical reducing agent itself.

5.3.2.i) Alkene hydroamination

The $CoCp_2$ showed a high percentage conversion of the alkene substrate (Table 5.3–7, Figures H.1–5 and H.1–6) but a low conversion of the amine substrate and very low overall yield of products, similar to what was observed for complex **1d** alone (Table 5.3–2, Figures H.1–3 and H.1–4). The mixture of complex **1d** and $CoCp_2$ showed a notable increase in the conversion of the amine substrate, however, the overall yields of the 1,1– and 1,2–addition products (Scheme 5.3–2) recorded were similar to those of as the original reaction. The chemically reduced **2b** displayed a decrease in percentage conversion of both alkene and amine substrates, but a minor increase in the percentage yield of 1,2–addition product. The regioselectivity of complexes **3a** and **4c** in the presence of $CoCp_2$ improved slightly, favouring the formation of the 1,1–addition product, albeit at decreased overall yields.

Table 5–8: Catalysis results for Alkene Hydroamination recorded in 0.5 mL C_6D_6. Reactions performed with 2 mol% complex. Substrate 1: 1-hexene, Substrate 2: nBu-NH_2; $CoCp_2$: Cobaltocene. Conversion and Yield based on NMR integration. ‡ Yields in excess of substrate 2 Conversion are due to the formation of alkene dimerization products. † Traces of dimerization products were observed. § Significant brown staining of the sample tube was noted after the experiment.

Complex	Catalyst Mass (mg)	Additives (eq)	Conv. Sub.1 (%)	Conv. Sub.2 (%)	Total Yield (%)	Yield of 1,1 (%)	Yield of 1,2 (%)	Ratio 1,1 : 1,2
$CoCp_2$ §	1.5	K_2CO_3 (0.25)	68	10	3	2	1	2:1
1d	5.6	K_2CO_3 (0.25); ±1.5 mg $CoCp_2$	56	25	5 †	5	0	5:0
2b	5.9	K_2CO_3 (0.25); ±1.5 mg $CoCp_2$	69	16	9	6	3	2:1
3a	5.4	K_2CO_3 (0.25); ±1.5 mg $CoCp_2$	59	14	9	8	1	8:1
4c	4.8	K_2CO_3 (0.25); ±1.5 mg $CoCp_2$	29	9	9 ‡	9	< 1	9:1

© University of Pretoria

5.3.2.ii) Alkene hydrothiolation

A substantial amount of conversion by $CoCp_2$ of both the alkene and thiol substrates was observed (Table 5.3–8, Figures H.1–9 and H.1–10), however, only 1 % yield if the 1,2–addition product was detected in the reaction solution (Scheme 5.3–3). The percentage conversions and overall yields of the chemically reduced **1d** decreased slightly compared to those recorded for the unaltered complex (Table 5.3–3, Figures H.1–7 and H.1–8). While the conversion percentages of complex **3a** showed a marked increase, no product formation was detected. In contrast, the amount of substrate conversion by complexes **2b** and **4c** in the presence of $CoCp_2$ was observed to increase, as did their regioselectivity for production of the 1,1–addition product (Scheme 5.3–3).

Table 5–9: Catalysis results for Alkene Hydrothiolation recorded in 0.5 mL C_6D_6. Reactions performed with 2 mol% complex. Substrate 1: 1-hexene, Substrate 2: tBu-SH; $CoCp_2$: Cobaltocene. Conversion and Yield based on NMR integration. § Reaction mixture became dark red in colour after reflux.

Complex	Catalyst Mass (mg)	Additives (eq)	Conv. Sub.1 (%)	Conv. Sub.2 (%)	Total Yield (%)	Yield of 1,1 (%)	Yield of 1,2 (%)	Ratio 1,1 : 1,2
$CoCp_2$	1.5	K_2CO_3 (0.25)	60	66	1	0	1	0:1
1d	4.9	K_2CO_3 (0.25); ±1.5 mg $CoCp_2$	43	29	11	8	3	3:1
2b	6.3	K_2CO_3 (0.25); ±1.5 mg $CoCp_2$	68	54	8	8	0	8:0
3a	4.7	K_2CO_3 (0.25); ±1.5 mg $CoCp_2$	74	58	0	0	0	-
4c §	4.4	K_2CO_3 (0.25); ±1.5 mg $CoCp_2$	47	39	8	8	0	8:0

5.3.2.iii) Alkyne hydroamination

Cobaltocene displayed a poor degree of alkyne conversion (Table 5.3–9, Figures H.1–15 and H.1–16), but no amine conversion or product formation were detected in the reaction sample.

Table 5–10: Catalysis results for Alkyne Hydroamination recorded in 0.5 mL C_6D_6. Reactions performed with 2 mol% complex. Substrate 1: 1-hexyne, Substrate 2: nBu-NH_2; $CoCp_2$: Cobaltocene. Conversion and Yield based on NMR integration. ‡ Yields in excess of substrate 2 Conversion are due to the formation of alkene dimerization products. † Significant brown staining of the sample tube was noted after the experiment. § Reaction mixture became purple during reflux.

Complex	Catalyst Mass (mg)	Additives (eq)	Conv. Sub.1 (%)	Conv. Sub.2 (%)	Total Yield (%)	Yield of 1,1 (%)	Yield of 1,2 (%)	Ratio 1,1 : 1,2
$CoCp_2$ †	1.5	K_2CO_3 (0.25)	14	0	0	0	0	-
1d	5.3	K_2CO_3 (0.25); ±1.5 mg $CoCp_2$	19	13	2	< 1	1	1:1
2b §	6.0	K_2CO_3 (0.25); ±1.5 mg $CoCp_2$	18	0	< 1 ‡	0	< 1	0:1
3a	6.0	K_2CO_3 (0.25); ±1.5 mg $CoCp_2$	28	17	0	0	0	-
4c	4.7	K_2CO_3 (0.25); ±1.5 mg $CoCp_2$	21	0	6 ‡	3	3	1:1

© University of Pretoria

As noted for the alkyne hydroamination reactions of complexes **1d**, **2b**, **3a** and **4c** in Section 5.3.1.v (Table 5.3–5, Figures H.1–13 and H.1–14), very little product formation was observed even after chemical reduction of these complexes. However, traces of alkyne dimerization were observed in the reactions of complexes **2b** and **4c**.

5.3.2.iv) Alkyne hydrothiolation

The $CoCp_2$ showed a poor percentage of substrate conversion with a minimal amount of product formation detectable in the solution (Table 5.3–10, Figures H.1–19 and H.1–20). The conversion of mercaptan substrate by complex **1d** in the presence of $CoCp_2$ decreased slightly compared to what was recorded in Section 5.3.1.vi (Table 5.3–6, Figures H.1–17 and H.1–18), with the overall yields remained comparably similar. However, precipitation of fine particulates with an off-white colouration were observed in the sample tubes of both the $CoCp_2$ and reduced **1d** reactions after reflux, suggesting possible polymerisation product formation. In addition, the stereoselective production of the 1,1-(E)-product which was previously observed is diminished in the presence of the chemical reducing agent. The percentage conversion of the thiol substrate by the chemically reduced **2b**, and the overall yield of the reaction, decreased by nearly 30 % compared to the previous results (Table 5.3–6). However, the regioselectivity of the reaction clearly shifted from favouring 1,1–addition products to forming chiefly the geminal 1,2–addition product (Scheme 5.3–6).

Table 5–11: Catalysis results for Alkyne Hydrothiolation recorded in 0.5 mL C_6D_6. Reactions performed with 2 mol% complex. Substrate 1: 1-hexyne, Substrate 2: tBu-SH; $CoCp_2$: Cobaltocene. Conversion and Yield based on NMR integration. ‡ The sample tubes were stained with an off-white residue after reflux. § Reaction mixture became dark red in colour after reflux.

Complex	Catalyst Mass (mg)	Additives (eq)	Conv. Sub.1 (%)	Conv. Sub.2 (%)	Total Yield (%)	Yield of 1,1–*Z* (%)	Yield of 1,1–*E* (%)	Yield of 1,2 (%)	Ratio 1,1 : 1,2
$CoCp_2$ ‡	1.5	K_2CO_3 (0.25)	14	24	1	1	0	0	1:0
1d ‡	5.4	K_2CO_3 (0.25); ±1.5 mg $CoCp_2$	41	45	17	3	11	3	5:1
2b	6.0	K_2CO_3 (0.25); ±1.5 mg $CoCp_2$	77	58	27	2	8	17	3:5
3a	5.6	K_2CO_3 (0.25); ±1.5 mg $CoCp_2$	57	61	33	4	3	25	2:7
4c §	5.3	K_2CO_3 (0.25); ±1.5 mg $CoCp_2$	47	45	22	3	13	5	3:1

The catalytic reactivity of complex **3a** in the presence of $CoCp_2$ showed a comparable degrees of substrate conversion as noted in the original reaction (Table 5.3–6), although the reduced **3a** catalyst favoured formation of the geminal 1,2–addition product instead of the 1,1–(*E*)–addition product (Scheme 5.3–6). While the conversion and overall yield percentages recorded for the chemically

© University of Pretoria

reduced **4c** were comparable to those observed for the neutral complex, its regioselective formation of primarily the 1,1–(*E*)–addition product was diminished (Table 5.3–6, Scheme 5.3–6).

© University of Pretoria

5.3.3) CO_2 Electrochemical Reduction and Interactions

The reactivity testing of the complex series **1**–**4** towards electrochemical CO_2 reduction was done using the same sample solutions as prepared for their electrochemical characterisation (Chapter 3), however, the solutions were purged with technical grade CO_2 (g) for 30 minutes before initiation of the analysis. An atmosphere of CO_2 was maintained inside the electrochemical cell throughout the analyses.

*Table 5–12: A summary of the DPV peak potentials (V vs Ag/Ag^+) recorded for DippBIAN, MesBIAN, and complex series **1**–**4** in solutions saturated with either Ar (g) or CO_2 (g). Assignments are presented as revised after application of the Peak Characterisation Model (Chapter 4). Key: * Electrochemically reversible events. ‡ Events were not observed in the CO_2 saturated solutions. § New peak observed in the CO_2 saturated solutions. † CV potentials measured at half peak height.*

Compound	Red. 4	Red. 3	Red. 2	Red. 1	Ox. 1	Ox. 2	Ox. 3
DippBIAN			–1.51	–0.85	+1.26		
DippBIAN + CO_2		–1.95	–1.47	‡	+1.25		
MesBIAN			–1.92	–1.43	+1.20	+1.73	
MesBIAN + CO_2			‡	–1.40	+1.20†	‡	
1a			–1.53	–0.56*	+1.31*	+1.61	
1a + CO_2			–1.56	–0.60*	+1.40*	+1.69	
1b			–1.64	–0.70*	+1.26	+1.63	
1b + CO_2			–1.64	–0.72*	+1.21	+1.59	
1c	–1.53	–1.14*	–0.91	–0.19*	+0.58	+1.24	+1.50
1c + CO_2	–1.53	–1.16*	–0.92	–0.20*	+0.57	+1.24	+1.50
1d	–1.52	–1.11*	–0.85	–0.21*	+0.58	+1.23	+1.47
1d + CO_2	–1.51	–1.11*	–0.85	–0.21*	+0.58	+1.23	+1.48
2a	–1.68	–1.41*	–0.70	–0.43*	+1.12	+1.40	
2a + CO_2	–1.69	–1.44*	–0.73*	–0.45*	+1.18	+1.47	
2b	–1.84	–1.54	–0.90*	–0.61	+1.04	+1.41	+1.72
2b + CO_2	–1.77†	–1.48†	–0.82†*	–0.54†	+1.09†	+1.43†	‡
2c			–1.19*	–0.22*	+1.56		
2c + CO_2			–1.19*	–0.21*	+1.58		
2d			–1.18*	–0.25*	+1.56		
2d + CO_2			–1.14*	–0.22*	+1.61		
3a			–1.79	–0.77*	+1.36	+1.60	
3a + CO_2		–1.76	–1.14§	–0.75*	+1.38	+1.61	
3b		–1.78	–1.70	–0.82*	+1.25	+1.59	
3b + CO_2		–1.74	–1.67	–0.82*	+1.21	+1.55	
4a	–1.88	–1.37	–1.15	–0.18*	+0.77	+1.46	
4a + CO_2	‡	–1.30	–1.14	–0.18*	+0.79	+1.48	
4b	–1.78	–1.53	–1.14	–0.20*	+0.89	+1.74	
4b + CO_2	–1.81	‡	–1.13	–0.20*	+0.88	+1.73	
4c	–1.79	–1.45	–1.02*	–0.16*	+0.70	+1.64	
4c + CO_2	–1.80	–1.46	–1.03*	–0.16*	+0.70	+1.64	
4d		–1.40	–1.00*	–0.16*	+0.67	+1.58	
4d + CO_2		–1.41	–1.01*	–0.17*	+0.67	+1.57	

© University of Pretoria

The results presented here are for the initial quantitative investigation into the application of the series of complexes **1**–**4** as CO_2 electroreduction catalysts. As such, the following discussions will focus chiefly on the changes that were observed in the electrochemical behaviour of the compounds upon addition of CO_2 to the electrochemical solution (e.g., changes in peak potentials and/or current), and not the identification of formed products or determination of the catalytic efficiency of the complexes. The reactivity of the free Dipp- and MesBIAN ligands towards CO_2 were assessed in addition to those of the complex series **1**–**4** to ensure that any positive catalytic results may not be attributable to the presence and action of the free ligands in the electrochemical solutions. The DPV peak potentials as recorded under Ar (g) and CO_2 (g) atmosphere for the free ligands and complexes **1**–**4** are summarised in Table 5.3–11, and visualisations of the CVs and DPVs as recorded under Ar (g) and CO_2 (g) atmosphere for the free ligands and complex series **1**–**4** are presented in the sections below and in Appendix I.1.

5.3.3.i) Dipp- and MesBIAN

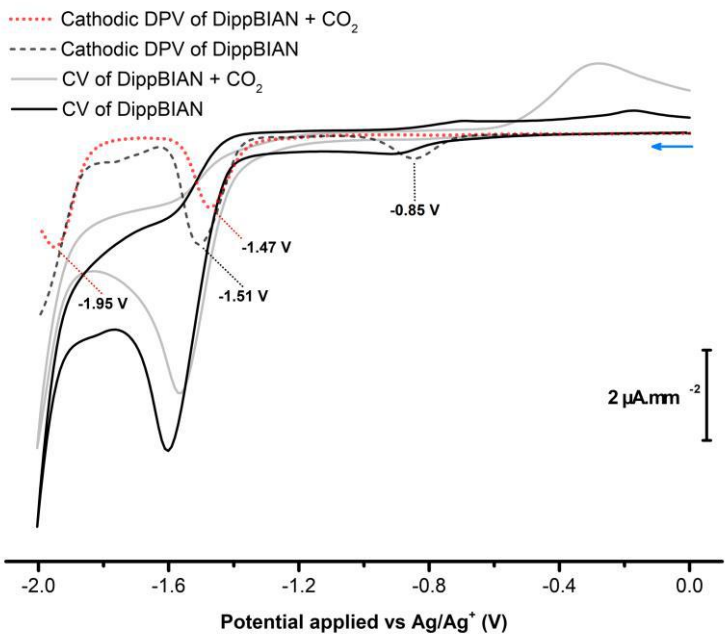


Figure 5.3–1: Cathodic CVs and DPVs of the free DippBIAN ligand recorded in CH_2Cl_2 saturated with either CO_2 (g) or Ar (g), with 1.0 mM analyte and 0.1 M $TBAPF_6$ supporting electrolyte.

The first reduction potential of the free MesBIAN ligand in the presence of CO_2 is shifted to more positive potentials by 30 mV (Table 5.3–11), however, the second reduction and second oxidation events are not clearly resolved and a decrease (40 µA) in cathodic current at potentials below –1.6 V

© University of Pretoria

was noted (Figure I.1–2). An additional broad anodic counter peak is observed in the CO_2 containing CV scans at +0.1 V (Figure I.1–3).

5.3.3.ii) Complexes 1a–d

The reduction potentials of complex **1a** are shifted to more negative potentials by 30–40 mV (Table 5.3–11) with a slight decrease in cathodic current at potentials below –1.6 V (Figure I.1–4), whereas the oxidation potentials are shifted to more positive potentials by 80–90 mV and slightly increased anodic peak currents (8 µA) at potentials above +1.1 V (Figure I.1–5).

The first reduction event of complex **1b** shows a small negative potential shift (–20 mV, Table 5.3–11) with a decrease in cathodic current (20 µA) evident at potentials below –1.7 V (Figure I.1–6), while its two oxidation potentials are shifted to more negative potentials by 40–50 mV (Figure I.1–7).

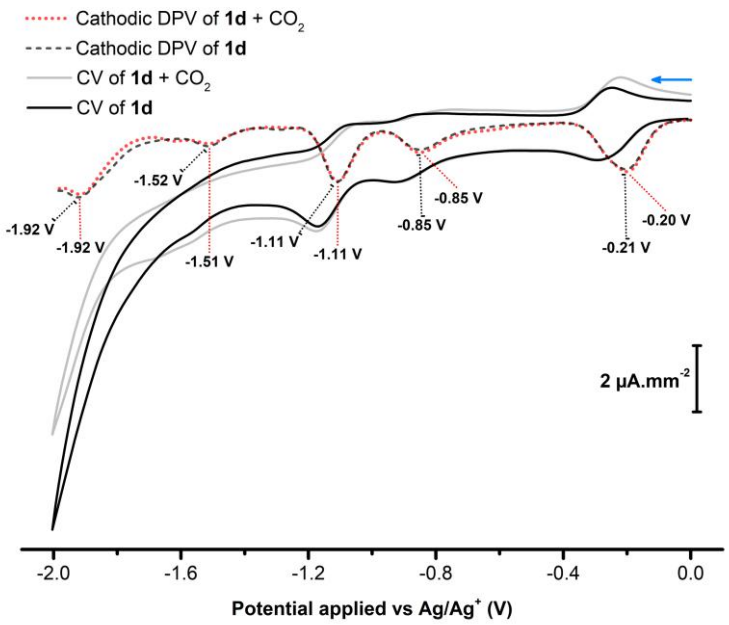


*Figure 5.3–2: Cathodic CVs and DPVs of **1d** recorded in CH_2Cl_2 saturated with either CO_2 (g) or Ar (g), with 1.0 mM analyte and 0.1 M $TBAPF_6$ supporting electrolyte.*

The reaction potentials of complex **1c** showed a slight negative shift (0–20 mV) in the presence of CO_2 (Table 5.3–11), but the reversibility of the first and third reduction events remained unaffected (Figure I.1–8). Even though the DPV peak current for the third reduction event at –1.53 V was diminished in the presence of CO_2, the irreversible reduction event was still visible in CV containing CO_2 with a similarly decreased cathodic peak current (20 µA).

© University of Pretoria

Very little change was observed in the CV and DPV of complex **1d** in the presence of CO_2 (Table 5.3–11), with only minor positive potentials shifts (0–10 mV) visible beyond +1.4 V and –1.4 V and a decrease in maximum cathodic current (20 µA) at potentials below –1.7 V (Figures 5.3–2 and I.1–10).

5.3.3.iii) Complexes 2a–d

The reduction potentials of complex **2a** showed a small shift to more negative potentials (10–30 mV, Table 5.3–11), and the reversibility of the second reduction event improved in the presence of CO_2 (Figure I.1–11). In contrast, the first oxidation event showed a small positive shift in reaction potential (20 mV) whereas the second oxidation event shifted by 70 mV and a significant decrease in oxidation current (40 µA) at potentials above +1.3 V (Figure I.1–12).

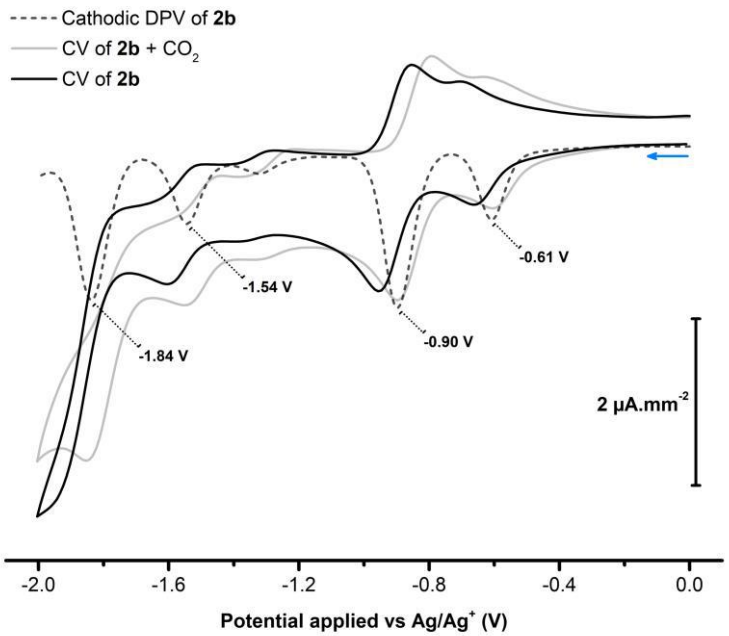


*Figure 5.3–3: Cathodic CVs and DPVs of **2b** recorded in CH_2Cl_2 saturated with either CO_2 (g) or Ar (g), with 1.0 mM analyte and 0.1 M $TBAPF_6$ supporting electrolyte.*

All the reduction events of complex **2b** showed a considerable positive shift in reaction potentials (70–80 mV) in the presence of CO_2 (Table 5.3–11), with a slight increase in cathodic current (5–10 µA) between –1.0 V and –1.9 V (Figure 5.3–3), however, the development of additional reduction events were observed. The first two oxidation events displayed a much more moderated positive shift in reaction potentials (20–30 mV) with slightly decreased anodic current (10 µA) at potentials above +1.2 V (Figure I.1–13), however, the third oxidation potential was not clearly observable.

© University of Pretoria

The first reduction potential of **2c** is shifted slightly more negative (10 mV) in the presence of CO_2 (Table 5.3–11), whereas the oxidation reaction potential is shifted slightly more positive (20 mV). The reversibility of the reduction event was largely unaffected by the presence of CO_2 (Figures I.1–14 and I.1–15).

The reduction and oxidation reaction potentials of complex **2d** showed a moderate positive shift (30–50 mV, Table 5.3–11) and slight increase in cathodic current (10 µA) at potentials below –1.6 V in the presence of CO_2 (Figures I.1–16 and I.1–17), however, the reversibility of the reduction events remained unchanged (Figures I.1–16).

5.3.3.iv) Complexes 3a–b

In the presence of CO_2, the reduction and oxidation reaction potentials of complex **3a** showed a slight positive shift (10–30 mV, Table 5.3–11), and the reversibility of the first reduction event was not affected (Figure 5.3–4 and Figure I.1–18). However, an additional reduction peak developed at –1.14 V that displayed very high current density in the CV between –1.3 V and –1.6 V (5 µA.mm^{-2}) (Figure 5.3–4).

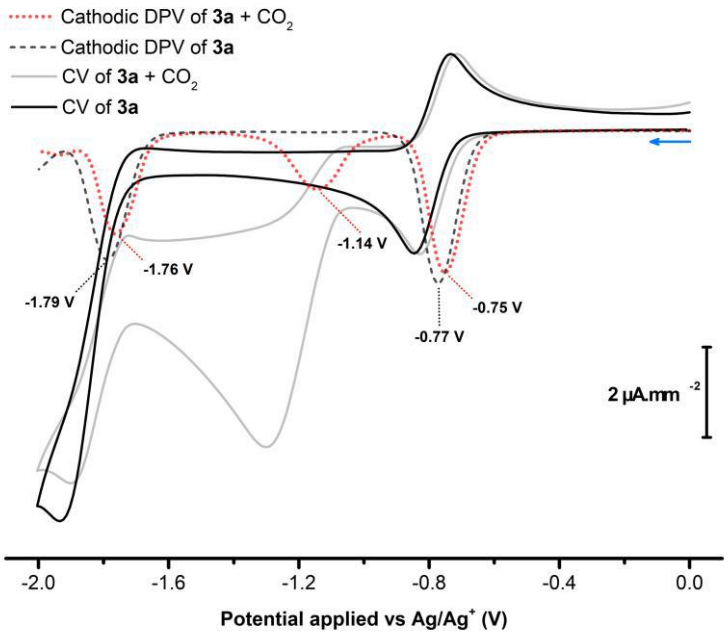


*Figure 5.3–4: Cathodic CVs and DPVs of **3a** recorded in CH_2Cl_2 saturated with either CO_2 (g) or Ar (g), with 1.0 mM analyte and 0.1 M $TBAPF_6$ supporting electrolyte.*

The second and third reduction events of complex **3b** showed a slight (20–30 mV, Table 5.3–11) positive shift in reaction potential in the presence of CO_2 and decrease in cathodic current (15 µA) at

© University of Pretoria

potentials below –1.8 V (Figure I.1–19), whereas the oxidation events were shifted to more negative potentials by 40 mV (Figure I.1–20). The reversibility of the first reduction event remained unchanged.

5.3.3.v) Complexes 4a–d

While the first and second reduction potentials of complex **4a** did not change significantly in the presence of CO_2 (Table 5.3–11), a positive shift of 70 mV was noted for the third reduction event with significantly decreased cathodic current (20–30 µA) below –1.3 V (Figure I.1–21), whereas the fourth reduction event was not clearly observable. The oxidation events showed a small positive shift of 20 mV, with the minor DPV peaks between +0.9 V and +1.3 V that were observed in the Ar samples no longer visible (Figure I.1–22). The reversibility of the first reduction event were unaffected.

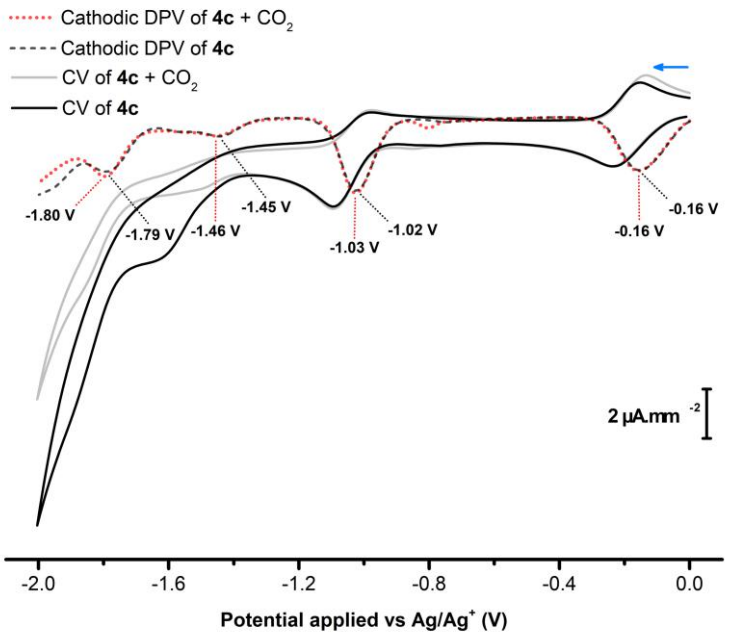


*Figure 5.3–5: Cathodic CVs and DPVs of **4c** recorded in CH_2Cl_2 saturated with either CO_2 (g) or Ar (g), with 1.0 mM analyte and 0.1 M $TBAPF_6$ supporting electrolyte.*

The first and second reduction events of **4b** were largely unaffected by the presence of CO_2 in the solution (Table 5.3–11), however, the third reduction event at –1.53 V was not observed, and the fourth reduction event showed a negative shift reaction potential of 30 mV, with a significant decrease in cathodic current (35–50 µA) at potentials below –1.2 V (Figure I.1–23). The oxidation events were also slightly shifted to more negative potentials (10 mV). The reversibility of the first reduction event remained unchanged.

© University of Pretoria

The reaction potentials of complex **4c** were not greatly affected by the presence of CO_2 (Table 5.3–11), with a slight 10 mV negative shift noted for the second, third and fourth reduction potentials, however, a substantial decrease in cathodic current (20–35 µA) at potentials below –1.45 V was observed (Figure 5.3–5). The reversibility of the first and second reduction events were unaffected.

Complex **4d** showed a slight negative shift in all reaction potentials (10 mV) except the first oxidation potentials (Table 5.3–11). A decrease in the cathodic current (10–25 µA) was noted at potentials below –1.1 V (Figure I.1–26). The reversibility of the first and second reduction events remained unchanged.

5.3.3.vi) Comparative Discussion

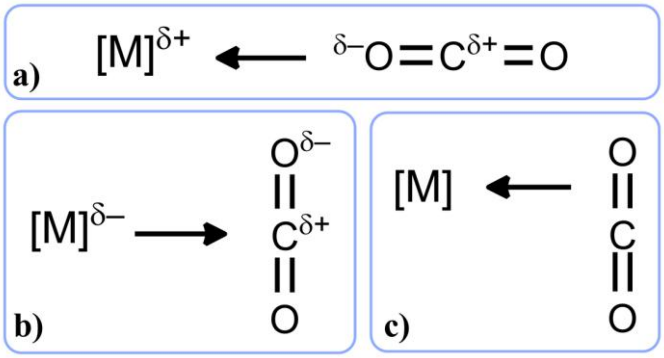
The free Dipp- and MesBIAN ligands as well as the series of complexes **1**–**4** may be divided into five broad groups based on the changes observed in their electrochemical potentials in the CO_2 saturated solutions compared to those recorded under Ar (g):

- Group **α** – The overall positive shift in peak potentials noted for free MesBIAN and complexes **2b**, **2d**, **3a** and **4a** indicate a slight to moderate decrease in the amount of energy required to electrochemically reduces the compounds in the presence of dissolved CO_2, however, additional energy is required to oxidise the compounds.
- Group **β** – The overall negative shift of reaction potentials observed for complexes **1b** and **4b** in the presence of dissolved CO_2 indicate an increase in the energy requirement for electrochemical reduction, but a decrease in the amount of energy needed for oxidation of these compounds.
- Group **γ** – Complexes **1a**, **2a** and **2c** showed a negative shift in reduction potentials but a positive shift in oxidation potentials in CO_2 saturated solutions, signifying an increase in these complexes' resistance to electrochemical reactions, requiring additional energy to affect the same changes in reduction and/or oxidation state.
- Group **δ** – The free DippBIAN ligand and complex **3b**, on the other hand, displayed the opposite reactivity – with an overall positive shift of reduction potentials and negative shift of oxidation potentials – suggesting a decreased resistance to electrochemical charge transfer reactions in the presence of CO_2.
- Group **ε** – Lastly, the peak potentials of the Ir(I)-cod complexes **1c**, **1d**, **4c** and **4d** showed little to no changes in the CO_2 saturated solutions, although the maximum cathodic currents of all four complexes were decreased by at least 20 µA.

© University of Pretoria

An examination of the variable modes of interaction between CO_2 and a coordination complex may shed light on the shifts in reaction potentials observed for the various compounds. Three main modes of associative interactions between CO_2 and a complex, without the formation of formal coordination attachment to the metal or its electrochemically generated charged intermediates, may be described as (Scheme 5.3–7):[30,56]

- An electrostatic associative interaction between the complex and a partially negative oxygen terminus of the CO_2 (a).
- An electrostatic associative interaction between the complex and the partially positive carbon centre of the CO_2 (b).
- An associative interaction between the complex MOs and the π-electron cloud between the oxygen and carbon atoms of the CO_2 (c).



Scheme 5.3–7: Simplified representation of three possible modes of non-coordinating associative interaction between a transition metal complex [M] and CO_2 molecule: a) electrostatic association with the partially negatively charged oxygen terminus of a CO_2 molecule; b) electrostatic association with the partially positive carbon of a CO_2 molecule; and c) a partial associative interaction between the complex [M] and the π-bond electron cloud between the oxygen and carbon atoms of a CO_2 molecule.[30,56]

Such non-coordinating associative interactions are projected to result in modest changes of the electrochemical potentials of the complex without affecting its coordination geometry, oxidation state, or ligand composition – all of which would inevitably modify the characteristic electrochemical profile of the complex. Electrostatic association with the oxygen atom of CO_2 (Scheme 5.3–7a) is anticipated to have an electron donating effect on the complex, increasing the ease with which the complex may be oxidised but also increasing the amount of energy required to reduce the complex (such as Group **β**). Conversely, electrostatic interaction with the carbon atom of CO_2 (Scheme 5.3–7b) would induce an electron withdrawing effect on the complex, improving the ease with which the complex may be reduced but increasing the energy required for oxidation (such as Group **α**).

© University of Pretoria

Side-on interaction between the complex and the π-bond electron cloud between the carbon and oxygen atoms (Scheme 5.3–7c) is anticipated to provide an associative interaction that is more yielding to changes in the charge of the complex during the electrochemical analysis, allowing the interaction between the complex and CO_2 to easily transform to either the electron donating (Scheme 5.3–7a) or electron withdrawing (Scheme 5.3–7b) modes. Complexes with this side-on π-electron cloud interaction may thus display contradictory shifts in electrochemical potentials. For example, they may be more difficult to oxidise and to reduce (such as Group **γ**), or they may be easier reduce and to oxidise (such as Group **δ**).

The positive potential shift that is observed for the first reduction events of complexes **2b**, **2d**, **3a** correlate with literature reports of CO_2 electroreduction activity (Table 5.3–11).[16,52,57–59,61] The altered cathodic behaviour recorded for the complex series **1**–**4** relate well to the results recently reported for a series of Ag(I)BIAN$_2$ complexes that showed electrocatalytic CO_2 reduction activity,[15] providing further evidence to support the conclusion that the reported complexes are interacting with CO_2 in solution.

The new reduction peak observed in the CO_2-containing DPV of DippBIAN at –1.95 V is due to positive shift of the reduction potentials for the ligand. The new reduction peak observed in both the CV and DPV of complex **3a** in the presence of CO_2 (–1.14 V) is due to an interaction between the dissolved CO_2 and the reduced intermediate [**3a**$^-$], resulting in a pronounced increase in cathodic CV current (50 µA) over a broad potential range (–1.1 V to –1.7 V) due to CO_2 electroreduction, even in the absence of a proton source.[16,18,46,52,56,57,60]

The disappearance of DPV peaks from the voltammograms of the free Dipp- and MesBIAN ligands may be the result of their charged radicals reacting with the CO_2 as a pseudo-ketone moiety following an associative electrostatic interaction as depicted in Scheme 5.3–7b.[61] Reactivity of the ligands' radical [BIAN^{1-}] state with the CO_2 would increase the degree of disproportionation normally observed between the [BIAN^{1-}] and [BIAN^{2-}] charged states,[66,67] compounding the irreversibility of these reduction events as observed in Figure 5.3–1 and Figure I.1–2. Such associate chemical reactions have previously been reported between doubly reduced quinones (Q^{2-}) and dissolved CO_2, accompanied by a positive shift in reduction potentials of a magnitude proportional to the molar equivalents of CO_2 that the quinones reacted with.[62]

© University of Pretoria

The decreased cathodic current and absence of the reduction peak at –1.80 V in the CO_2-containing DPV of complex **4a** suggest a decrease in the degree of decomposition of the complex during the electrochemical analysis, whereas the disappearance of complex **4b**'s third reduction peak at –1.53 V indicates possible CO_2-adduct formation at low potentials.[16,18,46,52,56,57,60]

The reduction CV of **4a** in the presence of CO_2 (Figure I.1–21) shows a +20 µA decrease in cathodic current at potentials below –1.3 V, and the DPV peak for **4a** at –1.88 V is not observed. The reduction potentials of **1a** are negative shifted by 30–40 mV in the presence of CO_2, and a slight decrease in cathodic CV current is also noted. The previously reported CO_2 reduction activity of **4a**, as well as **1a**, was not observed under the experimental conditions employed in this study.[16,18] However, this may be attributed to a combination of factors including:

- 1) The series of complexes **1**–**4** was not stable in the coordinating solvents dimethyl formamide (DMF) and CH_3CN that are often used in literature for electrochemical analysis, limiting our experiments to the non-coordinating CH_2Cl_2 solvent.
- 2) The lower solubility of CO_2 in CH_2Cl_2 compared to CH_3CN or DMF, resulting in decreased CO_2 concentrations at the electrode surface under the present experimental conditions.
- 3) The electrolyte solutions did not contain any proton sources, limiting the number of possible CO_2 reduction mechanisms which may occur.[15,16,46,56,57,60]

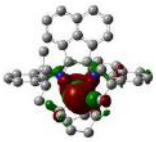
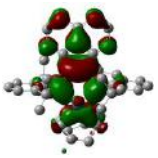
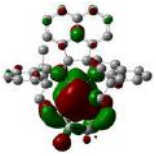
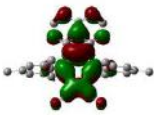
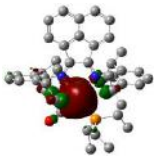
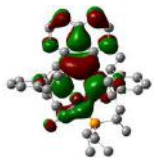
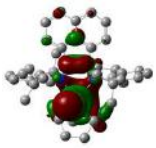
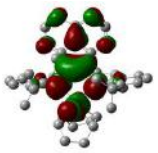
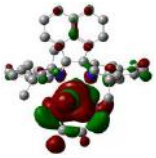
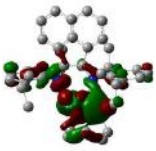
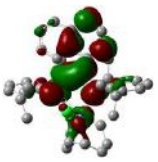
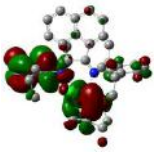
5.3.3.vii) Potential Drop and Future Prospects

The electroreduction of CO_2 has been established to occur as part of an inner sphere electron transport mechanism.[68] The application of Walsh diagrams have unequivocally shown that electron density transfer occurs from a donor species to the LUMO orbital of CO_2, thereby favouring its reduction.[69] Bearing these facts in mind, we visually inspected the spatial orientations of the HOMO, LUMO, and higher order LUMOs for the (n = 0) states for all the complexes in an effort to understand the difference in their CO_2 reactivity. Higher order LUMOs (LUMO+x) with orbital spatial distributions of near-HOMO character, not orbital composition, were identified for all complexes and utilised to calculate potential drops ($\Delta E_{(LUMO)}$) as illustrated in Table 5.3–12 (and Table I.2–1).

The LUMO+x for **3a** with near-HOMO character was identified as LUMO+4, yielding a potential drop value of 2.58 eV. In contrast, the LUMO+x for the series of complexes **1**, **2**, and **4** are found beyond LUMO+3 with potential drop values greater than 2.7 eV. The low lying LUMO+x of **3a** in addition to its small $\Delta E_{(LUMO)}$ value may facilitate the movement of electrons from a donor to an acceptor,[70,71] thus promoting the reduction of CO_2.

© University of Pretoria

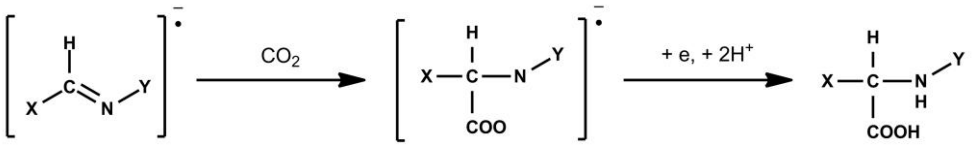
*Table 5–13: A summary of the DPV peak potentials (V vs Ag/Ag⁺) recorded for complex series **1–4** in solutions saturated with either Ar (g) or CO_2 (g). Key: * Electrochemically reversible events. ‡ Events were not observed in the CO_2 saturated solutions. § New peak observed in the CO_2 saturated solutions. † CV potentials measured at half peak height. # $\Delta E_{(LUMO)} = E_{LUMO+x} - E_{LUMO}$ (in eV), where LUMO +x is the higher order LUMO with near-HOMO character based on orbital spatial distribution.*

Compound	Red. 2	Red. 1	Ox. 1	$\Delta E_{(LUMO)}$#	HOMO	LUMO	LUMO + x
1a	–1.53	–0.56*	+1.31*	2.73			 LUMO +4
1a + CO_2	–1.56	–0.60*	+1.40*				
2b	–0.90*	–0.61	+1.04	2.82			 LUMO +6
2b + CO_2	–0.82†*	–0.54†	+1.09†				
3a	–1.79	–0.77*	+1.36	2.58			 LUMO +4
3a + CO_2	–1.14§	–0.75*	+1.38				
4a	–1.15	–0.18*	+0.77	2.99			 LUMO +8
4a + CO_2	–1.14	–0.18*	+0.79				
4c	–1.02*	–0.16*	+0.70	2.86			 LUMO +7
4c + CO_2	–1.03*	–0.16*	+0.70				

Minor variances between the Dipp- and MesBIAN analogue complexes of Rh(I), and Ir(I), are noted upon closer inspection of the $\Delta E_{(LUMO)}$ value in Table 5.3–12 and Table I.2–1. Seeing as the aryl-units of an Ar-BIAN are not co-planar with the delocalised aromatic orbitals of the bisimine nitrogens and acenaphthene rings, the substituents on the aryl-units of the Ar-BIAN may be expected not to significantly influence the electron density of the bisimine moiety itself.[72] However, a linear correlation has been observed between the electron donating or electron withdrawing strength of the substituents on the aryl-units of an Ar-BIAN, and the electrochemical reaction potentials of the Ar-BIAN compound.[72,73]

© University of Pretoria

Comparing the first reduction potentials of the DippBIAN and MesBIAN complexes reveal a shift to more negative potentials for MesBIAN complexes, corresponding to literature reports attributed to the increased electron donating strength of the *para*-methyl substituent.[72,73] It is therefore feasible that the electrocatalytic reactivity of complexes bearing Ar-BIAN ligands may be modulated, much as the redox potentials of the free ligands are, by selective variation of the aryl-substituents on the Ar-BIAN ligand to include stronger electron donating and withdrawing functionalities.



Scheme 5.3–8: The mechanism proposed by Koshechko et al.[61] for the electrochemical reactivity between CO_2 and imines.

The enhanced CO_2 reduction activity of a complex bearing two π-acceptor ancillary ligands may at first be counter intuitive, as π-acceptor ligands are anticipated to decrease the electron density on the metal centre, consequently decreasing its electron donor ability.[15] However, in light of the electrochemical reactivity of imine containing compounds with CO_2 (Scheme 5.3–8),[61] the electroreduction reactivity of **3a** may be localised on the bisimine moiety and not the metal centre as classically envisioned for catalytic reactions. This hypothesis is at present strictly restricted to an academic discussion in lieu of additional experimental evidence. Determination of the electroreduction mechanism may only be feasible once the reported reactivity of the complexes with CO_2 have been quantitatively investigated.

In a recent publication by Krisch *et al*. on the electrocatalytic activity of their Ag(I) bis-BIAN complexes with CO_2, the authors noted a pronounced increase in the cathodic CO_2 reduction current upon addition of a proton source to their electrolytic solutions.[15] Similarly, Vollmer *et al*. observed a near two-fold increase in the cathodic current associated with CO_2 reduction activity for their α-diimine complexes following the addition of 2,2,2-trifluoroethanol (TFE) to the electrochemical cell as a proton source.[60] The octahedral $Re(CO)_3Cl$ complexes of Dipp- and MesBIAN were shown to be active CO_2 reduction catalysts producing CO (g), with their activity substantially increasing after addition of 2 % H_2O to the CH_3CN solution and forming H_2 (g) in addition to CO.[46] While the presence of protons in the electrolyte solution is anticipated to increase the solubility of CO_2, their enhancement of the cathodic currents and CO_2 electroreduction activity is also due to an increase in the number of possible reaction mechanisms by which CO_2 may be reduced.[56]

© University of Pretoria

In an aprotic reaction environment, reduction of CO_2 can result in the formation of either oxalate anions ($C_2O_4^{2-}$) through reductive addition, or CO (g) and CO_3^{2-} anions through disproportionation of two CO_2^{1-} anions. However, with H^+ ions available in solution, a wide variety of compounds may be formed through alternative reaction mechanism, including methane (CH_4), methanol (CH_3OH), formaldehyde (HCHO), formic acid (HCOOH) and ethylene (C_2H_4).[16,56,57] In order to propose a fully informed reaction mechanisms by which complexes such as **3a** may electrocatalytically reduce CO_2, additional experimentation in both protic and aprotic mediums is essential, as well as the characterisation and quantification of products that are formed during the reactions.

5.4) Conclusion

The catalytic reactivity screening assays for the series of complexes **1**–**4** towards dimerization, hydroamination and hydrothiolation of both alkene and alkyne substrates were performed by monitoring NMR-scale reactions. The results of this investigation will be assessed to inform the feasibility of our future research into the catalytic reactivity of the reported series of complexes.

It was observed that all complexes displayed enhanced catalytic conversion of substrate in the non-polar solvent C_6D_6 for most reactions compared to the polar aprotic $CDCl_3$. In addition, it was observed that the polarity of the solvent also influenced the stereo- and regioselectivity of the catalysts in many reactions.

It was noted for many of the catalytic reactions that the total yield of 1,1- and 1,2-addition products which could be detected, as determined by integration of the NMR signals (see Section 5.2.2.ii), were much lower than the total conversion of substrate(s) that were observed in the samples. In conjunction with the experimental observations of changes in the reaction solutions before and after reflux, such as the development of off-white precipitates and increases in the viscosity of reaction solutions, it is postulated that polymerisation products formed in addition to the anticipated 1,1– and 1,2–addition products. Future investigation of these experiments on a larger reaction scale may enable both the detection and identification of any polymerisation products that are formed.

The Ir(I)-cod complexes **1c**, **1d**, **4c** and **4d** displayed the highest percentage yield of alkene dimerization products in both $CDCl_3$ and C_6D_6 solutions. Interestingly, the DippBIAN complexes **1c** and **4c** produced the 1,1–addition products exclusively in C_6D_6, whereas the MesBIAN complexes **1d** and **4d** produced the 1,2–addition products.

© University of Pretoria

All complexes showed poor conversion in the alkyne dimerization reactions, with 4 % being the highest total yield recorded. The complex series **1**–**4** is therefore not deemed active towards alkyne dimerization under the reaction conditions employed in this study.

The Rh(I)-phosphine complex **3a** showed an unusual regioselectivity for 1,2–addition during alkene hydroamination in $CDCl_3$, albeit in very low yields (6 %), whereas many of the other complexes favoured 1,1–addition product formation. However, it was noted that although the reactions performed in C_6D_6 showed an increased degree of substrate conversion, they also showed a decreased selectivity for the hydroamination of the alkene substrate. Indeed, a marked increase in alkene dimerization by-products were noted in the C_6D_6 reactions.

Although the highest total yield recorded for the alkyne hydroamination reactions was a low 6 % (for complex **4d**), it was observed that the percentage conversion of the 1-hexyne and n-butylamine substrates in most of the test reactions exceeded the total yield of 1,1- and 1,2-addition products that could be detected as determined by integration of the NMR signals.

The results for the alkene hydrothiolation reactions were similarly disproportionate in the low amounts of product that were detectable in the reaction solutions compared to the degree of substrate conversion displayed by the catalysts. As noted earlier, the percentage conversion of both alkene and thiol substrates in the $CDCl_3$ solutions were far exceeded by those of the analogous reactions done in C_6D_6. Complexes **2a** and **4a** showed near quantitative conversion of the substrates, however, only 1 % and 2 % total yield of product was observed in the NMR spectra of the samples. Therefore, it is recommended that future investigation into these reactions be done on a larger molar scale to enable the isolation and characterisation of the reaction products.

It is postulated that the divergent conversion and yield percentages, in combination with the precipitation that is observed in some of the catalytic reactivity assays, may indicate the formation of polymerisation products that were insoluble in the reaction solvents. Future research into these catalytic reactions should therefore be conducted on a larger molar scale to enable the isolation, purification, and characterization of the end-products, not only to eliminate the possibility that the observed precipitates are due to the decomposition of the catalysts, but also to establish the chemical and structural nature of the polymerisation product (if detected).

© University of Pretoria

By far the best catalytic reactivity among the complex series **1**–**4** was observed in the alkyne hydrothiolation reactions, with minimal amounts of dimerization by-products detected and yields near equivalent to the percentage conversion of substrates suggesting minimal polymerisation side-reactions. The Ir(I)-cod chloride complexes **4c** and **4d** displayed the highest overall yields in the $CDCl_3$ solutions, regioselectively forming the 1,1–addition products with the 1,1–(*E*) stereoisomer in enantiomeric excess of 82 %. While the total yield and regioselectivity achieved by complexes **4c** and **4d** in C_6D_6 was somewhat decreased, their stereoselectivity for the formation of the 1,1–(*E*)–addition product was greatly enhanced to 100 % enantiomeric excess. Although the stereoselectivity of the reactions of complexes **4a** and **4b** in C_6D_6 favoured the production of the 1,1-addition product, these reactions showed the highest recorded yields for production of the geminal 1,2–addition product, forming 15 % and 10 % respectively.

The alkyne dimerization reactions of the series of complexes **1**–**4** displayed poorer conversions compared to the alkene dimerization reactions. This result was unexpected seeing as catalytic alkyne transformations are generally more favourable than alkene transformations due to the greater ease with which the C≡C bond of the alkyne undergoes oxidative addition/reductive elimination compared to the C=C of the alkene.

The catalysed alkyne hydrothiolation reactions displayed the highest conversions, which could potentially be rationalized by considering two factors. Firstly, the ease with which the alkyne C≡C bonds may undergo oxidative addition/reductive elimination. And secondly, the more acidic S–H bond of the thiol hydrothiolation substrate, compared to that of the N–H bond in the amine hydroamination substrate, is more susceptible to the oxidative addition/reductive elimination steps that constitute the individual catalytic reaction steps.

It was also demonstrated that the catalytic reactivity of the Dipp- and MesBIAN complexes may be altered by *in situ* chemical reduction of the complexes through the addition of catalytic amounts of $CoCp_2$ to the reaction mixture. Perhaps the most notable perturbation of reactivity was observed in the alkyne hydrothiolation of the chemically reduced **2b** and **3a**. While the overall yield delivered by both of these reactions were decreased compared to their original reactivity, the regioselectivity of the complexes changed to favour the production of the geminal 1,2–addition product over the 1,1–addition product as observed in the original reactions.

© University of Pretoria

As noted in Chapter 2, several of the reported complexes proved to be air-sensitive following prolonged exposure to atmospheric conditions. To mitigate decomposition of the complexes in solution, care was taken to prepare the reaction solutions fresh before each measurement of the t=0 NMR spectra. In this preliminary study, tests to rule out heterogeneous catalytic activity have not been conducted (e.g., a Hg-drop test).[74] The possibility of conversion due to the catalytic activity of decomposition products of the metal complex (pre)catalyst therefore cannot be excluded.

Lastly, in the presence of CO_2, the reduction events of complex **2b** and **2d** displayed a positive shift in reaction potentials, and modest upturn in cathodic current between –1.0 V and –1.9 V, indicative of an associative interaction between the complex and CO_2. While the reduction potentials of complex **3a** in the presence of CO_2 did not show the same extent of positive shift as observed for **2b**, an addition reduction peak was observed at –1.14 V producing a 50 µA increase in cathodic peak current –1.0 V and –1.7 V. Future experimentation on the catalytic CO_2 electroreductive ability of the series of complexes **1**–**4** should therefore also include experimental procedures with a proton source to evaluate whether these complexes are catalytically active towards the formation of CO_2 reduction products other than oxalate and CO (g).[16,56,57] In addition, computational modelling of the complex-CO_2 interactions will expedite elucidation of the reaction mechanisms by which the electrocatalytically active complexes facilitate CO_2 electroreduction.

© University of Pretoria

5.5) References

(1) Johnson, L. K.; Killian, C. M.; Brookhart, M. New Pd(II)- and Ni(II)-Based Catalysts for Polymerization of Ethylene and α-Olefins. *J Am Chem Soc* **1995**, *117* (23), 6414–6415. https://doi.org/10.1021/ja00128a054.

(2) Liu, W.; Brookhart, M. Mechanistic Studies of Palladium(II)-a-Diimine-Catalyzed Polymerizations of Cis- and Trans-2-Butenes. *Organometallics* **2004**, *23* (26), 6099–6107. https://doi.org/10.1021/om040077m.

(3) Williams, B. S.; Leatherman, M. D.; White, P. S.; Brookhart, M. Reactions of Vinyl Acetate and Vinyl Trifluoroacetate with Cationic Diimine Pd(II) and Ni(II) Alkyl Complexes: Identification of Problems Connected with Copolymerizations of These Monomers with Ethylene. *J Am Chem Soc* **2005**, *127* (14), 5132–5146. https://doi.org/10.1021/ja045969s.

(4) Shiotsuki, M.; White, P. S.; Brookhart, M.; Templeton, J. L. Mechanistic Studies of Platinum(II)-Catalyzed Ethylene Dimerization: Determination of Barriers to Migratory Insertion in Diimine Pt(II) Hydrido Ethylene and Ethyl Ethylene Intermediates. *J Am Chem Soc* **2007**, *129* (13), 4058–4067. https://doi.org/10.1021/ja068118o.

(5) Khlebnikov, V.; Meduri, A.; Mueller-Bunz, H.; Montini, T.; Fornasiero, P.; Zangrando, E.; Milani, B.; Albrecht, M. Palladium Carbene Complexes for Selective Alkene Di- and Oligomerization. *Organometallics* **2012**, *31* (3), 976–986. https://doi.org/10.1021/om201027y.

(6) Zhang, D.; Nadres, E. T.; Brookhart, M.; Daugulis, O. Synthesis of Highly Branched Polyethylene Using “Sandwich” (8-p-Tolyl Naphthyl α-Diimine)Nickel(II) Catalysts. *Organometallics* **2013**, *32* (18), 5136–5143. https://doi.org/10.1021/om400704h.

(7) Daugulis, O.; Macarthur, A. H. R.; Rix, F. C.; Templeton, J. L. A Career in Catalysis: Maurice Brookhart. *ACS Catal* **2016**, *6* (3), 1518–1532. https://doi.org/10.1021/acscatal.5b02216.

(8) van Asselt, R.; Gielens, E. E. C. G.; Rulke, R. E.; Vrieze, K.; Elsevier, C. J. Rigid Bidentate Nitrogen Ligands in Organometallic Chemistry and Homogeneous Catalysis. 3. Insertion of Carbon Monoxide and Alkenes into Palladium-Carbon Bonds of Complexes Containing Rigid Bidentate Nitrogen Ligands: The First Example of Isolated Complex. *J Am Chem Soc* **1994**, *116* (3), 977–985. https://doi.org/10.1021/ja00082a020.

(9) van Laren, M. W.; Elsevier, C. J. Selective Homogeneous Palladium(0)- Catalyzed Hydrogenation of Alkynes to (Z)- Alkenes. *Angew. Chem. Int. Ed.* **1999**, *38* (24), 3715–3717.

(10) Nunes, C. D.; Vaz, P. D.; Félix, V.; Veiros, L. F.; Moniz, T.; Rangel, M.; Realista, S.; Mourato, A. C.; Calhorda, M. J. Vanadyl Cationic Complexes as Catalysts in Olefin Oxidation. *Dalton Transactions* **2015**, *44* (11), 5125–5138. https://doi.org/10.1039/C4DT03174A.

© University of Pretoria

(11) Fomenko, I. S.; Gushchin, A. L.; Shul'pina, L. S.; Ikonnikov, N. S.; Abramov, P. A.; Romashev, N. F.; Poryvaev, A. S.; Sheveleva, A. M.; Bogomyakov, A. S.; Shmelev, N. Y.; Fedin, M. V.; Shul'pin, G. B.; Sokolov, M. N. New Oxidovanadium(Iv) Complex with a BIAN Ligand: Synthesis, Structure, Redox Properties and Catalytic Activity. *New Journal of Chemistry* **2018**, *42* (19), 16200–16210. https://doi.org/10.1039/C8NJ03358G.

(12) Supej, M. J.; Volkov, A.; Darko, L.; West, R. A.; Darmon, J. M.; Schulz, C. E.; Wheeler, K. A.; Hoyt, H. M. Aryl-Substituted BIAN Complexes of Iron Dibromide: Synthesis, X-Ray and Electronic Structure, and Catalytic Hydrosilylation Activity. *Polyhedron* **2016**, *114*, 403–414. https://doi.org/10.1016/j.poly.2016.02.020.

(13) Omosun, N. N.; Smith, G. S. Water-Soluble, Disulfonated Alpha-Diimine Rhodium(I) Complexes: Synthesis, Characterisation and Application as Catalyst Precursors in the Hydroformylation of 1-Octene. *Eur J Inorg Chem* **2019**, *2019* (20), 2558–2564. https://doi.org/10.1002/ejic.201900317.

(14) Williams, O. M.; Cowley, A. H.; Rose, M. J. Structural and Electronic Characterization of Multi-Electron Reduced Naphthalene (BIAN) Cobaloximes. *Dalton Transactions* **2015**, *44* (29), 13017–13029. https://doi.org/10.1039/C5DT00924C.

(15) Krisch, D.; Sun, H.; Pellumbi, K.; Faust, K.; Apfel, U.-P.; Schöfberger, W. Tuning the Electronic Properties of Homoleptic Silver(I) Bis-BIAN Complexes towards Efficient Electrocatalytic CO2 Reduction. *Catalysts* **2022**, *12* (5), 545. https://doi.org/10.3390/catal12050545.

(16) Gushchin, A. L.; Romashev, N. F.; Shmakova, A. A.; Abramov, P. A.; Ryzhikov, M. R.; Fomenko, I. S.; Sokolov, M. N. Novel Redox Active Rhodium(III) Complex with Bis(Arylimino)Acenaphthene Ligand: Synthesis, Structure and Electrochemical Studies. *Mendeleev Communications* **2020**, *30* (1), 81–83. https://doi.org/10.1016/j.mencom.2020.01.027.

(17) Hasan, K.; Wang, J.; Pal, A. K.; Hierlinger, C.; Guerchais, V.; Sen Soo, H.; García, F.; Zysman-Colman, E. Bay-Region Functionalisation of Ar-BIAN Ligands and Their Use Within Highly Absorptive Cationic Iridium(III) Dyes. *Sci Rep* **2017**, *7* (1), 15520. https://doi.org/10.1038/s41598-017-14996-4.

(18) Romashev, N. F.; Gushchin, A. L.; Fomenko, I. S.; Abramov, P. A.; Mirzaeva, I. V.; Kompan'kov, N. B.; Kal'nyi, D. B.; Sokolov, M. N. A New Organometallic Rhodium(I) Complex with Dpp-Bian Ligand: Synthesis, Structure and Redox Behaviour. *Polyhedron* **2019**, *173*, 114110. https://doi.org/10.1016/j.poly.2019.114110.

(19) Rumble, S. L. The Synthesis of Amines and Imines Using Organometallic Catalysts. Doctor of Philosophy, University of New South Wales, 2005.

© University of Pretoria

(20) Rumble, S. L.; Page, M. J.; Field, L. D.; Messerle, B. A. In Situ Catalysts for the Intramolecular Hydroamination of Aminoalkynes - What Ligand Properties Determine Catalyst Activity? *Eur J Inorg Chem* **2012**, *2012* (13), 2226–2231. https://doi.org/10.1002/ejic.201101307.

(21) Hua, C.; Vuong, K. Q.; Bhadbhade, M.; Messerle, B. A. New Rhodium(I) and Iridium(I) Complexes Containing Mixed Pyrazolyl-1,2,3-Triazolyl Ligands as Catalysts for Hydroamination. *Organometallics* **2012**, *31* (5), 1790–1800. https://doi.org/10.1021/om201171b.

(22) Tregubov, A. A.; Vuong, K. Q.; Luais, E.; Gooding, J. J.; Messerle, B. A. Rh(I) Complexes Bearing N, N and N,P Ligands Anchored on Glassy Carbon Electrodes: Toward Recyclable Hydroamination Catalysts. *J Am Chem Soc* **2013**, *135* (44), 16429–16437. https://doi.org/10.1021/ja405783g.

(23) Colby, D. A.; Bergman, R. G.; Ellman, J. A. Rhodium-Catalyzed C-C Bond Formation via Heteroatom-Directed C-H Bond Activation. *Chem Rev* **2010**, *110* (2), 624–655. https://doi.org/10.1021/cr900005n.

(24) Burling, S.; Field, L. D.; Messerle, B. A.; Vuong, K. Q.; Turner, P. Rhodium(I) and Iridium(I) Complexes with Bidentate N,N and P,N Ligands as Catalysts for the Hydrothiolation of Alkynes. *Dalton Transactions* **2003**, *3* (21), 4181–4191. https://doi.org/10.1039/B303774F.

(25) Strydom, I.; Guisado-Barrios, G.; Fernández, I.; Liles, D. C.; Peris, E.; Bezuidenhout, D. I. A Hemilabile and Cooperative N-Donor-Functionalized 1,2,3-Triazol-5-Ylidene Ligand for Alkyne Hydrothiolation Reactions. *Chemistry - European Journal* **2017**, *1* (I), 1393–1401. https://doi.org/10.1002/chem.201604567.

(26) Kleinhans, G.; Guisado-Barrios, G.; Liles, D. C.; Bertrand, G.; Bezuidenhout, D. I. A Rhodium(i)-Oxygen Adduct as a Selective Catalyst for One-Pot Sequential Alkyne Dimerization-Hydrothiolation Tandem Reactions. *Chemical Communications* **2016**, *52* (17), 3504–3507. https://doi.org/10.1039/c6cc00029k.

(27) Bourissou, D.; Guerret, O.; Gabbaï, F. P.; Bertrand, G. Stable Carbenes. *Chem Rev* **2000**, *100* (1), 39–91. https://doi.org/10.1021/cr940472u.

(28) Bikrani, M.; Garralda, M. A.; Ibarlucea, L.; Pinilla, E.; Torres, M. R. Pentacoordinated Cationic Rhodium(I) and Iridium(I) Organocomplexes with α-Diimine Ligands Derived from Glyoxal: Crystal Structure of [Rh(Norbornadiene) (Glyoxalbis(4-Dimethylamino-Anil))-(PPh3)]BF4·1/2CH2Cl2. *Inorganica Chim Acta* **1998**, *282* (2), 230–236. https://doi.org/10.1016/s0020-1693(98)00237-0.

(29) Aucamp, D.; Witteler, T.; Dielmann, F.; Siangwata, S.; Liles, D. C.; Smith, G. S.; Bezuidenhout, D. I. A Triarylated 1,2,3-Triazol-5-Ylidene Ligand with a Redox-Active Ferrocenyl Substituent for

© University of Pretoria

Rhodium(I)-Catalyzed Hydroformylation of 1-Octene. *Eur J Inorg Chem* **2017**, *2017* (9), 1227–1236. https://doi.org/10.1002/ejic.201700164.

(30) Fernández-Alvarez, F. J.; Iglesias, M.; Oro, L. A.; Polo, V. CO2 Activation and Catalysis Driven by Iridium Complexes. *ChemCatChem* **2013**, *5* (12), 3481–3494. https://doi.org/10.1002/cctc.201300559.

(31) Munz, D. Pushing Electrons - Which Carbene Ligand for Which Application? *Organometallics* **2018**, *37* (3), 275–289. https://doi.org/10.1021/acs.organomet.7b00720.

(32) Field, L. D.; Messerle, B. A.; Vuong, K. Q.; Turner, P. Rhodium(I) and Iridium(I) Complexes Containing Bidentate Phosphine-Imidazolyl Donor Ligands as Catalysts for the Hydroamination and Hydrothiolation of Alkynes. *Dalton Transactions* **2009**, *38* (18), 3599. https://doi.org/10.1039/b821188d.

(33) Gunanathan, C.; Milstein, D. Bond Activation and Catalysis by Ruthenium Pincer Complexes. *Chem Rev* **2014**, *114* (24), 12024–12087. https://doi.org/10.1021/cr5002782.

(34) Wang, Z.; Lu, S. M.; Li, J.; Wang, J.; Li, C. Unprecedentedly High Formic Acid Dehydrogenation Activity on an Iridium Complex with an N,N'-Diimine Ligand in Water. *Chemistry - European Journal* **2015**, *21* (36), 12592–12595. https://doi.org/10.1002/chem.201502086.

(35) Valdés, H.; García-Eleno, M. A.; Canseco-Gonzalez, D.; Morales-Morales, D. Recent Advances in Catalysis with Transition-Metal Pincer Compounds. *ChemCatChem* **2018**, *10* (15), 3136–3172. https://doi.org/10.1002/cctc.201702019.

(36) Shaffer, D. W.; Ryken, S. A.; Zarkesh, R. A.; Heyduk, A. F. Redox Behavior of Rhodium 9,10-Phenanthrenediimine Complexes. *Inorg Chem* **2011**, *50* (1), 13–21. https://doi.org/10.1021/ic1007632.

(37) Liu, X.; Wang, F. Transition Metal Complexes That Catalyze Oxygen Formation from Water: 1979-2010. *Coord Chem Rev* **2012**, *256* (11–12), 1115–1136. https://doi.org/10.1016/j.ccr.2012.01.015.

(38) Petronilho, A.; Rahman, M.; Woods, J. A.; Al-Sayyed, H.; Müller-Bunz, H.; Don MacElroy, J. M.; Bernhard, S.; Albrecht, M. Photolytic Water Oxidation Catalyzed by a Molecular Carbene Iridium Complex. *Dalton Transactions* **2012**, *41* (42), 13074. https://doi.org/10.1039/c2dt30403a.

(39) Navarro, M.; Li, M.; Müller-Bunz, H.; Bernhard, S.; Albrecht, M. Donor-Flexible Nitrogen Ligands for Efficient Iridium-Catalyzed Water Oxidation Catalysis. *Chemistry - European Journal* **2016**, *22* (20), 6740–6745. https://doi.org/10.1002/chem.201600875.

(40) Broere, D. L. J.; Plessius, R.; Van Der Vlugt, J. I. New Avenues for Ligand-Mediated Processes-Expanding Metal Reactivity by the Use of Redox-Active Catechol, o-Aminophenol and o-

© University of Pretoria

Phenylenediamine Ligands. *Chem Soc Rev* **2015**, *44* (19), 6886–6915. https://doi.org/10.1039/c5cs00161g.

(41) Luca, O. R.; Crabtree, R. H. Redox-Active Ligands in Catalysis. *Chem. Soc. Rev.* **2013**, *42* (4), 1440–1459. https://doi.org/10.1039/C2CS35228A.

(42) Larson, P. J.; Wekesa, F. S.; Singh, A.; Smith, C. R.; Rajput, A.; McGovern, G. P.; Unruh, D. K.; Cozzolino, A. F.; Findlater, M. Synthesis, Characterization, Electrochemical Properties and Theoretical Calculations of (BIAN) Iron Complexes. *Polyhedron* **2019**, *159*, 365–374. https://doi.org/10.1016/j.poly.2018.11.060.

(43) Jay, R. M.; Banerjee, A.; Leitner, T.; Wang, R.-P.; Harich, J.; Stefanuik, R.; Wikmark, H.; Coates, M. R.; Beale, E. V.; Kabanova, V.; Kahraman, A.; Wach, A.; Ozerov, D.; Arrell, C.; Johnson, P. J. M.; Borca, C. N.; Cirelli, C.; Bacellar, C.; Milne, C.; Huse, N.; Smolentsev, G.; Huthwelker, T.; Odelius, M.; Wernet, P. Tracking C–H Activation with Orbital Resolution. *Science (1979)* **2023**, *380* (6648), 955–960. https://doi.org/10.1126/science.adf8042.

(44) van Asselt, R.; Elsevier, C. J. New Palladium Complexes of Cis-Fixed Bidentate Nitrogen Ligands as Catalysts for Carbon-Carbon Bond Formation. *Organometallics* **1992**, *11* (6), 1999–2001.

(45) van Asselt, R.; Elsevier, C. J. Homogeneous Catalytic Hydrogenation of Alkenes by Zero-Valent Palladium Complexes of Cis-Fixed Dinitrogen Ligands. *Journal of Molecular Catalysis* **1991**, *65* (3). https://doi.org/10.1016/0304-5102(91)85057-9.

(46) Portenkirchner, E.; Kianfar, E.; Sariciftci, N. S.; Knör, G. Two-Electron Carbon Dioxide Reduction Catalyzed by Rhenium(I) Bis(Imino)Acenaphthene Carbonyl Complexes. *ChemSusChem* **2014**, *7* (5), 1347–1351. https://doi.org/10.1002/cssc.201301116.

(47) Kianfar, E.; Monkowius, U.; Portenkirchner, E.; Knör, G. Synthesis and Characterization of Novel Re(BIAN)(CO)3Cl Derivatives Including the First Example of a Water-Soluble Tricarbonyl Rhenium(I) Complex with Bis(Imino)Acenaphthene Ligands. *Zeitschrift fur Naturforschung - Section B Journal of Chemical Sciences* **2014**, *69* (6), 691–698. https://doi.org/10.5560/ZNB.2014-4016.

(48) Abramov, P. A.; Dmitriev, A. A.; Kholin, K. V.; Gritsan, N. P.; Kadirov, M. K.; Gushchin, A. L.; Sokolov, M. N. Mechanistic Study of the [(Dpp-Bian)Re(CO)3Br] Electrochemical Reduction Using in Situ EPR Spectroscopy and Computational Chemistry. *Electrochim Acta* **2018**, *270*, 526–534. https://doi.org/10.1016/j.electacta.2018.03.111.

(49) Wang, W.; Wang, S.; Ma, X.; Gong, J. Recent Advances in Catalytic Hydrogenation of Carbon Dioxide. *Chem Soc Rev* **2011**, *40* (7), 3703. https://doi.org/10.1039/c1cs15008a.

© University of Pretoria

(50) Jessop, P. G.; Joó, F.; Tai, C.-C. Recent Advances in the Homogeneous Hydrogenation of Carbon Dioxide. *Coord Chem Rev* **2004**, *248* (21–24), 2425–2442. https://doi.org/10.1016/j.ccr.2004.05.019.

(51) Caix, C.; Chardon-Noblat, S.; Deronzier, A. Electrocatalytic Reduction of CO2 into Formate with [(H5-Me5C5)M(L)Cl]+ Complexes (L = 2,2′-Bipyridine Ligands; M = Rh(III) and Ir(III)). *Journal of Electroanalytical Chemistry* **1997**, *434* (1–2), 163–170. https://doi.org/10.1016/S0022-0728(97)00058-2.

(52) Elgrishi, N.; Chambers, M. B.; Wang, X.; Fontecave, M. Molecular Polypyridine-Based Metal Complexes as Catalysts for the Reduction of CO2. *Chemical Society Reviews*. 2017, pp 761–796. https://doi.org/10.1039/c5cs00391a.

(53) Makuve, N.; Mehlana, G.; Tia, R.; Darkwa, J.; Makhubela, B. C. E. Hydrogenation of Carbon Dioxide to Formate by α-Diimine RuII, RhIII, IrIII Complexes as Catalyst Precursors. *J Organomet Chem* **2019**, *899*, 120892. https://doi.org/10.1016/j.jorganchem.2019.120892.

(54) Sato, S.; Morikawa, T.; Kajino, T.; Ishitani, O. A Highly Efficient Mononuclear Iridium Complex Photocatalyst for CO 2 Reduction under Visible Light. *Angewandte Chemie - International Edition* **2013**, *52* (3), 988–992. https://doi.org/10.1002/anie.201206137.

(55) Kang, P.; Cheng, C.; Chen, Z.; Schauer, C. K.; Meyer, T. J.; Brookhart, M. Selective Electrocatalytic Reduction of CO2 to Formate by Water-Stable Iridium Dihydride Pincer Complexes. *J Am Chem Soc* **2012**, *134* (12), 5500–5503. https://doi.org/10.1021/ja300543s.

(56) Francke, R.; Schille, B.; Roemelt, M. Homogeneously Catalyzed Electroreduction of Carbon Dioxide - Methods, Mechanisms, and Catalysts. *Chem Rev* **2018**, *118* (9), 4631–4701. https://doi.org/10.1021/acs.chemrev.7b00459.

(57) Elouarzaki, K.; Kannan, V.; Jose, V.; Sabharwal, H. S.; Lee, J. Recent Trends, Benchmarking, and Challenges of Electrochemical Reduction of CO 2 by Molecular Catalysts. *Adv Energy Mater* **2019**, *9* (24), 1900090. https://doi.org/10.1002/aenm.201900090.

(58) Collin, J. P.; Sauvage, J. P. Electrochemical Reduction of Carbon Dioxide Mediated by Molecular Catalysts. *Coord Chem Rev* **1989**, *93* (2), 245–268. https://doi.org/10.1016/0010-8545(89)80018-9.

(59) Becker, J. Y.; Vainas, B.; Eger, R.; Kaufman, L. Electrocatalytic Reduction of CO2 to Oxalate by Ag II and Pd II Porphyrins. *Journal of the Chemical Society - Series Chemical Communications* **1985**, *0* (21), 1471–1472. https://doi.org/10.1039/C39850001471.

(60) Vollmer, M. V.; Machan, C. W.; Clark, M. L.; Antholine, W. E.; Agarwal, J.; Schaefer, H. F.; Kubiak, C. P.; Walensky, J. R. Synthesis, Spectroscopy, and Electrochemistry of (α-Diimine)M(CO)3Br,

© University of Pretoria

M = Mn, Re, Complexes: Ligands Isoelectronic to Bipyridyl Show Differences in CO2 Reduction. *Organometallics* **2015**, *34* (1), 3–12. https://doi.org/10.1021/om500838z.

(61) Koshechko, V. G.; Titov, V. E.; Bondarenko, V. N.; Pokhodenko, V. D. Electrochemical Carboxylation of Fluorocontaining Imines with Preparation of Fluorinated N-Phenylphenylglycines. *J Fluor Chem* **2008**, *129* (8), 701–706. https://doi.org/10.1016/j.jfluchem.2008.06.010.

(62) Yin, W.; Grimaud, A.; Azcarate, I.; Yang, C.; Tarascon, J. M. Electrochemical Reduction of CO2 Mediated by Quinone Derivatives: Implication for Li-CO2 Battery. *Journal of Physical Chemistry C* **2018**, *122* (12), 6546–6554. https://doi.org/10.1021/acs.jpcc.8b00109.

(63) Rosa, V.; Carabineiro, S. A.; Avilés, T.; Gomes, P. T.; Welter, R.; Campos, J. M.; Ribeiro, M. R. Synthesis, Characterisation and Solid State Structures of α-Diimine Cobalt(II) Complexes: Ethylene Polymerisation Tests. *J Organomet Chem* **2008**, *693* (4), 769–775. https://doi.org/10.1016/j.jorganchem.2007.12.007.

(64) Villa, M.; Miesel, D.; Hildebrandt, A.; Ragaini, F.; Schaarschmidt, D.; Jacobi von Wangelin, A. Synthesis and Catalysis of Redox-Active Bis(Imino)Acenaphthene (BIAN) Iron Complexes. *ChemCatChem* **2017**, *9* (16), 3203–3209. https://doi.org/10.1002/cctc.201700144.

(65) Connelly, N. G.; Geiger, W. E. Chemical Redox Agents for Organometallic Chemistry. *Chem Rev* **1996**, *96* (2), 877–910. https://doi.org/10.1021/cr940053x.

(66) Hill, N. J.; Vargas-Baca, I.; Cowley, A. H. Recent Developments in the Coordination Chemistry of Bis(Imino)Acenaphthene (BIAN) Ligands with s- and p-Block Elements. *Dalton Transactions* **2009**, *9226* (2), 240–253. https://doi.org/10.1039/b815079f.

(67) Fedushkin, I. L.; Skatova, A. A.; Chudakova, V. A.; Cherkasov, V. K.; Fukin, G. K.; Lopatin, M. A. Reduction of 1,2-Bis[(2,6-Diisopropylphenyl)Imino]Acenaphthene (Dpp-Bian) with Alkali Metals− A Study of the Solution Behaviour of (Dpp-Bian)N−[M^+]n (M = Li, Na;n = 1–4) with UV/Vis, ESR and 1H NMR Spectroscopy. *Eur J Inorg Chem* **2004**, *2004* (2), 388–393. https://doi.org/10.1002/ejic.200300351.

(68) Dunwell, M.; Yan, Y.; Xu, B. Understanding the Influence of the Electrochemical Double-Layer on Heterogeneous Electrochemical Reactions. *Current Opinion in Chemical Engineering*. June 2018, pp 151–158. https://doi.org/10.1016/j.coche.2018.05.003.

(69) Aresta, M.; Dibenedetto, A.; Quaranta, E. Reaction Mechanisms in Carbon Dioxide Conversion. *Reaction Mechanisms in Carbon Dioxide Conversion* **2015**, 1–409. https://doi.org/10.1007/978-3-662-46831-9/COVER.

© University of Pretoria

(70) Gayathri, S. S.; Patnaik, A. Electrical Rectification from a Fullerene[60]-Dyad Based Metal–Organic–Metal Junction. *Chem. Commun.* **2006**, No. 18, 1977–1979. https://doi.org/10.1039/B602203K.

(71) Gayathri, S. S.; Patnaik, A. A New Fullerene C60-Didodecyloxy Benzene Dyad: An Evidence for Ground State Electron Transfer. *Chem Phys Lett* **2005**, *414* (1–3), 198–203. https://doi.org/10.1016/j.cplett.2005.08.043.

(72) Viganò, M.; Ferretti, F.; Caselli, A.; Ragaini, F.; Rossi, M.; Mussini, P.; Macchi, P. Easy Entry into Reduced Ar-BIANH 2 Compounds: A New Class of Quinone/Hydroquinone-Type Redox-Active Couples with an Easily Tunable Potential. *Chemistry - European Journal* **2014**, *20* (44), 14451–14464. https://doi.org/10.1002/chem.201403594.

(73) Sprengers, J. W.; de Greef, M.; Duin, M. A.; Elsevier, C. J. Stable Platinum(0) Catalysts for Catalytic Hydrosilylation of Styrene and Synthesis of [Pt(Ar-bian)(η 2 -alkene)] Complexes. *Eur J Inorg Chem* **2003**, *2003* (20), 3811–3819. https://doi.org/10.1002/ejic.200300088.

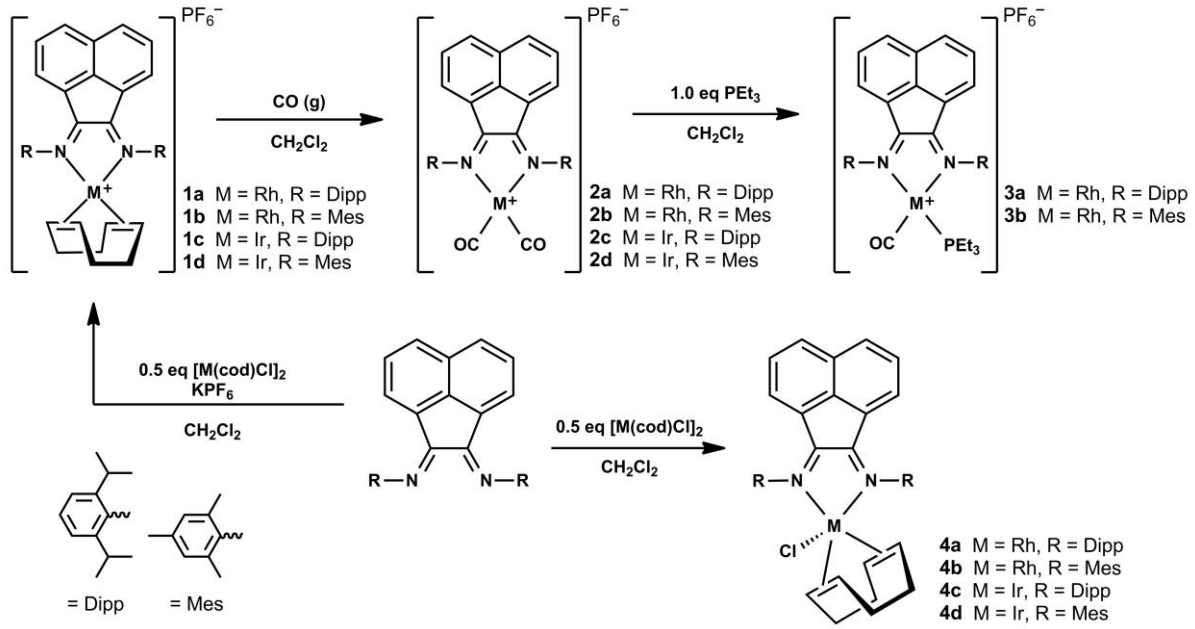
(74) Crabtree, R. H. Resolving Heterogeneity Problems and Impurity Artifacts in Operationally Homogeneous Transition Metal Catalysts. *Chem Rev* **2012**, *112* (3), 1536–1554. https://doi.org/10.1021/cr2002905.

© University of Pretoria

Chapter 6: Conclusions and Research Outlook

6.1) Conclusions

New Rh(I) and Ir(I) complexes of 4- and 5-coordinate geometries were synthesised utilising two traditional bis(aryl-imino)acenaphthene (BIAN) ligands, Dipp- and MesBIAN. Four groups of derivative complexes with ancillary ligands from across the spectrochemical series (low, mid and high field) were prepared and included σ-donor/π-donor (chloride), and σ-donor/π-acceptor ligands (1,5-cyclooctadiene, triethylphosphine and carbonyl) functionalities (Scheme 6.1-1).



Scheme 6–1: A schematic summary displaying the Number Convention used for the series of Rh(I)- and Ir(I)-BIAN complexes and derivatives that were investigated in this study.

6.1.1) Critical Comparison and Evaluation

The cod complex series **1a**–**d**, dicarbonyl complex series **2a**–**d**, and MesBIAN complexes **4b** and **4d** of Rh(I) and Ir(I) with cod and chloride are observed to adopt symmetrical molecular geometries in solution, as indicated by the BIAN–C**H** characteristic "*d-dd-d*" splitting patterns observed in the ^{1}H NMR spectra of these complexes. The ^{1}H and ^{13}C NMR signals associated with the aromatic-C**H** protons of the acenaphthene rings and the diimine quaternary carbons (N=**C$_q$**) showed a downfield shift compared to the spectra of the free BIAN ligands due to electron withdrawal by the coordinated metal centre. Complexes bearing the high field carbonyl ligands (**2a**–**d**) showed the greatest degree of downfield shift. The NMR spectra of the heteroleptic Rh(I)-carbonyl-triethylphosphine complex series **3a**–**b**, as well as the DippBIAN complexes **4a** and **4c** of Rh(I) and Ir(I) did not show the characteristic

© University of Pretoria

downfield "*d-dd-d*" peaks of the BIAN–C**H** protons, indicating that these complexes adopted asymmetric molecular geometries in solution. In addition, multiple upfield alkyl signals that are attributed to the Dipp- and Mes-C**H₃** groups were observed, illustrating the variance of the electronic environment in which each methyl-functional group is located. The asymmetric substitution characteristics observed in the NMR spectra of complexes **4a** and **4c** result from steric interactions between the isopropyl-moiety of the Dipp-substituent with the ancillary chlorido and cod ligands.

Single crystal X-ray Diffraction analyses of complexes **1b**, **1d**, **2a**–**c** and **3a** indicated that the Rh(I) and Ir(I) coordination spheres adopt slightly distorted square planar coordination geometries, with the dicarbonyl complex series **2a**–**c** showing the greatest extent of geometry deformation (τ_4 = 0.09–0.10). The neutral 5-coordinate Ir(I) complex **4c** adopts a square pyramidal coordination geometry (τ_5 = 0.00) with slight angular distortion of the axial Ir–Cl bond due to steric interactions between the chlorido and cod ancillary ligands, correlating well with the previously reported crystal structure of **4a**.[1]

6.1.2) Systematic Electrochemical Characterisation

Electrochemical measurements recorded in the non-coordinating solvent CH_2Cl_2, showed at least one electrochemically reversible, ligand-centred, reduction event for the complex series **1**–**4** at more positive potentials than the first reduction potentials of the free ligands. Electrochemically reversible, ligand-centred second reduction events were observed for the series of complexes **2a**–**d** and **4c**–**d**, indicating improved stabilisation of the reduced ligand by the electron withdrawing dicarbonyl ligands and the Ir(I)-chlorido coordination spheres. Evidence of metal-centred third reduction events were noted for the series of complexes **1c**–**d**, **2a**–**b** and **4a**–**d**, however, these reduction events were mostly irreversible and resulted in ligand dissociation and/or complex decomposition at potentials lower than –1.6 V (V vs Ag/Ag^+).

Complex **1a** was the only complex to show a fully reversible metal-centred oxidation event, while complexes **1c**, **2b**, and **4c** showed metal-centred oxidation events which were electrochemically reversible, but not chemically reversible on the timescale of the analyses. The irreversible second oxidation events observed for the series of complexes **1a**–**d**, **2a**–**b**, **3a**–**b**, and **4a**–**c** were determined to be ligand-centred. Interestingly, the ligand-centred second oxidation of complex **4d** showed electrochemically reversible characteristics, however, it was not chemically reversible on the timescale of the analysis.

© University of Pretoria

6.1.3) Computational Analysis of Electronic Structure

The optimised molecular geometries and thermal energies of the free DippBIAN and MesBIAN ligands, as well as the series of complexes **1**–**4**, in both gas phase and CH_2Cl_2 solution were determined computationally using DFT calculations. The compounds were modelled in eight different charged states (n = +4 to n = –3), where the integer "n" is representative of the number of electrons that have been added or removed. Linear Free Energy Relationships (LFERs) were investigated between the experimentally recorded DPV peak potentials of each compound, and various calculated theoretical properties of each compound (ex. HOMO/LUMO energies, Electron Affinity and Reaction Free Energy Change).

A high degree of linear correlation was observed in the "reactive" FMO vs E_{DPV} correlation plots, between the Frontier Molecular Orbital Energies of each modelled charged state and the experimental reaction potentials that were recorded using Differential Pulse Voltammetry (E_{DPV}). The development of LFERs such as these may facilitate the interpretation of electrochemical data for compounds that undergo multi-electron redox reactions.

Similar LFERs were drawn up for the theoretically calculated Electron Affinity (-EA(M)), Free energy change of reaction ($-\Delta G_{rxn}$), and theoretical half-reaction potentials (E_{cell}) for all of the reported compounds with only a modest linear correlation ($0.84 \leq R^2 \geq 0.92$). However, these relationships proved to be more sensitive to structural differences (functional groups) and chemical dissimilarities (identity of the coordinated metal) among the individual compounds that were being compared due to the underlying thermodynamic basis from which the properties are calculated. Comparison of chemically and/or structurally closer related compounds yielded a more accurate reflection of linear correlation, and excellent linear correlations ($0.93 \leq R^2 \geq 0.99$) were noted in the LFERs of –EA(M), $-\Delta G_{rxn}$, and E_{cell} vs E_{DPV} plots among the groups of complexes (**1a**–**b**, **2a**–**b**, etc.), and data for the individual complexes.

6.1.4) Peak Characterisation Model and Revised E_{DPV} Assignments

Following the identification of excellent LFERs between various theoretically calculated properties (e.g., "reactive" FMO, –EA(M), $-\Delta G_{rxn}$, and E_{cell}) and the experimentally determined E_{DPV} potentials among each group of complexes with similar ancillary ligands, and their modelled charged states, a Peak Characterisation Model integrating computational and experimental data was developed to assist in the analysis of convoluted voltammograms. Application of the Peak Characterisation Model enables the researcher to differentiate voltametric peaks associated with the primary electrochemical

© University of Pretoria

reaction of the analyte, from voltammetry peaks of impurities or secondary reactions that take place in the electrolyte solution.

The Peak Characterisation Model probes the statistical influence of introducing the queried voltametric peak potential on the aforementioned LFERs of a group of chemically and structurally closely related compounds/complexes. Inclusion of peak potentials that were not associated with the characteristic electrochemical reactivity of the complex series **1**–**4** decreased the linear correlation factor (R^2) and increased the Mean Absolute Deviation (MAD) and Root Mean Standard Deviation (RMSD) of the LFERs. In contrast, introduction of addition peak potentials (which were not utilised to set up the LFERs) which result in an increased linear correlation (R^2) and/or decreased absolute deviation in the LFERs of a complex, indicates that these potentials form part of the characteristic electrochemical reactivity description of that complex.

Application of the Peak Characterisation Model revealed that, in the DPVs of complexes **1c**, **1d**, **2b** and **4b**, the voltametric oxidation peaks with reaction potentials comparable to those observed in the DPVs of the free ligands were not due to ligand dissociation taking place during the course of the electrochemical analyses. These peaks are instead part of the characteristic electrochemical reactivity of the complexes, yielding valuable information about the metal-BIAN interactions within these complexes, and resulted in the revision of some the electrochemical potential assignments which had been made for these complexes. It is suggested that the ligand centred oxidation events of these complexes are less affected by the σ-basic interaction of the ligand with the metal and the electronic influence of the ancillary ligands due to the ligand centred nature of the molecular orbital composition of the respective charged states, featuring minimal to no contributions from the coordination sphere or ancillary ligands.

6.1.5) Catalytic Reactivity Screening and Redox Activation

The catalytic reactivity of the series of complexes **1**–**4** towards the dimerization, hydroamination and hydrothiolation of 1-hexene and 1-hexyne substrates were qualitatively screened using NMR-scale reaction assays in a non-polar solvent (C_6D_6) as well as a polar aprotic solvent ($CDCl_3$). It was observed that all complexes displayed an enhanced degree of catalytic conversion activity in non-polar solutions. In addition, the stereo- and regioselectivity of the various complexes towards many reactions were notably altered by the polarity of the solvent employed for the reaction.

© University of Pretoria

The Ir(I)-cod complexes **1c**, **1d**, **4c** and **4d** displayed the highest percentage yield of alkene dimerization products in both $CDCl_3$ and C_6D_6 solutions, with the DippBIAN complexes **1c** and **4c** producing exclusively the 1,1–addition products in C_6D_6, while the MesBIAN complexes **1d** and **4d** exclusively produced the 1,2–addition products in C_6D_6.

The series of complexes **1**–**4** are deemed to be inactive towards alkyne dimerization under the reaction conditions employed in this study, as they showed a poor degree of conversion. The Rh(I)-phosphine complex **3a** showed an unusual regioselectivity for 1,2–addition during alkene hydroamination in $CDCl_3$, albeit in very low yields (6 %), whereas many of the other complexes favoured 1,1–addition formation.

The percentage substrate conversions recorded in most of the alkene hydrothiolation and alkyne hydroamination reactions far exceeded the product yields that were detected, suggesting that polymerisation is taking place. Complexes **2a** and **4a** showed near quantitative conversion of the alkene hydrothiolation substrates, however, a total yield of only 1 % and 2 % respectively was observed.

The series of complexes **1**–**4** showed the best catalytic reactivity in the alkyne hydrothiolation reactions, with yields near equivalent to the percentage substrate conversions and minimal dimerization by-products detected. The Ir(I)-cod chlorido complexes **4c** and **4d** displayed the highest overall yields in $CDCl_3$, forming the 1,1–addition products regioselectively with the 1,1–(*E*) stereoisomer in enantiomeric excess (47 % yield with 64 % $ee_{(1,1\text{-}E)}$, and 43 % yield with 65 % $ee_{(1,1\text{-}E)}$ respectively). In contrast, complex **4b** outperformed all other complexes in term of total yields in C_6D_6. The stereoselectivity of **4c** and **4d** were greatly enhanced in the non-polar C_6D_6 solvent (100 % $ee_{(1,1\text{-}E)}$) but with notable decreases in total yield. Although the Rh(I)-cod chlorido complexes **4a** and **4b** did not show similar stereoselectivity, they produced the largest amounts of the geminal thiol 1,2–addition product, with 15 % and 10 % yield respectively.

The catalytic reactivity of a representative selection of the reported Dipp- and MesBIAN complexes (**1d**, **2b**, **3a**, and **4c**) was examined in the presence of a chemical reductant ($CoCp_2$) to investigate the possibility of *in situ* redox activation of these complexes through exploitation of the redox non-innocent properties of the BIAN ligand. The most prominent changes in catalytic reactivity were noted for the chemically reduced complexes **2b** and **3a** towards alkyne hydrothiolation. Although the overall product yield of these reactions decreased slightly compared to the reactions done in the

© University of Pretoria

absence of a reductant, the regioselectivity of the catalysts changed to favour the production of the geminal 1,2–addition product over the formation of the 1,1–addition products as observed in the original reactions.

6.1.6) Electrocatalytic CO_2 Reduction Ability Screening

Lastly, the reactivity of complex series **1**–**4** with CO_2 in solution was investigated to ascertain their potential as catalysts for CO_2 electroreduction. Alterations of the cathodic and/or anodic peak currents and peak potentials of electrochemical events observed in the CVs and DPVs of complexes in the presence of CO_2 are indicative of interactions between the CO_2 and the complexes. While minor modifications of the peak currents were observed in the CVs recorded for most of the complexes in the presence of CO_2, changes in the electrochemical reactivity of complexes **2b** and **3a** were most pronounced. The reduction events of complex **2b** displayed a prominent positive shift in reaction potentials in the presence of CO_2, indicative of an associate interaction between the complex and CO_2. The reduction potentials of complex **3a** also shifted to slightly more positive potentials upon introduction of CO_2 to the electrolytic solution, accompanied by the formation of a prominent new reduction peak at –1.14 V (V vs Ag/Ag^+) and concomitant 50 µA increase in cathodic peak current. Given the potential at which the new reduction event initiates, it is proposed that the first reduced state of complex **3a** (i.e. [**3a**$^{1-}$]) is the electrocatalytically active species.

6.1.7) Non-innocent Behaviour of BIANs

The non-innocent behaviour of the BIAN ligands among the series of complexes **1**–**4** is perhaps most evident in the abnormalities observed in the structural characterisation data of complexes **2a** and **4c** compared to those of **1b**, **1d**, **2b**–**c** and **3a**. As noted previously, determination of the oxidation state of the BIAN ligand in a coordination complex is largely substantiated in literature by the experimental determination of the C–N and C–C bond lengths within the BIAN bisimine N=C–C=N moiety and critically compared to literature values (Scheme 1.1–3).[2–7]

The crystal structures of complexes of **2a** and **4c** revealed that their bisimine C–N bonds are slightly longer compared to those in complexes **1b**, **1d**, **2b**–**c** and **3a**, indicating an increase in the C–N single bond character. Conversely, the bisimine C–C bond lengths in complexes **2a** and **4c** are slightly shorter than those observed in the crystal structures of complexes **1b**, **1d**, **2b**–**c** and **3a**, indicating an increase in C–C double bond character. The augmented bond lengths seen in the crystal structures of complexes **2a** and **4c** parallel the changes in bond character of the bisimine N=C–C=N moiety upon reduction which have been reported.[1,2,5,6,8–11] The structural deviations observed suggest that the

© University of Pretoria

DippBIAN ligand in complex **2a** is present as the doubly reduced [DippBIAN^{2-}] quinonate anion,[2–4,9,11] whereas in complex **4c** it presents features akin to the radical [DippBIAN^{1-}] semiquinonate monoanion.[2–6,9]

Based on the collective results of our multi-technique analyses,[7,12] however, it is imperative to note that no additional evidence was obtained to support the observation of the DippBIAN ligands in complexes **2a** and **4c** bearing an anodic charge. In fact, the crystal structures of **2a** and **4c** lack the additional counter ions necessary to stabilise the charge associated with reduced ligands. The square pyramidal coordination structure of the reported structure for **4a**,[1] in which rhodium is in oxidation state +1, is strikingly similar to that of **4c**. In addition, the electrochemical reactivity of complex **2a** and **4c** are comparable to those recorded for complexes **2b** and **4a**, respectively, having shown four successive reduction events between 0.0 V and –2.0 V (V vs Ag/Ag$^+$).

It is therefore implausible that the DippBIAN ligand in complexes **2a** and **4c** could be coordinated in an anionic state. The structural variances observed are in the crystal structures of complexes **2a** and **4c** are thus likely the result of electronic interactions of the ancillary ligands (carbonyl and chlorido) with the DippBIAN, evidencing the non-innocent behaviour of the DippBIAN ligand in complexes **2a** and **4c**. These observations and conclusions correlate well with the observations which have been drawn from the experimental results of electrochemical, EPR and computational analyses of previously reported BIAN complexes of various transition metals.[1,13–19]

6.2) Notes on Prospective Research

The conclusion of this study brings forth a number of conceivable research projects which may address latent queries and points of interest regarding the current Rh(I) and Ir(I) complexes of with Dipp- and MesBIAN. Following the promising catalytic reactivity and CO_2 electroreduction ability observed for the Rh(I)-phosphine complex **3a**, it is suggested that the synthesis and isolation of the analogous Ir(I)-phosphine complexes under more stringent inert conditions be perused to appraise and relate their reactivity with those of the complex series **1**–**4**.

During the catalytic reactivity screening assays performed on the series of complexes **1**–**4**, many of the catalytic reactions displayed a total product yield far lower than the total percentage of substrate(s) that reacted. In addition, the formation of off-white precipitates as well as changes in the viscosity of the reaction solutions before and after refluxing were noted in a number of reaction

© University of Pretoria

mixtures. It is proposed that polymerisation products may be formed alongside the expected 1,1– and 1,2–addition products of the catalytic dimerization, hydroamination, and hydrothiolation reactions. The researcher would advise that future studies into the catalytic reactivity of the series of complexes **1**–**4** towards alkene and/or alkyne polymerisation be performed on a larger mass scale to facilitate the isolation, purification, and characterisation of the polymerisation products, as well as the other catalysis by-products which are formed during the reactions.

The electroreduction of CO_2 in the absence of a proton source is known to form either oxalate dianions, or carbonate anions and CO (g).[8,20–22] However, numerous other CO_2 electroreductive products may be formed by including a proton source as part of the reductive reactions mechanism.[8,20,21,23] It is therefore recommended that additional CO_2 electroreduction studies be performed with complex series **1**–**4** in an electrolytic solution containing a sacrificial proton donor source (e.g. trifluoroethanol), to evaluate whether these complexes show electrocatalytic activity in the formation of electroreductive products other than the aforementioned oxalate, carbonate and CO (g). Computationally modelling the interactions of CO_2 with the electrocatalytically active complexes will facilitate elucidation of the CO_2 electroreduction reaction mechanisms. An informed understanding of the reaction mechanism will guide the development of novel electrocatalysts bearing modified BIAN or ancillary ligands to enhance their reactivity. In addition, chronoamperometric analysis of active electrocatalysts is proposed to establish the activity lifetime of the catalyst, and gas chromatographic head-space analysis of the electrochemical cell may assist in identification of the products formed.[21,22]

With the performance of computer hardware ever improving and becoming more affordable, more researchers around the world are readily gaining access to computational infrastructure thanks in part to initiatives such as the Centre for High Performance Computing (CHPC) that offers communal access to their computational clusters. Although the initial computational investment required to optimise and calculate the theoretical thermodynamic energies with sufficient accuracy may appear daunting, the Peak Characterisation Model described herein may be applied to different chemical systems irrespective of their molecular geometry or elemental composition. The accuracy with which the Model can be applied to characterise multi-electron electrochemical events may be refined semi-quantitatively by illustrating the functioning of the Model when applied to different test groups of compounds ranging from organic to organometallic.

© University of Pretoria

It is proposed that the reduced and/or oxidised derivatives of complex series **1**–**4** be synthesised and isolated in a future study to expand on the investigation of how their catalytic reactivity is affected by a change in their initial oxidation state. Isolating the purified reduced and/or oxidised derivatives for the catalytic studies precludes interference and secondary reactivity from chemical reducing/oxidising agent(s) in the reaction mixtures.

BIAN ligands featuring *para*-functionalised aryl-substituents have been reported to show low energy (376–448 nm) intra-ligand charge transfer absorptions between the acenaphthene and aryl-substituents,[24] which contributed to the photoluminescence observed in their zinc(II) complexes and the promising photovoltaic activity of their copper(I) complexes as visible light harvesters.[25–27] Complexes of Rh(I)- and Ir(I)-BIAN with such *para*-functionalised aryl-substituents are envisaged to display enhanced non-innocent behaviour and catalytic activity due to the low lying molecular orbitals of the acenaphthene rings and aryl-substituents.

Lastly, it is proposed that novel heterocyclic biscarbene-bisimine complexes may be synthesised through the continued development of the 1,2,3-triazolium derivatised BIAN ligand systems.[28] The *trans*-coordinated carbene and imine moieties are anticipated to show electron push-pull interactions between one another. The influence of these ostensibly conflicting interactions on the BIAN scaffold may thus be examined, in conjunction with the photochemical and molecular orbital distributions of the expanded aromatic ring systems in these complexes.

© University of Pretoria

6.3) References

(1) Romashev, N. F.; Gushchin, A. L.; Fomenko, I. S.; Abramov, P. A.; Mirzaeva, I. V.; Kompan'kov, N. B.; Kal'nyi, D. B.; Sokolov, M. N. A New Organometallic Rhodium(I) Complex with Dpp-Bian Ligand: Synthesis, Structure and Redox Behaviour. *Polyhedron* **2019**, *173*, 114110. https://doi.org/10.1016/j.poly.2019.114110.

(2) Khusniyarov, M. M.; Harms, K.; Burghaus, O.; Sundermeyer, J. Molecular and Electronic Structures of Homoleptic Nickel and Cobalt Complexes with Non-Innocent Bulky Diimine Ligands Derived from Fluorinated 1,4-Diaza-1,3-Butadiene (DAD) and Bis(Arylimino)Acenaphthene (BIAN). *Eur J Inorg Chem* **2006**, No. 15, 2985–2996. https://doi.org/10.1002/ejic.200600236.

(3) Viganò, M.; Ferretti, F.; Caselli, A.; Ragaini, F.; Rossi, M.; Mussini, P.; Macchi, P. Easy Entry into Reduced Ar-BIANH 2 Compounds: A New Class of Quinone/Hydroquinone-Type Redox-Active Couples with an Easily Tunable Potential. *Chemistry - European Journal* **2014**, *20* (44), 14451–14464. https://doi.org/10.1002/chem.201403594.

(4) Fedushkin, I. L.; Skatova, A. A.; Chudakova, V. A.; Fukin, G. K. Four-Step Reduction of Dpp-bian with Sodium Metal: Crystal Structures of the Sodium Salts of the Mono-, Di-, Tri- and Tetraanions of Dpp-bian. *Angewandte Chemie* **2003**, *115* (28), 3416–3420. https://doi.org/10.1002/ange.200351408.

(5) Clark, K. M.; Bendix, J.; Heyduk, A. F.; Ziller, J. W. Synthesis and Characterization of a Neutral Titanium Tris(Iminosemiquinone) Complex Featuring Redox-Active Ligands. *Inorg Chem* **2012**, *51* (14), 7457–7459. https://doi.org/10.1021/ic301059p.

(6) Bendix, J.; Clark, K. M. Delocalization and Valence Tautomerism in Vanadium Tris(Iminosemiquinone) Complexes. *Angewandte Chemie - International Edition* **2016**, *55* (8), 2748–2752. https://doi.org/10.1002/anie.201510403.

(7) Larson, P. J.; Wekesa, F. S.; Singh, A.; Smith, C. R.; Rajput, A.; McGovern, G. P.; Unruh, D. K.; Cozzolino, A. F.; Findlater, M. Synthesis, Characterization, Electrochemical Properties and Theoretical Calculations of (BIAN) Iron Complexes. *Polyhedron* **2019**, *159*, 365–374. https://doi.org/10.1016/j.poly.2018.11.060.

(8) Gushchin, A. L.; Romashev, N. F.; Shmakova, A. A.; Abramov, P. A.; Ryzhikov, M. R.; Fomenko, I. S.; Sokolov, M. N. Novel Redox Active Rhodium(III) Complex with Bis(Arylimino)Acenaphthene Ligand: Synthesis, Structure and Electrochemical Studies. *Mendeleev Communications* **2020**, *30* (1), 81–83. https://doi.org/10.1016/j.mencom.2020.01.027.

© University of Pretoria

(9) Vasudevan, K.; Cowley, A. H. Synthesis and Structures of 1,2-Bis(Imino)Acenaphthene (BIAN) Lanthanide Complexes That Involve the Transfer of Zero, One, or Two Electrons. *Chemical Communications* **2007**, No. 33, 3464–3466. https://doi.org/10.1039/b708758f.

(10) Moore, J. A.; Vasudevan, K.; Hill, N. J.; Reeske, G.; Cowley, A. H. Facile Routes to Alkyl-BIAN Ligands. *Chemical Communications* **2006**, *2006* (27), 2913–2915. https://doi.org/10.1039/b606390j.

(11) Reeske, G.; Hoberg, C. R.; Hill, N. J.; Cowley, A. H. Capture of Phosphorus(I) and Arsenic(I) Moieties by a 1,2-Bis(Arylimino) Acenaphthene (Aryl-BIAN) Ligand. A Case of Intramolecular Charge Transfer. *J Am Chem Soc* **2006**, *128* (9), 2800–2801. https://doi.org/10.1021/ja058459m.

(12) Butschke, B.; Fillman, K. L.; Bendikov, T.; Shimon, L. J. W.; Diskin-Posner, Y.; Leitus, G.; Gorelsky, S. I.; Neidig, M. L.; Milstein, D. How Innocent Are Potentially Redox Non-Innocent Ligands? Electronic Structure and Metal Oxidation States in Iron-PNN Complexes as a Representative Case Study. *Inorg Chem* **2015**, *54* (10), 4909–4926. https://doi.org/10.1021/acs.inorgchem.5b00509.

(13) Mahabiersing, T.; Luytenn, H.; Nieuwendam, R. C.; Hartl, F. Synthesis, Spectroscopy and Spectroelectrochemistry of Chlorocarbonyl {1,2-Bis[(2,6-Diisopropylphenyl)Imino]-Acenaphthene-K2-N, N'}rhodium(I). *Collect Czechoslov Chem Commun* **2003**, *68* (9), 1687–1709. https://doi.org/10.1135/cccc20031687.

(14) Singha Hazari, A.; Ray, R.; Hoque, M. A.; Lahiri, G. K. Electronic Structure and Multicatalytic Features of Redox-Active Bis(Arylimino)Acenaphthene (BIAN)-Derived Ruthenium Complexes. *Inorg Chem* **2016**, *55* (16), 8160–8173. https://doi.org/10.1021/acs.inorgchem.6b01280.

(15) Allan, C. J.; Cooper, B. F. T.; Cowley, H. J.; Rawson, J. M.; Macdonald, C. L. B. Non-Innocent Ligand Effects on Low-Oxidation-State Indium Complexes. *Chemistry - European Journal* **2013**, *19* (43), 14470–14483. https://doi.org/10.1002/chem.201301881.

(16) Abramov, P. A.; Dmitriev, A. A.; Kholin, K. V.; Gritsan, N. P.; Kadirov, M. K.; Gushchin, A. L.; Sokolov, M. N. Mechanistic Study of the [(Dpp-Bian)Re(CO)3Br] Electrochemical Reduction Using in Situ EPR Spectroscopy and Computational Chemistry. *Electrochim Acta* **2018**, *270*, 526–534. https://doi.org/10.1016/j.electacta.2018.03.111.

(17) Williams, O. M.; Cowley, A. H.; Rose, M. J. Structural and Electronic Characterization of Multi-Electron Reduced Naphthalene (BIAN) Cobaloximes. *Dalton Transactions* **2015**, *44* (29), 13017–13029. https://doi.org/10.1039/C5DT00924C.

© University of Pretoria

(18) Hazari, A. S.; Das, A.; Ray, R.; Agarwala, H.; Maji, S.; Mobin, S. M.; Lahiri, G. K. Tunable Electrochemical and Catalytic Features of BIAN- and BIAO-Derived Ruthenium Complexes. *Inorg Chem* **2015**, *54* (10), 4998–5012. https://doi.org/10.1021/acs.inorgchem.5b00615.

(19) Mondal, P.; Agarwala, H.; Jana, R. D.; Plebst, S.; Grupp, A.; Ehret, F.; Mobin, S. M.; Kaim, W.; Lahiri, G. K. Sensitivity of a Strained C-C Single Bond to Charge Transfer: Redox Activity in Mononuclear and Dinuclear Ruthenium Complexes of Bis(Arylimino)Acenaphthene (BIAN) Ligands. *Inorg Chem* **2014**, *53* (14), 7389–7403. https://doi.org/10.1021/ic500730m.

(20) Francke, R.; Schille, B.; Roemelt, M. Homogeneously Catalyzed Electroreduction of Carbon Dioxide - Methods, Mechanisms, and Catalysts. *Chem Rev* **2018**, *118* (9), 4631–4701. https://doi.org/10.1021/acs.chemrev.7b00459.

(21) Elouarzaki, K.; Kannan, V.; Jose, V.; Sabharwal, H. S.; Lee, J. Recent Trends, Benchmarking, and Challenges of Electrochemical Reduction of CO 2 by Molecular Catalysts. *Adv Energy Mater* **2019**, *9* (24), 1900090. https://doi.org/10.1002/aenm.201900090.

(22) Krisch, D.; Sun, H.; Pellumbi, K.; Faust, K.; Apfel, U.-P.; Schöfberger, W. Tuning the Electronic Properties of Homoleptic Silver(I) Bis-BIAN Complexes towards Efficient Electrocatalytic CO2 Reduction. *Catalysts* **2022**, *12* (5), 545. https://doi.org/10.3390/catal12050545.

(23) Vollmer, M. V.; Machan, C. W.; Clark, M. L.; Antholine, W. E.; Agarwal, J.; Schaefer, H. F.; Kubiak, C. P.; Walensky, J. R. Synthesis, Spectroscopy, and Electrochemistry of (α-Diimine)M(CO)3Br, M = Mn, Re, Complexes: Ligands Isoelectronic to Bipyridyl Show Differences in CO2 Reduction. *Organometallics* **2015**, *34* (1), 3–12. https://doi.org/10.1021/om500838z.

(24) Hasan, K.; Zysman-Colman, E. Synthesis, UV-Vis and CV Properties of a Structurally Related Series of Bis(Arylimino)Acenaphthenes (Ar-BIANs). *J Phys Org Chem* **2013**, *26* (3), 274–279. https://doi.org/10.1002/poc.3081.

(25) Evans, D. A.; Lee, L. M.; Vargas-Baca, I.; Cowley, A. H. Aggregation-Induced Emission of Bis(Imino)Acenaphthene Zinc Complexes: Photophysical Tuning via Methylation of the Flanking Aryl Substituents. *Organometallics* **2015**, *34* (11), 2422–2428. https://doi.org/10.1021/om501191c.

(26) Evans, D. A.; Lee, L. M.; Vargas-Baca, I.; Cowley, A. H. Photophysical Tuning of the Aggregation-Induced Emission of a Series of Para-Substituted Aryl Bis(Imino)Acenaphthene Zinc Complexes. *Dalton Transactions* **2015**, *44* (26), 11984–11996. https://doi.org/10.1039/C5DT01529D.

(27) Kee, J. W.; Ng, Y. Y.; Kulkarni, S. A.; Muduli, S. K.; Xu, K.; Ganguly, R.; Lu, Y.; Hirao, H.; Soo, H. S. Development of Bis(Arylimino)Acenaphthene (BIAN) Copper Complexes as Visible Light Harvesters for Potential Photovoltaic Applications. *Inorg Chem Front* **2016**, *3* (5), 651–662. https://doi.org/10.1039/c5qi00221d.

© University of Pretoria

(28) Li, L.; Gomes, C. S. B.; Gomes, P. T.; Duarte, M. T.; Fan, Z. New Tetradentate N,N,N,N-Chelating α-Diimine Ligands and Their Corresponding Zinc and Nickel Complexes: Synthesis, Characterisation and Testing as Olefin Polymerisation Catalysts. *Dalton Transactions* **2011**, *40* (13), 3365–3380. https://doi.org/10.1039/c0dt01308k.

© University of Pretoria

Appendices and Additional Results

Appendix A: NMR Spectra

A.1) NMR Spectra

A.1.1) DippBIAN

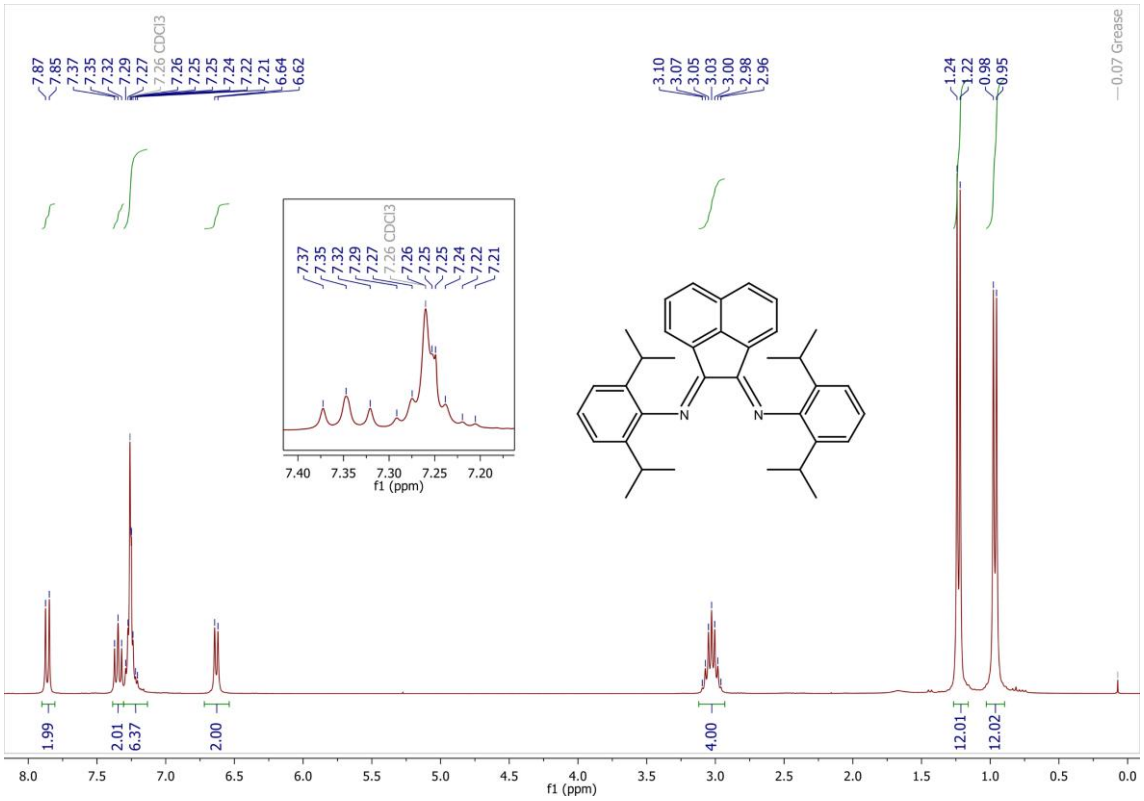


Figure A.1–1: ^{1}H NMR spectrum of DippBIAN in $CDCl_3$.

^{1}H NMR (300 MHz, $CDCl_3$) δ 7.86 (d, *J* = 8.3 Hz, 2H, BIAN-C**H**), 7.35 (dd, *J* = 8.3, 7.2 Hz, 2H, BIAN-C**H**), 7.31–7.19 (m, 6H, Dipp-C**H**), 6.63 (d, *J* = 7.2 Hz, 2H, BIAN-C**H**), 3.03 (sept, *J* = 6.8 Hz, 4H, Dipp(iso)-C**H**), 1.23 (d, *J* = 6.8 Hz, 12H, Dipp(iso)-C**H**$_3$), 0.97 (d, *J* = 6.8 Hz, 12H, Dipp(iso)-C**H**$_3$).

© University of Pretoria

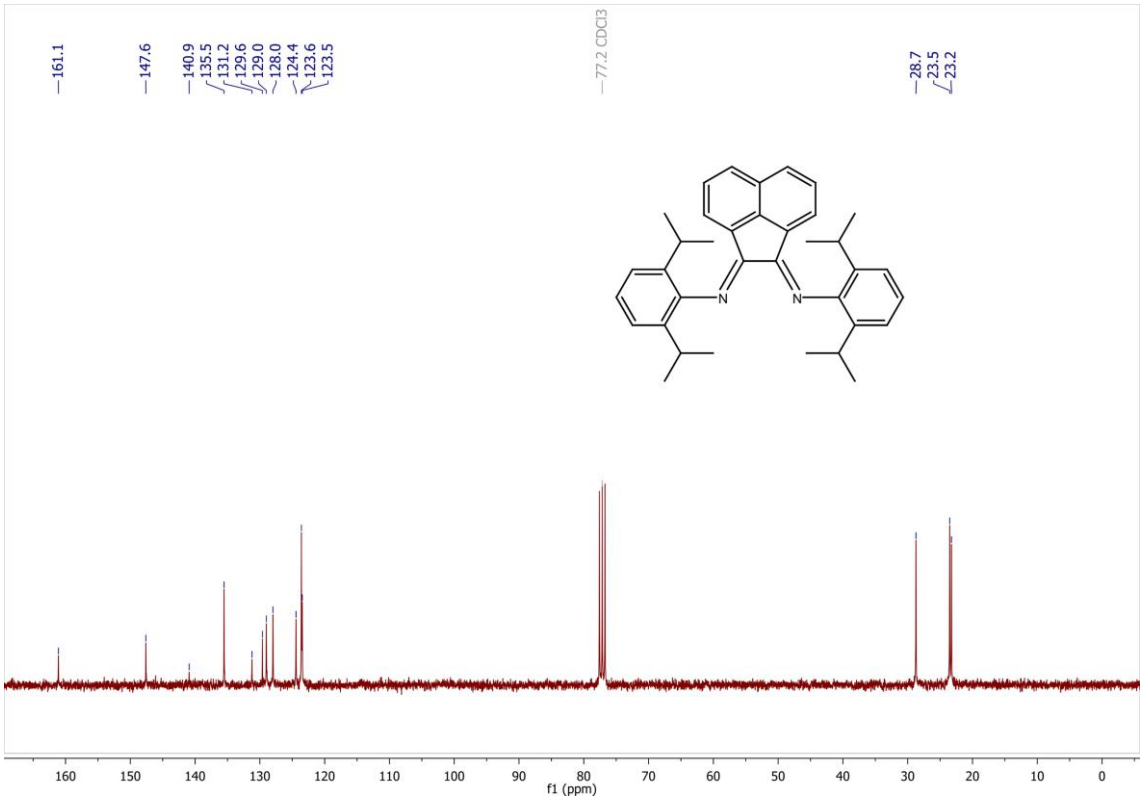


Figure A.1–2: ^{13}C NMR spectrum of DippBIAN in $CDCl_3$.

^{13}C NMR (75 MHz, $CDCl_3$) δ 161.1 (BIAN-**C_q**=N), 147.6 (Dipp-**C_q**-N), 140.9 (BIAN-**C_q**), 135.5 (Dipp-**C**H), 131.2 (BIAN-**C_q**), 129.6 (BIAN-**C_q**), 129.0 (Dipp(iso)-**C_q**), 128.0 (BIAN-**C**H), 124.4 (BIAN-**C**H), 123.6 (Dipp-**C**H), 123.5 (BIAN-**C**H), 28.7 (Dipp(iso)-**C**H), 23.5, 23.3 (Dipp(iso)-**C**H_3).

© University of Pretoria

A.1.2) MesBIAN

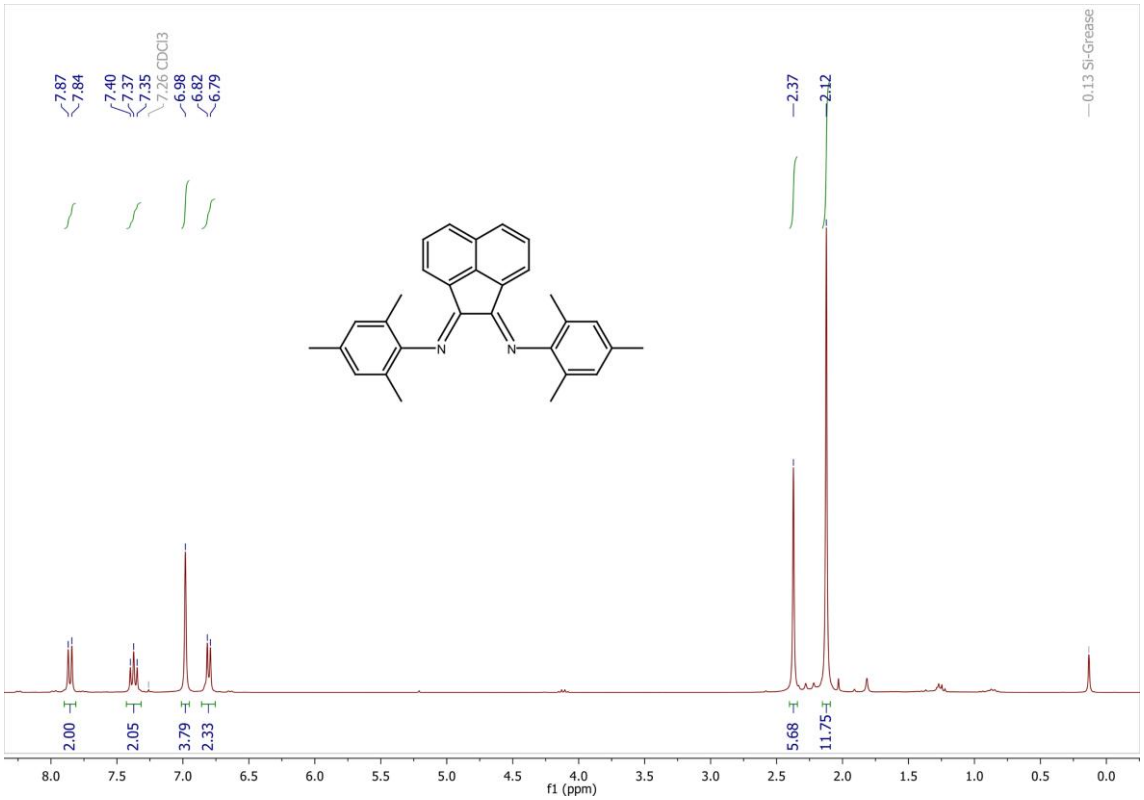


Figure A.1–3: ^{1}H NMR spectrum of MesBIAN in $CDCl_3$.

^{1}H NMR (300 MHz, $CDCl_3$) δ 7.89 (d, J = 8.3 Hz, 2H, BIAN-C**H**), 7.37 (dd, J = 8.3, 7.1 Hz, 2H, BIAN-C**H**), 6.98 (s, 4H, Mes-C**H**), 6.80 (d, J = 7.1 Hz, 2H, BIAN-C**H**), 2.37 (s, 6H, Mes-C**H**$_3$), 2.12 (s, 12H, Mes-C**H**$_3$).

© University of Pretoria

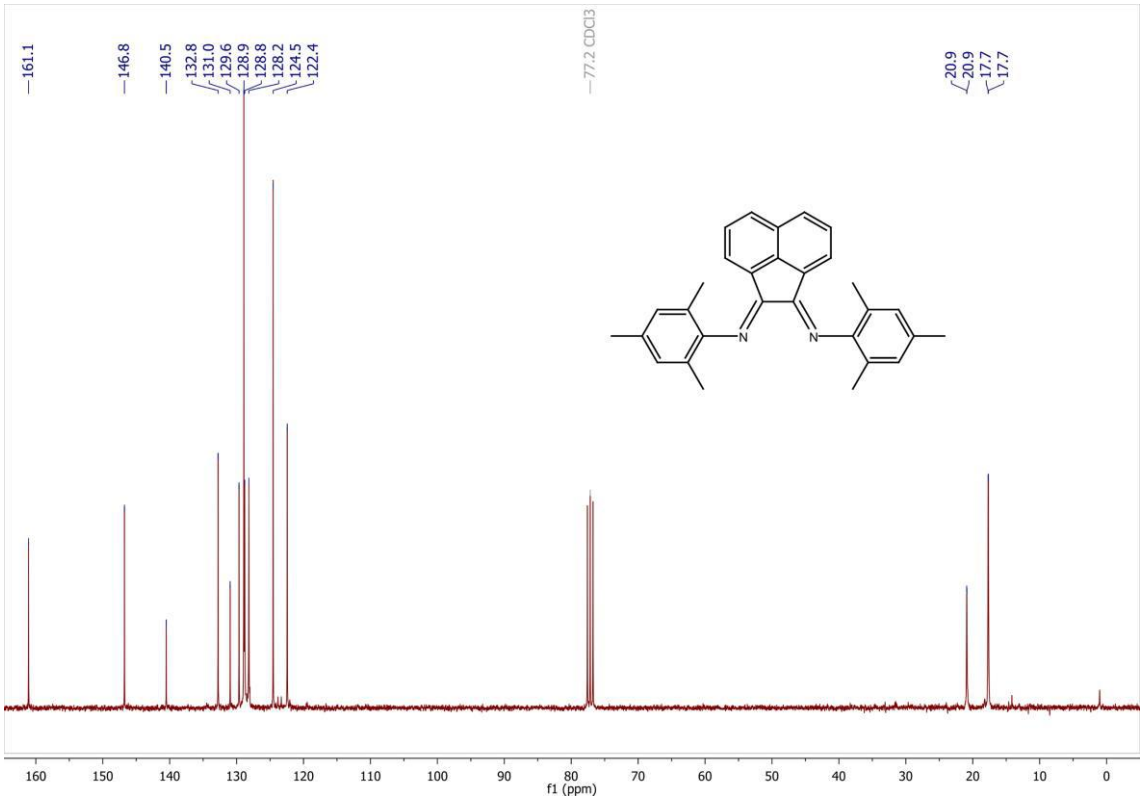


Figure A.1–4: ^{13}C NMR spectrum of DippBIAN in $CDCl_3$.

^{13}C NMR (75 MHz, $CDCl_3$) δ 161.1 (BIAN-**C_q**=N), 146.8 (Mes-**C_q**-N), 140.5 (BIAN-**C_q**), 132.8 (Mes-**C_q**), 131.0 (BIAN-**C_q**), 129.6 (BIAN-**C**H), 128.9 (Mes-**C**H), 128.8 (BIAN-**C_q**), 128.2 (Mes-**C_q**), 124.5 (BIAN-**C**H), 122.4 (BIAN-**C**H), 20.90, 20.87 (*p*-Mes-**C**H_3), 17.70, 17.66 (*o*-Mes-**C**H_3).

© University of Pretoria

A.1.3) **1a** [RhDB(cod)]PF_6

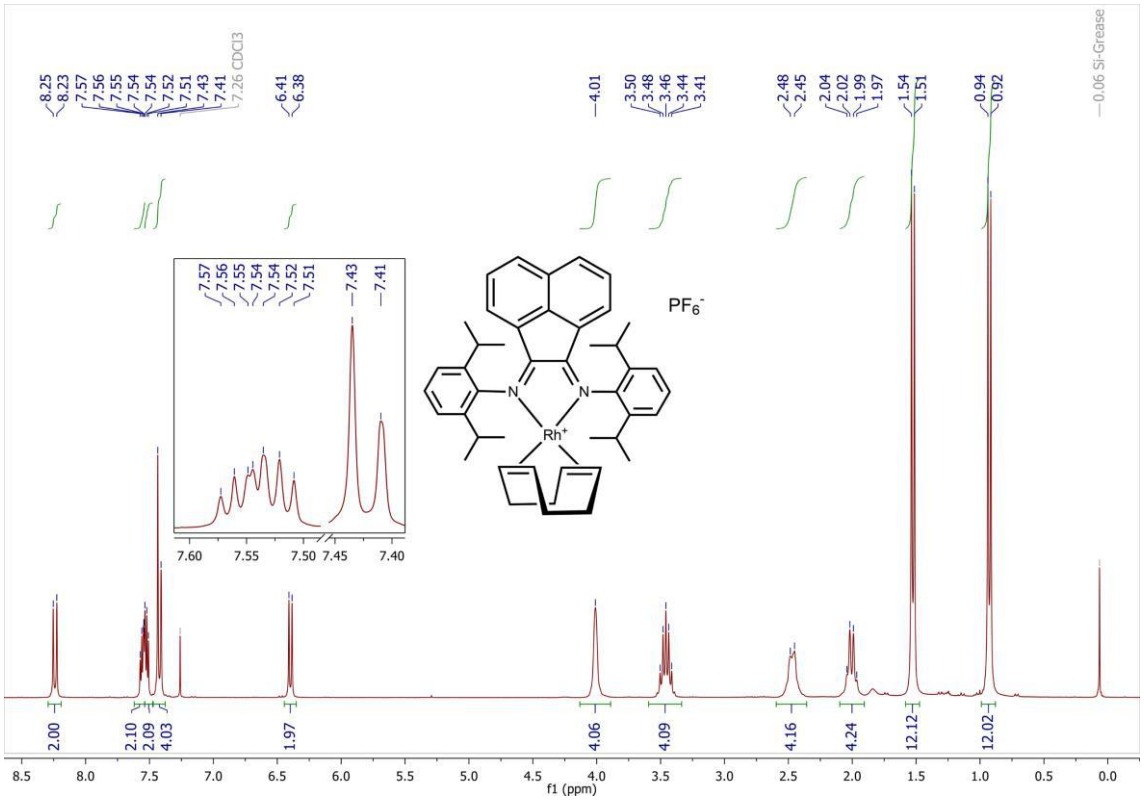


*Figure A.1–5: ^{1}H NMR spectrum of complex **1a** in $CDCl_3$.*

^{1}H NMR (300 MHz, $CDCl_3$) δ 8.24 (d, *J* = 8.3 Hz, 2H, BIAN-Ar-C**H**), 7.56 (dd, *J* = 7.3, 3.6 Hz, 2H, BIAN-Ar-C**H**), 7.53 (dd, *J* = 7.5, 3.3 Hz, 2H, Dipp-Ar-C**H**), 7.42 (d, *J* = 7.5 Hz, 4H, Dipp-Ar-C**H**), 6.40 (d, *J* = 7.3 Hz, 2H, BIAN-Ar-C**H**), 4.01 (br, 4H, cod-C**H**), 3.46 (sept, *J* = 6.7 Hz, 4H, Dipp(iso)-C**H**), 2.59–2.36 (m, 4H, cod-C$\mathbf{H}_2$), 2.10–1.91 (m, 4H, cod-C$\mathbf{H}_2$), 1.52 (d, *J* = 6.8 Hz, 12H, Dipp(iso)-C$\mathbf{H}_3$), 0.93 (d, *J* = 6.8 Hz, 12H, Dipp(iso)-C$\mathbf{H}_3$).

© University of Pretoria

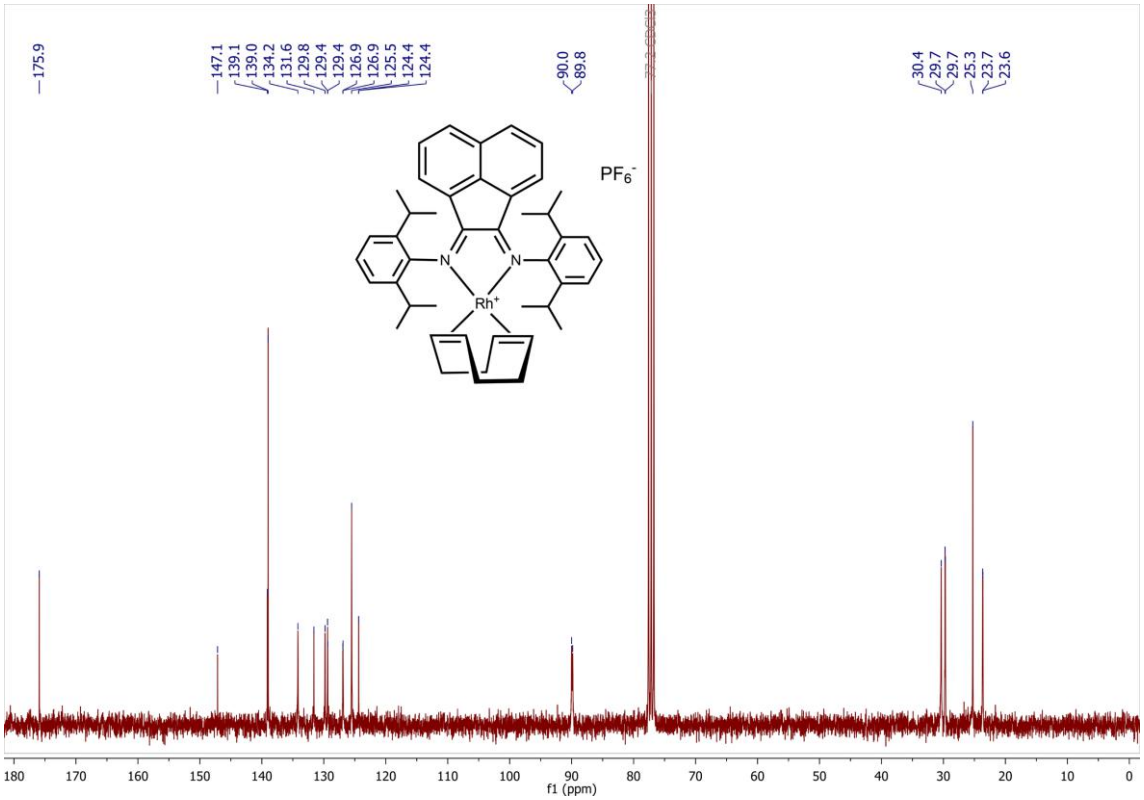


*Figure A.1–6: ^{13}C NMR spectrum of complex **1a** in $CDCl_3$.*

^{13}C NMR (75 MHz, $CDCl_3$) δ 175.9 (BIAN-N=**C**$_q$), 147.1 (Dipp-N-**C**$_q$), 139.1 (BIAN-**C**$_q$), 139.00 (Dipp(iso)-**C**$_q$), 134.2 (BIAN-**C**H), 131.6 (**C**$_q$), 129.8 (**C**$_q$), 129.4 (Dipp-**C**H), 129.4 (Dipp-**C**H), 126.9 (BIAN-**C**H), 126.9 (BIAN-**C**H), 125.5 (Dipp-**C**H), 124.4 (BIAN-**C**$_q$), 124.4 (BIAN-**C**$_q$), 89.9 (d, $J_{C\text{-}Rh}$ = 12.2 Hz, cod-**C**H), 30.4 (cod-**C**H$_2$), 29.7 (Dipp(iso)-**C**H), 29.7 (cod-**C**H$_2$), 25.3 (Dipp(iso)-**C**H$_3$), 23.7, 23.6 (Dipp(iso)-**C**H$_3$).

^{19}F NMR (282 MHz, $CDCl_3$) δ –73.8 (d, $J_{F\text{-}P}$ = 712.3 Hz, P**F**$_6$). **^{31}P NMR** (121 MHz, $CDCl_3$) δ –144.3 (sept, $J_{P–F}$ = 712.4 Hz, **P**F$_6$).

© University of Pretoria

A.1.4) **1b** [RhMB(cod)]PF_6

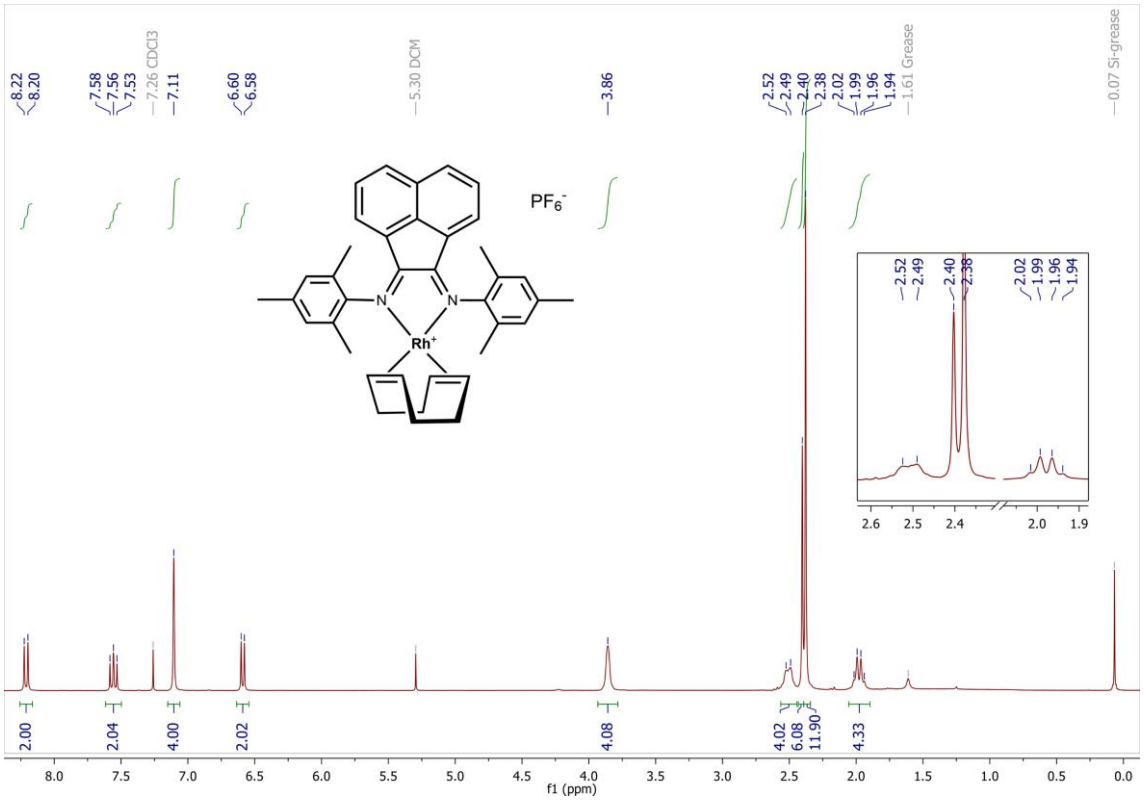


*Figure A.1–7: ^{1}H NMR spectrum of complex **1b** in $CDCl_3$.*

^{1}H NMR (300 MHz, $CDCl_3$) δ 8.21 (d, *J* = 8.3 Hz, 2H, BIAN-C**H**), 7.56 (dd, *J* = 8.3, 7.3 Hz, 2H, BIAN-C**H**), 7.11 (s, 3H, Mes-C**H**), 6.59 (d, *J* = 7.3 Hz, 2H, BIAN-C**H**), 3.86 (br, 4H, cod-C**H**), 2.51 (br, 4H, cod-C$\mathbf{H}_2$), 2.40 (s, 6H, Mes-C$\mathbf{H}_3$), 2.38 (s, 12H, Mes-C$\mathbf{H}_3$), 2.06–1.90 (m, 4H, cod-C$\mathbf{H}_2$).

© University of Pretoria

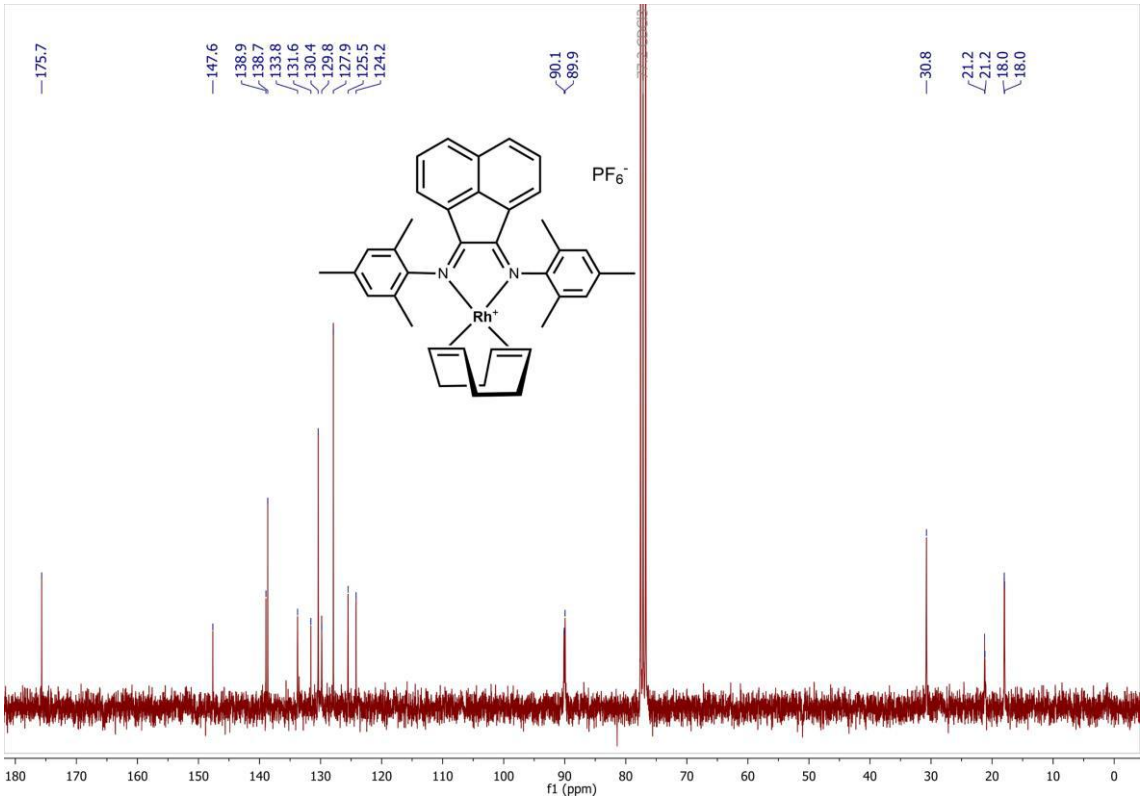


*Figure A.1–8: ^{13}C NMR spectrum of complex **1b** in $CDCl_3$.*

^{13}C NMR (75 MHz, $CDCl_3$) δ 175.7 (BIAN-N=**C**$_q$), 147.6 (Mes-N-**C**$_q$), 138.9 (BIAN-**C**$_q$), 138.7 (BIAN-**C**H), 133.8 (BIAN-**C**H), 131.6 (**C**$_q$), 130.4 (BIAN-**C**H), 129.8 (**C**$_q$), 127.9 (Mes-**C**H), 125.5 (**C**$_q$), 124.2 (BIAN-**C**$_q$), 90.0 (d, $J_{C\text{-}Rh}$ = 10.1 Hz, cod-**C**H), 30.8 (cod-**C**H$_2$), 21.22, 21.17, 18.00, 17.95 (Mes-**C**H$_3$).

^{19}F NMR (282 MHz, $CDCl_3$) δ –73.9 (d, $J_{F\text{-}P}$ = 712.4 Hz, P**F**$_6$). **^{31}P NMR** (121 MHz, $CDCl_3$) δ –144.4 (sept, $J_{P\text{–}F}$ = 712.1 Hz, **P**F$_6$).

© University of Pretoria

A.1.5) **1c** [IrDB(cod)]PF_6

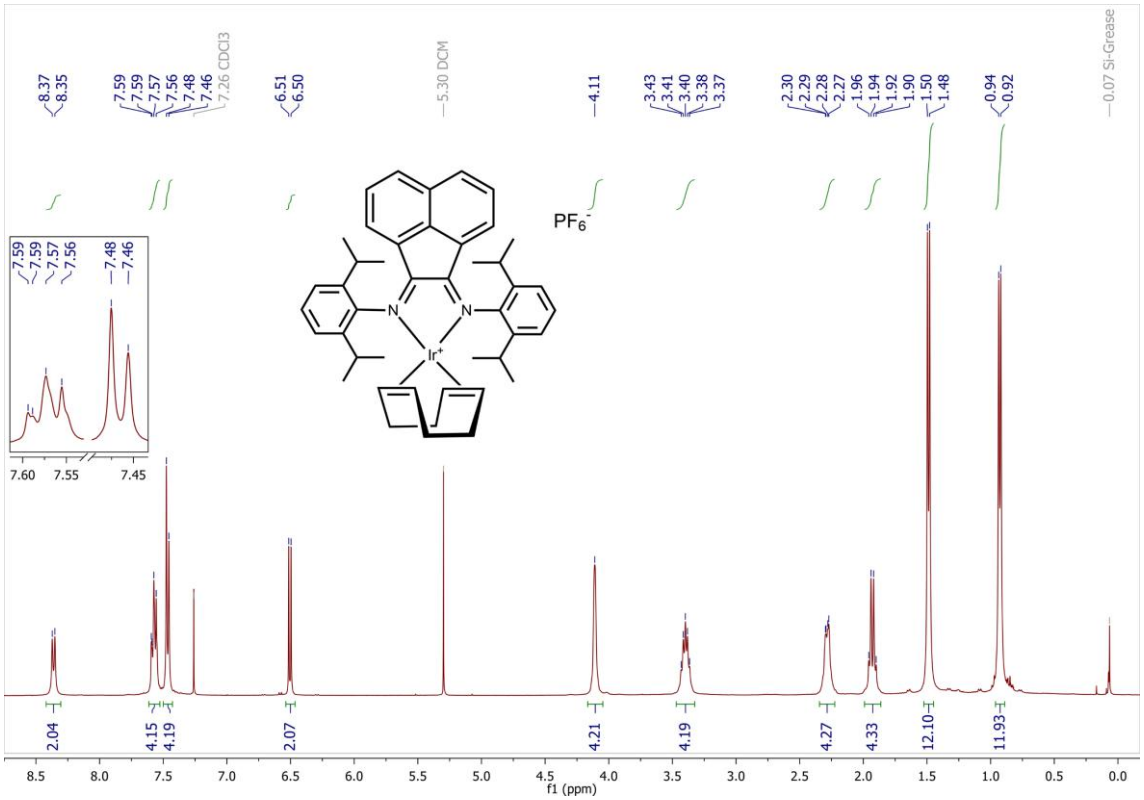


*Figure A.1–9: ^{1}H NMR spectrum of complex **1c** in $CDCl_3$.*

^{1}H NMR (300 MHz, $CDCl_3$) δ 8.36 (d, *J* = 8.2 Hz, 2H, BIAN-C**H**), 7.61–7.53 (m, 4H, Dipp-C**H** and BIAN-C**H**), 7.47 (d, *J* = 7.8 Hz, 4H, Dipp-C**H**), 6.50 (d, *J* = 7.3 Hz, 2H, BIAN-C**H**), 4.11 (br, 4H, cod-C**H**), 3.40 (sept, *J* = 6.4 Hz, 4H, Dipp(iso)C**H**), 2.35–2.22 (m, 4H, cod-C$\mathbf{H}_2$), 1.99–1.86 (m, 4H, cod-C$\mathbf{H}_2$), 1.49 (d, *J* = 6.7 Hz, 12H, Dipp(iso)C$\mathbf{H}_3$), 0.93 (d, *J* = 6.7 Hz, 12H, Dipp(iso)C$\mathbf{H}_3$).

© University of Pretoria

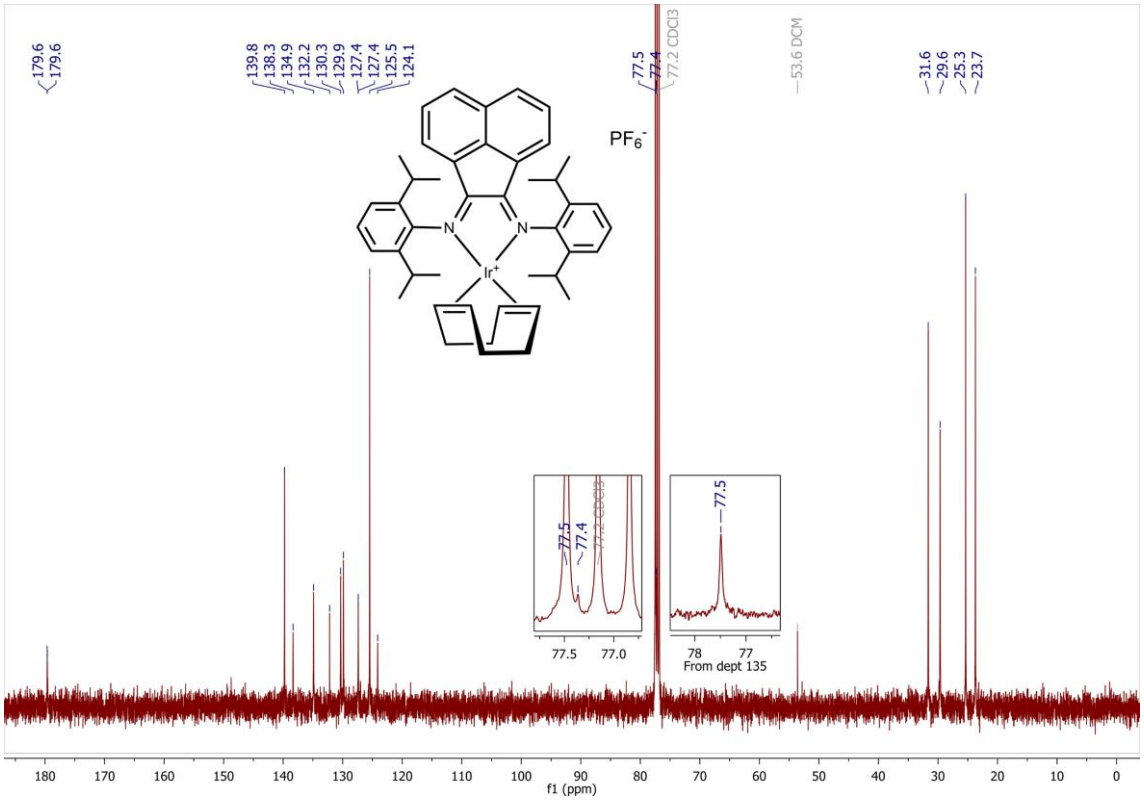


*Figure A.1–10: ^{13}C NMR spectrum of complex **1c** in $CDCl_3$.*

^{13}C NMR (75 MHz, $CDCl_3$) δ 179.6 (BIAN-N=**C**$_q$), 179.6 (BIAN-N=**C**$_q$), 139.8 (Dipp(iso)-**C**$_q$), 138.3 (Dipp-N-**C**$_q$), 134.9 (BIAN-**C**H), 132.2 (BIAN-**C**$_q$), 130.3 (Dipp-**C**H), 129.9 (BIAN-**C**H), 127.4 (BIAN-**C**H), 127.4 (BIAN-**C**H), 125.5 (Dipp-**C**H), 124.1 (BIAN-**C**$_q$), 77.5 (from dept135, cod-**C**H), 77.4 (cod-**C**H), 31.6 (cod-**C**H_2), 29.6 (Dipp(iso)-**C**H), 25.3 (Dipp(iso)-**C**H_3), 23.7 (Dipp(iso)-**C**H_3).

^{19}F NMR (282 MHz, $CDCl_3$) δ –73.8 (d, J_{F-P} = 712.5 Hz, P**F**$_6$). **^{31}P NMR** (121 MHz, $CDCl_3$) δ –144.4 (sept, $J_{P–F}$ = 712.6 Hz, **P**F_6).

© University of Pretoria

A.1.6) **1d** [IrMB(cod)]PF_6

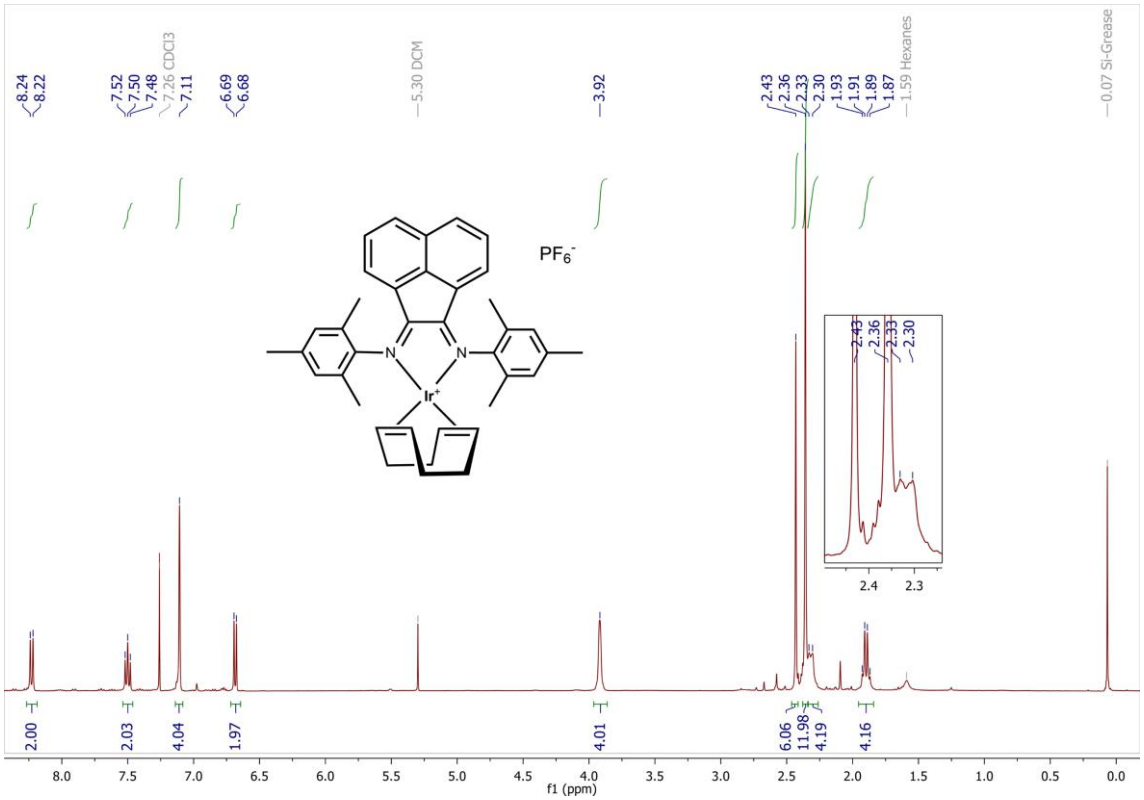


*Figure A.1–11: ^{1}H NMR spectrum of complex **1d** in $CDCl_3$.*

^{1}H NMR (300 MHz, $CDCl_3$) δ 8.23 (d, *J* = 8.3 Hz, 2H, BIAN-C**H**), 7.50 (dd, *J* = 8.3, 7.2 Hz, 2H, BIAN-C**H**), 7.11 (s, 4H, Mes-C**H**), 6.68 (d, *J* = 7.2 Hz, 2H, BIAN-C**H**), 3.92 (br, 4H, cod-C**H**), 2.43 (s, 6H, Mes-C**H**$_3$), 2.36 (s, 12H, Mes-C**H**$_3$), 2.32 (br, 4H, cod-C**H**$_2$), 1.90 (br, 4H, cod-C**H**$_2$).

© University of Pretoria

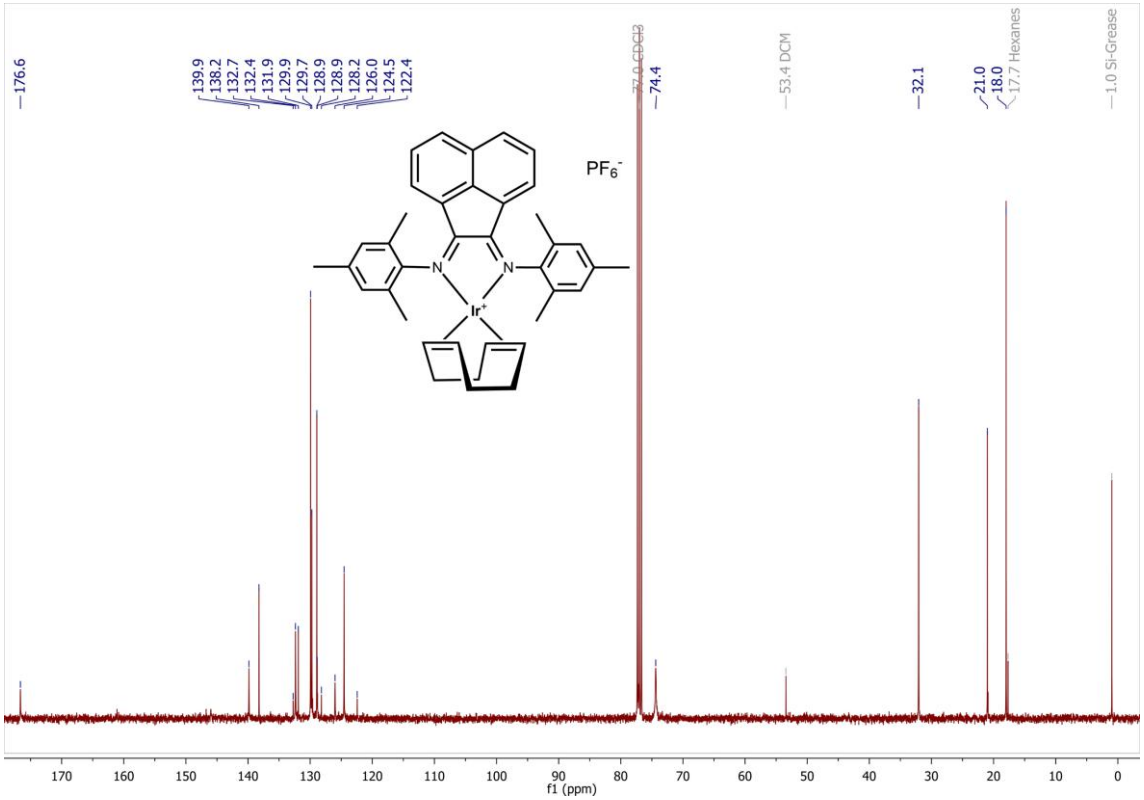


*Figure A.1–12: ^{13}C NMR spectrum of complex **1d** in $CDCl_3$.*

^{13}C NMR (75 MHz, $CDCl_3$) δ 176.6 (BIAN-N=**C**$_q$), 139.9 (Mes-N-**C**$_q$), 138.2 (BIAN-**C**$_q$), 132.7 (BIAN-**C**H), 132.4, 131.9, 129.9 (Mes-**C**H), 129.7 (BIAN-**C**H), 128.93, 128.87, 128.2, 126.0, 124.5 (BIAN-**C**H), 122.4 (BIAN-**C**$_q$), 74.4 (cod-**C**H), 32.1 (cod-**C**H_2), 21.0, 18.0 (Mes-**C**H_3).

^{19}F NMR (282 MHz, $CDCl_3$) δ –73.8 (d, $J_{F\text{-}P}$ = 712.6 Hz, P**F**$_6$). **^{31}P NMR** (121 MHz, $CDCl_3$) δ –144.5 (sept, $J_{P–F}$ = 712.2 Hz, **P**F_6).

© University of Pretoria

A.1.7) **2a** $[RhDB(CO)_2]PF_6$

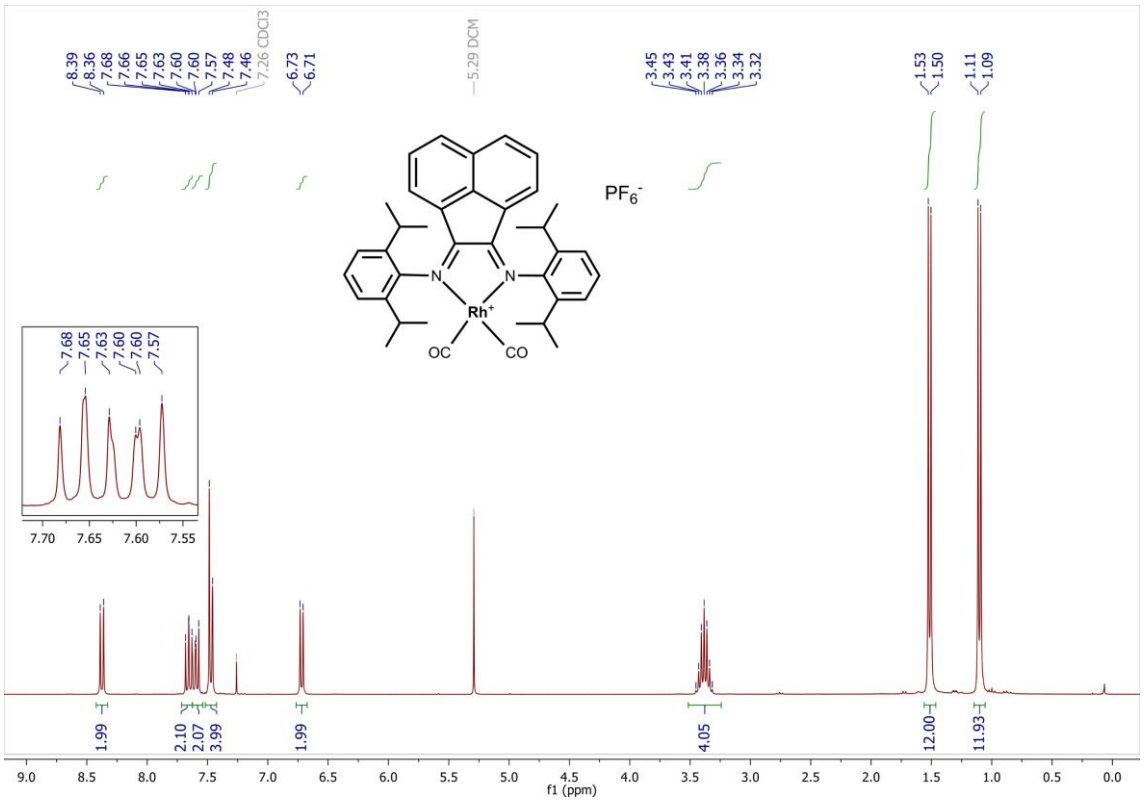


*Figure A.1–13: ^{1}H NMR spectrum of complex **2a** in $CDCl_3$.*

^{1}H NMR (300 MHz, $CDCl_3$) δ 8.37 (d, *J* = 8.3 Hz, 2H, BIAN-C**H**), 7.66 (dd, *J* = 8.3, 7.4 Hz, 2H, BIAN-C**H**), 7.60 (dd, *J* = 8.7, 7.1 Hz, 2H, Dipp-C**H**), 7.47 (d, *J* = 7.9 Hz, 2H, Dipp-C**H**), 6.72 (d, *J* = 7.4 Hz, 2H, BIAN-C**H**), 3.38 (sept, *J* = 6.7 Hz, 4H, Dipp(iso)C**H**), 1.51 (d, *J* = 6.8 Hz, 12H, Dipp(iso)C**H**$_3$), 1.10 (d, *J* = 6.8 Hz, 12H, Dipp(iso)C**H**$_3$).

© University of Pretoria

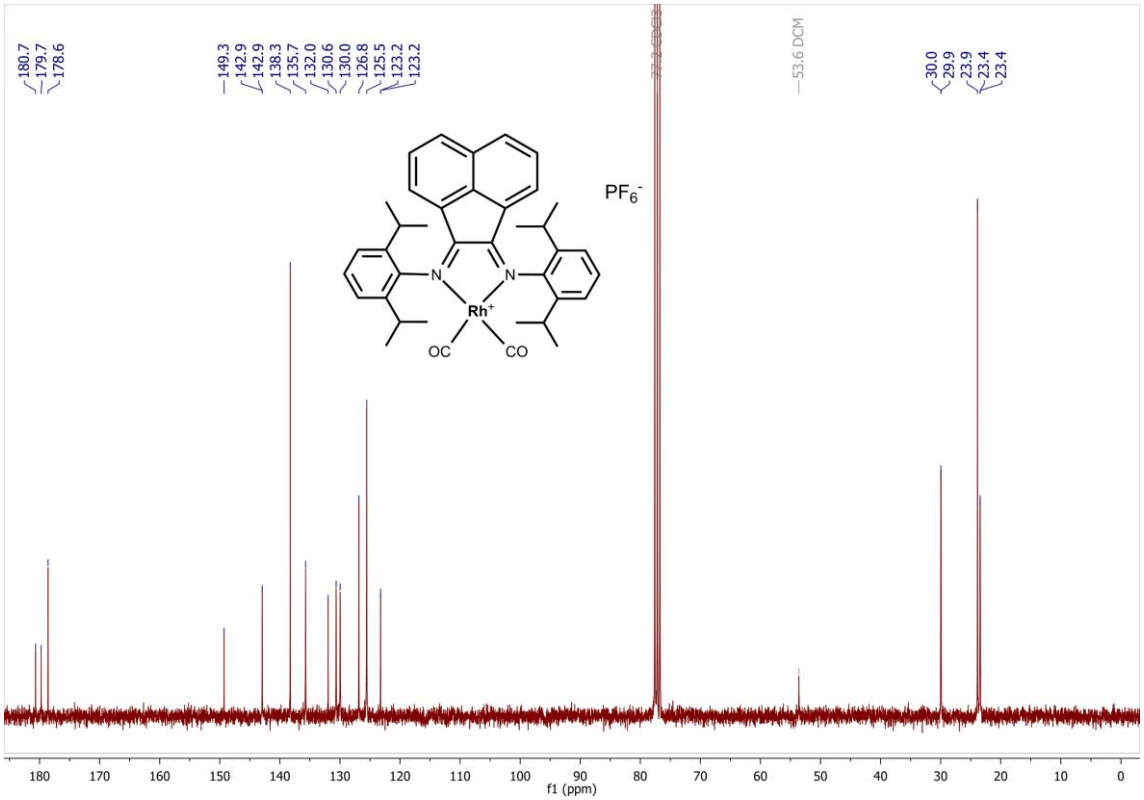


*Figure A.1–14: ^{13}C NMR spectrum of complex **2a** in $CDCl_3$.*

^{13}C NMR (75 MHz, $CDCl_3$) δ 180.2 (d, $J_{CO\text{-}Rh}$ = 70.3 Hz, **C**O), 178.6 (BIAN-N=**C**$_q$), 149.3 (Dipp-N-**C**$_q$), 142.9 (BIAN-**C**$_q$), 142.9 (BIAN-**C**$_q$), 138.3 (Dipp-**C**H), 135.7 (BIAN-**C**H), 132.0 (Dipp-**C**H), 130.6 (Dipp(iso)-**C**$_q$), 130.0 (Dipp(iso)-**C**$_q$), 126.8 (BIAN-**C**H), 125.5 (BIAN-**C**H), 123.2 (Dipp-**C**H), 123.2 (Dipp-**C**H), 30.0, 29.9 (Dipp(iso)-**C**H), 23.9, 23.4, 23.4 (Dipp(iso)-**C**H).

^{19}F NMR (377 MHz, $CDCl_3$) δ –73.7 (d, $J_{F\text{-}P}$ = 712.6 Hz, P**F**$_6$). **^{31}P NMR** (162 MHz, $CDCl_3$) δ –144.5 (sept, $J_{P–F}$ = 712.4 Hz, **P**F$_6$).

© University of Pretoria

A.1.8) **2b** $[RhMB(CO)_2]PF_6$

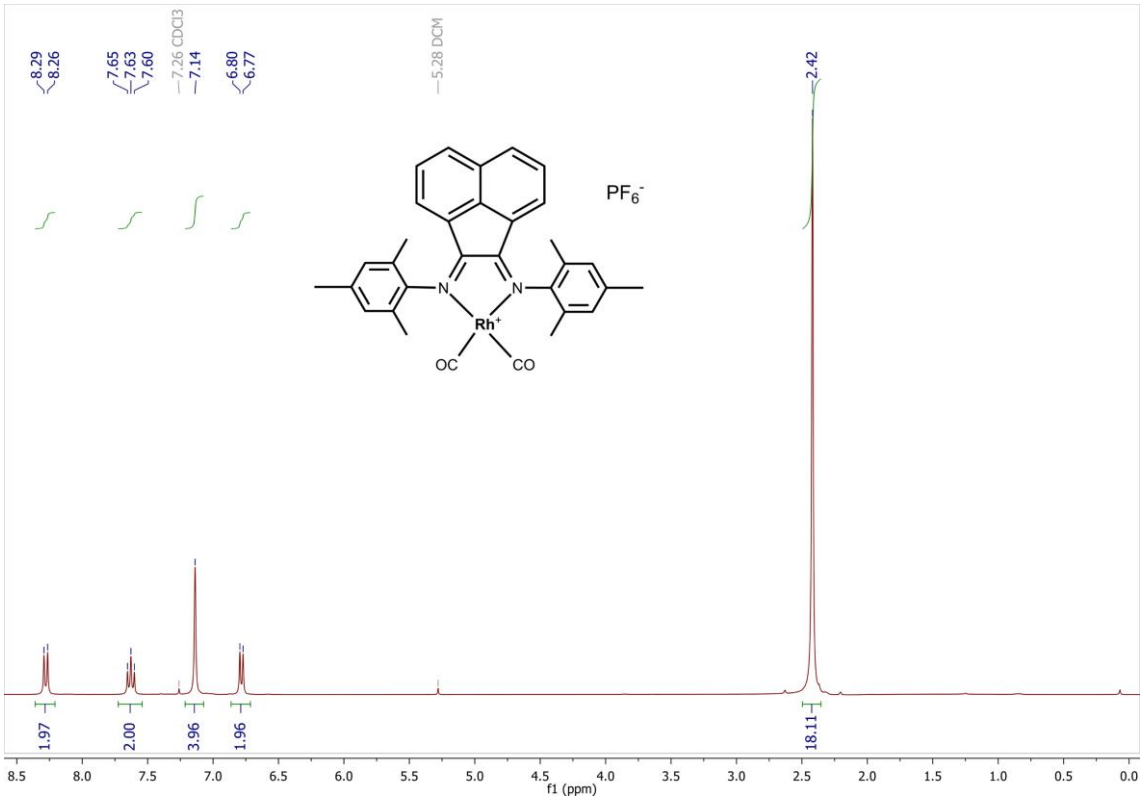


*Figure A.1–15: ^{1}H NMR spectrum of complex **2b** in $CDCl_3$.*

^{1}H NMR (300 MHz, $CDCl_3$) δ 8.28 (d, *J* = 8.3 Hz, 2H, BIAN-C**H**), 7.63 (dd, *J* = 8.3, 7.3 Hz, 2H, BIAN-C**H**), 7.14 (s, 4H, Mes-C**H**), 6.78 (d, *J* = 7.3 Hz, 2H, BIAN-C**H**), 2.42 (s, 18H, Mes-C**H**$_3$).

© University of Pretoria

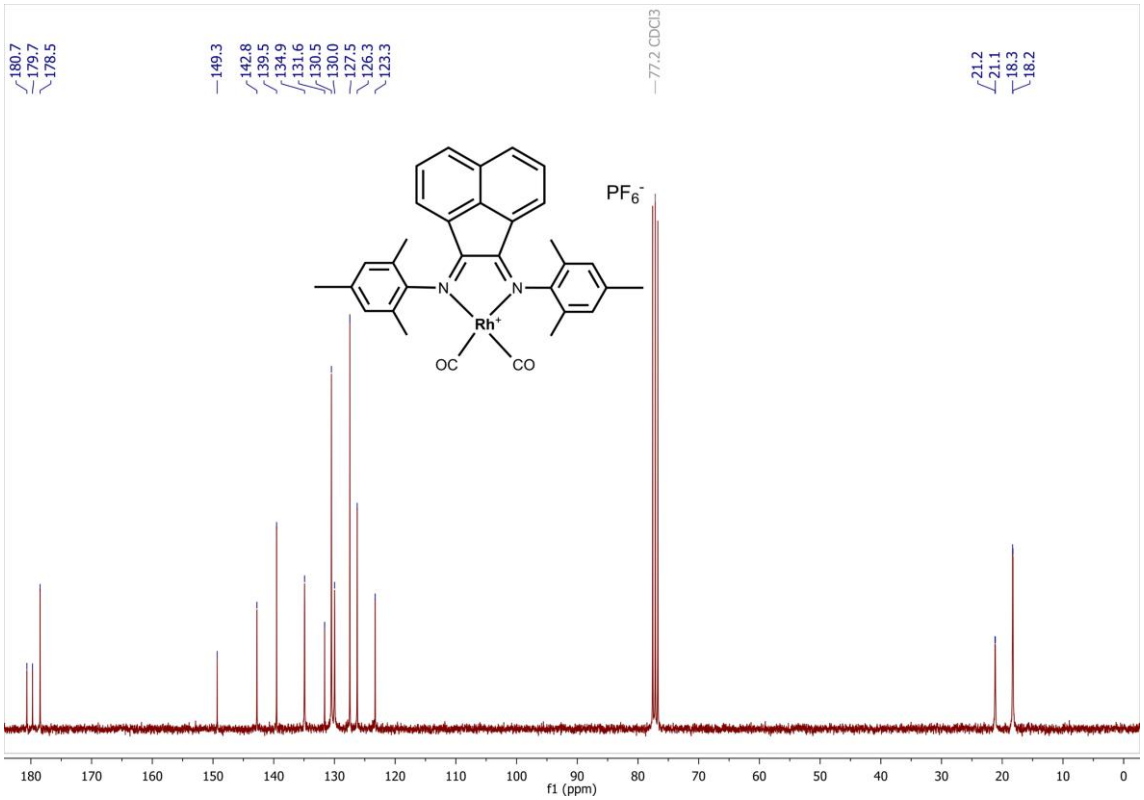


*Figure A.1–16: ^{13}C NMR spectrum of complex **2b** in $CDCl_3$.*

^{13}C NMR (75 MHz, $CDCl_3$) δ 180.19 (d, $J_{C\text{-}Rh}$ = 70.1 Hz, Rh=**C**=O), 178.5 (BIAN-N=**C**$_q$), 149.3 (Mes-N-**C**$_q$), 142.8 (BIAN-**C**$_q$), 139.5 (BIAN-**C**H), 134.9 (BIAN-**C**H), 131.6 (**C**$_q$), 130.5 (Mes-**C**H), 130.0 (**C**$_q$), 127.5 (BIAN-**C**H), 126.3 (BIAN-**C**$_q$), 123.3 (**C**$_q$), 21.2, 21.1, 18.3, 18.2 (Mes-**C**H$_3$).

^{19}F NMR (282 MHz, $CDCl_3$) δ –73.7 (d, $J_{F\text{-}P}$ = 712.9 Hz, P**F**$_6$). **^{31}P NMR** (121 MHz, $CDCl_3$) δ –144.6 (sept, $J_{P\text{–}F}$ = 713.3 Hz, **P**F$_6$).

© University of Pretoria

A.1.9) **2c** $[IrDB(CO)_2]PF_6$

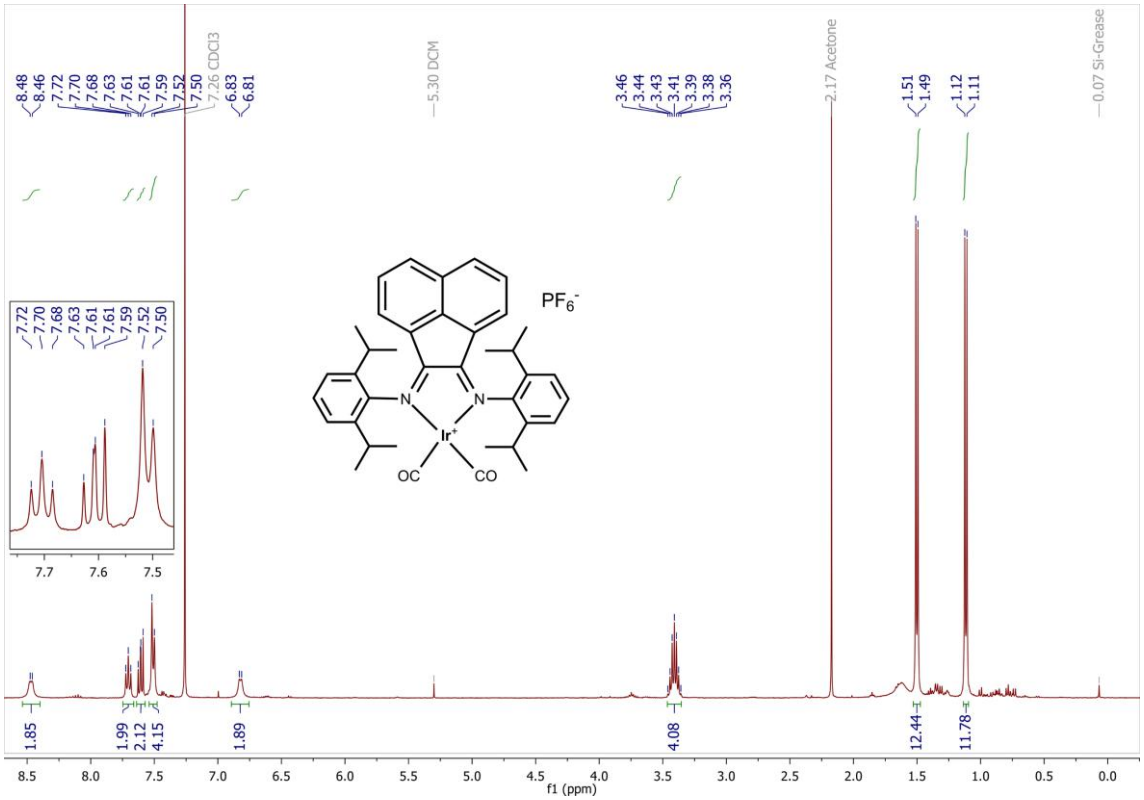


*Figure A.1–17: ^{1}H NMR spectrum of complex **2c** in $CDCl_3$.*

^{1}H NMR (300 MHz, $CDCl_3$) δ 8.45 (br, 2H, BIAN-C**H**), 7.70 (dd, *J* = 7.9, 7.3 Hz, 2H, BIAN-C**H**), 7.61 (dd, *J* = 8.7, 6.8 Hz, 2H, Dipp-C**H**), 7.51 (d, *J* = 7.7 Hz, 4H, Dipp-C**H**), 6.82 (d, *J* = 7.3 Hz, 2H, BIAN-C**H**), 3.39 (sept, *J* = 6.8 Hz, 4H, Dipp(iso)C**H**), 1.50 (d, *J* = 6.8 Hz, 12H, Dipp(iso)C**H**$_3$), 1.11 (d, *J* = 6.8 Hz, 12H, Dipp(iso)C**H**$_3$).

No well-resolved **^{13}C NMR** spectrum of this compound could be obtained, even after extended data acquisition times.

^{19}F NMR (282 MHz, $CDCl_3$) δ –73.7 (d, J_{F-P} = 712.7 Hz, P**F**$_6$). **^{31}P NMR** (121 MHz, $CDCl_3$) δ –144.5 (sept, J_{P-F} = 712.3 Hz, **P**F$_6$).

© University of Pretoria

A.1.10) **2d** $[IrMB(CO)_2]PF_6$

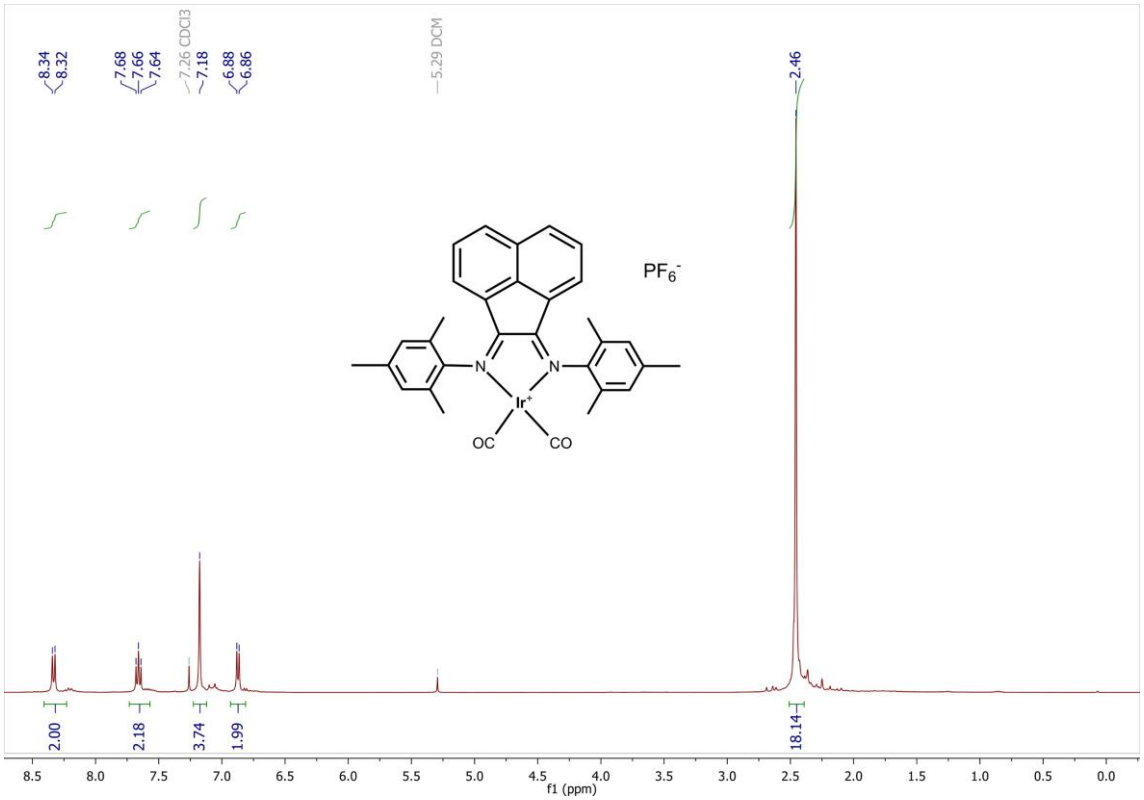


*Figure A.1–18: ^{1}H NMR spectrum of complex **2d** in $CDCl_3$.*

^{1}H NMR (300 MHz, $CDCl_3$) δ 8.33 (d, *J* = 8.3 Hz, 2H, BIAN-C**H**), 7.66 (dd, *J* = 8.3, 7.3 Hz, 2H, BIAN-C**H**), 7.18 (s, 4H, Mes-C**H**), 6.87 (d, *J* = 7.3 Hz, 2H, BIAN-C**H**), 2.46 (s, 18H, Mes-C**H**$_3$).

© University of Pretoria

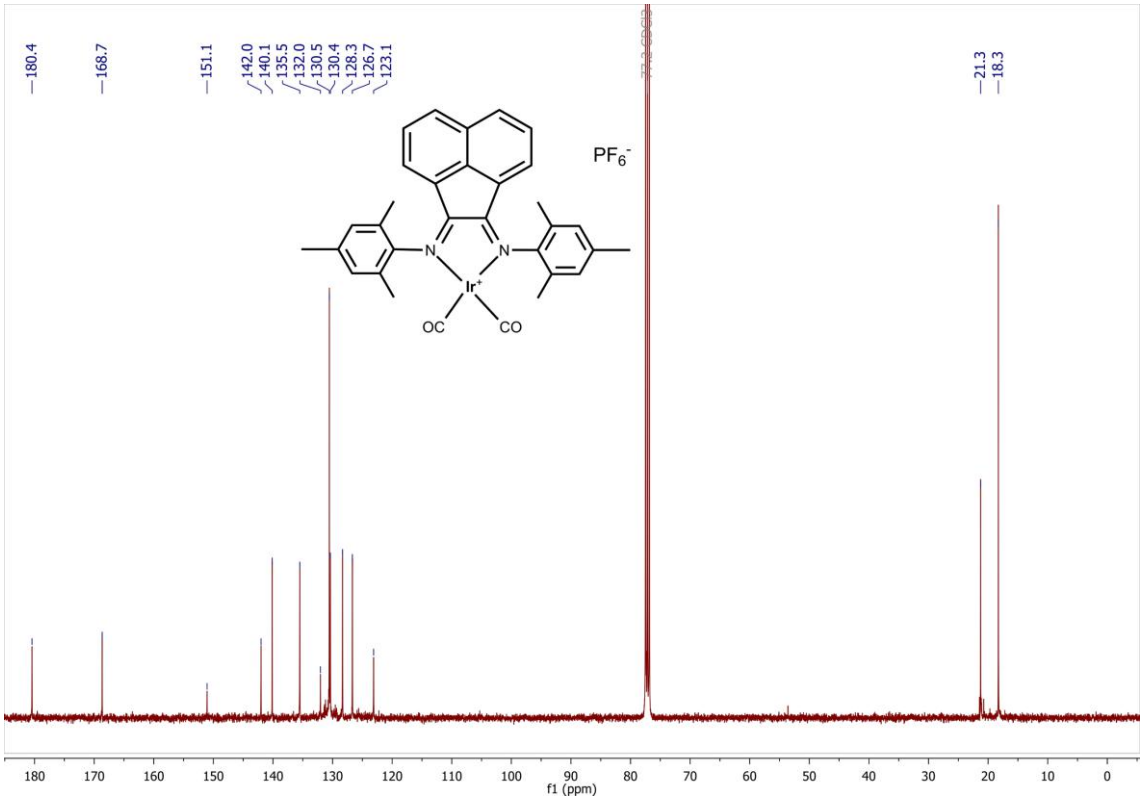


*Figure A.1–19: ^{13}C NMR spectrum of complex **2d** in $CDCl_3$.*

^{13}C NMR (75 MHz, $CDCl_3$) δ 180.4 (Ir=**C**=O), 168.7 (BIAN-N=**C**$_q$), 151.1 (Mes-N-**C**$_q$), 142.0 (BIAN-**C**$_q$), 140.1 (BIAN-**C**H), 135.5 (BIAN-**C**H), 132.0, 130.5 (Mes-**C**H), 130.4, 128.3 (BIAN-**C**H), 126.7, 123.1, 21.3, 18.3 (Mes-**C**H$_3$).

^{19}F NMR (282 MHz, $CDCl_3$) δ –73.7 (d, J_{F-P} = 712.9 Hz, P**F**$_6$). **^{31}P NMR** (121 MHz, $CDCl_3$) δ –144.8 (sept, J_{P-F} = 712.9 Hz, **P**F$_6$).

© University of Pretoria

A.1.11) **3a** [RhDB(CO)(PEt_3)]PF_6

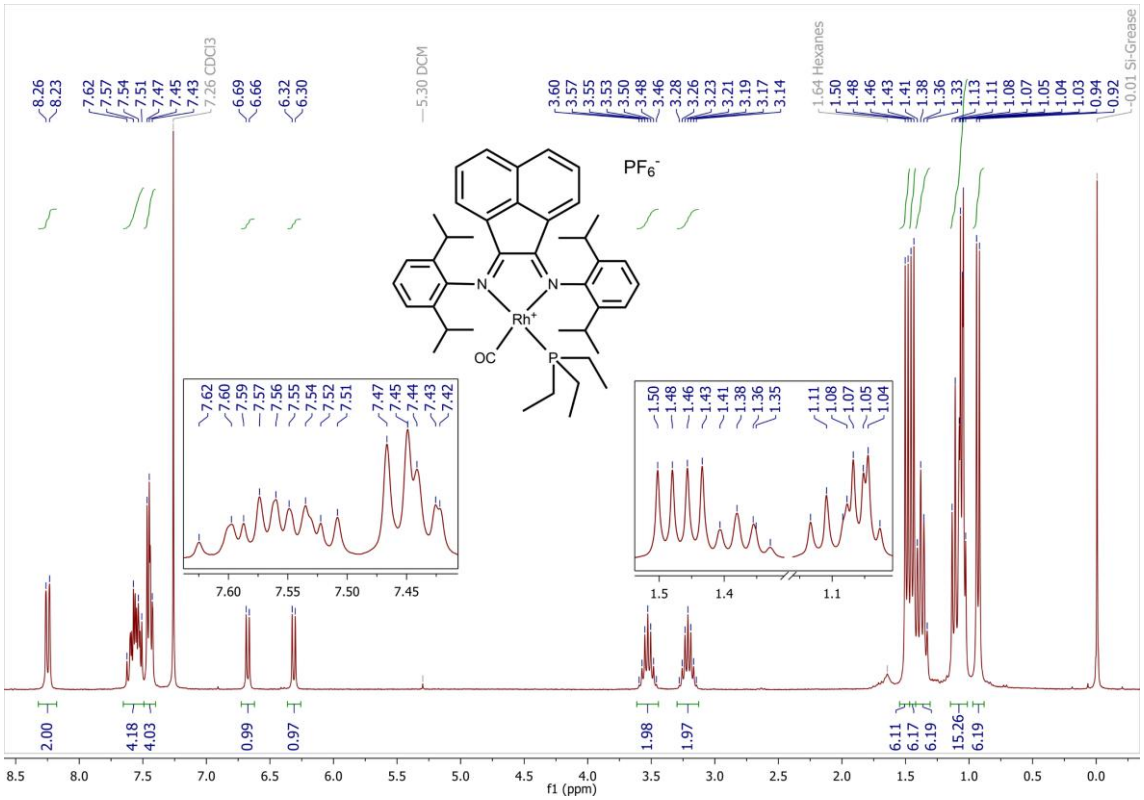


*Figure A.1–20: ^{1}H NMR spectrum of complex **3a** in $CDCl_3$.*

^{1}H NMR (300 MHz, $CDCl_3$) δ 8.25 (d, *J* = 8.4 Hz, 2H, BIAN-C**H**), 7.63–7.50 (m, 4H, Dipp-C**H** and BIAN-C**H**), 7.48–7.41 (m, 4H, Dipp-C**H** and BIAN-C**H**), 6.67 (d, *J* = 7.3 Hz, 1H, BIAN-C**H**), 6.31 (d, *J* = 7.4 Hz, 1H, BIAN-C**H**), 3.53 (sept, *J* = 6.9 Hz, 2H, Dipp(iso)C**H**), 3.21 (sept, *J* = 6.7 Hz, 2H, Dipp(iso)C**H**), 1.49 (d, *J* = 6.8 Hz, 6H, Dipp(iso)C$\mathbf{H}_3$), 1.45 (d, *J* = 6.8 Hz, 6H, Dipp(iso)C$\mathbf{H}_3$), 1.37 (q, *J* = 7.9 Hz, 6H, PEt_3-C$\mathbf{H}_2$), 1.15–1.01 (m, 15H, Dipp(iso)C$\mathbf{H}_3$ and PEt_3-C$\mathbf{H}_3$), 0.93 (d, *J* = 6.8 Hz, 6H, Dipp(iso)C$\mathbf{H}_3$).

© University of Pretoria

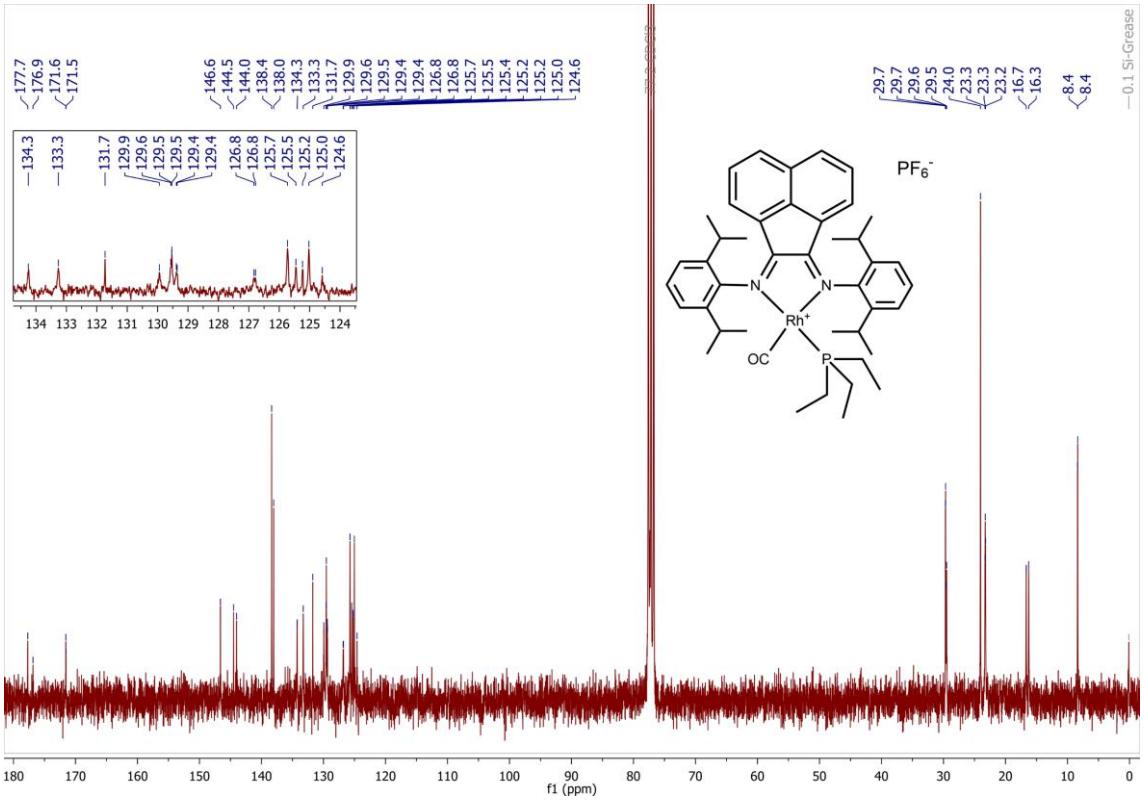


*Figure A.1–21: ^{13}C NMR spectrum of complex **3a** in $CDCl_3$.*

^{13}C NMR (75 MHz, $CDCl_3$) δ 177.27 (d, $J_{C\text{-}Rh}$ = 63.2 Hz, **C**O), 171.6 (BIAN-N=**C**$_q$), 171.5 (BIAN-N=**C**$_q$), 146.6 (BIAN-**C**$_q$), 144.5 (Dipp-N-**C**$_q$), 144.0(Dipp-N-**C**$_q$), 138.4 (BIAN-**C**$_q$), 138.0 (BIAN-**C**$_q$), 134.3 (BIAN-**C**H), 133.3 (BIAN-**C**H), 131.7 (BIAN-**C**$_q$), 129.9 (Dipp-**C**H), 129.6, 129.5 (Dipp-**C**H), 129.4 (Dipp-**C**H), 129.4 (BIAN-**C**$_q$), 126.83 (BIAN-**C**H), 126.78 (BIAN-**C**H), 125.7 (BIAN-**C**H), 125.5 (Dipp(iso)-**C**$_q$), 125.4 (Dipp(iso)-**C**$_q$), 125.23 (Dipp-**C**H), 125.21 (BIAN-**C**H), 125.0 (Dipp-**C**H), 124.6 (Dipp-**C**H), 29.69, 29.66, 29.6, 29.5 (Dipp(iso)-**C**H), 24.0, 23.31, 23.26, 23.21 (Dipp(iso)-**C**H_3), 16.45 (d, $J_{C\text{-}P}$ = 30.1 Hz, PEt_3-**C**H_2), 8.38, 8.35 (PEt_3-**C**H_3).

© University of Pretoria

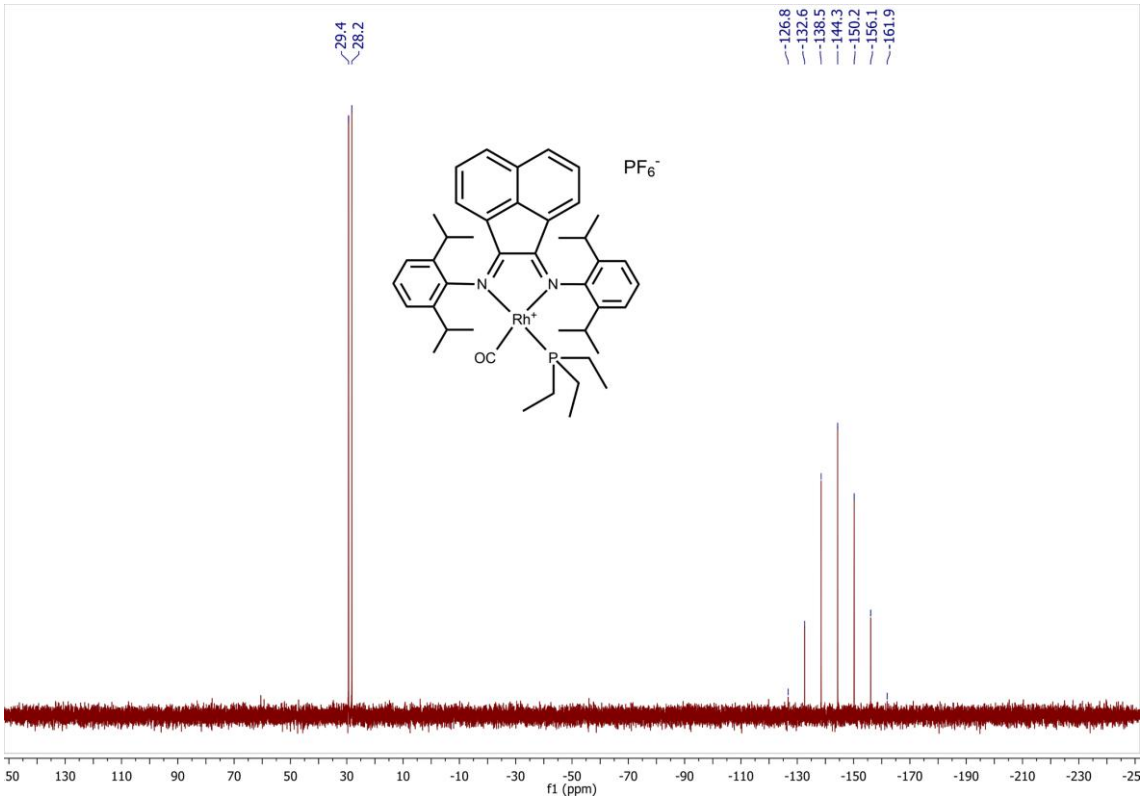


*Figure A.1–22: ^{31}P NMR spectrum of complex **3a** in $CDCl_3$.*

^{19}F NMR (282 MHz, $CDCl_3$) δ –73.8 (d, $J_{F\text{-}P}$ = 712.5 Hz, P**F**$_6$). **^{31}P NMR** (121 MHz, $CDCl_3$) δ –144.4 (sept, $J_{P\text{–}F}$ = 712.2 Hz, **P**F_6), 28.8 (d, $J_{P\text{-}Rh}$ = 141.4 Hz, **P**Et_3).

© University of Pretoria

A.1.12) **3b** [RhMB(CO)(PEt_3)]PF_6

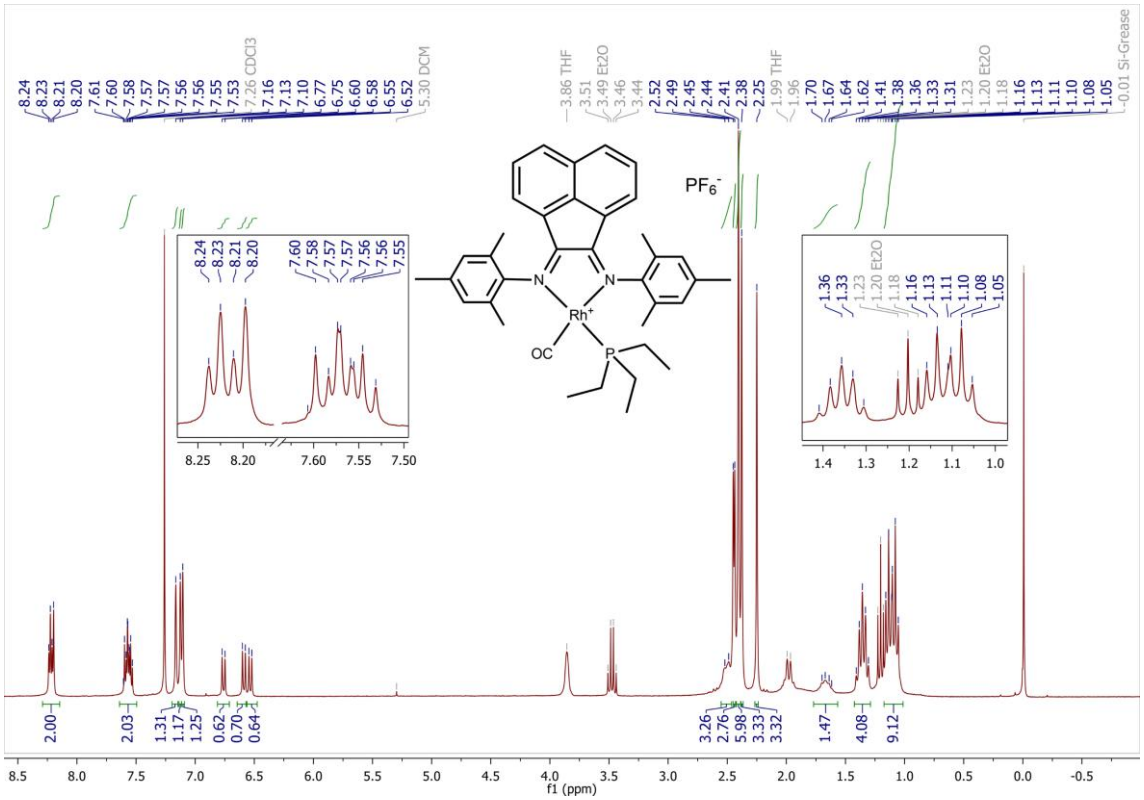


*Figure A.1–23: ^{1}H NMR spectrum of complex **3b** in $CDCl_3$.*

^{1}H NMR (300 MHz, $CDCl_3$) δ 8.22 (dd, *J* = 8.3, 3.9 Hz, 2H, BIAN-C**H**), 7.56 (m, 2H, Mes-C**H** and BIAN-C**H**), 7.16 (s, 1H, Mes-C**H**), 7.13 (s, 1H, Mes-C**H**), 7.10 (s, 1H, Mes-C**H**), 6.76 (d, *J* = 7.2 Hz, 1H, BIAN-C**H**), 6.59 (d, *J* = 7.2 Hz, 1H, BIAN-C**H**), 6.53 (d, *J* = 7.3 Hz, 1H, BIAN-C**H**), 2.55–2.46 (m, 3H, Mes-C$\mathbf{H}_3$), 2.44 (d, *J* = 3.8 Hz, 3H, Mes-C$\mathbf{H}_3$), 2.41 (s, 6H, Mes-C$\mathbf{H}_3$), 2.38 (s, 3H, Mes-C$\mathbf{H}_3$), 2.25 (s, 3H, Mes-C$\mathbf{H}_3$), 1.66 (br, 2H, PEt_3-C$\mathbf{H}_2$), 1.36 (dq, $J_{P\text{-}H}$ = 8.0 Hz, $J_{H\text{-}H}$ = 7.6, 7.4 Hz, 4H, PEt_3-C$\mathbf{H}_2$), 1.11 (dt, $J_{P\text{-}H}$ = 17.0 Hz, $J_{H\text{-}H}$ = 7.4, 7.4 Hz, 9H, PEt_3-C$\mathbf{H}_3$).

© University of Pretoria

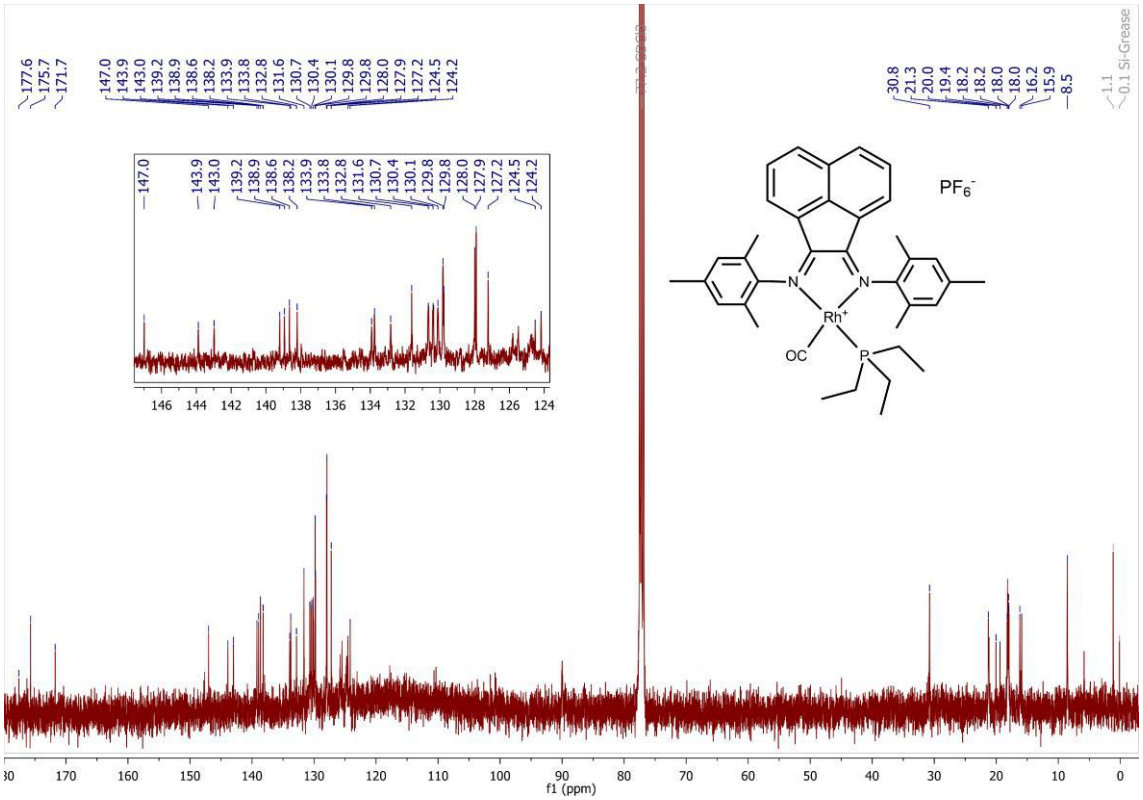


*Figure A.1–24: ^{13}C NMR spectrum of complex **3b** in $CDCl_3$.*

^{13}C NMR (75 MHz, $CDCl_3$) δ 177.6 (Rh=**C**=O), 175.7 (BIAN-N=**C**$_q$), 171.7 (BIAN-N=**C**$_q$), 147.0 (BIAN-**C**$_q$), 143.9 (Mes-N-**C**$_q$), 143.0 (Mes-N-**C**$_q$),139.2, 138.9, 138.6, 138.2, 133.9 (BIAN-**C**H), 133.8, 132.8 (BIAN-**C**H), 131.6, 130.7 (Mes-**C**H), 130.4 (Mes-**C**H), 130.1 (Mes-**C**H), 129.82 (Mes-**C**H), 129.77 (BIAN-**C**H), 128.0, 127.9, 127.2 (BIAN-**C**$_q$), 125.8 (BIAN-**C**H), 125.5 (BIAN-**C**H), 124.5 (BIAN-**C**H), 124.2, 30.88, 21.3, 21.2 (Mes-**C**H$_3$), 19.71 (d, $J_{C\text{-}P}$ = 65.8 Hz, PEt$_3$-**C**H$_2$), 18.24, 18.19, 17.96 (Mes-**C**H$_3$), 16.06 (d, $J_{C\text{-}P}$ = 29.7 Hz, PEt$_3$-**C**H$_2$), 8.5, 5.8 (PEt$_3$-**C**H$_3$).

© University of Pretoria

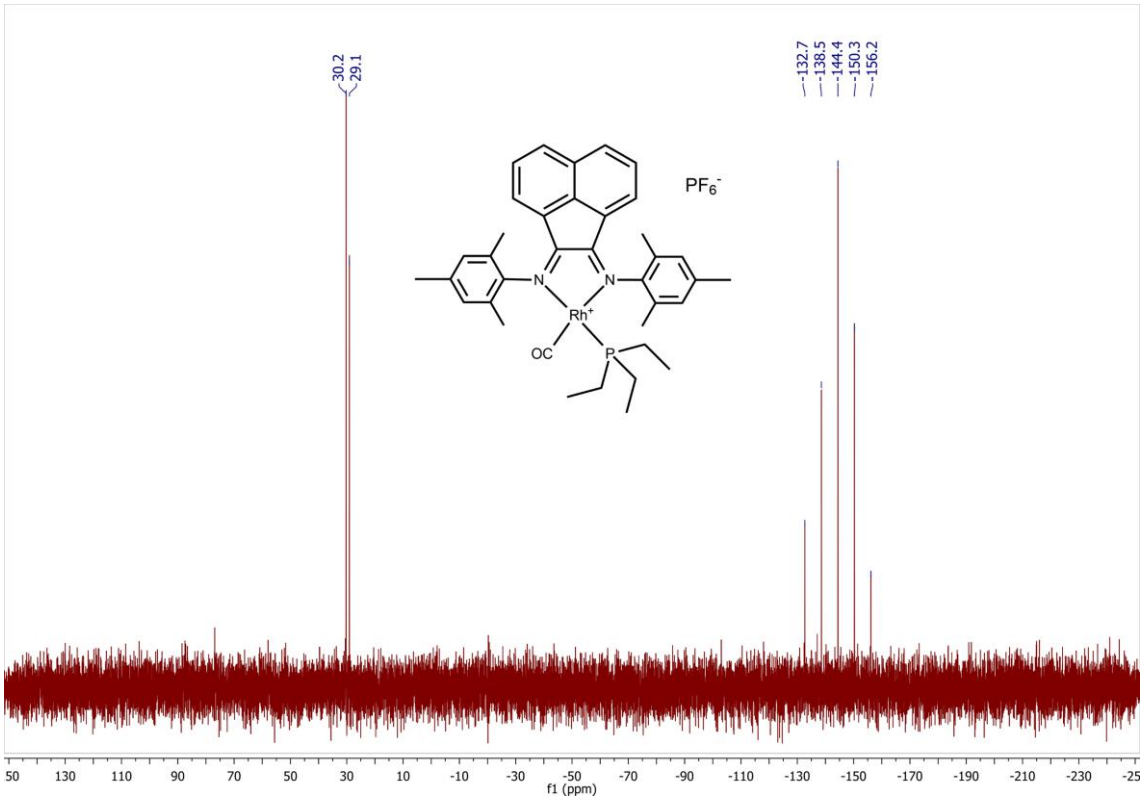


*Figure A.1–25: ^{31}P NMR spectrum of complex **3b** in $CDCl_3$.*

^{19}F NMR (282 MHz, $CDCl_3$) δ –73.5 (d, $J_{F\text{-}P}$ = 713.1 Hz, P**F**$_6$). **^{31}P NMR** (121 MHz, $CDCl_3$) δ 29.7 (d, $J_{P\text{-}Rh}$ = 143.0 Hz), –144.4 (sept, $J_{P–F}$ = 712.4 Hz, **P**F$_6$).

© University of Pretoria

A.1.13) **4a** [RhDB(cod)Cl]

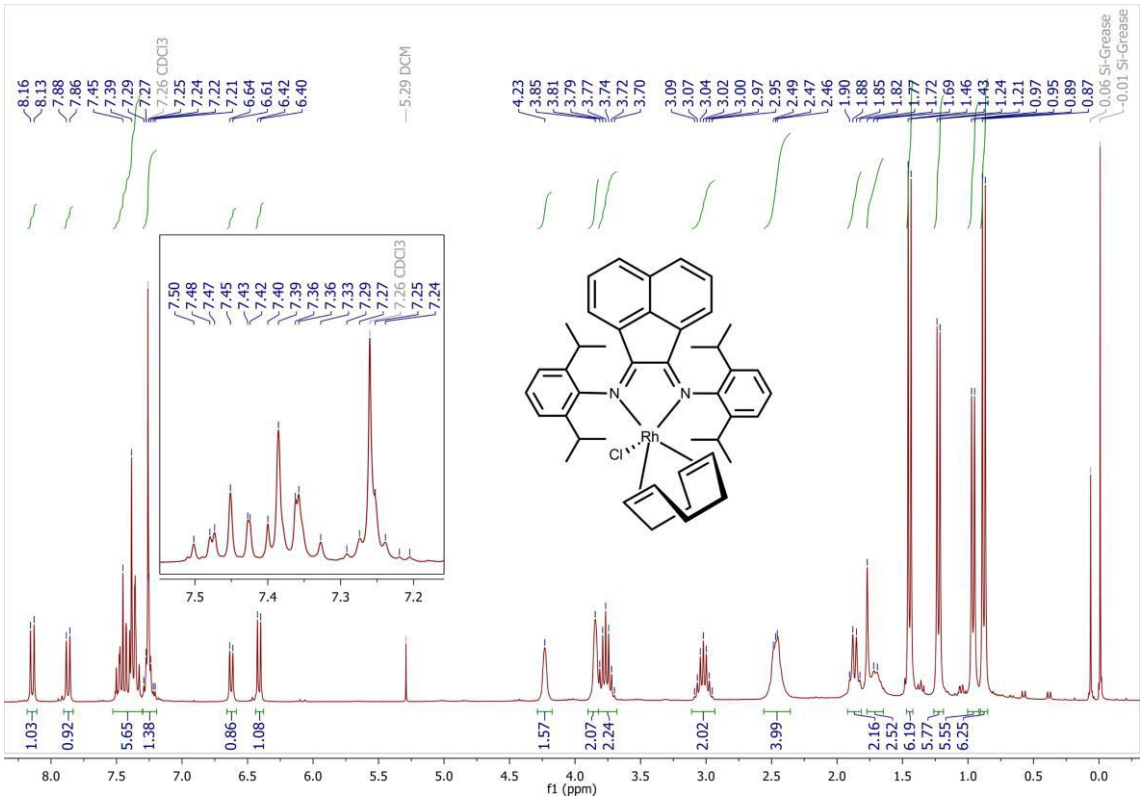


*Figure A.1–26: ^{1}H NMR spectrum of complex **4a** in $CDCl_3$.*

^{1}H NMR (300 MHz, $CDCl_3$) δ 8.14 (d, *J* = 8.3 Hz, 1H, BIAN-C**H**), 7.87 (d, *J* = 8.3 Hz, 1H, BIAN-C**H**), 7.42 (br, 6H, Dipp-C**H** and BIAN-C**H**), 7.31–7.19 (m, 1H), 6.62 (d, *J* = 7.2 Hz, 1H, BIAN-C**H**), 6.41 (d, *J* = 7.3 Hz, 1H, BIAN-C**H**), 4.23 (br, 2H, cod-C**H**), 3.85 (s, 2H, cod-C**H**), 3.75 (sept, *J* = 6.7 Hz, 2H, Dipp(iso)C**H**), 3.02 (sept, *J* = 6.7 Hz, 2H, Dipp(iso)C**H**), 2.55–2.36 (m, 4H, cod-C$\mathbf{H}_2$), 1.93–1.81 (m, 2H, cod-C$\mathbf{H}_2$), 1.77–1.64 (m, 2H, cod-C$\mathbf{H}_2$), 1.45 (d, *J* = 6.8 Hz, 6H, Dipp(iso)C$\mathbf{H}_3$), 1.23 (d, *J* = 6.9 Hz, 6H, Dipp(iso)C$\mathbf{H}_3$), 0.96 (d, *J* = 6.9 Hz, 6H, Dipp(iso)C$\mathbf{H}_3$), 0.88 (d, *J* = 6.8 Hz, 6H, Dipp(iso)C$\mathbf{H}_3$).

© University of Pretoria

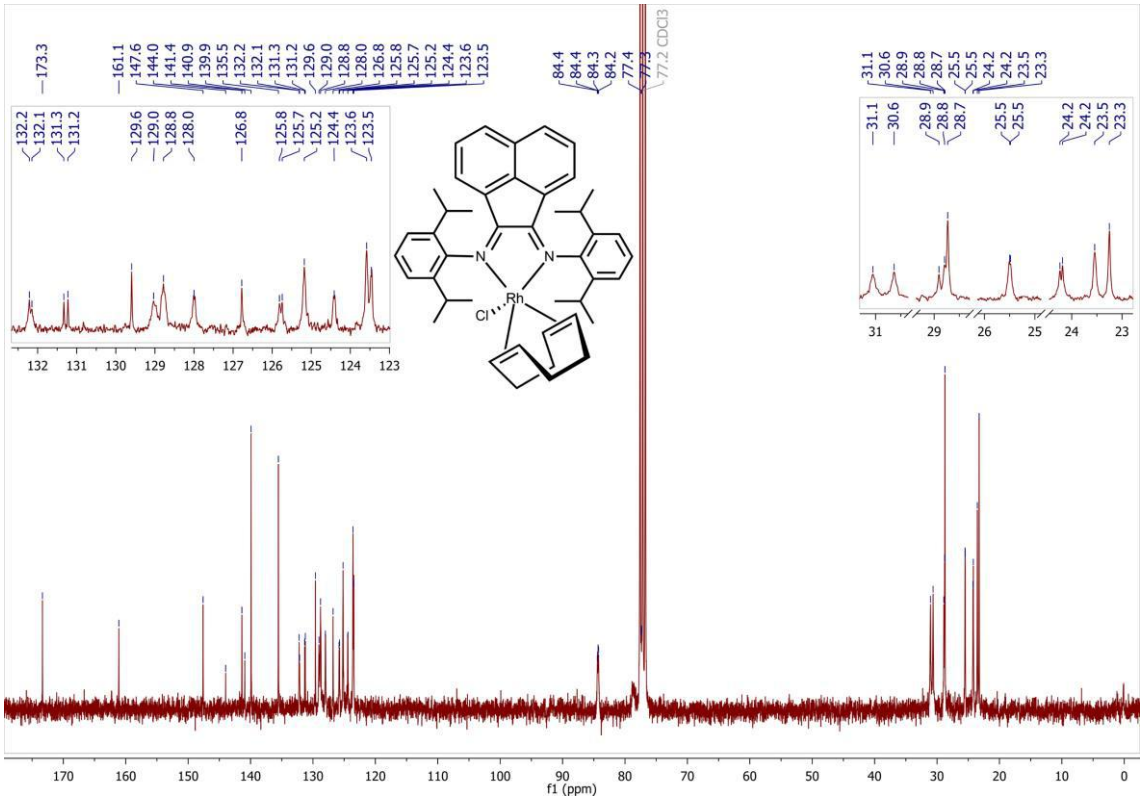


*Figure A.1–27: ^{13}C NMR spectrum of complex **4a** in $CDCl_3$.*

^{13}C NMR (75 MHz, $CDCl_3$) δ 173.3 (BIAN-N=**C**$_q$), 161.1 (BIAN-N=**C**$_q$), 147.6 (Dipp-N-**C**$_q$), 144.0 (Dipp-N-**C**$_q$), 141.4 (BIAN-**C**$_q$), 140.9 (BIAN-**C**$_q$), 139.9 (**C**$_q$), 135.5 (**C**$_q$), 132.2, 132.1 (BIAN-**C**H), 131.3, 131.2 (Dipp(iso)-**C**$_q$), 129.6 (**C**$_q$), 129.0, 128.8 (Dipp-**C**H), 128.0 (BIAN-**C**H), 126.8 (**C**$_q$), 125.8, 125.7 (Dipp-**C**H), 125.2, 124.4 (BIAN-**C**H), 123.6, 123.5 (Dipp-**C**H), 84.35 (dd, $J_{C\text{-}Rh}$ = 10.9, 4.9 Hz, cod-**C**H), 77.36 (d, $J_{C\text{-}Rh}$ = 4.8 Hz, cod-**C**H), 31.1 (cod-**C**H$_2$), 30.6 (cod-**C**H$_2$), 28.9, 28.8, 28.7 (Dipp(iso)-**C**H), 25.5 (cod-**C**H$_2$), 25.5 (Dipp(iso)-**C**H$_3$), 24.2 (cod-**C**H$_2$), 24.2, 23.5, 23.3 (Dipp(iso)-**C**H$_3$).

© University of Pretoria

A.1.14) **4b** [RhMB(cod)Cl]

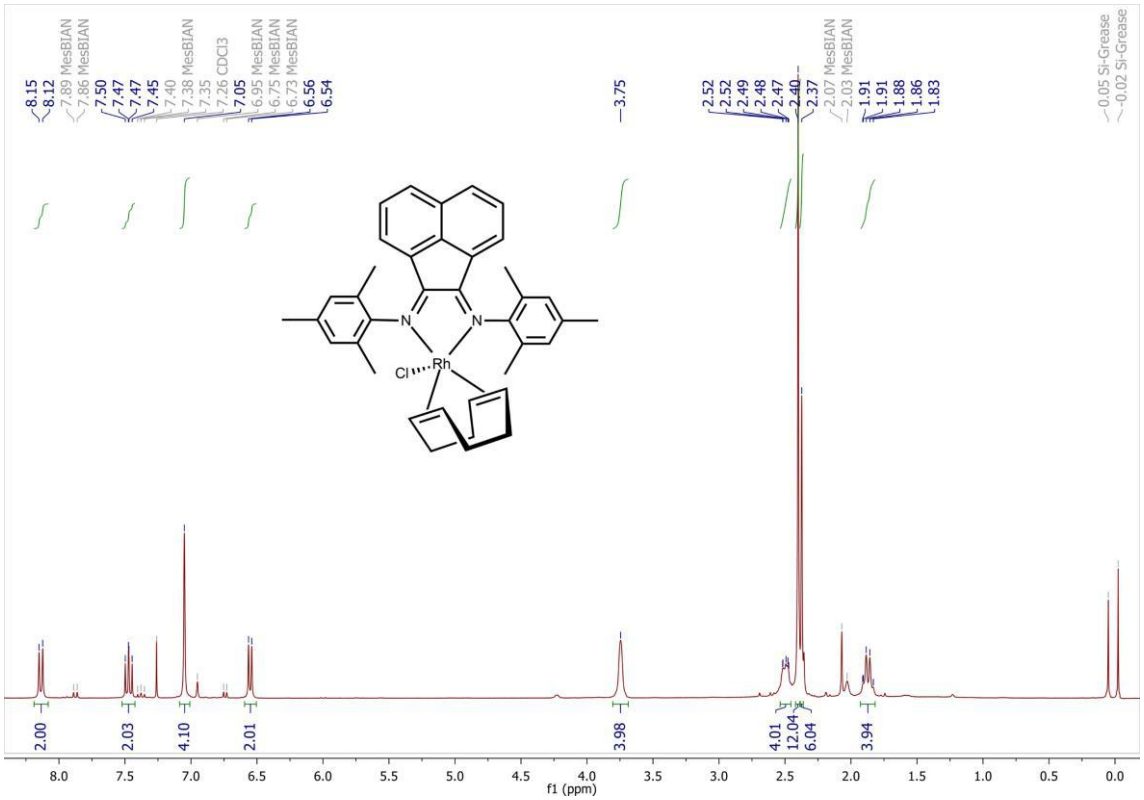


*Figure A.1–28: ^{1}H NMR spectrum of complex **4b** in $CDCl_3$. A small amount of the MesBIAN ligand dissociates from the complex over time, and the associated peaks have been marked as "MesBIAN".*

^{1}H NMR (300 MHz, $CDCl_3$) δ 8.14 (d, *J* = 8.3 Hz, 2H, BIAN-C**H**), 7.47 (dd, *J* = 8.3, 7.3 Hz, 2H, BIAN-C**H**), 7.05 (s, 4H, Mes-C**H**), 6.55 (d, *J* = 7.2 Hz, 2H, BIAN-C**H**), 3.75 (br, 4H, cod-C**H**), 2.52–2.47 (m, 4H, cod-C**H**$_2$), 2.40 (s, 12H, Mes-C**H**$_3$), 2.37 (s, 6H, Mes-C**H**$_3$), 1.98–1.81 (m, 4H, cod-C**H**$_2$).

© University of Pretoria

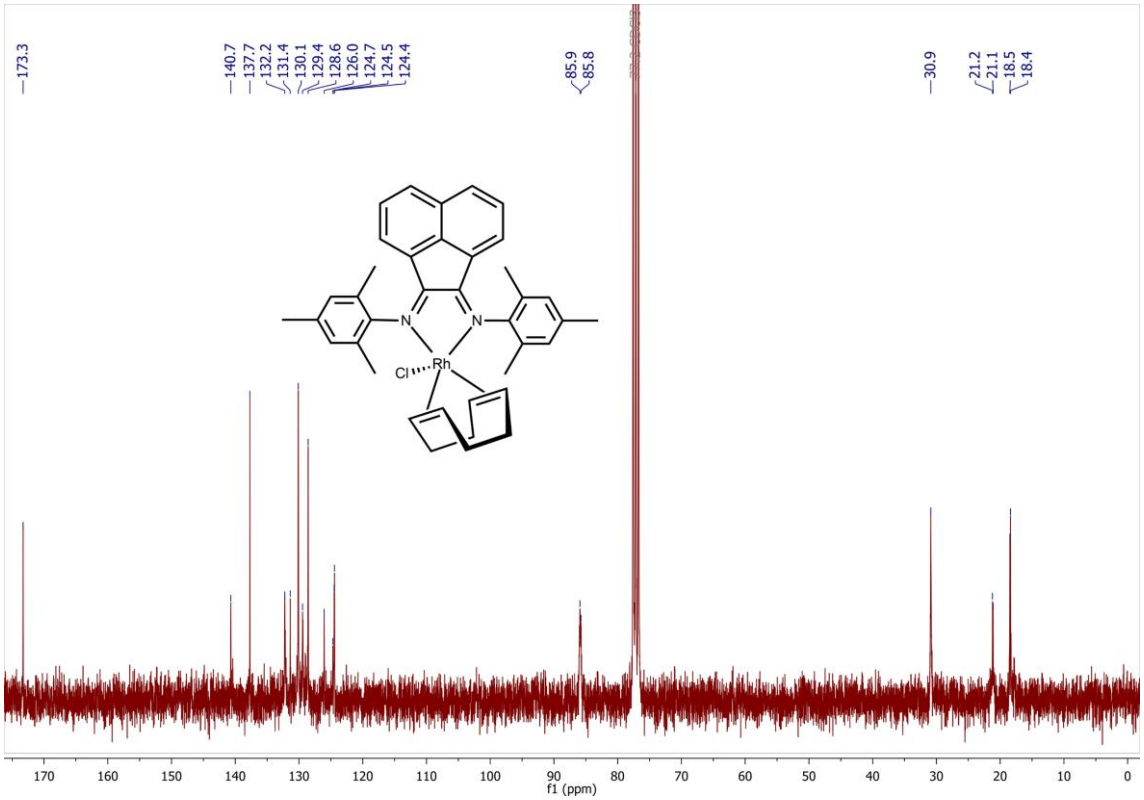


*Figure A.1–29: ^{13}C NMR spectrum of complex **4b** in $CDCl_3$.*

^{13}C NMR (75 MHz, $CDCl_3$) δ 173.3 (BIAN-N=**C**$_q$), 140.7 (Mes-N-**C**$_q$), 137.7 (BIAN-**C**H), 132.2 (BIAN-**C**$_q$), 132.2 (BIAN-**C**$_q$), 131.4 (**C**$_q$), 130.1 (Mes-**C**H), 129.4 (**C**$_q$), 128.6 (BIAN-**C**H), 126.0 (**C**$_q$), 124.7 (BIAN-**C**$_q$), 124.5 (BIAN-**C**H), 124.4 (BIAN-**C**H), 85.9 (d, $J_{C\text{-}Rh}$ = 11.0 Hz, cod-**C**H), 30.9 (cod-**C**H_2), 21.2, 21.1, 18.5, 18.4 (Mes-**C**H_3).

© University of Pretoria

A.1.15) **4c** [IrDB(cod)Cl]

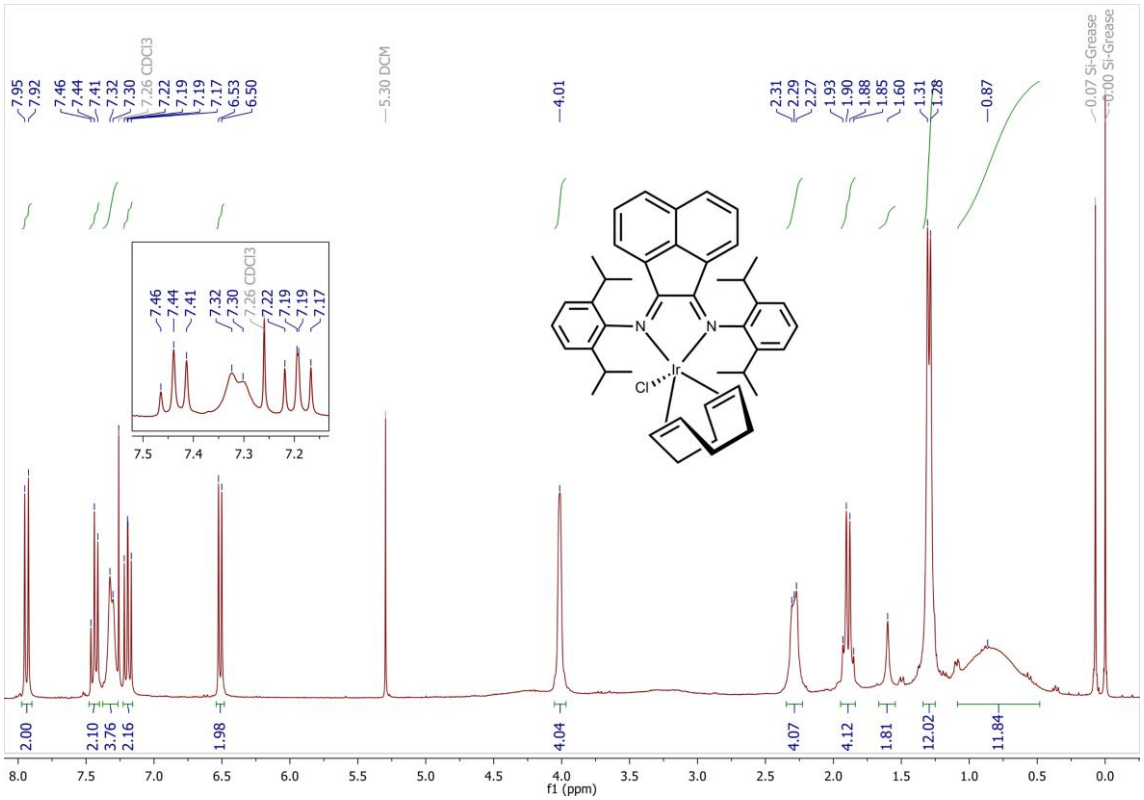


*Figure A.1–30: ^{1}H NMR spectrum of complex **4c** in $CDCl_3$.*

^{1}H NMR (300 MHz, $CDCl_3$) δ 7.94 (d, *J* = 8.2 Hz, 2H, BIAN-C**H**), 7.44 (dd, *J* = 7.6 Hz, 2H, Dipp-C**H**), 7.31 (br, 4H, Dipp-C**H**), 7.19 (dd, *J* = 8.3, 7.2 Hz, 2H, 2H, BIAN-C**H**), 6.51 (d, *J* = 7.2 Hz, 2H, BIAN-C**H**), 4.01 (br, 4H, cod-C**H**), 2.29 (br, 4H, Dipp(iso)C**H**), 1.95–1.84 (m, 4H, cod-C$\mathbf{H}_2$), 1.60 (br, 2H, cod-C$\mathbf{H}_2$), 1.30 (d, *J* = 6.7 Hz, 12H, Dipp(iso)C$\mathbf{H}_3$), 0.87 (br, 12H, Dipp(iso)C$\mathbf{H}_3$).

© University of Pretoria

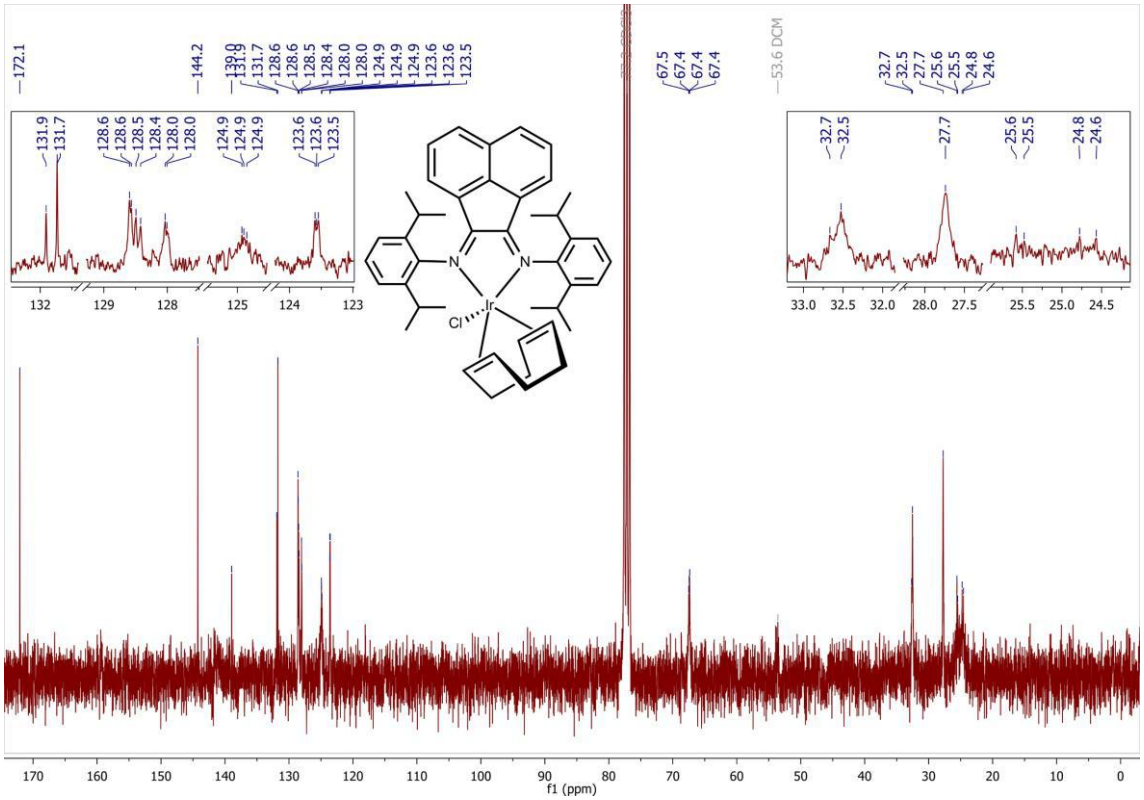


*Figure A.1–31: ^{13}C NMR spectrum of complex **4c** in $CDCl_3$.*

^{13}C NMR (75 MHz, $CDCl_3$) δ 172.1 (BIAN-N=**C_q**), 144.2 (Dipp-N-**C_q**), 139.0 (BIAN-**C_q**), 131.9, 131.7 (Dipp(iso)-**C_q**), 128.59, 128.57 (BIAN-**C**H), 128.5, 128.4 (BIAN-**C_q**), 128.03, 128.00 (BIAN-**C**H), 124.93, 124.90, 124.85 (Dipp-**C**H), 123.6 (BIAN-**C**H), 123.6 (BIAN-**C_q**), 123.5 (BIAN-**C**H), 67.4 (br, cod-**C**H), 32.7 (cod-**C**H_2), 32.5 (br, Dipp(iso)-**C**H), 27.7 (br, cod-**C**H_2), 25.6, 25.5, 24.8, 24.6 (Dipp(iso)-**C**H_3).

© University of Pretoria

A.1.16) **4d** [IrMB(cod)Cl]

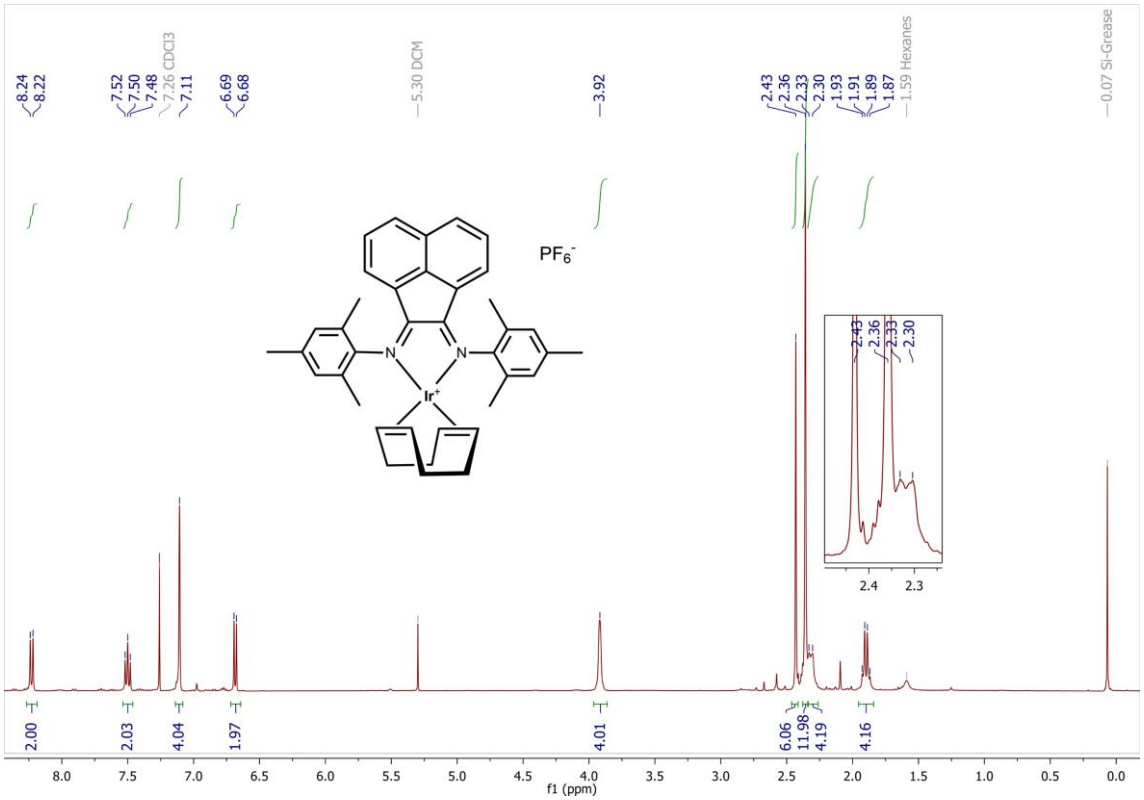


*Figure A.1–32: ^{1}H NMR spectrum of complex **4d** in $CDCl_3$.*

^{1}H NMR (300 MHz, $CDCl_3$) δ 7.96 (d, *J* = 8.2 Hz, 2H, BIAN-C**H**), 7.26–7.20 (m, 2H, BIAN-C**H**), 6.99 (s, 4H, Mes-C**H**), 6.64 (d, *J* = 7.1 Hz, 2H, BIAN-C**H**), 3.92 (br, 4H, cod-C**H**), 2.39 (s, 6H, Mes-C**H**$_3$), 2.32 (br, 16H, Mes-C**H**$_3$ and cod-C**H**$_2$), 1.95–1.83 (m, 4H, cod-C**H**$_2$).

© University of Pretoria

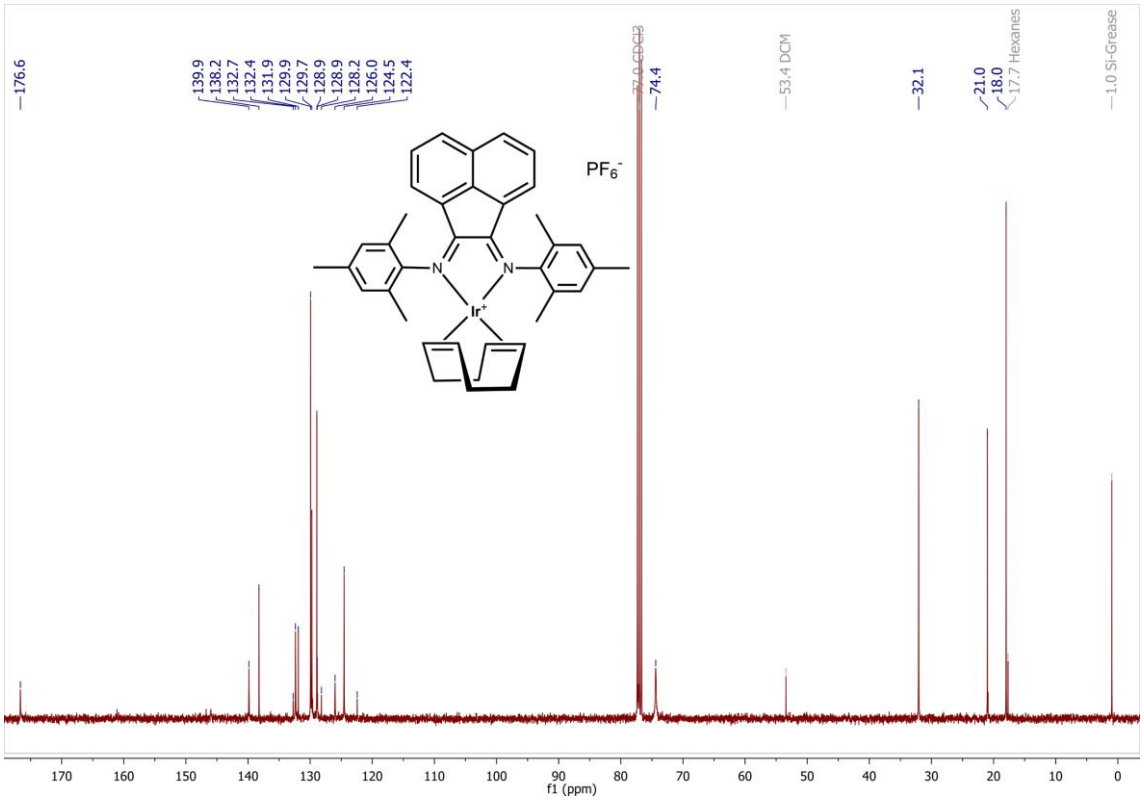


*Figure A.1–33: ^{13}C NMR spectrum of complex **4d** in $CDCl_3$.*

^{13}C NMR (75 MHz, $CDCl_3$) δ 171.3 (BIAN-N=**C_q**), 144.1 (Mes-N-**C_q**), 139.3 (BIAN-**C_q**), 136.6, 132.0 (BIAN-**C_q**), 131.3, 129.8 (Mes-**C**H), 129.1 (BIAN-**C**H), 128.4 (BIAN-**C**H), 121.9 (BIAN-**C**H), 77.4 (cod-**C**H), 32.8, 32.8, 32.7, 32.6 (cod-**C**H_2), 21.1, 18.8 (Mes-**C**H_3).

© University of Pretoria

A.2) NMR Data Tables

*Table A.2–1: :Selected ^{1}H NMR chemical shifts, multiplicity and coupling constants for DippBIAN, MesBIAN, and the series of complexes **1–4** as recorded in $CDCl_3$ at 25 °C.*

Compound	BIAN-C**H**	Ar-C**H**	Ar-C**H$_3$**	^{i}Pr-C**H**
DippBIAN	7.86 (d, J = 8.3 Hz, 2H) 7.35 (dd, J = 8.3, 7.2 Hz, 2H) 6.63 (d, J = 7.2 Hz, 2H)	7.31–7.19 (m, 6H)	1.23 (d, J = 6.8 Hz, 12H) 0.97 (d, J = 6.8 Hz, 12H)	3.03 (sept, J = 6.8 Hz, 4H)
MesBIAN	7.89 (d, J = 8.3 Hz, 2H) 7.37 (dd, J = 8.3, 7.1 Hz, 2H) 6.80 (d, J = 7.1 Hz, 2H)	6.98 (s, 4H)	2.37 (s, 6H) 2.12 (s, 12H)	
1a	8.24 (d, J = 8.3 Hz, 2H) 7.56 (dd, J = 7.3, 3.6 Hz, 2H) 6.40 (d, J = 7.3 Hz, 2H)	7.53 (dd, J = 7.5, 3.3 Hz, 2H) 7.42 (d, J = 7.5 Hz, 4H)	1.52 (d, J = 6.8 Hz, 12H) 0.93 (d, J = 6.8 Hz, 12H)	3.46 (sept, J = 6.7 Hz, 4H)
1b	8.21 (d, J = 8.3 Hz, 2H) 7.56 (dd, J = 8.3, 7.3 Hz, 2H) 6.59 (d, J = 7.3 Hz, 2H)	7.11 (s, 4H)	2.40 (s, 6H) 2.38 (s, 12H)	
1c	8.36 (d, J = 8.2 Hz, 2H) 7.61–7.53 (m, 4H)* 6.50 (d, J = 7.3 Hz, 2H)	7.61–7.53 (m, 4H)* 7.47 (d, J = 7.8 Hz, 4H) * Overlapping peaks	1.49 (d, J = 6.7 Hz, 12H) 0.93 (d, J = 6.7 Hz, 12H)	3.40 (sept, J = 6.4 Hz, 4H)
1d	8.23 (d, J = 8.3 Hz, 2H) 7.50 (dd, J = 8.3, 7.2 Hz, 2H) 6.68 (d, J = 7.2 Hz, 2H)	7.11 (s, 4H)	2.43 (s, 6H) 2.36 (s, 12H)	
2a	8.37 (d, J = 8.3 Hz, 2H) 7.66 (dd, J = 8.3, 7.4 Hz, 2H) 6.72 (d, J = 7.4 Hz, 2H)	7.60 (dd, J = 8.7, 7.1 Hz, 2H) 7.47 (d, J = 7.9 Hz, 4H)	1.51 (d, J = 6.8 Hz, 12H) 1.10 (d, J = 6.8 Hz, 12H)	3.38 (sept, J = 6.7 Hz, 4H)
2b	8.28 (d, J = 8.3 Hz, 2H) 7.63 (dd, J = 8.3, 7.3 Hz, 2H) 6.78 (d, J = 7.3 Hz, 2H)	7.14 (s, 4H)	2.42 (s, 18H)	
2c	8.45 (br, 2H) 7.70 (dd, J = 7.9, 7.3 Hz, 2H) 6.82 (d, J = 7.3 Hz, 2H)	7.61 (dd, J = 8.7, 6.8 Hz, 2H) 7.51 (d, J = 7.7 Hz, 4H)	1.50 (d, J = 6.8 Hz, 12H) 1.11 (d, J = 6.8 Hz, 12H)	3.39 (sept, J = 6.8 Hz, 4H)
2d	8.33 (d, J = 8.3 Hz, 2H) 7.66 (dd, J = 8.3, 7.3 Hz, 2H) 6.87 (d, J = 7.3 Hz, 2H)	7.18 (s, 4H)	2.46 (s, 18H)	
3a	8.25 (d, J = 8.4 Hz, 2H) 7.63–7.50 (m, 4H)* 7.48–7.41 (m, 4H)† 6.67 (d, J = 7.3 Hz, 1H) 6.31 (d, J = 7.4 Hz, 1H)	7.63–7.50 (m, 4H)* 7.48–7.41 (m, 4H)† *, † Overlapping peaks ‡ Overlaps with a PEt_3 signal	1.49 (d, J = 6.8 Hz, 6H) 1.45 (d, J = 6.8 Hz, 6H) 1.15–1.01 (m, 15H)‡ 0.93 (d, J = 6.8 Hz, 6H)	3.53 (sept, J = 6.9 Hz, 2H) 3.21 (sept, J = 6.7 Hz, 2H)
3b	8.22 (dd, J = 8.3, 3.9 Hz, 2H) 7.56 (m, 2H)* 6.76 (d, J = 7.2 Hz, 1H) 6.59 (d, J = 7.2 Hz, 1H) 6.53 (d, J = 7.3 Hz, 1H)	7.56 (m, 2H)* 7.16 (s, 1H) 7.13 (s, 1H) 7.10 (s, 1H) * Overlapping peaks	2.55–2.46 (m, 3H) 2.44 (d, J = 3.8 Hz, 3H) 2.41 (s, 6H) 2.38 (s, 3H) 2.25 (s, 3H)	
4a	8.14 (d, J = 8.3 Hz, 1H) 7.87 (d, J = 8.3 Hz, 1H) 7.52–7.31 (m, 6H)* 7.31–7.19 (m, 1H)‡ 6.62 (d, J = 7.2 Hz, 1H) 6.41 (d, J = 7.3 Hz, 1H)	7.52–7.31 (m, 6H)* * Overlapping peaks ‡ Overlap with $CDCl_3$	1.45 (d, J = 6.8 Hz, 6H) 1.23 (d, J = 6.9 Hz, 6H) 0.96 (d, J = 6.9 Hz, 6H) 0.88 (d, J = 6.8 Hz, 6H)	3.75 (sept, J = 6.7 Hz, 2H) 3.02 (sept, J = 6.7 Hz, 2H)
4b	8.14 (d, J = 8.3 Hz, 2H) 7.47 (dd, J = 8.3, 7.3 Hz, 2H) 6.55 (d, J = 7.2 Hz, 2H)	7.05 (s, 4H)	2.40 (s, 12H) 2.37 (s, 6H)	
4c	7.94 (d, J = 8.2 Hz, 2H) 7.19 (dd, J = 8.3, 7.2 Hz, 2H) 6.51 (d, J = 7.2 Hz, 2H)	7.44 (dd, J = 7.6 Hz, 2H) 7.31 (br, 4H)	1.30 (d, J = 6.7 Hz, 12H) 0.87 (br, 12H)	2.29 (br, 4H)
4d	7.96 (d, J = 8.2 Hz, 2H) 7.26–7.20 (m, 2H) 6.64 (d, J = 7.1 Hz, 2H)	6.99 (s, 4H)	2.39 (s, 6H) 2.32 (br, 16H)† † Signals overlap with cod–CH_2	

© University of Pretoria

*Table A.2–2: Selected ^{13}C NMR chemical shifts, multiplicity and coupling constants for DippBIAN, MesBIAN, and the series of complexes **1–4** as recorded in $CDCl_3$ at 25 °C. † A fully resolved ^{13}C NMR spectrum for **2c** could not be obtained, even after prolonged acquisition times.*

Compound	BIAN–**C**H	BIAN–N=**C**$_q$	Ar–**C**H	Ar–N–**C**$_q$	Ar–**C**H$_3$	Miscellaneous
DippBIAN	128.0, 124.4, 123.5	161.1	135.5, 123.6	147.6	23.5, 23.3	28.7 (Dipp(iso)–**C**H)
MesBIAN	129.6, 124.5, 122.4	161.1	128.9	146.8	20.90, 20.87 (*p*) 17.70, 17.66 (*o*)	
1a	134.2, 129.4, 126.9	175.9	129.4, 125.5	147.1	25.3, 23.7, 23.6	89.9 (d, $J_{C–Rh}$ = 12.2 Hz, cod–**C**H), 29.7 (Dipp(iso)–**C**H)
1b	138.7, 133.8, 130.4	175.7	127.9	147.6	21.22, 21.17, 18.00, 17.95	90.0 (d, $J_{C–Rh}$ = 10.1 Hz, cod–**C**H)
1c	134.9, 129.9, 127.4	179.63, 179.61	130.3, 125.5	138.3	25.3, 23.7	77.5, 77.4 (cod–**C**H), 29.6 (Dipp(iso)–**C**H)
1d	132.7, 129.7, 124.5	176.6	132.4, 131.9, 129.9	139.9	21.0, 18.0	74.4 (cod–**C**H)
2a	135.7, 126.8, 125.5	178.6	138.3, 132.0, 123.2, 123.2	149.3	23.9, 23.4, 23.4	180.2 (d, $J_{C–Rh}$ = 70.3 Hz, Rh=**C**O), 30.0, 29.9 (Dipp(iso)–**C**H)
2b	139.5, 134.9, 127.5	178.5	130.5	149.3	21.2, 21.1, 18.3, 18.2	180.19 (d, $J_{C–Rh}$ = 70.1 Hz, Rh=**C**O)
2c †	-	-	-	-	-	-
2d	140.1, 135.5, 128.3	168.7	132.0, 130.5	151.1	21.3, 18.3	180.4 (Ir=**C**O)
3a	134.3, 133.3, 126.83, 126.78, 125.7, 125.21	171.6, 171.5	129.9, 129.6, 129.5, 129.4, 125.2, 125.0, 124.6	144.5, 144.0	24.0, 23.31, 23.26, 23.21	177.27 (d, $J_{C–Rh}$ = 63.2 Hz, Rh=**C**O), 29.69, 29.66, 29.6, 29.5 (Dipp(iso)–**C**H), 16.45 (d, $J_{C–P}$ = 30.1 Hz, PEt$_3$–**C**H$_2$), 8.38, 8.35 (PEt$_3$–**C**H$_3$)
3b	133.9, 133.8, 132.8, 129.8, 125.8, 125.5, 124.5	175.7, 171.7	131.6, 130.7, 130.4, 130.1, 129.8	143.9, 143.0	30.88, 21.3, 21.2, 18.24, 18.19, 17.96	177.6 (Rh=**C**O), 19.71 (d, $J_{C–P}$ = 65.8 Hz, PEt$_3$–**C**H$_2$), 16.06 (d, $J_{C–P}$ = 29.7 Hz, PEt$_3$–**C**H$_2$), 8.5, 5.8 (PEt$_3$–**C**H$_3$)
4a	132.2, 132.1, 128.0, 125.2, 124.4	173.3, 161.1	129.0, 128.8, 125.8, 125.7, 123.6, 123.5	147.6, 144.0	25.5, 24.2, 23.5, 23.3	84.35 (dd, $J_{C–Rh}$ = 10.9, 4.9 Hz, cod–**C**H), 77.36 (d, $J_{C–Rh}$ = 4.8 Hz, cod–**C**H), 28.9, 28.8, 28.7 (Dipp(iso)–**C**H)
4b	137.7, 128.6, 124.5, 124.4	173.3	130.1	140.7	21.2, 21.1, 18.5, 18.4	85.90 (d, $J_{C–Rh}$ = 11.0 Hz, cod–**C**H)
4c	128.59, 128.57, 128.03, 128.00, 123.6, 123.5	172.1	124.93, 124.90, 124.85	144.2	25.6, 25.5, 24.8, 24.6	67.4 (br, cod–**C**H), 32.5 (br, Dipp(iso)–**C**H)
4d	129.1, 128.4, 121.9	171.3	131.3, 129.8	144.1	21.1, 18.8	77.4 (cod–**C**H)

© University of Pretoria

Appendix B: Mass Spectrometry

B.1) Mass Spectrometry

B.1.1) **1a** [RhDB(cod)]PF_6

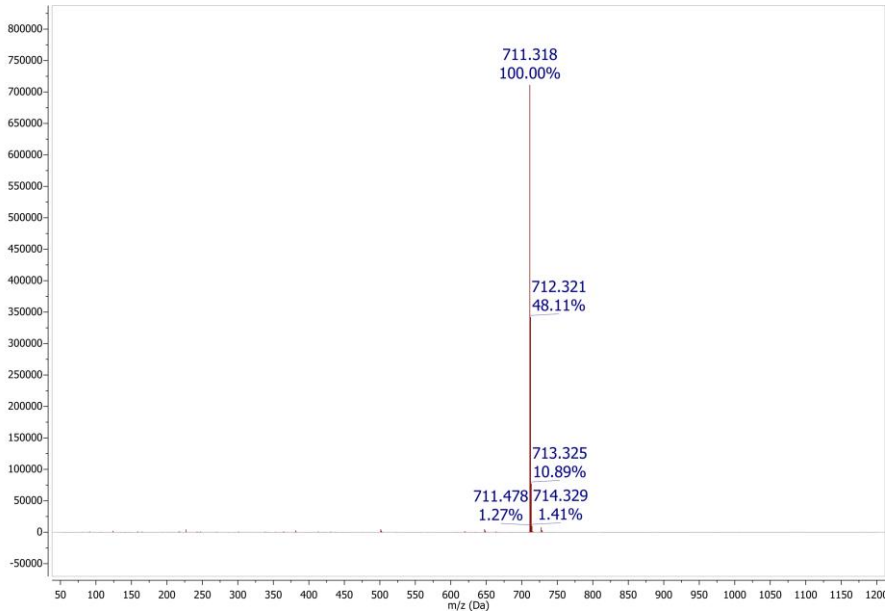


*Figure B.1–1: Mass Spectroscopy spectrum of **1a** recorded in methanol: Positive mode, Electron Spray Ionisation.*

MS (ESI+, CH_3OH): m/z [**1a**]$^+$ calculated 711.31855; found 711.318.

B.1.2) **1b** [RhMB(cod)]PF_6

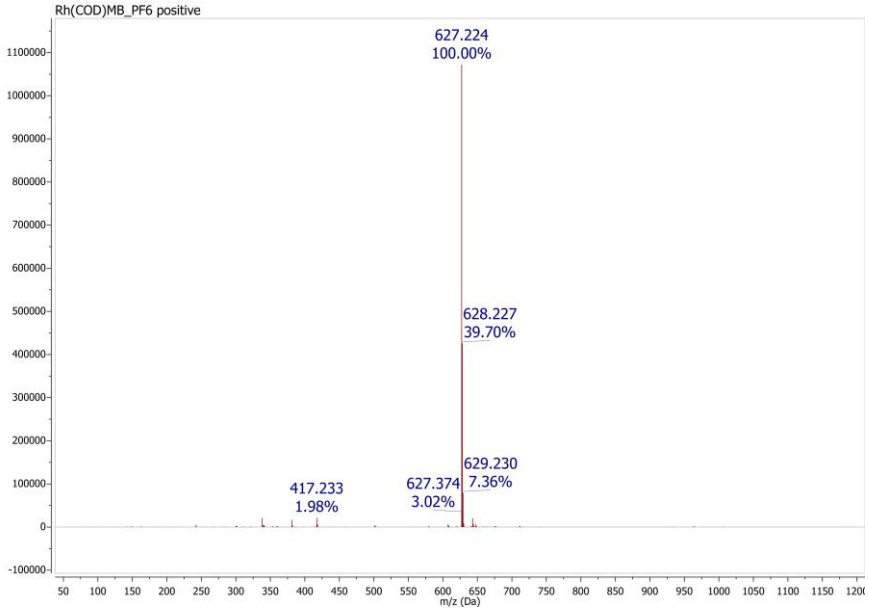


*Figure B.1–2: Mass Spectroscopy spectrum of **1b** recorded in methanol: Positive mode, Electron Spray Ionisation.*

MS (ESI+, CH_3OH): m/z [**1b**]$^+$ calculated 627.225; found 627.224.

© University of Pretoria

B.1.3) **1c** [IrDB(cod)]PF_6

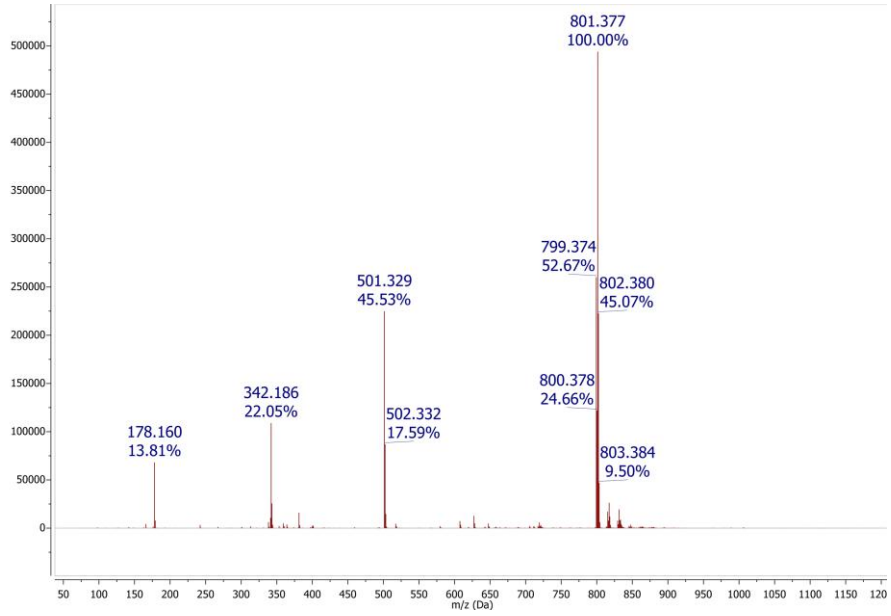


*Figure B.1–3: Mass Spectroscopy spectrum of **1c** recorded in methanol: Positive mode, Electron Spray Ionisation.*

MS (ESI+, CH_3OH): m/z [**1c**]$^+$ calculated 801.3759; found 801.377.

B.1.4) **1d** [IrMB(cod)]PF_6

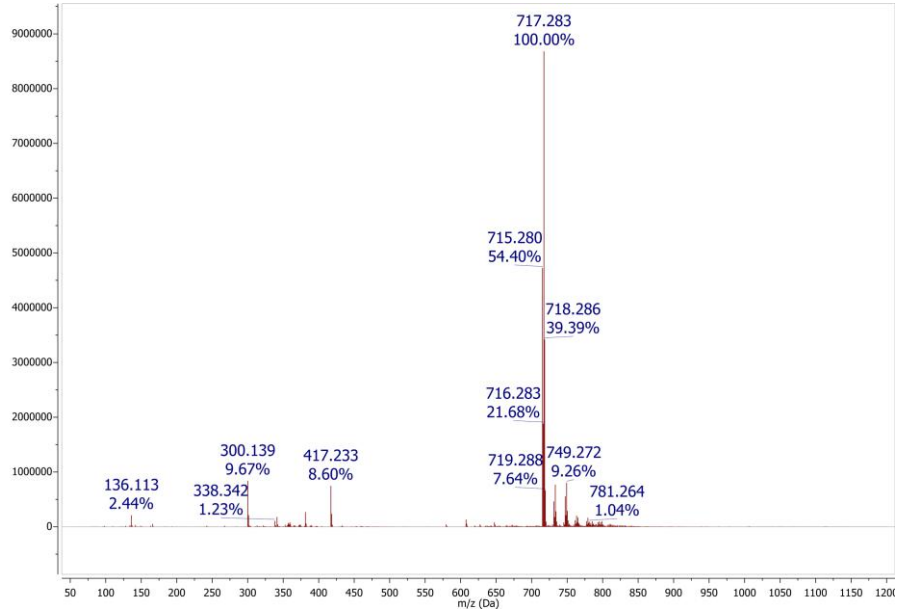


*Figure B.1–4: Mass Spectroscopy spectrum of **1d** recorded in methanol: Positive mode, Electron Spray Ionisation.*

MS (ESI+, CH_3OH): m/z [**1d**]$^+$ calculated 717.28207; found 717.283.

© University of Pretoria

B.1.5) **2a** [RhDB(CO)$_2$]PF$_6$

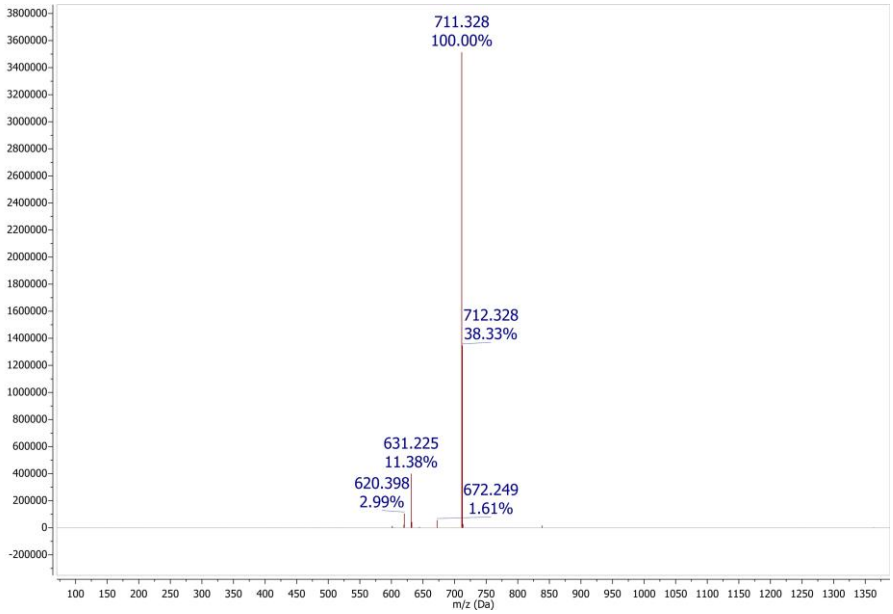


*Figure B.1–5: Mass Spectroscopy spectrum of **2a** recorded in methanol: Positive mode, Electron Spray Ionisation.*

MS (ESI+, CH_3OH): m/z [**2a**-CO]$^+$ calculated 631.220; found 631.225.

B.1.6) **2b** [RhMB(CO)$_2$]PF$_6$

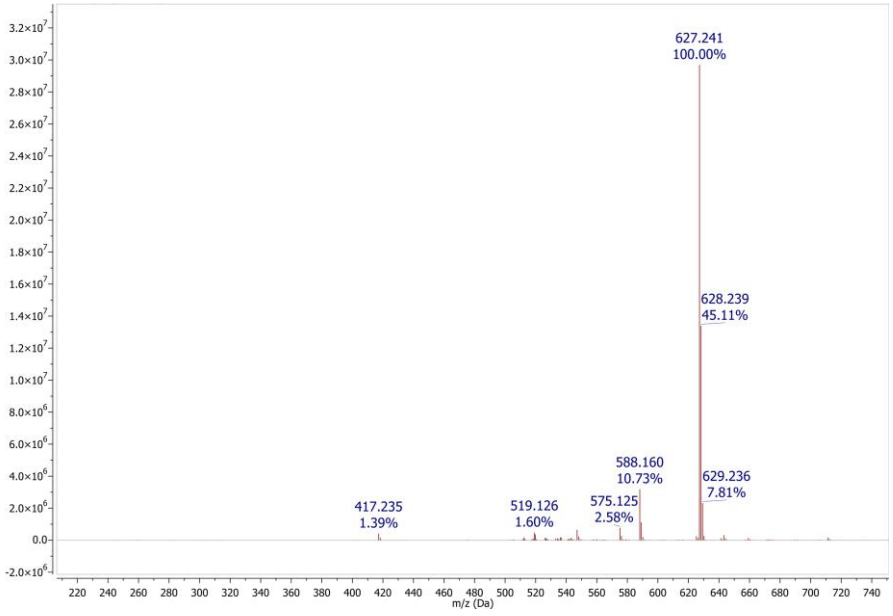


*Figure B.1–6: Mass Spectroscopy spectrum of **2b** recorded in methanol: Positive mode, Electron Spray Ionisation.*

MS (ESI+, CH_3OH): m/z [**2b**]$^+$ calculated 575.121; found 575.125, [**2b**-CO]$^+$ calculated 547.126; found 547.125, [**2b**-(CO)$_2$]$^+$ calculated 519.131; found 519.126.

© University of Pretoria

B.1.7) **2c** $[IrDB(CO)_2]PF_6$

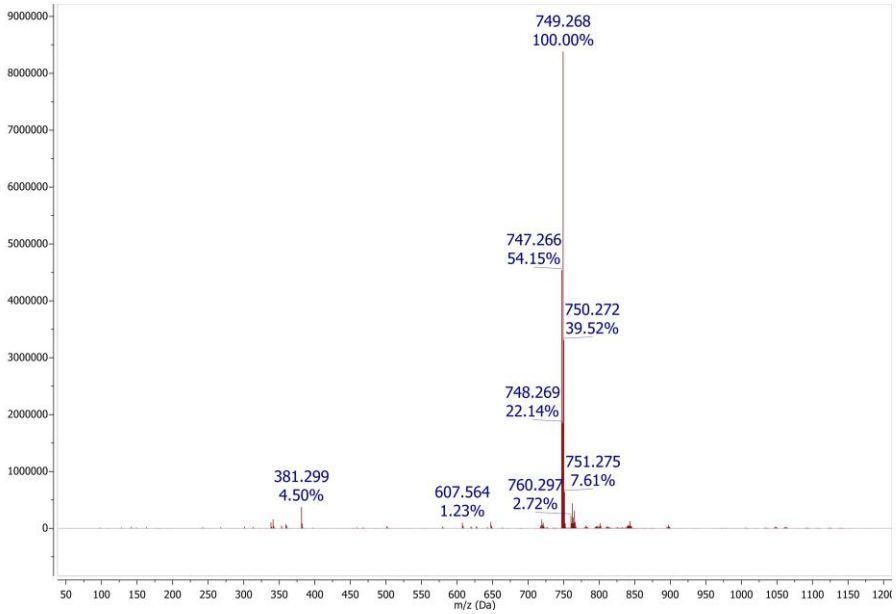


*Figure B.1–7: Mass Spectroscopy spectrum of **2c** recorded in methanol: Positive mode, Electron Spray Ionisation.*

MS (ESI+, CH_3OH): m/z $[\mathbf{2c}]^+$ calculated 749.27190; found 749.268.

B.1.8) **2d** $[IrMB(CO)_2]PF_6$

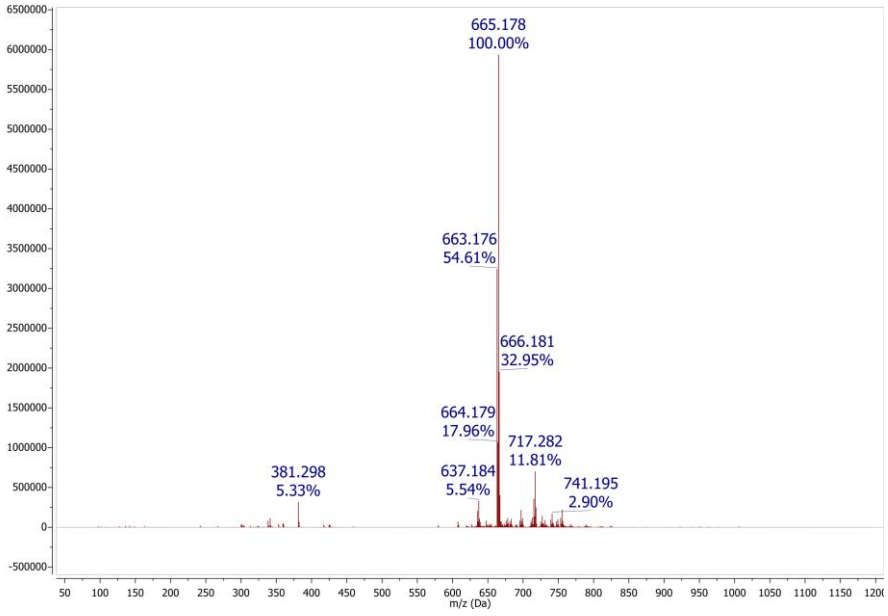


*Figure B.1–8: Mass Spectroscopy spectrum of **2d** recorded in methanol: Positive mode, Electron Spray Ionisation.*

MS (ESI+, CH_3OH): m/z $[\mathbf{2d}]^+$ calculated 665.178; found 665.178.

© University of Pretoria

B.1.9) **3a** [RhDB(CO)(PEt_3)]PF_6

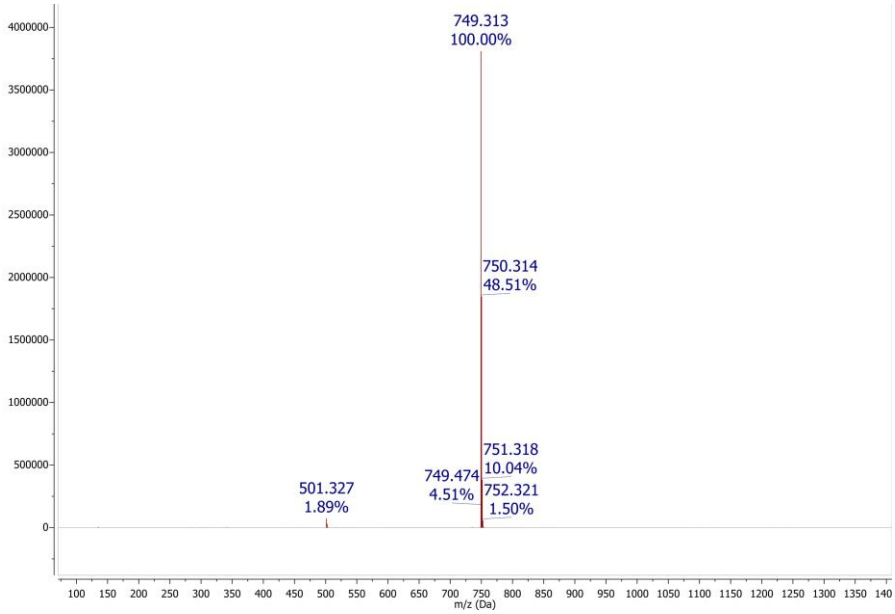


*Figure B.1–9: Mass Spectroscopy spectrum of **3a** recorded in methanol: Positive mode, Electron Spray Ionisation.*

MS (ESI+, CH_3OH): m/z [**3a**]$^+$ calculated 749.310; found 749.313.

B.1.10) **3b** [RhMB(CO)(PEt_3)]PF_6

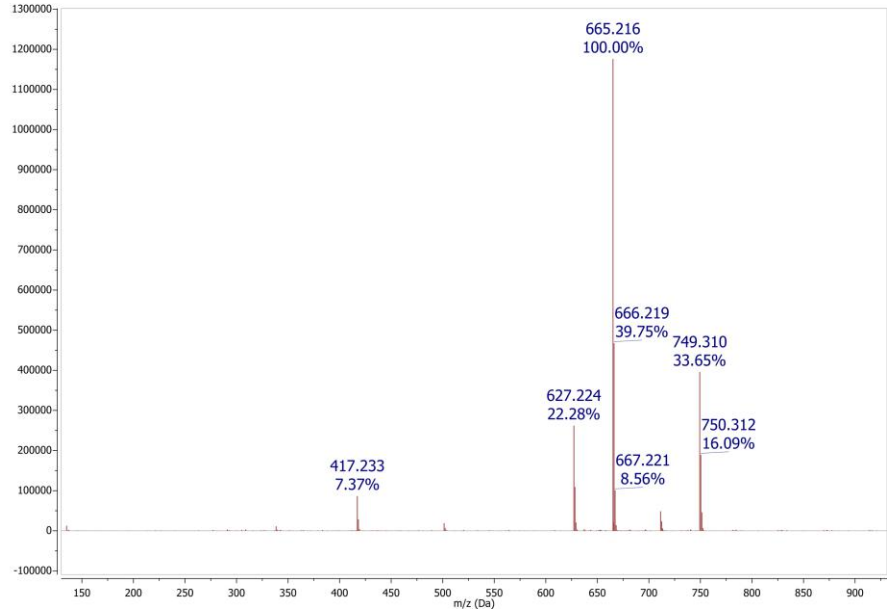


*Figure B.1–10: Mass Spectroscopy spectrum of **3b** recorded in methanol: Positive mode, Electron Spray Ionisation.*

MS (ESI+, CH_3OH): m/z [**3b**]$^+$ calculated 749.311; found 749.310.

© University of Pretoria

B.1.11) **4a** [RhDB(cod)Cl]

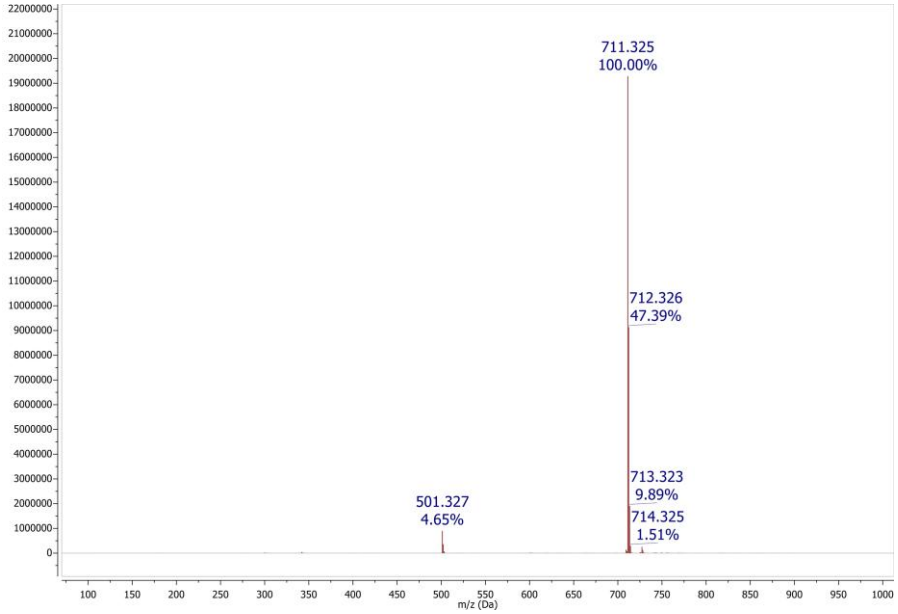


*Figure B.1–11: Mass Spectroscopy spectrum of **4a** recorded in methanol: Positive mode, Electron Spray Ionisation.*

MS (ESI+, CH_3OH): m/z [**4a**-Cl]$^+$ calculated 711.3186; found 711.325.

B.1.12) **4b** [RhMB(cod)Cl]

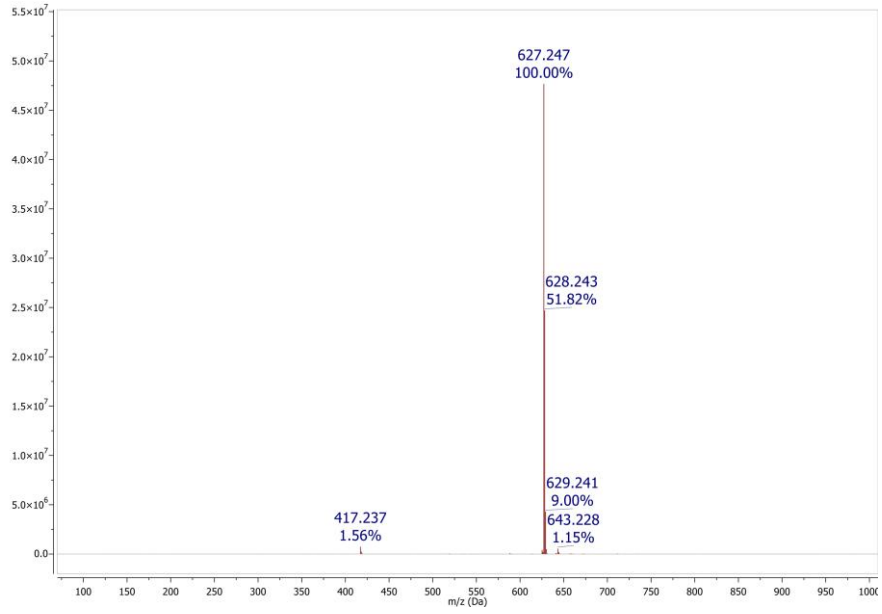


*Figure B.1–12: Mass Spectroscopy spectrum of **4b** recorded in methanol: Positive mode, Electron Spray Ionisation.*

MS (ESI+, CH_3OH): m/z [**4b**-Cl]$^+$ calculated 627.225; found 627.247.

© University of Pretoria

B.1.13) **4c** [IrDB(cod)Cl]

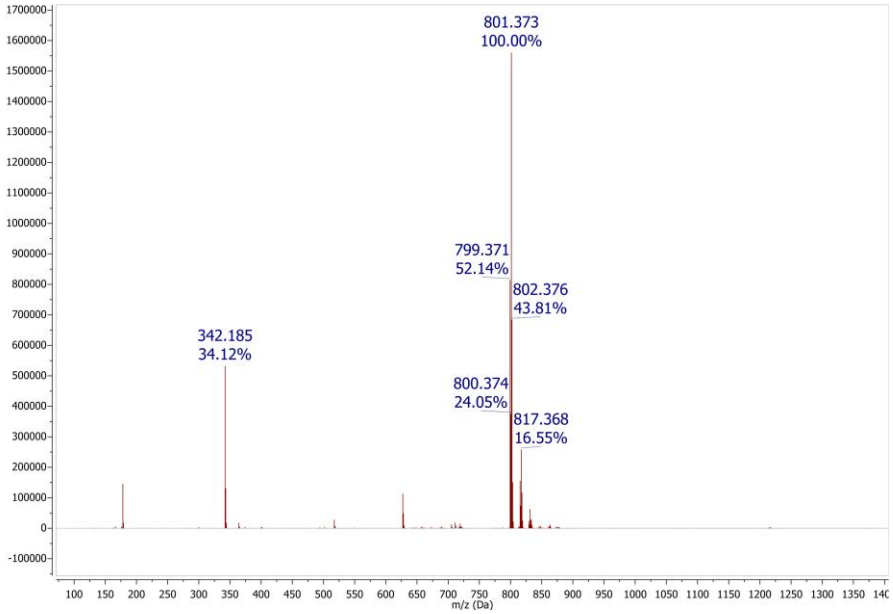


*Figure B.1–13: Mass Spectroscopy spectrum of **4c** recorded in methanol: Positive mode, Electron Spray Ionisation.*

MS (ESI+, CH_3OH): m/z [**4c**-Cl]$^+$ calculated 801.376; found 801.373.

B.1.14) **4d** [IrMB(cod)Cl]

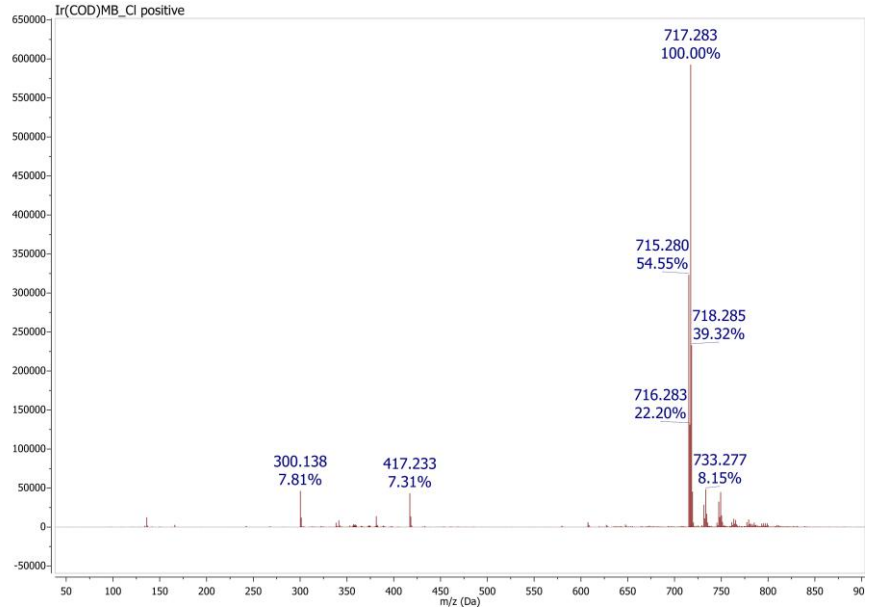


*Figure B.1–14: Mass Spectroscopy spectrum of **4d** recorded in methanol: Positive mode, Electron Spray Ionisation.*

MS (ESI+, CH_3OH): m/z [**4d**-Cl]$^+$ calculated 717.282; found 717.283.

© University of Pretoria

Appendix C: Infrared Spectroscopy

C.1) IR spectra

C.1.1) DippBIAN

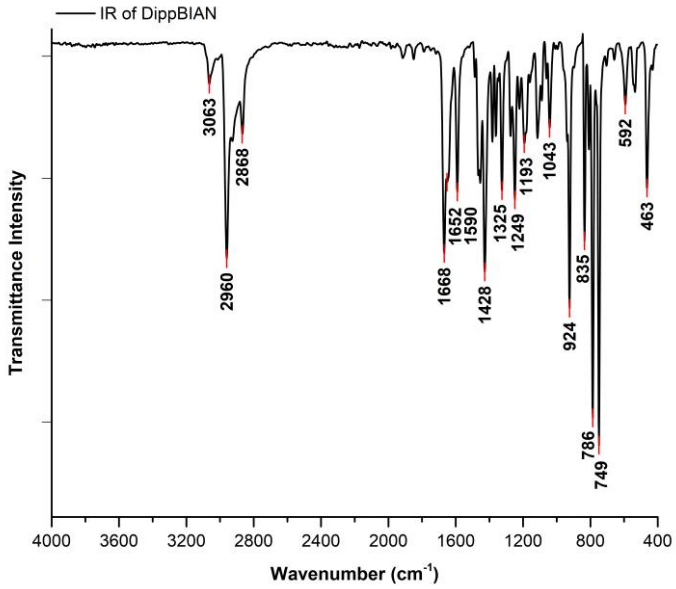


Figure C.1–1: Solid state infrared transmittance spectrum of DippBIAN recorded with a platinum-ATR module (monolithic diamond crystal window).

IR (cm^{-1}) **ν(C=N)** 1668 (m), 1652 (m, sh), 1590 (m).

C.1.2) MesBIAN

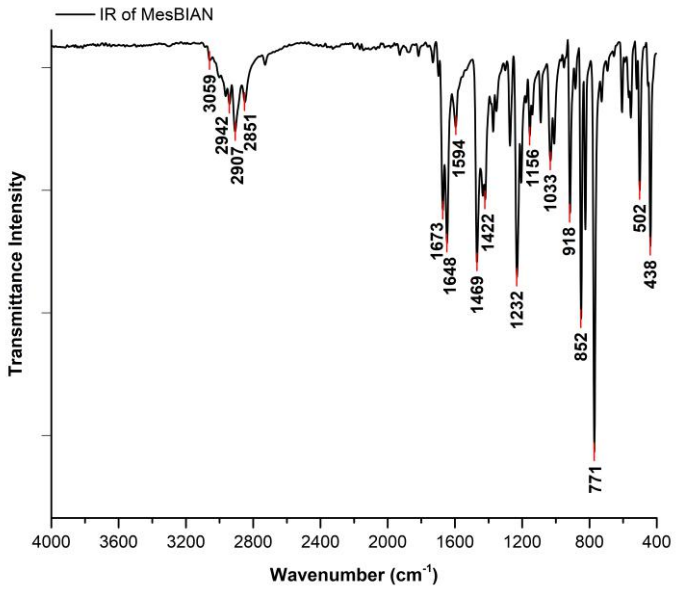


Figure C.1–2: Solid state infrared transmittance spectrum of MesBIAN recorded with a platinum-ATR module (monolithic diamond crystal window).

IR (cm^{-1}) **ν(C=N)** 1673 (m), 1648 (m), 1594 (w).

© University of Pretoria

C.1.3) **1a** [RhDB(cod)]PF_6

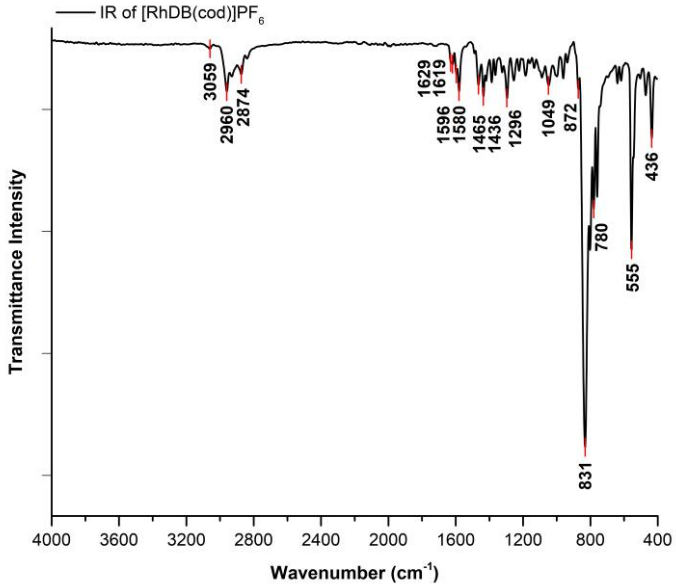


*Figure C.1–3: Solid state infrared transmittance spectrum of **1a** recorded with a platinum-ATR module (monolithic diamond crystal window).*

IR (cm^{-1}) **ν(C=N)** 1629 (vw), 1619 (vw), 1596 (w, sh), 1580 (w); **ν(P–F)** 831 (vs); **δ(P–F)** 555 (vs).

C.1.4) **1b** [RhMB(cod)]PF_6

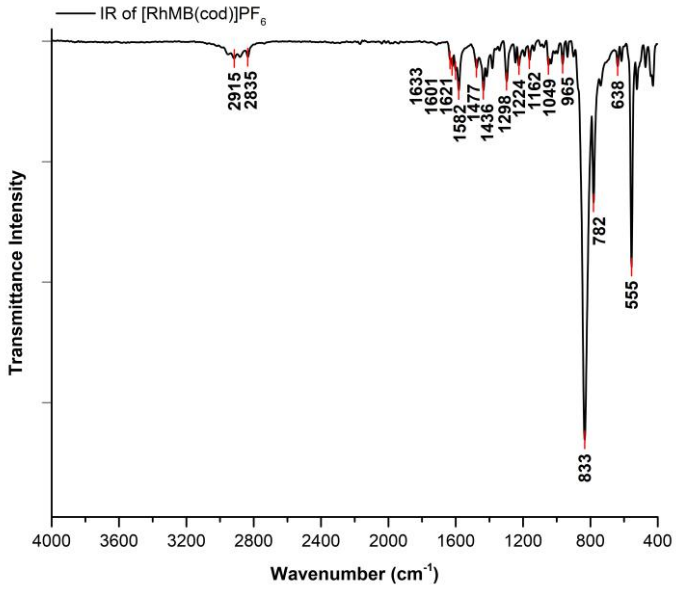


*Figure C.1–4: Solid state infrared transmittance spectrum of **1b** recorded with a platinum-ATR module (monolithic diamond crystal window).*

IR (cm^{-1}) **ν(C=N)** 1633 (vw), 1601 (vw), 1621 (vw, sh), 1582 (w); **ν(P–F)** 833 (vs); **δ(P–F)** 555 (s).

© University of Pretoria

C.1.5) **1c** [IrDB(cod)]PF_6

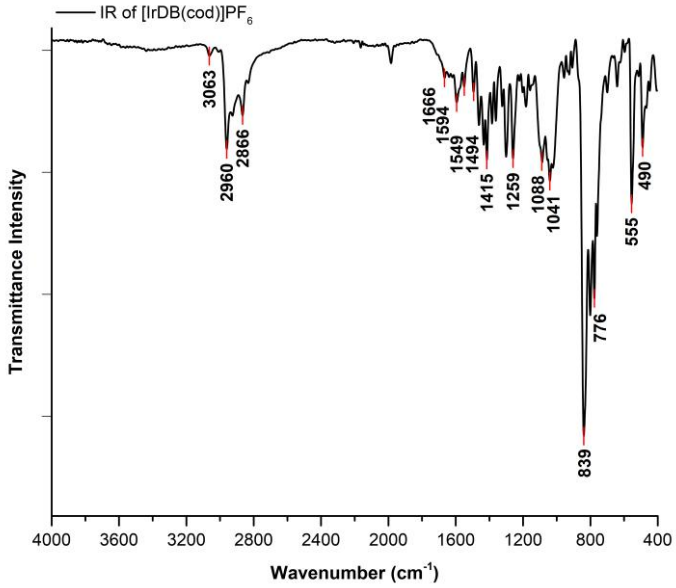


*Figure C.1–5: Solid state infrared transmittance spectrum of **1c** recorded with a platinum-ATR module (monolithic diamond crystal window).*

IR (cm^{-1}) **ν(C=N str)** 1666 (vw), 1594(w), 1549 (vw, sh); **ν(P–F)** 839 (vs); **δ(P–F)** 555 (s).

C.1.6) **1d** [IrMB(cod)]PF_6

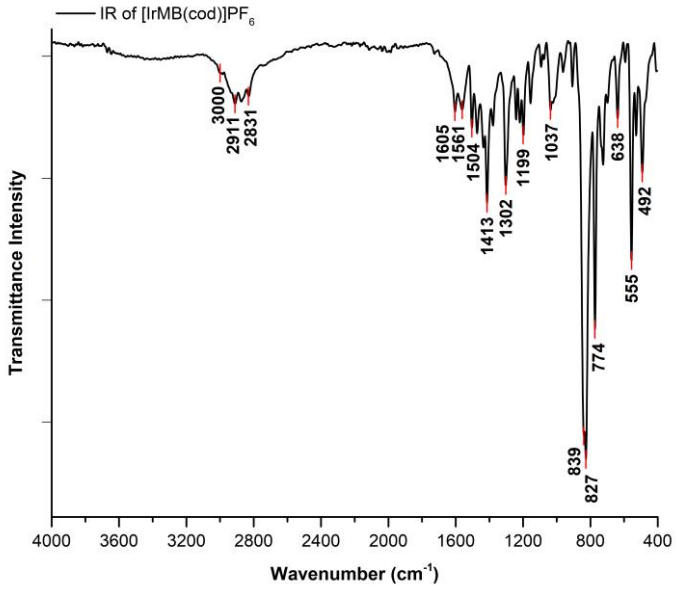


*Figure C.1–6: Solid state infrared transmittance spectrum of **1d** recorded with a platinum-ATR module (monolithic diamond crystal window).*

IR (cm^{-1}) **ν(C=N str)** 1605 (w), 1561 (w); **ν(P–F)** 839 (vs, sh); **δ(P–F)** 555 (s).

© University of Pretoria

C.1.7) **2a** [RhDB(CO)$_2$]PF$_6$

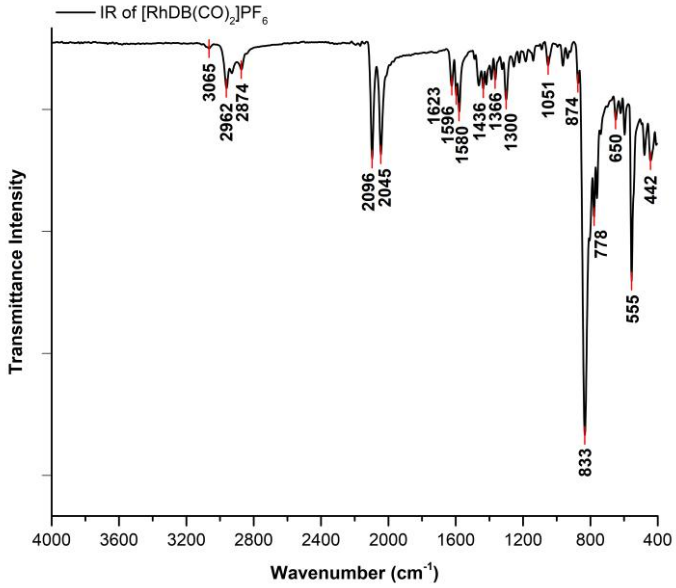


*Figure C.1–7: Solid state infrared transmittance spectrum of **2a** recorded with a platinum-ATR module (monolithic diamond crystal window).*

IR (cm^{-1}) **ν(CO)** 2096 (m), 2045 (m); **ν(C=N)** 1623 (w), 1596 (w, sh), 1580 (w); **ν(P–F)** 833 (vs); **δ(P–F)** 555 (s).

C.1.8) **2b** [RhMB(CO)$_2$]PF$_6$

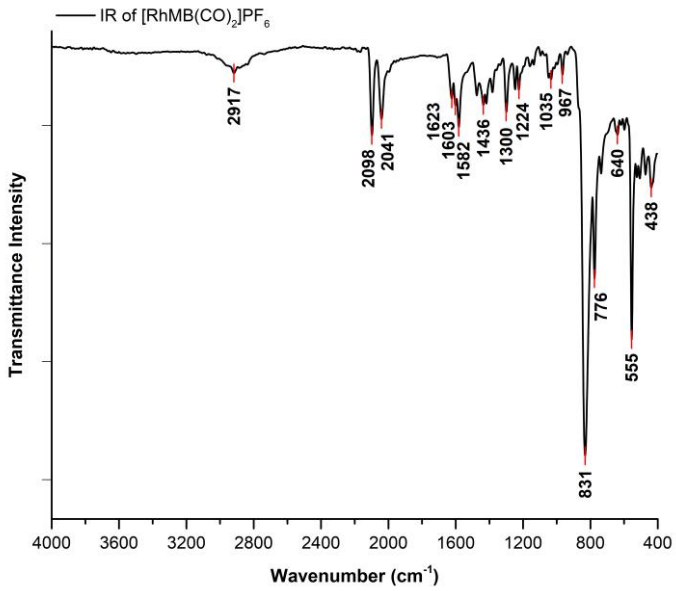


*Figure C.1–8: Solid state infrared transmittance spectrum of **2b** recorded with a platinum-ATR module (monolithic diamond crystal window).*

IR (cm^{-1}) **ν(CO)** 2098 (m), 2041 (m); **ν(C=N)** 1623 (w), 1603 (vw, sh), 1582 (m); **ν(P–F)** 831 (vs); **δ(P–F)** 555 (vs).

© University of Pretoria

C.1.9) **2c** $[IrDB(CO)_2]PF_6$

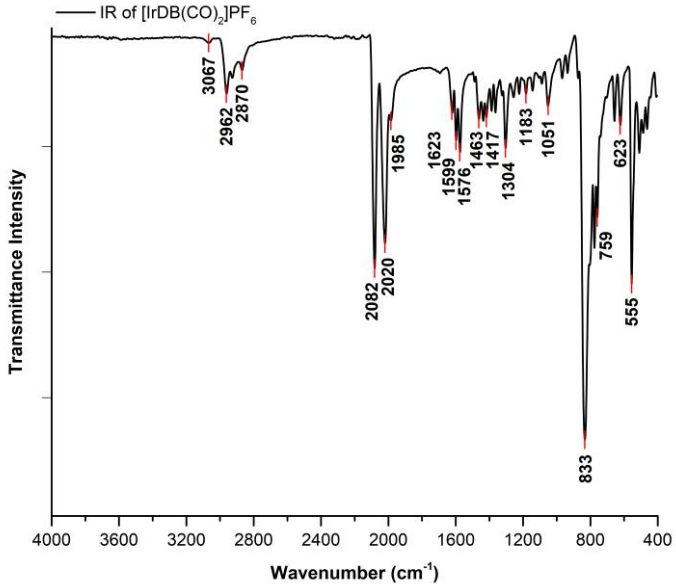


*Figure C.1–9: Solid state infrared transmittance spectrum of **2c** recorded with a platinum-ATR module (monolithic diamond crystal window).*

IR (cm^{-1}) **ν(CO)** 2082 (s), 2020 (s), 1985 (vw, sh); **ν(C=N)** 1623 (w), 1599 (w), 1576 (m); **ν(P–F)** 833 (vs); **δ(P–F)** 555 (s).

C.1.10) **2d** $[IrMB(CO)_2]PF_6$

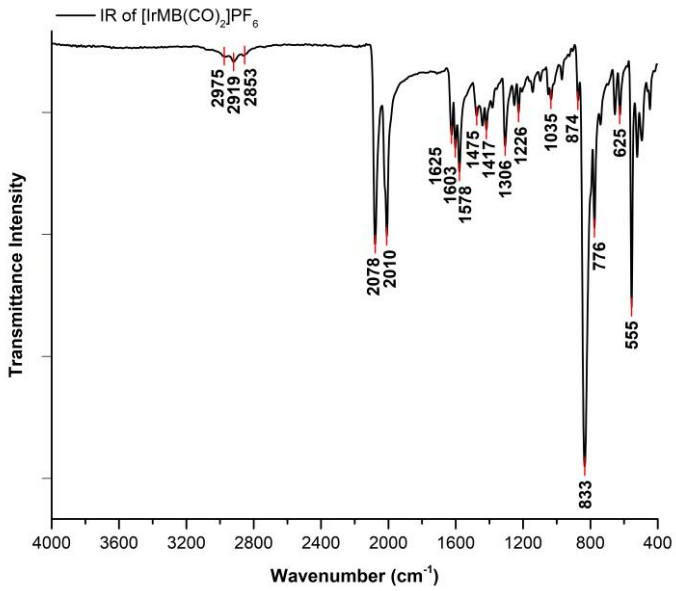


*Figure C.1–10: Solid state infrared transmittance spectrum of **2d** recorded with a platinum-ATR module (monolithic diamond crystal window).*

IR (cm^{-1}) **ν(C=O)** 2078 (s), 2010 (s); **ν(C=N)** 1625 (w), 1603 (vw), 1578 (m); **ν(P–F)** 833 (vs); **δ(P–F)** 555 (s).

© University of Pretoria

C.1.11) **3a** [RhDB(CO)(PEt_3)]PF_6

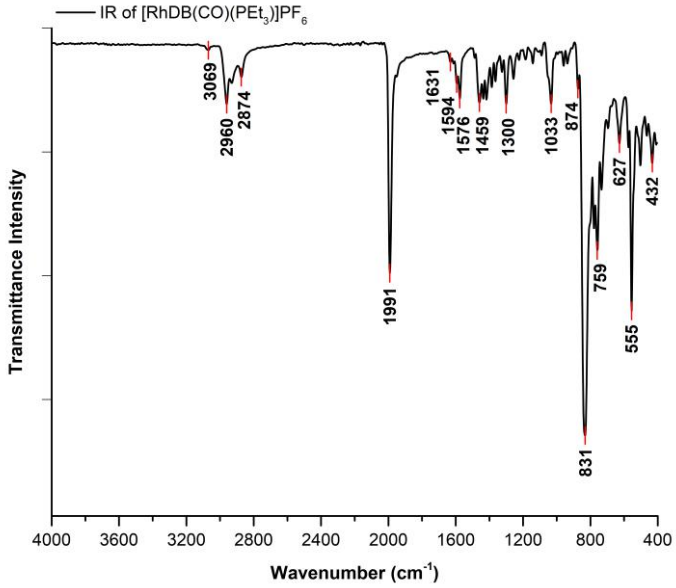


*Figure C.1–11: Solid state infrared transmittance spectrum of **3a** recorded with a platinum-ATR module (monolithic diamond crystal window).*

IR (cm^{-1}) **ν(CO)** 1991 (s); **ν(C=N)** 1631 (vw), 1594 (vw, sh), 1576 (w); **ν(P–F)** 831 (vs); **δ(P–F)** 555 (s).

C.1.12) **3b** [RhMB(CO)(PEt_3)]PF_6

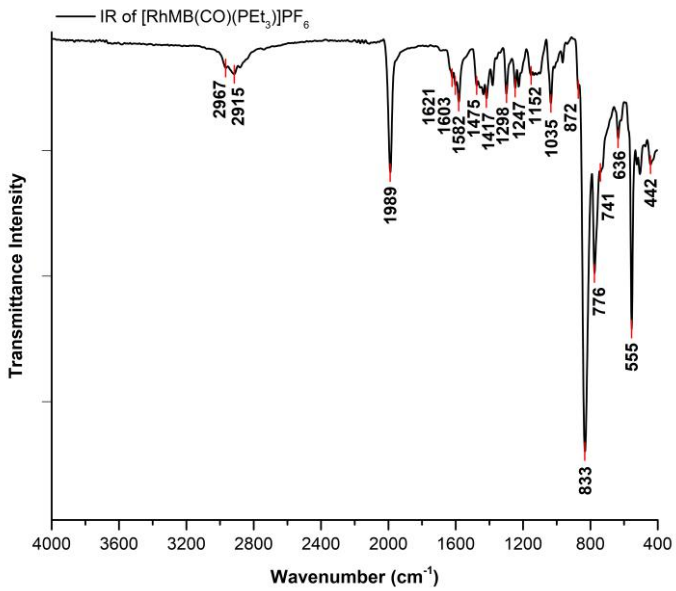


*Figure C.1–12: Solid state infrared transmittance spectrum of **3b** recorded with a platinum-ATR module (monolithic diamond crystal window).*

IR (cm^{-1}) **ν(CO)** 1989 (m); **ν(C=N)** 1621 (vw), 1603 (vw, sh), 1582 (w); **ν(P–F)** 833 (vs); **δ(P–F)** 555 (s).

© University of Pretoria

C.1.13) **4a** [RhDB(cod)Cl]

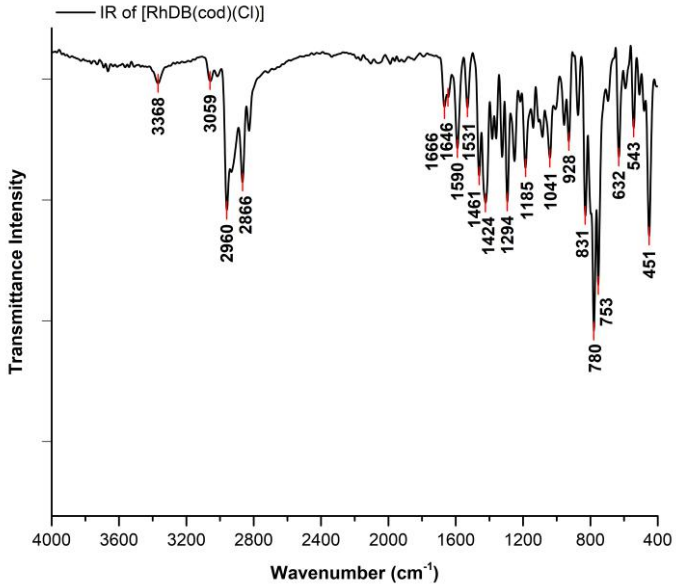


*Figure C.1–13: Solid state infrared transmittance spectrum of **4a** recorded with a platinum-ATR module (monolithic diamond crystal window).*

IR (cm^{-1}) **ν(C=N)** 1666 (m), 1646 (w, sh), 1590 (m).

C.1.14) **4b** [RhMB(cod)Cl]

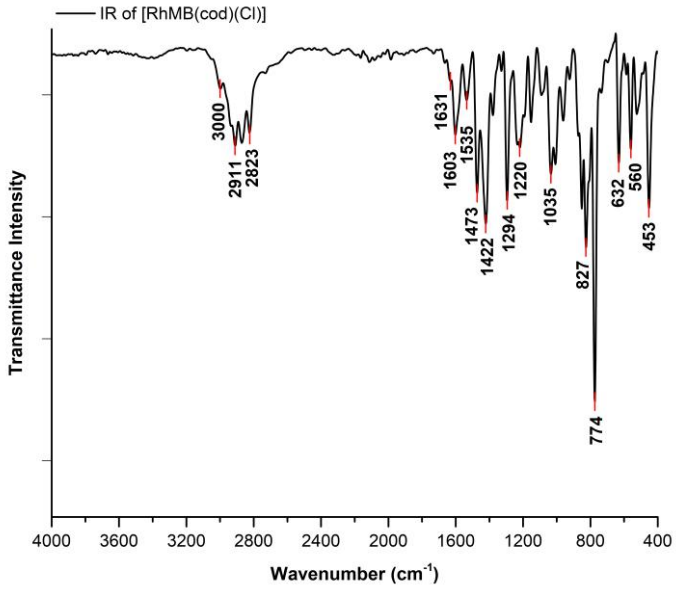


*Figure C.1–14: Solid state infrared transmittance spectrum of **4b** recorded with a platinum-ATR module (monolithic diamond crystal window).*

IR (cm^{-1}) **ν(C=N)** 1631 (vw, sh), 1603 (m), 1535 (w).

© University of Pretoria

C.1.15) **4c** [IrDB(cod)Cl]

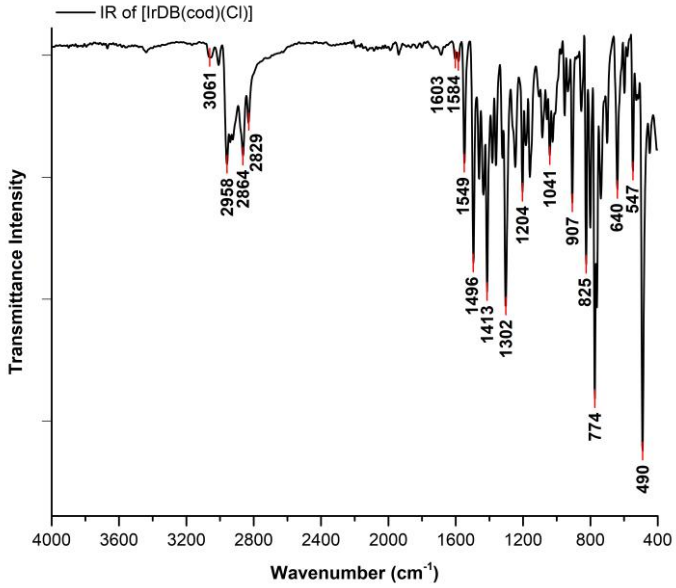


*Figure C.1–15: Solid state infrared transmittance spectrum of **4c** recorded with a platinum-ATR module (monolithic diamond crystal window).*

IR (cm^{-1}) **ν(C=N)** 1603 (vw), 1584 (vw), 1549 (m).

C.1.16) **4d** [IrMB(cod)Cl]

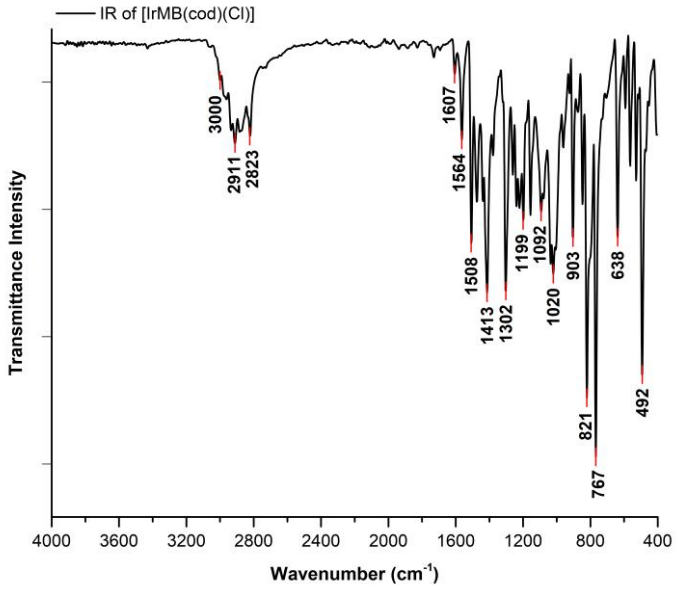


*Figure C.1–16: Solid state infrared transmittance spectrum of **4d** recorded with a platinum-ATR module (monolithic diamond crystal window).*

IR (cm^{-1}) **ν(C=N)** 1607 (vw), 1564 (m).

© University of Pretoria

C.2) IR Data Tables

*Table C.2–1: Selected solid state infrared bond vibrations (in cm^{-1}) of DippBIAN, MesBIAN, and the series of complexes **1a–d**. Abbreviations in parentheses denote the relative intensity of the vibration: (w) weak, (m) moderate, (s) strong, (vs) very strong, (sh) shoulder.*

Compound	ν(C=N)	ν(P–F)	δ(P–F)	ν(CO)
DippBIAN	1668 (m), 1652 (m, sh), 1590 (m)			
MesBIAN	1673 (m), 1648 (m), 1594 (w)			
1a	1629 (vw), 1619 (vw), 1596 (w, sh), 1580 (w)	831 (vs)	555 (vs)	
1b	1633 (vw), 1601 (vw), 1621 (vw, sh), 1582 (w)	833 (vs)	555 (s)	
1c	1666 (vw), 1594(w), 1549 (vw, sh)	839 (vs)	555 (s)	
1d	1605 (w), 1561 (w)	839 (vs, sh)	555 (s)	
2a	1623 (w), 1596 (w, sh), 1580 (w)	833 (vs)	555 (s)	2096 (m), 2045 (m)
2b	1623 (w), 1603 (vw, sh), 1582 (m)	831 (vs)	555 (vs)	2098 (m), 2041 (m);
2c	1623 (w), 1599 (w), 1576 (m)	833 (vs)	555 (s)	2082 (s), 2020 (s), 1985 (vw, sh)
2d	1625 (w), 1603 (vw), 1578 (m)	833 (vs)	555 (s)	2078 (s), 2010 (s)
3a	1631 (vw), 1594 (vw, sh), 1576 (w)	831 (vs)	555 (s)	1991 (s)
3b	1621 (vw), 1603 (vw, sh), 1582 (w)	833 (vs)	555 (s)	1989 (m)
4a	1666 (m), 1646 (w, sh), 1590 (m)			
4b	1631 (vw, sh), 1603 (m), 1535 (w)			
4c	1603 (vw), 1584 (vw), 1549 (m)			
4d	1607 (vw), 1564 (m)			

© University of Pretoria

Appendix D: UV-Vis Spectroscopy

D.1) UV-Vis Spectra

D.1.1) DippBIAN

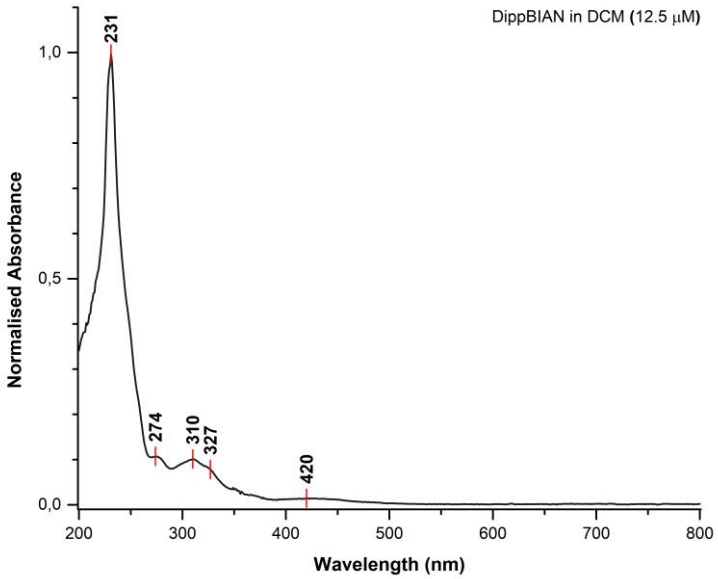


Figure D.1–1: Normalised UV-Vis absorption spectrum of DippBIAN recorded in CH_2Cl_2 using 10 mm quarts cuvettes.

UV-Vis in CH_2Cl_2, $\boldsymbol{\lambda_{max}}$ [nm] ($\boldsymbol{\varepsilon}$ [M^{-1} cm^{-1}]): 231 (45 126), 274 (4 699), 310 (4 436), 327 (3 372), 420 (501).

D.1.2) MesBIAN

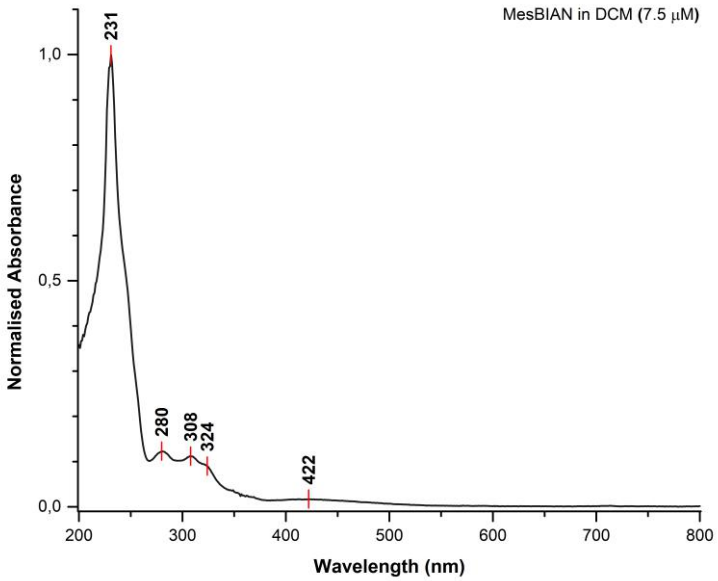


Figure D.1–2: Normalised UV-Vis absorption spectrum of MesBIAN recorded in CH_2Cl_2 using 10 mm quarts cuvettes.

UV-Vis in CH_2Cl_2, $\boldsymbol{\lambda_{max}}$ [nm] ($\boldsymbol{\varepsilon}$ [M^{-1} cm^{-1}]): 231 (91 675), 280 (11 090), 308 (10 139), 324 (8 082), 422 (1 397).

© University of Pretoria

D.1.3) **1a** [RhDB(cod)]PF_6

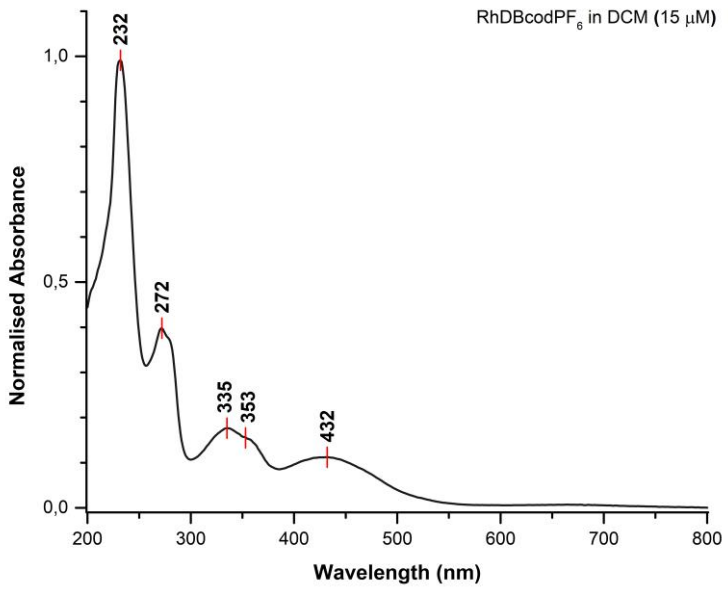


*Figure D.1–3: Normalised UV-Vis absorption spectrum of **1a** recorded in CH_2Cl_2 using 10 mm quarts cuvettes.*

UV-Vis in CH_2Cl_2, $\boldsymbol{\lambda_{max}}$ [nm] ($\boldsymbol{\varepsilon}$ [M^{-1} cm^{-1}]): 232 (43 928), 272 (17 744), 335 (8 024), 353 (7 069), 432 (5 188).

D.1.4) **1b** [RhMB(cod)]PF_6

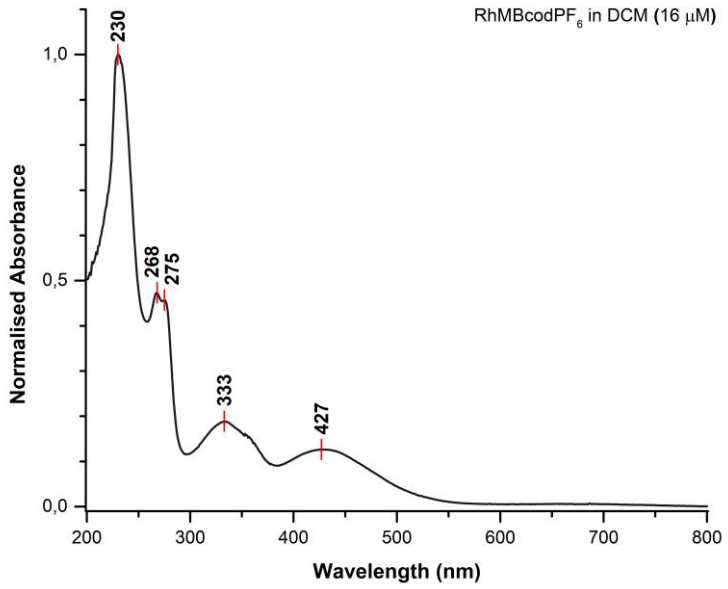


*Figure D.1–4: Normalised UV-Vis absorption spectrum of **1b** recorded in CH_2Cl_2 using 10 mm quarts cuvettes.*

UV-Vis in CH_2Cl_2, $\boldsymbol{\lambda_{max}}$ [nm] ($\boldsymbol{\varepsilon}$ [M^{-1} cm^{-1}]): 230 (49 406), 268 (23 442), 275 (22 616), 333 (9 404), 427 (6 324).

© University of Pretoria

D.1.5) **1c** [IrDB(cod)]PF_6

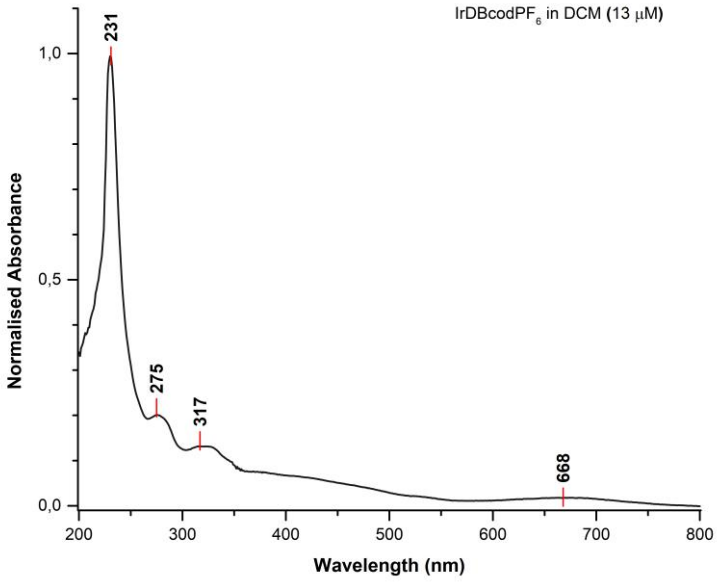


*Figure D.1–5: Normalised UV-Vis absorption spectrum of **1c** recorded in CH_2Cl_2 using 10 mm quarts cuvettes.*

UV-Vis in CH_2Cl_2, $\boldsymbol{\lambda_{max}}$ [nm] (**ε** [M^{-1} cm^{-1}]): 231 (53 363), 275 (10 798), 317 (7 063), 668 (1 005).

D.1.6) **1d** [IrMB(cod)]PF_6

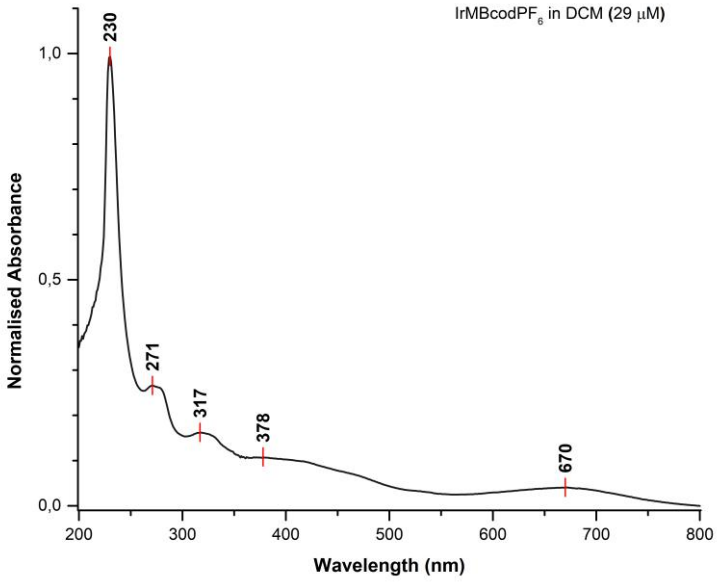


*Figure D.1–6: Normalised UV-Vis absorption spectrum of **1d** recorded in CH_2Cl_2 using 10 mm quarts cuvettes.*

UV-Vis in CH_2Cl_2, $\boldsymbol{\lambda_{max}}$ [nm] (**ε** [M^{-1} cm^{-1}]): 230 (34 200), 271 (9 319), 317 (5 795), 378 (3 955), 670 (1 663).

© University of Pretoria

D.1.7) **2a** $[RhDB(CO)_2]PF_6$

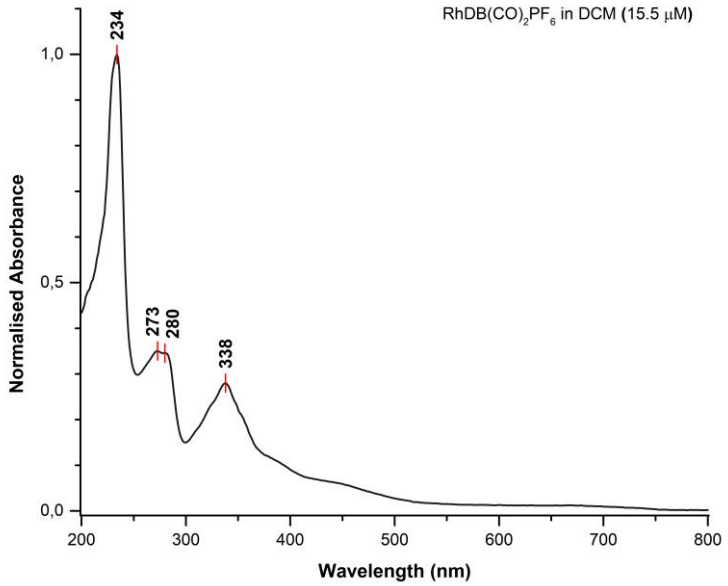


*Figure D.1–7: Normalised UV-Vis absorption spectrum of **2a** recorded in CH_2Cl_2 using 10 mm quarts cuvettes.*

UV-Vis in CH_2Cl_2, $\boldsymbol{\lambda_{max}}$ [nm] ($\boldsymbol{\varepsilon}$ [M^{-1} cm^{-1}]): 234 (75 053), 273 (26 503), 280 (26 323), 338 (21 691).

D.1.8) **2b** $[RhMB(CO)_2]PF_6$

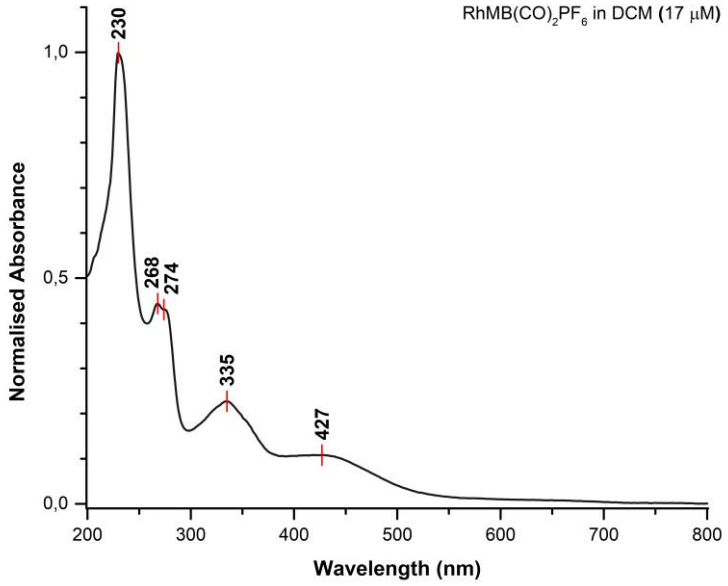


*Figure D.1–8: Normalised UV-Vis absorption spectrum of **2b** recorded in CH_2Cl_2 using 10 mm quarts cuvettes.*

UV-Vis in CH_2Cl_2, $\boldsymbol{\lambda_{max}}$ [nm] ($\boldsymbol{\varepsilon}$ [M^{-1} cm^{-1}]): 230 (30 050), 268 (13 438), 274 (12 901), 335 (6 936), 427 (3 376).

© University of Pretoria

D.1.9) **2c** $[IrDB(CO)_2]PF_6$

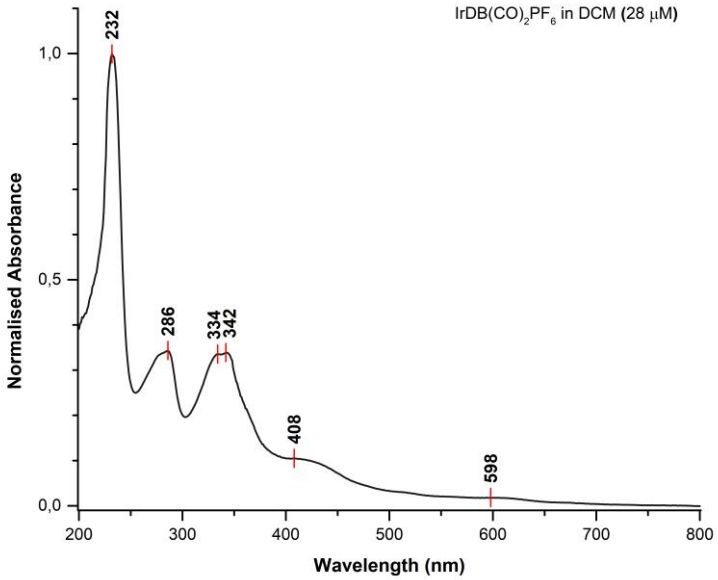


*Figure D.1–9: Normalised UV-Vis absorption spectrum of **2c** recorded in CH_2Cl_2 using 10 mm quarts cuvettes.*

UV-Vis in CH_2Cl_2, $\boldsymbol{\lambda_{max}}$ [nm] (**ε** [M^{-1} cm^{-1}]): 232 (30 303), 286 (10 477), 334 (10 253), 342 (10 353), 408 (3 285), 598 (682).

D.1.10) **2d** $[IrMB(CO)_2]PF_6$

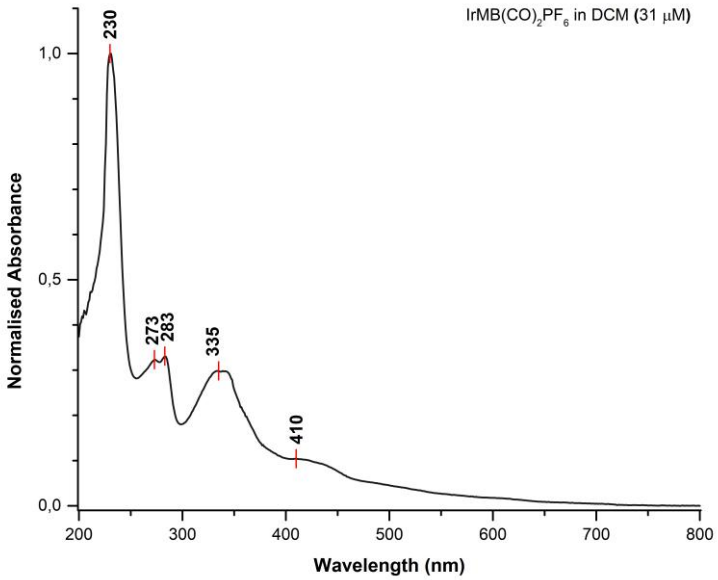


*Figure D.1–10: Normalised UV-Vis absorption spectrum of **2d** recorded in CH_2Cl_2 using 10 mm quarts cuvettes.*

UV-Vis in CH_2Cl_2, $\boldsymbol{\lambda_{max}}$ [nm] (**ε** [M^{-1} cm^{-1}]): 230 (21 646), 273 (7 033), 283 (7 201), 335 (6 506), 410 (2 289).

© University of Pretoria

D.1.11) **3a** [RhDB(CO)(PEt_3)]PF_6

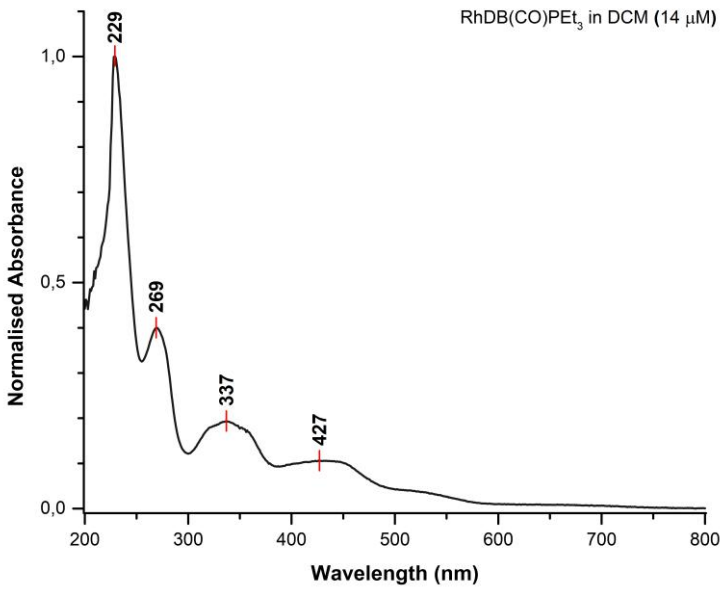


*Figure D.1–11: Normalised UV-Vis absorption spectrum of **3a** recorded in CH_2Cl_2 using 10 mm quarts cuvettes.*

UV-Vis in CH_2Cl_2, $\boldsymbol{\lambda_{max}}$ [nm] ($\boldsymbol{\varepsilon}$ [M^{-1} cm^{-1}]): 229 (28 804), 269 (11 525), 337 (5 571), 427 (3 050).

D.1.12) **3b** [RhMB(CO)(PEt_3)]PF_6

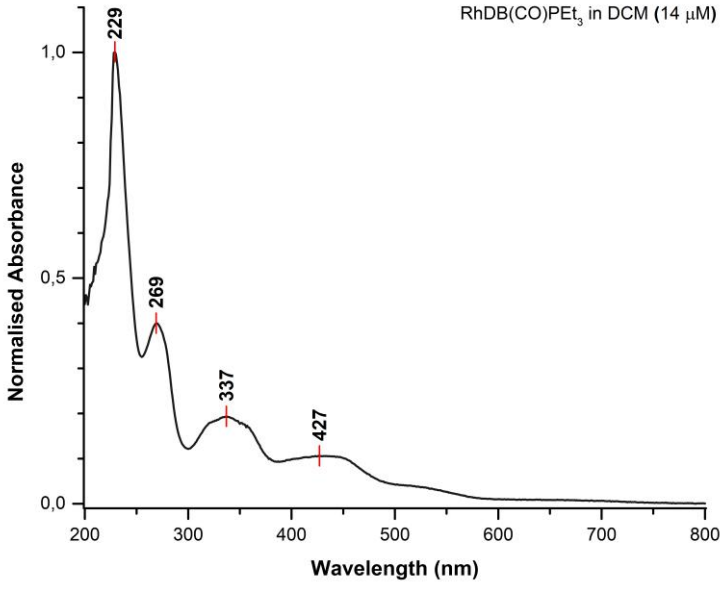


*Figure D.1–12: Normalised UV-Vis absorption spectrum of **3b** recorded in CH_2Cl_2 using 10 mm quarts cuvettes.*

UV-Vis in CH_2Cl_2, $\boldsymbol{\lambda_{max}}$ [nm] ($\boldsymbol{\varepsilon}$ [M^{-1} cm^{-1}]): 229 (31 589), 269 (13 742), 337 (6 010), 427 (3 373).

© University of Pretoria

D.1.13) 4a [RhDB(cod)Cl]

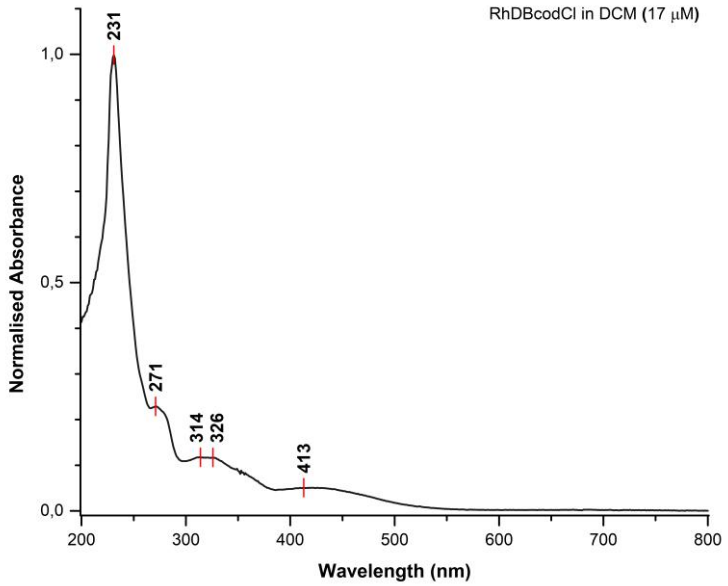


*Figure D.1–13: Normalised UV-Vis absorption spectrum of **4a** recorded in CH_2Cl_2 using 10 mm quarts cuvettes.*

UV-Vis in CH_2Cl_2, $\boldsymbol{\lambda_{max}}$ [nm] ($\boldsymbol{\varepsilon}$ [M^{-1} cm^{-1}]): 231 (37 783), 271 (8 664), 314 (4 445), 326 (4 414), 413 (1 913).

D.1.14) 4b [RhMB(cod)Cl]

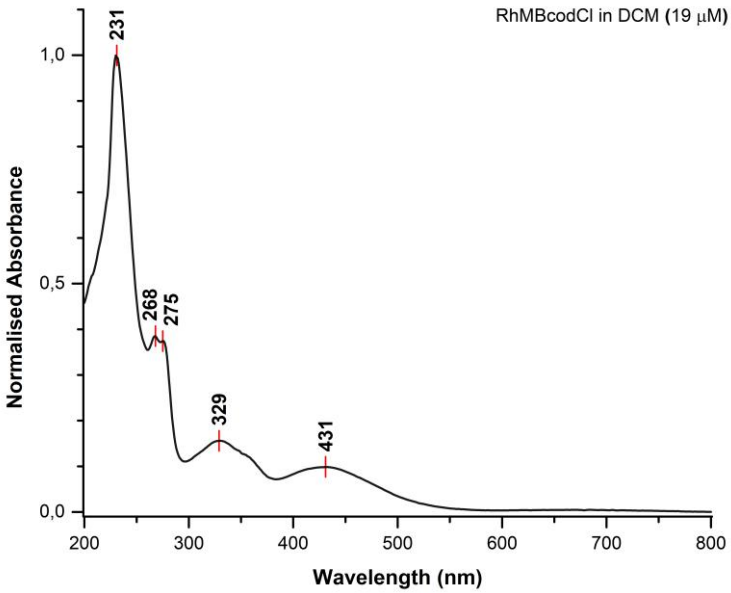


*Figure D.1–14: Normalised UV-Vis absorption spectrum of **4b** recorded in CH_2Cl_2 using 10 mm quarts cuvettes.*

UV-Vis in CH_2Cl_2, $\boldsymbol{\lambda_{max}}$ [nm] ($\boldsymbol{\varepsilon}$ [M^{-1} cm^{-1}]): 231 (44 817), 268 (17 306), 275 (16 828), 329 (7 067), 431 (4 523).

© University of Pretoria

D.1.15) 4c [IrDB(cod)Cl]

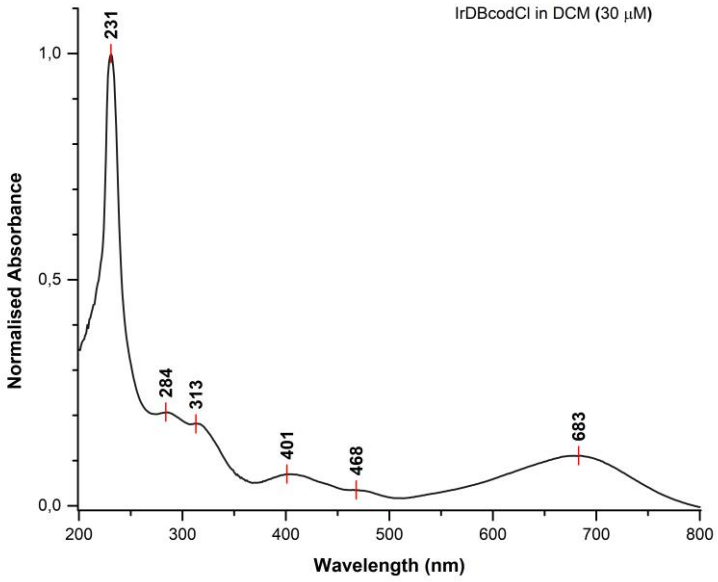


*Figure D.1–15: Normalised UV-Vis absorption spectrum of **4c** recorded in CH_2Cl_2 using 10 mm quarts cuvettes.*

UV-Vis in CH_2Cl_2, $\boldsymbol{\lambda_{max}}$ [nm] ($\boldsymbol{\varepsilon}$ [M^{-1} cm^{-1}]): 231 (31 161), 284 (6 980), 313 (6 188), 401 (2 809), 468 (1 734), 683 (4 043).

D.1.16) 4d [IrMB(cod)Cl]

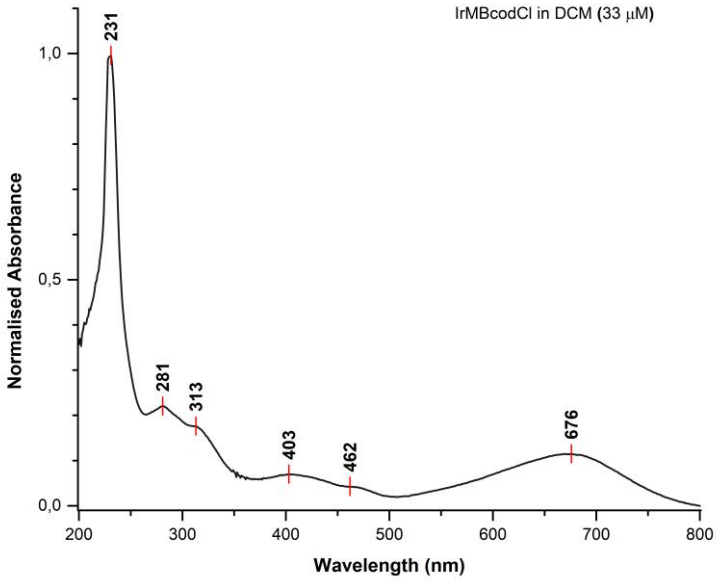


*Figure D.1–16: Normalised UV-Vis absorption spectrum of **4d** recorded in CH_2Cl_2 using 10 mm quarts cuvettes.*

UV-Vis in CH_2Cl_2, $\boldsymbol{\lambda_{max}}$ [nm] ($\boldsymbol{\varepsilon}$ [M^{-1} cm^{-1}]): 231 (14 169), 281 (3 348), 313 (2 740), 403 (1 234), 462 (848), 676 (1 862).

© University of Pretoria

D.2) UV-Vis Data Tables

*Table D.2–1: UN-Vis spectroscopic data for DippBIAN, MesBIAN and the series of complexes **1–4** recorded in Ar (g) degassed CH_2Cl_2 under ambient conditions. Key: λ_{max} = Absorption peak maxima; ε = Molar Absorptivity; LC = Ligand Centred transition; ILCT = Intra-Ligand Charge Transfer; MLCT = Metal-to-Ligand Charge Transfer; * = Shoulder peak.*

Compound	Conc. (μM)	LC and ILCT: λ_{max} [nm] (ε [x10^3 M^{-1} cm^{-1}])					MLCT: λ_{max} [nm] (ε [x10^3 M^{-1} cm^{-1}])	
DippBIAN	12.5	231 (45.1)	274 (4.7)	310 (4.4)	327* (3.4)	420 (0.5)		
MesBIAN	7.5	231 (91.7)	280 (11.1)	308 (10.1)	324* (8.1)	422 (1.4)		
1a	15	232 (43.9)	272 (17.7)	335 (8.0)	353* (7.1)	432 (5.2)		
1b	16	230 (49.4)	268 (23.4)	275* (22.6)	333 (9.4)	427 (6.3)		
1c	13	231 (53.4)	275 (10.8)	317 (7.1)				668 (1.0)
1d	29	230 (34.2)	271 (9.3)	317 (5.8)	378 (4.0)			670 (1.7)
2a	15.5	234 (75.1)	273 (26.5)	280* (26.3)	338 (21.7)			
2b	17	230 (30.1)	268 (13.4)	274* (12.9)	335 (6.9)	427 (3.4)		
2c	28	232 (30.3)	286 (10.5)	334 (10.3)	342* (10.4)	408 (3.3)		598 (0.7)
2d	31	230 (21.4)	273 (7.0)	283* (7.2)	335 (6.5)	410 (2.3)		
3a	14	229 (28.8)	269 (11.5)	337 (5.6)	427 (3.1)			
3b	15	229 (31.6)	269 (13.7)	337 (6.0)	427 (3.4)			
4a	17	231 (37.8)	271 (8.7)	314* (4.4)	326 (4.4)	413 (1.9)		
4b	19	231 (44.8)	268 (17.3)	275* (16.8)	329 (7.1)	431 (4.5)		
4c	30	231 (31.2)	284 (7.0)	313* (6.2)	401 (2.8)		468* (1.7)	683 (4.0)
4d	33	231 (14.2)	281 (3.3)	313* (2.7)	403 (1.2)		462* (0.8)	676 (1.9)

© University of Pretoria

Appendix E: Single Crystal X-ray Diffractometry

E.1) SC-XRD

E.1.1) **1b** [RhMB(cod)]PF_6

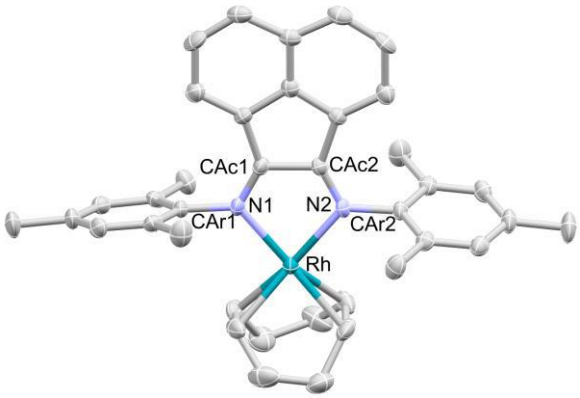


*Figure E.1–1: The molecular structure of **1b** [RhMB(cod)]PF_6 with partial atom-numbering scheme, thermal ellipsoids shown at 50% probability. Hydrogen atoms, PF_6 counterion and CH_2Cl_2 solvent molecule are omitted for clarity.*

$C_{38.91}H_{41.82}Cl_{1.82}F_6N_2PRh$ (*M* = 849.74 g/mol): hexagonal, space group *P6₅22*, *a* = 12.2066(7) Å, *b* = 12.2066(7) Å, *c* = 43.710(3) Å, *γ* = 120°, V = 5640.3(8) Å^3, *Z* = 6, *T* = 150(2) K, μ(MoKα) = 0.687 mm^{-1}, *Dcalc* = 1.501 g/cm^3, 166775 reflections measured (4.28° ≤ 2Θ ≤ 52.742°), 3853 unique (R_{int} = 0.0575, R_{sigma} = 0.0146) which were used in all calculations. The final R_1 was 0.0442 (I > 2σ(I)) and wR_2 was 0.1059 (all data). CCDC 2161247.

Complex **1b** is accompanied by one molecule of CH_2Cl_2 in the unit cell, along with one PF_6^- counter ion.

E.1.2) **1d** [IrMB(cod)]PF_6

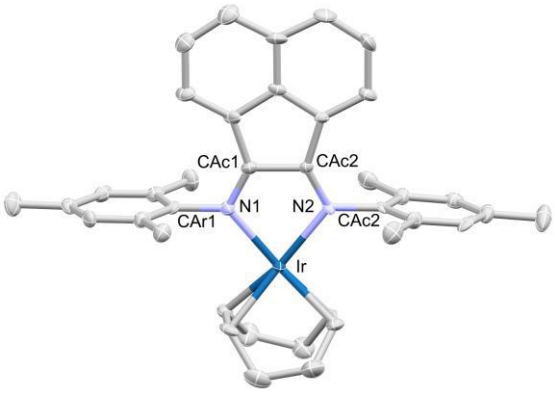


*Figure E.1–2: The molecular structure of **1d** [IrMB(cod)]PF_6 with partial atom-numbering scheme, thermal ellipsoids shown at 50% probability. Hydrogen atoms, PF_6 counterion and two $CDCl_3$ solvent molecules are omitted for clarity.*

$C_{40}H_{42}Cl_6F_6IrN_2P$ (*M* = 1100.62 g/mol): monoclinic, space group *P2₁/n*, *a* = 12.0546(7) Å, *b* = 22.1106(11) Å, *c* = 15.8673(9) Å, *β* = 100.789(2)°, V = 4154.4(4) Å^3, *Z* = 4, *T* = 150(2) K, μ(MoKα) = 3.698 mm^{-1}, *Dcalc* = 1.760 g/cm^3, 25383 reflections measured (4.694° ≤ 2Θ ≤ 52.74°), 8202 unique (R_{int} = 0.0912, R_{sigma} = 0.0963) which were used in all calculations. The final R_1 was 0.0639 (I > 2σ(I)) and wR_2 was 0.1624 (all data). CCDC 2161249.

Complex **1d** is accompanied by two molecules of $CDCl_3$ in the unit cell, along with one PF_6^- counter ion.

© University of Pretoria

E.1.3) **2a** [RhDB(CO)$_2$]PF$_6$

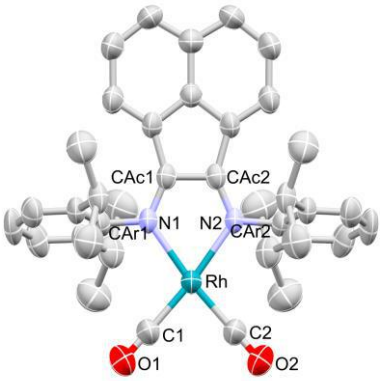


*Figure E.1–3: The molecular structure of **2a** [RhDB(CO)$_2$]PF$_6$ with partial atom-numbering scheme, thermal ellipsoids shown at 50% probability. Hydrogen atoms and PF$_6$ counterion are omitted for clarity.*

$C_{38}H_{40}F_6N_2O_2PRh$ (*M* = 804.60 g/mol): orthorhombic, space group *Pnma*, *a* = 16.6885(3) Å, *b* = 14.9252(3) Å, *c* = 16.2846(3) Å, V = 4056.16(13) Å^3, *Z* = 4, *T* = 149.98(10) K, μ(MoKα) = 4.296 mm^{-1}, *Dcalc* = 1.318 g/cm^3, 13585 reflections measured (7.936° ≤ 2Θ ≤ 151.48°), 4009 unique (R_{int} = 0.1612, R_{sigma} = 0.0564) which were used in all calculations. The final R_1 was 0.0698 (I > 2σ(I)) and wR_2 was 0.2070 (all data). CCDC 2161246.

E.1.4) **2b** [RhMB(CO)$_2$]PF$_6$

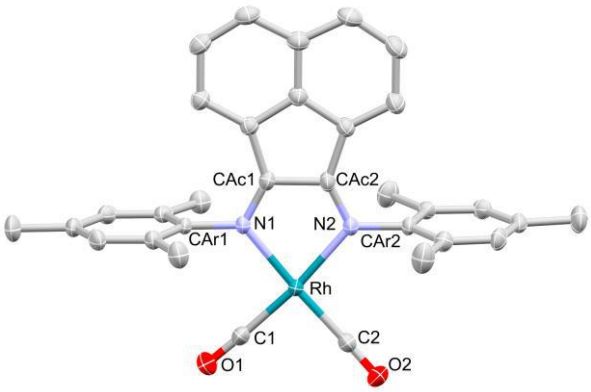


*Figure E.1–4: The molecular structure of **2b** [RhMB(CO)$_2$]PF$_6$ with partial atom-numbering scheme, thermal ellipsoids shown at 50% probability. Hydrogen atoms and PF$_6$ counterion are omitted for clarity.*

$C_{32}H_{28}F_6N_2O_2PRh$ (*M* = 720.44 g/mol): orthorhombic, space group *Pbcn*, *a* = 25.6796(4) Å, *b* = 10.7759(2) Å, *c* = 21.8263(3) Å, V = 6039.79(17) Å^3, *Z* = 8, *T* = 150(2) K, μ(MoKα) = 0.689 mm^{-1}, *Dcalc* = 1.585 g/cm^3, 98928 reflections measured (4.1° ≤ 2Θ ≤ 52.744°), 6173 unique (R_{int} = 0.1040, R_{sigma} = 0.0344) which were used in all calculations. The final R_1 was 0.0294 (I > 2σ(I)) and wR_2 was 0.0835 (all data). CCDC 2161251.

© University of Pretoria

E.1.5) **2c** $[IrDB(CO)_2]PF_6$

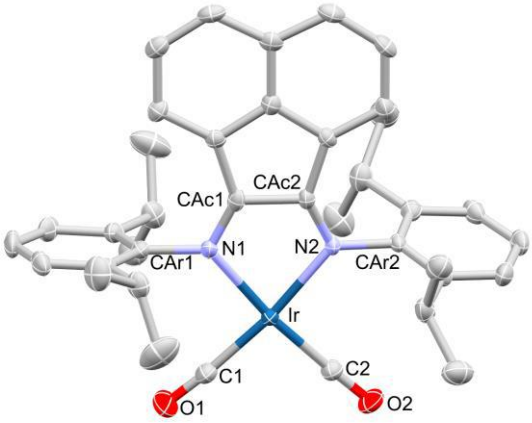


Figure E.1–5: The molecular structure of ***2c*** *$[IrDB(CO)_2]PF_6$ with partial atom-numbering scheme, thermal ellipsoids shown at 50% probability. Hydrogen atoms and PF_6 counterion are omitted for clarity.*

$C_{38}H_{40}F_6IrN_2O_2P$ (*M* = 893.91 g/mol): orthorhombic, space group $P2_12_12_1$, *a* = 12.5684(2) Å, *b* = 12.6901(2) Å, *c* = 22.7161(3) Å, V = 3623.09(9) Å^3, *Z* = 4, *T* = 149.98(10) K, μ(MoKα) = 3.796 mm^{-1}, *Dcalc* = 1.639 g/cm^3, 74771 reflections measured (3.74° ≤ 2Θ ≤ 62.522°), 7400 unique (R_{int} = 0.0731, R_{sigma} = 0.0319) which were used in all calculations. The final R_1 was 0.0200 (I > 2σ(I)) and wR_2 was 0.0459 (all data). CCDC 2161248.

E.1.6) **3a** $[RhDB(CO)(PEt_3)]PF_6$

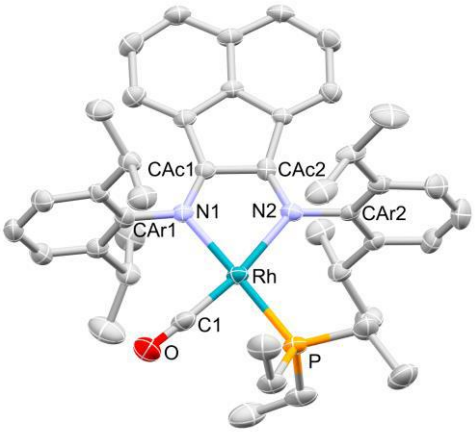


Figure E.1–6: The molecular structure of ***3a*** *$[RhDB(CO)(PEt_3)]PF_6$ with partial atom-numbering scheme, thermal ellipsoids shown at 50% probability. Hydrogen atoms and PF_6 counterion are omitted for clarity.*

$C_{43}H_{55}F_6N_2OP_2Rh$ (*M* = 894.74 g/mol): orthorhombic, space group *Pbca*, *a* = 17.3549(15) Å, *b* = 15.2081(15) Å, *c* = 33.675(3) Å, V = 8888.0(14) Å^3, *Z* = 8, *T* = 150(2) K, μ(MoKα) = 0.515 mm^{-1}, *Dcalc* = 1.337 g/cm^3, 546214 reflections measured (5.08° ≤ 2Θ ≤ 52.76°), 9113 unique (R_{int} = 0.0650, R_{sigma} = 0.0128) which were used in all calculations. The final R_1 was 0.0647 (I > 2σ(I)) and wR_2 was 0.1446 (all data). CCDC 2161252.

© University of Pretoria

E.1.7) **4c** [IrDB(cod)Cl]

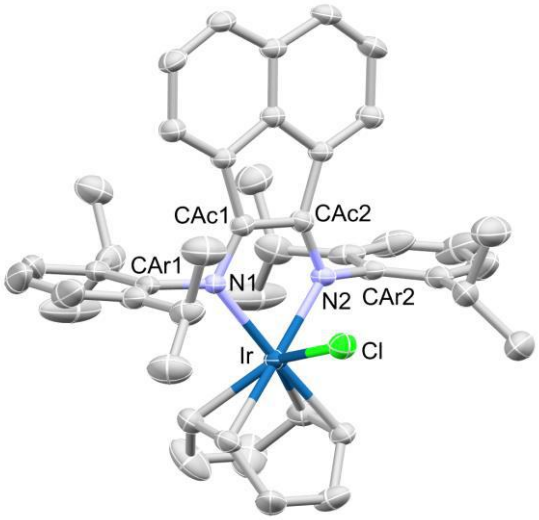


*Figure E.1–7: The molecular structure of **4c** [IrDB(cod)Cl] with partial atom-numbering scheme, thermal ellipsoids shown at 50% probability. Hydrogen atoms are omitted for clarity.*

$C_{44}H_{52}ClIrN_2$ (*M* = 836.55 g/mol): orthorhombic, space group *Pnma, a* = 18.6186(3) Å, *b* = 19.3903(3) Å, *c* = 10.2238(2) Å, V = 3691.00(11) Å^3, *Z* = 4, *T* = 149.99(10) K, μ(MoKα) = 3.723 mm^{-1}, *Dcalc* = 1.505 g/cm^3, 60960 reflections measured (4.202° ≤ 2Θ ≤ 52.74°), 3889 unique (R_{int} = 0.0804, R_{sigma} = 0.0282) which were used in all calculations. The final R_1 was 0.0250 (I > 2σ(I)) and wR_2 was 0.0622 (all data). CCDC 2161250.

© University of Pretoria

E.2) Crystallographic Data Tables

Table E.2–1: Selected bond lengths (Å) from SC-XRD data and DFT optimised molecular geometries, modelled in CH_2Cl_2 solution using cPCM. M = Metal; C_{Ac} = Acenaphthalene imine carbon; C_{Ar} = Aromatic substituent's imine carbon, i.e. Dipp or Mes; L = ancillary ligand. Standard uncertainties are reported in parenthesis.

Complex	M–N	*cPCM*	N–C_{Ac}	*cPCM*	N–C_{Ar}	*cPCM*	C_{Ac}–C_{Ac}	*cPCM*	Miscellaneous	*cPCM*
1b	Rh–N1 2.100(4) Rh–N2 2.100(4)	*2.1270* *2.1270*	N1–C_{Ac1} 1.276(7) N2–C_{Ac2} 1.276(7)	*1.2903* *1.2903*	N1–C_{Ar1} 1.445(6) N2–C_{Ar2} 1.445(6)	*1.4282* *1.4282*	C_{Ac1}–C_{Ac2} 1.492(10)	*1.5022*		
1d	Ir–N1 2.100(7) Ir–N2 2.097(7)	*2.1303* *2.1304*	N1–C_{Ac1} 1.291(11) N2–C_{Ac2} 1.280(11)	*1.2927* *1.2926*	N1–C_{Ar1} 1.451(11) N2–C_{Ar2} 1.456(11)	*1.4313* *1.4313*	C_{Ac2}–C_{Ac1} 1.495(13)	*1.5014*		
2a	Rh–N1 2.135(4) Rh–N2 2.135(4)	*2.1327* *2.1177*	N1–C_{Ac1} 1.350(6) N2–C_{Ac2} 1.350(6)	*1.2921* *1.2915*	N1–C_{Ar1} 1.328(5) N2–C_{Ar2} 1.328(5)	*1.4383* *1.4342*	C_{Ac2}–C_{Ac1} 1.381(9)	*1.5026*	Rh–C1 1.897(6) C1–O1 1.104(7) Rh–C2 1.897(6) C2–O2 1.104(7)	*1.8845* *1.1405* *1.8795* *1.1410*
2b	Rh–N1 2.0728(17) Rh–N2 2.0898(16)	*2.1204* *2.1205*	N1–C_{Ac1} 1.285(3) N2–C_{Ac2} 1.289(2)	*1.2909* *1.2909*	N1–C_{Ar1} 1.450(2) N2–C_{Ar2} 1.451(2)	*1.4335* *1.4335*	C_{Ac1}–C_{Ac2} 1.501(3)	*1.5038*	Rh–C1 1.871(2) C1–O1 1.124(3) Rh–C2 1.875(2) C2–O2 1.129(3)	*1.8824* *1.1411* *1.8825* *1.1410*
2c	Ir–N1 2.082(3) Ir–N2 2.083(3)	*2.1368* *2.1379*	N1–C_{Ac1} 1.279(5) N2–C_{Ac2} 1.277(5)	*1.2935* *1.2941*	N1–C_{Ar1} 1.452(5) N2–C_{Ar2} 1.455(5)	*1.4409* *1.4380*	C_{Ac1}–C_{Ac2} 1.500(5)	*1.5004*	Ir–C1 1.873(5) C1–O1 1.124(6) Ir–C2 1.861(4) C2–O2 1.134(5)	*1.8788* *1.1449* *1.8783* *1.1453*
3a	Rh–N1 2.3053(13) ‡ Rh–N2 2.163(4) ‡ *trans* to PEt_3	*2.1257‡* *2.1799*	N1–C_{Ac1} 1.278(6) N2–C_{Ac2} 1.289(6)	*1.2895* *1.2928*	N1–C_{Ar1} 1.443(6) N2–C_{Ar2} 1.434(6)	*1.4343* *1.4303*	C_{Ac1}–C_{Ac2} 1.495(6)	*1.4947*	Rh–P 2.3053(13) Rh–C1 1.814(6) C1–O 1.155(7)	*2.3465* *1.8304* *1.1518*
4c	Ir–N1 2.096(2) Ir–N2 2.096(2)	*2.9839* *2.1819*	N1–C_{Ac1} 1.321(4) N2–C_{Ac2} 1.321(4)	*1.2760* *1.2970*	N1–C_{Ar1} 1.443(4) N2–C_{Ar2} 1.443(4)	*1.4200* *1.4511*	C_{Ac1}–C_{Ac2} 1.447(6)	*1.5286*	Ir–Cl 2.4754(11)	*2.4269*

© University of Pretoria

Table E.2–2: Selected bond and dihedral angles (°) from SC-XRD data and DFT optimised molecular geometries, modelled in CH_2Cl_2 solution using cPCM. M = Metal; C_{Ac} = Acenaphthalene imine carbon; C_{Ar} = Aromatic substituent's imine carbon, i.e. Dipp or Mes; L = ancillary ligand; plane = least squares plane of aromatic ring(s). Standard uncertainties are reported in parenthesis.

Complex	N–M–N	*cPCM*	N–M–L	*cPCM*	Miscellaneous	*cPCM*	M–N–C_{Ac1}–C_{Ac2}	cPCM	Miscellaneous Dihedrals	*cPCM*
1b	N1–Rh–N2 78.9(2)	*78.86*					Rh–N1–C_{Ac1}–C_{Ac2} 2.2(8) Rh–N2–C_{Ac2}–C_{Ac1} -2.2(8)	*–0.62* *–0.62*		
1d	N2–Ir–N1 78.8(3)	*78.36*					Ir–N1–C_{Ac1}–C_{Ac2} 2.6(10) Ir–N2–C_{Ac2}–C_{Ac1} -6.4(10)	*–0.45* *–0.45*		
2a	N1–Rh–N2 69.4(2)	*78.92*	C1–Rh–N1 104.9(2) C1–Rh–N2 173.9(2) C2–Rh–N1 173.9(2) C2–Rh–N2 104.9(2)	*95.01* *173.86* *173.18* *94.48*	C1–Rh–C2 80.8(4) O1–C1–Rh 177.6(7) O2–C2–Rh 177.6(7)	*91.62* *177.12* *177.20*	Rh–N2–C_{Ac2}–C_{Ac1} 4.3(4) Rh–N1–C_{Ac1}–C_{Ac2} -4.3(4)	*0.80* *0.26*	O1–C1–C2–O2 0.0(1)	*–1.66*
2b	N1–Rh–N2 79.78(6)	*79.02*	C1–Rh–N1 94.31(8) C1–Rh–N2 172.50(8) C2–Rh–N1 174.17(8) C2–Rh–N2 96.35(8)	*94.60* *173.59* *173.59* *94.60*	C1–Rh–C2 89.89(8) O1–C1–Rh 177.9(2) O2–C2–Rh 175.6(2)	*91.79* *177.36* *177.35*	Rh–N1–C_{Ac1}–C_{Ac2} 1.5(2) Rh–N2–C_{Ac2}–C_{Ac1} -2.0(2)	*0.54* *0.54*	O1–C1–C2–O2 –7.3(4)	*–0.47*
2c	N1–Ir–N2 78.47(13)	*77.85*	C1–Ir–N1 94.74(17) C1–Ir–N2 172.92(17) C2–Ir–N1 173.47(15) C2–Ir–N2 95.07(16)	*95.46* *172.59* *173.17* *95.09*	C2–Ir–C1 91.69(19) O1–C1–Ir 175.8(4) O2–C2–Ir 177.9(4)	*91.64* *177.02* *176.76*	Ir–N1–C_{Ac1}–C_{Ac2} 0.6(5) Ir–N2–C_{Ac2}–C_{Ac1} -4.5(5)	*2.17* *–0.49*	O1–C1–C2–O2 –0.7(9)	*–2.77*
3a	N1–Rh–N2 77.30(15)	*77.29*	C1–Rh–N1 93.53(19) C1–Rh–N2 170.76(19) N2–Rh–P 103.90(11) N1–Rh–P 178.38(11)	*93.32* *169.69* *103.42* *178.33*	C1–Rh–P 85.24(16) O–C1–Rh 176.9(5)	*86.08* *176.26*	Rh–N1–C_{Ac1}–C_{Ac2} -0.2(5) Rh–N2–C_{Ac2}–C_{Ac1} -0.1(5)	*–2.80* *–1.03*		
4c	N2–Ir–N1 78.49(13)	*66.77*	N1–Ir–Cl 88.32(6) N2–Ir–Cl 88.33(6)	*80.63* *88.41*	Cl–Ir–Ac_{plane} 79.66	*71.99*	Ir–N1–C_{Ac1}–C_{Ac2} 12.12(9) Ir–N2–C_{Ac2}–C_{Ac1} -12.12(9)	*17.19* *–19.33*		

© University of Pretoria

Table E.2–3: : Selected bond and dihedral angles (°) from SC-XRD data and DFT optimised molecular geometries, modelled in CH_2Cl_2 solution using cPCM. M = Metal; C_{Ac} = Acenaphthalene imine carbon; C_{Ar} = Aromatic substituent's imine carbon, i.e. Dipp or Mes; L = ancillary ligand; plane = least squares plane of aromatic ring(s). Standard uncertainties are reported in parenthesis.

Complex	C_{Ar}–N–C_{Ac}	*cPCM*	N–C_{Ac}–C_{Ac}	*cPCM*	N–C_{Ac1}–C_{Ac2}–N	*cPCM*	Miscellaneous Dihedrals	*cPCM*
1b	C_{Ac1}–N1–C_{Ar1} 120.6(5) C_{Ac2}–N2–C_{Ar2} 120.6(5)	*120.66* *120.66*	N1–C_{Ac1}–C_{Ac2} 117.5(3) N2–C_{Ac2}–C_{Ac1} 117.5(3)	*117.70* *117.70*	N1–C_{Ac1}–C_{Ac2}–N2 –3.0(8)	*0.88*	Mes_{plane1}–Mes_{plane2} 23.97 Ac_{plane}–Mes_{plane1} 79.62 Ac_{plane}–Mes_{plane2} 79.62	*11.46* *86.82* *86.82*
1d	C_{Ac1}–N1–C_{Ar1} 118.9(7) C_{Ac2}–N2–C_{Ar2} 120.3(7)	*120.70* *120.71*	N1–C_{Ac1}–C_{Ac2} 117.4(8) N2–C_{Ac2}–C_{Ac1} 116.7(8)	*117.41* *117.42*	N2–C_{Ac2}–C_{Ac1}–N1 2.6(12)	*0.63*	Mes_{plane1}–Mes_{plane2} 7.31 Ac_{plane}–$Mes_{plane1(CAr1)}$ 89.60 Ac_{plane}–$Mes_{plane2(CAr2)}$ 87.62	*11.82* *87.04* *87.03*
2a	C_{Ac1}–N1–C_{Ar1} 116.0(4) C_{Ar2}–N2–C_{Ac2} 116.0(4)	*119.50* *121.25*	N1–C_{Ac1}–C_{Ac2} 112.9(2) N2–C_{Ac2}–C_{Ac1} 112.9(2)	*117.72* *117.56*	N1–C_{Ac2}–C_{Ac1}–N2 0.0(6)	*–0.75*	$Dipp_{plane1}$–$Dipp_{plane2}$ 0.91 Ac_{plane}–$Dipp_{plane1}$ 76.69 Ac_{plane}–$Dipp_{plane2}$ 76.69	*13.65* *89.65* *77.60*
2b	C_{Ar1}–N1–C_{Ac1} 119.84(16) C_{Ac2}–N2–C_{Ar2} 118.96(17)	*120.83* *120.83*	N1–C_{Ac1}–C_{Ac2} 116.96(17) N2–C_{Ac2}–C_{Ac1} 117.04(17)	*117.56* *117.55*	N1–C_{Ac1}–C_{Ac2}–N2 0.4(3)	*–0.75*	Mes_{plane1}–Mes_{plane2} 5.18 Ac_{plane}–$Mes_{plane1(CAr1)}$ 87.49 Ac_{plane}–$Mes_{plane2(CAr2)}$ 84.12	*9.94* *87.46* *87.45*
2c	C_{Ar1}–N1–C_{Ac1} 118.9(3) C_{Ac2}–N2–C_{Ar2} 120.6(3)	*119.56* *121.13*	N1–C_{Ac1}–C_{Ac2} 116.5(4) N2–C_{Ac2}–C_{Ac1} 116.1(4)	*117.32* *117.21*	N1–C_{Ac1}–C_{Ac2}–N2 2.7(6)	*–1.17*	$Dipp_{plane1}$–$Dipp_{plane2}$ 17.41 Ac_{plane}–$Dipp_{plane(CAr1)}$ 89.34 Ac_{plane}–$Dipp_{plane(CAr2)}$ 75.36	*14.31* *89.81* *77.32*
3a	C_{Ar1}–N1–C_{Ac1} 121.1(4) C_{Ac2}–N2–C_{Ar2} 118.1(4)	*119.46* *119.28*	N1–C_{Ac1}–C_{Ac2} 117.3(4) N2–C_{Ac2}–C_{Ac1} 117.1(4)	*117.27* *117.81*	N1–C_{Ac1}–C_{Ac2}–N2 0.2(7)	*2.65*	$Dipp_{plane1}$–$Dipp_{plane2}$ 7.30 Ac_{plane}–$Dipp_{plane1(CO\ side)}$ 82.04 Ac_{plane}–$Dipp_{plane2(PEt3\ side)}$ 81.52	*15.77* *87.38* *77.53*
4c	C_{Ar1}–N1–C_{Ac1} 116.8(2) C_{Ac2}–N2–C_{Ar2} 116.8(2)	*121.41* *117.96*	N1–C_{Ac1}–C_{Ac2} 117.14(16) N2–C_{Ac2}–C_{Ac1} 117.14(16)	*122.07* *123.33*	N1–C_{Ac1}–C_{Ac2}–N2 0.0(4)	*–5.12*	$Dipp_{plane1}$–$Dipp_{plane2}$ 5.27 Ac_{plane}–$Dipp_{plane1}$ 83.32 Ac_{plane}–$Dipp_{plane2}$ 83.32	*0.84* *82.60* *83.19*

© University of Pretoria

Appendix F: Electrochemical Characterisation

F.1) CVs and DPVs

F.1.1) DippBIAN

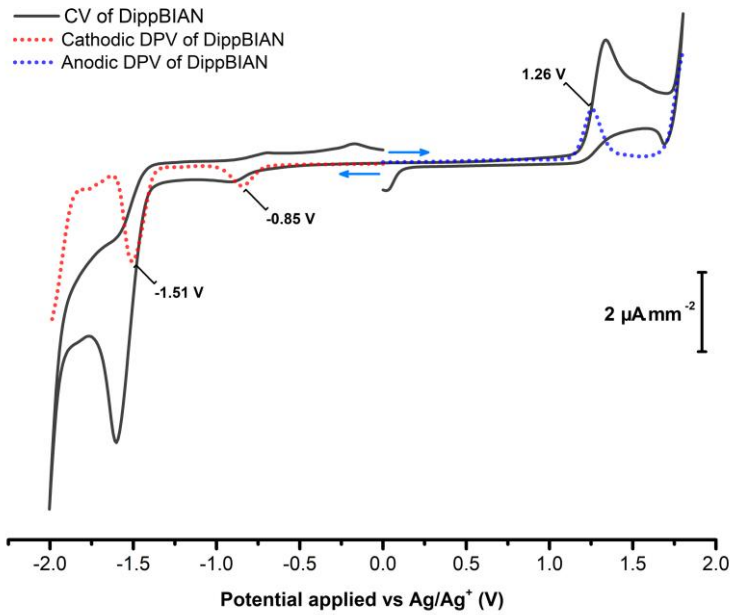


Figure F.1–1: CV and DPV of DippBIAN recorded in CH_2Cl_2 with 1.0 mM analyte and 0.1 M $TBAPF_6$ supporting electrolyte.

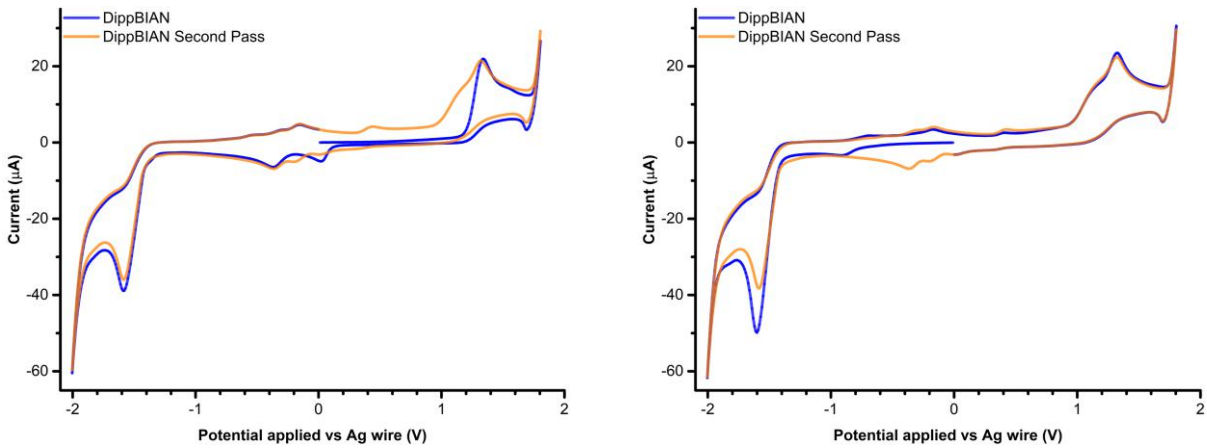


Figure F.1–2: Anodic first (left) and Cathodic first (right) CVs of the free DippBIAN ligand recorded in CH_2Cl_2 with 1.0 mM analyte and 0.1 M $TBAPF_6$ supporting electrolyte. Second pass scans (orange) are included to assist in differentiating compound peaks from decomposition or secondary reaction peaks.

© University of Pretoria

F.1.2) **1a** [RhDB(cod)]PF_6

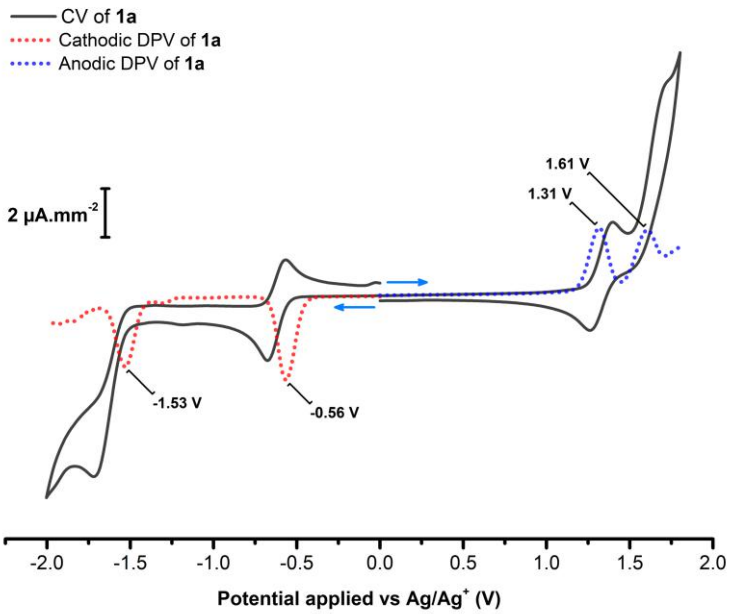


*Figure F.1–3: CV and DPV of **1a** [RhDB(cod)]PF_6 recorded in CH_2Cl_2 with 1.0 mM analyte and 0.1 M $TBAPF_6$ supporting electrolyte.*

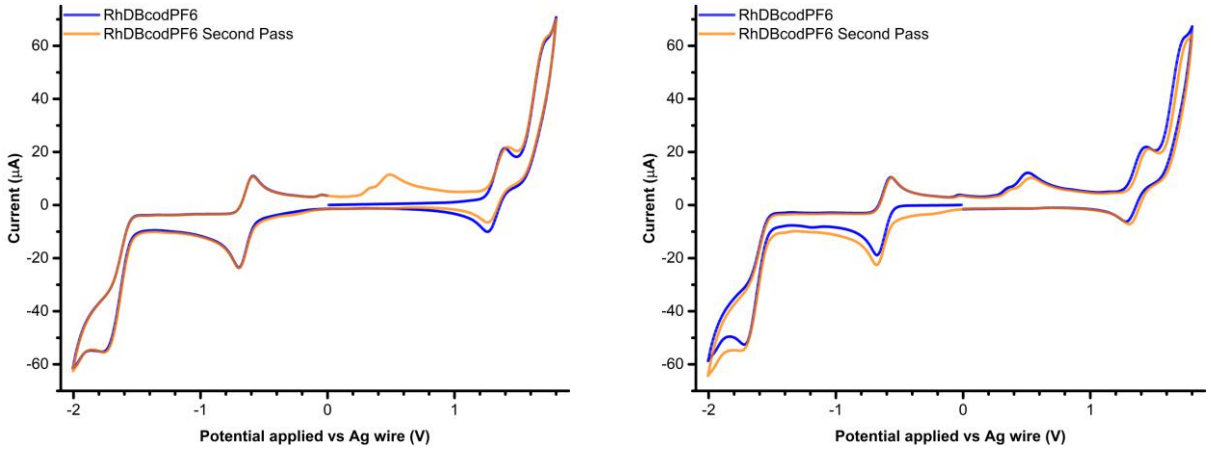


*Figure F.1–4: Anodic first (left) and Cathodic first (right) CVs of **1a** recorded in CH_2Cl_2 with 1.0 mM analyte and 0.1 M $TBAPF_6$ supporting electrolyte. Second pass scans (orange) are included to assist in differentiating compound peaks from decomposition or secondary reaction peaks.*

© University of Pretoria

F.1.3) **1b** [RhMB(cod)]PF_6

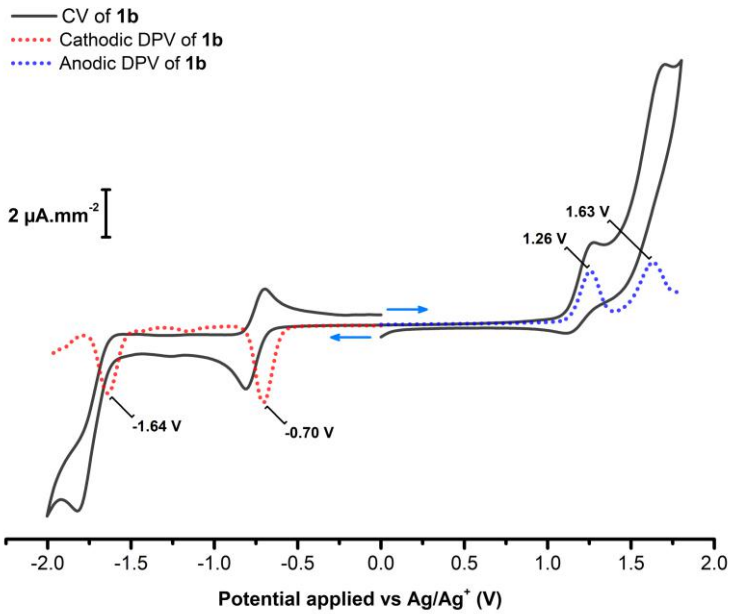


*Figure F.1–5: CV and DPV of **1b** [RhMB(cod)]PF_6 recorded in CH_2Cl_2 with 1.0 mM analyte and 0.1 M $TBAPF_6$ supporting electrolyte.*

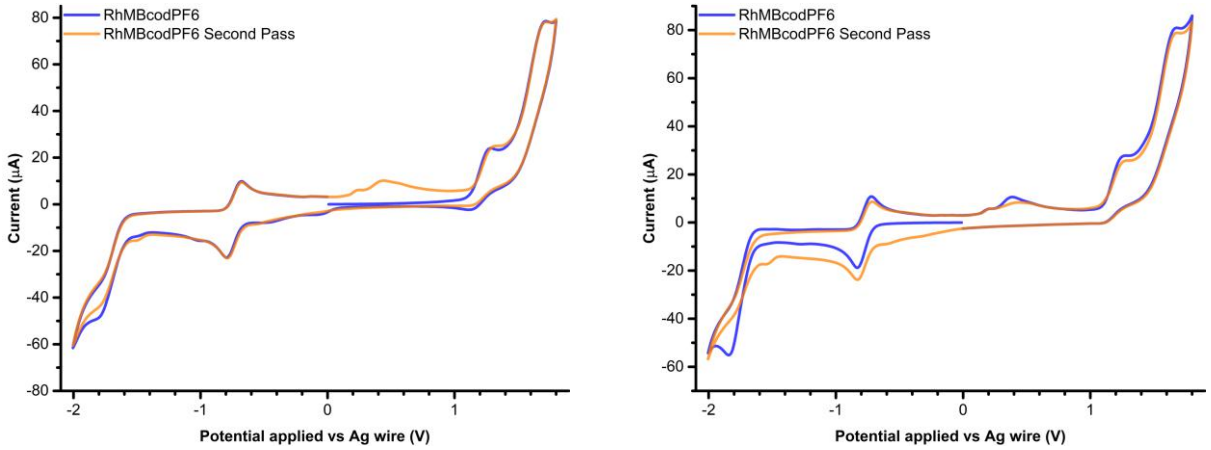


*Figure F.1–6: Anodic first (left) and Cathodic first (right) CVs of **1b** recorded in CH_2Cl_2 with 1.0 mM analyte and 0.1 M $TBAPF_6$ supporting electrolyte. Second pass scans (orange) are included to assist in differentiating compound peaks from decomposition or secondary reaction peaks.*

© University of Pretoria

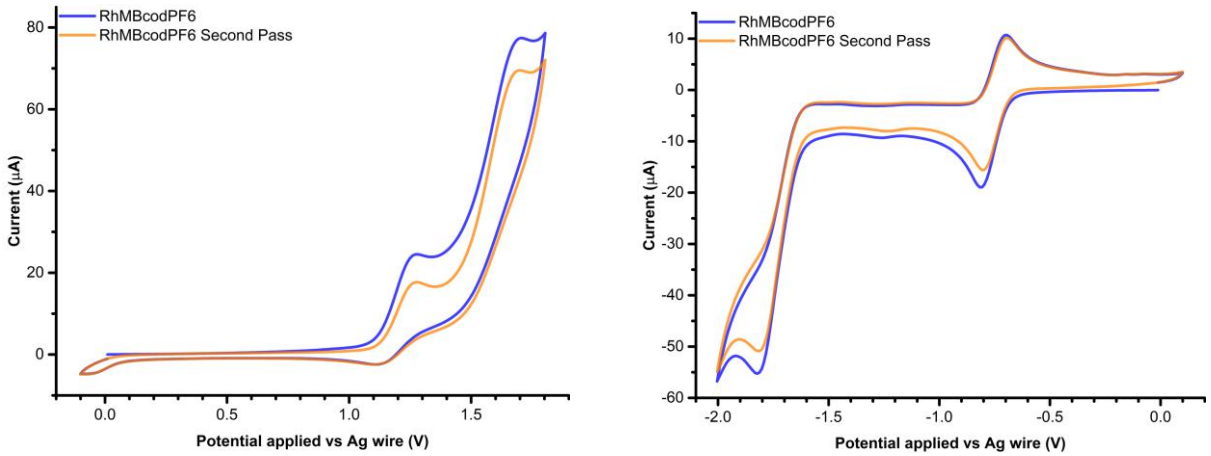


*Figure F.1–7: Narrowed potential window CVs of **1b**, anodic first (left) and cathodic first (right), recorded in CH_2Cl_2 with 1.0 mM analyte and 0.1 M $TBAPF_6$ supporting electrolyte. Second pass scans (orange) are included to assist in differentiating compound peaks from decomposition or secondary reaction peaks.*

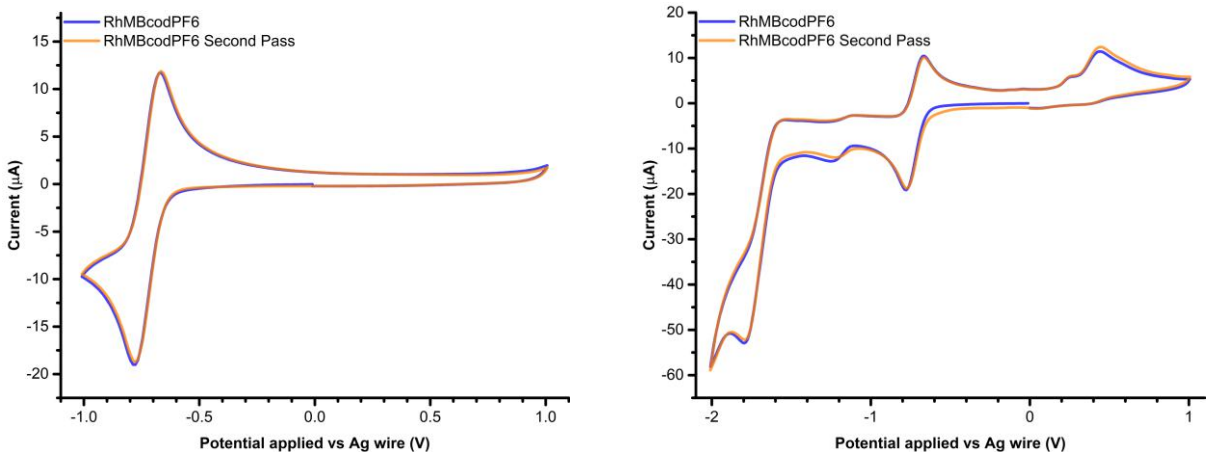


*Figure F.1–8: Narrowed potential window cathodic first CVs of **1b**, recorded in CH_2Cl_2 with 1.0 mM analyte and 0.1 M $TBAPF_6$ supporting electrolyte. Second pass scans (orange) are included to assist in differentiating compound peaks from decomposition or secondary reaction peaks.*

© University of Pretoria

F.1.4) **1c** [IrDB(cod)]PF_6

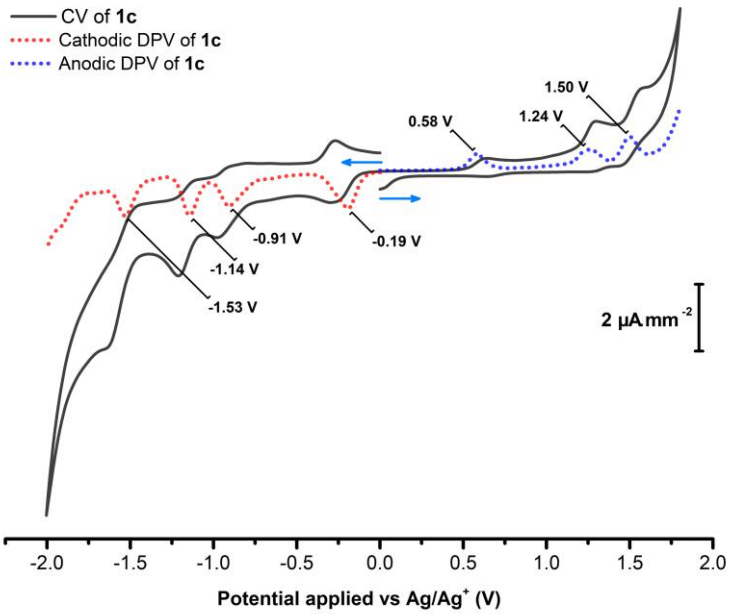


*Figure F.1–9: CV and DPV of **1c** [IrDB(cod)]PF_6 recorded in CH_2Cl_2 with 1.0 mM analyte and 0.1 M $TBAPF_6$ supporting electrolyte.*

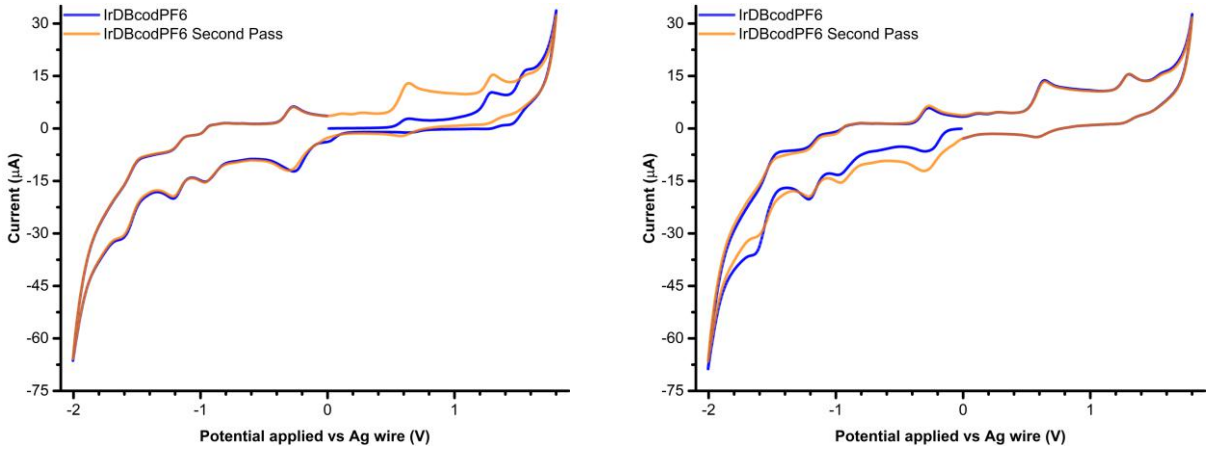


*Figure F.1–10: Anodic first (left) and Cathodic first (right) CVs of **1c** recorded in CH_2Cl_2 with 1.0 mM analyte and 0.1 M $TBAPF_6$ supporting electrolyte. Second pass scans (orange) are included to assist in differentiating compound peaks from decomposition or secondary reaction peaks.*

© University of Pretoria

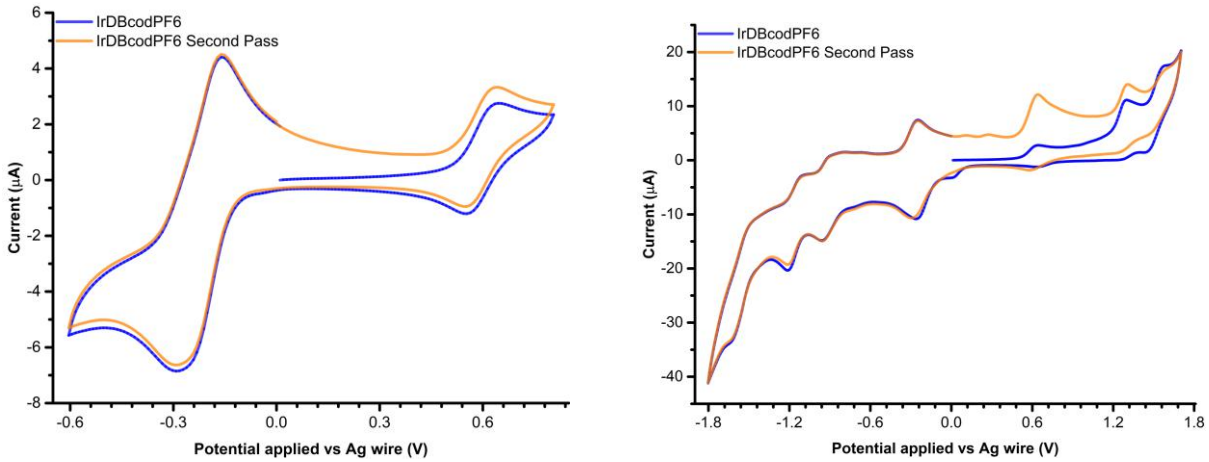


*Figure F.1–11: Narrowed potential window anodic first CVs of **1c**, recorded in CH_2Cl_2 with 1.0 mM analyte and 0.1 M $TBAPF_6$ supporting electrolyte. Second pass scans (orange) are included to assist in differentiating compound peaks from decomposition or secondary reaction peaks.*

© University of Pretoria

F.1.5) **1d** [IrMB(cod)]PF_6

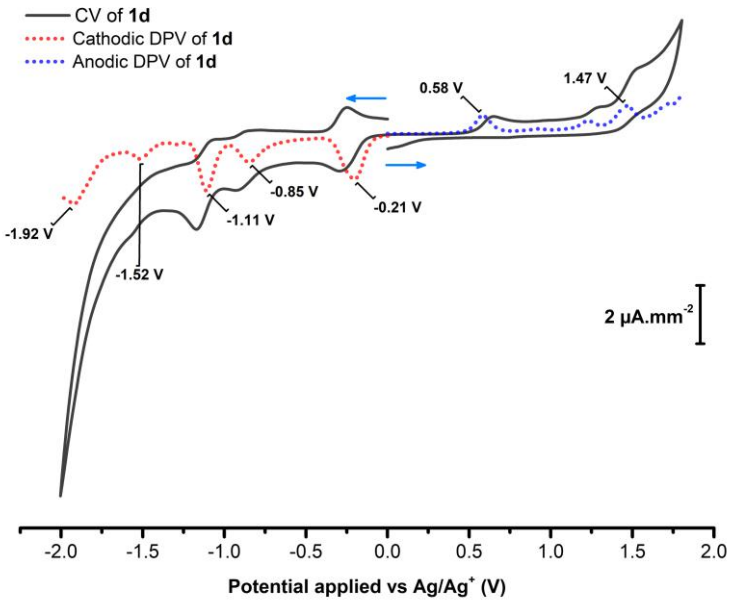


*Figure F.1–12: CV and DPV of **1d** [IrMB(cod)]PF_6 recorded in CH_2Cl_2 with 1.0 mM analyte and 0.1 M $TBAPF_6$ supporting electrolyte.*

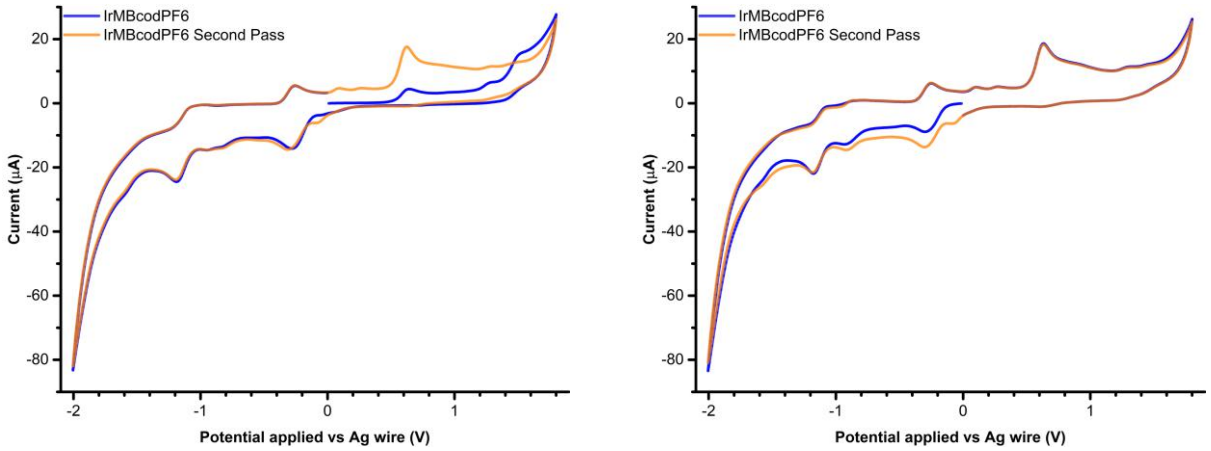


*Figure F.1–13: Anodic first (left) and Cathodic first (right) CVs of **1d** recorded in CH_2Cl_2 with 1.0 mM analyte and 0.1 M $TBAPF_6$ supporting electrolyte. Second pass scans (orange) are included to assist in differentiating compound peaks from decomposition or secondary reaction peaks.*

© University of Pretoria

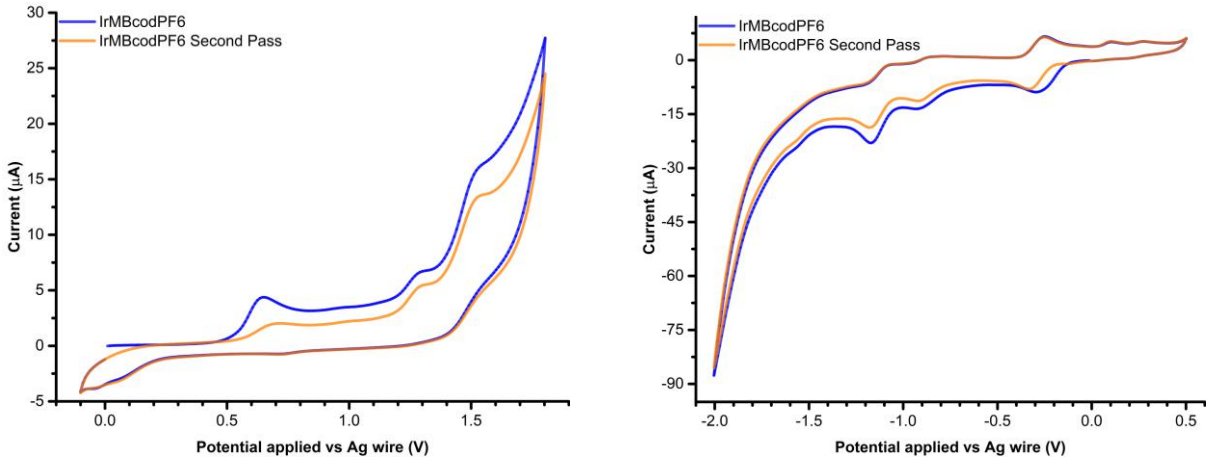


*Figure F.1–14: Narrowed potential window CVs of **1d**, anodic first (left) and cathodic first (right), recorded in CH_2Cl_2 with 1.0 mM analyte and 0.1 M $TBAPF_6$ supporting electrolyte. Second pass scans (orange) are included to assist in differentiating compound peaks from decomposition or secondary reaction peaks.*

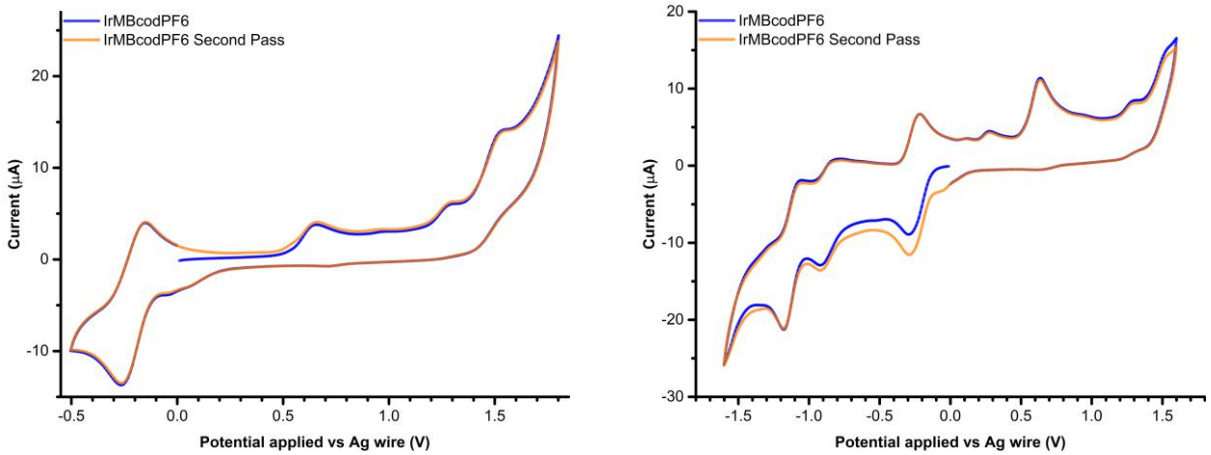


*Figure F.1–15: Narrowed potential window anodic first CVs of **1d**, recorded in CH_2Cl_2 with 1.0 mM analyte and 0.1 M $TBAPF_6$ supporting electrolyte. Second pass scans (orange) are included to assist in differentiating compound peaks from decomposition or secondary reaction peaks.*

© University of Pretoria

F.1.6) **2a** $[RhDB(CO)_2]PF_6$

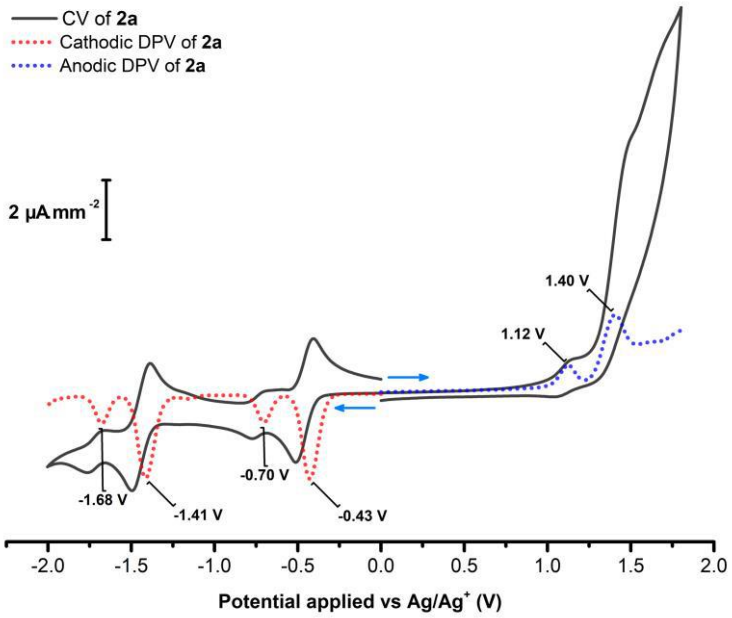


*Figure F.1–16: CV and DPV of **2a** $[RhDB(CO)_2]PF_6$ recorded in CH_2Cl_2 with 1.0 mM analyte and 0.1 M $TBAPF_6$ supporting electrolyte.*

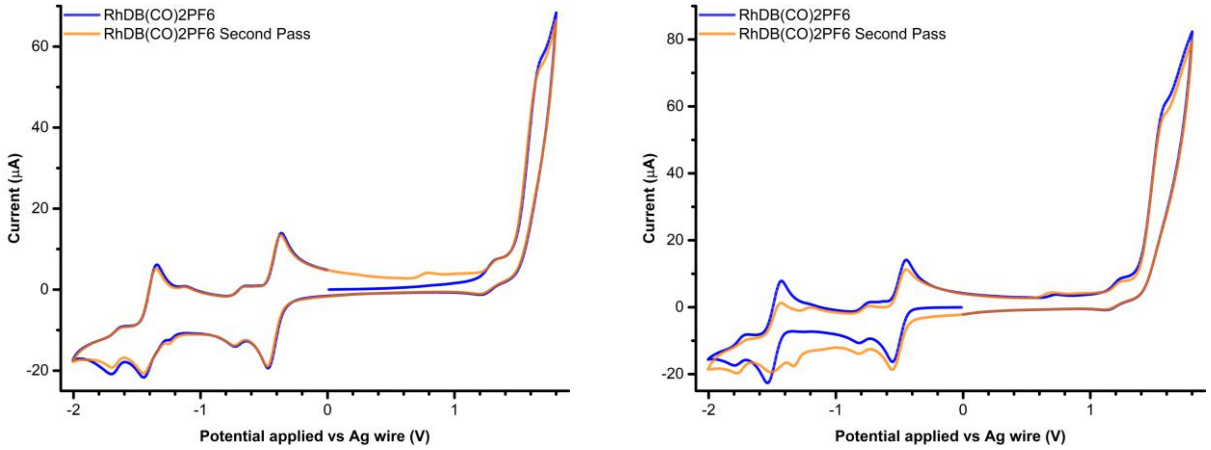
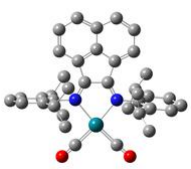
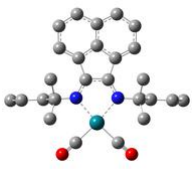
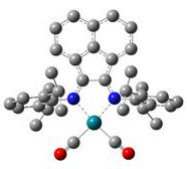
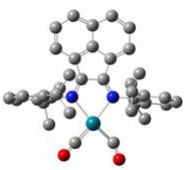
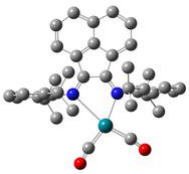


*Figure F.1–17: Anodic first (left) and Cathodic first (right) CVs of **2a** recorded in CH_2Cl_2 with 1.0 mM analyte and 0.1 M $TBAPF_6$ supporting electrolyte. Second pass scans (orange) are included to assist in differentiating compound peaks from decomposition or secondary reaction peaks.*

*Table F.1–1: Optimised molecular geometries of **2a** modelled in different charged states. All calculations were performed at B3LYP-D3/def2-SVP level of theory in CH_2Cl_2 using cPCM. The integer "n" designates the number of electrons that were added to the starting geometry before optimisation to simulate the effect of electrochemical reduction.*

n = 0	n = +1	n = +2	n = +3	n = +4
				

© University of Pretoria

F.1.7) **2c** $[IrDB(CO)_2]PF_6$

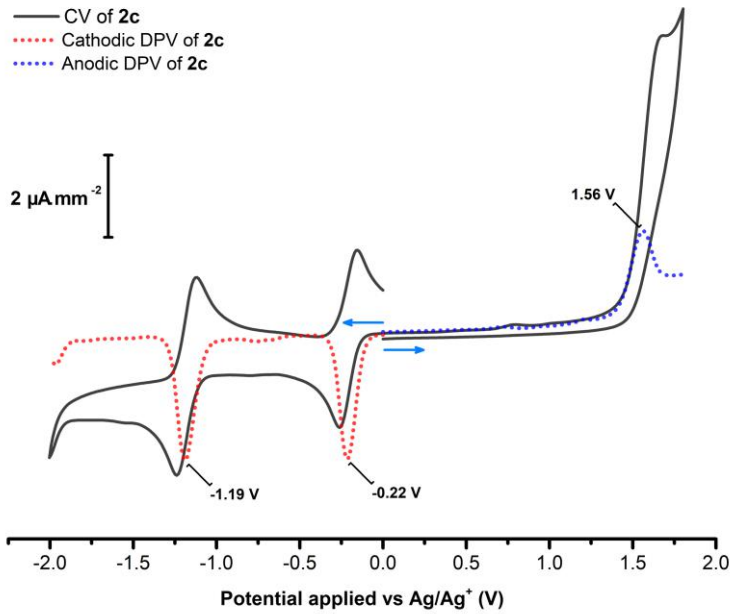


*Figure F.1–18: CV and DPV of **2c** $[IrDB(CO)_2]PF_6$ recorded in CH_2Cl_2 with 1.0 mM analyte and 0.1 M $TBAPF_6$ supporting electrolyte.*

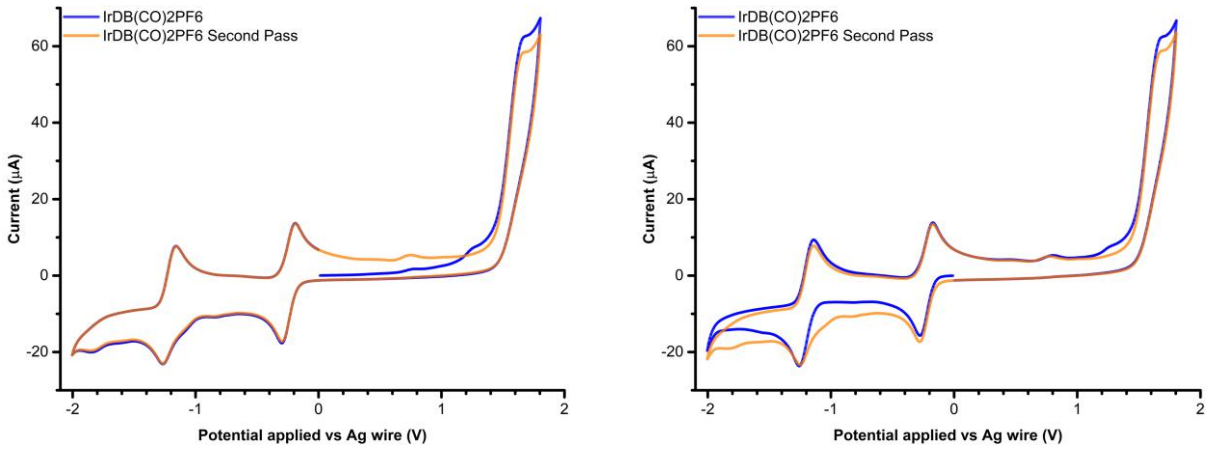


*Figure F.1–19: Anodic first (left) and Cathodic first (right) CVs of **2c** recorded in CH_2Cl_2 with 1.0 mM analyte and 0.1 M $TBAPF_6$ supporting electrolyte. Second pass scans (orange) are included to assist in differentiating compound peaks from decomposition or secondary reaction peaks.*

© University of Pretoria

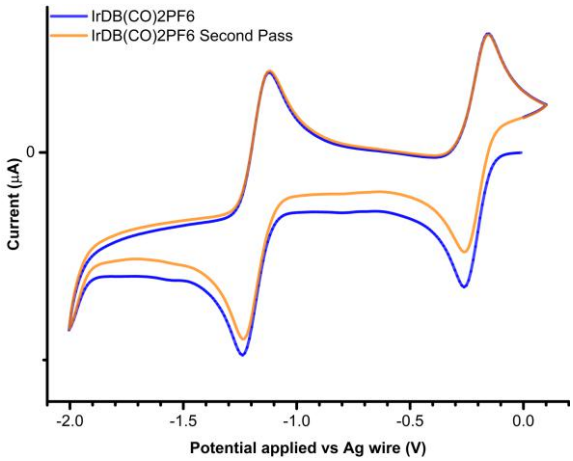


*Figure F.1–20: Narrowed potential window cathodic first CV of **2c**, recorded in CH_2Cl_2 with 1.0 mM analyte and 0.1 M $TBAPF_6$ supporting electrolyte. Second pass scans (orange) are included to assist in differentiating compound peaks from decomposition or secondary reaction peaks.*

© University of Pretoria

F.1.8) **2d** $[IrMB(CO)_2]PF_6$

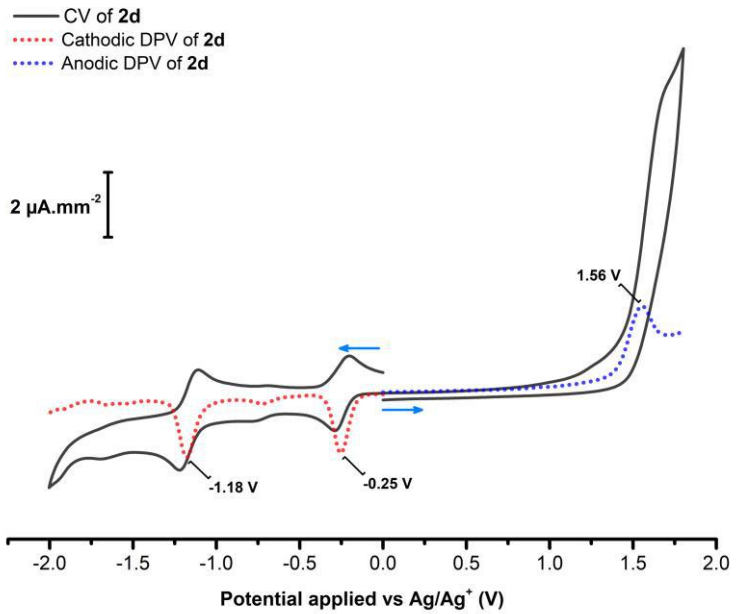


*Figure F.1–21: CV and DPV of **2d** $[IrMB(CO)_2]PF_6$ recorded in CH_2Cl_2 with 1.0 mM analyte and 0.1 M $TBAPF_6$ supporting electrolyte.*

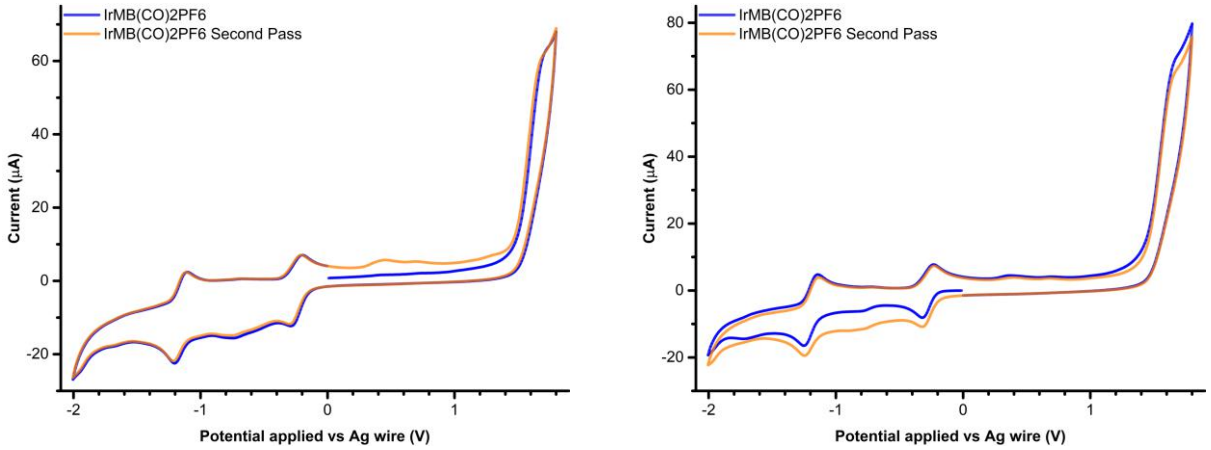


*Figure F.1–22: Anodic first (left) and Cathodic first (right) CVs of **2d** recorded in CH_2Cl_2 with 1.0 mM analyte and 0.1 M $TBAPF_6$ supporting electrolyte. Second pass scans (orange) are included to assist in differentiating compound peaks from decomposition or secondary reaction peaks.*

© University of Pretoria

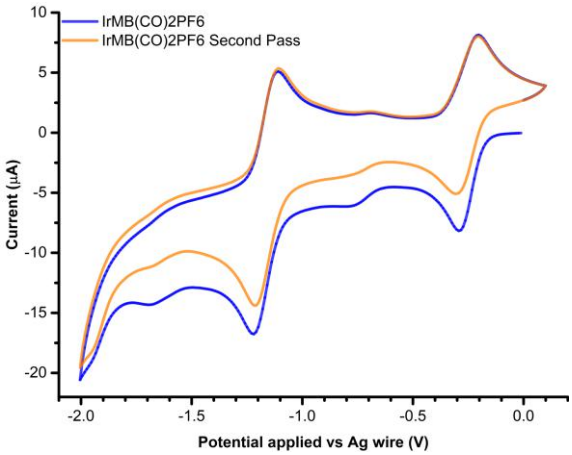


*Figure F.1–23: Narrowed potential window cathodic first CVs of **2d**, recorded in CH_2Cl_2 with 1.0 mM analyte and 0.1 M $TBAPF_6$ supporting electrolyte. Second pass scans (orange) are included to assist in differentiating compound peaks from decomposition or secondary reaction peaks.*

© University of Pretoria

F.1.9) **3a** [RhDB(CO)(PEt_3)]PF_6

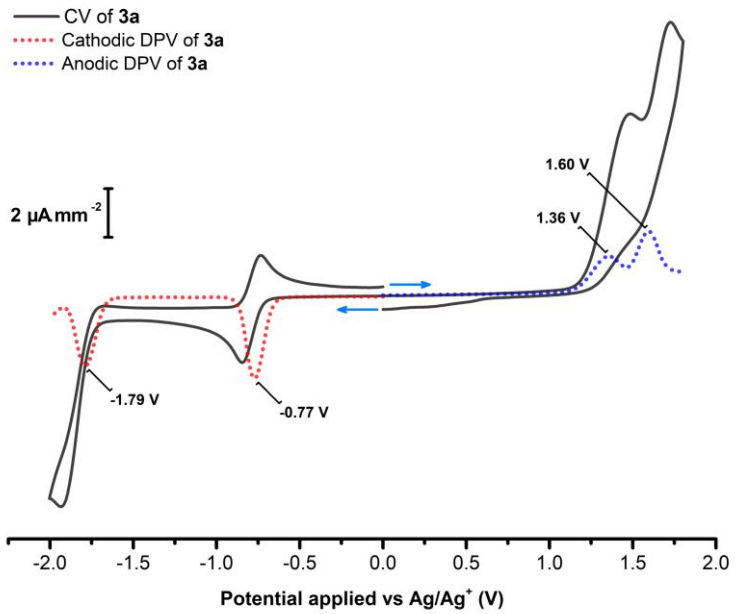


*Figure F.1–24: CV and DPV of **3a** [RhDB(CO)(PEt_3)]PF_6 recorded in CH_2Cl_2 with 1.0 mM analyte and 0.1 M $TBAPF_6$ supporting electrolyte.*

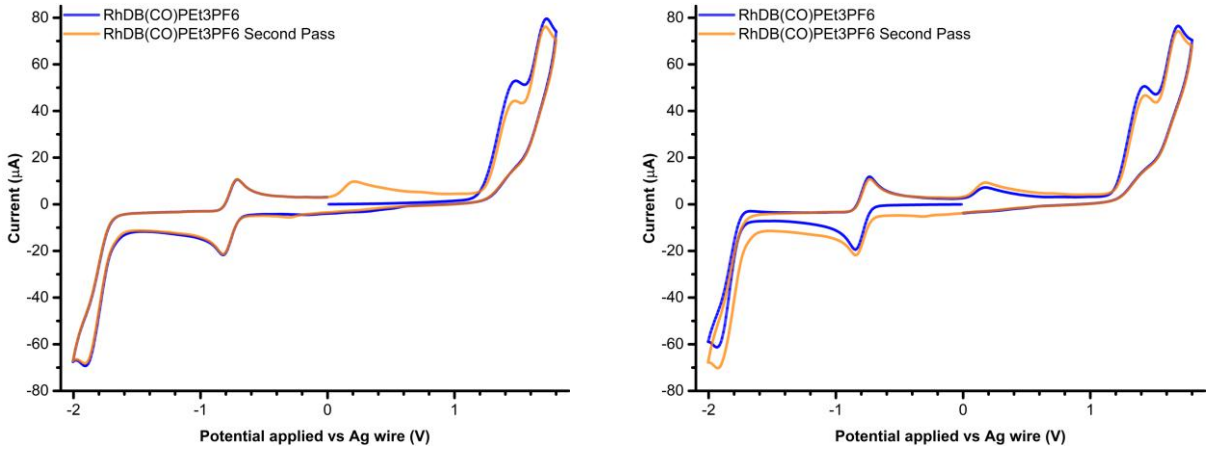


*Figure F.1–25: Anodic first (left) and Cathodic first (right) CVs of **3a** recorded in CH_2Cl_2 with 1.0 mM analyte and 0.1 M $TBAPF_6$ supporting electrolyte. Second pass scans (orange) are included to assist in differentiating compound peaks from decomposition or secondary reaction peaks.*

© University of Pretoria

F.1.10) **3b** [RhMB(CO)(PEt_3)]PF_6

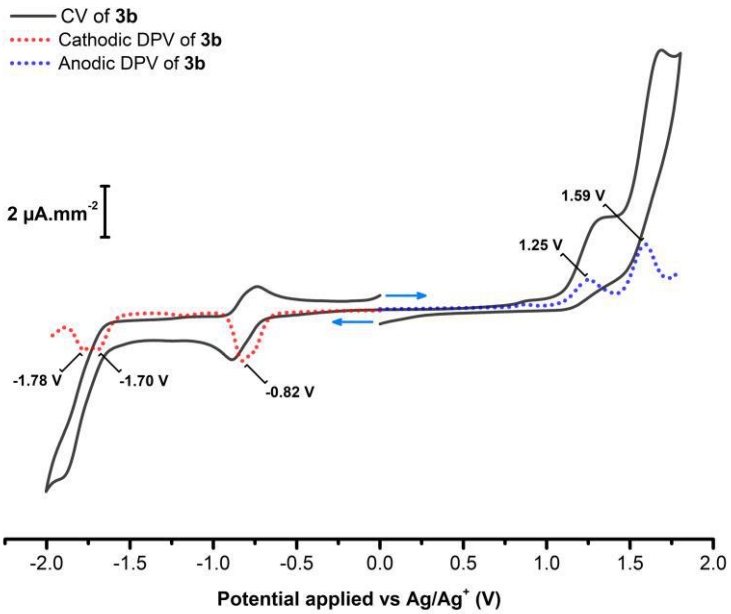


*Figure F.1–26: CV and DPV of **3b** [RhMB(CO)(PEt_3)]PF_6 recorded in CH_2Cl_2 with 1.0 mM analyte and 0.1 M $TBAPF_6$ supporting electrolyte.*

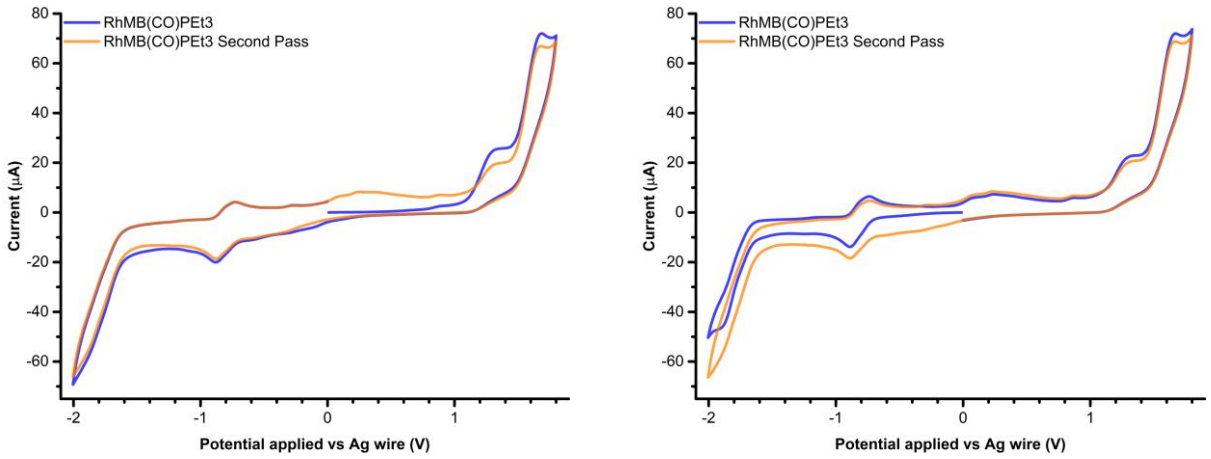


*Figure F.1–27: Anodic first (left) and Cathodic first (right) CVs of **3b** recorded in CH_2Cl_2 with 1.0 mM analyte and 0.1 M $TBAPF_6$ supporting electrolyte. Second pass scans (orange) are included to assist in differentiating compound peaks from decomposition or secondary reaction peaks.*

© University of Pretoria

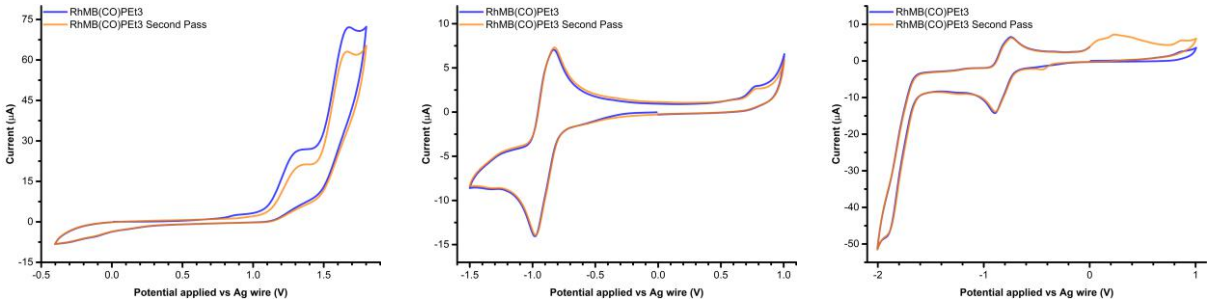


*Figure F.1–28: Narrowed potential window CVs of **3b**, anodic first (left and right) and cathodic first (middle), recorded in CH_2Cl_2 with 1.0 mM analyte and 0.1 M $TBAPF_6$ supporting electrolyte. Second pass scans (orange) are included to assist in differentiating compound peaks from decomposition or secondary reaction peaks.*

*Table F.1–2: Optimised molecular geometries of **3b** modelled in different charged states. All calculations were performed at B3LYP-D3/def2-SVP level of theory in CH_2Cl_2 using cPCM. The integer "n" designates the number of electrons that were added to the starting geometry before optimisation to simulate the effect of electrochemical reduction.*

n = 0	n = +1	n = +2	n = +3	n = +4
				

© University of Pretoria

F.1.11) **4a** [RhDB(cod)Cl]

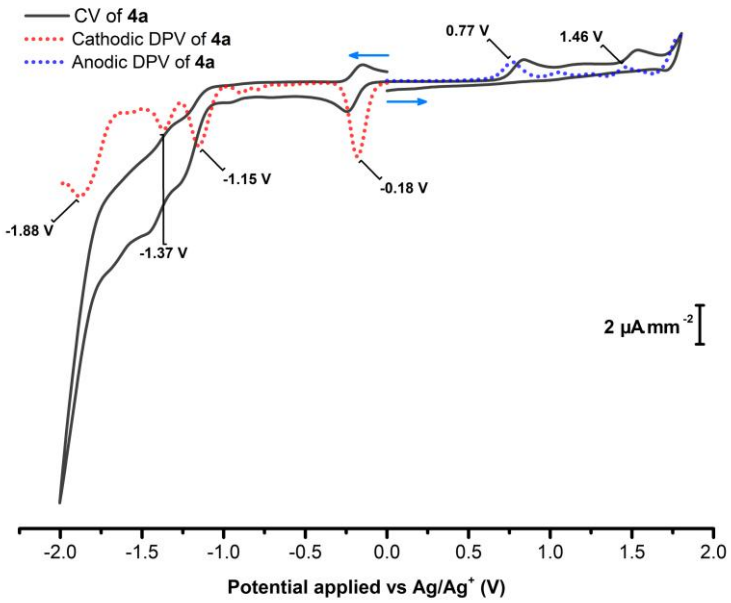


*Figure F.1–29: CV and DPV of **4a** [RhDB(cod)Cl] recorded in CH_2Cl_2 with 1.0 mM analyte and 0.1 M $TBAPF_6$ supporting electrolyte.*

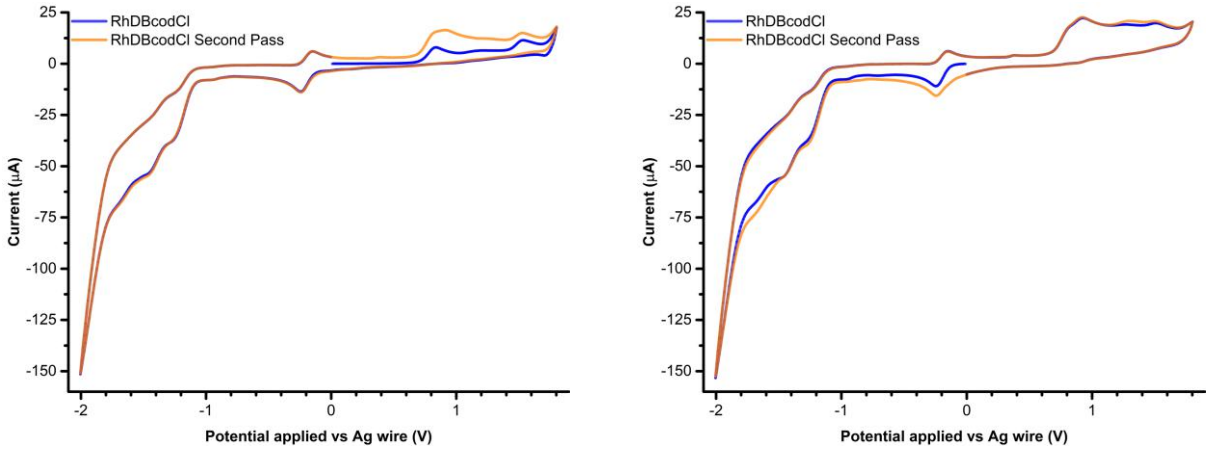
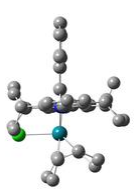
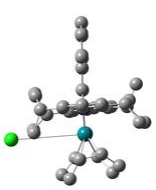
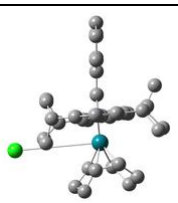
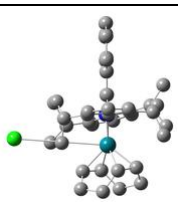
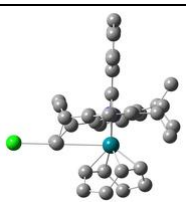


*Figure F.1–30: Anodic first (left) and Cathodic first (right) CVs of **4a** recorded in CH_2Cl_2 with 1.0 mM analyte and 0.1 M $TBAPF_6$ supporting electrolyte. Second pass scans (orange) are included to assist in differentiating compound peaks from decomposition or secondary reaction peaks.*

*Table F.1–3: Optimised molecular geometries of **4a** modelled in different charged states. All calculations were performed at B3LYP-D3/def2-SVP level of theory in CH_2Cl_2 using cPCM. The integer "n" designates the number of electrons that were added to the starting geometry before optimisation to simulate the effect of electrochemical reduction.*

n = 0	n = +1	n = +2	n = +3	n = +4
				
Rh–Cl 2.613 Å	Rh–Cl 4.689 Å	Rh–Cl 5.033 Å	Rh–Cl 5.542 Å	Rh–Cl 5.632 Å

© University of Pretoria

F.1.12) **4b** [RhMB(cod)Cl]

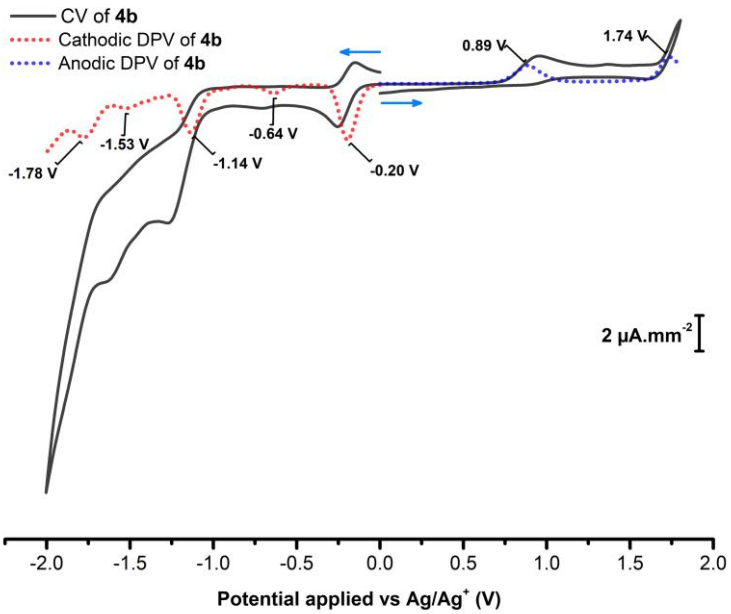


*Figure F.1–31: CV and DPV of **4b** [RhMB(cod)Cl] recorded in CH_2Cl_2 with 1.0 mM analyte and 0.1 M $TBAPF_6$ supporting electrolyte.*

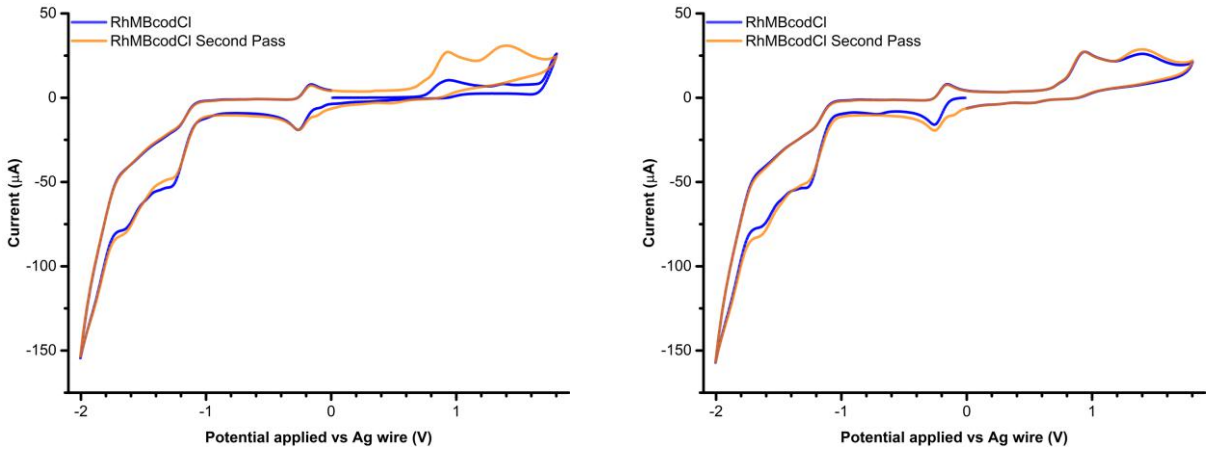


*Figure F.1–32: Anodic first (left) and Cathodic first (right) CVs of **4b** recorded in CH_2Cl_2 with 1.0 mM analyte and 0.1 M $TBAPF_6$ supporting electrolyte. Second pass scans (orange) are included to assist in differentiating compound peaks from decomposition or secondary reaction peaks.*

© University of Pretoria

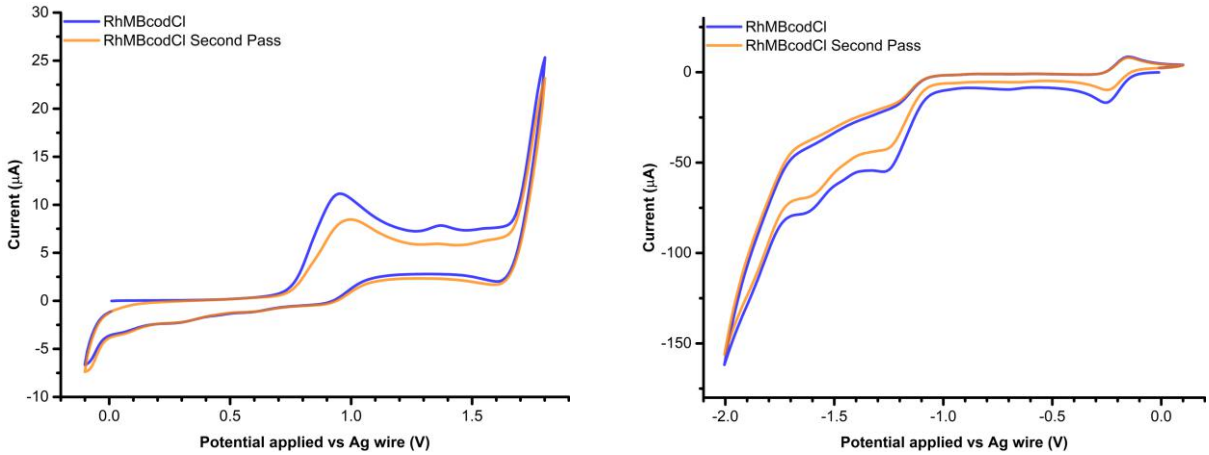
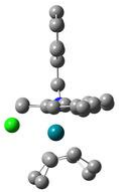
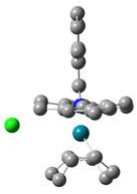
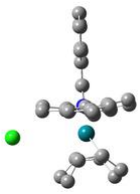
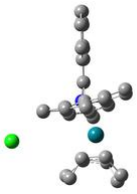
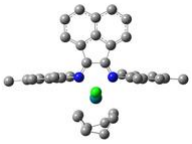
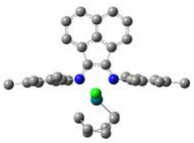
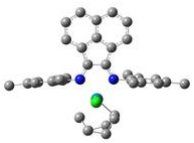
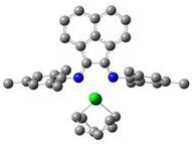
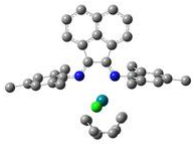


*Figure F.1–33: Narrowed potential window CVs of **4b**, anodic first (left) and cathodic first (right), recorded in CH_2Cl_2 with 1.0 mM analyte and 0.1 M $TBAPF_6$ supporting electrolyte. Second pass scans (orange) are included to assist in differentiating compound peaks from decomposition or secondary reaction peaks.*

*Table F.1–4: Optimised molecular geometries of **4b** modelled in different charged states. All calculations were performed at B3LYP-D3/def2-SVP level of theory in CH_2Cl_2 using cPCM. The integer "n" designates the number of electrons that were added to the starting geometry before optimisation to simulate the effect of electrochemical reduction.*

n = 0	n = +1	n = +2	n = +3	n = +4
				
Rh–Cl 2.593 Å	Rh–Cl 4.052 Å	Rh–Cl 4.303 Å	Rh–Cl 4.529 Å	Rh–Cl 5.057 Å
				
Rh–N 2.131 Å	Rh–N 2.108 Å	Rh–N 2.096 Å	Rh–N 2.250 Å	$Rh–N_1$ 2.859 Å $Rh–N_2$ 2.357 Å

© University of Pretoria

F.1.13) **4c** [IrDB(cod)Cl]

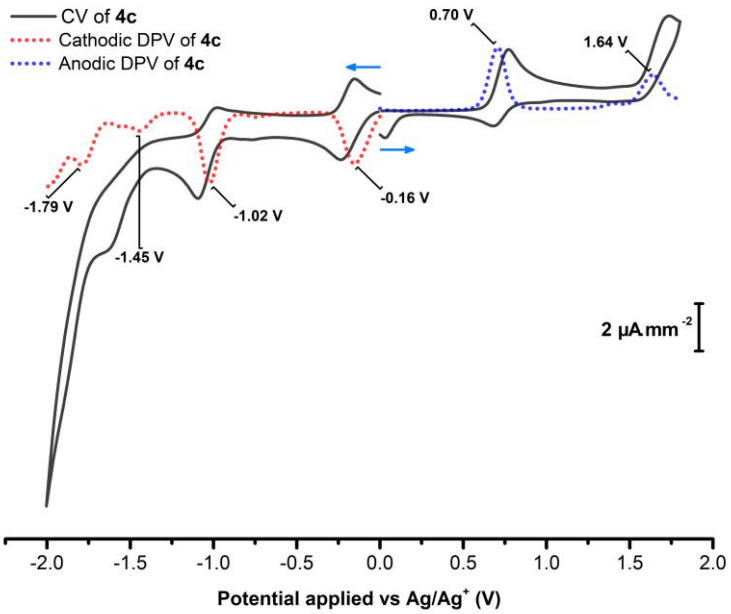


*Figure F.1–34: CV and DPV of **4c** [IrDB(cod)Cl] recorded in CH_2Cl_2 with 1.0 mM analyte and 0.1 M $TBAPF_6$ supporting electrolyte.*

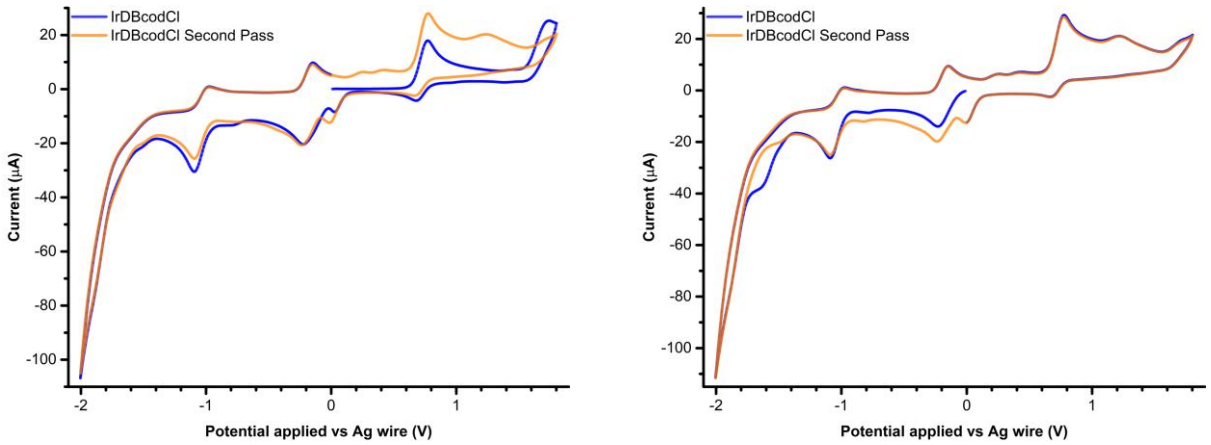


*Figure F.1–35: Anodic first (left) and Cathodic first (right) CVs of **4c** recorded in CH_2Cl_2 with 1.0 mM analyte and 0.1 M $TBAPF_6$ supporting electrolyte. Second pass scans (orange) are included to assist in differentiating compound peaks from decomposition or secondary reaction peaks.*

© University of Pretoria

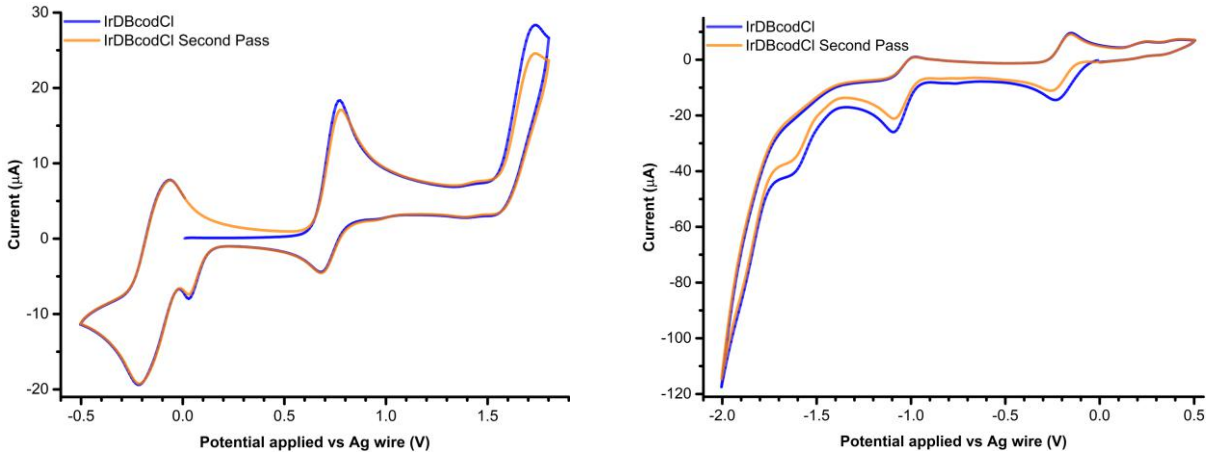


*Figure F.1–36: Narrowed potential window CVs of **4c**, anodic first (left) and cathodic first (right), recorded in CH_2Cl_2 with 1.0 mM analyte and 0.1 M $TBAPF_6$ supporting electrolyte. Second pass scans (orange) are included to assist in differentiating compound peaks from decomposition or secondary reaction peaks.*

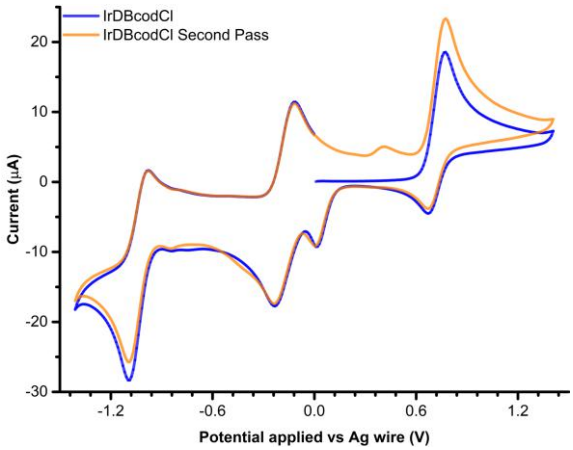
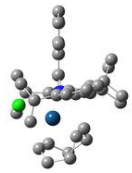
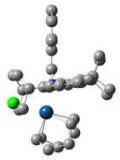
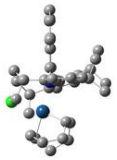
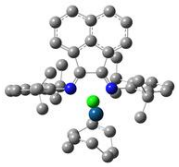
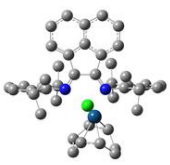
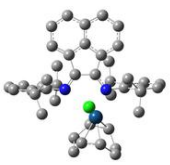
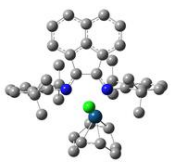
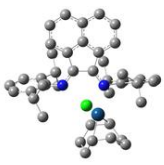
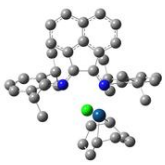


*Figure F.1–37: Narrowed potential window anodic first CV of **4c**, recorded in CH_2Cl_2 with 1.0 mM analyte and 0.1 M $TBAPF_6$ supporting electrolyte. Second pass scans (orange) are included to assist in differentiating compound peaks from decomposition or secondary reaction peaks.*

*Table F.1–5: Optimised molecular geometries of **4c** modelled in different charged states. All calculations were performed at B3LYP-D3/def2-SVP level of theory in CH_2Cl_2 using cPCM. The integer "n" designates the number of electrons that were added to the starting geometry before optimisation to simulate the effect of electrochemical reduction.*

n = –1	n = 0	n = +1	n = +2	n = +3	n = +4
 Ir–Cl 2.411 Å	 Ir–Cl 2.427 Å	 Ir–Cl 2.448 Å	 Ir–Cl 2.464 Å	 Ir–Cl 2.590 Å	 Ir–Cl 2.719 Å
 $Ir–N_1$ 2.513 Å $Ir–N_2$ 2.128 Å	 $Ir–N_1$ 2.984 Å $Ir–N_2$ 2.182 Å	 $Ir–N_1$ 3.068 Å $Ir–N_2$ 2.169 Å	 $Ir–N_1$ 2.928 Å $Ir–N_2$ 2.181 Å	 $Ir–N_1$ 3.500 Å $Ir–N_2$ 2.280 Å	 $Ir–N_1$ 3.623 Å $Ir–N_2$ 2.363 Å

© University of Pretoria

F.1.14) **4d** [IrMB(cod)Cl]

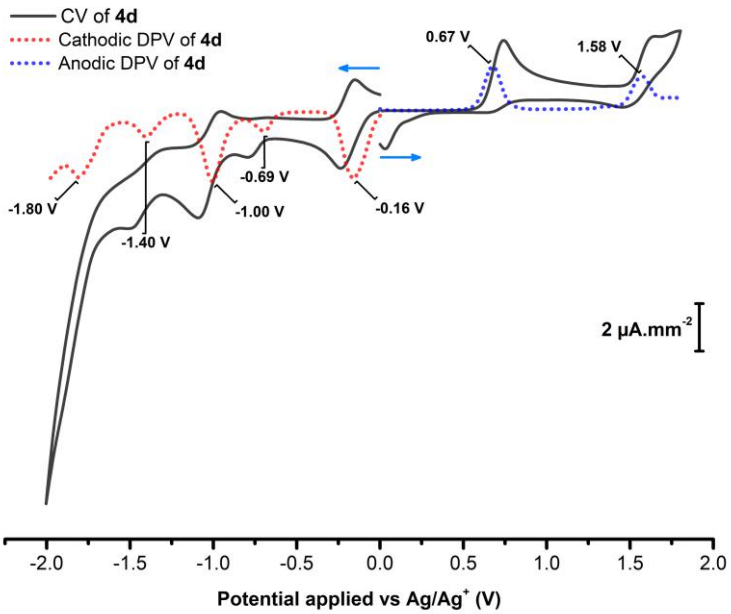


*Figure F.1–38: CV and DPV of **4d** [IrMB(cod)Cl] recorded in CH_2Cl_2 with 1.0 mM analyte and 0.1 M $TBAPF_6$ supporting electrolyte.*

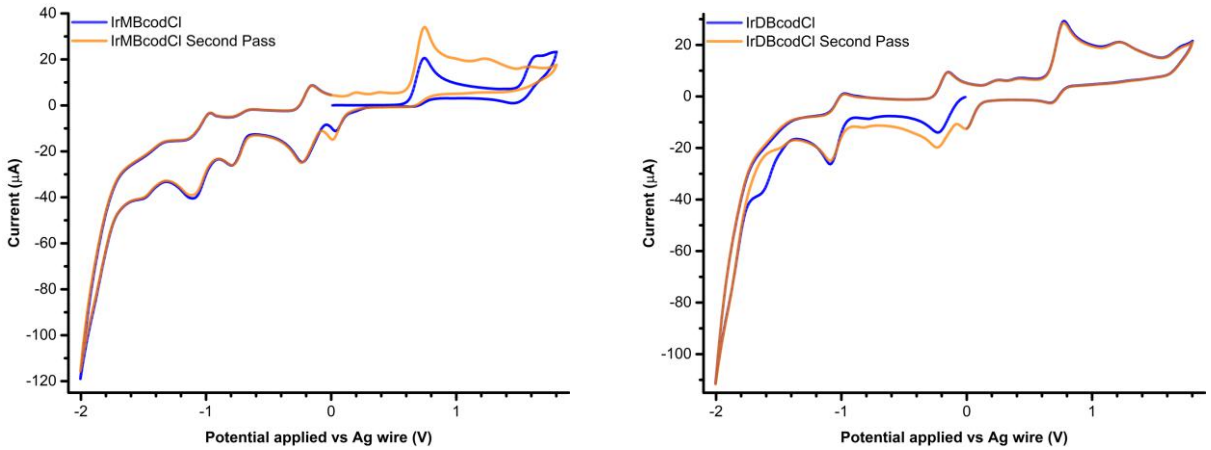


*Figure F.1–39: Anodic first (left) and Cathodic first (right) CVs of **4d** recorded in CH_2Cl_2 with 1.0 mM analyte and 0.1 M $TBAPF_6$ supporting electrolyte. Second pass scans (orange) are included to assist in differentiating compound peaks from decomposition or secondary reaction peaks.*

© University of Pretoria

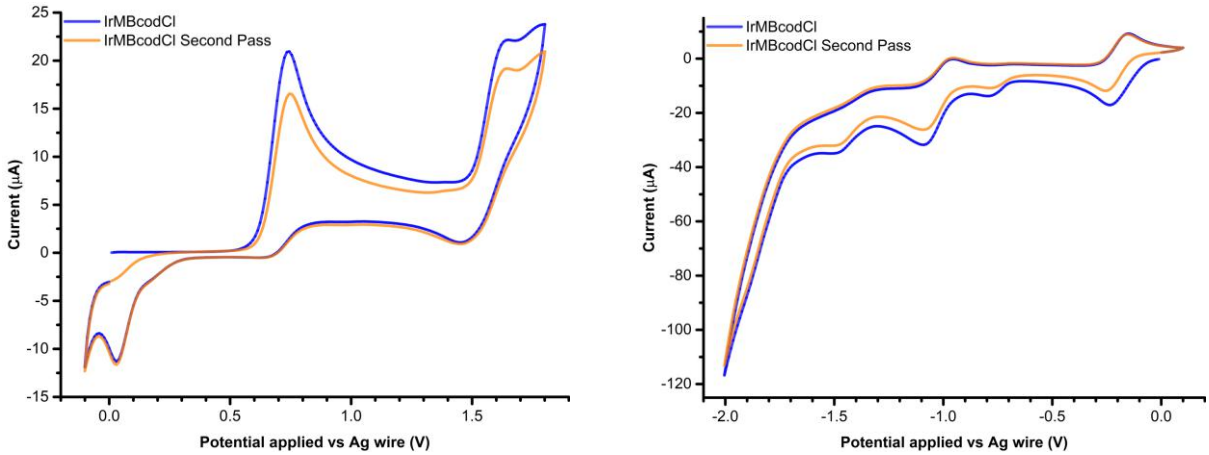


*Figure F.1–40: Narrowed potential window CVs of **4d**, anodic first (left) and cathodic first (right), recorded in CH_2Cl_2 with 1.0 mM analyte and 0.1 M $TBAPF_6$ supporting electrolyte. Second pass scans (orange) are included to assist in differentiating compound peaks from decomposition or secondary reaction peaks.*

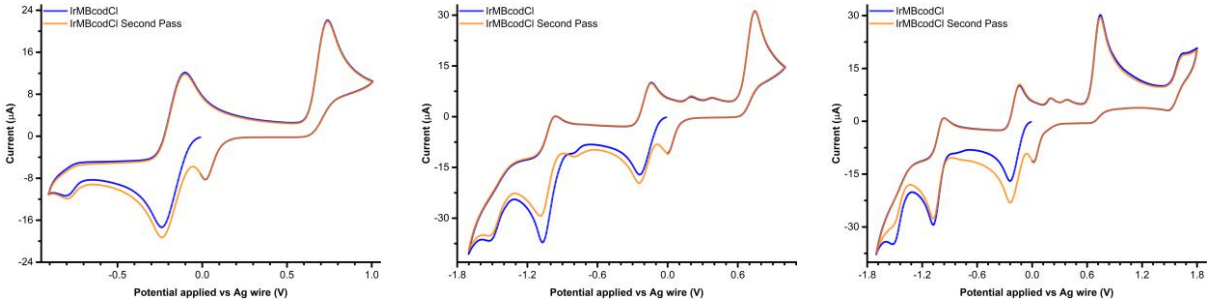


*Figure F.1–41: Narrowed potential window cathodic first CVs of **4d**, recorded in CH_2Cl_2 with 1.0 mM analyte and 0.1 M $TBAPF_6$ supporting electrolyte. Second pass scans (orange) are included to assist in differentiating compound peaks from decomposition or secondary reaction peaks.*

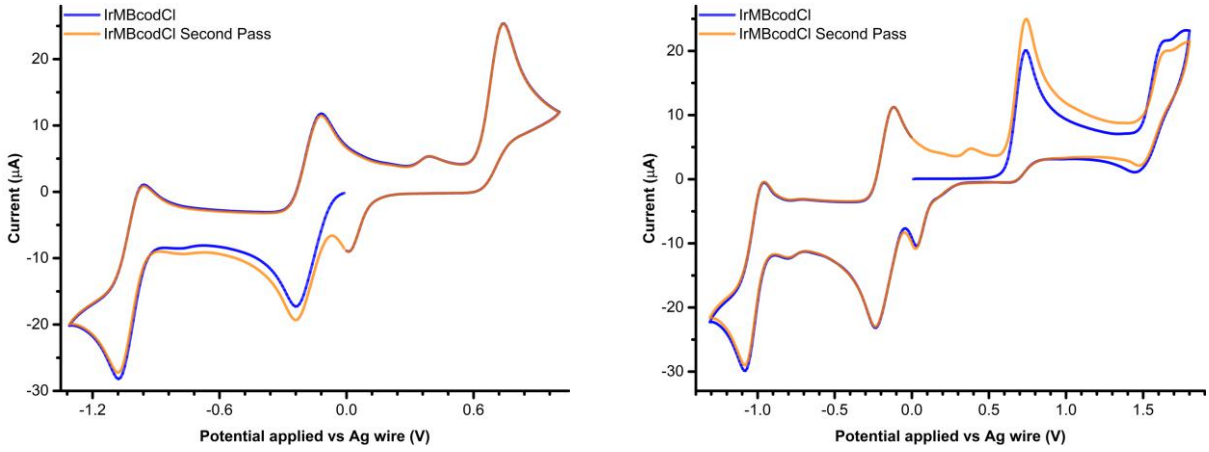
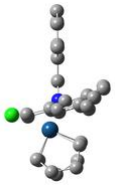
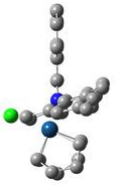
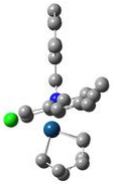
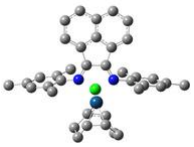
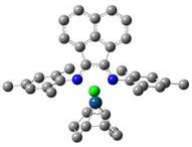
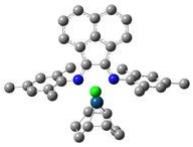
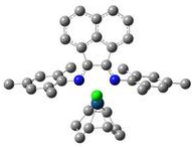


*Figure F.1–42: Narrowed potential window anodic first CVs of **4d**, recorded in CH_2Cl_2 with 1.0 mM analyte and 0.1 M $TBAPF_6$ supporting electrolyte. Second pass scans (orange) are included to assist in differentiating compound peaks from decomposition or secondary reaction peaks.*

© University of Pretoria

*Table F.1–6: Optimised molecular geometries of **4d** modelled in different charged states. All calculations were performed at B3LYP-D3/def2-SVP level of theory in CH_2Cl_2 using cPCM. The integer "n" designates the number of electrons that were added to the starting geometry before optimisation to simulate the effect of electrochemical reduction.*

n = 0	n = +1	n = +2	n = +3	n = +4
				
Ir–Cl 2.441 Å	Ir–Cl 2.470 Å	Ir–Cl 2.486 Å	Ir–Cl 4.157 Å	Ir–Cl 2.533 Å
				
Ir–N_1 2.337 Å Ir–N_2 2.279 Å	Ir–N_1 2.346 Å Ir–N_2 2.285 Å	Ir–N_1 2.329 Å Ir–N_2 2.279 Å	Ir–N_1 2.289 Å Ir–N_2 2.265 Å	Ir–N_1 2.307 Å Ir–N_2 2.269 Å

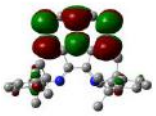
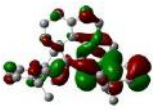
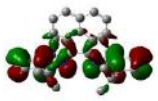
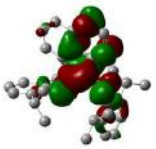
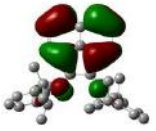
© University of Pretoria

Appendix G: DFT Modelling Results

G.1) Frontier Orbital Energies and various Diagrams

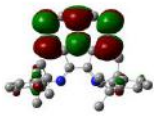
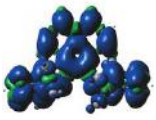
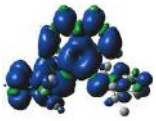
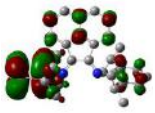
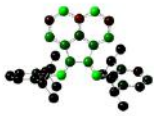
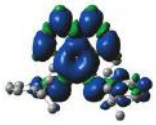
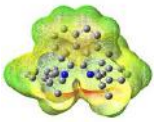
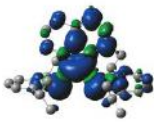
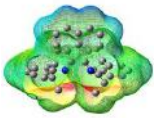
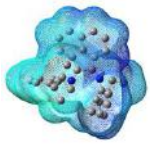
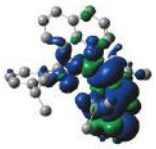
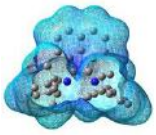
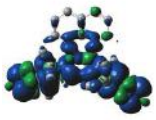
G.1.1) DippBIAN

Table G.1–1: H(S)OMO and LUMO Diagrams and Energies of DippBIAN, modelled in different charged states. Total Energies (EE_{ZPV}) in a.u. include zero-point vibrational correction. H(S)OMO and LUMO orbitals were generated with [Isovalue] = 0.02. All calculations were performed at B3LYP-D3/def2-SVP level of theory in CH_2Cl_2 using cPCM.

EE_{ZPV} (a.u.)	S	H(S)OMO$_\alpha$ (eV)	LUMO$_\alpha$ (eV)	H(S)OMO$_\beta$ (eV)	LUMO$_\beta$ (eV)	Other (eV)
–1503.91 (n = +4)	5/2	 0.776	 2.093	 –2.297	 1.116	 HOMO -1$_\alpha$ 0.746
–1503.94 (n = +3)	2	 0.525	 1.243	 –2.911	 0.348	
–1503.96 (n = +2)	3/2	 –1.547	 0.876	 –3.569	 –0.052	
–1503.90 (n = +1)	1	 –2.836	 –1.310	 –4.705	 –1.090	
–1503.80 (n = 0)	1/2	 –5.975	 –2.424			
–1503.59 (n = –1)	1	 –6.716	 –3.666	 –6.727	 –5.191	
–1503.36 (n = –2)	3/2	 –7.765	 –4.757	 –7.802	 –6.017	

© University of Pretoria

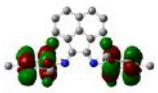
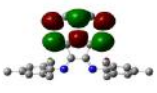
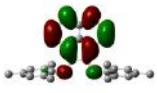
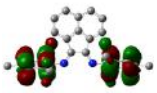
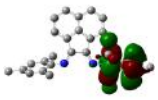
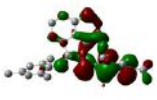
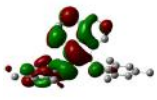
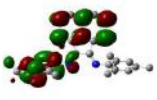
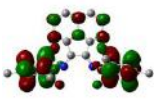
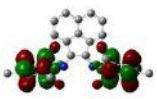
Table G.1–2: Electrostatic Surface Potential (ESP) (ESP) and Spin Density diagrams of DippBIAN. Total Energies (EE_{ZPV}) in a.u. include zero-point vibrational correction. H(S)OMO and LUMO orbitals were generated with [Isovalue] = 0.02, and Spin Density plots with [Isovalue] = 0.0004. Mulliken Spin diagrams were generated with symmetric colour shading, where brightly coloured areas indicate the localisation of unpaired alpha- or beta-spin densities. Alpha FMOs are presented for reduced species (n > 0), and Beta FMOs for oxidised species (n < 0). All calculations were performed at B3LYP-D3/def2-SVP level of theory in CH_2Cl_2 using cPCM.

EE_{ZPV} (a.u.)	S	H(S)OMO	LUMO	ESP	Mulliken Spin	Spin Density
–1503.91 (n = +4)	5/2					
–1503.94 (n = +3)	2					
–1503.96 (n = +2)	3/2					
–1503.90 (n = +1)	1					
–1503.80 (n = 0)	1/2					
–1503.59 (n = –1)	1					
–1503.36 (n = –2)	3/2					

© University of Pretoria

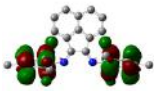
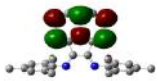
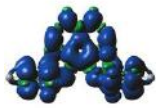
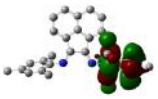
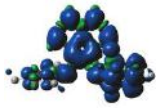
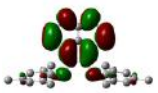
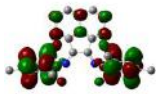
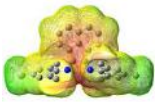
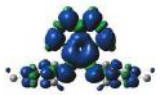
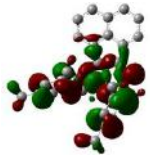
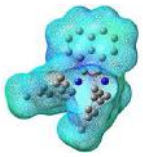
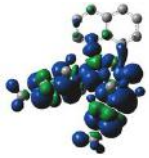
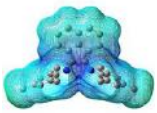
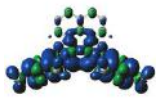
G.1.2) MesBIAN

Table G.1–3: H(S)OMO and LUMO Diagrams and Energies of MesBIAN, modelled in different charged states. Total Energies (EE_{ZPV}) in a.u. include zero-point vibrational correction. H(S)OMO and LUMO orbitals were generated with [Isovalue] = 0.02. All calculations were performed at B3LYP-D3/def2-SVP level of theory in CH_2Cl_2 using cPCM.

EE_{ZPV} (a.u.)	S	H(S)OMO$_\alpha$ (eV)	LUMO$_\alpha$ (eV)	H(S)OMO$_\beta$ (eV)	LUMO$_\beta$ (eV)	Other (eV)
–1268.36 (n = +4)	5/2	 0.712	 2.127	 –2.328	 1.136	 HOMO -1$_\alpha$ 0.703
–1268.39 (n = +3)	2	 0.432	 1.337	 –2.770	 0.291	 LUMO +1$_\alpha$ 1.632
–1268.41 (n = +2)	3/2	 –1.602	 0.999	 –3.534	 –0.204	 LUMO +1$_\alpha$ 1.022
–1268.35 (n = +1)	1	 –2.800	 –1.298	 –4.678	 –1.071	 HOMO -1$_\beta$ –4.715
–1268.25 (n = 0)	1/2	 –5.827	 –2.375			
–1268.06 (n = –1)	1	 –6.442	 –3.513	 –6.646	 –4.951	
–1267.83 (n = –2)	3/2	 –7.630	 –4.485	 –7.660	 –5.637	 LUMO +1$_\beta$ –5.594

© University of Pretoria

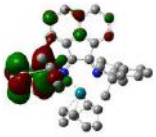
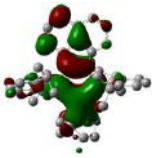
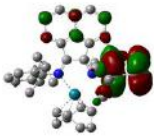
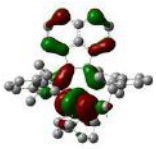
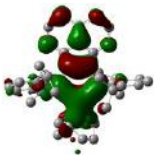
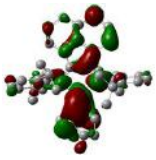
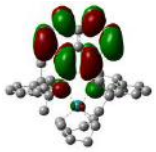
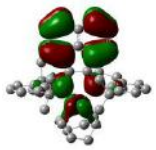
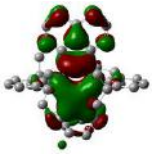
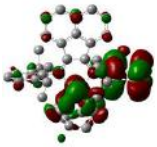
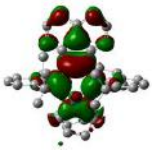
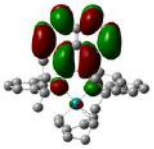
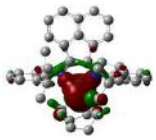
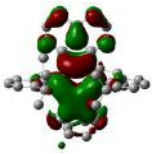
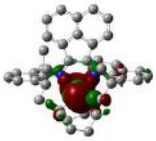
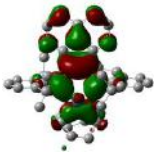
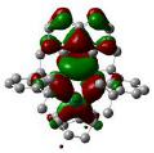
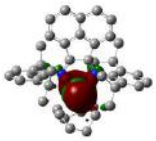
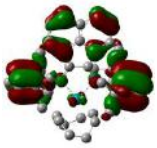
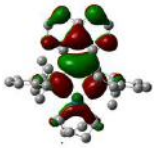
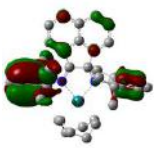
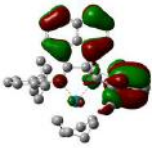
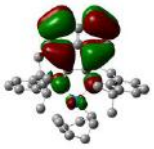
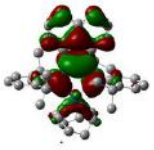
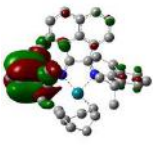
Table G.1–4: Electrostatic Surface Potential (ESP) (ESP) and Spin Density diagrams of MesBIAN. Total Energies (EE_{ZPV}) in a.u. include zero-point vibrational correction. H(S)OMO and LUMO orbitals were generated with [Isovalue] = 0.02, and Spin Density plots with [Isovalue] = 0.0004. Mulliken Spin diagrams were generated with symmetric colour shading, where brightly coloured areas indicate the localisation of unpaired alpha- or beta-spin densities. Alpha FMOs are presented for reduced species (n > 0), and Beta FMOs for oxidised species (n < 0). All calculations were performed at B3LYP-D3/def2-SVP level of theory in CH_2Cl_2 using cPCM.

EE_{ZPV} (a.u.)	S	H(S)OMO	LUMO	ESP	Mulliken Spin	Spin Density
–1268.36 (n = +4)	5/2					
–1268.39 (n = +3)	2					
–1268.41 (n = +2)	3/2					
–1268.35 (n = +1)	1					
–1268.25 (n = 0)	1/2					
–1268.06 (n = –1)	1					
–1267.83 (n = –2)	3/2					

© University of Pretoria

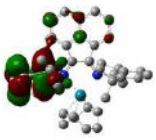
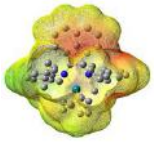
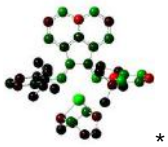
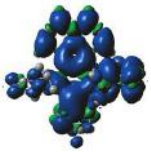
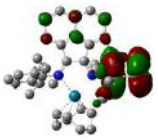
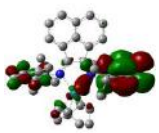
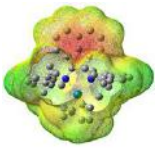
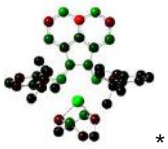
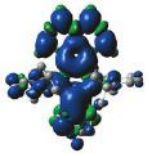
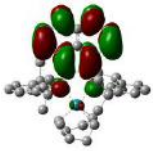
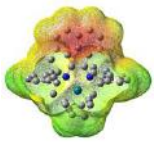
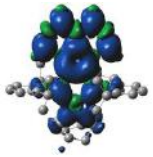
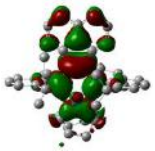
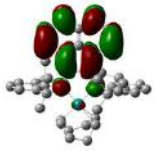
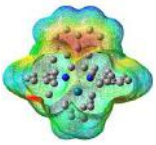
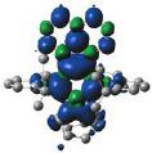
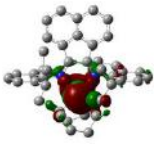
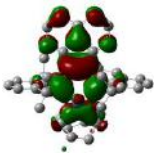
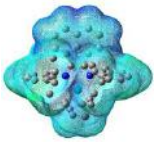
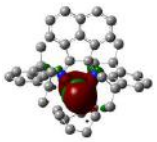
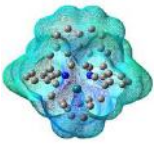
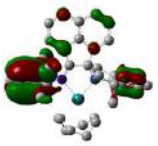
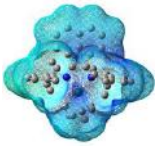
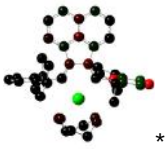
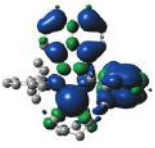
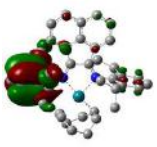
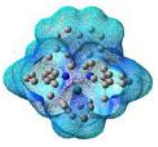
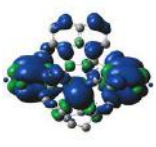
G.1.3) **1a** [RhDB(cod)]PF_6

*Table G.1–5: H(S)OMO and LUMO Diagrams and Energies of **1a**, modelled in different charged states. Total Energies (EE_{ZPV}) in a.u. include zero-point vibrational correction. H(S)OMO and LUMO orbitals were generated with [Isovalue] = 0.02. All calculations were performed at B3LYP-D3/def2-SVP level of theory in CH_2Cl_2 using cPCM.*

EE_{ZPV} (a.u.)	S	H(S)OMO$_\alpha$ (eV)	LUMO$_\alpha$ (eV)	H(S)OMO$_\beta$ (eV)	LUMO$_\beta$ (eV)	Other (eV)
–1926.25 (n = +4)	5/2	 0.331	 1.121	 –2.831	 –0.079	
–1926.26 (n = +3)	2	 –1.632	 0.655	 –3.277	 –0.558	 HOMO -1$_\alpha$ –1.762
–1926.23 (n = +2)	3/2	 –2.326	 –0.143	 –4.392	 –1.410	 LUMO +1$_\alpha$ 0.088
–1926.14 (n = +1)	1	 –4.157	 –2.080	 –5.337	 –2.426	
–1925.99 (n = 0)	1/2	 –6.203	 –3.789			
–1925.78 (n = –1)	1	 –7.543	 –4.595	 –7.535	 –5.252	 HOMO -1$_\beta$ –7.481
–1925.51 (n = –2)	3/2	 –8.009	 –5.292	 –7.984	 –7.385	
–1925.22 (n = –3)	2	 –8.585	 –5.727	 –8.484	 –7.796	

© University of Pretoria

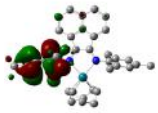
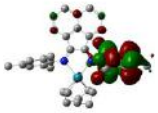
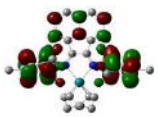
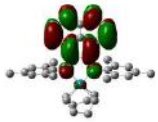
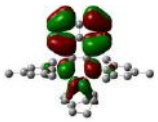
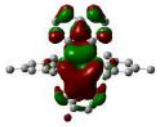
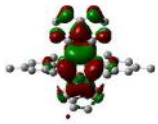
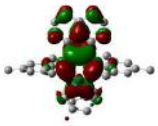
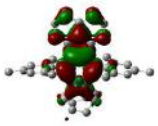
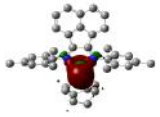
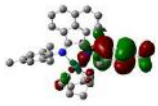
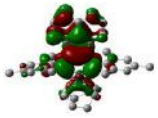
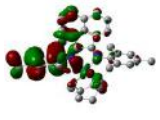
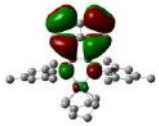
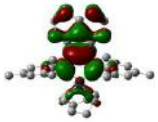
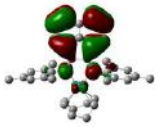
*Table G.1–6: Electrostatic Surface Potential (ESP) and Spin Density diagrams of **1a**. Total Energies (EE_{ZPV}) in a.u. include zero-point vibrational correction. H(S)OMO and LUMO orbitals were generated with [Isovalue] = 0.02, and Spin Density plots with [Isovalue] = 0.0004. Mulliken Spin diagrams were generated with symmetric colour shading, where brightly coloured areas indicate the localisation of unpaired alpha- or beta-spin densities. Alpha FMOs are presented for reduced species (n > 0), and Beta FMOs for oxidised species (n < 0). All calculations were performed at B3LYP-D3/def2-SVP level of theory in CH_2Cl_2 using cPCM. *Asymmetric colour shading applied for clarity.*

EE_{ZPV} (a.u.)	S	H(S)OMO	LUMO	ESP	Mulliken Spin	Spin Density
–1926.25 (n = +4)	5/2				 *	
–1926.26 (n = +3)	2				 *	
–1926.23 (n = +2)	3/2					
–1926.14 (n = +1)	1					
–1925.99 (n = 0)	1/2					
–1925.78 (n = –1)	1					
–1925.51 (n = –2)	3/2				 *	
–1925.22 (n = –3)	2				 *	

© University of Pretoria

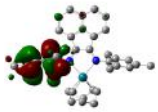
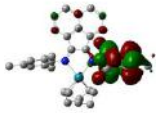
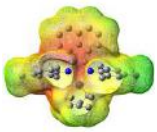
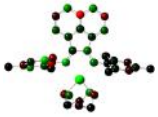
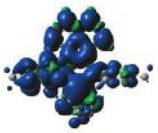
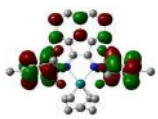
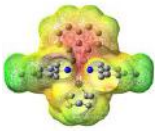
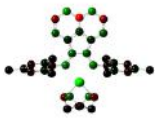
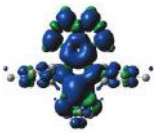
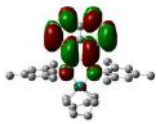
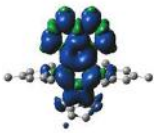
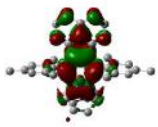
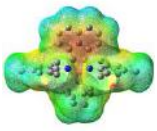
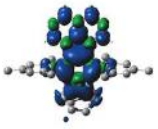
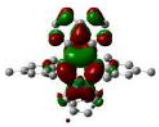
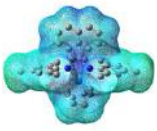
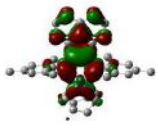
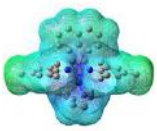
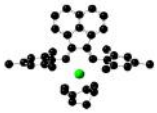
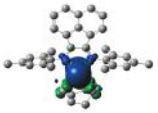
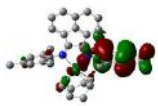
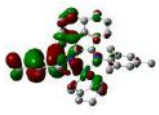
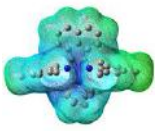
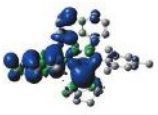
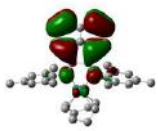
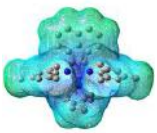
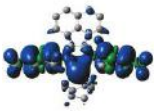
G.1.4) **1b** [RhMB(cod)]PF_6

*Table G.1–7: H(S)OMO and LUMO Diagrams and Energies of **1b**, modelled in different charged states. Total Energies (EE_{ZPV}) in a.u. include zero-point vibrational correction. H(S)OMO and LUMO orbitals were generated with [Isovalue] = 0.02. All calculations were performed at B3LYP-D3/def2-SVP level of theory in CH_2Cl_2 using cPCM.*

EE_{ZPV} (a.u.)	S	H(S)OMO$_\alpha$ (eV)	LUMO$_\alpha$ (eV)	H(S)OMO$_\beta$ (eV)	LUMO$_\beta$ (eV)	Other (eV)
–1690.71 (n = +4)	5/2	 0.276	 1.134	 –2.912	 –0.222	
–1690.72 (n = +3)	2	 –1.524	 0.814	 –3.339	 –0.709	 LUMO +1$_\alpha$ 0.822
–1690.69 (n = +2)	3/2	 –2.338	 –0.128	 –4.435	 –1.455	 LUMO +1$_\alpha$ 0.013
–1690.60 (n = +1)	1	 –4.170	 –2.076	 –5.404	 –2.447	
–1690.46 (n = 0)	1/2	 –6.199	 –3.760			
–1690.24 (n = –1)	1	 –7.447	 –4.526	 –7.465	 –5.240	 HOMO -1$_\beta$ –7.481
–1689.97 (n = –2)	3/2	 –7.839	 –5.245	 –7.823	 –7.185	
–1689.69 (n = –3)	2	 –8.560	 –5.814	 –8.542	 –7.575	

© University of Pretoria

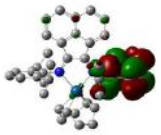
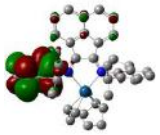
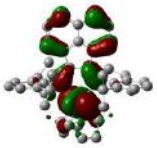
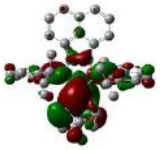
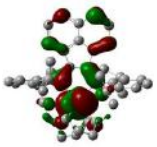
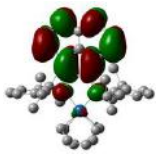
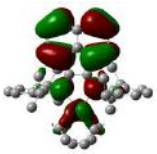
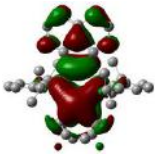
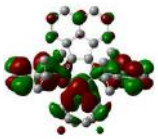
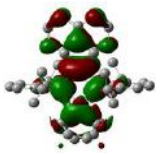
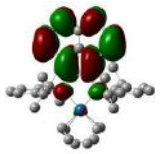
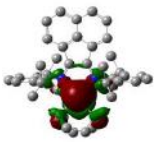
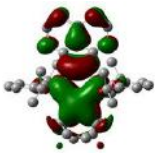
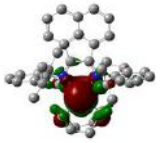
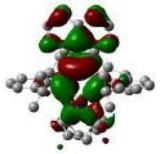
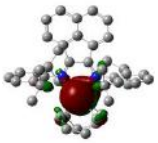
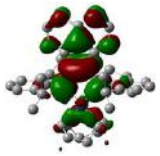
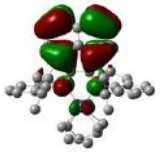
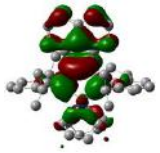
*Table G.1–8: Electrostatic Surface Potential (ESP) and Spin Density diagrams of **1b**. Total Energies (EE_{ZPV}) in a.u. include zero-point vibrational correction. H(S)OMO and LUMO orbitals were generated with [Isovalue] = 0.02, and Spin Density plots with [Isovalue] = 0.0004. Mulliken Spin diagrams were generated with symmetric colour shading, where brightly coloured areas indicate the localisation of unpaired alpha- or beta-spin densities. Alpha FMOs are presented for reduced species (n > 0), and Beta FMOs for oxidised species (n < 0). All calculations were performed at B3LYP-D3/def2-SVP level of theory in CH_2Cl_2 using cPCM. *Asymmetric colour shading applied for clarity.*

EE_{ZPV} (a.u.)	S	H(S)OMO	LUMO	ESP	Mulliken Spin	Spin Density
–1690.71 (n = +4)	5/2				 *	
–1690.72 (n = +3)	2				 *	
–1690.69 (n = +2)	3/2					
–1690.60 (n = +1)	1					
–1690.46 (n = 0)	1/2					
–1690.24 (n = –1)	1					
–1689.97 (n = –2)	3/2				 *	
–1689.69 (n = –3)	2				 *	

© University of Pretoria

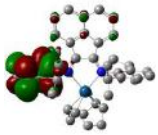
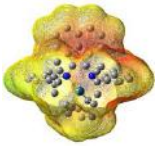
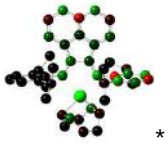
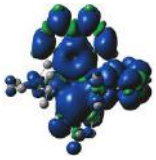
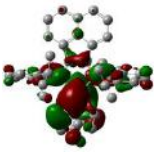
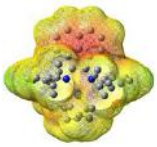
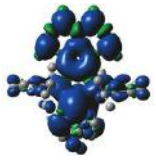
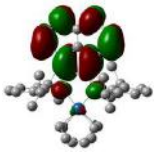
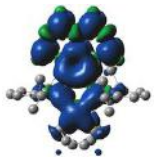
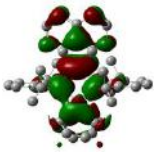
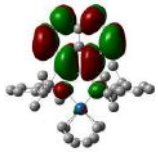
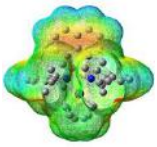
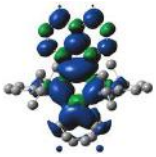
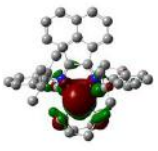
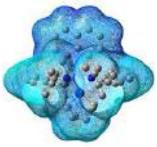
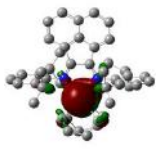
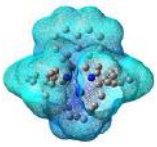
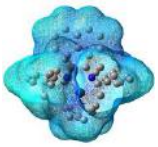
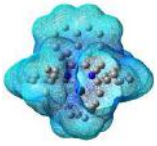
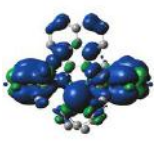
G.1.5) **1c** [IrDB(cod)]PF_6

*Table G.1–9: H(S)OMO and LUMO Diagrams and Energies of **1c**, modelled in different charged states. Total Energies (EE_{ZPV}) in a.u. include zero-point vibrational correction. H(S)OMO and LUMO orbitals were generated with [Isovalue] = 0.02. All calculations were performed at B3LYP-D3/def2-SVP level of theory in CH_2Cl_2 using cPCM.*

EE_{ZPV} (a.u.)	S	H(S)OMO$_\alpha$ (eV)	LUMO$_\alpha$ (eV)	H(S)OMO$_\beta$ (eV)	LUMO$_\beta$ (eV)	Other (eV)
–1920.06 (n = +4)	5/2	 0.297	 0.982	 –2.835	 –0.258	
–1920.07 (n = +3)	2	 –1.128	 0.649	 –3.253	 –0.751	 LUMO +1$_\alpha$ 0.723
–1920.05 (n = +2)	3/2	 –2.421	 0.030	 –4.476	 –1.576	 LUMO +1$_\alpha$ 0.121
–1919.96 (n = +1)	1	 –4.317	 –2.161	 –5.293	 –2.603	
–1919.81 (n = 0)	1/2	 –6.140	 –3.928			
–1919.59 (n = –1)	1	 –7.551	 –4.683	 –7.543	 –5.314	
–1919.32 (n = –2)	3/2	 –8.172	 –5.509	 –8.048	 –7.458	
–1919.03 (n = –3)	2	 –8.624	 –5.826	 –8.510	 –7.824	

© University of Pretoria

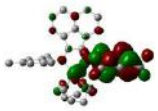
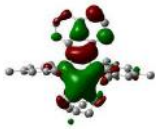
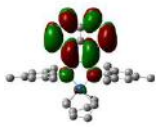
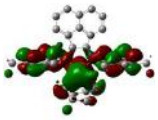
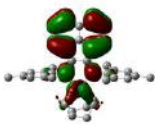
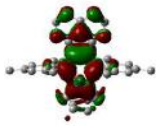
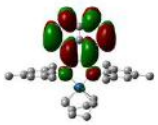
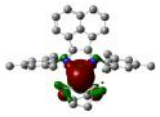
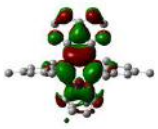
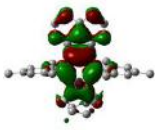
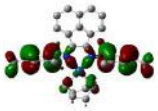
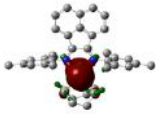
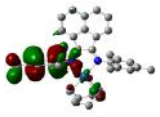
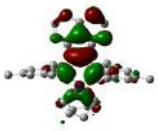
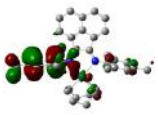
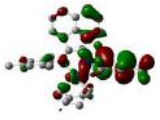
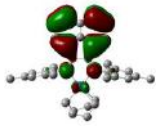
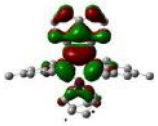
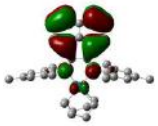
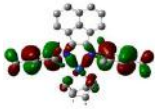
*Table G.1–10: Electrostatic Surface Potential (ESP) and Spin Density diagrams of **1c**. Total Energies (EE_{ZPV}) in a.u. include zero-point vibrational correction. H(S)OMO and LUMO orbitals were generated with [Isovalue] = 0.02, and Spin Density plots with [Isovalue] = 0.0004. Mulliken Spin diagrams were generated with symmetric colour shading, where brightly coloured areas indicate the localisation of unpaired alpha- or beta-spin densities. Alpha FMOs are presented for reduced species (n > 0), and Beta FMOs for oxidised species (n < 0). All calculations were performed at B3LYP-D3/def2-SVP level of theory in CH_2Cl_2 using cPCM. *Asymmetric colour shading applied for clarity.*

EE_{ZPV} (a.u.)	S	H(S)OMO	LUMO	ESP	Mulliken Spin	Spin Density
–1920.06 (n = +4)	5/2				 *	
–1920.07 (n = +3)	2				 *	
–1920.05 (n = +2)	3/2					
–1919.96 (n = +1)	1					
–1919.81 (n = 0)	1/2					
–1919.59 (n = –1)	1					
–1919.32 (n = –2)	3/2				 *	
–1919.03 (n = –3)	2				 *	

© University of Pretoria

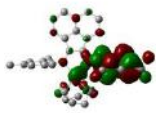
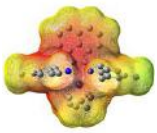
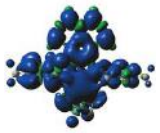
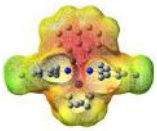
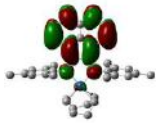
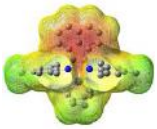
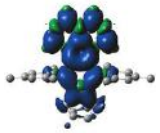
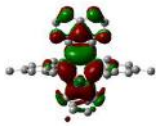
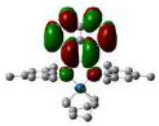
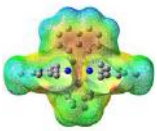
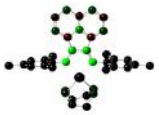
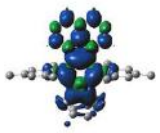
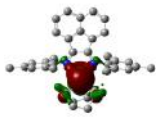
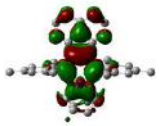
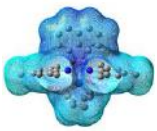
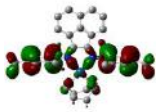
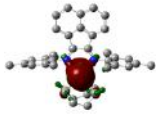
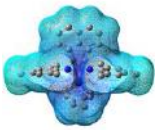
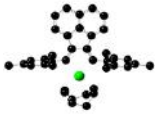
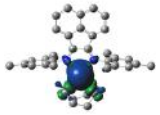
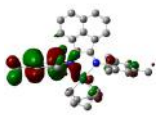
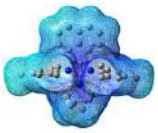
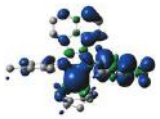
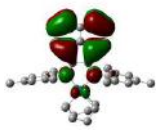
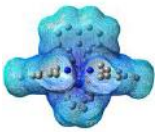
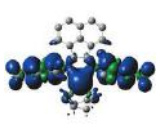
G.1.6) **1d** [IrMB(cod)]PF_6

*Table G.1–11: H(S)OMO and LUMO Diagrams and Energies of **1d**, modelled in different charged states. Total Energies (EE_{ZPV}) in a.u. include zero-point vibrational correction. H(S)OMO and LUMO orbitals were generated with [Isovalue] = 0.02. All calculations were performed at B3LYP-D3/def2-SVP level of theory in CH_2Cl_2 using cPCM.*

EE_{ZPV} (a.u.)	S	H(S)OMO$_\alpha$ (eV)	LUMO$_\alpha$ (eV)	H(S)OMO$_\beta$ (eV)	LUMO$_\beta$ (eV)	Other (eV)
–1684.52 (n = +4)	5/2	 0.235	 1.086	 –3.082	 –0.383	 HOMO -1$_\alpha$ –0.412
–1684.53 (n = +3)	2	 –0.999	 0.714	 –3.447	 –0.868	
–1684.51 (n = +2)	3/2	 –2.425	 0.060	 –4.518	 –1.626	
–1684.42 (n = +1)	1	 –4.326	 –2.155	 –5.334	 –2.635	
–1684.27 (n = 0)	1/2	 –6.115	 –3.914			
–1684.05 (n = –1)	1	 –7.469	 –4.636	 –7.465	 –5.286	 HOMO -1$_\beta$ –7.489
–1683.79 (n = –2)	3/2	 –7.880	 –5.344	 –7.835	 –7.188	
–1683.50 (n = –3)	2	 –8.581	 –5.903	 –8.567	 –7.584	 LUMO +1$_\beta$ –7.551

© University of Pretoria

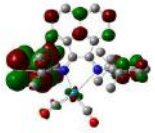
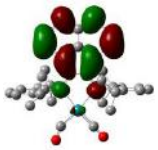
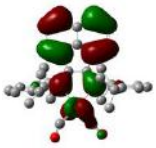
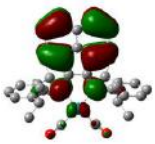
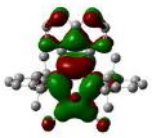
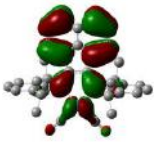
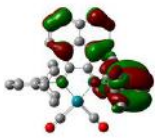
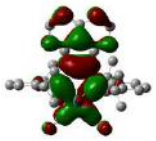
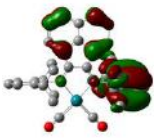
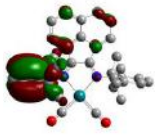
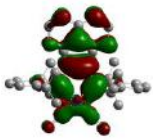
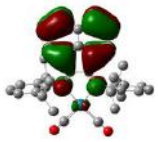
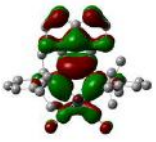
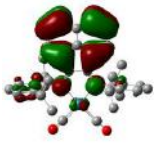
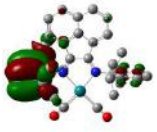
*Table G.1–12: Electrostatic Surface Potential (ESP) and Spin Density diagrams of **1d**. Total Energies (EE_{ZPV}) in a.u. include zero-point vibrational correction. H(S)OMO and LUMO orbitals were generated with [Isovalue] = 0.02, and Spin Density plots with [Isovalue] = 0.0004. Mulliken Spin diagrams were generated with symmetric colour shading, where brightly coloured areas indicate the localisation of unpaired alpha- or beta-spin densities. Alpha FMOs are presented for reduced species (n > 0), and Beta FMOs for oxidised species (n < 0). All calculations were performed at B3LYP-D3/def2-SVP level of theory in CH_2Cl_2 using cPCM. *Asymmetric colour shading applied for clarity.*

EE_{ZPV} (a.u.)	S	H(S)OMO	LUMO	ESP	Mulliken Spin	Spin Density
–1684.52 (n = +4)	5/2				 *	
–1684.53 (n = +3)	2					
–1684.51 (n = +2)	3/2					
–1684.42 (n = +1)	1					
–1684.27 (n = 0)	1/2					
–1684.05 (n = –1)	1					
–1683.79 (n = –2)	3/2				 *	
–1683.50 (n = –3)	2				 *	

© University of Pretoria

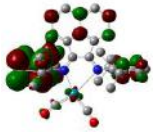
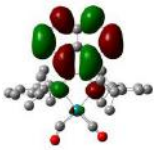
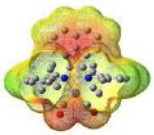
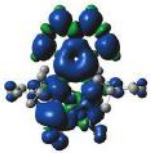
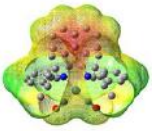
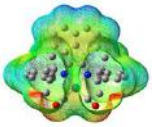
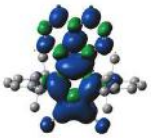
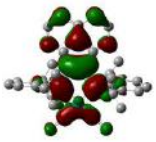
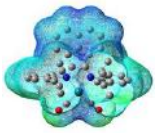
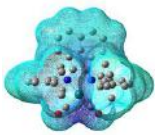
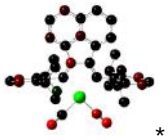
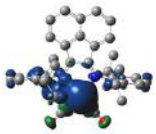
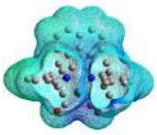
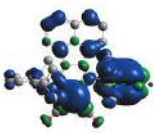
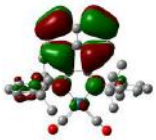
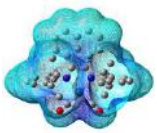
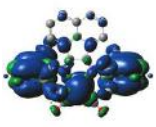
G.1.7) **2a** $[RhDB(CO)_2]PF_6$

*Table G.1–13: H(S)OMO and LUMO Diagrams and Energies of **2a**, modelled in different charged states. Total Energies (EE_{ZPV}) in a.u. include zero-point vibrational correction. H(S)OMO and LUMO orbitals were generated with [Isovalue] = 0.02. All calculations were performed at B3LYP-D3/def2-SVP level of theory in CH_2Cl_2 using cPCM.*

EE_{ZPV} (a.u.)	S	H(S)OMO$_\alpha$ (eV)	LUMO$_\alpha$ (eV)	H(S)OMO$_\beta$ (eV)	LUMO$_\beta$ (eV)	Other (eV)
–1841.14 (n = +4)	5/2	 –0.789	 1.002	 –3.399	 –0.077	
–1841.13 (n = +3)	2	 –1.887	 0.305	 –3.920	 –0.808	 HOMO -1$_\alpha$ –2.364
–1841.08 (n = +2)	3/2	 –2.526	 –0.867	 –4.646	 –1.852	 LUMO +1$_\alpha$ –0.435
–1840.99 (n = +1)	1	 –4.480	 –2.248	 –6.086	 –2.816	
–1840.82 (n = 0)	1/2	 –6.905	 –4.061			
–1840.58 (n = –1)	1	 –7.700	 –4.911	 –7.697	 –6.113	
–1840.30 (n = –2)	3/2	 –8.156	 –5.493	 –8.132	 –7.549	
–1840.01 (n = –3)	2	 –8.701	 –6.019	 –8.653	 –7.871	

© University of Pretoria

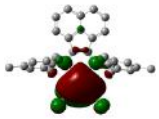
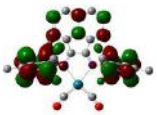
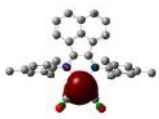
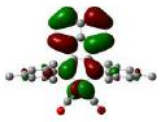
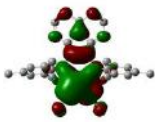
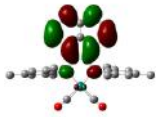
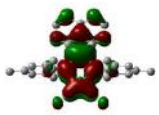
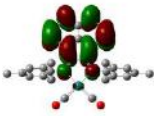
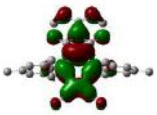
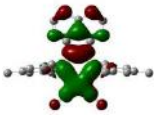
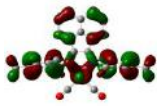
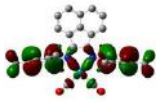
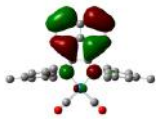
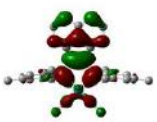
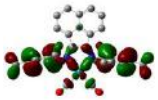
*Table G.1–14: Electrostatic Surface Potential (ESP) and Spin Density diagrams of **2a**. Total Energies (EE_{ZPV}) in a.u. include zero-point vibrational correction. H(S)OMO and LUMO orbitals were generated with [Isovalue] = 0.02, and Spin Density plots with [Isovalue] = 0.0004. Mulliken Spin diagrams were generated with symmetric colour shading, where brightly coloured areas indicate the localisation of unpaired alpha- or beta-spin densities. Alpha FMOs are presented for reduced species (n > 0), and Beta FMOs for oxidised species (n < 0). All calculations were performed at B3LYP-D3/def2-SVP level of theory in CH_2Cl_2 using cPCM. *Asymmetric colour shading applied for clarity.*

EE_{ZPV} (a.u.)	S	H(S)OMO	LUMO	ESP	Mulliken Spin	Spin Density
–1841.14 (n = +4)	5/2					
–1841.13 (n = +3)	2					
–1841.08 (n = +2)	3/2					
–1840.99 (n = +1)	1					
–1840.82 (n = 0)	1/2					
–1840.58 (n = –1)	1				 *	
–1840.30 (n = –2)	3/2				 *	
–1840.01 (n = –3)	2				 *	

© University of Pretoria

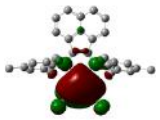
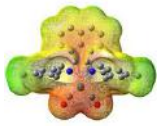
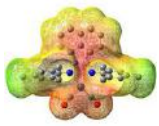
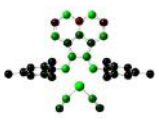
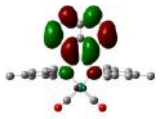
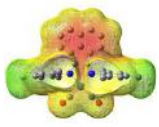
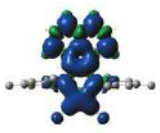
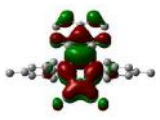
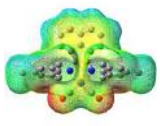
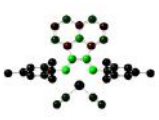
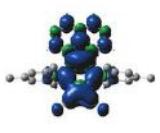
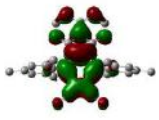
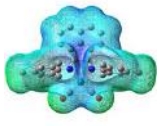
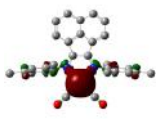
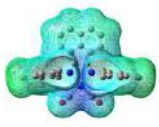
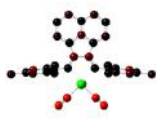
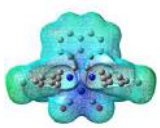
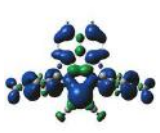
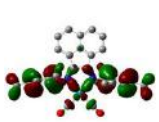
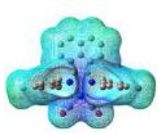
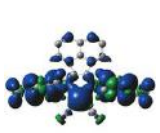
G.1.8) **2b** $[RhMB(CO)_2]PF_6$

*Table G.1–15: H(S)OMO and LUMO Diagrams and Energies of **2b**, modelled in different charged states. Total Energies (EE_{ZPV}) in a.u. include zero-point vibrational correction. H(S)OMO and LUMO orbitals were generated with [Isovalue] = 0.02. All calculations were performed at B3LYP-D3/def2-SVP level of theory in CH_2Cl_2 using cPCM.*

EE_{ZPV} (a.u.)	S	H(S)OMO$_\alpha$ (eV)	LUMO$_\alpha$ (eV)	H(S)OMO$_\beta$ (eV)	LUMO$_\beta$ (eV)	Other (eV)
–1605.60 (n = +4)	5/2	 –0.716	 1.123	 –3.427	 –0.203	
–1605.59 (n = +3)	2	 –1.932	 –0.841	 –3.928	 –1.014	 HOMO -1$_\alpha$ –2.240
–1605.53 (n = +2)	3/2	 –2.488	 –0.841	 –4.634	 –1.817	 LUMO +1$_\alpha$ –0.386
–1605.44 (n = +1)	1	 –4.432	 –2.206	 –6.076	 –2.756	 HOMO -1$_\beta$ –6.115
–1605.28 (n = 0)	1/2	 –6.880	 –4.037			
–1605.04 (n = –1)	1	 –7.543	 –4.817	 –7.577	 –5.979	 HOMO -1$_\beta$ –7.590
–1604.77 (n = –2)	3/2	 –8.346	 –5.562	 –8.023	 –7.305	
–1604.48 (n = –3)	2	 –8.744	 –6.107	 –8.716	 –7.718	 LUMO +1$_\beta$ –7.704

© University of Pretoria

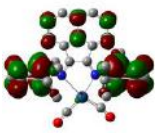
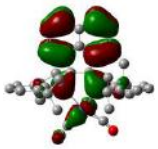
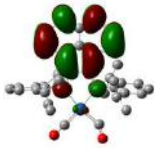
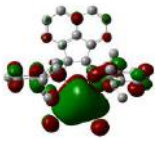
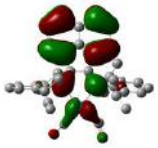
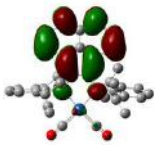
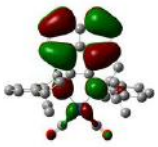
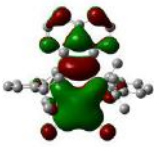
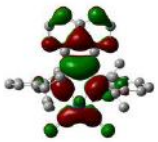
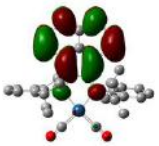
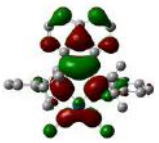
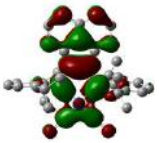
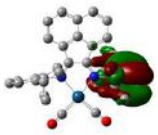
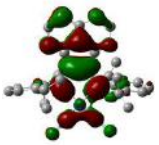
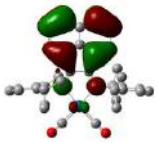
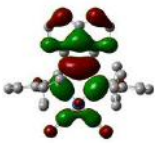
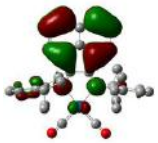
*Table G.1–16: Electrostatic Surface Potential (ESP) and Spin Density diagrams of **2b**. Total Energies (EE_{ZPV}) in a.u. include zero-point vibrational correction. H(S)OMO and LUMO orbitals were generated with [Isovalue] = 0.02, and Spin Density plots with [Isovalue] = 0.0004. Mulliken Spin diagrams were generated with symmetric colour shading, where brightly coloured areas indicate the localisation of unpaired alpha- or beta-spin densities. Alpha FMOs are presented for reduced species (n > 0), and Beta FMOs for oxidised species (n < 0). All calculations were performed at B3LYP-D3/def2-SVP level of theory in CH_2Cl_2 using cPCM. *Asymmetric colour shading applied for clarity.*

EE_{ZPV} (a.u.)	S	H(S)OMO	LUMO	ESP	Mulliken Spin	Spin Density
–1605.60 (n = +4)	5/2				 *	
–1605.59 (n = +3)	2					
–1605.53 (n = +2)	3/2					
–1605.44 (n = +1)	1					
–1605.28 (n = 0)	1/2					
–1605.04 (n = –1)	1				 *	
–1604.77 (n = –2)	3/2				 *	
–1604.48 (n = –3)	2				 *	

© University of Pretoria

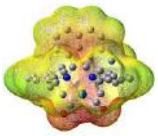
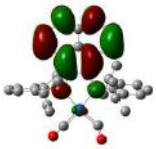
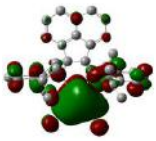
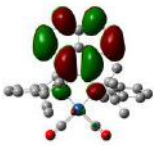
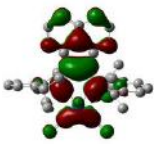
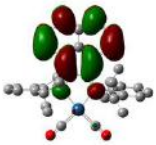
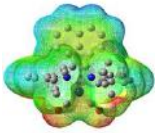
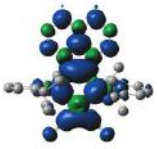
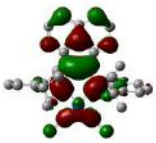
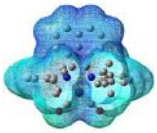
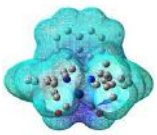
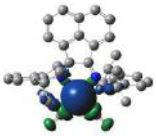
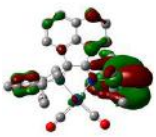
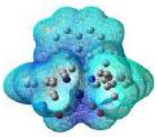
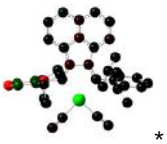
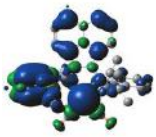
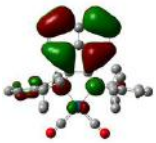
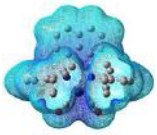
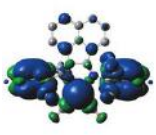
G.1.9) **2c** $[IrDB(CO)_2]PF_6$

*Table G.1–17: H(S)OMO and LUMO Diagrams and Energies of **2c**, modelled in different charged states. Total Energies (EE_{ZPV}) in a.u. include zero-point vibrational correction. H(S)OMO and LUMO orbitals were generated with [Isovalue] = 0.02. All calculations were performed at B3LYP-D3/def2-SVP level of theory in CH_2Cl_2 using cPCM.*

EE_{ZPV} (a.u.)	S	H(S)OMO$_\alpha$ (eV)	LUMO$_\alpha$ (eV)	H(S)OMO$_\beta$ (eV)	LUMO$_\beta$ (eV)	Other (eV)
–1834.96 (n = +4)	5/2	 –0.618	 0.965	 –3.470	 –0.182	
–1834.95 (n = +3)	2	 –1.966	 0.396	 –4.021	 –0.930	 HOMO -1$_\alpha$ –2.208
–1834.90 (n = +2)	3/2	 –2.544	 –0.571	 –4.673	 –1.884	 LUMO +1$_\alpha$ –0.281
–1834.81 (n = +1)	1	 –4.557	 –2.281	 –6.097	 –2.896	
–1834.65 (n = 0)	1/2	 –6.930	 –4.206			
–1834.41 (n = –1)	1	 –7.670	 –4.958	 –7.666	 –6.028	
–1834.13 (n = –2)	3/2	 –8.105	 –5.587	 –8.078	 –7.511	
–1833.84 (n = –3)	2	 –8.686	 –6.041	 –8.640	 –7.815	

© University of Pretoria

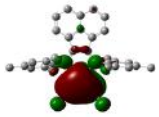
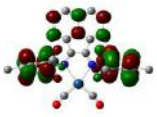
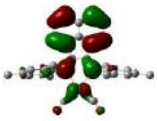
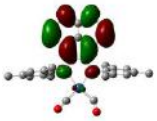
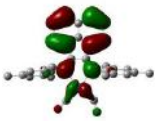
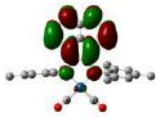
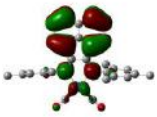
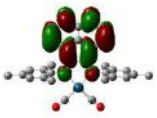
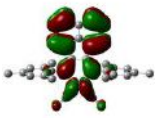
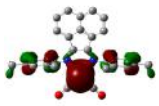
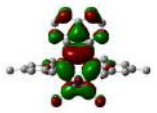
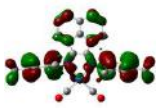
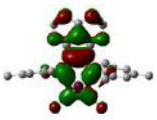
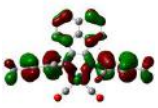
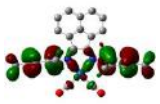
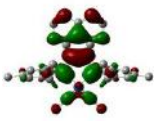
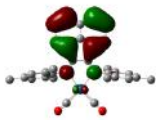
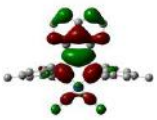
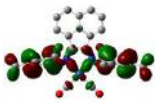
*Table G.1–18: Electrostatic Surface Potential (ESP) and Spin Density diagrams of **2c**. Total Energies (EE_{ZPV}) in a.u. include zero-point vibrational correction. H(S)OMO and LUMO orbitals were generated with [Isovalue] = 0.02, and Spin Density plots with [Isovalue] = 0.0004. Mulliken Spin diagrams were generated with symmetric colour shading, where brightly coloured areas indicate the localisation of unpaired alpha- or beta-spin densities. Alpha FMOs are presented for reduced species (n > 0), and Beta FMOs for oxidised species (n < 0). All calculations were performed at B3LYP-D3/def2-SVP level of theory in CH_2Cl_2 using cPCM. *Asymmetric colour shading applied for clarity.*

EE_{ZPV} (a.u.)	S	H(S)OMO	LUMO	ESP	Mulliken Spin	Spin Density
–1834.96 (n = +4)	5/2					
–1834.95 (n = +3)	2					
–1834.90 (n = +2)	3/2					
–1834.81 (n = +1)	1					
–1834.65 (n = 0)	1/2					
–1834.41 (n = –1)	1				 *	
–1834.13 (n = –2)	3/2				 *	
–1833.84 (n = –3)	2				 *	

© University of Pretoria

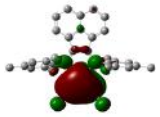
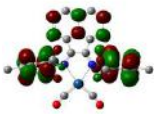
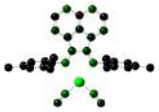
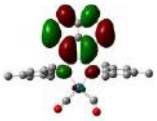
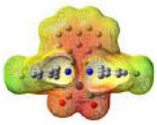
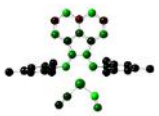
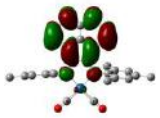
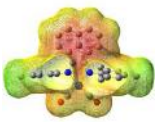
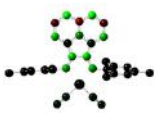
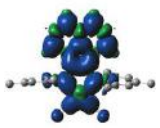
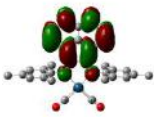
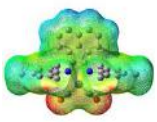
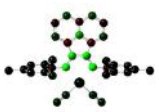
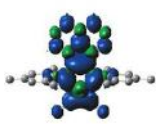
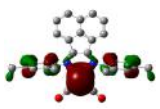
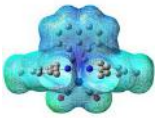
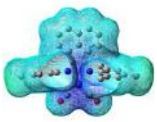
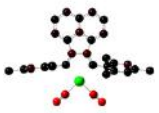
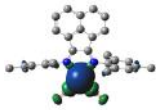
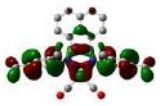
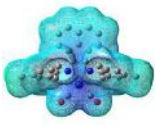
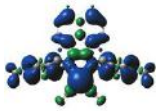
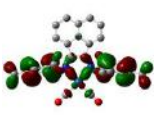
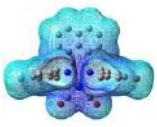
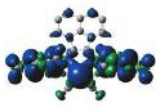
G.1.10) **2d** $[IrMB(CO)_2]PF_6$

*Table G.1–19: H(S)OMO and LUMO Diagrams and Energies of **2d**, modelled in different charged states. Total Energies (EE_{ZPV}) in a.u. include zero-point vibrational correction. H(S)OMO and LUMO orbitals were generated with [Isovalue] = 0.02. All calculations were performed at B3LYP-D3/def2-SVP level of theory in CH_2Cl_2 using cPCM.*

EE_{ZPV} (a.u.)	S	H(S)OMO$_\alpha$ (eV)	LUMO$_\alpha$ (eV)	H(S)OMO$_\beta$ (eV)	LUMO$_\beta$ (eV)	Other (eV)
–1599.41 (n = +4)	5/2	 –0.617	 1.105	 –3.539	 –0.273	 LUMO +1$_\alpha$ 1.116
–1599.40 (n = +3)	2	 –2.002	 0.278	 –4.065	 –1.000	 LUMO +1$_\alpha$ 0.661
–1599.36 (n = +2)	3/2	 –2.558	 –0.629	 –4.699	 –1.906	 LUMO +1$_\alpha$ –0.275
–1599.26 (n = +1)	1	 –4.547	 –2.273	 –6.119	 –2.882	
–1599.10 (n = 0)	1/2	 –6.940	 –4.158			
–1598.86 (n = –1)	1	 –7.565	 –4.873	 –7.575	 –5.961	 HOMO -1$_\beta$ –7.589
–1598.59 (n = –2)	3/2	 –8.347	 –5.607	 –7.999	 –7.323	
–1598.30 (n = –3)	2	 –8.750	 –6.139	 –8.726	 –7.702	 LUMO +1$_\beta$ –7.692

© University of Pretoria

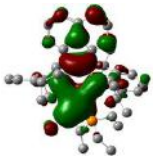
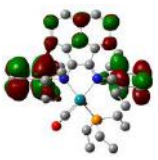
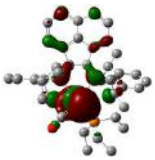
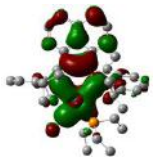
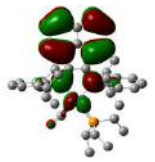
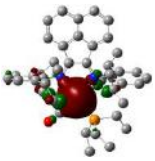
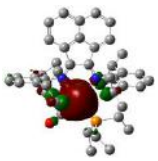
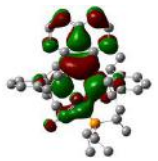
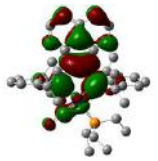
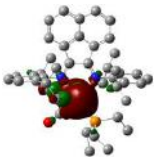
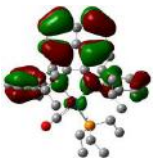
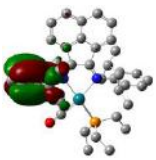
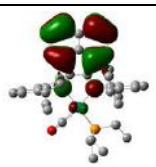
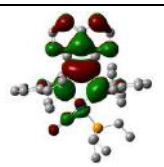
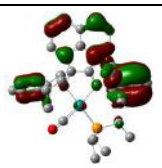
*Table G.1–20: Electrostatic Surface Potential (ESP) and Spin Density diagrams of **2d**. Total Energies (EE_{ZPV}) in a.u. include zero-point vibrational correction. H(S)OMO and LUMO orbitals were generated with [Isovalue] = 0.02, and Spin Density plots with [Isovalue] = 0.0004. Mulliken Spin diagrams were generated with symmetric colour shading, where brightly coloured areas indicate the localisation of unpaired alpha- or beta-spin densities. Alpha FMOs are presented for reduced species (n > 0), and Beta FMOs for oxidised species (n < 0). All calculations were performed at B3LYP-D3/def2-SVP level of theory in CH_2Cl_2 using cPCM. *Asymmetric colour shading applied for clarity.*

EE_{ZPV} (a.u.)	S	H(S)OMO	LUMO	ESP	Mulliken Spin	Spin Density
–1599.41 (n = +4)	5/2					
–1599.40 (n = +3)	2					
–1599.36 (n = +2)	3/2					
–1599.26 (n = +1)	1					
–1599.10 (n = 0)	1/2					
–1598.86 (n = –1)	1				 *	
–1598.59 (n = –2)	3/2				 *	
–1598.30 (n = –3)	2				 *	

© University of Pretoria

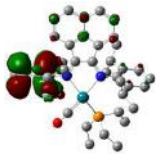
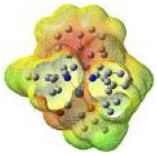
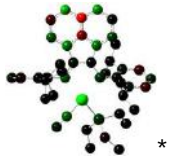
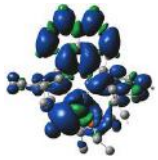
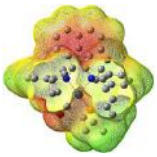
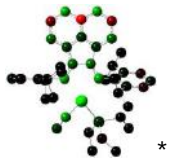
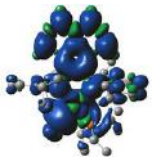
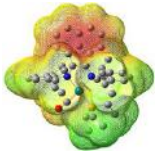
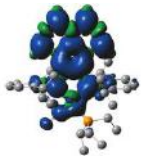
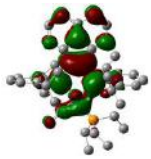
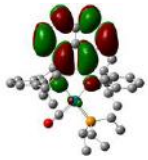
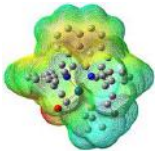
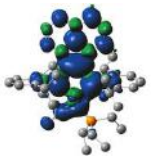
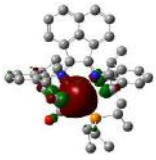
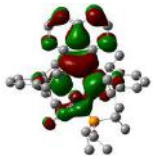
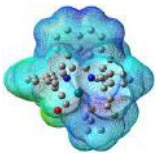
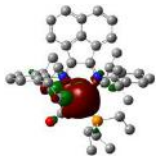
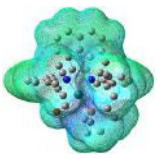
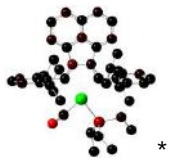
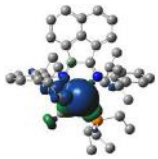
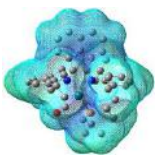
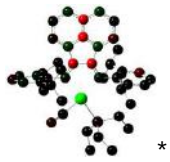
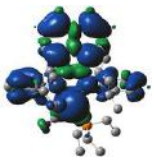
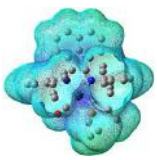
G.1.11) **3a** [RhDB(CO)(PEt_3)]PF_6

*Table G.1–21: H(S)OMO and LUMO Diagrams and Energies of **3a**, modelled in different charged states. Total Energies (EE_{ZPV}) in a.u. include zero-point vibrational correction. H(S)OMO and LUMO orbitals were generated with [Isovalue] = 0.02. All calculations were performed at B3LYP-D3/def2-SVP level of theory in CH_2Cl_2 using cPCM.*

EE_{ZPV} (a.u.)	S	H(S)OMO$_\alpha$ (eV)	LUMO$_\alpha$ (eV)	H(S)OMO$_\beta$ (eV)	LUMO$_\beta$ (eV)	Other (eV)
–2306.51 (n = +4)	5/2	 –0.869	 1.209	 –1.229	 0.507	 HOMO -1$_\alpha$ –0.983
–2306.48 (n = +3)	2	 –1.717	 0.684	 –3.327	 –0.517	 HOMO -1$_\alpha$ –1.782
–2306.44 (n = +2)	3/2	 –2.265	 –0.221	 –4.340	 –1.292	 LUMO +1$_\alpha$ 0.040
–2306.36 (n = +1)	1	 –4.057	 –2.021	 –5.326	 –2.299	
–2306.21 (n = 0)	1/2	 –6.153	 –3.687			
–2306.00 (n = –1)	1	 –7.510	 –4.448	 –7.505	 –4.430	
–2305.73 (n = –2)	3/2	 –8.266	 –5.343	 –8.059	 –7.375	 HOMO -1$_\alpha$ –8.298
–2305.44 (n = –3)	2	 –8.704	 –5.659	 –8.439	 –7.795	

© University of Pretoria

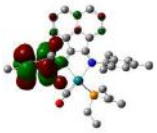
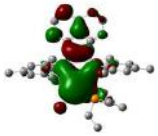
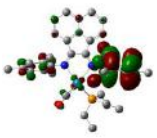
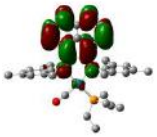
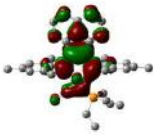
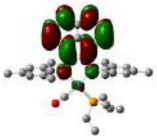
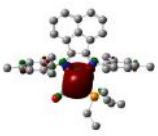
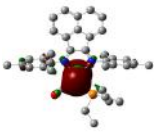
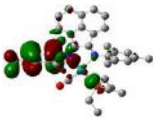
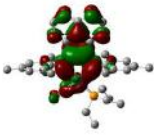
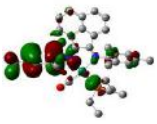
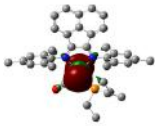
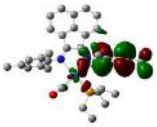
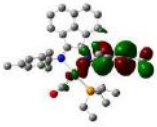
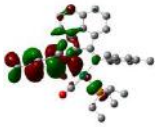
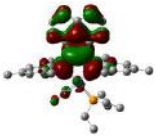
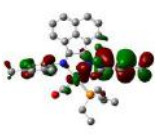
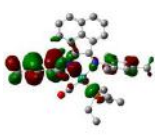
*Table G.1–22: Electrostatic Surface Potential (ESP) and Spin Density diagrams of **3a**. Total Energies (EE_{ZPV}) in a.u. include zero-point vibrational correction. H(S)OMO and LUMO orbitals were generated with [Isovalue] = 0.02, and Spin Density plots with [Isovalue] = 0.0004. Mulliken Spin diagrams were generated with symmetric colour shading, where brightly coloured areas indicate the localisation of unpaired alpha- or beta-spin densities. Alpha FMOs are presented for reduced species (n > 0), and Beta FMOs for oxidised species (n < 0). All calculations were performed at B3LYP-D3/def2-SVP level of theory in CH_2Cl_2 using cPCM. *Asymmetric colour shading applied for clarity.*

EE_{ZPV} (a.u.)	S	H(S)OMO	LUMO	ESP	Mulliken Spin	Spin Density
–2306.51 (n = +4)	5/2				 *	
–2306.48 (n = +3)	2				 *	
–2306.44 (n = +2)	3/2					
–2306.36 (n = +1)	1					
–2306.21 (n = 0)	1/2					
–2306.00 (n = –1)	1				 *	
–2305.73 (n = –2)	3/2				 *	
–2305.44 (n = –3)	2				 *	

© University of Pretoria

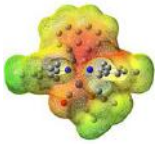
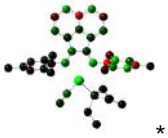
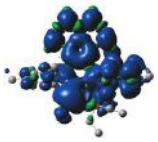
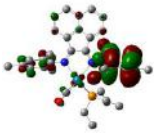
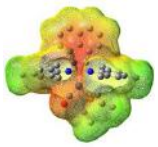
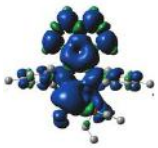
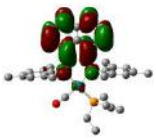
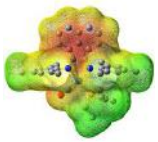
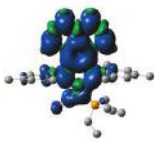
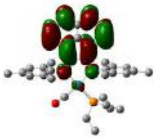
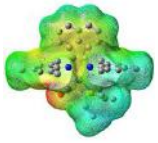
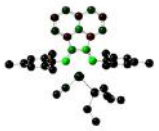
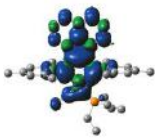
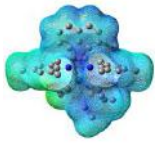
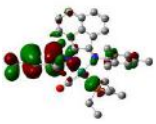
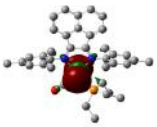
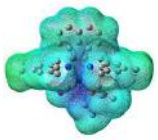
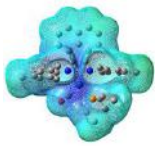
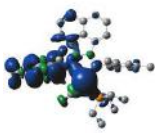
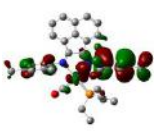
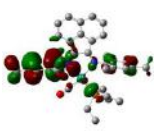
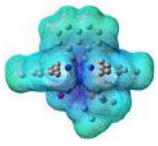
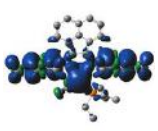
G.1.12) **3b** [RhMB(CO)(PEt_3)]PF_6

*Table G.1–23: H(S)OMO and LUMO Diagrams and Energies of **3b**, modelled in different charged states. Total Energies (EE_{ZPV}) in a.u. include zero-point vibrational correction. H(S)OMO and LUMO orbitals were generated with [Isovalue] = 0.02. All calculations were performed at B3LYP-D3/def2-SVP level of theory in CH_2Cl_2 using cPCM.*

EE_{ZPV} (a.u.)	S	H(S)OMO$_\alpha$ (eV)	LUMO$_\alpha$ (eV)	H(S)OMO$_\beta$ (eV)	LUMO$_\beta$ (eV)	Other (eV)
–2070.92 (n = +4)	5/2	 0.165	 1.140	 –3.029	 –0.205	
–2070.93 (n = +3)	2	 –1.801	 0.704	 –3.481	 –0.673	 HOMO -1$_\alpha$ –1.898
–2070.89 (n = +2)	3/2	 –2.297	 –0.135	 –4.385	 –1.365	 LUMO +1$_\alpha$ –0.107
–2070.81 (n = +1)	1	 –4.075	 –2.027	 –5.431	 –2.324	
–2070.66 (n = 0)	1/2	 –6.194	 –3.657			
–2070.45 (n = –1)	1	 –7.315	 –4.382	 –7.314	 –5.166	
–2070.19 (n = –2)	3/2	 –7.817	 –5.094	 –7.817	 –7.007	
–2069.91 (n = –3)	2	 –8.4820	 –5.655	 –8.470	 –7.513	

© University of Pretoria

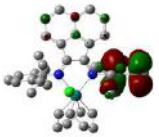
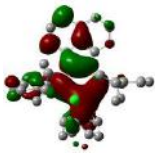
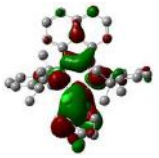
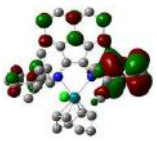
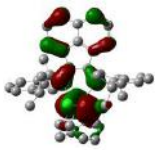
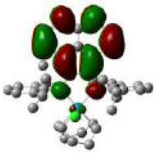
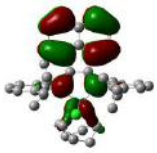
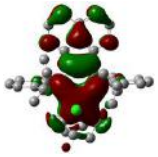
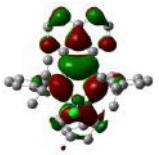
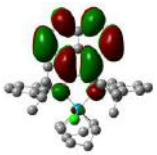
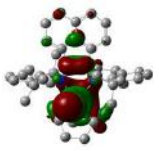
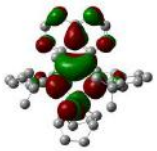
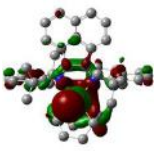
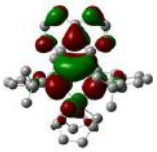
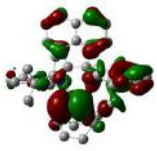
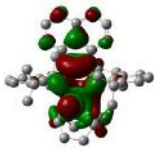
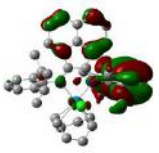
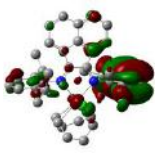
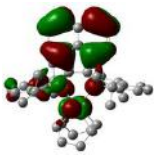
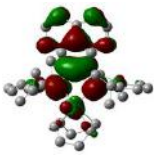
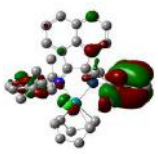
*Table G.1–24: Electrostatic Surface Potential (ESP) and Spin Density diagrams of **3b**. Total Energies (EE_{ZPV}) in a.u. include zero-point vibrational correction. H(S)OMO and LUMO orbitals were generated with [Isovalue] = 0.02, and Spin Density plots with [Isovalue] = 0.0004. Mulliken Spin diagrams were generated with symmetric colour shading, where brightly coloured areas indicate the localisation of unpaired alpha- or beta-spin densities. Alpha FMOs are presented for reduced species (n > 0), and Beta FMOs for oxidised species (n < 0). All calculations were performed at B3LYP-D3/def2-SVP level of theory in CH_2Cl_2 using cPCM. *Asymmetric colour shading applied for clarity.*

EE_{ZPV} (a.u.)	S	H(S)OMO	LUMO	ESP	Mulliken Spin	Spin Density
–2070.92 (n = +4)	5/2				 *	
–2070.93 (n = +3)	2				 *	
–2070.89 (n = +2)	3/2					
–2070.81 (n = +1)	1					
–2070.66 (n = 0)	1/2					
–2070.45 (n = –1)	1				 *	
–2070.19 (n = –2)	3/2				 *	
–2069.91 (n = –3)	2				 *	

© University of Pretoria

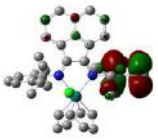
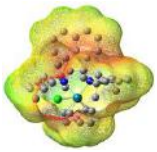
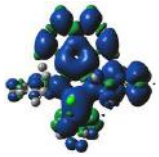
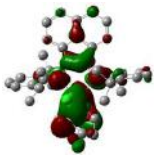
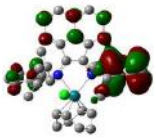
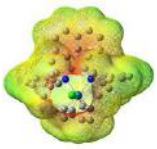
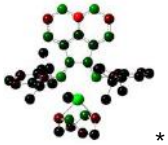
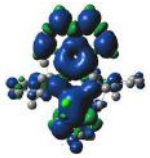
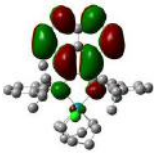
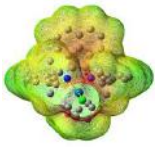
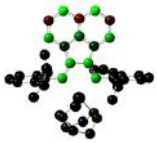
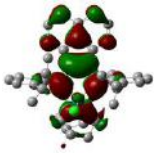
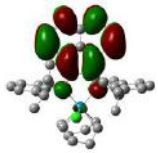
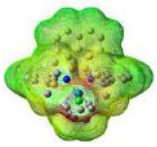
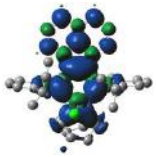
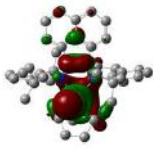
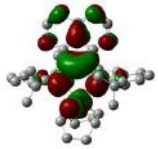
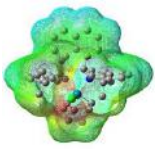
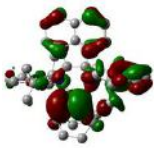
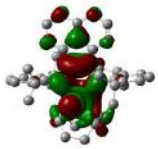
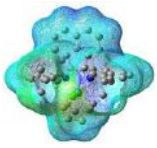
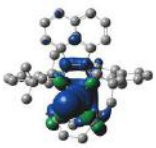
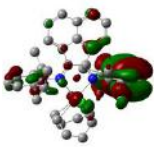
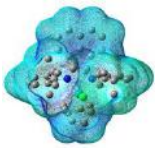
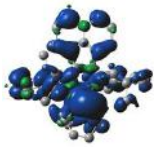
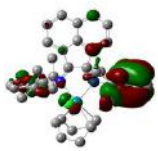
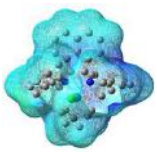
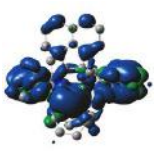
G.1.13) **4a** [RhDB(cod)Cl]

*Table G.1–25: H(S)OMO and LUMO Diagrams and Energies of **4a**, modelled in different charged states. Total Energies (EE_{ZPV}) in a.u. include zero-point vibrational correction. H(S)OMO and LUMO orbitals were generated with [Isovalue] = 0.02. All calculations were performed at B3LYP-D3/def2-SVP level of theory in CH_2Cl_2 using cPCM.*

EE_{ZPV} (a.u.)	S	H(S)OMO$_\alpha$ (eV)	LUMO$_\alpha$ (eV)	H(S)OMO$_\beta$ (eV)	LUMO$_\beta$ (eV)	Other (eV)
–2386.45 (n = +4)	5/2	 0.518	 1.297	 –2.629	 0.115	
–2386.47 (n = +3)	2	 –1.397	 0.918	 –3.021	 –0.313	
–2386.44 (n = +2)	3/2	 –2.078	 0.149	 –4.141	 –1.152	 LUMO +2$_\alpha$ 0.415
–2386.37 (n = +1)	1	 –3.853	 –1.805	 –4.898	 –2.119	 HOMO -1$_\beta$ –4.929
–2386.24 (n = 0)	1/2	 –5.135	 –2.858			
–2386.07 (n = –1)	1	 –6.637	 –3.834	 –6.916	 –4.222	 HOMO -1$_\beta$ –7.068
–2385.82 (n = –2)	3/2	 –7.592	 –4.708	 –7.571	 –6.643	
–2385.55 (n = –3)	2	 –8.123	 –5.141	 –8.060	 –7.271	

© University of Pretoria

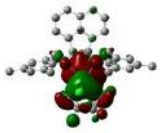
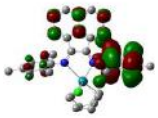
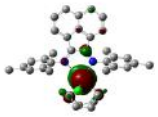
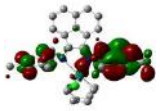
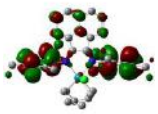
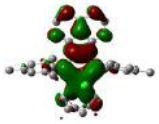
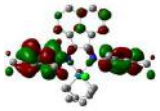
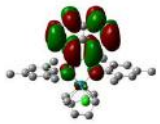
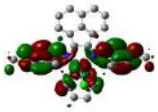
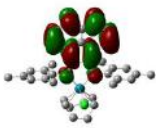
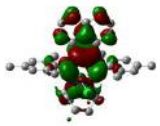
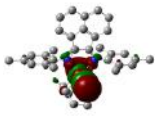
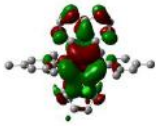
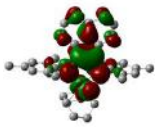
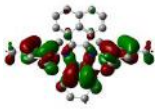
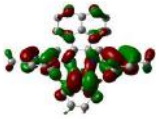
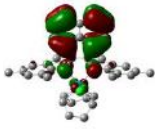
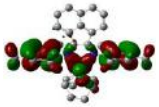
*Table G.1–26: Electrostatic Surface Potential (ESP) and Spin Density diagrams of **4a**. Total Energies (EE_{ZPV}) in a.u. include zero-point vibrational correction. H(S)OMO and LUMO orbitals were generated with [Isovalue] = 0.02, and Spin Density plots with [Isovalue] = 0.0004. Mulliken Spin diagrams were generated with symmetric colour shading, where brightly coloured areas indicate the localisation of unpaired alpha- or beta-spin densities. Alpha FMOs are presented for reduced species (n > 0), and Beta FMOs for oxidised species (n < 0). All calculations were performed at B3LYP-D3/def2-SVP level of theory in CH_2Cl_2 using cPCM. *Asymmetric colour shading applied for clarity.*

EE_{ZPV} (a.u.)	S	H(S)OMO	LUMO	ESP	Mulliken Spin	Spin Density
–2386.45 (n = +4)	5/2				 *	
–2386.47 (n = +3)	2				 *	
–2386.44 (n = +2)	3/2					
–2386.37 (n = +1)	1					
–2386.24 (n = 0)	1/2					
–2386.07 (n = –1)	1				 *	
–2385.82 (n = –2)	3/2				 *	
–2385.55 (n = –3)	2				 *	

© University of Pretoria

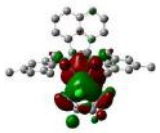
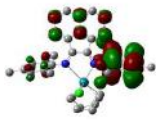
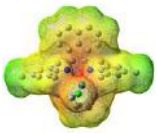
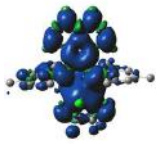
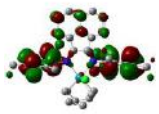
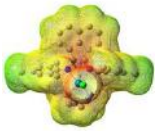
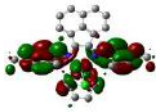
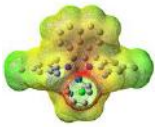
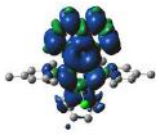
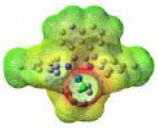
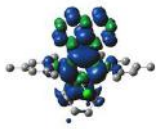
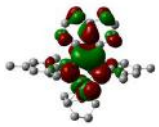
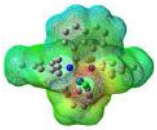
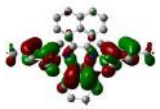
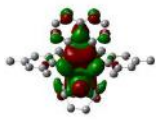
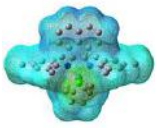
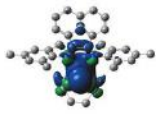
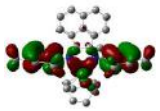
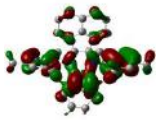
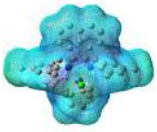
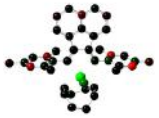
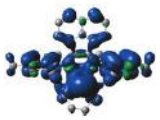
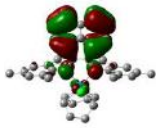
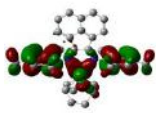
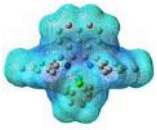
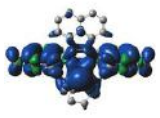
G.1.14) **4b** [RhMB(cod)Cl]

*Table G.1–27: H(S)OMO and LUMO Diagrams and Energies of **4b**, modelled in different charged states. Total Energies (EE_{ZPV}) in a.u. include zero-point vibrational correction. H(S)OMO and LUMO orbitals were generated with [Isovalue] = 0.02. All calculations were performed at B3LYP-D3/def2-SVP level of theory in CH_2Cl_2 using cPCM.*

EE_{ZPV} (a.u.)	S	H(S)OMO$_\alpha$ (eV)	LUMO$_\alpha$ (eV)	H(S)OMO$_\beta$ (eV)	LUMO$_\beta$ (eV)	Other (eV)
–2150.90 (n = +4)	5/2	 –0.206	 1.473	 –2.280	 0.358	 LUMO +1$_\alpha$ 1.541
–2150.92 (n = +3)	2	 –1.116	 1.079	 –3.035	 –0.343	 LUMO +1$_\alpha$ 1.085
–2150.90 (n = +2)	3/2	 –2.062	 0.211	 –4.139	 –1.103	 LUMO +1$_\alpha$ 0.444
–2150.83 (n = +1)	1	 –3.804	 –1.783	 –4.753	 –2.060	
–2150.71 (n = 0)	1/2	 –5.119	 –2.800			
–2150.54 (n = –1)	1	 –6.541	 –3.770	 –6.819	 –4.139	
–2150.29 (n = –2)	3/2	 –7.460	 –4.606	 –7.424	 –6.579	
–2150.03 (n = –3)	2	 –7.975	 –5.208	 –8.141	 –7.114	

© University of Pretoria

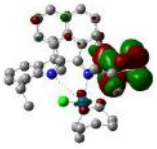
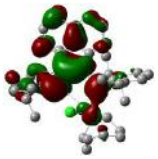
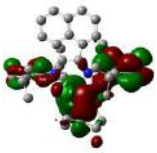
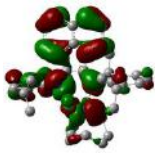
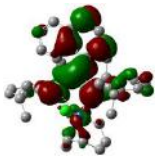
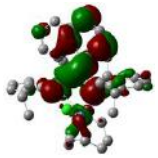
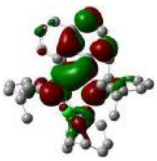
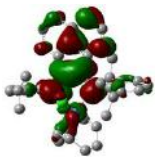
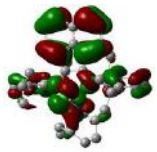
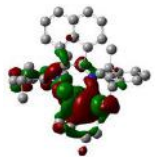
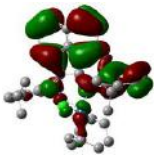
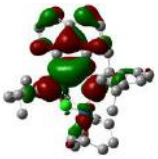
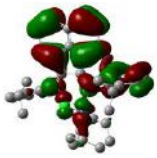
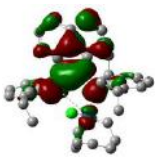
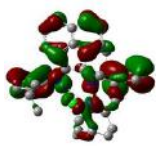
*Table G.1–28: Electrostatic Surface Potential (ESP) and Spin Density diagrams of **4b**. Total Energies (EE_{ZPV}) in a.u. include zero-point vibrational correction. H(S)OMO and LUMO orbitals were generated with [Isovalue] = 0.02, and Spin Density plots with [Isovalue] = 0.0004. Mulliken Spin diagrams were generated with symmetric colour shading, where brightly coloured areas indicate the localisation of unpaired alpha- or beta-spin densities. Alpha FMOs are presented for reduced species (n > 0), and Beta FMOs for oxidised species (n < 0). All calculations were performed at B3LYP-D3/def2-SVP level of theory in CH_2Cl_2 using cPCM. *Asymmetric colour shading applied for clarity.*

EE_{ZPV} (a.u.)	S	H(S)OMO	LUMO	ESP	Mulliken Spin	Spin Density
–2150.90 (n = +4)	5/2				 *	
–2150.92 (n = +3)	2				 *	
–2150.90 (n = +2)	3/2					
–2150.83 (n = +1)	1					
–2150.71 (n = 0)	1/2					
–2150.54 (n = –1)	1				 *	
–2150.29 (n = –2)	3/2				 *	
–2150.03 (n = –3)	2				 *	

© University of Pretoria

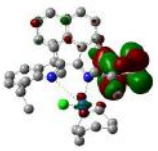
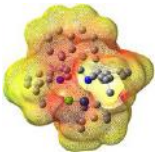
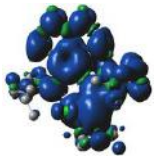
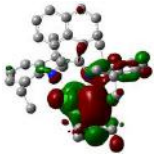
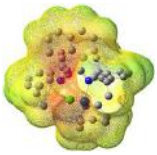
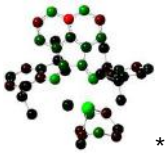
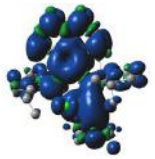
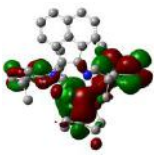
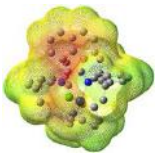
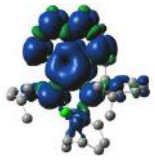
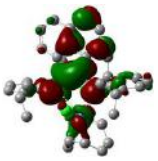
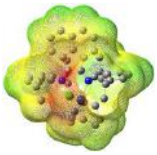
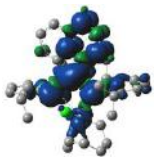
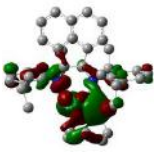
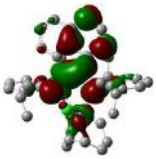
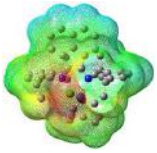
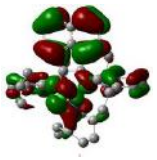
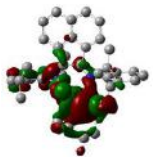
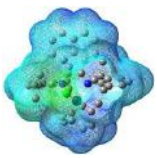
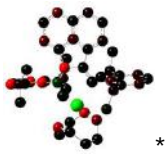
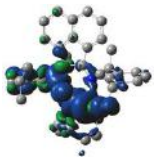
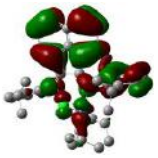
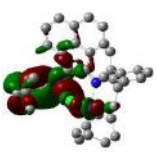
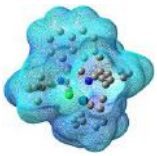
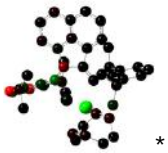
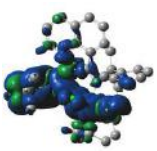
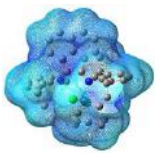
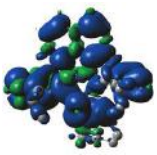
G.1.15) **4c** [IrDB(cod)Cl]

*Table G.1–29: H(S)OMO and LUMO Diagrams and Energies of **4c**, modelled in different charged states. Total Energies (EE_{ZPV}) in a.u. include zero-point vibrational correction. H(S)OMO and LUMO orbitals were generated with [Isovalue] = 0.02. All calculations were performed at B3LYP-D3/def2-SVP level of theory in CH_2Cl_2 using cPCM.*

EE_{ZPV} (a.u.)	S	H(S)OMO$_\alpha$ (eV)	LUMO$_\alpha$ (eV)	H(S)OMO$_\beta$ (eV)	LUMO$_\beta$ (eV)	Other (eV)
–2380.22 (n = +4)	5/2	 –0.669	 0.638	 –2.567	 0.529	
–2380.24 (n = +3)	2	 –0.783	 1.059	 –2.969	 0.029	
–2380.24 (n = +2)	3/2	 –1.751	 0.454	 –3.637	 –0.461	
–2380.17 (n = +1)	1	 –3.324	 –1.487	 –4.388	 –1.481	
–2380.05 (n = 0)	1/2	 –5.257	 –2.886			
–2379.87 (n = –1)	1	 –6.734	 –3.847	 –6.976	 –4.299	 HOMO -1$_\beta$ –7.168
–2379.63 (n = –2)	3/2	 –7.521	 –4.645	 –7.492	 –5.907	
–2379.36 (n = –3)	2	 –8.380	 –5.475	 –8.163	 –7.309	 HOMO -1$_\alpha$ –8.430

© University of Pretoria

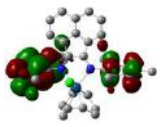
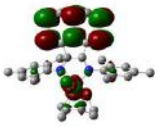
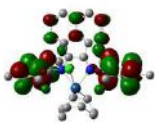
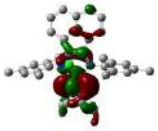
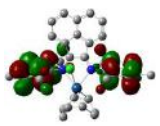
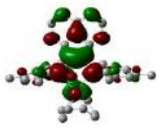
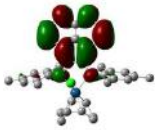
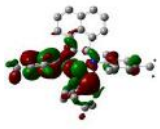
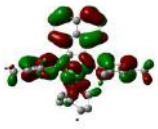
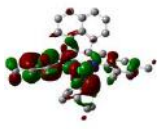
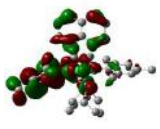
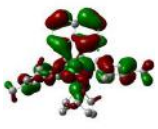
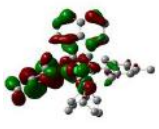
*Table G.1–30: Electrostatic Surface Potential (ESP) and Spin Density diagrams of **4c**. Total Energies (EE_{ZPV}) in a.u. include zero-point vibrational correction. H(S)OMO and LUMO orbitals were generated with [Isovalue] = 0.02, and Spin Density plots with [Isovalue] = 0.0004. Mulliken Spin diagrams were generated with symmetric colour shading, where brightly coloured areas indicate the localisation of unpaired alpha- or beta-spin densities. Alpha FMOs are presented for reduced species (n > 0), and Beta FMOs for oxidised species (n < 0). All calculations were performed at B3LYP-D3/def2-SVP level of theory in CH_2Cl_2 using cPCM. *Asymmetric colour shading applied for clarity.*

EE_{ZPV} (a.u.)	S	H(S)OMO	LUMO	ESP	Mulliken Spin	Spin Density
–2380.22 (n = +4)	5/2				 *	
–2380.24 (n = +3)	2				 *	
–2380.24 (n = +2)	3/2					
–2380.17 (n = +1)	1					
–2380.05 (n = 0)	1/2					
–2379.87 (n = –1)	1				 *	
–2379.63 (n = –2)	3/2				 *	
–2379.36 (n = –3)	2				 *	

© University of Pretoria

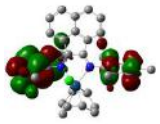
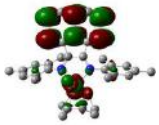
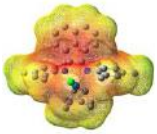
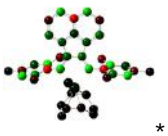
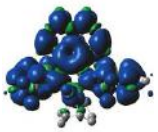
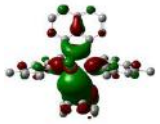
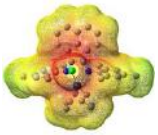
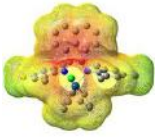
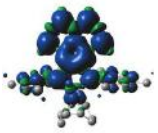
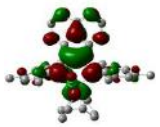
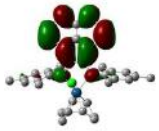
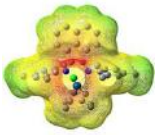
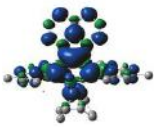
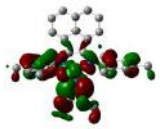
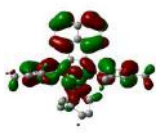
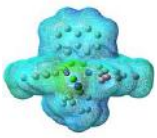
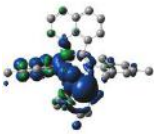
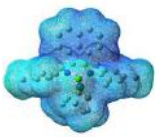
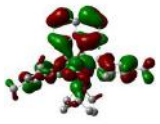
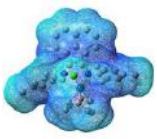
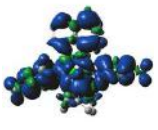
G.1.16) **4d** [IrMB(cod)Cl]

*Table G.1–31: H(S)OMO and LUMO Diagrams and Energies of **4d**, modelled in different charged states. Total Energies (EE_{ZPV}) in a.u. include zero-point vibrational correction. H(S)OMO and LUMO orbitals were generated with [Isovalue] = 0.02. All calculations were performed at B3LYP-D3/def2-SVP level of theory in CH_2Cl_2 using cPCM.*

EE_{ZPV} (a.u.)	S	H(S)OMO$_\alpha$ (eV)	LUMO$_\alpha$ (eV)	H(S)OMO$_\beta$ (eV)	LUMO$_\beta$ (eV)	Other (eV)
–2144.67 (n = +4)	5/2	 0.537	 1.849	 –2.535	 0.685	 LUMO +1$_\alpha$ 1.855
–2144.72 (n = +3)	2	 –1.430	 1.063	 –3.094	 –0.313	 LUMO +1$_\alpha$ 1.139
–2144.70 (n = +2)	3/2	 –1.862	 0.696	 –3.773	 –0.548	
–2144.63 (n = +1)	1	 –3.240	 –1.588	 –4.545	 –1.470	
–2144.52 (n = 0)	1/2	 –5.570	 –2.777			
–2144.34 (n = –1)	1	 –6.372	 –3.770	 –6.858	 –3.889	
–2144.10 (n = –2)	3/2	 –7.209	 –4.798	 –7.500	 –6.587	
–2143.83 (n = –3)	2	 –8.184	 –5.527	 –8.302	 –7.011	

© University of Pretoria

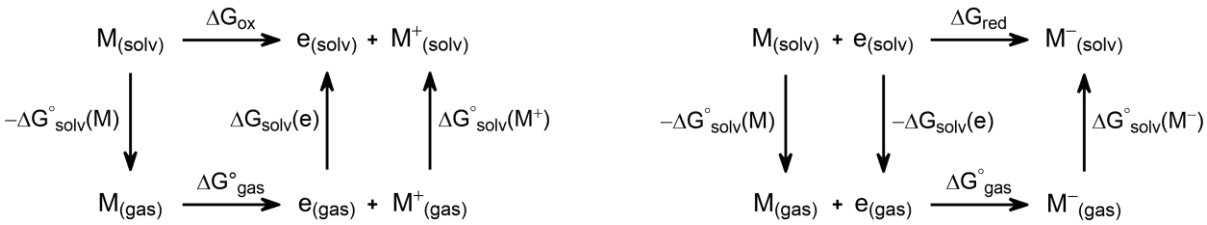
*Table G.1–32: Electrostatic Surface Potential (ESP) and Spin Density diagrams of **4d**. Total Energies (EE_{ZPV}) in a.u. include zero-point vibrational correction. H(S)OMO and LUMO orbitals were generated with [Isovalue] = 0.02, and Spin Density plots with [Isovalue] = 0.0004. Mulliken Spin diagrams were generated with symmetric colour shading, where brightly coloured areas indicate the localisation of unpaired alpha- or beta-spin densities. Alpha FMOs are presented for reduced species (n > 0), and Beta FMOs for oxidised species (n < 0). All calculations were performed at B3LYP-D3/def2-SVP level of theory in CH_2Cl_2 using cPCM. *Asymmetric colour shading applied for clarity.*

EE_{ZPV} (a.u.)	S	H(S)OMO	LUMO	ESP	Mulliken Spin	Spin Density
–2144.67 (n = +4)	5/2				 *	
–2144.72 (n = +3)	2				 *	
–2144.70 (n = +2)	3/2					
–2144.63 (n = +1)	1					
–2144.52 (n = 0)	1/2					
–2144.34 (n = –1)	1				 *	
–2144.10 (n = –2)	3/2				 *	
–2143.83 (n = –3)	2				 *	

© University of Pretoria

G.2) Linear Free Energy Relationships

G.2.1) Theoretical Oxidation Potential Equations



Scheme G.2–1: Thermodynamic reaction cycles were used to calculate the theoretical Gibbs Free Energy change of the reduction half-cell reaction (left), and oxidation half-cell reaction (right), of compound "M" in solution.

Theoretical E_{cell} potentials may be calculated by applying a half-cell reaction thermodynamic cycle method as depicted in Scheme G.2-1.[1–4] The oxidation potential (E_{cell}^{Ox}) of a reaction may be calculated from the standard state free energy change (ΔG_{Ox}) of the half-reaction using equation 1b.[1,3–8]

$$E_{cell}^{Ox} = \left(\frac{+\Delta G_{Ox}}{nF}\right) - E_{ref} \qquad (1b)$$

The number of electrons transferred during the reaction is represented by n, F is Faraday's constant (96.485 kJ/V.e) and E_{ref} is the standard reduction potential of a reference electrode, relative to which E_{cell}^{Ox} is being calculated. E_{ref} here serves a similar function as a reference electrode in an electrochemical cell, whereby the reaction potential is measured relative to the potential of the reference electrode.[1–4] The ΔG_{Ox} is calculated as shown in the thermodynamic half-cell reaction cycle and equation 2b:

$$\Delta G_{Ox} = \Delta G_{gas}^{\circ} + \Delta G_{solv}(e) + \left[\Delta G_{solv}^{\circ}(M^{+}) - \Delta G_{solv}^{\circ}(M)\right] \qquad (2b)$$

where ΔG_{gas}° is the standard state free energy change of the gaseous reduction reaction, and ΔG_{solv}° denotes the free energy of solvation. Note: as previously reported in literature, the $\Delta G_{solv}(e)$ was treated as 0 (zero).[1,3,5,6]

The ΔG_{gas}° may be calculated as a function of the product's and reactants' Electronic Energy "EE" and the thermal correction to their free energy "ΔG_{corr}" (Equation 3b) – which include contributions for zero-point energy corrections "E_{ZPV}" (Equation 4).[1,3,4,9,10] The free energy contribution of the gaseous electron at 298.15 K (in kJ/mol) is also taken into account, $G_{gas}^{\circ}(e)$, as determined using Fermi-Direc statistics.[1,11]

© University of Pretoria

$$\Delta G^{\circ}_{gas} = G^{\circ}_{gas}(M^{+}) - G^{\circ}_{gas}(M) + G^{\circ}_{gas}(e) \qquad (3b)$$
$$= \left[EE(M^{+})_{gas} + \Delta G_{corr}(M^{+})_{gas}\right] - \left[EE(M)_{gas} + \Delta G_{corr}(M)_{gas}\right] + (-3.6106)$$

and

$$\Delta G_{corr} = H_{corr} - TS_{corr} = (ZPE_{corr} + k_B T) - TS_{tot} \qquad (4)$$

The "S_{tot}" represents the total Entropy, and the thermal correction factor to enthalpy "H_{corr}" includes the zero-point vibrational correction energy "ZPE_{corr}".[1,3,4,9,10]

The last remaining variables in equation 2b are the solvation free energies "ΔG°_{solv}" of the product and reactant, which are critical to account for energy differences between the two states that are not directly associated with the reaction itself.[1,3,4,9,10] For example, conformational changes that are induced by solvation between the optimised gas-phase and solvated geometries will result in energy differences between the two states that is not related to the reduction/oxidation reaction. Equation 5b, written here for the oxidised "(M^{+})" species, also includes the change in the thermal correction to free energy.

$$\Delta G^{\circ}_{solv}(M^{+}) = G^{\circ}_{solv}(M^{+}) - G^{\circ}_{gas}(M^{+}) \qquad (5b)$$
$$= [EE(M^{+})_{solv} + \Delta G_{corr}(M^{+})_{solv}] - \left[EE(M^{+})_{gas} + \Delta G_{corr}(M^{+})_{gas}\right]$$

The energy that is released by the addition of one electron to compound "*M*" may be described as the Electron Affinity (EA),[3,12] and the energy required to remove an electron from "*M*" as the Ionisation Energy (IE),[3,12] which may be estimated using equations 6 and 7b:

$$EA(M) = EE(M) - EE(M^{-}) \qquad (6)$$
$$IE(M) = EE(M^{+}) - EE(M) \qquad (7b)$$

Substituting equation 6 into equation 3b yields:

$$\Delta G^{\circ}_{gas} = \left[EE(M^{+})_{gas} + \Delta G_{corr}(M^{+})_{gas}\right] - \left[EE(M)_{gas} + \Delta G_{corr}(M)_{gas}\right] + G^{\circ}_{gas}(e)$$
$$= IE(M)_{gas} + \left[\Delta G_{corr}(M^{+})_{gas} - \Delta G_{corr}(M)_{gas}\right] + (-3.6106)$$
$$= IE(M)_{gas} + \Delta\Delta G_{corr} - 3.6106 \qquad (8b)$$

© University of Pretoria

(1) Marenich, A. V.; Ho, J.; Coote, M. L.; Cramer, C. J.; Truhlar, D. G. Computational Electrochemistry: Prediction of Liquid-Phase Reduction Potentials. *Physical Chemistry Chemical Physics* **2014**, *16* (29), 15068–15106. https://doi.org/10.1039/c4cp01572j.

(2) Winget, P.; Weber, E. J.; Cramer, C. J.; Truhlar, D. G. Computational Electrochemistry: Aqueous One-Electron Oxidation Potentials for Substituted Anilines. *Physical Chemistry Chemical Physics* **2000**, *2* (6), 1231–1239. https://doi.org/10.1039/a909076b.

(3) Ho, J.; Coote, M. L.; Cramer, C. J.; Truhlar, D. G. Theoretical Calculation Of Reduction Potentials. In *Organic Electrochemistry*; CRC Press, 2015; pp 249–280. https://doi.org/10.1201/b19122-12.

(4) Schultz, F. A.; Lord, R. L.; Baik, M.-H. Multifaceted Examination of Multielectron Transfer Reactions. *Inorganica Chim Acta* **2020**, *510*, 119746. https://doi.org/10.1016/j.ica.2020.119746.

(5) Adeniyi, A. A.; Conradie, J. Computational Insight into the Contribution of Para-Substituents on the Reduction Potential, Proton Affinity, and Electronic Properties of Nitrobenzene Compounds. *J Mol Model* **2019**, *25* (3), 78. https://doi.org/10.1007/s00894-019-3946-2.

(6) Fu, Y.; Liu, L.; Yu, H. Z.; Wang, Y. M.; Guo, Q. X. Quantum-Chemical Predictions of Absolute Standard Redox Potentials of Diverse Organic Molecules and Free Radicals in Acetonitrile. *J Am Chem Soc* **2005**, *127* (19), 7227–7234. https://doi.org/10.1021/ja0421856.

(7) Baik, M.-H.; Friesner, R. A. Computing Redox Potentials in Solution: Density Functional Theory as A Tool for Rational Design of Redox Agents. *J Phys Chem A* **2002**, *106* (32), 7407–7412. https://doi.org/10.1021/jp025853n.

(8) Roy, L. E.; Jakubikova, E.; Guthrie, M. G.; Batista, E. R. Calculation of One-Electron Redox Potentials Revisited. Is It Possible to Calculate Accurate Potentials with Density Functional Methods? *J Phys Chem A* **2009**, *113* (24), 6745–6750. https://doi.org/10.1021/jp811388w.

(9) Ryu, H.; Park, J.; Kim, H. K.; Park, J. Y.; Kim, S.-T.; Baik, M.-H. Pitfalls in Computational Modeling of Chemical Reactions and How To Avoid Them. *Organometallics* **2018**, *37* (19), 3228–3239. https://doi.org/10.1021/acs.organomet.8b00456.

(10) Ochterski, J. W. Thermochemistry in Gaussian. *Gaussian Inc Pittsburgh PA* **2000**, *264* (1), 1–19.

(11) Fifen, J. J. Thermodynamics of the Electron Revisited and Generalized. *J Chem Theory Comput* **2013**, *9* (7), 3165–3169. https://doi.org/10.1021/ct400212t.

(12) Foresman, J. B.; Frisch, Æ. *Exploring Chemistry with Electronic Structure Methods*, 3rd ed.; Gaussian, Inc.: Wallingford, CT, 2015.

© University of Pretoria

G.3) Dataset Comparison Tables

G.3.1) All compounds *vs* Complex Series **1–4**

*Table G.3–1: Comparison of the linear correlations' statistical analysis data, for all computed compounds (All) and all computed complexes (**1–4**), as determined using the three datasets. The X- and Y-intercepts are reported under the (x, 0) and (0, y) columns, respectively.*

	Full Dataset						All – Outlier Dataset						Limited Dataset					
Plot	**(0, y)**	**Slope**	**(x, 0)**	**R^2**	**RMSD**	**MAD**	**(0, y)**	**Slope**	**(x, 0)**	**R^2**	**RMSD**	**MAD**	**(0, y)**	**Slope**	**(x, 0)**	**R^2**	**RMSD**	**MAD**
HOMO: All	4.706	2.175	-2.164	0.9274	0.78484	0.08612	4.721	2.158	-2.188	0.92761	0.77429	0.08548	4.780	2.040	-2.344	0.93114	0.68623	0.08029
HOMO: **1–4**	4.713	2.235	-2.109	0.92995	0.7818	0.08965	4.728	2.217	-2.133	0.92982	0.77252	0.08917	4.794	2.095	-2.289	0.93111	0.93111	0.08498
LUMO: All	2.952	2.361	-1.251	0.93774	0.78449	0.08608	2.958	2.353	-1.257	0.93655	0.7868	0.08686	2.911	2.285	-1.274	0.93144	0.76706	0.08974
LUMO: **1–4**	2.970	2.428	-1.223	0.94339	0.75813	0.08693	2.976	2.421	-1.229	0.94211	0.7614	0.08789	2.925	2.360	-1.239	0.93631	0.74628	0.09182
FMO: All	3.624	2.852	-1.270	0.9467	0.87284	0.0954	3.628	2.848	-1.274	0.94559	0.87744	0.09687	3.602	2.824	-1.275	0.93771	0.90073	0.10538
FMO: **1–4**	3.622	2.908	-1.246	0.94753	0.8721	0.100	3.625	2.904	-1.248	0.94628	0.87767	0.10131	3.597	2.892	-1.244	0.93748	0.90537	0.11139
-EA: All (eV)	-4.536	-4.615	-0.983	0.84313	2.54297	0.28246	-4.590	-4.550	-1.009	0.84249	2.50114	0.27954	-4.560	-4.215	-1.082	0.84217	2.25765	0.26413
-EA: **1–4** (eV)	-4.616	-4.830	-0.956	0.85423	2.51448	0.29219	-4.672	-4.761	-0.981	0.85305	2.47553	0.28962	-4.658	-4.414	-1.055	0.84971	2.25031	0.27686
$-\Delta G_{rxn}$: All (eV)	4.066	1.859	-2.187	0.8804	0.87516	0.09721	4.092	1.827	-2.239	0.88428	0.84029	0.09392	4.106	1.725	-2.380	0.88364	0.77471	0.09064
$-\Delta G_{rxn}$: **1–4** (eV)	4.075	1.930	-2.111	0.88596	0.87269	0.10141	4.103	1.896	-2.164	0.88918	0.83857	0.09811	4.124	1.791	-2.302	0.88569	0.78009	0.09598
E_{cell}: All	-0.375	1.859	0.202	0.8804	0.87515	0.09337	-0.348	1.827	0.191	0.88428	0.84029	0.09392	-0.334	1.725	0.193	0.88364	0.77470	0.00131
E_{cell}: **1–4**	-0.365	1.930	0.189	0.88596	0.87269	0.10141	-0.337	1.896	0.178	0.88918	0.83857	0.09811	-0.316	1.791	0.177	0.88569	0.78009	0.09598

© University of Pretoria

G.3.2) Rhodium complexes *vs* Iridium complexes

Table G.3–2: Comparison of the linear correlations' statistical analysis data, for all computed Rhodium and Iridium complexes, as determined using the three datasets. The X- and Y-intercepts are reported under the (x, 0) and (0, y) columns, respectively.

	Full Dataset						All – Outlier Dataset						Limited Dataset					
Plot	**(0, y)**	**Slope**	**(x, 0)**	**R^2**	**RMSD**	**MAD**	**(0, y)**	**Slope**	**(x, 0)**	**R^2**	**RMSD**	**MAD**	**(0, y)**	**Slope**	**(x, 0)**	**R^2**	**RMSD**	**MAD**
HOMO: Rh	4.866	-2.049	-2.374	0.95076	0.6354	0.09568	4.866	2.049	-2.374	0.95076	0.6354	0.09568	4.943	2.001	-2.470	0.95637	0.55883	0.08824
HOMO: **Ir**	4.524	-2.551	-1.773	0.94115	0.76361	0.13070	4.536	2.538	-1.787	0.93683	0.77344	0.13436	4.560	2.320	-1.965	0.91957	0.75819	0.14286
LUMO: Rh	3.119	-2.292	-1.361	0.95544	0.67424	0.10153	3.119	2.292	-1.361	0.95544	0.67424	0.10153	3.128	2.271	-1.377	0.94868	0.69055	0.10904
LUMO: **Ir**	2.785	-2.660	-1.047	0.94952	0.73425	0.12568	2.779	2.673	-1.040	0.94506	0.75621	0.13137	2.611	2.587	-1.009	0.94723	0.67463	0.12712
FMO: Rh	3.764	-2.746	-1.370	0.96844	0.67538	0.1017	3.764	2.746	-1.370	0.96844	0.67538	0.1017	3.797	2.768	-1.372	0.96567	0.68210	0.10770
FMO: **Ir**	3.447	-3.181	-1.084	0.93928	0.96803	0.16569	3.434	3.207	-1.071	0.93548	0.98826	0.17168	3.281	3.193	-1.027	0.92023	1.03872	0.19572
-EA: Rh (eV)	-5.038	-4.294	-1.173	0.85636	2.35737	0.36344	-5.038	-4.294	-1.173	0.85636	2.3583	0.36344	-5.006	-4.263	-1.174	0.85405	2.30395	0.36378
-EA: **Ir** (eV)	-4.177	-5.637	-0.741	0.89322	2.33289	0.39931	-4.233	-5.551	-0.763	0.88675	2.3277	0.40436	-4.122	-4.797	-0.859	0.86619	2.08331	0.39254
$-\Delta G_{rxn}$: Rh (eV)	4.258	1.706	-2.496	0.89606	0.77923	0.12009	4.258	1.706	-2.496	0.89606	0.77923	0.12009	4.258	1.707	-2.495	0.88941	0.78662	0.12420
$-\Delta G_{rxn}$: **Ir** (eV)	3.879	2.267	-1.711	0.92434	0.77653	0.13291	3.916	2.218	-1.766	0.92351	0.74871	0.13006	3.911	1.996	-1.959	0.90883	0.69851	0.13162
E_{cell}: Rh	-0.182	1.706	0.107	0.89606	0.77923	0.12009	-0.182	1.706	0.107	0.89606	0.77923	0.12009	-0.182	1.707	0.106	0.88941	0.78661	0.12420
E_{cell}: **Ir**	-0.540	2.271	0.238	0.92395	0.77982	0.13348	-0.524	2.217	0.237	0.92351	0.74871	0.13006	-0.529	1.996	0.265	0.90883	0.69851	0.13161

© University of Pretoria

G.3.3) DippBIAN complexes *vs* MesBIAN complexes

Table G.3–3: Comparison of the linear correlations' statistical analysis data, for all computed DippBIAN and MesBIAN complexes, as determined using the three datasets. The X- and Y-intercepts are reported under the (x, 0) and (0, y) columns, respectively.

	Full Dataset						All – Outlier Dataset						Limited Dataset					
Plot	**(0, y)**	**Slope**	**(x, 0)**	**R^2**	**RMSD**	**MAD**	**(0, y)**	**Slope**	**(x, 0)**	**R^2**	**RMSD**	**MAD**	**(0, y)**	**Slope**	**(x, 0)**	**R^2**	**RMSD**	**MAD**
HOMO: DB	4.689	-2.307	-2.032	0.93431	0.77562	0.12563	4.689	2.307	-2.033	0.93453	0.77433	0.12542	4.762	2.145	-2.220	0.93498	0.69113	0.11830
HOMO: **MB**	4.736	-2.172	-2.180	0.9276	0.79826	0.12604	4.768	2.133	-2.235	0.92825	0.77356	0.12369	4.819	2.048	-2.353	0.92811	0.70627	0.12089
LUMO: DB	2.973	-2.448	-1.215	0.94164	0.77258	0.12514	2.973	2.447	-1.215	0.94167	0.77238	0.1251	2.913	2.398	-1.215	0.93778	0.75444	0.12913
LUMO: **MB**	2.968	-2.411	-1.231	0.94508	0.76467	0.12074	2.979	2.398	-1.242	0.9427	0.77102	0.12328	2.932	2.325	-1.261	0.93494	0.75991	0.13007
FMO: DB	3.625	-2.943	-1.232	0.94738	0.87937	0.14243	3.625	2.942	-1.232	0.94739	0.87925	0.14241	3.565	2.933	-1.216	0.9392	0.91157	0.15603
FMO: **MB**	3.620	-2.877	-1.258	0.9479	0.8873	0.1401	3.627	2.869	-1.264	0.94548	0.89845	0.14366	3.623	2.855	-1.269	0.93596	0.92529	0.15838
-EA: DB (eV)	-4.545	-4.831	-0.941	0.85556	2.48100	0.40721	-4.546	-4.830	-0.941	0.85578	2.47916	0.4069	-4.609	-4.404	-1.047	0.85381	2.22606	0.38102
-EA: **MB** (eV)	-4.684	-4.830	-0.970	0.85328	2.61377	0.41793	-4.796	-4.696	-1.021	0.85132	2.53411	0.4145	-4.709	-4.428	-1.064	0.84539	2.34618	0.40158
$-\Delta G_{rxn}$: DB (eV)	4.087	1.958	-2.088	0.89044	0.85842	0.14089	4.088	1.958	-2.088	0.89066	0.85756	0.14075	4.117	1.828	-2.252	0.88588	0.80137	0.13717
$-\Delta G_{rxn}$: **MB** (eV)	4.063	1.906	-2.132	0.8822	0.90890	0.14533	4.119	1.840	-2.239	0.88945	0.83752	0.13565	4.126	1.756	-2.349	0.88564	0.78196	0.13384
E_{cell}: DB	-0.353	1.958	0.180	0.89044	0.85842	0.14089	-0.352	1.958	0.180	0.89066	0.85756	0.14075	-0.323	1.828	0.177	0.88588	0.80137	0.13717
E_{cell}: **MB**	-0.377	1.906	0.198	0.8822	0.9089	0.14533	-0.321	1.840	0.174	0.88945	0.83752	0.13565	-0.314	1.756	0.179	0.88564	0.78196	0.13384

© University of Pretoria

G.3.4) Grouped complexes' MO correlations

Table G.3–4: Comparison of the MO linear correlations' statistical analysis data, for each group of computed complexes, as determined using the three datasets. The X- and Y-intercepts are reported under the (x, 0) and (0, y) columns, respectively.

	Full Dataset						All – Outlier Dataset						Limited Dataset					
Plot	**(0, y)**	**Slope**	**(x, 0)**	**R^2**	**RMSD**	**MAD**	**(0, y)**	**Slope**	**(x, 0)**	**R^2**	**RMSD**	**MAD**	**(0, y)**	**Slope**	**(x, 0)**	**R^2**	**RMSD**	**MAD**
HOMO: 1a–d	4.768	2.421	-1.982	0.91668	0.9131	0.18561	4.800	2.421	-1.983	0.91702	0.91124	0.18524	4.886	2.148	-2.274	0.90585	0.84061	0.18680
HOMO: **2a–d**	4.918	2.152	-2.285	0.97328	0.46748	0.10144	4.918	2.142	-2.285	0.97328	0.46748	0.10144	4.911	2.145	-2.290	0.96959	0.48115	0.10692
HOMO: 3a–d	5.223	1.712	-3.051	0.99514	0.19669	0.05782	5.223	1.712	-3.051	0.99514	0.19669	0.05782	5.223	1.712	-3.051	0.99514	0.19669	0.05782
HOMO: **4a–d**	4.280	2.332	-1.835	0.9638	0.57681	0.11273	4.299	2.305	-1.865	0.96287	0.57295	0.11416	4.410	2.284	-1.931	0.95898	0.53998	0.11718
HOMO: 1a–b	5.174	1.745	-2.965	0.99691	0.14914	0.04568	5.174	1.745	-2.965	0.99691	0.14917	0.04568	5.174	1.745	-2.965	0.99691	0.14917	0.04568
HOMO: **1c–d**	4.683	2.960	-1.582	0.97154	0.60064	0.14862	4.685	2.958	-1.584	0.97172	0.59872	0.14814	4.727	2.729	-1.732	0.93134	0.79617	0.22519
LUMO: 1a–d	3.160	2.663	-1.187	0.9416	0.82968	0.16866	3.161	2.662	-1.188	0.94162	0.82955	0.16863	3.046	2.511	-1.213	0.93257	0.81935	0.18208
LUMO: **2a–d**	3.207	2.424	-1.323	0.97332	0.5261	0.11417	3.207	2.424	-1.323	0.97332	0.5261	0.11417	3.183	2.398	-1.327	0.97	0.53413	0.11869
LUMO: 3a–d	3.413	1.983	-1.721	0.96808	0.59166	0.17393	3.413	1.983	-1.721	0.96808	0.59166	0.17393	3.413	1.983	-1.721	0.96808	0.59166	0.17393
LUMO: **4a–d**	2.391	2.355	-1.015	0.98356	0.38859	0.07594	2.391	2.355	-1.015	0.98252	0.39773	0.07925	2.327	2.456	-0.947	0.98403	0.35768	0.07762
LUMO: 1a–b	3.333	2.046	-1.629	0.96828	0.56873	0.17414	3.333	2.046	-1.629	0.96828	0.56873	0.17414	3.333	2.046	-1.629	0.96828	0.56873	0.17414
LUMO: **1c–d**	3.153	3.174	-0.994	0.98843	0.40714	0.10074	3.155	3.171	-0.995	0.98817	0.41167	0.10186	2.900	3.186	-0.910	0.99032	0.33852	0.09575

© University of Pretoria

Table G.3–5: Comparison of the FMO linear correlations' statistical analysis data, for each group of computed complexes, as determined using the three datasets. The X- and Y-intercepts are reported under the (x, 0) and (0, y) columns, respectively.

	Full Dataset						All – Outlier Dataset						Limited Dataset					
Plot	**(0, y)**	**Slope**	**(x, 0)**	**R^2**	**RMSD**	**MAD**	**(0, y)**	**Slope**	**(x, 0)**	**R^2**	**RMSD**	**MAD**	**(0, y)**	**Slope**	**(x, 0)**	**R^2**	**RMSD**	**MAD**
FMO: 1a–d	3.743	3.112	-1.203	0.94002	0.98332	0.19989	3.744	3.111	-1.204	0.94001	0.98335	0.19989	3.649	2.999	-1.217	0.91823	1.08593	0.24132
FMO: **2a–d**	3.717	2.870	-1.295	0.98049	0.53068	0.11516	3.717	2.870	-1.295	0.98049	0.53068	0.11516	3.713	2.865	-1.296	0.97781	0.54675	0.12150
FMO: 3a–d	4.109	2.441	-1.684	0.99476	0.29097	0.08554	4.409	2.441	-1.684	0.99476	0.29097	0.08554	4.109	2.441	-1.684	0.99476	0.29097	0.08554
FMO: **4a–d**	3.234	2.932	-1.103	0.94596	0.89414	0.17475	3.228	2.940	-1.098	0.94312	0.91409	0.18213	3.203	3.178	-1.008	0.94227	0.89924	0.19514
FMO: 1a–b	3.968	2.527	-1.570	0.99374	0.3081	0.09434	3.968	2.527	-1.570	0.99374	0.3081	0.09434	3.968	2.527	-1.570	0.99374	0.3091	0.09434
FMO: **1c–d**	3.700	3.589	-1.031	0.95641	0.90838	0.22477	3.703	3.585	-1.033	0.95616	0.91097	0.22541	3.478	3.679	-0.945	0.92548	1.12183	0.3173
FMO: 2a–b							3.901	2.988	-1.306	0.98877	0.44231	0.11284						
FMO: **2c–d**							3.378	2.612	-1.293	0.98624	0.43008	0.14336						

© University of Pretoria

G.3.5) Grouped complexes' thermodynamic correlations

Table G.3–6: Comparison of the theoretical thermodynamics' linear correlation statistical analysis data, for each group of computed complexes, as determined using the three datasets. The X- and Y-intercepts are reported under the (x, 0) and (0, y) columns, respectively.

	Full Dataset						All – Outlier Dataset						Limited Dataset					
Plot	**(0, y)**	**Slope**	**(x, 0)**	**R^2**	**RMSD**	**MAD**	**(0, y)**	**Slope**	**(x, 0)**	**R^2**	**RMSD**	**MAD**	**(0, y)**	**Slope**	**(x, 0)**	**R^2**	**RMSD**	**MAD**
-EA (eV): 1a–d	-5.584	-5.220	-1.070	0.88314	2.37489	0.48276	-5.586	-5.218	-1.070	0.88353	2.37097	0.48197	-5.663	-4.349	-1.302	0.88151	1.93491	0.42998
-EA (eV): **2a–d**	-5.446	-4.927	-1.105	0.92146	1.88542	0.40925	-5.446	-4.927	-1.105	0.92146	1.88541	0.40915	-5.292	-4.765	-1.111	0.91391	1.85232	0.41163
-EA (eV): 3a–d	-6.229	-3.444	-1.809	0.9299	1.55391	0.45681	-6.229	-3.444	-1.809	0.9299	1.5539	0.4568	-6.229	-3.444	-1.809	0.9299	1.55391	0.45681
-EA (eV): **4a–d**	-2.224	-4.910	-0.459	0.97279	1.02388	0.20813	-2.293	-4.807	-0.477	0.97433	0.95536	0.1983	-2.431	-4.717	-0.515	0.97707	0.82604	0.17926
-EA (eV): 1a–b	-6.432	-3.328	-1.933	0.96039	1.03786	0.31778	-6.432	-3.33	-1.933	0.96039	1.03786	0.31778	-6.432	-3.328	-1.933	0.96039	1.03786	0.31778
-EA (eV): **1c–d**	-5.378	-6.749	-0.797	0.98357	1.03400	0.25582	-5.383	-6.744	-0.798	0.98375	1.02845	0.25448	-5.229	-5.809	-0.900	0.95725	1.31924	0.37314
-EA (eV): 2a–b							-5.582	-5.543	-1.007	0.95792	1.61345	0.41163						
-EA (eV): **2c–d**							-5.478	-3.253	-1.684	0.97695	0.69657	0.23219						
-ΔG_{rxn} (eV): 1a–d	4.221	2.100	-2.011	0.88753	0.93489	0.19004	4.222	2.099	-2.012	0.88785	0.93358	0.18978	4.280	1.819	-2.353	0.87356	0.83986	0.18664
-ΔG_{rxn} (eV): **2a–d**	4.422	1.937	-2.284	0.93956	0.64389	0.13973	4.422	1.937	-2.284	0.93956	0.64389	0.13973	4.417	1.931	-2.287	0.93149	0.66345	0.14743
-ΔG_{rxn} (eV): 3a–d	4.539	1.423	-3.190	0.93151	0.63406	0.18640	4.539	1.423	-3.190	0.93151	0.63405	0.18639	4.539	1.423	-3.190	0.93151	0.63406	0.18640
-ΔG_{rxn} (eV): **4a–d**	3.426	1.996	-1.716	0.96018	0.50687	0.10304	3.480	1.917	-1.815	0.97207	0.39784	0.08258	3.522	1.888	-1.866	0.96993	0.37995	0.08245
-ΔG_{rxn} (eV): 1a–b	4.602	1.387	-3.317	0.9514	0.48154	0.14744	4.602	1.387	-3.317	0.9514	0.48154	0.14744	4.602	1.387	-3.317	0.9514	0.48154	0.14744
-ΔG_{rxn} (eV): **1c–d**	4.109	2.669	-1.540	0.97869	0.46688	0.11552	4.110	2.666	-1.542	0.97876	0.46602	0.11531	4.100	2.437	-1.682	0.95066	0.59662	0.16875
-ΔG_{rxn} (eV): 2a–b							4.464	2.115	-2.111	0.95784	0.61615	0.1572						
-ΔG_{rxn} (eV): **2c–d**							4.425	1.454	-3.044	0.97723	0.30935	0.10312						

© University of Pretoria

Table G.3–7: Comparison of the theoretical E_{cell} linear correlation statistical analysis data, for each group of computed complexes, as determined using the three datasets. The X- and Y-intercepts are reported under the (x, 0) and (0, y) columns, respectively.

	Full Dataset						All – Outlier Dataset						Limited Dataset					
Plot	**(0, y)**	**Slope**	**(x, 0)**	**R^2**	**RMSD**	**MAD**	**(0, y)**	**Slope**	**(x, 0)**	**R^2**	**RMSD**	**MAD**	**(0, y)**	**Slope**	**(x, 0)**	**R^2**	**RMSD**	**MAD**
E_{cell}: 1a–d	-0.219	2.100	0.104	0.88753	0.93488	0.18991	-0.218	2.099	0.104	0.88785	0.93358	0.18978	-0.160	1.819	0.088	0.87356	0.83986	0.18663
E_{cell}: **2a–d**	-0.018	1.937	0.009	0.93956	0.64386	0.13973	-0.018	1.937	0.009	0.93956	0.64389	0.13973	-0.023	1.931	0.012	0.93149	0.66345	0.14743
E_{cell}: 3a–d	0.099	1.423	-0.070	0.93151	0.63405	0.18639	0.099	1.423	-0.070	0.93151	0.63405	0.18639	0.099	1.423	-0.070	0.93151	0.63405	0.18639
E_{cell}: **4a–d**	-1.014	1.996	0.508	0.96018	0.50687	0.10304	-0.960	1.917	0.501	0.97207	0.39784	0.08258	-0.918	1.888	0.487	0.96993	0.37995	0.08245
E_{cell}: 1a–b	0.162	1.387	-0.117	0.9514	0.48154	0.14744	0.162	1.387	-0.117	0.9514	0.48154	0.14744	0.162	1.387	-0.117	0.9514	0.48154	0.14744
E_{cell}: **1c–d**	-0.331	2.669	0.124	0.97869	0.46688	0.11552	-0.330	2.666	0.124	0.97876	0.46602	0.11531	-0.340	2.437	0.140	0.95066	0.59662	0.16875
E_{cell}: 2a–b							0.024	2.115	-0.012	0.95784	0.61615	0.1572						
E_{cell}: **2c–d**							-0.015	1.454	0.010	0.97723	0.30935	0.10312						

© University of Pretoria

G.3.6) Individual complexes' Reaction free energy correlations ($-\Delta G_{rxn}$)

Table G.3–8: Comparison of the theoretical reaction free energy (eV) linear correlations' statistical analysis data, for individual computed complexes, as determined using the three datasets. The X- and Y-intercepts are reported under the (x, 0) and (0, y) columns, respectively.

	Full Dataset						All – Outlier Dataset						Limited Dataset					
$-\Delta G_{rxn}$ (eV)	(0, y)	Slope	(x, 0)	R^2	RMSD	MAD	(0, y)	Slope	(x, 0)	R^2	RMSD	MAD	(0, y)	Slope	(x, 0)	R^2	RMSD	MAD
1a	4.575	1.430	-3.199	0.95436	0.57629	0.20375	4.575	1.430	-3.199	0.95436	0.57629	0.20372	4.575	1.430	-3.199	0.95436	0.57629	0.20375
1b	4.626	1.349	-3.431	0.95018	0.59193	0.20928	4.626	1.349	-3.431	0.95018	0.59193	0.20928	4.626	1.349	-3.431	0.95018	0.59193	0.20928
1c	4.161	2.651	-1.570	0.97946	0.50258	0.16054	4.164	2.647	-1.573	0.97968	0.49981	0.15966	4.123	2.419	-1.702	0.94753	0.71693	0.24835
1d	4.057	2.687	-1.510	0.97863	0.51144	0.16337	4.057	2.687	-1.510	0.97863	0.51144	0.16337	4.076	2.453	-1.662	0.95419	0.65770	0.22783
2a	4.423	2.257	-1.959	0.95153	0.73032	0.24344	4.423	2.257	-1.959	0.95153	0.73031	0.24344	4.423	2.258	-1.959	0.95153	0.73032	0.24344
2b	4.525	2.017	-2.243	0.96902	0.57912	0.18499	4.525	2.017	-2.243	0.96902	0.57912	0.18499	4.570	2.058	-2.221	0.95912	0.63779	0.21156
2c	4.464	1.458	-3.063	0.98336	0.37393	0.12464	4.464	1.458	-3.063	0.98336	0.37393	0.12464	4.464	1.458	-3.063	0.98336	0.37393	0.13069
2d	4.387	1.450	-3.026	0.97216	0.48342	0.16114	4.387	1.450	-3.026	0.97216	0.48342	0.16114	4.387	1.450	-3.026	0.97216	0.48342	0.16114
3a	4.700	1.309	-3.592	0.94349	0.64710	0.22878	4.700	1.309	-3.592	0.94349	0.64709	0.22878	4.700	1.309	-3.592	0.94349	0.64710	0.22878
3b	4.439	1.490	-2.978	0.93289	0.74409	0.25776	4.439	1.490	-2.978	0.93289	0.74408	0.25776	4.439	1.490	-2.978	0.93289	0.74409	0.25776
4a	3.710	1.880	-1.973	0.9627	0.51952	0.17997	3.710	1.880	-1.973	0.9627	0.51952	0.17997	3.710	1.880	-1.973	0.9627	0.51952	0.17997
4b	3.457	1.700	-2.034	0.97191	0.45651	0.15814	3.457	1.700	-2.034	0.97191	0.45651	0.15814	3.356	1.586	-2.116	0.94203	0.51996	0.18383
4c	3.356	2.068	-1.623	0.98946	0.31713	0.10571	3.356	2.068	-1.623	0.98946	0.31713	0.10571	3.406	1.993	-1.709	0.98904	0.30478	0.10558
4d	3.316	2.214	-1.498	0.967	0.59375	0.19792	3.472	1.960	-1.771	0.994	0.21377	0.07405	3.472	1.960	-1.771	0.994	0.21377	0.07405

© University of Pretoria

G.3.7) Individual complexes' Theoretical cell potential correlations (E_{cell})

Table G.3–9: Comparison of the theoretical reaction cell potential (V vs NHE) linear correlations' statistical analysis data, for individual computed complexes, as determined using the three datasets.

	Full Dataset						All – Outlier Dataset						Limited Dataset					
E_{cell} vs NHE	**(0, y)**	**Slope**	**(x, 0)**	**R^2**	**RMSD**	**MAD**	**(0, y)**	**Slope**	**(x, 0)**	**R^2**	**RMSD**	**MAD**	**(0, y)**	**Slope**	**(x, 0)**	**R^2**	**RMSD**	**MAD**
1a	0.135	1.430	-0.094	0.95436	0.57629	0.20375	0.135	1.430	-0.094	0.95436	0.57629	0.20375	0.135	1.430	-0.094	0.95436	0.57629	0.20375
1b	0.186	1.349	-0.138	0.95018	0.59193	0.20928	0.186	1.349	-0.138	0.95018	0.59193	0.20928	0.186	1.349	-0.138	0.95018	0.59193	0.16742
1c	-0.279	2.651	0.105	0.97946	0.50258	0.16124	-0.276	2.647	0.104	0.97968	0.49981	0.15966	-0.317	2.422	0.131	0.94753	0.71693	0.24835
1d	-0.383	2.687	0.143	0.97863	0.51144	0.16337	-0.383	2.687	0.143	0.97863	0.51144	0.16337	-0.364	2.453	0.149	0.95419	0.65770	0.22783
2a	-0.017	2.257	0.008	0.95153	0.73031	0.24344	-0.017	2.257	0.008	0.95153	0.73031	0.24344	-0.017	2.257	0.008	0.95153	0.73031	0.24344
2b	0.085	2.017	-0.042	0.96902	0.57912	0.18499	0.085	2.017	-0.042	0.96902	0.57912	0.18499	0.130	2.058	-0.063	0.95912	0.63778	0.21260
2c	0.024	1.458	-0.017	0.98336	0.37393	0.12464	0.024	1.458	-0.017	0.98336	0.37393	0.12464	0.024	1.458	-0.017	0.98336	0.37393	0.12464
2d	-0.053	1.450	0.037	0.97216	0.48342	0.16114	-0.053	1.450	0.369	0.97216	0.48342	0.16114	-0.053	1.450	0.037	0.97216	0.48342	0.16114
3a	0.260	1.308	-0.199	0.94349	0.64709	0.22878	0.260	1.309	-0.199	0.94349	0.64709	0.22878	0.260	1.309	-0.199	0.94349	0.64709	0.22878
3b	-0.001	1.490	0.001	0.93289	0.74408	0.25776	-0.001	0.001	0.001	0.93289	0.74408	0.25776	-0.001	1.490	0.001	0.93289	0.74408	0.25776
4a	-0.730	1.880	0.388	0.9627	0.51952	0.17997	-0.730	1.880	0.388	0.9627	0.51952	0.17997	-0.730	1.880	0.388	0.9627	0.51952	0.17997
4b	-0.983	1.700	0.579	0.97191	0.45651	0.15814	-0.983	1.700	0.579	0.97191	0.45651	0.15814	-1.084	1.586	0.683	0.94203	0.51995	0.18383
4c	-1.084	2.068	0.524	0.98946	0.31713	0.10571	-1.084	2.068	0.524	0.98946	0.31713	0.10571	-1.034	1.993	0.519	0.98904	0.30478	0.10558
4d	-1.124	2.214	0.508	0.967	0.59374	0.19792	-0.968	1.960	0.494	0.994	0.21377	0.07405	-0.968	1.960	0.494	0.994	0.21377	0.07405

© University of Pretoria

G.4) LFER Plots – All – Outlier dataset

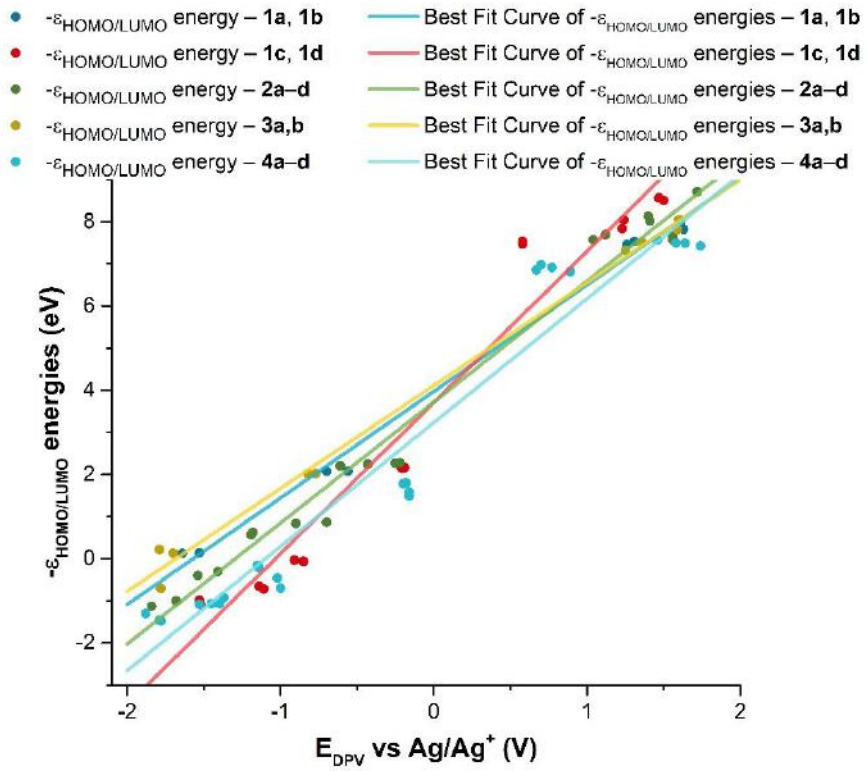


*Figure G.4–1: LFER between the reactive FMO energies ($-\varepsilon_{HOMO/LUMO}$) and experimental DPV reaction potentials (E_{DPV}) for all modelled states of the complex series **1**–**4**. LUMO energies were used at negative potentials, and HOMO energies at positive potentials, to model reductive and oxidative reactivity respectively.*

© University of Pretoria

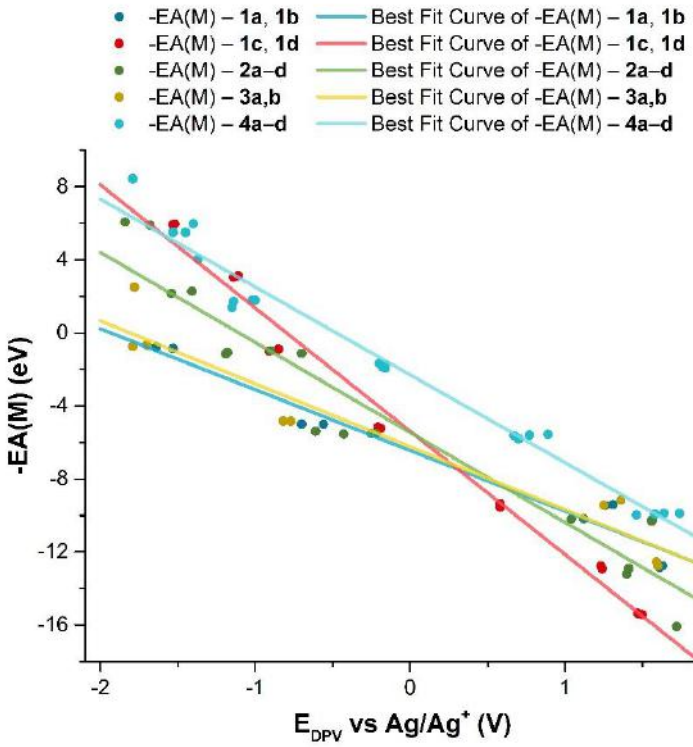


*Figure G.4–2: LFER between the theoretical Electron Affinity ($-EA_{gas}$) and the experimental DPV reaction potentials (E_{DPV}) for all modelled states of the complex series **1–4**.*

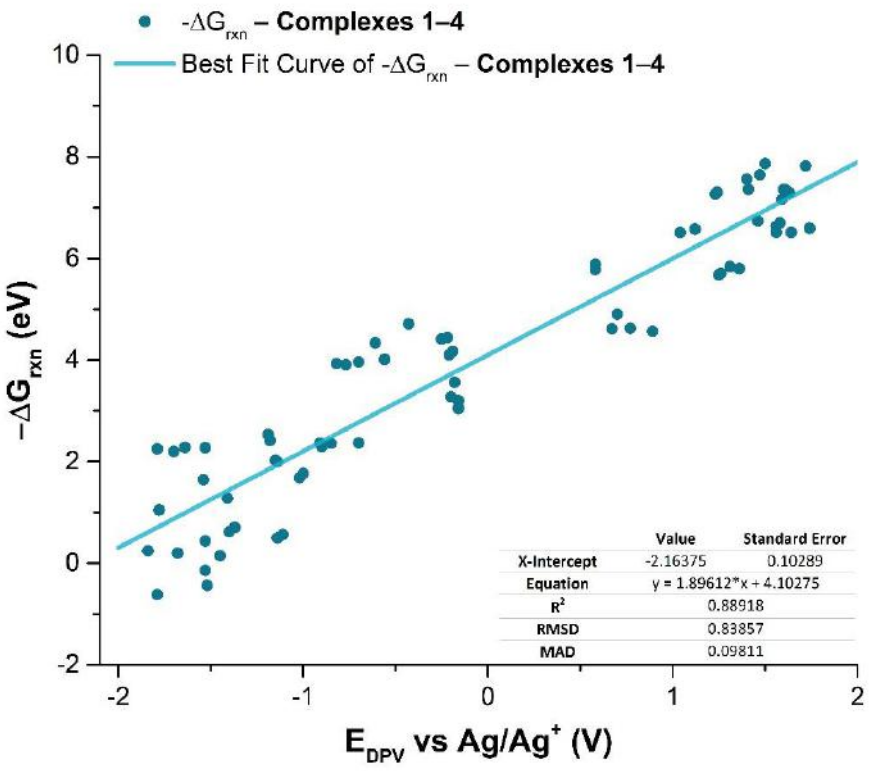


*Figure G.4–3: LFER between the theoretical reaction free energy change ($-\Delta G_{rxn}$) and the experimental DPV reaction potentials (E_{DPV}) for all modelled states of the complex series **1–4**.*

© University of Pretoria

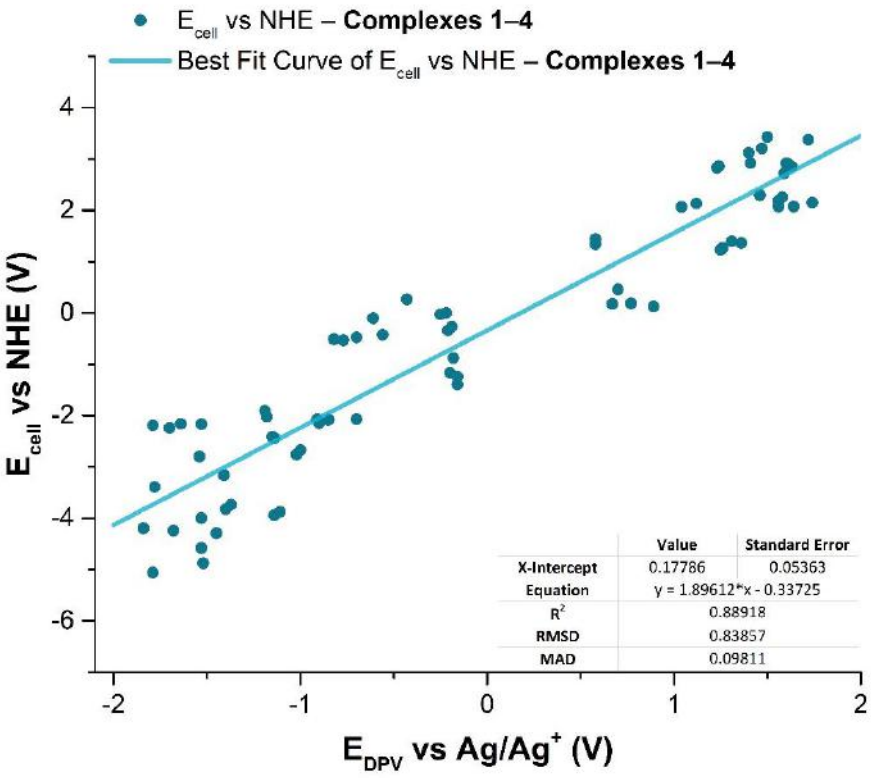


*Figure G.4–4: LFER between the theoretical reaction cell potential (E_{cell}) and the experimental DPV reaction potentials (E_{DPV}) for all modelled states of the complex series **1–4**.*

© University of Pretoria

Appendix H: Catalysis – NMR Studies

H.1) Representative Catalytic Activity NMR Spectra

H.1.1) Alkene Dimerization

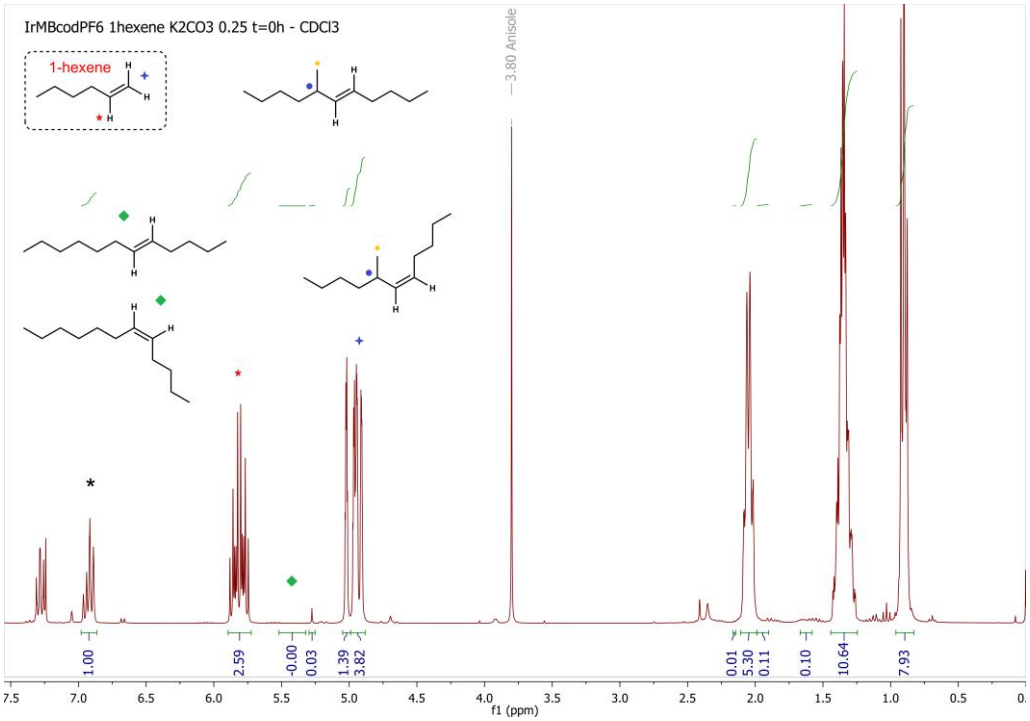


*Figure H.1–1: ^{1}H NMR spectra for the catalytic dimerization activity of 1-hexene by **1d** in $CDCl_3$, recorded at t=0h.*

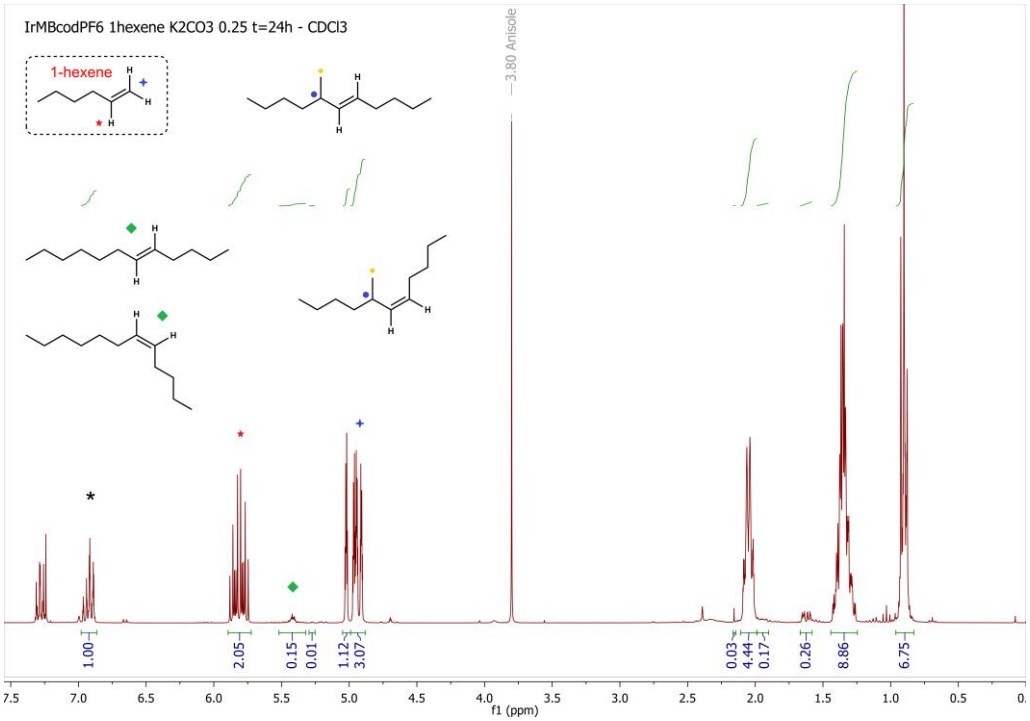


*Figure H.1–2: ^{1}H NMR spectra for the catalytic dimerization activity of 1-hexene by **1d** in $CDCl_3$, recorded at t=24h.*

© University of Pretoria

H.1.2) Alkene Hydroamination

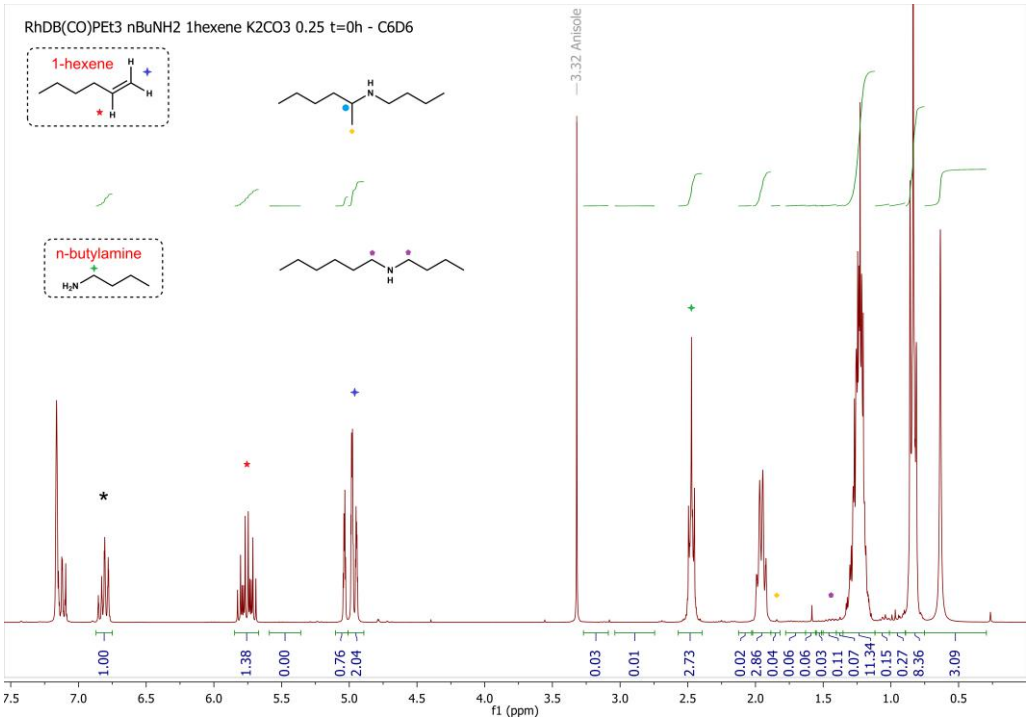


*Figure H.1–3: ^{1}H NMR spectra for the catalytic hydroamination activity of 1-hexene with n-butylamine by **3a** in C_6D_6, recorded at t=0h.*

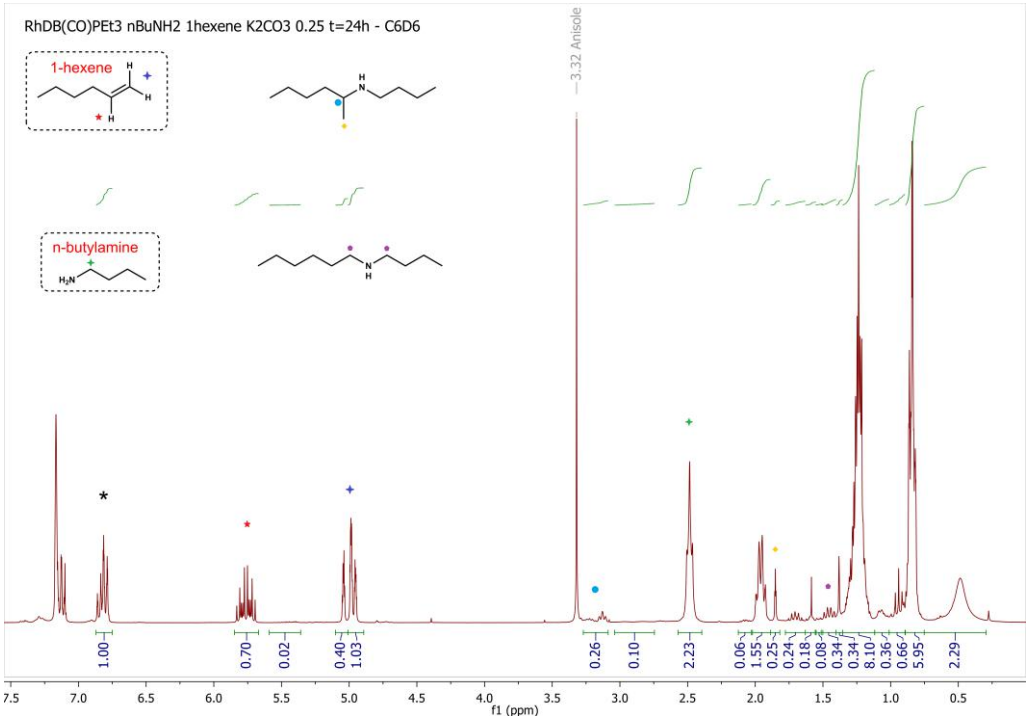


*Figure H.1–4: ^{1}H NMR spectra for the catalytic hydroamination activity of 1-hexene with n-butylamine by **3a** in C_6D_6, recorded at t=24h.*

© University of Pretoria

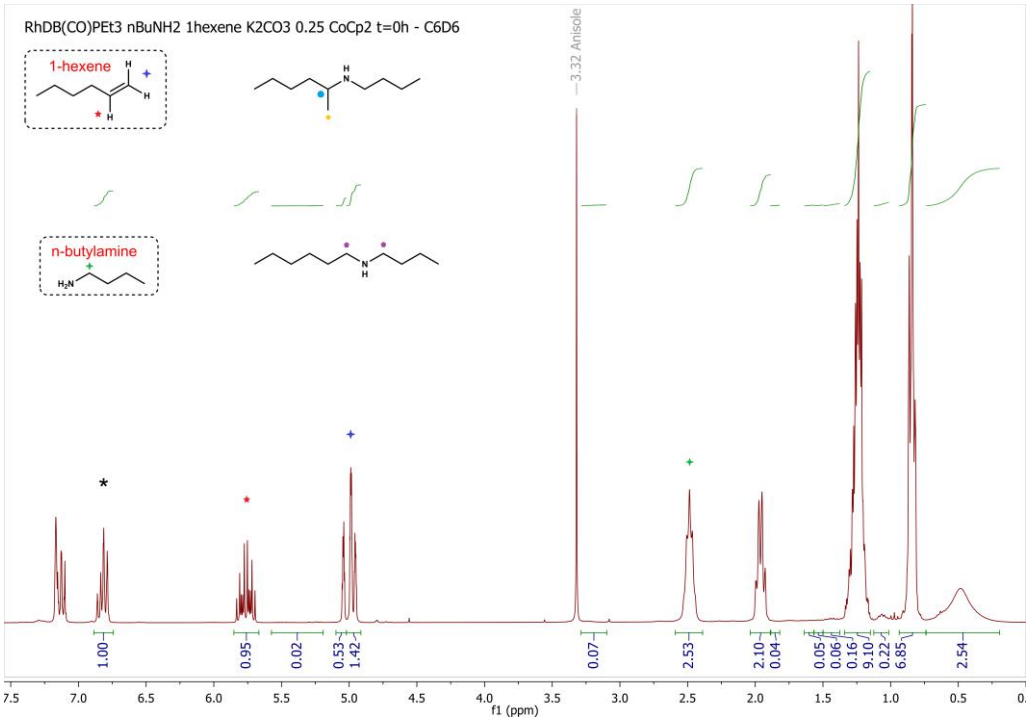


*Figure H.1–5: ^{1}H NMR spectra for the catalytic activity test of the hydroamination of 1-hexene with n-butylamine by **3a** in C_6D_6, in the presence of the chemical reductant $CoCp_2$, recorded at t=0h.*

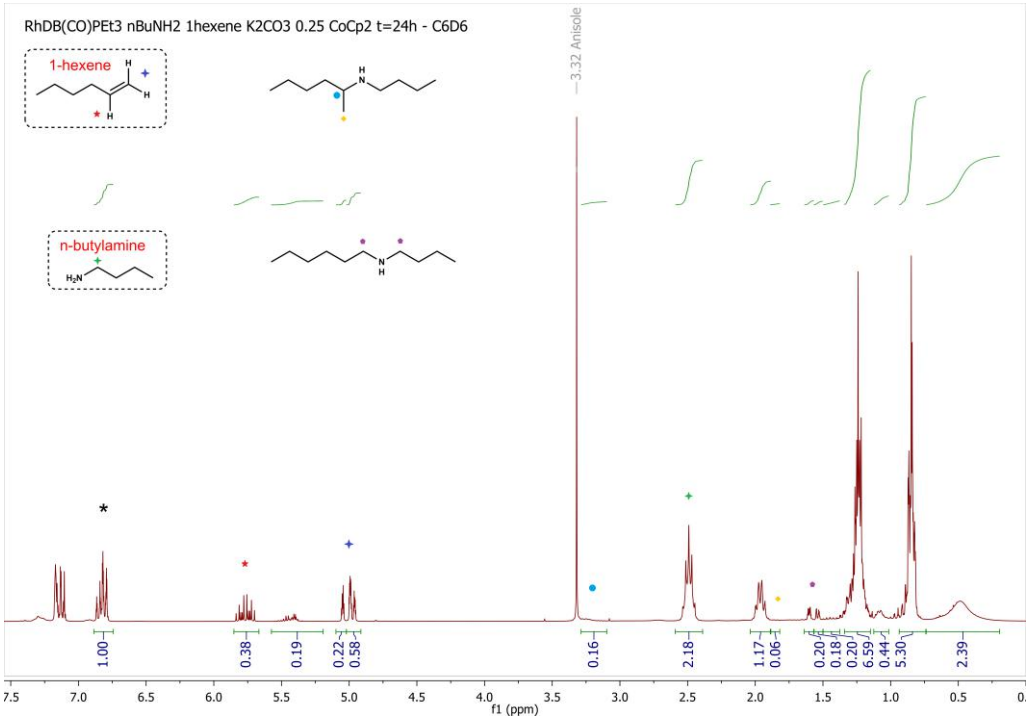


*Figure H.1–6: ^{1}H NMR spectra for the catalytic activity test of the hydroamination of 1-hexene with n-butylamine by **3a** in C_6D_6, in the presence of the chemical reductant $CoCp_2$, recorded at t=24h.*

© University of Pretoria

H.1.3) Alkene Hydrothiolation

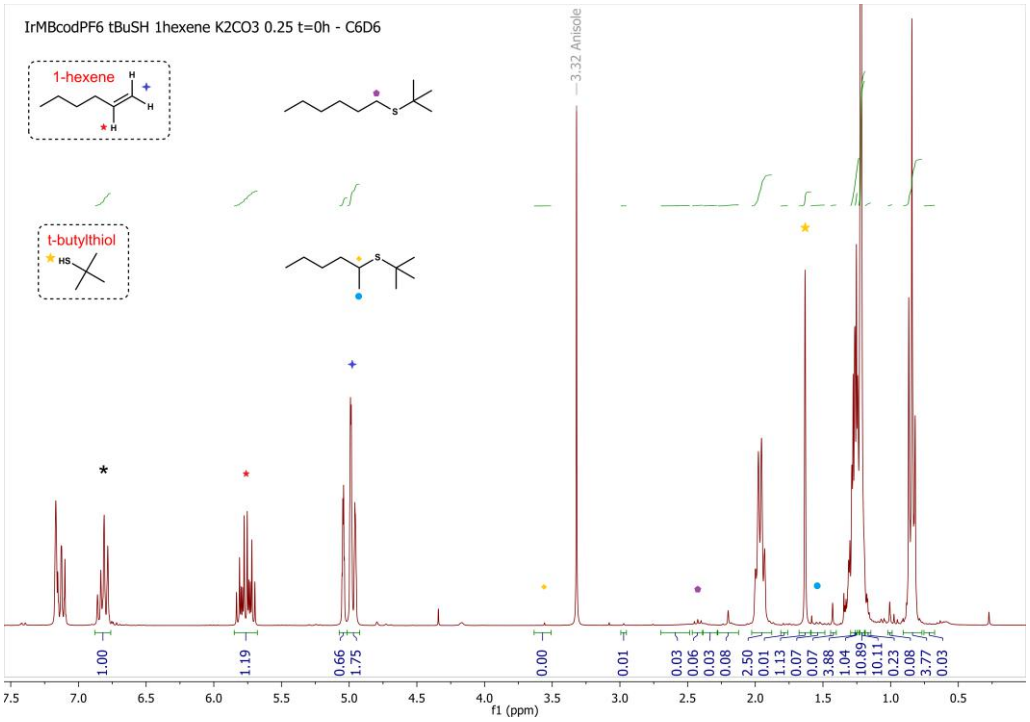


*Figure H.1–7: ^{1}H NMR spectra for the catalytic activity test of the hydrothiolation of 1-hexene with t-butylthiol by **1d** in C_6D_6, recorded at t=0h.*

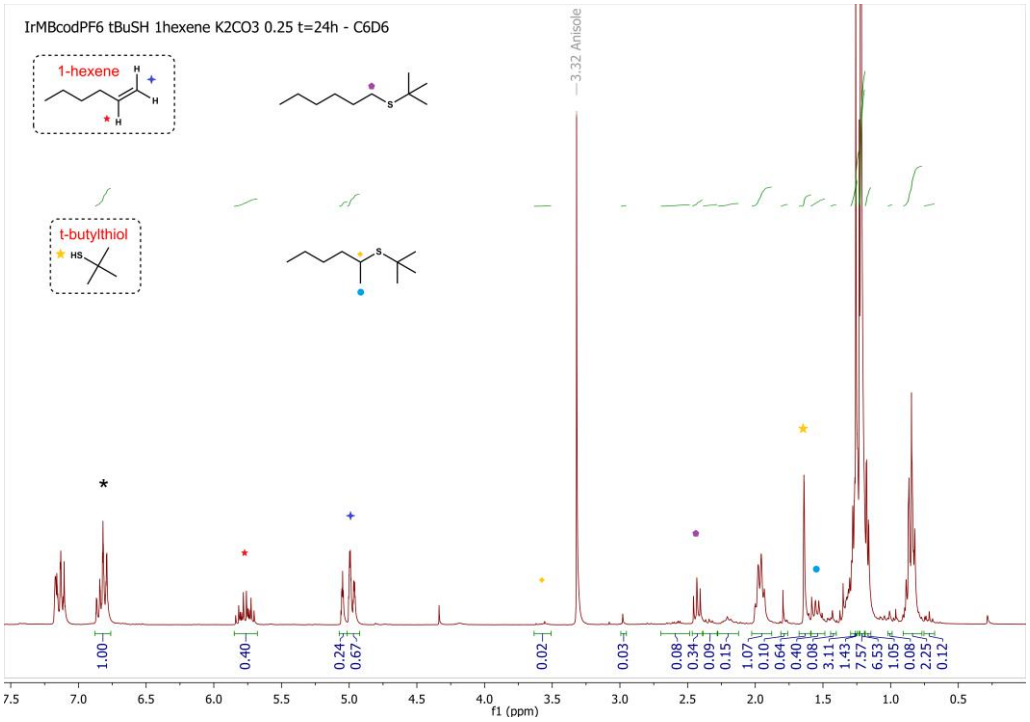


*Figure H.1–8: ^{1}H NMR spectra for the catalytic activity test of the hydrothiolation of 1-hexene with t-butylthiol by **1d** in C_6D_6, recorded at t=24h.*

© University of Pretoria

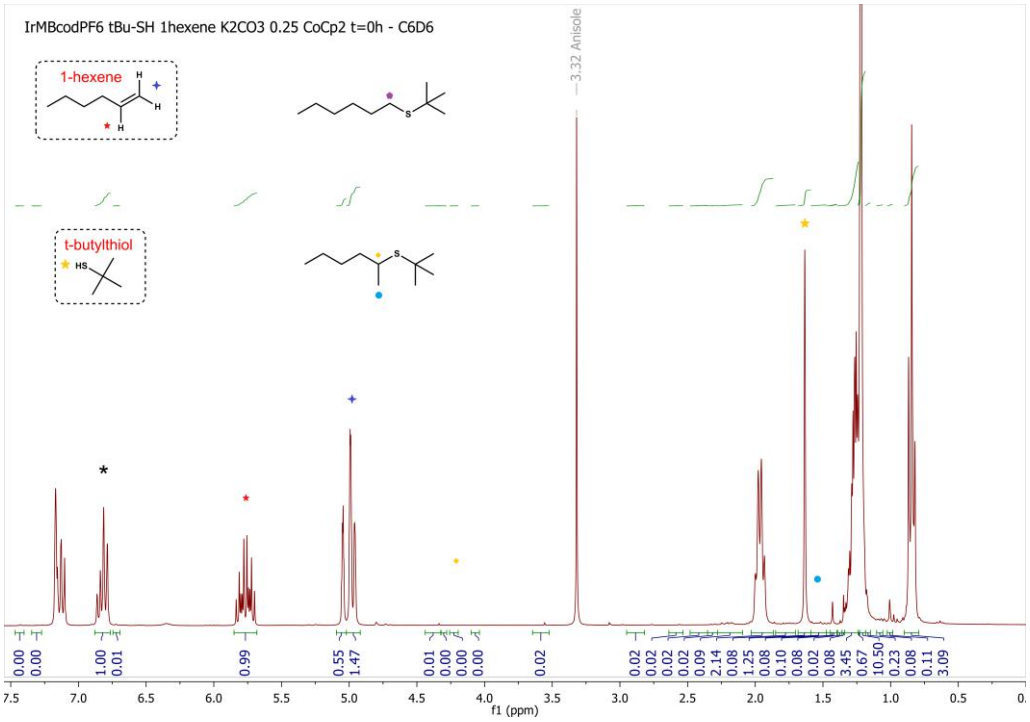


*Figure H.1–9: ^{1}H NMR spectra for the catalytic activity test of the hydrothiolation of 1-hexene with t-butylthiol by **1d** in C_6D_6, in the presence of the chemical reductant $CoCp_2$, recorded at t=0h.*

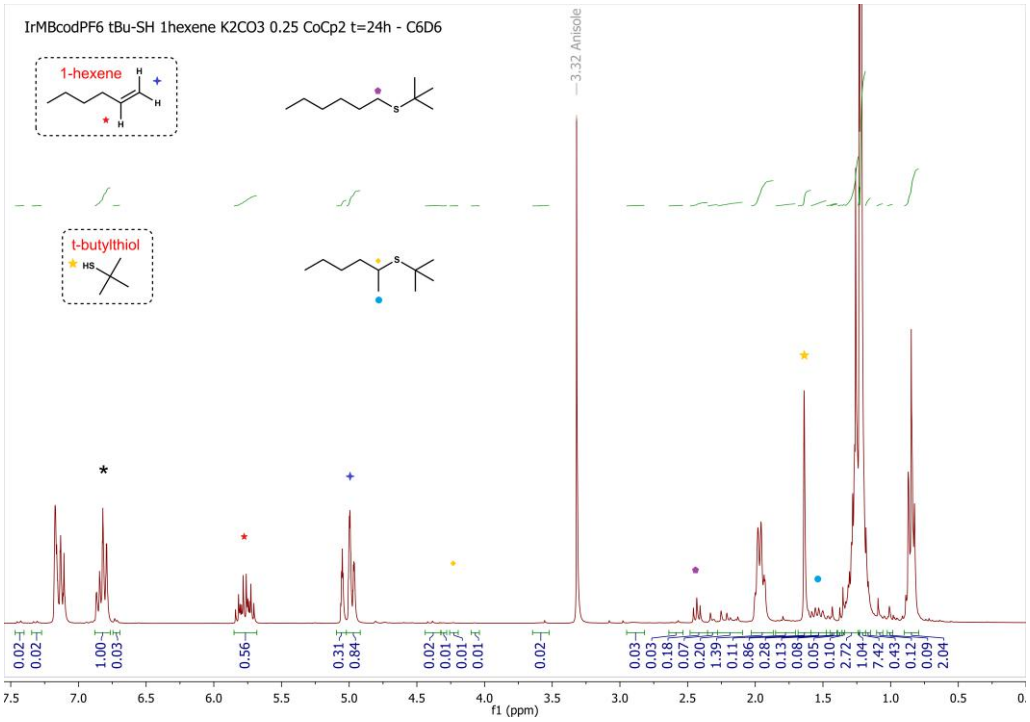


*Figure H.1–10: ^{1}H NMR spectra for the catalytic activity test of the hydrothiolation of 1-hexene with t-butylthiol by **1d** in C_6D_6, in the presence of the chemical reductant $CoCp_2$, recorded at t=24h.*

© University of Pretoria

H.1.4) Alkyne Dimerization

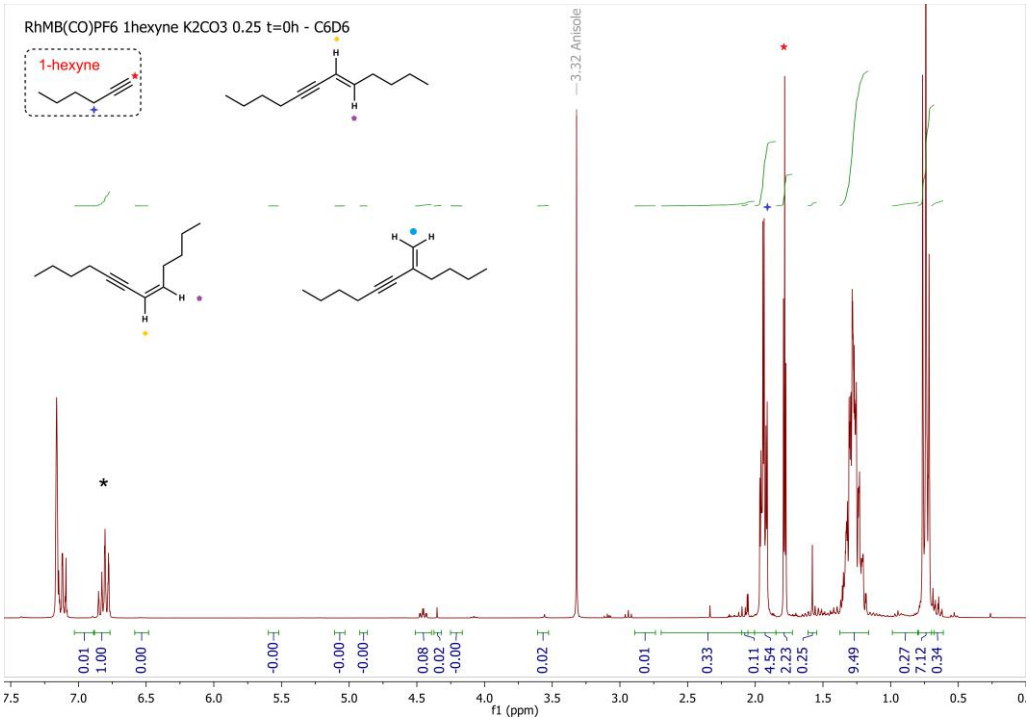


*Figure H.1–11: ^{1}H NMR spectra for the catalytic dimerization activity of 1-hexyne by **2b** in C_6D_6, recorded at t=0h.*

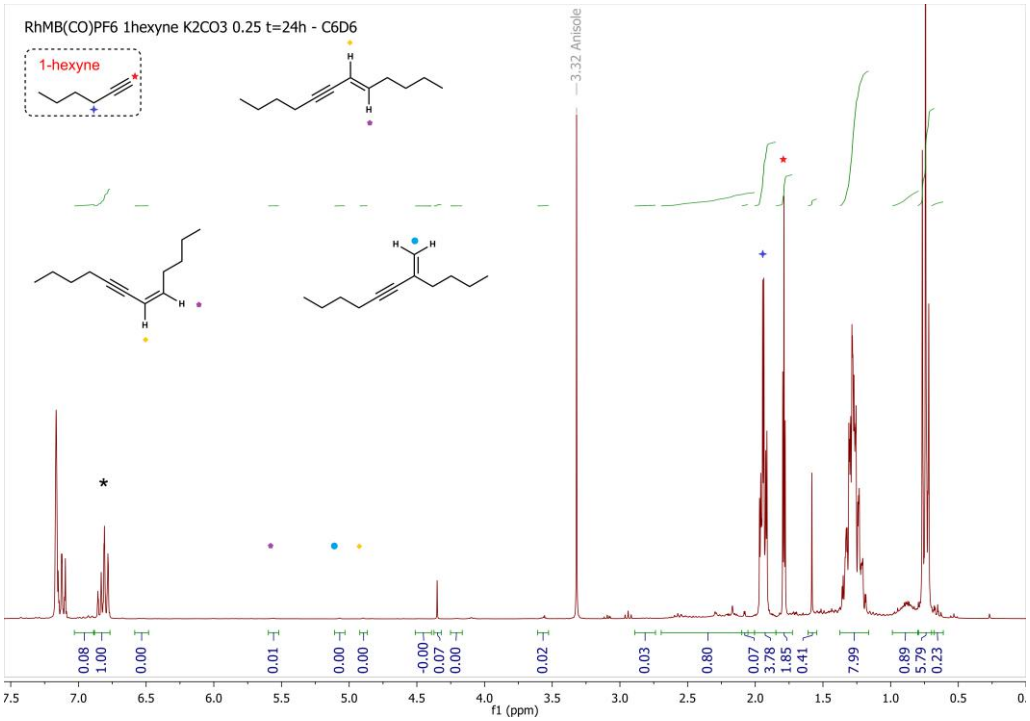


*Figure H.1–12: ^{1}H NMR spectra for the catalytic dimerization activity of 1-hexyne by **2b** in C_6D_6, recorded at t=24h.*

© University of Pretoria

H.1.5) Alkyne Hydroamination

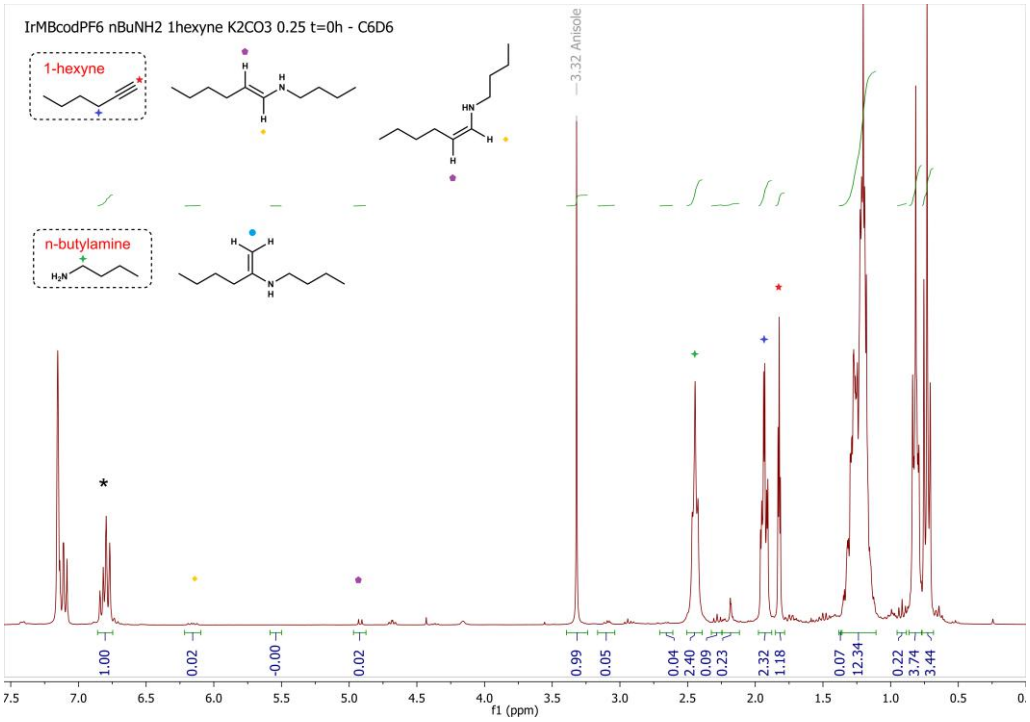


*Figure H.1–13: ^{1}H NMR spectra for the catalytic activity test of the hydroamination of 1-hexyne with n-butylamine by **1d** in C_6D_6, recorded at t=0h.*

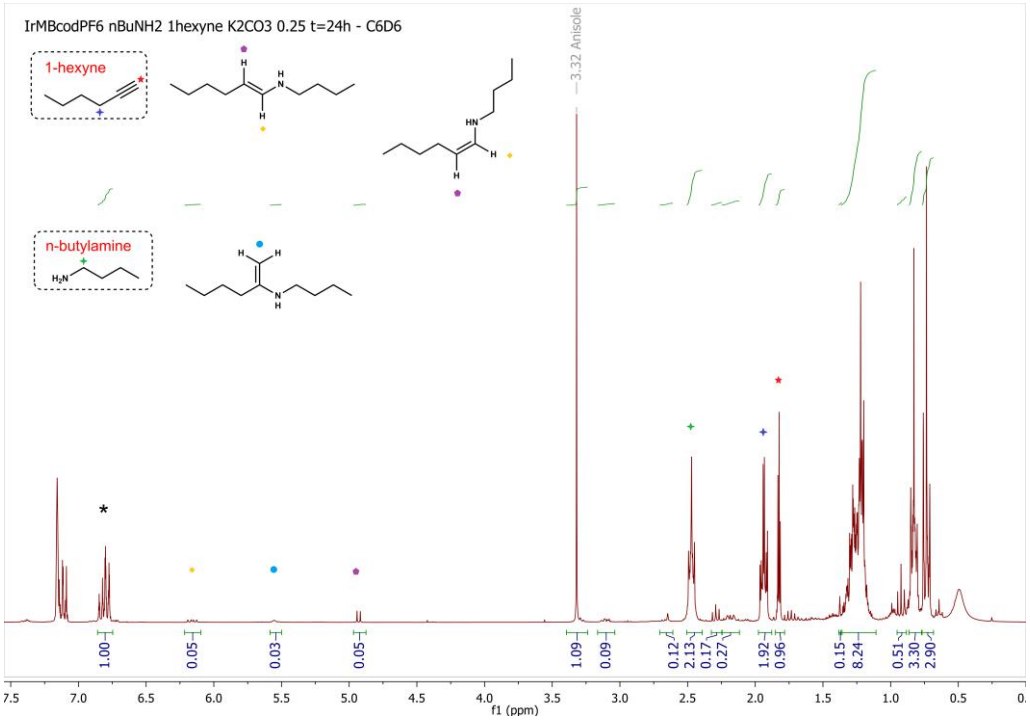


*Figure H.1–14: ^{1}H NMR spectra for the catalytic activity test of the hydroamination of 1-hexyne with n-butylamine by **1d** in C_6D_6, recorded at t=24h.*

© University of Pretoria

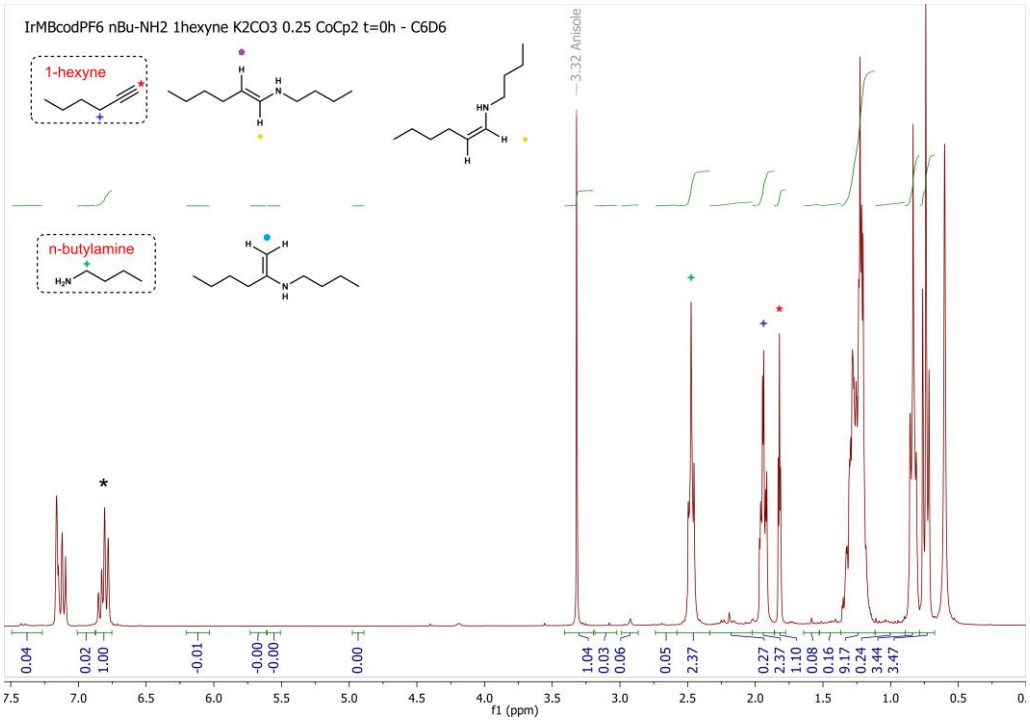


*Figure H.1–15: ^{1}H NMR spectra for the catalytic activity test of the hydroamination of 1-hexyne with n-butylamine by **1d** in C_6D_6, in the presence of the chemical reductant $CoCp_2$, recorded at t=0h.*

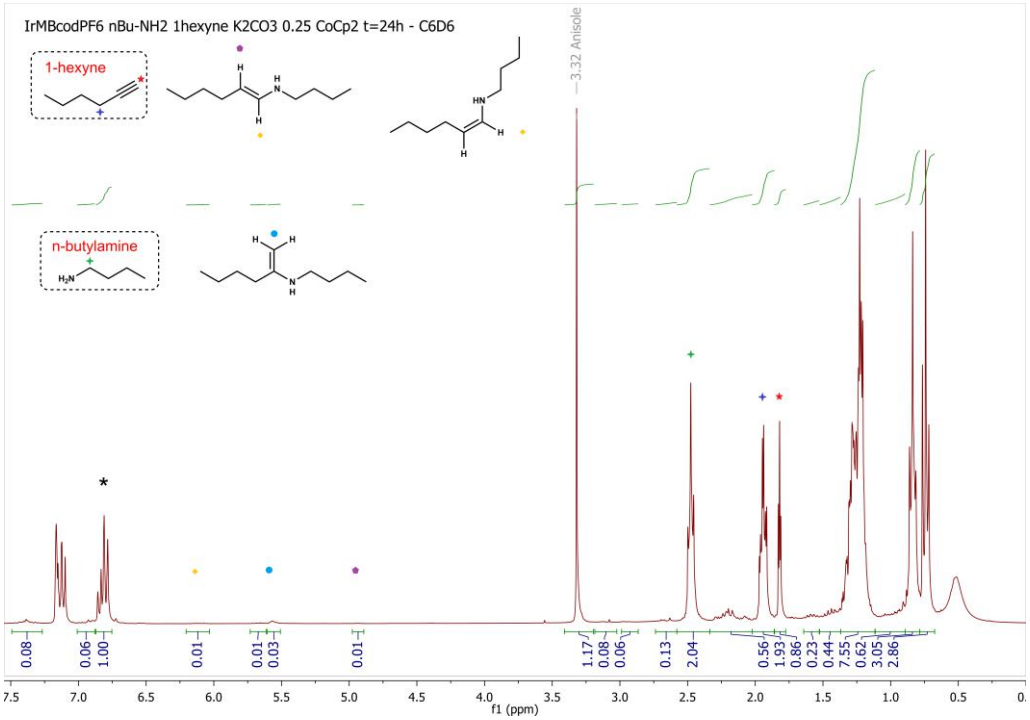


*Figure H.1–16: ^{1}H NMR spectra for the catalytic activity test of the hydroamination of 1-hexyne with n-butylamine by **1d** in C_6D_6, in the presence of the chemical reductant $CoCp_2$, recorded at t=24h.*

© University of Pretoria

H.1.1) Alkyne Hydrothiolation

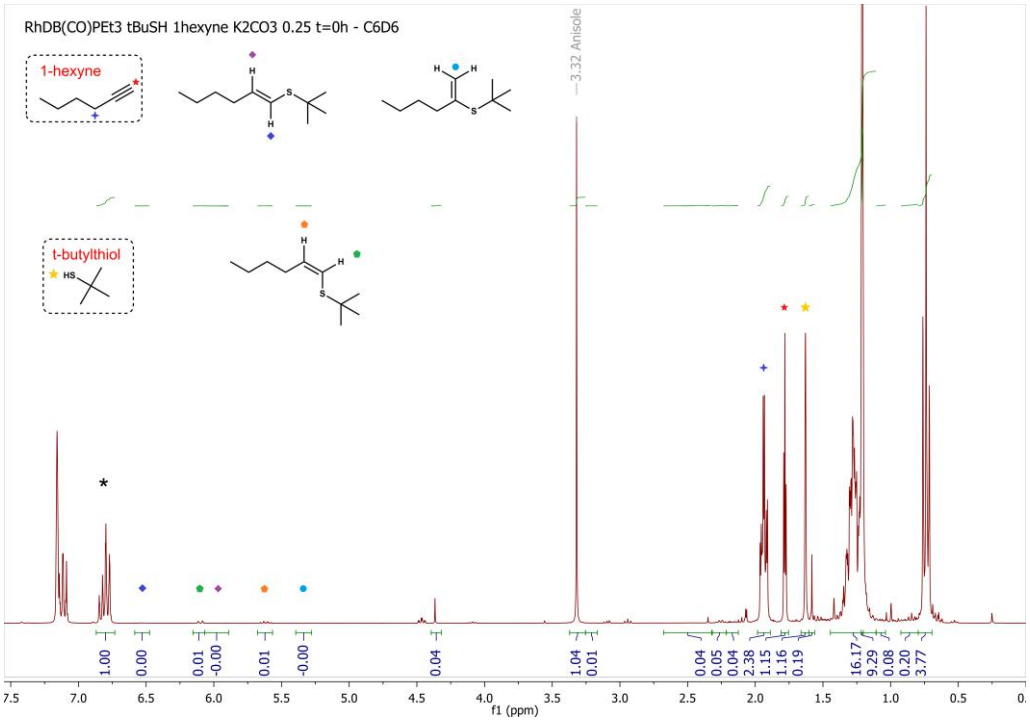


*Figure H.1–17: ^{1}H NMR spectra for the catalytic activity test of the hydrothiolation of 1-hexyne with t-butylthiol by **3a** in C_6D_6, recorded at t=0h.*

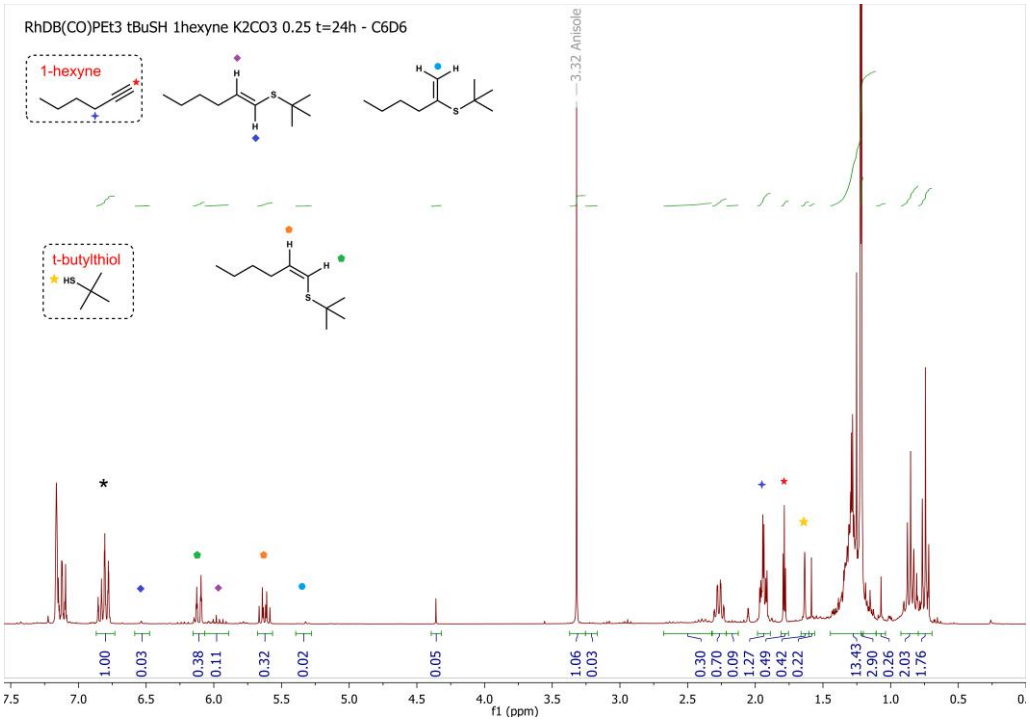


*Figure H.1–18: ^{1}H NMR spectra for the catalytic activity test of the hydrothiolation of 1-hexyne with t-butylthiol by **3a** in C_6D_6, recorded at t=24h.*

© University of Pretoria

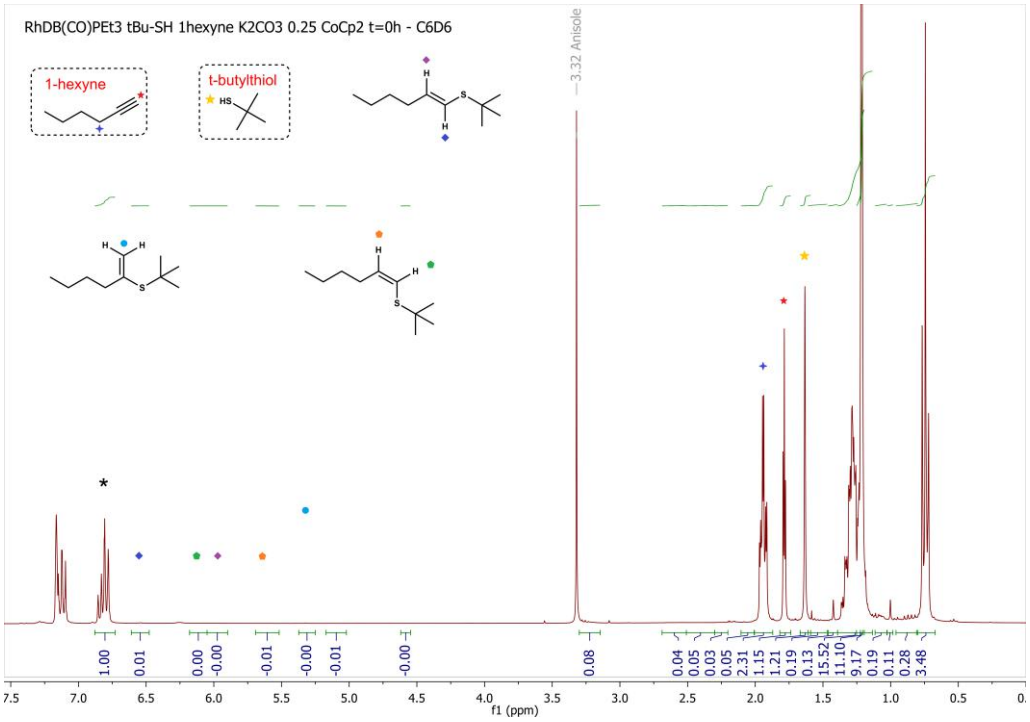


*Figure H.1–19: ^{1}H NMR spectra for the catalytic activity test of the hydrothiolation of 1-hexyne with t-butylthiol by **3a** in C_6D_6, in the presence of the chemical reductant $CoCp_2$, recorded at t=0h.*

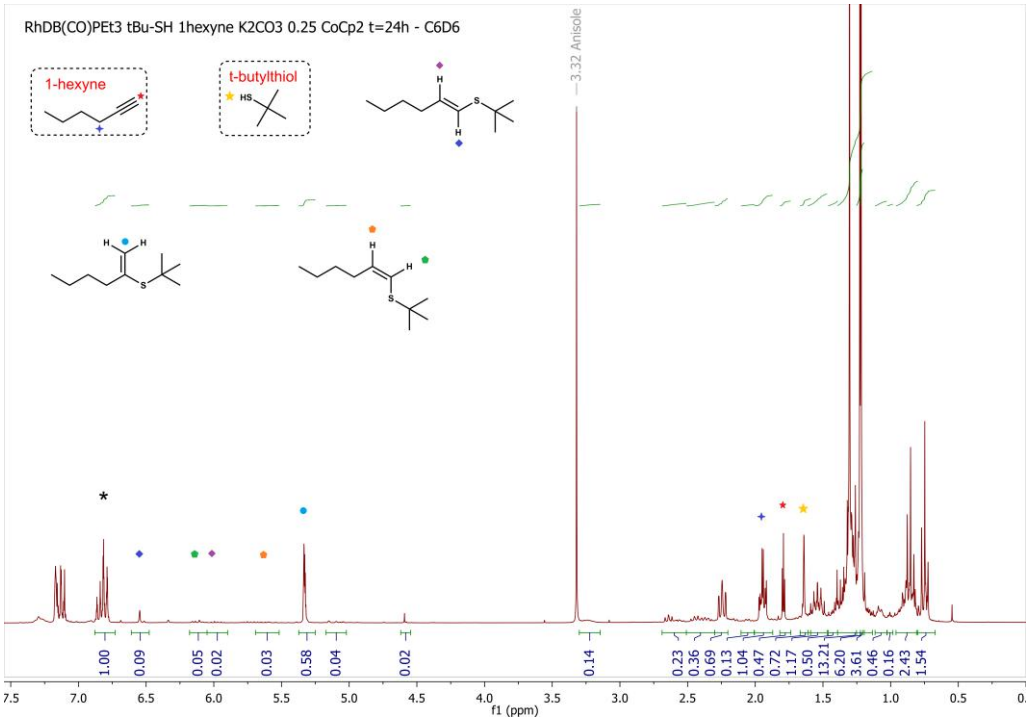


*Figure H.1–20: ^{1}H NMR spectra for the catalytic activity test of the hydrothiolation of 1-hexyne with t-butylthiol by **3a** in C_6D_6, in the presence of the chemical reductant $CoCp_2$, recorded at t=24h.*

© University of Pretoria

H.2) NMR scale Catalytic Activity Screening

H.2.1) Alkene Dimerization

H.2.1.i) Alkene dimerization – $CDCl_3$

Table H.2–1: Catalysis results for Alkene dimerization recorded in $CDCl_3$. Reactions performed with 2 mol% complex at 65 °C. Substrate 1 & 2: 1-hexene; Additives: 0.25 eq K_2CO_3. Conversion and Yield based on NMR integration. ‡ Yield in excess of Conversion % is likely due to the catalyst reacting with the products in addition to the substrate, resulting in the complex overlapping alkyl proton ^1H NMR peaks.

Complex	Catalyst Mass (mg)	Conversion (%)	Total Yield (%)	Yield of 1,1 (%)	Yield of 1,2 (%)	Ratio 1,1 : 1,2
1a	5.2	11.37	1.63	1.09	0.54	2:1
1b	4.8	14.51	2.31	2.31	0.00	2:0
1c	5.5	13.44	14.44 ‡	8.02	6.42	5:4
1d	5.1	20.21	5.77	5.77	0.00	6:0
2a	5.2	10.76	2.74	2.35	0.39	6:1
2b	5.0	11.91	0.40	0.40	0.00	-
2c	4.6	9.50	7.32	0.79	6.53	1:8
2d	5.3	16.38	7.16	5.32	1.84	3:1
3a	5.5	10.78	1.96	1.57	0.39	4:1
3b	5.0	17.41	0.80	0.80	0.00	1:0
4a	5.1	10.22	1.11	1.11	0.00	1:0
4b	4.5	14.55	1.83	1.22	0.61	2:1
4c	4.6	12.15	8.62	1.96	6.66	2:7
4d	5.5	13.93	6.10	6.10	0.00	6:0

H.2.1.ii) Alkene dimerization – C_6D_6

Table H.2–2: Catalysis results for Alkene dimerization recorded in C_6D_6. Reactions performed with 2 mol% complex at 80 °C. Substrate 1 & 2: 1-hexene; Additives: 0.25 eq K_2CO_3. Conversion and Yield based on NMR integration.

Complex	Catalyst Mass (mg)	Conversion (%)	Total Yield (%)	Yield of 1,1 (%)	Yield of 1,2 (%)	Ratio 1,1 : 1,2
1a	5.4	36.71	0.40	0.40	0.00	1:0
1b	5.4	92.68	0.20	0.00	0.20	0:1
1c	5.2	53.82	19.94	19.94	0.00	20:0
1d	5.1	48.75	10.81	0.00	10.81	0:11
2a	4.9	37.49	10.28	10.28	0.00	10:0
2b	5.4	56.57	6.23	6.23	0.00	6:0
2c	5.1	48.80	2.85	2.85	0.00	3:0
2d	4.8	35.12	2.37	0.00	2.37	0:2
3a	4.6	31.17	1.49	1.49	0.00	1:0
3b	4.7	49.41	8.25	8.25	0.00	8:0
4a	4.6	35.24	3.44	3.44	0.00	3:0
4b	4.8	77.54	1.38	0.39	0.99	2:5
4c	4.6	48.08	12.31	12.31	0.00	12:0
4d	4.9	36.21	8.82	0.38	8.44	1:22

© University of Pretoria

H.2.2) Alkene Hydroamination

H.2.2.i) Alkene hydroamination – $CDCl_3$

Table H.2–3: Catalysis results for Alkene hydroamination recorded in $CDCl_3$. Reactions performed with 2 mol% complex at 65 °C. Substrate 1: 1-hexene, Substrate 2: nBu-NH_2; Additives: 0.25 eq K_2CO_3. Conversion and Yield based on NMR integration. ‡ Yields in excess of substrate 2 Conversion are due to the formation of alkene dimerization products. † Yields are in excess of substrate 2 Conversion due to the catalyst reacting with the 1,1 products in addition to the substrate, and minimal dimerization by-products were observed. § Traces of dimerization noted.

Complex	Catalyst Mass (mg)	Conv. Sub.1 (%)	Conv. Sub.2 (%)	Total Yield (%)	Yield of 1,1 (%)	Yield of 1,2 (%)	Ratio 1,1 : 1,2
1a	5.2	29.32	12.13	19.81 ‡	13.65	6.16	2:1
1b	5.1	23.87	11.59	26.34 †	14.81	11.52	9:7
1c	4.8	15.46	3.04	7.66 ‡	5.54	2.11	5:2
1d	5.3	13.87	10.11	7.68 §	7.68	0.00	8:0
2a	4.7	7.78	10.47	4.30	1.24	3.06	2:5
2b	4.6	19.71	7.91	7.13 §	7.13	0.00	7:0
2c	5.2	7.89	2.48	6.48 ‡	1.48	5.00	2:7
2d	5.3	12.01	0.77	2.13 ‡	0.00	2.13	0:2
3a	5.3	13.72	11.70	5.84	0.00	5.84	0:6
3b	5.0	28.02	10.00	16.14 §	16.14	0.00	16:0
4a	4.5	23.78	15.08	26.84 †	18.65	8.20	16:7
4b	5.3	19.32	12.56	21.84 †	12.64	9.20	3:2
4c	5.2	8.14	1.51	6.58 ‡	6.58	0.00	7:0
4d	5.5	16.57	4.72	16.56 ‡	16.56	0.00	17:0

H.2.2.ii) Alkene hydroamination – C_6D_6

Table H.2–4: Catalysis results for Alkene hydroamination recorded in C_6D_6. Reactions performed with 2 mol% complex at 80 °C. Substrate 1: 1-hexene, Substrate 2: nBu-NH_2; Additives: 0.25 eq K_2CO_3. Conversion and Yield based on NMR integration. ‡ Yields in excess of substrate 2 Conversion are due to the formation of alkene dimerization products.

Complex	Catalyst Mass (mg)	Conv. Sub.1 (%)	Conv. Sub.2 (%)	Total Yield (%)	Yield of 1,1 (%)	Yield of 1,2 (%)	Ratio 1,1 : 1,2
1a	4.8	59.96	23.49	24.39 ‡	16.77	7.63	2:1
1b	4.6	52.84	23.08	12.52	10.18	2.35	4:1
1c	4.7	49.08	23.64	24.39 ‡	14.34	10.05	10:7
1d	5.4	63.51	9.41	4.39	4.39	0.00	4:0
2a	4.5	60.88	19.25	4.88	0.00	4.88	0:5
2b	4.8	75.94	25.27	7.21	5.74	1.47	4:1
2c	5.5	57.30	20.92	35.28 ‡	21.80	13.48	3:2
2d	4.8	30.37	6.97	1.10	0.83	0.28	3:1
3a	5.3	49.10	18.32	10.07	5.04	5.04	1:1
3b	4.6	91.20	25.00	5.36	4.51	0.86	11:2
4a	4.8	77.87	23.05	18.51	13.40	5.11	5:2
4b	4.7	83.80	18.28	5.87	4.00	1.87	2:1
4c	5.2	50.09	23.99	27.61 ‡	15.90	11.70	4:3
4d	5.0	28.72	10.88	7.16 ‡	5.74	1.42	4:1

© University of Pretoria

H.2.3) Alkene Hydrothiolation

H.2.3.i) Alkene hydrothiolation – $CDCl_3$

Table H.2–5: Catalysis results for Alkene hydrothiolation recorded in $CDCl_3$. Reactions performed with 2 mol% complex at 65 °C. Substrate 1: 1-hexene, Substrate 2: tBu-SH; Additives = 0.25 eq K_2CO_3. Conversion and Yield based on NMR integration. ‡ Yields in excess of substrate 2 Conversion are due to the formation of alkene dimerization products.

Complex	Catalyst Mass (mg)	Conv. Sub.1 (%)	Conv. Sub.2 (%)	Total Yield (%)	Yield of 1,1 (%)	Yield of 1,2 (%)	Ratio 1,1 : 1,2
1b	5.3	22.99	0.00	1.75 ‡	1.50	0.38	4:1
1c	4.8	15.59	0.00	0.77 ‡	0.77	0.00	1:0
1d	5.2	44.83	11.88	0.00	0.00	0.00	-
2b	4.8	22.38	0.00	1.34 ‡	1.34	0.00	1:0
2c	4.5	22.71	17.25	0.00	0.00	0.00	-
2d	4.8	15.15	1.15	0.00	0.00	0.00	-
3b	5.1	18.83	8.71	0.00	0.00	0.00	-
4b	5.0	33.62	41.37	0.00	0.00	0.00	-
4c	5.5	20.71	0.00	0.78 ‡	0.78	0.00	1:0
4d	4.2	20.66	1.90	3.81 ‡	3.27	0.54	6:1

H.2.3.ii) Alkene hydrothiolation – C_6D_6

Table H.2–6: Catalysis results for Alkene hydrothiolation recorded in C_6D_6. Reactions performed with 2 mol% complex at 80 °C. Substrate 1; 1-hexene, Substrate 2: tBu-SH; Additives = 0.25 eq K_2CO_3. Conversion and Yield based on NMR integration.

Complex	Catalyst Mass (mg)	Conv. Sub.1 (%)	Conv. Sub.2 (%)	Total Yield (%)	Yield of 1,1 (%)	Yield of 1,2 (%)	Ratio 1,1 : 1,2
1a	5.0	73.47	40.94	1.36	1.36	0.00	1:0
1b	4.7	78.15	46.65	1.78	1.64	0.14	12:1
1c	5.4	72.32	42.36	10.25	10.25	0.00	10:0
1d	5.3	64.31	35.41	17.08	11.67	5.42	2:1
2a	4.8	100.00	94.07	1.42	0.47	0.94	1:2
2b	5.0	82.91	55.39	3.66	3.53	0.13	27:1
2c	4.7	75.85	37.67	1.88	0.00	1.88	0:2
2d	4.8	55.31	32.02	0.00	0.00	0.00	-
3a	5.3	54.13	32.26	0.61	0.00	0.61	0:1
3b	5.0	55.71	32.18	1.01	0.43	0.58	3:4
4a	5.2	100.00	98.22	2.18	1.31	0.87	3:2
4b	4.5	61.78	38.14	1.64	0.82	0.82	1:1
4c	5.3	44.53	28.53	8.80	5.74	3.06	2:1
4d	4.6	57.83	18.84	11.03	9.77	1.25	8:1

© University of Pretoria

H.2.4) Alkyne Dimerization

H.2.4.i) Alkyne dimerization – $CDCl_3$

Table H.2–7: Catalysis results for Alkyne dimerization recorded in $CDCl_3$. Reactions performed with 2 mol% complex at 65 °C. Substrate 1 & 2: 1-hexyne; Additives: 0.25 eq K_2CO_3. Conversion and Yield based on NMR integration.

Complex	Catalyst Mass (mg)	Conversion (%)	Total Yield (%)	Yield of 1,1 (%)	Yield of 1,2 (%)	Ratio 1,1 : 1,2
1b	5.0	44.42	0.00	0.00	0.00	-
1c	4.7	11.82	0.00	0.00	0.00	-
1d	5.0	4.76	0.42	0.42	0.00	1:0
2a	4.8	22.77	0.74	0.74	0.00	1:0
2b	4.7	6.85	0.00	0.00	0.00	-
2c	5.3	3.95	0.00	0.00	0.00	-
2d	5.4	1.90	0.45	0.45	0.00	1:0
3a	5.4	10.27	0.00	0.00	0.00	-
3b	4.5	11.17	0.00	0.00	0.00	-
4a	5.0	5.52	0.00	0.00	0.00	-
4b	5.4	18.32	4.20	1.58	2.63	3:5
4c	4.6	12.26	2.10	1.68	0.42	4:1
4d	4.7	8.79	0.82	0.41	0.41	1:1

H.2.4.ii) Alkyne dimerization – C_6D_6

Table H.2–8: Catalysis results for Alkyne dimerization recorded in C_6D_6. Reactions performed with 2 mol% complex at 80 °C. Substrate 1 & 2: 1-hexyne; Additives: 0.25 eq K_2CO_3. Conversion and Yield based on NMR integration.

Complex	Catalyst Mass (mg)	Conversion (%)	Total Yield (%)	Yield of 1,1 (%)	Yield of 1,2 (%)	Ratio 1,1 : 1,2
1a	5.3	19.95	1.39	0.46	0.93	1:2
1b	4.9	58.00	1.35	0.45	0.90	1:2
1c	4.6	81.38	0.00	0.00	0.00	-
1d	5.2	14.56	0.44	0.00	0.44	0:1
2a	4.8	20.25	0.00	0.00	0.00	-
2b	4.6	16.89	0.44	0.00	0.44	0:1
2c	5.3	9.84	3.90	3.90	0.00	4:0
2d	4.5	16.59	0.00	0.00	0.00	-
3a	4.9	19.02	0.00	0.00	0.00	-
3b	4.9	23.34	0.94	0.94	0.00	1:0
4a	4.5	16.38	0.00	0.00	0.00	-
4b	4.9	31.37	0.00	0.00	0.00	-
4c	5.2	24.73	1.23	0.00	1.23	0:1
4d	5.3	13.49	2.37	0.00	2.37	0:2

© University of Pretoria

H.2.5) Alkyne Hydroamination

H.2.5.i) Alkyne hydroamination – $CDCl_3$

Table H.2–9: Catalysis results for Alkyne hydroamination recorded in $CDCl_3$. Reactions performed with 2 mol% complex at 65 °C. Substrate 1: 1-hexyne, Substrate 2: nBu-NH_2; Additives = 0.25 eq K_2CO_3. Conversion and Yield based on NMR integration. ‡ Yields in excess of substrate 2 Conversion are due to the formation of alkyne dimerization products.

Complex	Catalyst Mass (mg)	Conv. Sub.1 (%)	Conv. Sub.2 (%)	Total Yield (%)	Yield of 1,1 (%)	Yield of 1,2 (%)	Ratio 1,1 : 1,2
1a	4.7	0.00	11.45	3.33	2.50	0.83	3:1
1b	5.1	0.00	16.52	1.35	0.90	0.45	2:1
1c	4.7	0.00	10.80	1.27	1.27	0.00	1:0
1d	5.4	40.83	12.55	0.00	0.00	0.00	-
2a	4.7	10.20	6.90	0.99	0.50	0.50	1:1
2b	4.8	12.96	10.79	0.00	0.00	0.00	-
2c	5.0	9.43	2.05	1.42	0.94	0.47	2:1
2d	4.5	16.05	5.62	0.00	0.00	0.00	-
3a	5.1	3.75	9.30	0.37	0.37	0.00	1:0
3b	4.5	12.26	14.73	0.00	0.00	0.00	-
4a	4.8	7.69	6.86	0.00	0.00	0.00	-
4b	4.9	11.24	14.59	1.02	0.51	0.51	1:1
4c	5.2	20.54	0.00	3.52	2.64 ‡	0.88	3:1
4d	5.0	32.14	12.27	0.90	0.45	0.45	1:1

H.2.5.ii) Alkyne hydroamination – C_6D_6

Table H.2–10: Catalysis results for Alkyne hydroamination recorded in C_6D_6. Reactions performed with 2 mol% complex at 80 °C. Substrate 1: 1-hexyne, Substrate 2: nBu-NH_2; Additives = 0.25 eq K_2CO_3. Conversion and Yield based on NMR integration. § Orange reaction mixture changed colour to purple during reflux.

Complex	Catalyst Mass (mg)	Conv. Sub.1 (%)	Conv. Sub.2 (%)	Total Yield (%)	Yield of 1,1 (%)	Yield of 1,2 (%)	Ratio 1,1 : 1,2
1a	4.7	14.48	9.95	3.75	2.34	1.41	5:3
1b §	5.2	22.53	17.31	3.25	1.62	1.62	1:1
1c	5.3	20.23	12.46	3.85	2.57	1.28	2:1
1d	5.0	17.19	11.51	3.85	2.56	1.28	2:1
2a	4.7	10.38	5.44	0.98	0.98	0.00	1:0
2b §	4.6	14.36	7.44	1.60	1.20	0.40	3:1
2c	4.9	17.78	21.13	2.98	2.13	0.85	5:2
2d	5.0	7.43	5.27	2.43	2.43	0.00	2:0
3a	4.9	18.65	10.98	0.89	0.89	0.00	1:0
3b §	4.7	11.68	12.67	1.69	0.84	0.84	1:1
4a	4.7	9.46	13.36	1.63	0.41	1.22	1:3
4b §	4.7	36.00	14.51	2.18	0.87	1.31	2:3
4c	4.9	23.87	17.27	3.59	1.99	1.59	5:4
4d	4.7	19.33	7.48	6.27	3.37	2.89	7:6

© University of Pretoria

H.2.6) Alkyne Hydrothiolation

H.2.6.i) Alkyne hydrothiolation – $CDCl_3$

Table H.2–11: Catalysis results for Alkyne hydrothiolation recorded in $CDCl_3$. Reactions performed with 2 mol% complex at 65 °C. Substrate 1: 1-hexyne, Substrate 2: tBu-SH; Additives = 0.25 eq K_2CO_3. Conversion and Yield based on NMR integration. ‡ Yields in excess of substrate 2 Conversion are due to the formation of alkyne dimerization products. † Yields are in excess of substrate 1 Conversion due to the catalyst reacting with the alkene products in addition to the alkyne substrate. No dimerization by-products were observed.

Complex	Catalyst Mass (mg)	Conv. Sub.1 (%)	Conv. Sub.2 (%)	Total Yield (%)	Yield of 1,1–*Z* (%)	Yield of 1,1–*E* (%)	Yield of 1,2 (%)	Ratio 1,1 : 1,2	% ee^E
1a	5.2	28.53	29.34	14.61	9.07	5.04	0.50	28:1	36
1b	5.3	53.08	51.72	39.91	12.70	25.40	1.81	21:1	67
1c	5.5	16.80	22.78	18.63 †	0.00	18.63	0.00	19:0	100
1d	5.5	12.37	17.40	12.75 †	0.00	12.75	0.00	13:0	100
2a	5.2	26.69	19.29	12.65	4.38	8.27	0.00	13:0	65
2b	5.0	54.42	52.87	48.71	12.61	34.96	1.15	42:1	73
2c	4.6	6.90	6.84	3.67	2.75	0.92	0.00	4:0	25
2d	5.0	9.59	10.31	9.40	0.00	9.40	0.00	9:0	100
3a	4.9	16.26	11.80	7.08	2.18	4.90	0.00	7:0	69
4a	4.7	28.52	17.17	17.19 ‡	5.73	10.32	1.15	14:1	64
4b	4.9	46.25	44.85	39.18	7.02	31.58	0.58	67:1	82
4c	4.7	73.85	61.32	58.48	10.38	47.40	0.69	21:1	82
4d	4.9	50.70	58.48	53.00 †	9.22	43.32	0.46	114:1	82

H.2.6.ii) Alkyne hydrothiolation – C_6D_6

Table H.2–12: Catalysis results for Alkyne hydrothiolation recorded in C_6D_6. Reactions performed with 2 mol% complex at 80 °C. Substrate 1: 1-hexyne, Substrate 2: tBu-SH; Additives = 0.25 eq K_2CO_3. Conversion and Yield based on NMR integration.

Complex	Catalyst Mass (mg)	Conv. Sub.1 (%)	Conv. Sub.2 (%)	Total Yield (%)	Yield of 1,1–*Z* (%)	Yield of 1,1–*E* (%)	Yield of 1,2 (%)	Ratio 1,1 : 1,2	% ee^E
1a	5.4	58.19	74.72	34.26	9.72	23.61	0.93	33:1	71
1b	4.6	74.81	75.87	53.46	12.89	37.71	2.86	51:3	75
1c	4.9	53.81	65.94	40.43	0.00	38.83	1.60	24:1	100
1d	4.7	46.21	61.57	15.00	0.00	11.67	3.33	7:2	100
2a	4.6	42.64	55.98	23.93	7.67	16.25	0.00	24:0	68
2b	4.9	78.97	86.80	55.98	25.64	29.91	0.43	129:1	54
2c	4.6	31.72	60.54	18.31	4.34	13.01	0.96	18:1	75
2d	5.1	29.66	25.61	17.00	2.68	14.32	0.00	17:0	84
3a	4.7	52.01	68.78	35.90	5.98	29.06	0.85	41:1	83
3b	4.9	71.82	79.38	51.55	25.78	23.87	1.91	26:1	48
4a	4.8	66.25	71.54	47.21	9.44	23.18	14.59	9:4	71
4b	5.3	71.52	79.36	62.00	14.86	36.94	10.19	5:1	71
4c	5.5	41.21	37.27	22.40	0.00	20.80	1.60	13:1	100
4d	4.7	65.07	81.99	41.36	0.00	37.97	3.39	11:1	100

© University of Pretoria

Appendix I: Catalysis – Electrocatalysis Studies

I.1) Electrocatalytic CO_2 Reduction

I.1.1) DippBIAN

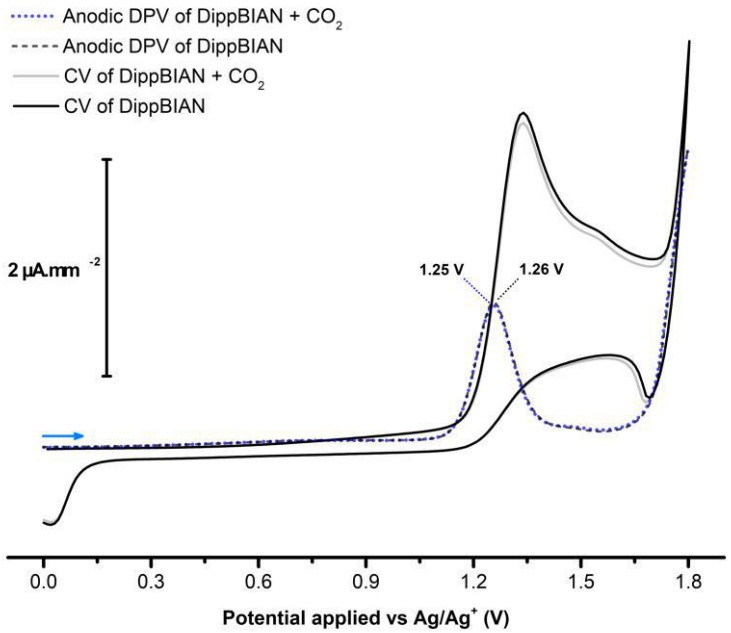


Figure I.1–1: Anodic CVs and DPVs of the free DippBIAN ligand recorded in CH_2Cl_2 saturated with either CO_2 (g) or Ar (g), with 1.0 mM analyte and 0.1 M $TBAPF_6$ supporting electrolyte.

© University of Pretoria

I.1.2) MesBIAN

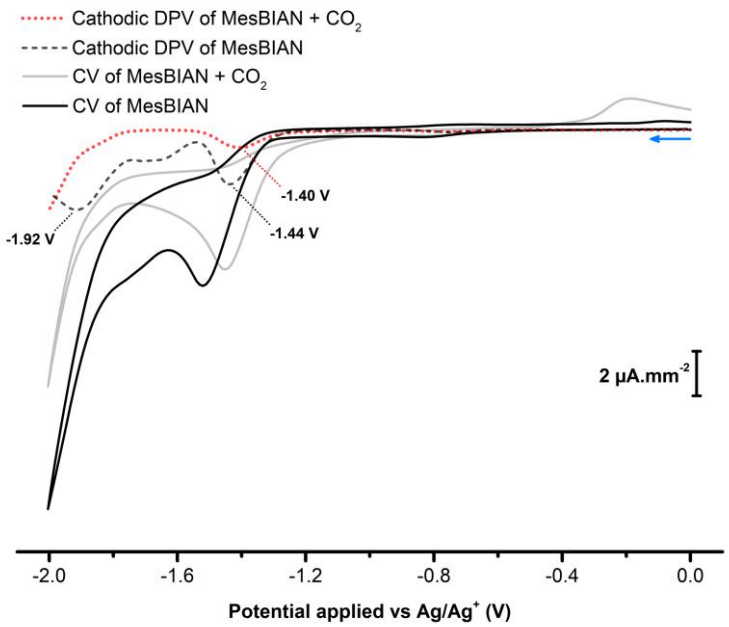


Figure I.1–2: Cathodic CVs and DPVs of the free MesBIAN ligand recorded in CH_2Cl_2 saturated with either CO_2 (g) or Ar (g), with 1.0 mM analyte and 0.1 M $TBAPF_6$ supporting electrolyte.

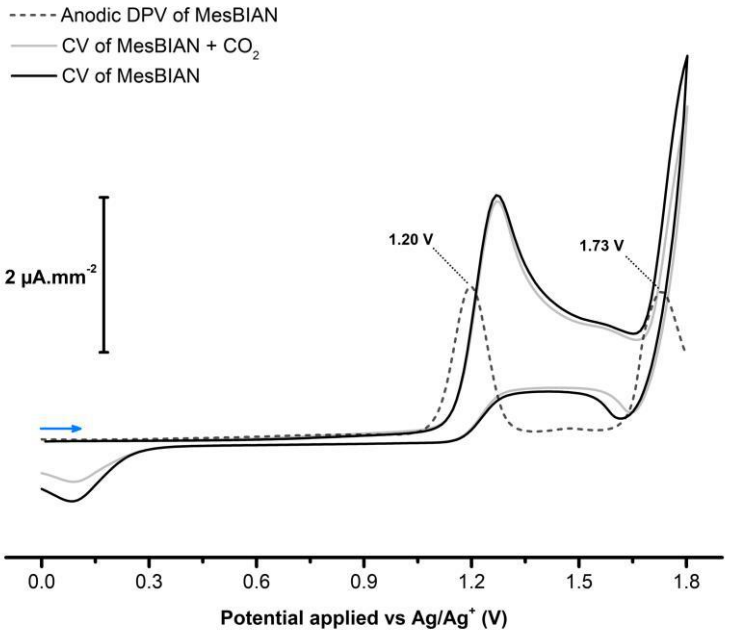


Figure I.1–3: Anodic CVs and DPVs of the free MesBIAN ligand recorded in CH_2Cl_2 saturated with either CO_2 (g) or Ar (g), with 1.0 mM analyte and 0.1 M $TBAPF_6$ supporting electrolyte.

© University of Pretoria

I.1.3) **1a** [RhDB(cod)]PF_6

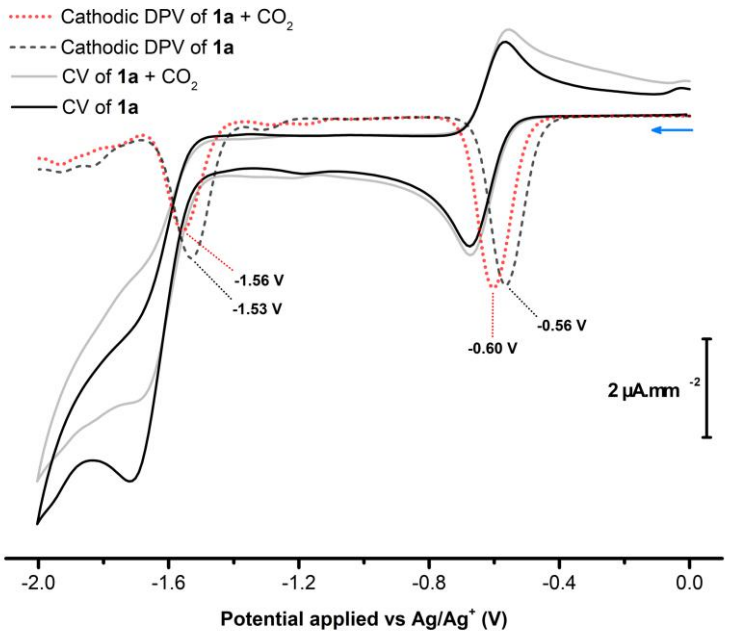


*Figure I.1–4: Cathodic CVs and DPVs of **1a** recorded in CH_2Cl_2 saturated with either CO_2 (g) or Ar (g), with 1.0 mM analyte and 0.1 M $TBAPF_6$ supporting electrolyte.*

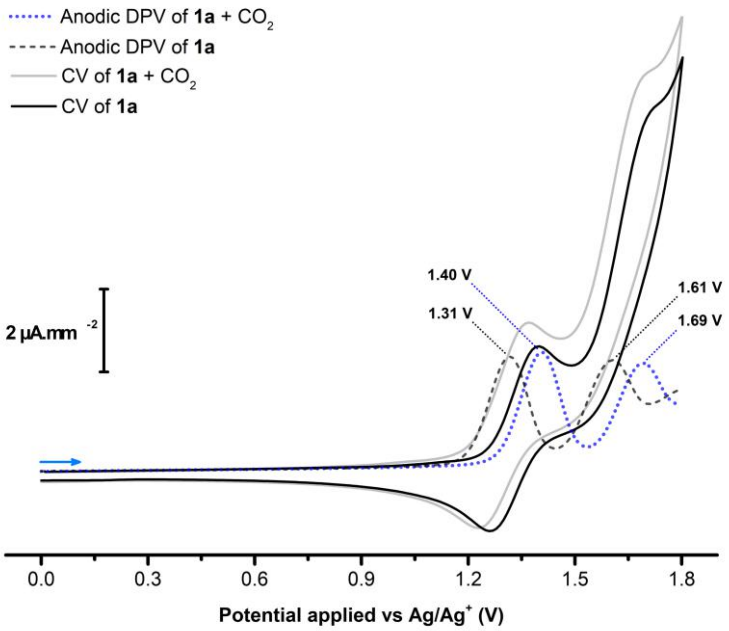


*Figure I.1–5: Anodic CVs and DPVs of **1a** recorded in CH_2Cl_2 saturated with either CO_2 (g) or Ar (g), with 1.0 mM analyte and 0.1 M $TBAPF_6$ supporting electrolyte.*

© University of Pretoria

I.1.4) **1b** [RhMB(cod)]PF_6

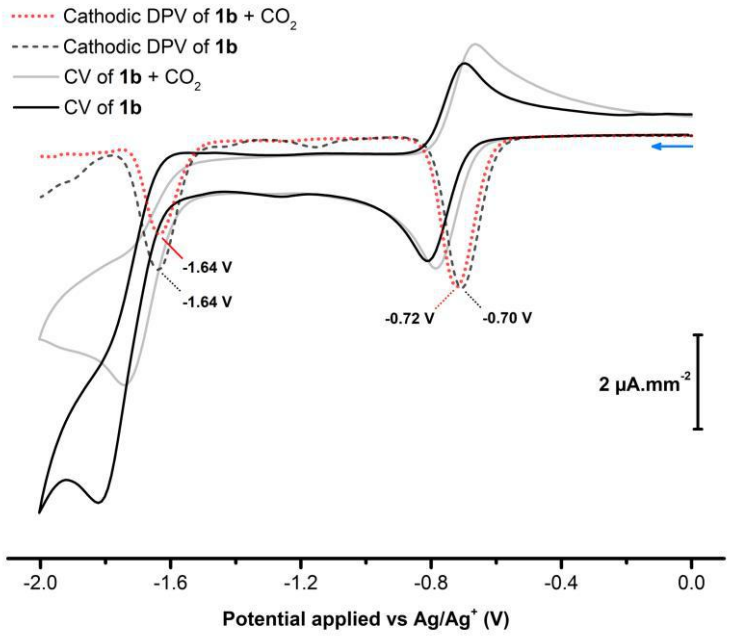


*Figure I.1–6: Cathodic CVs and DPVs of **1b** recorded in CH_2Cl_2 saturated with either CO_2 (g) or Ar (g), with 1.0 mM analyte and 0.1 M $TBAPF_6$ supporting electrolyte.*

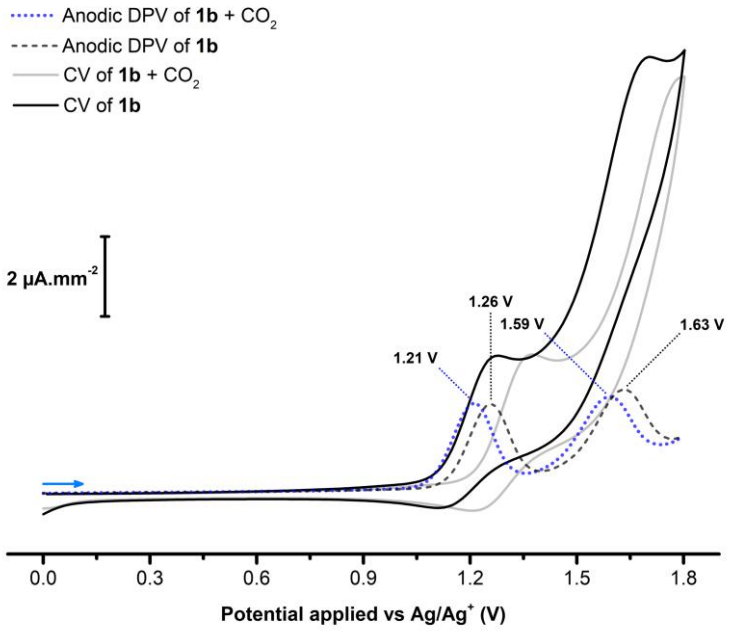


*Figure I.1–7: Anodic CVs and DPVs of **1b** recorded in CH_2Cl_2 saturated with either CO_2 (g) or Ar (g), with 1.0 mM analyte and 0.1 M $TBAPF_6$ supporting electrolyte.*

© University of Pretoria

I.1.5) **1c** [IrDB(cod)]PF_6

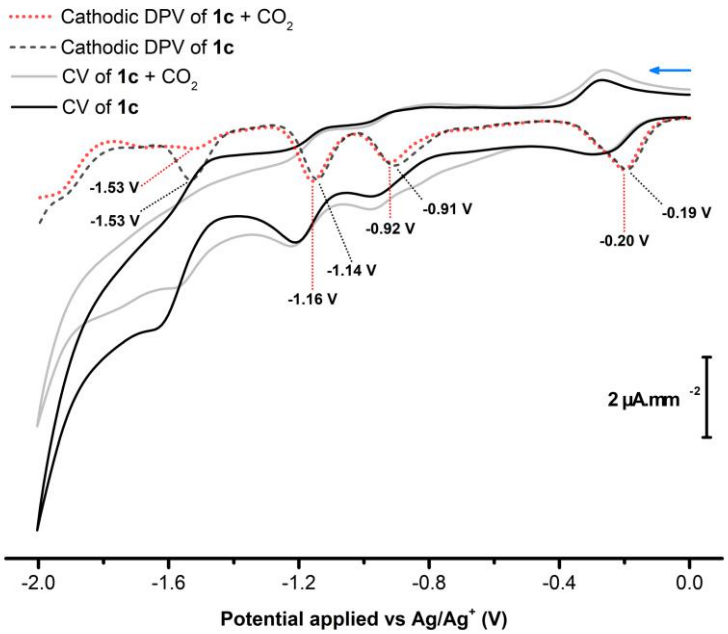


*Figure I.1–8: Cathodic CVs and DPVs of **1c** recorded in CH_2Cl_2 saturated with either CO_2 (g) or Ar (g), with 1.0 mM analyte and 0.1 M $TBAPF_6$ supporting electrolyte.*

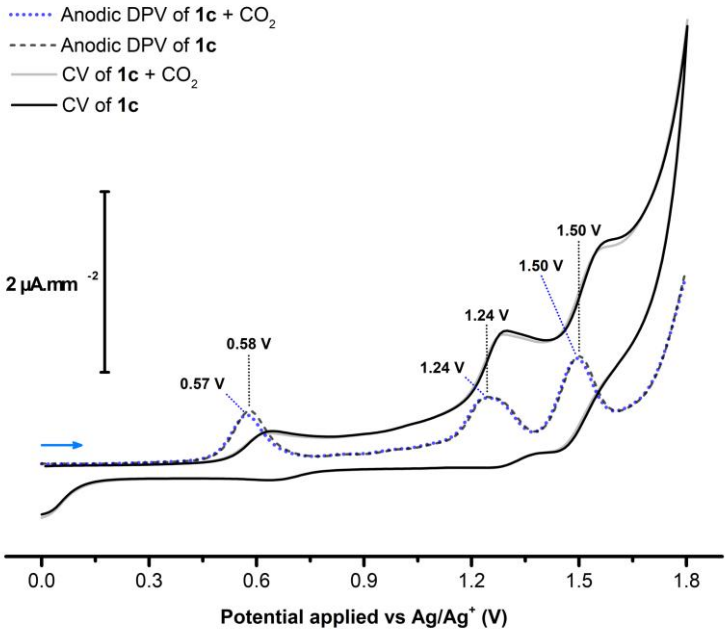


*Figure I.1–9: Anodic CVs and DPVs of **1c** recorded in CH_2Cl_2 saturated with either CO_2 (g) or Ar (g), with 1.0 mM analyte and 0.1 M $TBAPF_6$ supporting electrolyte.*

© University of Pretoria

I.1.6) **1d** [IrMB(cod)]PF_6

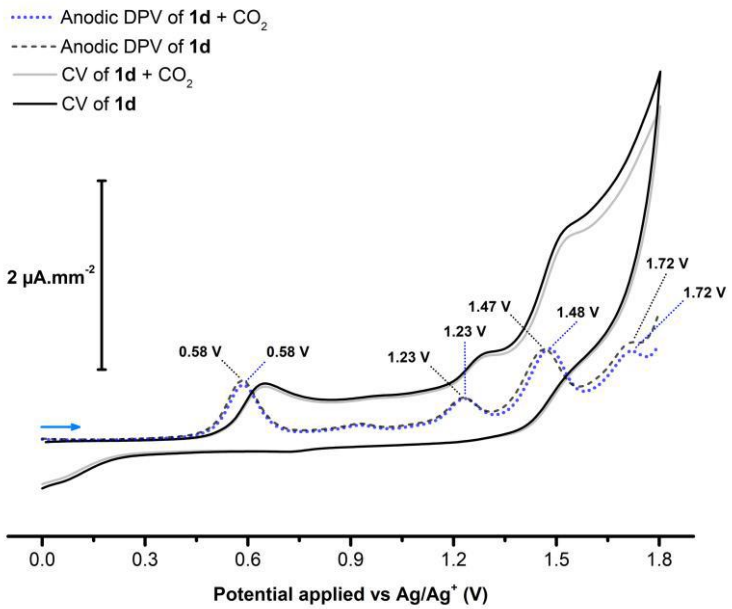


*Figure I.1–10: Anodic CVs and DPVs of **1d** recorded in CH_2Cl_2 saturated with either CO_2 (g) or Ar (g), with 1.0 mM analyte and 0.1 M $TBAPF_6$ supporting electrolyte.*

© University of Pretoria

I.1.7) **2a** $[RhDB(CO)_2]PF_6$

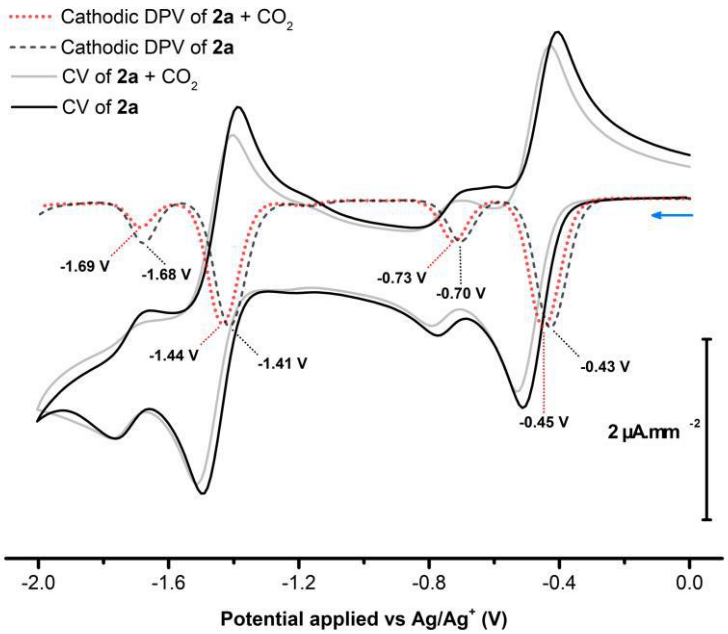


*Figure I.1–11: Cathodic CVs and DPVs of **2a** recorded in CH_2Cl_2 saturated with either CO_2 (g) or Ar (g), with 1.0 mM analyte and 0.1 M $TBAPF_6$ supporting electrolyte.*

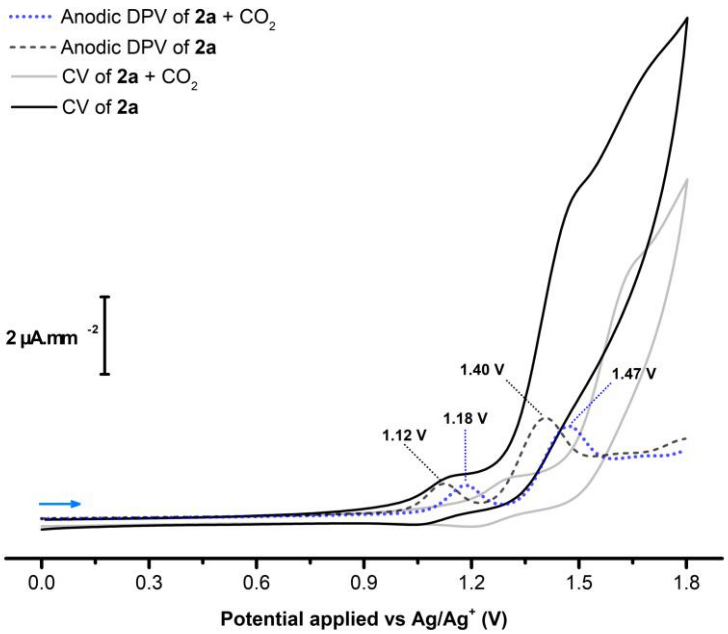


*Figure I.1–12: Anodic CVs and DPVs of **2a** recorded in CH_2Cl_2 saturated with either CO_2 (g) or Ar (g), with 1.0 mM analyte and 0.1 M $TBAPF_6$ supporting electrolyte.*

© University of Pretoria

I.1.8) **2b** $[RhMB(CO)_2]PF_6$

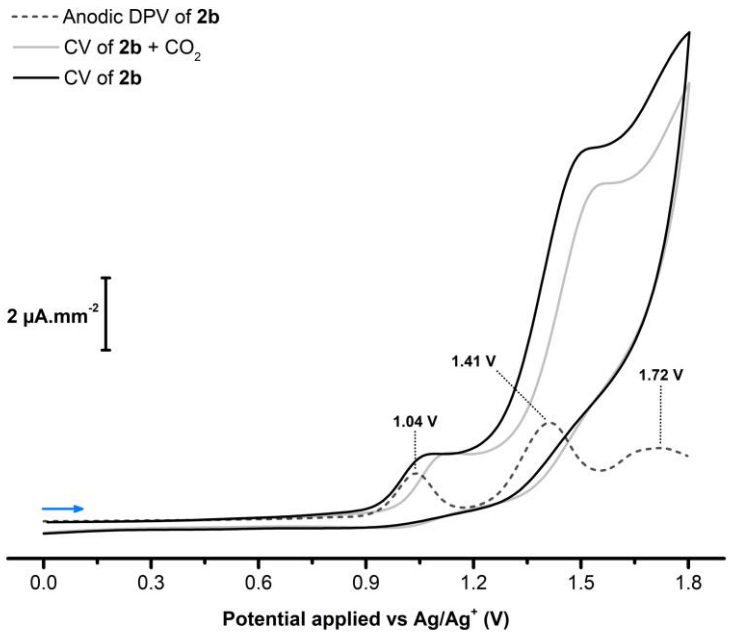


*Figure I.1–13: Anodic CVs and DPVs of **2b** recorded in CH_2Cl_2 saturated with either CO_2 (g) or Ar (g), with 1.0 mM analyte and 0.1 M $TBAPF_6$ supporting electrolyte.*

© University of Pretoria

I.1.9) **2c** $[IrDB(CO)_2]PF_6$

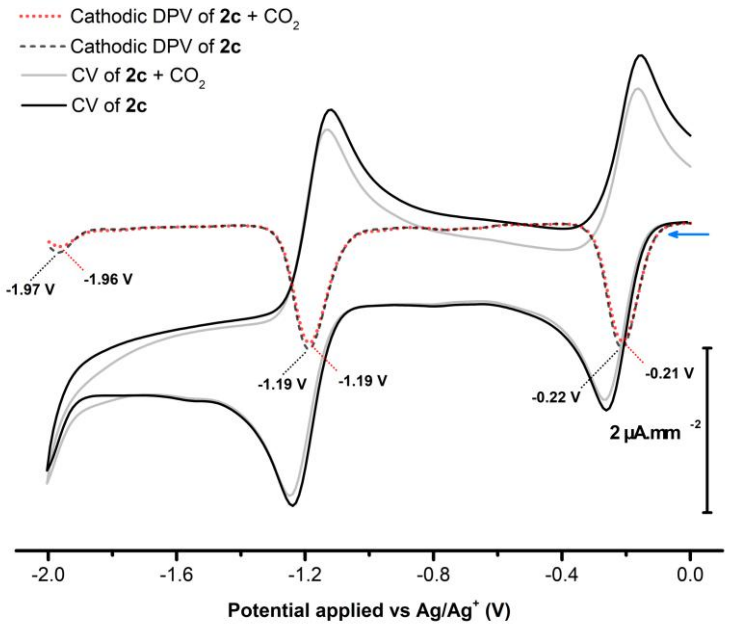


*Figure I.1–14: Cathodic CVs and DPVs of **2c** recorded in CH_2Cl_2 saturated with either CO_2 (g) or Ar (g), with 1.0 mM analyte and 0.1 M $TBAPF_6$ supporting electrolyte.*

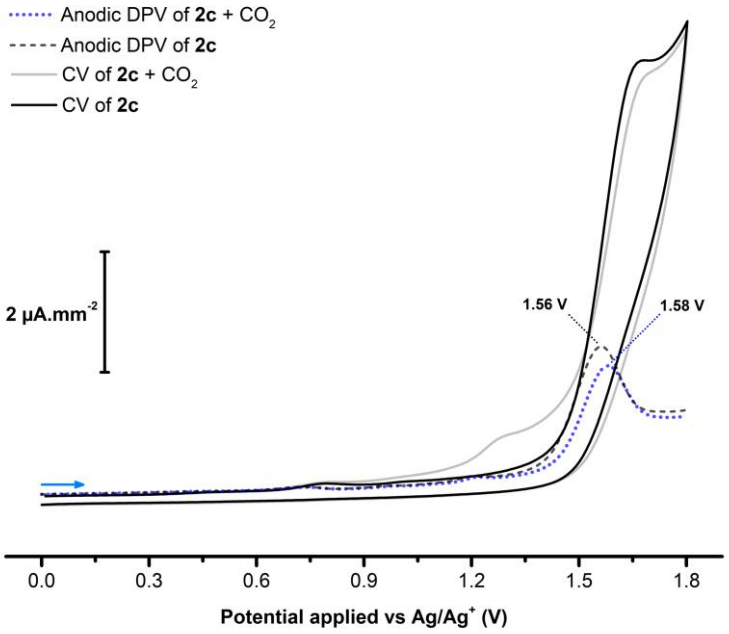


*Figure I.1–15: Anodic CVs and DPVs of **2c** recorded in CH_2Cl_2 saturated with either CO_2 (g) or Ar (g), with 1.0 mM analyte and 0.1 M $TBAPF_6$ supporting electrolyte.*

© University of Pretoria

I.1.10) **2d** $[IrMB(CO)_2]PF_6$

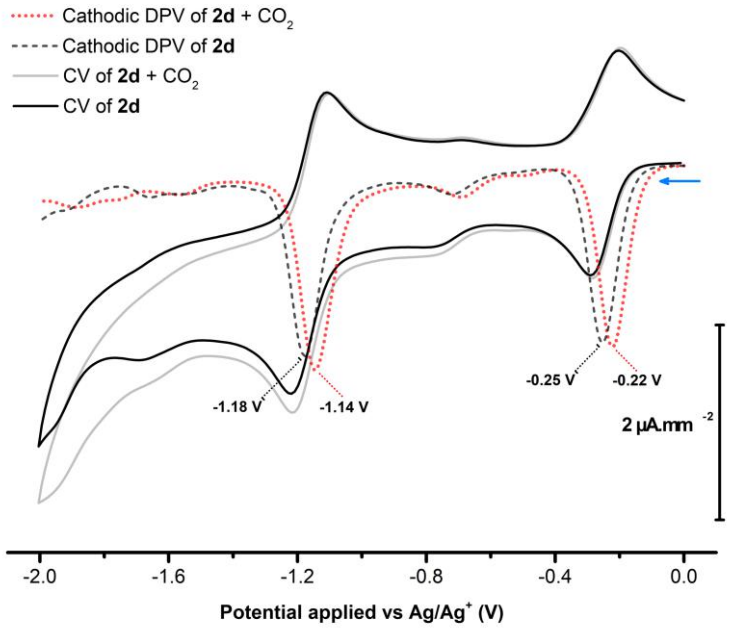


*Figure I.1–16: Cathodic CVs and DPVs of **2d** recorded in CH_2Cl_2 saturated with either CO_2 (g) or Ar (g), with 1.0 mM analyte and 0.1 M $TBAPF_6$ supporting electrolyte.*

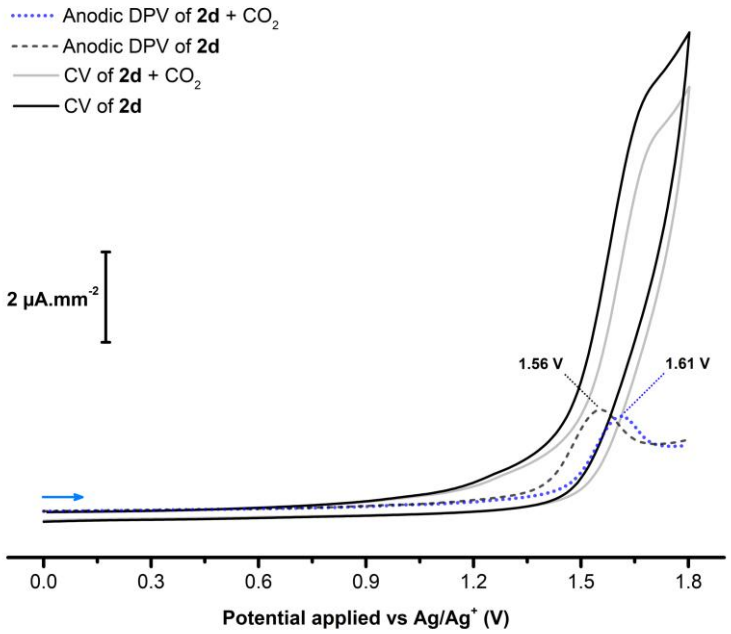


*Figure I.1–17: Anodic CVs and DPVs of **2d** recorded in CH_2Cl_2 saturated with either CO_2 (g) or Ar (g), with 1.0 mM analyte and 0.1 M $TBAPF_6$ supporting electrolyte.*

© University of Pretoria

I.1.11) **3a** [RhDB(CO)(PEt_3)]PF_6

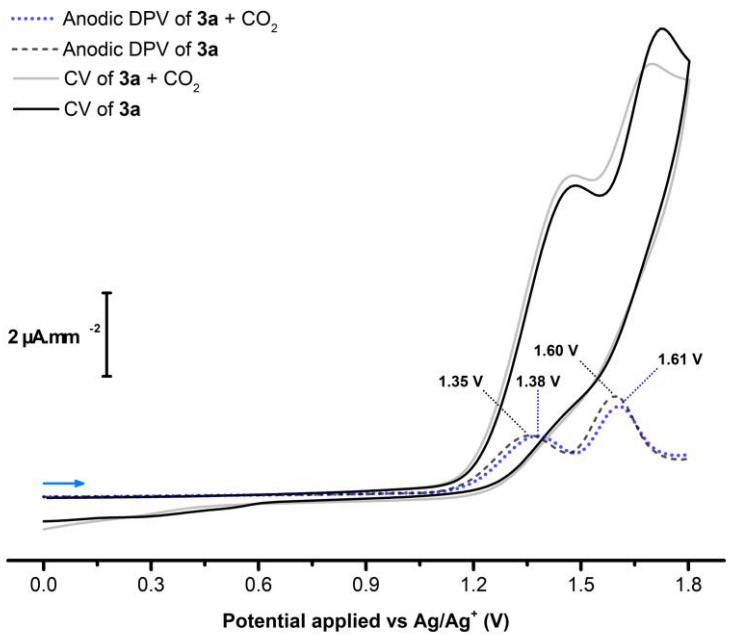


*Figure I.1–18: Anodic CVs and DPVs of **3a** recorded in CH_2Cl_2 saturated with either CO_2 (g) or Ar (g), with 1.0 mM analyte and 0.1 M $TBAPF_6$ supporting electrolyte.*

© University of Pretoria

I.1.12) **3b** [RhMB(CO)(PEt_3)]PF_6

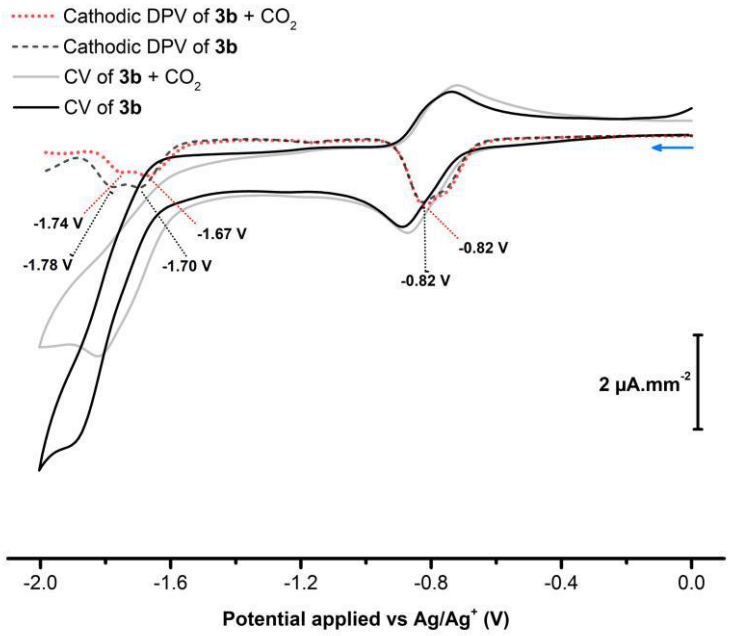


*Figure I.1–19: Cathodic CVs and DPVs of **3b** recorded in CH_2Cl_2 saturated with either CO_2 (g) or Ar (g), with 1.0 mM analyte and 0.1 M $TBAPF_6$ supporting electrolyte.*

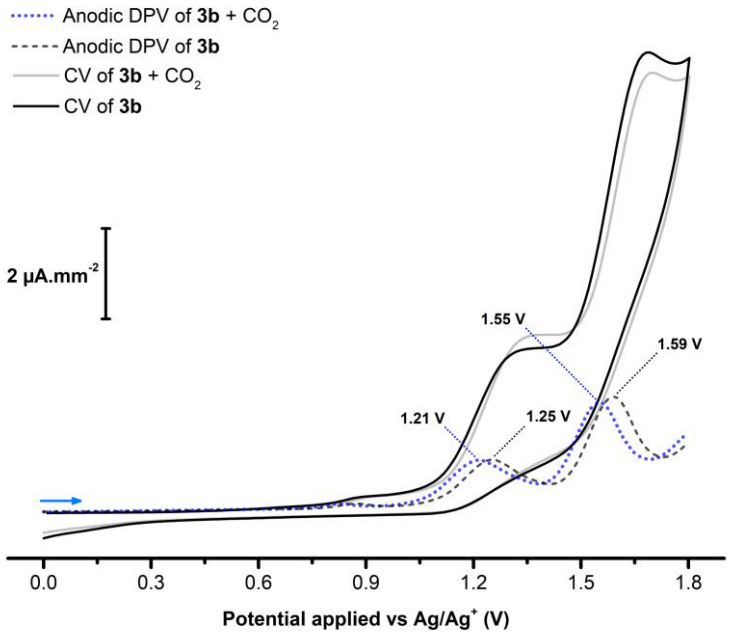


*Figure I.1–20: Anodic CVs and DPVs of **3b** recorded in CH_2Cl_2 saturated with either CO_2 (g) or Ar (g), with 1.0 mM analyte and 0.1 M $TBAPF_6$ supporting electrolyte.*

© University of Pretoria

I.1.13) **4a** [RhDB(cod)Cl]

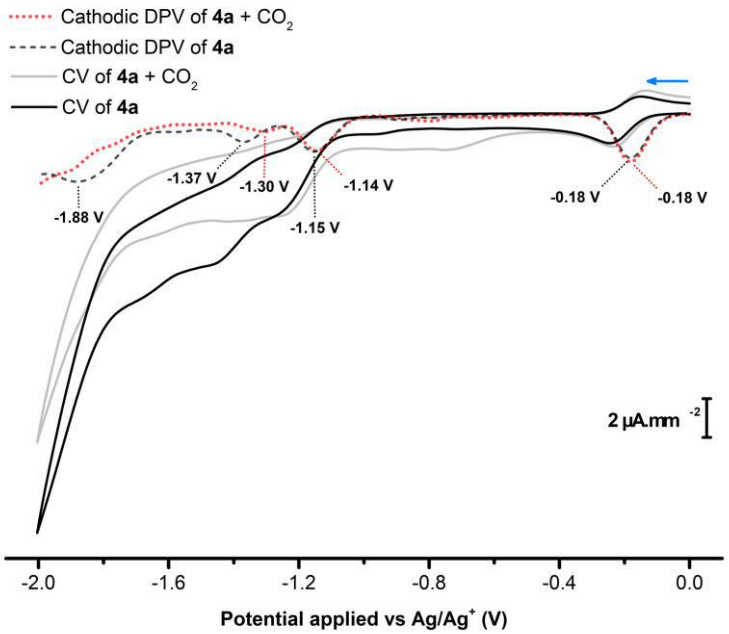


*Figure I.1–21: Cathodic CVs and DPVs of **4a** recorded in CH_2Cl_2 saturated with either CO_2 (g) or Ar (g), with 1.0 mM analyte and 0.1 M $TBAPF_6$ supporting electrolyte.*

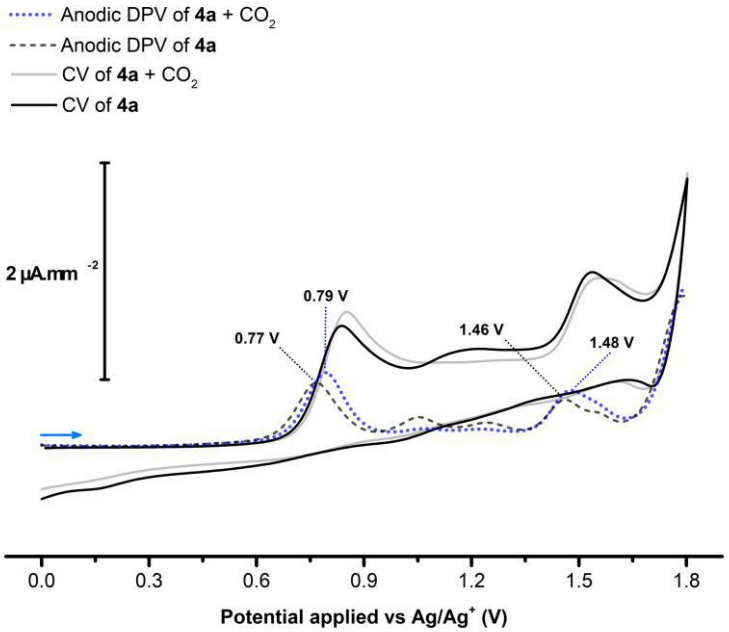


*Figure I.1–22: Anodic CVs and DPVs of **4a** recorded in CH_2Cl_2 saturated with either CO_2 (g) or Ar (g), with 1.0 mM analyte and 0.1 M $TBAPF_6$ supporting electrolyte.*

© University of Pretoria

I.1.14) **4b** [RhMB(cod)Cl]

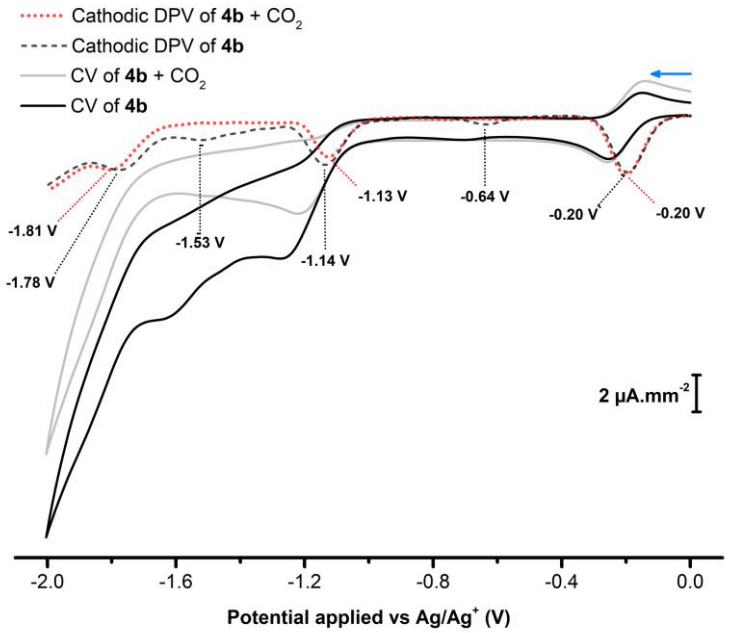


*Figure I.1–23: Cathodic CVs and DPVs of **4b** recorded in CH_2Cl_2 saturated with either CO_2 (g) or Ar (g), with 1.0 mM analyte and 0.1 M $TBAPF_6$ supporting electrolyte.*

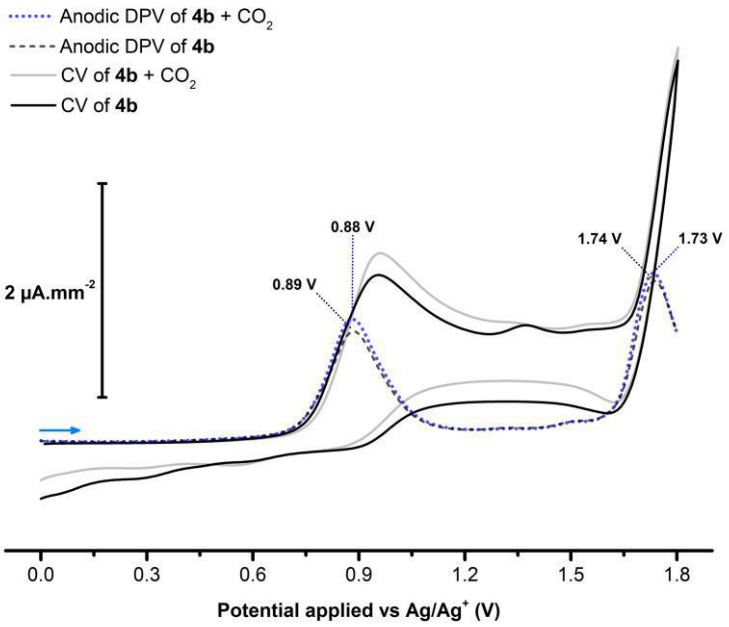


*Figure I.1–24: Anodic CVs and DPVs of **4b** recorded in CH_2Cl_2 saturated with either CO_2 (g) or Ar (g), with 1.0 mM analyte and 0.1 M $TBAPF_6$ supporting electrolyte.*

© University of Pretoria

I.1.15) **4c** [IrDB(cod)Cl]

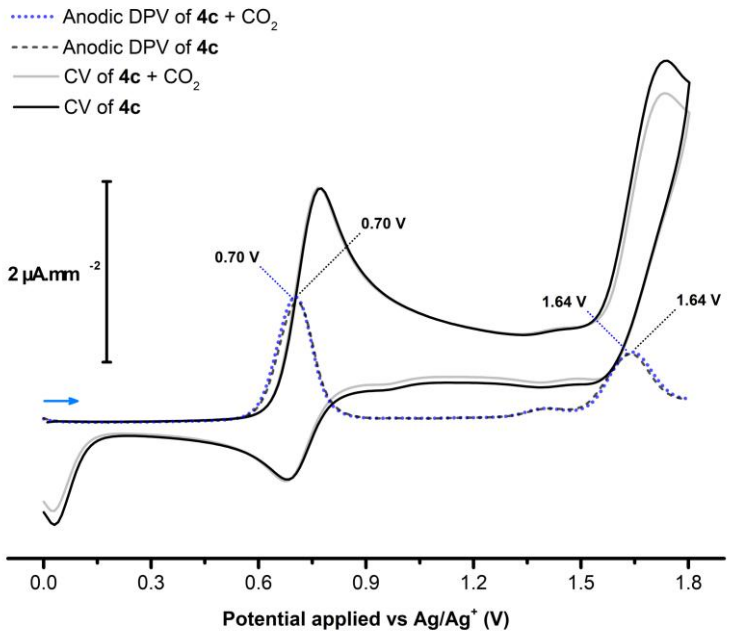


*Figure I.1–25: Anodic CVs and DPVs of **4c** recorded in CH_2Cl_2 saturated with either CO_2 (g) or Ar (g), with 1.0 mM analyte and 0.1 M $TBAPF_6$ supporting electrolyte.*

© University of Pretoria

I.1.16) 4d [IrMB(cod)Cl]

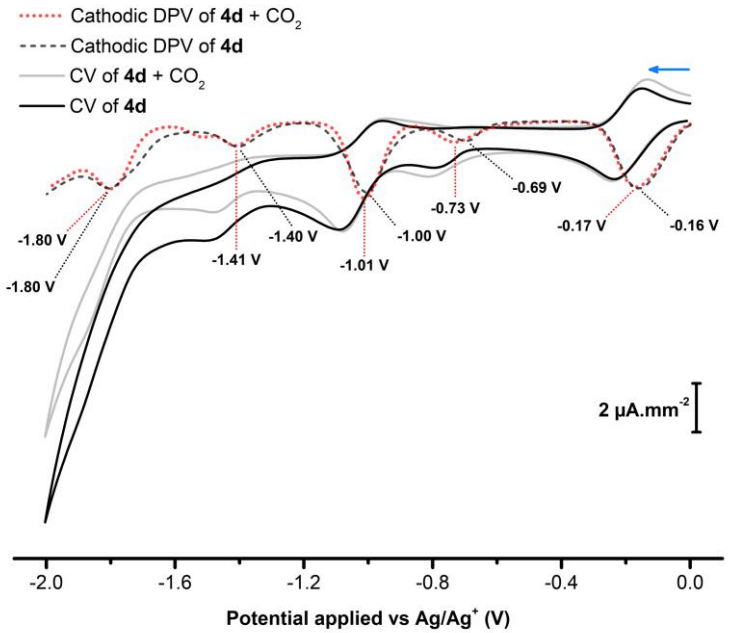


*Figure I.1–26: Cathodic CVs and DPVs of **4d** recorded in CH_2Cl_2 saturated with either CO_2 (g) or Ar (g), with 1.0 mM analyte and 0.1 M $TBAPF_6$ supporting electrolyte.*

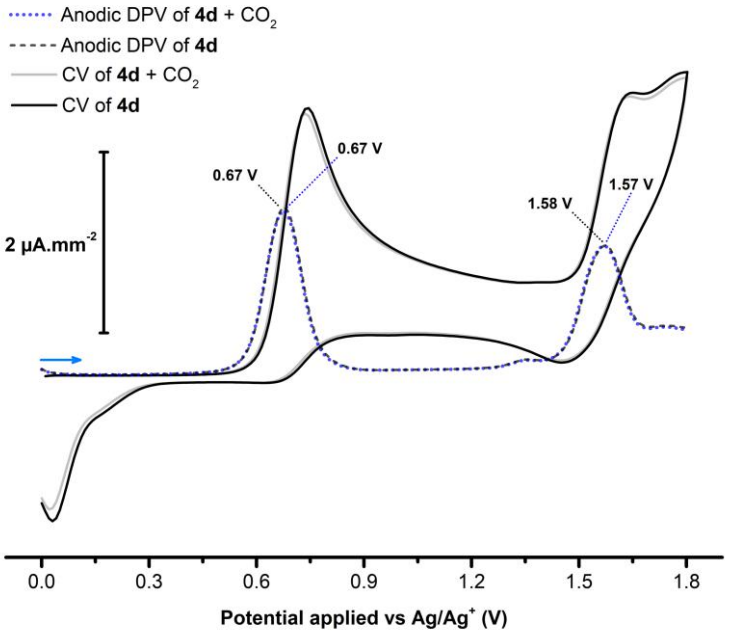


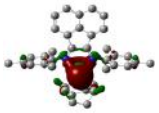
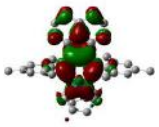
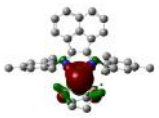
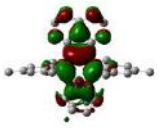
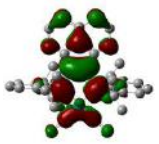
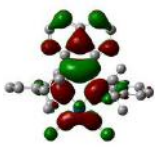
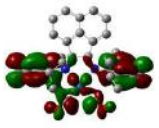
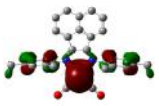
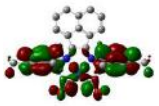
*Figure I.1–27: Anodic CVs and DPVs of **4d** recorded in CH_2Cl_2 saturated with either CO_2 (g) or Ar (g), with 1.0 mM analyte and 0.1 M $TBAPF_6$ supporting electrolyte.*

© University of Pretoria

Appendix J: Potential Drop Values and LUMO +x

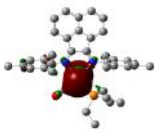
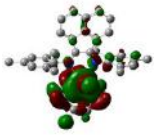
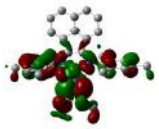
J.1) Theoretical Potential Drop, LUMO +x Orbitals and Electrochemical Data for Complex Series 1–4

*Table J.1–1: A summary of the DPV peak potentials (V vs Ag/Ag^+) recorded for complex series **1–4** in solutions saturated with either Ar (g) or CO_2 (g). Key: * Electrochemically reversible events. ‡ Events were not observed in the CO_2 saturated solutions. § New peak observed in the CO_2 saturated solutions. † CV potentials measured at half peak height. # $\Delta E_{(LUMO)} = E_{LUMO+x} - E_{LUMO}$ (in eV), where LUMO +x is the higher order LUMO with near-HOMO character based on orbital spatial distribution.*

Compound	Red. 2	Red. 1	Ox. 1	$\Delta E_{(LUMO)}^{\#}$	HOMO	LUMO	LUMO + x
1b	–1.64	–0.70*	+1.26	2.66			 LUMO +4
1b + CO_2	–1.64	–0.72*	+1.21				
1c	–0.91	–0.19*	+0.58	2.85			 LUMO +4
1c + CO_2	–0.92	–0.20*	+0.57				
1d	–0.85	–0.21*	+0.58	2.89			 LUMO +4
1d + CO_2	–0.85	–0.21*	+0.58				
2a	–0.70	–0.43*	+1.12	2.76			 LUMO +6
2a + CO_2	–0.73*	–0.45*	+1.18				
2c	–1.19*	–0.22*	+1.56	2.96			 LUMO +5
2c + CO_2	–1.19*	–0.21*	+1.58				
2d	–1.18*	–0.25*	+1.56	3.02			 LUMO +5
2d + CO_2	–1.14*	–0.22*	+1.61				

© University of Pretoria

*Table J.1–1(continued): A summary of the DPV peak potentials (V vs Ag/Ag^+) recorded for complex series **1–4** in solutions saturated with either Ar (g) or CO_2 (g). Key: * Electrochemically reversible events. ‡ Events were not observed in the CO_2 saturated solutions. § New peak observed in the CO_2 saturated solutions. † CV potentials measured at half peak height. # $\Delta E_{(LUMO)} = E_{LUMO+x} - E_{LUMO}$ (in eV), where LUMO +x is the higher order LUMO with near-HOMO character based on orbital spatial distribution.*

Compound	Red. 2	Red. 1	Ox. 1	$\Delta E_{(LUMO)}^{\#}$	HOMO	LUMO	LUMO + x
3b	–1.70	–0.82*	+1.25	2.48			 LUMO +4
3b + CO_2	–1.67	–0.82*	+1.21				
4b	–1.14	–0.20*	+0.89	2.96			 LUMO +8
4b + CO_2	–1.13	–0.20*	+0.88				
4d	–1.00*	–0.16*	+0.67	2.94			 LUMO +7
4d + CO_2	–1.01*	–0.17*	+0.67				

© University of Pretoria